MIXING IN NON-REACTING
GAS TURBINE COMBUSTOR FLOWS

by

JOSÉ MANUEL LAGINHA MESTRE DA PALMA

THESIS SUBMITTED FOR
THE DEGREE OF DOCTOR OF PHILOSOPHY IN THE UNIVERSITY OF LONDON
AND FOR
THE DIPLOMA OF MEMBERSHIP OF THE IMPERIAL COLLEGE

IMPERIAL COLLEGE OF SCIENCE AND TECHNOLOGY
(DEPARTMENT OF MECHANICAL ENGINEERING)
– NOVEMBER -1988 –

ABSTRACT

The present study examines the characteristics of the flow inside gas turbine combustors. Only non-reacting flows, but possibly non-isothermal, are considered. The work, both experimental and numerical, had the main objectives of: (i) providing experimental data to assist the development of mathematical models and (ii) assessing the ability of presently available numerical techniques and a two-equation turbulence model (k-ε) to calculate efficiently and accurately this type of flow.

Experiments were performed in a water model of a can-type gas turbine combustor. The model and the experimental conditions were typical of those found in realistic combustor geometries. Velocity measurements were taken by laser Doppler velocimetry. An extensive flow visualization study, using laser induced fluorescence and high speed photography, was also made; firstly to make sure that the mean flow pattern was similar to that found in a similar but combusting flow and secondly to observe the mixing phenomena inside the combustor and the dynamic behaviour of the jets. The low frequency characteristics and turbulence structure of the primary jet impingement, confirmed by both the flow visualization and spectral analysis, account for the high turbulence intensity and anisotropy measured in this region. A feasibility study of a quantitative application of laser induced fluorescence with the objective of measuring the concentration of a passive scalar inside the combustor was also performed.

The numerical work comprised the appraisal of both the computational efficiency of several alternative formulations of the pressure-velocity coupling (SIMPLE, SIMPLEC, SIMPLER, PISO and AVPI) and the ability of the k-ε turbulence model to predict accurately the characteristics of the non-reacting flow inside gas turbine combustors. Two test cases were used in the study of computational efficiency and both showed that the overall rate of convergence of the calculations was dominated by the convergence of the turbulence model equations. The use of more elaborate pressure velocity algorithms, requiring more than one pressure equation, led to a marginal reduction of the CPU time at the expense of increased memory requirements and the present test cases do not support the use of such algorithms.

A detailed comparison between predictions and experiments is also presented with attention paid to numerical accuracy, boundary condition sensitivity and validation of the turbulence model. Two combustor geometries were used: the dilution zone system of an annular combustor and the water model of a can-type combustor as in the experimental work. In the first case, the calculations evidenced lower levels of mixing compared to the experiments, and this resulted in the underprediction of the overall temperature distribution factor by 100%, even with a

reduction of the turbulent Prandtl number from 0.9 to 0.5. In case of the water model calculations, the complexity of the flow near the primary jet impingement led to the underprediction of the maximum negative axial velocity and turbulence kinetic energy in the primary region by 30% and 40%, respectively. The present work shows that numerically accurate solutions of realistic combustor flows are possible and the reasons for discrepancies observed in the primary region should be sought in the turbulence model. These deficiencies, however do not preclude the use of the model for design purposes, given the agreement between the numerical and experimental results in other regions of the combustor and the correct prediction of the main features of the combustor flow.

ACKNOWLEDGEMENTS

I am grateful to all those from whom I benefited throughout the course of this work. The staff of the Fluids Section, the Computer Centre and the Mechanical Engineering Library were very helpful in many ways.

I am particularly indebted to my supervisor, Dr. J.J. McGuirk, for the criticism, guidance and encouragement he gave me.

For their advice, discussions and generous help I would like also to acknowledge the contributions of Professor J.H. Whitelaw, Dr. A. Bicen, Dr. W.P. Jones, Dr. C. Priddin (Rolls-Royce), Dr. C. Arcoumanis, Dr. C. Papadimitriou, Dr. A. Taylor, Mr. H. Avis, Mr. W. Crew, Mr. J. Laker, Mr. T.S. - Dau, Mr. G. Tindall, Mrs. E. Archer and my colleagues: Mr. A. Tober, Mr. A. Pascau, Mr. F. Pinho, Mr. D. Tse, Mr. P. Oliveira, Mr. A. Urgueira, Miss. D. Lopes, Mr. S. Baker and Mr. P. Rogers. The original manuscript was typed by Mrs. E.A. Hall and I am grateful for her help and efficiency on the preparation of this thesis.

The work was carried out under a grant from the Ministry of Defence.

Finally, and most of all I wish to express my gratitude for the encouragement I received from my parents, to whom I dedicate this thesis.

CONTENTS

ABSTRACT I
ACKNOWLEDGEMENTS III
CONTENTS IV
LIST OF FIGURES X
LIST OF TABLES XIX
NOMENCLATURE XX

CHAPTER 1 - INTRODUCTION 1
1.1 REASONS FOR THE THESIS TITLE 1
1.2 THE MOTIVATION BEHIND RESEARCH ON GAS TURBINE COMBUSTOR FLOWS 1
1.3 THE CONTRIBUTION OF THE PRESENT WORK 3
1.4 REVIEW OF PREVIOUS WORK 3
1.4.1 Studies of gas turbine combustor geometries: experiments and calculations 8
1.4.2 Studies of Dilution Zone Systems (Row(s) of Jets Injected into a Crossflow) 13
1.4.3 The Numerical Solution of the Fluid Flow Equations 18
1.5 OUTLINE OF THE THESIS 23

CHAPTER 2 - THE MATHEMATICAL MODEL AND THE PRESSURE-CORRECTION APPROACH 25
2.1 INTRODUCTION 25
2.1.1 Objectives and Outline of the Chapter 25
2.2 MATHEMATICAL MODEL 25
2.2.1 Exact Equations 25
Turbulence modelling 28
2.2.2 Finite Difference Discretisation 31
Numerical Accuracy 33
2.3 CALCULATION PROCEDURE 36
2.3.1 Alternative Formulations of the Pressure-Velocity Coupling 36
SIMPLE 36
SIMPLEC 38

SIMPLER 39
PISO 40
AVPI 42
2.3.2 Details of the Calculation Procedure 43
The convergence of the calculations 44
Steady and unsteady formulations 45
The nature of the pressure-velocity coupling 47
The under-relaxation factor (and the time-step) 49
The solver (TDMA) 51
2.4 THE CONVERGENCE OF THE CALCULATION PROCEDURE 52
(Case Study 1 - Two-Dimensional Flow Over an Obstacle) 52
2.4.1 Solution Domain and Boundary Conditions 52
Inlet and outlet boundary conditions 53
Walls 54
Numerical grids 55
2.4.2 Results with the Upwind Quadratic (QUICK) Scheme 55
2.4.3 Results with the Hybrid Scheme
- Comparison of PISO and SIMPLE 57
PISO and SIMPLE in unsteady formulations 58
PISO and SIMPLE in steady-state formulations 58
2.4.4 Conclusions 59
2.5 SUMMARY 60
FIGURES 61

CHAPTER 3 - CALCULATIONS OF THE DILUTION SYSTEM IN AN ANNULAR COMBUSTOR GEOMETRY 69
3.1 INTRODUCTION 69
3.1.1 Objectives and Outline of the Chapter 69
3.1.2 Domain of integration 69
Holes and nozzle 70
3.1.3 Boundary Conditions 70
3.1.4 Numerical Meshes 71
3.2 THE CONVERGENCE OF THE CALCULATION PROCEDURE
(Case Study 2 - The Dilution System of an Annular Type Combustor) 72
3.2.1 Conditions of the Test and Presentation of Results 72
3.2.2 The Convergence of the Complete Set of Equations 73
3.2.2.1 Relative performance of SIMPLE and PISO 73
The under-relaxation of all the variables 73

The under-relaxation of the pressure 74
The under-relaxation of the
turbulence kinetic energy and its dissipation 74
3.2.2.2 The performance of AVPI 75
3.2.2.3 Conclusions 76
3.2.3 The 'Exact' Solution of the Complete Set of Equations 76
3.2.4 The Convergence of the Velocities and Pressure
Isolated from the Turbulence Model Equations 77
3.2.4.1 Relative performance of SIMPLE and PISO 77
The under-relaxation of the velocities
and pressure 78
The under-relaxation of the pressure 78
3.2.4.2 Relative performance of SIMPLE and PISO
(both in time-dependent formulation) and AVPI 79
3.2.4.3 Summary 79
3.2.5 Conclusions of the
Study of Convergence of the Calculation Procedure 80
3.3 DISCUSSION OF RESULTS 81
3.3.1 Presentation of Results 81
3.3.2 Constant Density Calculations 83
3.3.2.1 Grid resolution - numerical accuracy 83
3.3.2.2 Inclined and non-inclined jets 86
3.3.3 Variable Density Calculations 87
3.3.3.2 Comparison with experiments.
The turbulent Prandtl number 88
3.3.4 Conclusions 90
3.4 SUMMARY 90
FIGURES 92

**CHAPTER 4 - EXPERIMENTS IN A WATER MODEL
OF A CAN-TYPE GAS TURBINE COMBUSTOR** 120
4.1 INTRODUCTION 120
4.1.1 Objectives and Outline of the Chapter 120
4.1.2 Experimental Set Up and Geometry 120
4.1.3 Measurement Techniques and Post-Processing of Data 122
Statistical error analysis up to the 4th order moment 127
4.1.4 Flow Visualization 130
Photographic and visualization techniques 131

4.1.5 Experimental Conditions 133
4.2 TWO PRELIMINARY STUDIES 136
4.2.1 Swirl Number Evaluation
- Assessment of the Axisymmetry of the Swirler Flow 136
Results 137
4.2.2 Matching reacting and non-reacting conditions 138
Results 139
4.3 FLOW INSIDE A MODEL CAN-TYPE GAS TURBINE COMBUSTOR 141
4.3.1 Flow in the External Annulus 143
4.3.2 Standard Case (45° Swirler) 144
4.3.3 Parametric Study 148
4.3.4 PDFs and Higher Order Moments 152
Implications for the jet impingement process 154
4.3.5 The Transport of Fuel 156
4.3.6 Flow Visualization and Mixing 157
4.4 CONCLUSIONS 160
FIGURES 162

CHAPTER 5 - CALCULATION OF THE ISOTHERMAL FLOW INSIDE A GAS TURBINE COMBUSTOR 195
5.1 INTRODUCTION 195
5.1.1 Objectives and Outline of the Chapter 195
5.1.2 Domain of Integration 195
5.1.3 Boundary Conditions 196
5.1.4 Numerical Grids 197
5.1.5 Presentation of the Results 199
5.2 PRELIMINARY CALCULATIONS: SOME FUNDAMENTAL QUESTIONS 199
5.2.1 The convergence pattern 199
5.2.2 Results with four different grids 200
5.2.3 The radial velocity boundary condition
at the primary hole 201
5.2.4 Conclusions 202
5.3 BOUNDARY CONDITION STUDY 202
5.3.1 Choice of Grid for Boundary Condition Study 203
5.3.2 Swirler 203
Constant or linear (radial) profiles of azimuthal
velocity and blockage of the vanes (method 1) 204
The effect of the boundary conditions on

the primary hole 205
The blockage of the vanes (method 2) 205
The radial velocity 206
5.3.3 Primary and Dilution Holes 207
Reduction of hole diameter and increase in primary flow rate 208
The dilution flow rate 209
5.3.4 The Injection of Fuel 209
5.3.5 Conclusions 210
5.4 DISCUSSION OF RESULTS 210
5.4.1 The Importance of Some Geometrical Simplifications 211
5.4.2 The Numerical Accuracy 212
Systematic grid refinement: global and grid refinement in independent directions 212
Peclet number 213
5.4.3 Combustor Flow With Swirler 214
Standard case (45° swirler) 214
Higher swirler flow rate (30° swirler) 217
5.4.4 Combustor Flow Without Swirl 218
5.4.5 The Transport of Fuel 220
Scalar mixing - the turbulent Prandtl number 221
5.5 CONCLUSIONS 221
FIGURES 223

CHAPTER 6 - CLOSURE 253
6.1 CONCLUSIONS 253
Experimental 253
Numerical 254
6.2 SUGGESTIONS FOR FUTURE WORK 255
Numerical 255
Experimental 256

APPENDIX A - A FEASIBILITY STUDY OF LASER-INDUCED FLUORESCENCE (LIF) 257
A.1 INTRODUCTION 257
A.2 REVIEW OF PREVIOUS WORK 257

A.3 BASIC PRINCIPLES OF FLUORESCENCE 258
A.4 EXPERIMENTAL RESULTS 261
Selection of the Fluorescent Dye 261
Difficulties of Using the Technique in the Combustor Model 264
A.5 CONCLUSIONS 266
FIGURES 268

APPENDIX B - THE LUCAS DYE TRACER TECHNIQUE 272
FIGURES 274

REFERENCES 275

PHOTOGRAPHS

LIST OF FIGURES

2.1 - Control volume for one dimension. 61

2.2 - Domain of Integration. 61

2.3 - Staggered cells around the obstacle. 62

2.4 - Streamline pattern in the proximity of the obstacle. 62

2.5 - Convergence behaviour of SIMPLE using QUICK difference scheme. 63

2.6 - Convergence behaviour of SIMPLE using hybrid difference scheme. 63

2.7 - Convergence behaviour of AVPI using QUICK difference scheme for two different time steps: a) Δt = 0.002 sec; b) Δt = 0.001 sec. 64

2.8 - Convergence behaviour of AVPI using QUICK difference scheme - calculations in double precision (Δt=0.001 sec). 64

2.9 - SIMPLE and PISO in unsteady formulation with a criterion of convergence of the pressure of 10% (Δt_o = 0.001 sec). 65

2.10 - Influence of the under-relaxation of the pressure in PISO unsteady formulation (Δt_o = 0.001 sec). 65

2.11 - Influence of the criterion of convergence of the pressure in PISO unsteady formulation (Δt_o = 0.001 sec). 66

2.12 - The convergence of SIMPLE and PISO as a function of the under-relaxation factors. 66

2.13 - Identical to 2.12 but with the under-relaxation for pressure also being changed. 67

2.14 - Map of convergence of PISO. 68

2.15 - Map of convergence of SIMPLE. 68

3.1 - Geometry of the annular dilution system. 92

3.2 - Numerical simulation of the holes. 92

3.3 - Flow splits and inclination of the jets. 92

3.4 - Numerical meshes. 93

3.5 - Influence of the under-relaxation in PISO and SIMPLE. 94

3.6 - The reduction of the mass residual in PISO for various under-relaxation factors.: a) α_{all} = 0.1 b) α_{all} = 0.4. c) α_{all} = 0.6 d) α_{all} = 0.85. 94

3.7 - The reduction of the mass residuals in SIMPLE for various under-relaxation factors : a) $\alpha_{all} = 0.1$ b) $\alpha_{all} = 0.4$ c) $\alpha_{all} = 0.5$ d) $\alpha_{all} = 0.65$. 95

3.8 - Influence of the under-relaxation of the pressure in SIMPLE and PISO - α_p changed while $\alpha_{u,v,w,k,\varepsilon}$ were kept constant. 96

3.9 - Influence of the under-relaxation of the turbulence kinetic energy and its dissipation in SIMPLE and PISO - $\alpha_{k,\varepsilon}$ changed while $\alpha_{u,v,w,p}$ were kept constant (0.65 for SIMPLE and 0.88 for PISO). 96

3.10 - The reduction of the residual of all the equations in SIMPLE and PISO for various under-relaxation factors of the turbulence kinetic energy and its dissipation- : a) $\alpha_{k,\varepsilon} = 0.1$ b) $\alpha_{k,\varepsilon} = 0.6$ c) $\alpha_{k,\varepsilon} = 0.8$. 97

3.11 - Results from 3.5 and 3.9 plotted on logarithmic scales . 98

3.12 - Influence of the time step in AVPI ($\Delta t_o = 0.001$ sec). 98

3.13 - The reduction of the residual of all the equations in AVPI for various time steps:a) $\Delta t = 0.00001$ sec b) $\Delta t = 0.0001$ secc) $\Delta t = 0.002$ sec. 99

3.14 - The convergence of the calculations carried to the limits of machine accuracy: a) SIMPLE b) PISO c) AVPI. 100

3.15 - Influence of the under-relaxation of the velocities and pressure in SIMPLE and PISO (k-ε fields obtained from a previous run converged to machine accuracy). 101

3.16 - Results from 3.15 plotted on logarithmic scales 101

3.17 - The reduction of the mass residual (DSUM) in PISO for various under-relaxation factors $\alpha_{u,v,w,p}$ from 0.1 to 0.8 changed in steps of 0.1. 102

3.18 - Influence of the under-relaxation of the pressure in SIMPLE and PISO -α_p changed while $\alpha_{u,v,w}$ were kept constant. 102

3.19 - Map of convergence of SIMPLE. 102

3.20 - Influence of the time step in AVPI. 103

3.21 - Influence of the time step in SIMPLE and PISO. 104

3.22 - Streakline plots: longitudinal views (grid $17 \times 11 \times 6$) (case 1). 104

3.23 - Streakline plots: longitudinal views (grid $40 \times 30 \times 15$) (case 1). 105

3.24 - Streakline plots: longitudinal views (grid $70 \times 40 \times 25$) (case 1). 105

3.25 - Longitudinal contours of Φ^* (grid $40 \times 30 \times 15$) (case 1). 106

3.26 - Longitudinal contours of Φ^* (grid $70 \times 40 \times 25$) (case 1). 106

3.27 - Peclet number contours on centre plane (grid $70 \times 40 \times 25$) (case 1). 107

3.28 - Streakline plots: longitudinal views (grid $40 \times 30 \times 15$)- inclined jets. 107

3.29 - Streakline plots: longitudinal views (grid $40 \times 30 \times 15$) - double symmetry. 108

3.30 - Longitudinal contours of Φ (grid $40 \times 30 \times 15$)- double symmetry. 109

3.31 - Streakline plots: cross-sectional views (grid $40 \times 30 \times 15$)

- symmetry (case 1). 109
3.32 - Streakline plots: cross-sectional views (grid 40 × 30 × 15)
- double symmetry. 110
3.33 - Streakline plots: longitudinal views (grid 40 × 30 × 30)- inclined jets (case 2). 111
3.34 - Longitudinal contours of Φ^* (grid 40 × 30 × 30)- inclined jets (case 2).111
3.35 - Longitudinal contours of turbulence kinetic energy (grid 40 × 30 × 15) (case 1). 112
3.36 - Streakline plots: cross-sectional views (grid 40 × 30 × 30)
- inclined jets (case 2). 112
3.37 - Contours of Φ, cross-sectional views (grid 40 × 30 × 15) - symmetry (case 1). 113
3.38 - Contours of Φ^*, cross-sectional views (grid 40 × 30 × 30)
- inclined jets (case 2). 114
3.39 - Streakline plots: longitudinal views (grid 40 × 30 × 15)
- variable density calculations (case 3). 115
3.40 - Streakline plots: cross-sectional views (grid 40 × 30 × 15)
- variable density calculations (case 3). 115
3.41 - Longitudinal contours of Φ^* (grid 40 × 30 × 15)
- variable density calculations (case 4). 116
3.42 - Contours of T^*, cross-sectional views (grid 40 × 30 × 15)
- variable density calculations (case 4). 116
3.43 - Streakline plots: longitudinal views (grid 40 × 30 × 30)
- variable density calculations, inclined jets (case 4). 117
3.44 - Flow visualization (from Shaw [1981]).
3.45 - Streakline plots: cross-sectional views (grid 40 × 30 × 30)
- variable density calculations, inclined jets (case 4). 117
3.46 - Longitudinal radially averaged contours of mean radial temperature (grid 40 ×30 ×30)- variable density calculations, inclined jets (case 4).118
3.47 - Contours of T^*, cross-sectional views (grid 40 × 30 × 30)
- variable density calculations, inclined jets. 118
3.48 - Experimental temperature contours at the outlet section (from Shaw [1981]). 119
3.49 - Temperature contours at the outlet section (grid 40 × 30 × 30)
- variable density calculations, inclined jets (case 4): a) turbulent Prandtl number equal to 0.9 b) turbulent Prandtl number equal to 0.5. 119
3.50 - Experimental total pressure contours at the outlet section (from Shaw [1981]). 119

3.51 - Total pressure contours at the outlet section (grid 40 × 30 × 30)
- variable density calculations, inclined jets (case 4),
turbulent Prandtl number equal to 0.9. 119

4.1 - Experimental rig. 162
4.2 - Plexiglass combustor model. 162
4.3 - Swirlers. 163
4.4 - Fuel injector. 163
4.5 - Flow splits found in engine and model combustors. 163
4.6 - Diagram of the LDV system. 164
4.7 - Axial mean velocity and turbulence intensity profiles at Z/D=1
- 30 ° swirler 164
4.8 - Axial mean velocity profiles at Z/D=2 for two angular locations
120° apart - 30° swirler 164
4.9 - Azimuthal mean velocity and turbulence intensity profiles at Z/D=2
for two angular locations 120° apart - 30° swirler 164
4.10 - Axial and azimuthal mean velocities at Z/D=2 for two Reynolds number
- 30° swirler 165
4.11 - Axial and azimuthal mean velocities at 3 mm downstream from
the swirler and along the middle of the vane passage - 45° swirler 165
4.12 - Flow split (flow split 1) in a preliminary experiment to simulate
the flow pattern of the combusting rig in the water rig. 165
4.13 - Mean velocity profiles at Z = 8 mm, θ = 0° (flow split 1). 165
4.14 - Mean velocity profiles at Z = 50 mm, θ = 0° (flow split 1). 166
4.15 - Mean velocity profiles at Z = 8 mm, θ = 0° (flow split 1)
- no swirler flow). 166
4.16 - Mean azimuthal velocity profile at Z = 8 mm, θ = 0°
(flow split 1- no swirler flow). 166
4.17 - Mean velocity profiles at Z = 130 mm, θ = 0° (flow split 1). 167
4.18 - Centreline values of mean axial velocity (flow split 1). 167
4.19 - Axial mean velocity and turbulence intensity in the primary annulus,
65 mm upstream of the swirler. 167
4.20 - Axial mean velocity and turbulence intensity in the primary annulus,
10 mm upstream of the primary holes and at θ = 30°. 168
4.21 - Radial mean and turbulence intensity 3 mm above the outer
surface of the combustor along the primary hole diameter. 168
4.22 - Axial and azimuthal components (mean and turbulence intensity)

along the primary hole diameter in a plane tangential to the inner surface of the combustor. 168
4.23 - Axial mean velocity and turbulence intensity in the dilution annulus 90 mm upstream of the dilution holes. 169
4.24a - Radial mean velocity and turbulence intensity along the dilution hole diameter in a plane tangential to the outer surface of the combustor. 169
4.24b - Axial and azimuthal components (mean and turbulence intensity) along the dilution hole diameter in a plane tangential to the inner surface of the combustor. 169
4.25 - Schematic longitudinal views of the flow pattern inside the combustor.
4.26 - Schematic cross-sectional views of the flow pattern inside the combustor.170
4.27 - Measurements at Z = 8 mm, θ = 0° (case 1). 170
4.28 - Measurements at Z = 40 mm, θ = 0° (case 1). 171
4.29 - Measurements at Z = 40 mm, θ = 30° (case 1). 171
4.30 - Centreline mean axial velocity and turbulence intensity (case 1). 172
4.31 - Measurements at Z = 50 mm, θ = 0° (case 1). 172
4.32 - Measurements at Z = 50 mm, θ = 15° (case 1). 173
4.33 - Measurements at Z = 50 mm, θ = 30° (case 1). 174
4.34 - Measurements at Z = 60 mm, θ = 0° (case 1). 175
4.35 - Measurements at Z = 60 mm, θ = 15° (case 1). 176
4.36 - Measurements at Z = 60 mm, θ = 30° (case 1). 176
4.37 - Measurements at Z = 70 mm, θ = 0° (case 1). 177
4.38 - Measurements at Z = 70 mm, θ = 15° (case 1). 178
4.39 - Measurements at Z = 70 mm, θ = 30° (case 1). 179
4.40 - Measurements at Z = 85 mm, θ = 0° (case 1). 179
4.41 - Measurements at Z = 130 mm, θ = 30° (case 1). 180
4.42 - Measurements at Z = 130 mm, θ = 0° (case 1). 181
4.43 - Measurements at Z = 40 mm, θ = 0° (case 2). 182
4.44 - Measurements at Z = 40 mm, θ = 0° (case 5). 183
4.45 - Measurements at Z = 50 mm, θ = 30° (case 5). 183
4.46 - Measurements at Z = 50 mm, θ = 30° (case 6). 183
4.47 - Measurements at Z = 50 mm, θ = 30° (case 7). 186
4.48 - Measurements at Z = 50 mm, θ = 30° (case 2). 186
4.49 - Measurements at Z = 50 mm, θ = 0° (case 4). 187
4.50 - Measurements at Z = 50 mm, θ = 0° (case 2). 188
4.51 - Measurements at Z = 60 mm, θ = 15° (case 5). 188
4.52 - Measurements at Z = 60 mm, θ = 0° (case 2). 189
4.53 - Measurements at Z = 70 mm, θ = 0° (case 2). 190

4.54 - Measurements at Z = 85 mm, θ = 0° (case 2). 190
4.55 - Measurements at Z = 85 mm, θ = 0° (case 4). 191
4.56 - Measurements at Z = 110 mm, θ = 0° (case 2). 192
4.57 - Measurements at Z = 130 mm, θ = 0° (case 2). 192
4.58 - Spectrum of the W component on the combustor centreline at Z = 50 mm (case 2). 193
4.59 - Identical to 4.58 but with a longer sampling time.
4.60 - Spectrum of the W component on the combustor centreline at Z = 50 mm (case 6). 193
4.61 - Measurements at Z = 8 mm, θ = 0° (case 2 and case 3). 193
4.62 - Centreline values of mean axial components (case 2 and case 3). 194

5.1 - Numerical grids used in preliminary calculations. 223
5.2 - The relationship between the numerical grids. used in preliminary calculations. 224
5.3 - Numerical grids used in the final set of calculations. 224
5.4 - The relationship between the numerical grids used in the final set of calculations (total number of nodes within brackets). 225
5.5 - The convergence pattern of the calculations using three different grids. 226
5.6 - Axial velocity and turbulence kinetic energy along the combustor centreline using four different grids. 227
5.7 - Results at Z = 8 mm, θ = 0° using four different grids. 227
5.8 - Results at Z = 40 mm, θ = 0° using four different grids. 227
5.9 - Results at Z = 50 mm, θ = 0° using four different grids. 228
5.10 - Results at Z = 50 mm, θ = 0° using two primary flow rates. 228
5.11 - Axial velocity and turbulence kinetic energy along the combustor centreline for two primary flow rates. 228
5.12 - Results at Z = 50 mm, θ = 0° using three alternative boundary conditions for the radial velocity on the primary hole. 229
5.13 - Results at Z = 50 mm, θ = 0°, using three alternative boundary conditions for the radial velocity on the primary hole. 229
5.14 - Results at Z = 8 mm, θ = 0° using four alternative boundary conditions for the swirler. 229
5.15 - Axial velocity and turbulence kinetic energy along the combustor centreline with four alternative boundary conditions for the swirler. 230
5.16 - Results at Z = 8 mm, θ = 0° using two alternative boundary conditions for the swirler and two alternative

boundary conditions for the primary hole. 230
5.17 - As above but at Z = 40 mm, θ = 0°. 230
5.18 - Results at Z = 8 mm , θ = 0° using three alternative
boundary conditions for the swirler. 231
5.19 - The influence of the radial velocity at the outlet of the swirler.
Results at Z = 8 mm , θ = 0°. 231
5.20 - Results at Z = 8 mm , θ = 0° using four alternative boundary
conditions for the radial velocity in the primary hole. 231
5.21 - Identical to 5.20, but at Z = 40 mm, θ = 0°. 232
5.22 - Identical to 5.20, but at Z = 50 mm, θ = 0°. 232
5.23 - Axial velocity along the combustor centreline
with and without dilution flow 232
5.24 - Arrangement of cells simulating the injection of fuel. 233
5.25 - Results from calculations with three different castellations
to simulate the hemispherical head of the combustor. 233
5.26 - Similar to 5.25 but at Z = 40 mm, θ = 0°. 233
5.27 - Axial velocity and turbulence kinetic energy
along the combustor centreline. 234
5.28 - Results from calculations with and without area
correction factors for the primary holes. 234
5.29 - Similar to 5.28 but at Z = 55 mm, θ = 0°. 234
5.30 - Results from calculations with and without a castellated
approximation of the fuel injector shape at Z = 8 mm, θ = 0°. 234
5.31 - Axial velocity and turbulence kinetic energy along
the combustor centreline 235
5.32 - Axial velocity and turbulence kinetic energy along the
combustor centreline with four different grids. 235
5.33 - As in 5.32, but at Z = 50 mm θ = 0°. 235
5.34 - Peclet number along the axial direction (Pe_Z) in the longitudinal
plane containing the axis of the primary hole (grid 60 × 30 × 22). 236
5.35 - Peclet number along the axial direction (Pe_Z) in the longitudinal
plane containing the axis of the primary hole (grid 70 × 36 × 30). 236
5.36 - Peclet numbers along the radial (Pe_R)and angular (Pe_T) directions
in the longitudinal plane containing the axis of the holes
(grid 60 × 30 × 22). 236
5.37 - Streakline plots corresponding to case 1 - views in the longitudinal
planes containing the axis of the holes. 237
5.38 - As in 5.37, but views in the cross-sectional planes containing the axis

of the primary and dilution holes. 237
5.39 - Results corresponding to case 1 at Z = 8 mm, θ = 0°. 238
5.40 - Results corresponding to case 1 at Z = 40 mm, θ = 0°. 238
5.41 - Results corresponding to case 1 at Z = 40 mm, θ = 30°. 238
5.42 - Results corresponding to case 1 at Z = 50 mm, θ = 0°. 239
5.43 - Results corresponding to case 1 at Z = 50 mm, θ = 15°. 239
5.44 - Results corresponding to case 1 at Z = 50 mm, θ = 30°. 239
5.45 - Results corresponding to case 1 at Z = 60 mm, θ = 0°. 240
5.46 - Results corresponding to case 1 at Z = 60 mm, θ = 15°. 240
5.47 - Results corresponding to case 1 at Z = 60 mm, θ = 30°. 240
5.48 - Results corresponding to case 1 at Z = 70 mm, θ = 0°. 241
5.49 - Results corresponding to case 1 at Z = 70 mm, θ = 15°. 241
5.50 - Results corresponding to case 1 at Z = 70 mm, θ = 30°. 241
5.51 - Results corresponding to case 1 at Z = 85 mm, θ = 0°. 242
5.52 - Results corresponding to case 1 at Z = 130 mm, θ = 30° 242
5.53 - Contour plots of turbulence kinetic energy ($\sqrt{k}/U_b$) in the longitudinal planes containing the axis of the holes. 242
5.54 - Contour plots of turbulence kinetic energy ($\sqrt{k}/U_b$) in the transverse cross-sectional planes. 243
5.55 - Streakline plots corresponding to case 6 - views in the longitudinal planes containing the axis of the holes. 243
5.56 - As in 5.55 but views in the cross-sectional planes. 244
5.57 - Results corresponding to case 6 at Z = 50 θ = 30°. 244
5.58 - Results at Z = 50, θ = 0°, from two flow conditions with different primary to swirler flow ratio. 245
5.59 - Streakline plots corresponding to case 5 (without swirler flow) - views in the longitudinal planes containing the axis of the holes. 245
5.60 - Streakline plots from calculations with flow through the swirler gap without a swirl component of velocity - views in the longitudinal planes containing the axis of the holes. 245
5.61 - Experimental data from case 5 (without swirler flow). Numerical results from calculations without swirler flow and flow through the swirler gap with no azimuthal component of velocity. 246
5.62 - Results at Z = 50, θ = 0°, corresponding to case 5. 246
5.63 - Results at Z = 50, θ = 30°, corresponding to case 5. 246
5.64 - Results at Z = 60, θ = 15°, corresponding to case 5. 247
5.65 - Results at Z = 85, θ = 0°, corresponding to case 5. 247
5.66 - As in 5.61 to 5.65 but along the combustor centreline. 247

5.67 - Streakline plots from calculations in the planes containing the axis of the primary hole. 248
5.68 - Results at Z = 8, θ = 15°, corresponding to case 3. 248
5.69 - As in 5.68 but at Z = 8, θ = 30°. 248
5.70 - As in Figures 5.68 and 5.69 but along the combustor centreline. 249
5.71 - Fuel fraction field in the longitudinal planes (option 1). 249
5.72 - As in 5.69 but cross-sectional views. 249
5.73 - Fuel fraction field in the cross sectional planes (option 2). 250
5.74 - Fuel fraction field in the cross sectional planes (option 3). 251
5.75 - As in 5.73 but for a turbulent Prandtl number of 0.7. 251
5.76 - As in 5.73 but for a turbulent Prandtl number of 0.4. 252

A.1 - Energy diagram of photoluminiscence phenomena 268
A.2 - Spectra of three fluorescent substances. 268
A.3 - Experimental set-up used to assess the main characteristics of the dyes. 269
A.4 - Intensity of fluorescence versus time for fluorescein at a concentration of 40 $X10^{-3}$ mg/l. 269
A.5 - Intensity of fluorescence versus time for rhodamine B and rhodamine 6G at a concentration of 40 $X10^{-3}$ mg/l. 269
A.6 - Intensity of fluorescence versus distance for different concentrations of rhodamine B 269
A.7 - Intensity of fluorescence versus distance for low concentrations of rhodamine B. 270
A.8 - Intensity of fluorescence versus concentrations of rhodamine B. 270
A.9 - Intensity of fluorescence versus concentrations of rhodamine B (2^{nd} experimental arrangement). 270
A.10 - Intensity of fluorescence as a function of laser power and concentrations of rhodamine B (2^{nd} experimental arrangement). 270
A.11 - Intensity of fluorescence as a function of laser power, concentrations and photomultiplier voltage supply on the signal intensity. 271
A.12 - The location of the beam waist 271
A.13 - Fluorescence intensity along the centreline of the model combustor. 271

B.1 - Dye trace probe and data acquisition system. 274
B.2 - Calibration curve. 274
B.3 - Radial profiles of fuel fraction at the primary hole plane 274

LIST OF TABLES

1.1 - Books and review papers of significance to the study of gas turbine combustor flows in general (background literature) 4
1.2 - Studies originating from the main engine manufacturers 6
1.3 - Studies of gas turbine combustor geometries 9
1.4 - Review of dilution zone studies 14
1.5 - Solution of the elliptic fluid flow equations 19

2.1 - Standard constants of the k-e model 28
2.2 - Coefficient of "Diffusivity for the Pressure" (Γp) 48
2.3 - Boundary conditions at the inlet section 53
2.4 - Convergence tests with the Quadratic Upwind (QUICK) 56

3.1 - Boundary conditions of the annular dilution system and momentum flux and velocity ratio between the jets and the annular flow 71
3.2 - Numerical grids 72
3.3 - CPU time per iteration (sec) 73
3.4 - Integral parameters of mixing 89

4.1 - Characteristics of the Laser-Doppler anemometer 124
4.2 - Operating conditions of water rig 135
4.3 - Principal characteristics of the Laser-Doppler anemometer 139

5.1 - Boundary conditions (45° swirler, case 1 of Table 4.2). 197
5.2 - Numerical Grids 198

A.1 - Spectral Characteristics of Fluorescein, Rhodamine B and Rhodamine 6G 261

NOMENCLATURE

Roman Characters

a	:	cross sectional area
AFR_{PZ}	:	air fuel ratio in the primary zone
A	:	coefficients of the discretised transport equations
b	:	absorption path length
b_o	:	diameter of laser beam originating from the laser at $1/e^2$ intensity points
b_x, b_y	:	length of the major and minor axis of the ellipsoid control volume
c	:	concentration
C	:	passive scalar
$C_\mu, C_1, C_2,$	:	constants of k-ε turbulence model (table 2.1)
D	:	jet diameter
E	:	constant in the law of the wall
f_1, f_2, f_3	:	focal length of lenses L_1, L_2 and L_3
f_D	:	Doppler frequency
f_S	:	frequency shift
f_r	:	speed of rotation of the grating
F	:	flatness factor
F_i	:	source term (equation 2.2)
k	:	turbulence kinetic energy (equation 2.7)
If	:	fluorescence intensity
I_o	:	laser power
l_2	:	l_2 norm
$\dot{m}$	:	mass flow rate
N	:	total number of line pairs on radial diffraction grating or sample size
p	:	order of difraction of diffracted laser beams
P	:	static pressure (equation 2.2)
P_Z, P_R, P_T	:	local Peclet numbers along the main directions of the polar coordinate system
M_{ratio}	:	momentum flux ratio
N_{iter}	:	number of iterations
OTDF	:	overall temperature distribution factor

r, R	:	cylindrical polar coordinate
R_e	:	Reynolds number
R *	:	non-dimensioned radial coordinate
R_C	:	internal diameter of water model combustor
RTDF	:	radial temperature distribution factor
S	:	source term of the discretised transport equations, Swirl number, Strouhal number or skewness factor
S/D	:	pitch to diamter ratio
t	:	time (equation 2.1)
T	:	temperature
T *	:	nondimensioned temperature
U	:	velocity (equation 2.1)
U+	:	nondimensional velocity in wall law
U_b	:	bulk velocity
X	:	cartesian coordinate
x_i	:	spatial coordinates in tensor notation (equation 2.1)
$\rho\ \overline{u_i u_j}$	:	double correlation (Reynolds stress tensor) (equation 2.5)
$\rho\ \overline{u_i c}$	:	double correlation (equation 2.6)
Z	:	cylindrical polar coordinate
Y	:	cartesian coordinate
W_i	:	weighting factor used in polynomial fitting

Greek Characters

α	:	under-relaxation or angle in air between laser beams
δ	:	boundary layer thickness (Table 2.3)
Θ	:	cylindrical polar coordinate
ϕ	:	general variable (equation 2.17)
Φ	:	quantum efficiency
Φ^*	:	nondimensioned passive scalar
ε	:	rate of dissipation of turbulence kinetic energy or molar absorptivity
κ	:	von Karman constant
η	:	refractive index or mixedness parameter
ν	:	kinematic viscosity
σ	:	standard deviation
$\sigma_k, \sigma_\varepsilon, \sigma_\phi$	:	constants of k-ε turbulence model (table 2.1)
σ_t	:	turbulent Prandtl number
ρ	:	density (equation 2.1)

μ	:	dynamic viscosity (equation 2.2)
Ψ	:	unmixedness parameter
Γ	:	diffusivity (equation 2.3)

Operators

$\partial/\partial x_i$	:	partial derivative
$D/Dt = \partial/\partial t + U_i\ \partial/\partial x_i$	:	substantial derivative
$\hat{}$	:	instantaneous quantity
$\bar{}$	:	time averaged quantity
δ_{ij}	:	Kronecker delta (= 1 for i = j; = 0 for $i \neq j$)
$\partial/\partial x_i$, $\partial/\partial t$	:	partial derivatives
Σ	:	summation
$\|\|...\|\|$	:	absolute value

Subscripts

exp	:	explicit
imp	:	implicit
i, j, k, l	:	indices of the tensorial notation
L, R	:	left and right
max	:	maximum value
nb	:	neighbours
v	:	velocity
p	:	pressure

Superscripts

*	:	guessed velocity and pressure
'	:	velocity or pressure correction
Up	:	coefficient from the discretised momentum equations at the point U_p

CHAPTER 1
INTRODUCTION

1.1 REASONS FOR THE THESIS TITLE

The history of the gas turbine engine is the history of a constant search for more efficient and economical solutions to engine design. Efficiency of the engine depends above all on the efficiency of the thermodynamic operating cycle and the development of the gas turbine engine has followed a trend of increasing temperature of the gases at the turbine inlet. Following recent restrictions on pollution control, this trend has had to be accompanied by a reduction of the emission of pollutants. To achieve these objectives successfully clearly requires a detailed knowledge of the processes occurring inside the combustor – the engine component this work is concerned with.

The study of the flow inside the gas turbine combustor in its most general form involves an enormous variety of topics dispersed among such subjects as aerodynamics, thermodynamics and combustion. A complete study is far beyond the scope of the present work and attention has been given to aerodynamics phenomena under non-reacting conditions only. This methodological approach is justified by the important role aerodynamics plays in the combustor, guaranteeing a region of low velocities for flame stabilization and the appropriate mixing, either of fuel and air before combustion or products of combustion and air after combustion.

1.2 THE MOTIVATION BEHIND RESEARCH ON GAS TURBINE COMBUSTOR FLOWS

Recent design requirements for gas turbine combustors include the need to reduce the emission of pollutants (e.g. smoke, CO, NO_x) and design costs. Future combustors should be able to sustain higher temperatures at lower emission levels through a wider range of operating conditions and without impairing favourable features already achieved by current designs, Bahr [1987]. This is a difficult task because there are conflicting requirements to be satisfied which may require radical changes of existing combustor geometries, Jones [1978]. The successful design of new combustors requires an increased knowledge of the phenomena inside the combustor, particularly in the complex primary zone, where most of the combustion takes place. Unfortunately, in the past, attention has been restricted to the outlet of the combustor, not only because this is the region in which the designer is basically interested but,

undoubtedly also due to the difficulty of performing measurements in such a hostile environment as that prevailing inside the combustor. The current methodology of design, Lefebvre [1983], is therefore the result of a judicious blend of knowledge derived from the study of simpler flow constituents of the combustor flow, from previous designs and from semi-empirical correlations, all culminating in rig and engine tests. This is a well established, but costly, practice, able to produce combustors with good characteristics of, for instance, durability and high efficiency and stability of combustion. The main motivation behind research on gas turbine combustor flows is then to increase the understanding of this type of flow, with the objective of reducing both the emission of pollutants and above all the time and costs of design .

To facilitate the study of complex combustor flow, simplifications are often made. This has usually led to the use of simplified combustor geometries, for instance axisymmetric swirling flows, or isothermal models, as in the present work. As mentioned above, a main area of interest is the study of the mixing processes inside the combustor, and this is an area where isothermal experiments can play a vital role. The information given by isothermal models is limited to the fluid mechanics aspects of the combustor flow; however because many aspects of combustion depend strongly on mixing, controlled mainly by turbulent diffusion, isothermal models become particularly suitable since mixing can be studied without the additional complexities implied by, for instance, variable gas densities, turbulence/combustion interaction and spray/droplet dynamics.

Computational fluid dynamics (CFD) is already contributing to the reduction of design cost of new combustors by reducing rig testing time. This contribution is expected to increase due to the availability of more powerful computers and the confidence gained in the calculation of simpler laboratory flows. The progress in computing systems is likely to continue at the same rate for at least the next 10 or 15 years (Peled [1987]), but even so the cost of performing combustor flow calculations cannot be ignored and improved numerical techniques with higher numerical accuracy and faster convergence rate are clearly to be sought. Nevertheless, if the computational methods are to contribute to further reduction of design costs, more general and reliable mathematical models should also emerge and their capabilities and limitations should be fully assessed. This calls for both experimental and computational research programmes and if possible they should be closely linked – this view has influenced the present work.

1.3 THE CONTRIBUTION OF THE PRESENT WORK

The contribution of the present work is centred on the study of combustor flows in the absence of chemical reaction. Both experiments and calculations will be described. The work had the main objectives of providing experimental data to assist the development of mathematical models and assessing the ability of presently available numerical techniques to predict accurately and efficiently gas-turbine combustor flows. Emphasis was placed on realistic combustor geometries and realistic combustor flow patterns.

The experimental work involved both velocity measurements and flow visualization of the flow inside a water model of a can-type combustor. The model geometry is representative of currently available combustors and all the main features are represented apart from the wall cooling flows. The measurements were taken by laser Doppler velocimetry and the flow visualization involved the use of high speed photography and laser induced fluorescence techniques; the visualization was made to illustrate the process of mixing inside the combustor, particularly at the plane of the inflowing jets, which as will be described below dominate the combustor flow pattern. The application of this technique, laser induced fluorescence, for quantitative measurements of scalar concentration was also initiated.

A corresponding set of predictions of the flow above was made and the limitations of the turbulence model assessed. From a strictly numerical point of view the computational efficiency of several algorithms for solution of the fluid flow equations was tested and the nature of the coupling between the equations highlighted via two basic test cases: the flow over an obstacle attached to a flat plate and the flow in the dilution zone system of an annular combustor. The latter, because based on a full scale experiment, also provided the opportunity to assess the ability of the model to predict the overall mixing parameters.

1.4 REVIEW OF PREVIOUS WORK

The changing needs of engine manufacturers, the advent of more powerful computer systems and the development of advanced experimental techniques appropriate for recirculating flows have all given rise in recent years to a growth in literature of potential interest to the study of gas turbine combustors. The articles listed in the following table, by chronological order, are examples of this body of work, with Lefebvre [1983] being the most comprehensive text on traditional design methods for gas-turbine combustors.

TABLE 1.1 - Books and review papers of significance to the study of gas turbine combustor flows in general (background literature)

AUTHOR(S) YEAR	TITLE	REMARKS
Lefebvre [1965]	'Progress and problems in gas turbine combustion'	A useful overview of the requirements of gas turbine combustors in the era before optical experimental techniques and CFD (historical interest mainly).
Jones [1978]	'Gas turbine engine emissions-problems, progress and future'	Discussion of constraints imposed on combustor design due to pollution control. Detailed description of research programmes aimed at reduction of engine emissions.
Jones [1979]	'Models for turbulent flows with variable density and combustion'	Review and derivation of turbulence and combustion models for reacting flows. Discussion concentrates on the physical assumptions supporting the derivation of the models.
McDonald [1979]	'Combustion modelling in two and three dimensions - some numerical considerations'	An assessment of the numerical techniques available (1979) for combustor flow calculations. Emphasis on problems encountered in calculations of practical combustion systems.
Libby and Williams [1980],	*'Turbulent Reacting Flows'*	Research monograph on the interaction between turbulence and combustion.
Patankar [1980]	*'Numerical Heat Transfer and Fluid Flow'*	A textbook containing a practical description of the numerical methods incorporated in the finite difference computer programmes used in most of the calculations of combustor flows.
Durst, Melling and Whitelaw [1981]	*'Principles and Practice of Laser-Doppler Velocimetry'*	A textbook on laser-Doppler velocimetry (LDV).
Jones and Whitelaw [1982]	'Calculation methods for reacting turbulent flows: a review'	A review made in the context of gas turbine combustor flows. It is concluded that although calculations of real combustors show deficiencies of the numerical techniques, failures can also be attributed to physical models, especially the modelling of turbulent diffusion.
Lefebvre [1983]	*'Gas Turbine Combustion'*	A fundamental textbook on standard methods for gas-turbine combustor design.

TABLE 1.1 - continued

AUTHOR(S) YEAR	TITLE	REMARKS
Gupta,Lilley and Syred [1984]	*'Swirl Flows'*	A detailed treatment of swirl flows with emphasis on engineering applications.
Gupta and Lilley [1985]	*'Flowfield Modelling and Diagnostics'*	A complement of Gupta, Lilley and Syred [1984] oriented towards numerical techniques.
Williams [1985]	*'Combustion Theory'* 2nd edition	A fundamental textbook for study of reacting flows.
Sloan, Smith and Smoot [1986]	'Modeling of swirl in turbulent flow systems'	Evaluation of the k-ε model and algebraic stress models for prediction of swirl flows (both reacting and non-reacting). Importance of numerical techniques demonstrated once more. Improved turbulence models recommended.
Odgers and Kretschmer [1986]	*'Gas Turbine Fuels and Their Influence on Combustion'*	The evaluation of a large range of fuels as potential heat sources for gas turbine combustion systems.
Eckbreth [1987]	*'Laser Diagnostics for Temperature and Species'*	A book on laser based techniques (e.g. CARS-coherent anti-Stokes Raman spectroscopy, LIFS-laser induced fluorescence spectroscopy) for measurements of scalar quantities.

By sampling from this list, the reader can acquire an overview of the most recent work in all areas relevant to combustors. However, the objectives stated in the previous section require a few areas to be addressed in much more detail. This is achieved in subsections 1.4.1, 1.4.2 and 1.4.3 which are more selective and review the previous work in the context of each topic. Initially however, because the trends in research on gas turbine combustors are mainly set by the needs of the engine manufacturers it is informative first to see how the main companies are proceeding and use this context to guide the more detailed reviews. Attention will be given to the work originating from the main companies: General Electric, Pratt and Whitney, General Motors (Allison) and Rolls-Royce. It may be stated right away, that the need for joint experimental and computational research programmes is not reflected by the works originating from these companies and available in the open literature: emphasis has been put exclusively onto computational work, probably in the expectation that

computational fluid dynamics can reduce (in a very short time) the development costs of new engines. Table 1.2 lists the most significant work from each company.

TABLE 1.2 - Studies originating from the main engine manufacturers

AUTHOR(S) YEAR-COMPANY	TITLE	REMARKS
Bruce, Mongia and Reynolds [1979] Mongia, Reynolds, Coleman and Bruce [1979]	'Combustor design criteria validation'-Vol. I and Vol. II	Reports of development programmes of gas turbine combustors supported by CFD, experimentation and empirical correlations.
Srinivasan, Reynolds, Ball, Johnson and Mongia [1983]-General Motors (Allison)	'Aerothermal modelling program. Phase I- final report'	A long list of calculations performed in very simple flows relevant to g-t combustor flows. A short version of this report is available in Mongia et al. [1986].
Sturgess [1986] - Pratt and Whitney	'Calculations of aerospace propulsion combustors: a view from industry'	A very pragmatic view with applications of fairly well established numerical techniques and mathematical models with emphasis given to the need for an increased availability of the software.
Shyy, Correa and Braaten [1986], Correa and Shyy 1987] or Burrus, Shyy and Braaten [1987]-General Electric	'Computational models for gas turbine combustors', 'Computational models and methods for continuous gaseous turbulent combustion' or 'Numerical models for analytical predictions of combustor aerothermal performance characteristics'	Review papers containing short introductions to the mathematical models relevant to gas turbine combustors. Description of software capabilities with some original contributions as, for instance the generation of a versatile grid to simulate the dilution holes and the film cooling slots.
Priddin and Coupland [1986] Rolls-Royce	'Impact of numerical methods on gas turbine combustor design and development'	A list of practical applications of numerical methods in gas turbine combustor like flows.

Pratt and Whitney has concentrated on the use of straightforward applications of the TEACH code (Gosman and Ideriah [1976]) in simplified geometries (e.g. Syed and Sturgess [1980]; Sturgess, Syed and Sepulveda [1981]). There was also some time spent in searching for that chimera that is the "perfect" numerical scheme (Syed and Chiappetta [1985]) and in speculation about the impact of large scale coherent structures on the calculation of combustor flowfields (Sturgess [1984]). These latter two studies, can obviously not be considered as reflecting an objective need

of an engine manufacturer, but rather reflecting the influence upon the manufacturer of the main trend of research in CFD and of a line of thought that has had some impact in experimental fluid mechanics during the last years. More recently, Sturgess [1986], work seems to have concentrated on improving the "user-friendliness" of the codes and making a more extensive use of graphic facilities.

General Motors (Allison) has presented a very ambitious programme, Mongia and Reider [1985], from which some work on sprays has emerged (see Mongia [1987] for references). The objectives of this programme are very wide ranging and are practically identical to the objectives of combustion research in general. Little published work has originated from this company directly. Mostly, it has been carried out and published by university teams sub-contracted by GM; hence it is not possible to identify the specific philosophy underlying GM's approach.

General Electric and Rolls-Royce seem to have set their priorities on a much longer term basis and their research shows a more consistent trend. General Electric has spent some time on the development of numerical meshes able to resolve the geometrical features of a real combustor and this has produced some original work, summarized in Shyy, Correa and Braaten [1986], Burrus, Shyy and Braaten [1987] or Correa and Shyy [1987]. Rolls-Royce has, from the early papers by Jones, Clifford, Priddin and Chair [1977] to the more recent one by Coupland and Priddin [1987] followed a different route from that adopted by the two first companies above, little use has been made of very simplified geometries and they appear to be the first of these companies to have used CFD.

The impact of CFD within the main engine manufacturers is now a well established fact. Of the four companies above, all, except General Motors (Allison), seem to have adopted a pragmatic approach. Rather than being involved in research at a very fundamental level they are more concerned with increasing the availability and use of their computer programs as design tools. Geometric flexibility has for example been an overriding concern. This tendency to increase the realism of the calculations by firstly being able to reproduce the correct geometric shape of the real combustor may be expected to be valid also for experimental research. The recent trend is certainly to perform measurements under conditions and in geometries closer related to gas turbine combustor than the common axisymmetric flows of the past. This has become possible in the numerical field for the reasons stated above but, also in the experimental field new techniques are available (e.g. Durst, Melling and Whitelaw [1981]; Eckbreth [1987]) which are capable of accurate measurements, and under more difficult conditions than were possible before. The following subsection reviews relevant work on combustors in both experimental and computational branches.

1.4.1 Studies of gas turbine combustor geometries: experiments and calculations

The work published in the gas turbine combustor field is now examined. Only studies using geometries typical of gas-turbine combustors are reviewed and a few reacting studies are included. Table 1.3 provides a short description and summarizes the main findings of the most relevant work. The following text discusses the requirements of experimental data suitable for computer modelling and, without being exhaustive, describes the current status and identifies areas where development is still needed.

Two-dimensional, axisymmetric combustor geometries are not considered. A main characteristic of a typical gas-turbine combustor flow is the existence of radially injected jets and this is missing in most of the simpler flows used in the past, mainly to allow the use of two dimensional computer models. It has become possible to deal with more complex flows and there are recent examples (Amhed and So [1987] and Cameron, Brower, Wood and Samuelsen [1988]) where, by the simple expedient of drilling holes in the walls of previous cylindrical research combustors, the authors claim to have created a typical gas turbine combustor flow. This is, sadly, often not the case. Amhed and So [1987] used a single jet radially injected into a confined swirling flow with a high swirl number of 2.25. Not surprisingly, they discovered that the jet followed a spiral trajectory depending on the relative intensity of swirler and jet flow and limited by the tube walls. This type of flow is completely irrelevant. In practice, swirlers used in gas-turbine combustors are usually of a much lower swirl number and the interaction between one or several sets of circumferentially distributed jets (not a single jet) and the swirler is of prime importance. Cameron, Brown, Wood and Samuelsen [1988] recognized this and used two rows of four jets to simulate the primary and dilution holes of a can-type combustor. Now however, the momentum flux ratio between the jets and the crossflow was so high (425 and 140 in the first and second row of jets, respectively) compared to a typical gas-turbine combustor (about 20 according to Cox [1976]) that once again the practical interest of their experiment is very little. Even worse, such strong jets made the adjustment of the relative intensity of the opposite jets so critical that the deviations from cyclic symmetry were significant, which effectively precluded the numerical calculation of the flow.

The main problem in the simulation of a realistic combustor geometry is to simplify the real combustion system as little as possible but still allow the use of presently available experimental and computer techniques. Experiments in real combustion systems have only provided very limited data and are difficult to control in order to provide the type of flow adequate for numerical calculations. This is the case with the work of Goldstein, Lau and Leung [1983] where, due to experimental limitations, the measurements of velocity and temperature were restricted to the

outlet section of the can combustors. In addition, because of likely nonuniformities of the flow through the dilution holes the expected cyclic pattern of the temperature distribution was destroyed. Heitor and Whitelaw [1986] and Tse [1988] have traced one further cause of this phenomenon as the fuel injector: an asymmetric injection of fuel causes an asymmetric temperature pattern which the radial injection of primary and dilution flows cannot correct. It should also be mentioned that the exact simulation of the combusting system in a laboratory scale is not possible, because the strict obedience of the similarity laws imposes too many conflicting requirements (Spalding [1963]). Compromises have to be made and this adds to the practical difficulties mentioned above and increases the difficulties of performing experiments directly relevant to gas turbine combustors. Table 1.3 reviews the work considered to satisfy the appropriate requirements.

TABLE 1.3 - Studies of gas turbine combustor geometries

AUTHOR(S) YEAR	THEME	REMARKS
Jones, Clifford, Priddin and Chair [1977]	Experimental / Numerical A cylindrical combustor with a 20 degree swirler and six dilution holes.	Underpenetration of the fuel into the swirler air stream likely to be caused by insufficient number of grid nodes with implications on the concentration of the various species. The need for a more versatile system of coordinates emphasized.
Jones and Priddin [1978]	Numerical. Geometry as above.	Larger discrepancies in the proximity of the swirler with longer recirculation and underpredicted mixing and higher levels of CO and UHC. Beta and Double delta PDF functions give similar results.
Swithenbank, Turan and Felton [1978]	Cylindrical combustor with three sets of holes and a swirler with a swirl number of 0.6.	Limited measurements were available but the qualitative features of the combustor flow were all predicted. The use of more sophisticated models precluded by computer limitations. Results of the finite-difference calculations used to set-up a network of well stirred and plug flow reactors for prediction of combustion efficiency and pollutants emission.
Jones and McGuirk [1979]	Numerical. Coaxial jets with or without swirler discharging into a sudden expansion and cylindrical combustor with a 30 degree swirler and eight rows of holes.	Slow rate of mixing because of turbulence model. Inadequacy of the combustion model was established and improvements suggested with allowance for the finite rate oxidation of CO. Lack of detailed experiments precludes model improvements.

TABLE 1.3 - continued

AUTHOR(S) YEAR	THEME	REMARKS
Serag-Eldin and Spalding [1979]	Experimental / Numerical. Cylindrical combustor with 45 degree swirler and six dilution holes.	Good qualitative results on the study of influence of radially injected air. Main deficiencies attributed to the neglect of chemical kinetics on the rate of reaction.
Green and Whitelaw [1983]	Experimental / Numerical. 2 geometries: flow downstream of a baffle with either 1) 4 equally spaced jets fed from an annulus or 2) 2 rows of 4 equally spaced jets fed from an annulus radially discharging into it.	Deeper penetration in case of geometry 1). Discrepancies between measurements and calculations attributed to numerical errors. It is concluded that calculation methods are of qualitative use only.
Koutmos [1985]	Numerical / Experimental. Water model of a can-type combustor with a 45 degree swirler and 2 rows of holes.	Measurements and calculations of the water flow inside a can combustor. Agreement between calculations and measurements in the primary region improves as the swirler to primary flow ratio increases.
Heitor and Whitelaw [1986]	Experimental (reacting and non-reacting). Scale model of a can-type combustor with a 45 degree swirler and 2 rows of holes.	Discussion of results pointing towards the numerical modelling of the flow with comments on the validity of the assumptions of currently available models. Ability of the k-ε model to predict the primary region strongly questioned.
Bicen and Jones [1986]	Experimental (reacting and non-reacting). Geometry as above.	Extension of Heitor and Whitelaw [1986] to assess the effects of Reynolds number, fuel injection and transply flows.
Coupland and Priddin [1987]	Numerical. A production gas-turbine combustor with swirler, 3 rows of holes and cooling flows	k-ε turbulence model and fast-kinetics assumption give acceptable results for engineering calculations. Disagreement on the value of turbulent Prandtl number to be used. Orthogonal grid system.
Wild, Boysan and Swithenbank [1987]	Numerical / Experimental. 2 geometries: a cylindrical combustor with 3 rows of holes and a sector of a commercial annular combustor.	k-ε used together with an ASM model. The integration domain was split into two. Discrepancies between measurements and predictions attributed to the stepped wall approximation of the combustor head.

TABLE 1.3 - continued

AUTHOR(S) YEAR	THEME	REMARKS
Wittig, Bauer and Noll [1987]	Numerical / Experimental. 2 geometries: a dilution zone system and an annular combustor including the nozzle.	Application of a non-orthogonal grid.
Ikeda, Nakajima Matsumoto, Yamazaki and Horikawa [1987]	Experimental / Numerical. Cylindrical combustor with four holes and a 45 degree swirler.	k-ε with corrections increased the discrepancies between measurements and calculations. Influence of the boundary conditions at the dilution jet entry. Underprediction of the jet penetration without certainty about its cause.

Jones, Clifford, Priddin and Chair [1977] provided one of the first applications of computational fluid dynamics to prediction of a genuine gas turbine combustor flowfield. A density weighted version of the k-ε turbulence model was used together with a combustion model which solved equations for the mean mass fraction and variance of mixture fraction and carbon dioxide. A double delta PDF function was taken as representative of the two locally instantaneous extreme situations of fuel rich and lean mixtures. The numerical methods involved the use of the hybrid differencing scheme with the SIMPLE algorithm and a cylindrical polar system of coordinates. They concluded that the model was capable of predicting the main features quite well and that some deficiencies might have been caused by innacurate treatment of the swirler wake region since the initial mixing of the fuel and air strongly affects the distribution of the various products of combustion. Other studies have followed using the same solution procedure but with either additional physical models or slight variations. Jones and Priddin [1978] used a beta PDF function and allowed for liquid fuel and NO_x calculations; they concluded that there was a need for handling more complicated geometries and for more accurate measurements. Jones and McGuirk [1979] predicted a two dimensional axisymmetric and a three dimensional combustor and suggested the use of more sophisticated combustion models with the abandonment of the fast kinetics assumption and inclusion of a two dimensional joint PDF. Examples of the same calculation procedure used in more realistic applications can also be found in Priddin and Coupland [1986] and Coupland and Priddin [1987] where a body fitted orthogonal system of coordinates was used but the main physical assumptions were unaltered.

Serag-E ldin and Spalding [1979] predicted the reacting flow and made temperature measurements in a cylindrical combustor. They used the k-ε model in

Reynolds averaged form and assumed fast chemical reaction with a prescribed instantaneous distribution of concentration. Good qualitative agreement was obtained and the neglect of chemical kinetics was indicated as the most likely cause of disagreement.

Green and Whitelaw [1983] predicted and measured various water flows in simplified geometries of can combustors without a swirler. The need to resolve the high pressure gradient regions generated by the penetration of radial flows precluded grid independent solutions and they abstained from comments on the performance of the turbulence model (k-ε). Heitor and Whitelaw [1986] presented a set of measurements including both isothermal and combusting cases in a scaled model of a can type combustor. The work, dealing mainly with reacting flow, discusses in detail how the physical models included in the standard calculation procedures are likely to perform. In case of combusting flow, the application of the k-ε model in the primary region is questioned on the basis of production of turbulence by counter-gradient mechanisms. Koutmos [1985] predicted and measured the water flow model in a geometry similar to Heitor and Whitelaw [1986]; he showed that increasing the swirler to primary flow ratio reduces the primary jet penetration and the size of the primary zone vortex. The agreement between measurements and predictions in the primary region improved as the swirler to primary flow ratio increased from 0.29 to 0.88; underestimation of the turbulence kinetic energy by 40% in the least favourable case was attributed to the high turbulence anisotropy created by the primary jet impingement. Bicen and Jones [1986] in the same test facility used by Heitor and Whitelaw [1986] made velocity measurements for a wider range of conditions and showed the effects of increased fuel flow rate under isothermal and combusting conditions, transply flows and Reynolds number. Striking effects due to the fuel injection were reported, suggesting different flow patterns in the primary region due to fuel injection. The works of Heitor and Whitelaw [1986], Bicen and Jones [1986] and Koutmos [1985] being the predecessors of the present work will be referred to in more detail throughout the current thesis.

The k-ε model and the hybrid finite difference scheme have been used in all the above calculations involving combustor geometries. Wild, Boysan, Swithenbank and Lu [1987] tried to remove the eddy viscosity assumption and used an algebraic stress model of the Reynolds stresses, but concluded that its superiority was not clearly demonstrated. Ikeda, Nakajima, Matsumoto, Yamazaki and Horikawa [1987] tried k-ε with a Richardson number correction: the agreement with measurements was worse than using the standard k-ε; however, they also made measurements inside the combustor which showed that the boundary conditions used may have been the main source of error and this immediately invalidates their conclusions on the turbulence

modelling. Sloan, Smith and Smoot [1986] reviewed calculations of simplified combustor flows with swirl; they concluded that the k-ε model, either standard or with corrections, and algebraic stress models usually fail to predict the correct size of the toroidal reverse region created by the swirling flow and tend to show larger regions of forced vortex flow compared with the experiments. They also emphasized the importance of the boundary conditions and numerical accuracy and recommended the use of higher order closures. At the present stage, the use of higher order closures, e.g. Reynolds stress models, may be premature, because the larger number of equations, will in turn preclude the use of finer grids and consequently reduce the numerical accuracy – one may gain in sophistication of the physical model but lose on numerical accuracy.

The need for versatile grid systems has been stressed since the first applications of CFD to realistic combustor geometries. In aeronautical applications of CFD this need has given rise to a fruitful area of research (see, for instance, Thompson and Steger [1988]). Coupland and Priddin [1987] and Shyy, Braaten and Sober [1987] are two recent examples of calculations of gas-turbine combustors using grid generation techniques similar to those developed in the aeronautical field. Coupland and Priddin [1987] rotated an orthogonal two dimensional mesh around the axis of the engine to create a three dimensional grid for resolution of an annular combustor geometry. Shyy, Braaten and Sober [1987] used a non-orthogonal grid system which could simulate the shape of the liner holes. Simulation of smaller geometrical details is precluded by the limits of computer storage available and may require the splitting of the integration domain. With this need satisfied, further attention can be given to other areas also requiring improvements as, for instance the limitations of the physical models embedded in the calculation procedures; this will certainly increase the demand for detailed and accurate experimental data. These demands are less difficult to fulfil under non-reacting conditions and this is an area where water model experiments may be useful by providing information on the velocity and concentration fields of passive scalars.

More specific aspects of the calculations and experiments in gas turbine combustor flows are considered in the following subsection in the context of studies of dilution zone systems.

1.4.2 Studies of Dilution Zone Systems (Row(s) of Jets Injected into a Crossflow)

Although there has been an interest in the phenomena occurring in the primary region in recent years, the need to provide a suitable temperature distribution at the combustor outlet has always been one of the major parameters of design. The main

feature of a dilution system is the perpendicular injection of cold air, through row(s) of holes in the combustor walls, to be mixed with the hot combustion gases. Other applications exist with a similar arrangement and the flow of a single jet injected perpendicularly into a cross-stream has been the subject of many studies in the past (e.g. Crabb, Durão and Whitelaw [1981]; Andreopoulos and Rodi [1984]). Here, attention will be mainly focused on studies containing a row of holes and with a moderate ratio between the jet and the crossflow velocity ($1< V_{ratio}< 5$). Applications related either to film cooling flows or V/STOL (vertical/short take-off and landing) are outside this range and therefore are not included. Table 1.4 includes a brief description and conclusions of the work found to be more relevant.

TABLE 1.4 - Review of dilution zone studies

AUTHOR(S) YEAR	TEST CASE	REMARKS
Holdeman and Walker [1977]	Experimental. A row of jets. ($2< S/D<6$; $4< H/D <16$; $6< M_{ratio}<60$).	Probe measurements. The momentum flux ratio is the most important parameter influencing the penetration and mixing.
Crabb and Whitelaw [1979]	Experimental. Row of jets (Vratio=2.3).	Probe measurements. The effect in the mean velocity and concentration fields of unequal spacing between jets. The two nearest jets tend to merge and increase the blockage to the crossflow.
Sugiyama and Usami [1979]	Experimental. A single and a row of jets. (S/D=3; H/D=2.5; V_{ratio}=1.96).	Probe measurements and flow visualization. A comparative study between the flow induced by an isolated jet and a jet in a row of jets. The latter cannot be created by a superposition of modules of a single jet.
Khan and Whitelaw [1980]	Experimental. Row of opposed jets (also staggered) (V_{ratio}=2.3; H/D=4; S/D=2 and 4)	Probe measurements. A complement of Crabb and Whitelaw [1979]. Symmetrically opposed and axially transversely staggered jets studied together with the effect of geometrical asymmetries which are more relevant at the lower pitch to diameter ratio.
Shaw [1981]	Experimental. A full annular dilution system with 48 equally spaced jets (V_{ratio}=6.5).	Probe measurements. Experiments in a geometry similar to a real combustor.

TABLE 1.4 - continued

AUTHOR(S) YEAR	TEST CASE	REMARKS
Khan, McGuirk and Whitelaw [1981]	Experimental / Numerical. Row of jets (V_{ratio}=2.3; S/D=2 and 4; H/D=2, 4 and 8).	Probe measurements. Numerical inaccuracy still evident, but the influence of jet spacing and tunnel height correctly predicted. Two types of boundary conditions tested in the inlet plane of the jets.
Atkinson, Khan and Whitelaw [1982]	Experimental. Row of opposed jets (S/D=2, 4 and ∞; V_{ratio}=1 and 1.8; H/D=4).	Hot-wire and probe measurements. Reduced impingement of the jets for Vratio less than 1. The vertical trajectory of the jets increases as the V_{ratio} increases and S/D decreases, but at S/D=2 the free stream penetrates between opposed jets and inhibits mixing.
Chleboun, Craig, Sebbowa and Sheppard [1982]	Experimental / Numerical. Model of an annular combustor (V_{ratio}=1, 4.4 and 5.3).	Probe measurements. Both concentration measurements and streakline views show the existence of a backward flow region upstream created by the impingement of opposed dilution jets.
Demuren [1983]	Numerical. Row of jets (S/D=3; H/D=2.5; V_{ratio}=1.96).	Both hybrid and QUICK differencing schemes used in the calculations. Two boundary conditions tested at the inlet plane of the jets. Emphasis on the errors introduced by the numerics.
Holdeman, Srinivasan and Berenfeld [1984]	Experimental. Single row and also opposed row of holes with jets and mainstream at a different temperature (S/D=2 and 4; H/D=4 and 8; V_{ratio}=3.6, 5.5 and 6.5; 5.3< M_{ratio} <102).	Measurements of temperature for a large range of conditions to study the effect of flow and geometric variations. The momentum flux ratio is the most significant flow parameter. A convergent nozzle improves the mixing relative to a situation without nozzle.
Wittig, Elbahar and Noll [1984]	Experimental. Single row and also opposed row of holes with jets and mainstream at different temperatures (S/D=2.5, and 5; H/D=12.5 and 15.5; 8.9< M_{ratio}<60.24).	Probe measurements. A limited comparison between experimental and empirical correlations to conclude that they are not applicable to high momentum flux ratio.
Demuren [1986]	Review.	Review on the modelling of jets in crossflow (empirical, integral and numerical methods included).

TABLE 1.4 - continued

AUTHOR(S) YEAR	TEST CASE	REMARKS
Sivasegaram and Whitelaw [1986]	Experimental (visualization) Row of opposed jets without crossflow (S/D=2 and 4; H/D=4).	The effect of angular and axial misalignment of the jets results in large flow asymmetries. The effect of opposed jets with unequal strength is magnified at the larger pitch to diameter ratio.
Breidenthal, Tong, Wong, Hamerquist and Landry [1986]	Experimental. Row of opposed staggered jets (S/D=1).	Flow visualization in the transversal planes showing the formation of the vortices in between the jets.

D - jet diameter; H - tunnel height; S/D - pitch to diameter ratio
M - ratio between the the jet and cross stream momentum fluxes

The main flow parameter governing the penetration and mixing of the jets is the momentum flux ratio between jets and cross-stream (e.g. Holdeman and Walker [1977]). In applications such as the dilution zone of a gas turbine combustor, this assumes values usually in the range between 5 and 60. The geometrical parameters of design are the number of holes, their diameter, D, and the spacing between the holes in jet diameters, S/D (pitch to diameter ratio). Other geometrical variables, such as the angle of injection and the convergence of the walls, are also important, but are not included in the semi-empirical correlations (e.g. Holdeman and Walker [1977]; Holdeman, Srinivasan and Berenfeld [1984]; Kamotani and Greber [1982]) used in these types of flow. This seriously limits their applicability and reinforces the interest in the use and development of more versatile numerical models.

Khan, McGuirk and Whitelaw [1981] discuss the results of an application of CFD to a row of jets. They found that some discrepancies between the experimental and numerical results gave strong evidence of numerical errors, caused by the coarseness of the grid; nevertheless, the effect of the tunnel height and jet spacing could be predicted by the model. Problems associated with the numerical models are the need for fine grids to improve the numerical accuracy, the influence of the boundary condition used at the inlet plane of the jets and the appropriateness of the turbulence model. The first point has been addressed, in the context of a single jet in crossflow, by many authors (e.g. Jones and McGuirk [1979]; White [1980]; Claus [1983]; Marquis [1986]); Claus [1983], for instance stated that calculations with grids of 90 × 40 × 22 (79200 grid nodes) were still grid-dependent. This problem, however, is less critical in calculations of rows of jets, because only half of one jet is needed on the grounds of symmetry conditions. There are some difficulties in setting up a laboratory experiment where the flow pattern repeats transversely every half jet and these

conditions can be observed. It is even questionable whether it can even exist inside a gas turbine combustor; the reason being that, if two jets in the row are closer to each other, they tend to merge, increasing the blockage of the crossflow and giving rise to a wake region larger than that which is found in a single jet. Crabb and Whitelaw [1979], Khan and Whitelaw [1980] and Sivasegaram and Whitelaw [1986] are all a variation on this theme. They also concluded that stringent tolerances are needed in laboratory experiments to ensure that a symmetric flow pattern exists downstream of the plane of the jets; this becomes more critical as the momentum flux ratio increases. In the case of rows of opposed jets without crossflow (cf. Sivasegaram and Whitelaw [1986]), geometrical asymmetries are more influential than the uneven feeding of the jets.

The simplest boundary condition to use in the inlet plane of the jet is to assume a constant velocity profile; this is known to be incorrect, especially for low velocity ratios of 0.5 where the cross-stream distorts the velocity profile not only at the inlet plane of the jet, but also at a certain distance upstream (e.g. Andreopoulos [1982]). White [1980], Demuren [1983] and McGuirk, Khan and Whitelaw [1981] tested various boundary conditions in calculations with either a row of jets or a single jet configuration: plug flow profile, constant total pressure, and coupling between two sets of calculations (one inside the jet feed tube and the other with the actual jet in crossflow). White [1980] strongly favours coupling between the two sets of calculations, but the complexity of this approach has led investigators to prefer the constant total pressure boundary condition, or simply a plug flow velocity. This problem is more critical in real combustor geometries, since the dilution holes are fed through an annulus and deviations from the plug flow assumption are likely to occur. This was the reason why Chleboun, Craig, Sebbowa and Sheppard [1982] in their experiment, fed a dilution zone model through annular gaps to simulate a real dilution system. This implies that calculations of real combustors might have to be done in a domain of integration incorporating both the interior of the combustor and the annular passages feeding the holes in the combustor walls, as made in Green and Whitelaw [1983] and Manners [1988].

Many authors have commented on limitations of the turbulence model in this type of flow (the k-ε model is generally used), but the importance of the problems mentioned above has hindered progress in this area. Two aspects of the turbulence model need to be distinguished here: the modelling of the turbulent transport of momentum and the modelling of the turbulent transport of scalars, the scalar flux model. The latter directly affects the prediction of the mixing parameters; particularly in flows without chemical reaction, since the equation of conservation of a passive scalar is simply a balance between convection and diffusion, i.e. turbulent transport

(see Chapter 2 for the actual equations). In a manner consistent with the eddy viscosity concept, the scalar diffusion is also approximated by a gradient hypothesis; the respective coefficient is related to its counterpart in the momentum equations by the turbulent Prandtl number. This is presumed known beforehand and is a major parameter of the model. Controversy exists on the correct value of the turbulent Prandtl number (see further comments in subsection 2.2.1) and at the present the simple expedient of reducing its value for a better agreement with the experimental results has been often used (e.g. Sturgess, Syed and McManus [1983]; Coupland and Priddin [1987]).

1.4.3 The Numerical Solution of the Fluid Flow Equations

Any fluid mechanics problem may be reduced to the solution of a set of strongly coupled partial differential equations (momentum and continuity). Combustor flows are ones where the Mach number is low and are normally treated as incompressible flows. In this case, pressure is a variable for which there is no explicit conservation equation and this is usually circumvented by creating an equation for the pressure by manipulation of the momentum and continuity equations (the pressure-velocity, or primitive variables, formulation). The vorticity-stream function formulation is no longer in use (see Roache [1972] for a discussion on the relative merits of each formulation).

Because of the coupling and nonlinearity of the equations, the solution is usually sought in a sequential or segregated approach (according to the terminology used by Van Doormaal and Raithby [1985]). The momentum and the pressure correction (or continuity) equations are solved in a sequential fashion and tend to the final simultaneous solution by a sequence of steps that alternately satisfy principles of momentum and mass conservation. The solution of the momentum equations (the predictor step) is usually achieved by iterative methods for solution of the systems of linear algebraic equations. This followed by a step (the corrector step) using explicit formulae whereby the velocity fields satisfying continuity are re-established and the pressure field is changed by an amount proportional to the local mass inbalance. Efforts to improve the rate of convergence have concentrated on such aspects as (i) efficiency of the numerical technique used to solve each equation (the solver), and (ii) how the pressure-velocity coupling is addressed. Here, only studies concerned with the second aspect are reviewed. Table 2.5 reviews the work published concerned with this aspect.

The algorithm designated SIMPLE has been used in all the combustor flow calculations mentioned above and is the one incorporated in most computer programs to solve the elliptic flow equations. SIMPLE was first presented by Patankar and Spalding

[1972] but a clearer description of this algorithm and the coupling between velocity and pressure is provided by Patankar [1980]. The algorithms suggested by Harlow and Welch [1965] and Chorin [1967] (designated as the MAC and artificial compressibility methods, respectively) preceded SIMPLE. The main differences between SIMPLE and the other two are the use of a pressure correction equation and an implicit steady-state formulation rather than a pressure equation and an explicit time-dependent formulation; the greater popularity of the SIMPLE algorithm is probably due to the stringent limitations on the time step associated with the explicit time dependent formulation.

TABLE 1.5 - Solution of the elliptic fluid flow equations

AUTHOR(S) YEAR	TEST CASE (geometry, regime, grid)	REMARKS
Harlow and Welch [1965]	Flow under a fully or partially open sluice gate (laminar).	The original paper of the MAC method.
Chorin [1967]	Flow in cavities (two-dimensional and three-dimensional) heated from below.	The artificial compressibility method.
Patankar and Spalding [1972]	Duct of square cross-section with a laterally moving wall (laminar).	The SIMPLE algorithm and an application in a three-dimensional parabolic flow. Clearer discussion of SIMPLE in Patankar[1980].
Harlow and Amsden [1971]	Cylindrically symmetric explosion.	An extension of the MAC method to enable the calculation of flows for all Mach numbers.
Raithby and Schneider [1979]	Flow in rectangular and square boxes with the entry and outlet sections and perpendicularly oriented to each other (laminar) - 10 x 10.	Tests with SIMPLE, SIMPLER (PUP) and others. Various ways of treating the velocity-pressure coupling and equations for the velocity correction emerged and were evaluated.
Benodekar, Goddard, Gosman and Issa [1983]	Flow over a surface mounted thin rib (turbulent) - 36 x 33 and 49 x 47.	An early paper with comparative tests of PISO and SIMPLE. No optimization of numerical parameters.
Van Doormaal and Raithby[1984]	Backward facing step and flow in a rectangular box with the entry and outlet sections perpendicular to each other (laminar).	Discussion of the convergence of SIMPLE and of some modifications as SIMPLEC. Performance tests using the two algorithms above and SIMPLER showed superiority of SIMPLEC.

TABLE 1.5 - continued

AUTHOR(S) YEAR	TEST CASE (geometry, regime, grid)	REMARKS
Zedan and Schneider [1983,1985]	Driven cavity and rectangular box with entry and outlet sections perpendicularly oriented to each other (laminar) - 18 x 18.	Presentation of a coupled strongly procedure (CSIP). Compared with SIMPLE and claimed to be superior.
Galpin, and Van Doormaal and Raithby [1985]	Backward facing step. Rectangular box with entry inlet and outlet sections perpendicularly oriented.	Presentation of a coupled equation line solver (CELS) and comparisons against SIMPLER and SIMPLEC.
Latimer and Pollard [1985]	Sudden expansion in a duct - 14 x 14. Driven cavity - 14 x 14. Plane duct with a porous wall - 18 x 18. All laminar.	Tests with SIMPLE, SIMPLEC and SIMPLER.
Connel and Stow [1985]	Driven cavity (laminar) - 15 x 15.	Tests with SIMPLE, PISO and others. No optimization of the numerical parameters.
Issa [1986] and Issa, Gosman and Watkins [1986]	Flow in a duct with a sudden expansion with a time dependent boundary condition at the inlet and the downstream end closed for compressible test case (laminar)- 20 x 20.	The PISO algorithm and a companion paper with test cases and results in favour of PISO. Comparisons against SIMPLE.
Jang, Jetli and Acharya [1986]	Sudden expansion in a plane channel (laminar) - 7 x 12 and 20 x 20. Annular flow in a duct with a contraction at the outlet (turbulent)-20 x 20. Swirling flow in an axisymmetric furnace (reacting and turbulent)- 7 x 12, 20 x 20.	Performance tests of SIMPLE, SIMPLER and PISO. Tests with both steady and time-dependent formulation. There is no consistent superiority of any algorithm in all the test cases tested.
Wilkes, Thompson, Hightley, Jones and Burns [1986]	Rectangular box with inlet and outlet of different dimension facing each other - 20 x 20 x 20 (reacting, turbulent). Natural convection in an enclosure (laminar) -20 x 20.	SIMPLE and PISO were used. Comparison between line relaxation and conjugate gradients. Results show that SIMPLE and line relaxation techniques are as good as the others.

TABLE 1.5 - continued

AUTHOR(S) YEAR	TEST CASE (geometry, regime, grid)	REMARKS
Galpin and Raithby [1986]	Natural convection in a polar annulus - 22 x 22, 82 x 82 and 62 x 62.	Tests with SIMPLEC, SIMPLER and ST-CELS (a simultaneous solution method). ST-CELS found to be insensitive to the time step.
Van Doormaal and Raithby [1985]	Driven cavity (laminar) - 14 x 14 and 25 x 25.	Tests with SIMPLE, SIMPLEC, SIMPLER and SIMPLEX. A clear discussion on the influence of flow and numerical parameters on convergence and pressure-velocity coupling.

New algorithms have appeared, as alternatives or modifications of SIMPLE. SIMPLER (Patankar [1980]) and SIMPLEC (Van Doormaal and Raithby [1984]) followed directly from SIMPLE. The PISO algorithm is in Issa [1986] and a fourth algorithm, AVPI, was suggested by Jones [1984] and is described in detail in subsection 2.3.1. All the above claim to improve the convergence rate of SIMPLE and are therefore candidates for inclusion in a more efficient combustor code.

In order to maintain the pressure cell coupled only to its immediate neighbours and lead to a matrix of coefficients with the minimum number of diagonals (four in a two-dimensional flow and six in a three-dimensional flow), the velocity/pressure linking formula has to be simplified in the derivation of the pressure correction equation (see subsection 2.3.1 for details). It is usually thought that this simplification is mainly responsible for the convergence rate and suggestions have been made to modify it. Van Doormaal and Raithby [1984] presented one of these suggestions, designated by SIMPLEC, which they claimed to be superior to both SIMPLE and SIMPLER. They also experienced difficulties with SIMPLER and preferred to use it in a version with a pressure correction equation (the original SIMPLER version used a pressure equation, Patankar [1980]). However, as Van Doormaal and Raithby [1984] noticed themselves, SIMPLEC can in many circumstances be converted to SIMPLE provided a certain relationship (see subsection 2.3.1 for details) between the under-relaxation factors of velocity and pressure is obeyed. The lesson to learn from the performance tests of Van Doormaal and Raithby [1984] is that SIMPLE can actually be superior to SIMPLER, depending on the under-relaxation factors being used.

The PISO algorithm has been described by Issa [1986], but an earlier application of PISO had been reported by Benodekar, Goddard, Gosman and Issa [1983] where limited comparisons against SIMPLE showed that PISO was faster by a factor of 6. Gosman, Watkins and Issa [1986], the companion paper of Issa [1986], is intended

to show the superiority of PISO by comparing PISO in time-dependent formulation against SIMPLE in steady-state formulation. This is incorrect because the two formulations may have different rates of convergence (as can be observed in, for instance, Jang, Jetli and Acharya [1986]). However, their purposes seem to have been achieved and they concluded the superiority of PISO.

SIMPLEC and both SIMPLER and PISO are two different strategies to improve the rate of convergence of SIMPLE. SIMPLEC uses one pressure correction equation with different coefficients. SIMPLER and PISO maintain the same pressure correction as SIMPLE, but include an extra pressure or pressure correction equation; this leads to an increased CPU time per iteration, may or may not reduce the total number of iterations, but will usually allow higher under-relaxation factors, i.e. a more robust algorithm. Robustness can usually be improved by increasing the number of diagonals of the matrix of the coefficients of the pressure correction equation (Connel and Stow [1986], and Raithby and Schneider [1979]), or, in PISO, improved even further by increasing the number of pressure correction equations; however, these techniques require a more accurate solution of the pressure correction equation(s) (Connel and Stow [1986], Issa [1986]) and this may also add to an increased CPU time per iteration, stretching the need for an even more reduced number of iterations if any advantage is to be taken. There is no guarantee that the increase of complexity relative to SIMPLE will lead to a more robust algorithm. Latimer and Pollard [1985] suggested another technique where the velocity predictor step is solved in an implicit manner; their figures showed that this technique required lower under-relaxation factors and converged in twice the time of SIMPLER, but nevertheless they concluded that the results were similar.

Tests of performance of the four algorithms mentioned above in turbulent flows have been reported by Jang, Jetli and Acharya [1986] and Wilkes, Thompson, Hightley, Jones and Borns [1986]. None of the algorithms emerged as superior in terms of the CPU time needed to reach convergence. Wilkes, Thompson, Hightley, Jones and Borns calculated the flow inside an industrial furnace using SIMPLE and PISO; their results did not show any advantages of PISO. Nevertheless, it is possible that the performance of these algorithms is to some extent flow dependent and how they would perform in a combustor like flow has not yet been established.

There are alternatives to the segregated algorithms described above, where a stronger coupling between velocity and pressure is sought by a direct solution of momentum and continuity as, for instance, in Vanka [1985] and Galpin, Van Doormaal and Raithby [1985]. These methods usually allow higher under-relaxation factors; their use is justifiable only when simpler techniques fail to converge, as in Galpin and Raithby [1986]. Some authors overemphasize the increased robustness of this type of

algorithm to claim their superiority relative to the segregated approach, even when the algorithms they propose are 'scandalously' slower (e.g. Zedan and Schneider [1985]).

The picture that emerges from the above remarks is that it is difficult to ascertain the superiority of any algorithm. What is important? The CPU time needed to achieve convergence, the robustness, the computer storage requirements, or the simplicity of the method? There is no fully representative test case and the rate of convergence, apart from depending on the flow characteristics, can also be influenced by the boundary conditions, grid size and grid distribution. In addition, some of the previous tests of performance have been made without optimization of the under-relaxation factors and authors tend to claim the superiority of the methods they propose on insufficient evidence. It is thus clear from this literature survey that one cannot with certainty draw conclusions on the superiority of any of these algorithms relative to the others. To reach a conclusion specific to the calculation of combustor flows, tests have to be made and this was therefore one of the tasks selected for study here.

1.5 OUTLINE OF THE THESIS

The bulk of the work is contained in chapters 2, 3, 4 and 5. Chapters 1 and 6 are a short introduction and a list of the main conclusions of the current work, respectively.

Chapter 2 describes the mathematical model and assesses the performance of various algorithms for solving the fluid flow equations using primitive variables formulation and a two equation model of turbulence, k-ε. The SIMPLE algorithm provided the reference against which others had to be judged; two variations of SIMPLE, SIMPLEC and SIMPLER, were assessed together with PISO and AVPI. Detailed discussions of the similarities between the algorithms and aspects that can contribute to the rate of convergence are presented. The two dimensional flow over an obstacle attached to a flat plate was used as a test case believed to be representative of many recirculating flows.

Chapter 3 includes the calculation of the flow inside a dilution zone system of an annular combustor. The first part of the chapter deals with a convergence study for this flow to confirm the conclusions reached for the two-dimensional test problem of Chapter 2. The second part is concerned with the ability of the mathematical model to predict accurately the mixing parameters at the outlet of the combustor; two basic sets of predictions are included with constant and variable density calculations.

Chapter 4 contains an experimental study of the flow inside a water model of a can-type combustor. This includes flow visualization and detailed velocity

measurements. The main part of the work is preceded by two studies: (i) to evaluate experimentally the swirl number of the swirlers to be used in the combustor model and (ii) to establish the operating conditions of the water rig in order to closely simulate the flow pattern observed in a geometrically similar but combusting rig. The velocity data covers flows with different swirl intensities and with or without the simulation of the fuel injection.

The numerical prediction of the flow studied in Chapter 4 is the subject of Chapter 5. The effect of the numerical simplifications is fully investigated, for instance the difficulty of prescribing the boundary conditions in regions where measurements were not possible and the level of grid refinement needed to resolve this type of flow. Only then was the assessment of the limitations of the turbulence model possible and this is the subject of the last part of the chapter with the comparison between the numerical and experimental results of various operating conditions.

Chapter 6 contains a summary of the conclusions and suggestions for future work.

Two appendices are included which deal with the application of a laser induced fluorescence technique and an intrusive probe (designated the Lucas dye probe) with the objective of measuring the concentration in the combustor model. Further development is needed before the data provided by these two techniques can be used for model validation and the main objective of these two appendices is the description of the difficulties experienced and suggestions for improvements.

CHAPTER 2
THE MATHEMATICAL MODEL AND THE PRESSURE-CORRECTION APPROACH

2.1 INTRODUCTION

2.1.1 Objectives and Outline of the Chapter

The objectives of this chapter are threefold: (i) to introduce the governing equations for the calculation of non-reacting turbulent flows, (ii) to describe the numerical techniques used to solve these equations in the present work and (iii) to examine closely one part of the overall numerical procedure, the pressure correction formulation, and to assess the performance of five of its variants.

Section 2.2 deals with the mathematical model; both the exact and the modelled equations are presented (subsection 2.2.1) together with the finite difference techniques (subsection 2.2.2). The calculation procedure is described in Section 2.3; the algorithms (SIMPLE, SIMPLEC, SIMPLER, PISO and AVPI) used in the current work are treated in separate subsections, followed by a discussion on the influence of numerical and flow parameters on the rate of convergence. Section 2.4 discusses the convergence of calculations for the first test case shown: the two dimensional flow over an obstacle. Section 2.5 is a summary of the main conclusions.

2.2 MATHEMATICAL MODEL

2.2.1 Exact Equations

The equations governing the fluid motion of an incompressible, constant property, Newtonian fluid are, in an Eulerian description (cf. Hinze [1975]):

Continuity equation:

$$\frac{\partial \hat{U}_i}{\partial x_i} = 0 \qquad [2.1]$$

Momentum (or Navier-Stokes) equation:

$$\rho \frac{D\hat{U}_i}{Dt} = -\frac{\partial \hat{P}}{\partial x_i} + \frac{\partial}{\partial x_j}\left[\mu \left(\frac{\partial \hat{U}_i}{\partial x_j} + \frac{\partial \hat{U}_j}{\partial x_i}\right)\right] + \hat{F}_i \ . \qquad [2.2]$$

The equation of transport of a scalar is:

$$\rho \frac{D\hat{C}}{Dt} = \frac{\partial}{\partial x_i}(\Gamma \frac{\partial \hat{C}}{\partial x_i}) + \hat{F}_c \qquad [2.3]$$

It is well known that, in the majority of flows of engineering interest, the solution of these equations is not possible. There is in general no analytical solution and, at the high Reynolds numbers found in practice, the range of time and length scales present in these flows is so wide that, were the equations to be solved numerically, the required computer storage and time (Saffmann [1978], Rogallo and Moin [1984]) would far exceed the limits of what is available in today's computers. Therefore, equations [2.1] to [2.3] are usually converted into their averaged form – the Reynolds-averaged Navier-Stokes equations. The instantaneous quantities are decomposed into mean (upper case) and fluctuating (lower case) contributions:

$$\hat{U} = U + u$$

The time-average mean velocity is usually defined as: $U = \lim_{T \to \infty} \frac{1}{T} \int_{t_o}^{t_o+T} \hat{U}\, dt$, which is independent of t_o. Equations [2.1] to [2.3] then become:

Continuity:

$$\frac{\partial U_i}{\partial x_i} = 0 \qquad [2.4]$$

Momentum equation:

$$\rho \frac{DU_i}{Dt} = -\frac{\partial P}{\partial x_i} + \frac{\partial}{\partial x_j}\left[\mu \left(\frac{\partial U_i}{\partial x_j} + \frac{\partial U_j}{\partial x_i}\right) - \rho \overline{u_i u_j}\right] + F_i \qquad [2.5]$$

The equation of transport of a scalar is:

$$\rho \frac{DC}{Dt} = \frac{\partial}{\partial x_i}(\Gamma \frac{\partial C}{\partial x_i} - \rho \overline{u_i c}) + F_c \qquad [2.6]$$

These equations are not a closed set; new terms, $\rho\overline{u_i u_j}$ and $\rho\overline{u_i c}$ have been introduced and extra equations are needed. This is designated the closure problem and constitutes the main objective of turbulence modelling. Transport equations can be derived for the double correlations $\rho\overline{u_i u_j}$ and $\rho\overline{u_i c}$, but this introduces correlations of

higher order, which still need to be closed, and more than doubles the number of equations to be solved. Here, a simpler approach is followed, in which the turbulent fluxes, the double correlations above, are found by gradient diffusion hypothesis from two extra equations accounting for the transport of turbulence kinetic energy, k, and its rate of dissipation, ε. For closure of the above equations, following an analogy with laminar flows, the Reynolds stresses, $\rho\overline{u_i u_j}$, are related to the local strain rate through the Boussinesq eddy viscosity concept:

$$\rho \overline{u_i u_j} = \frac{2}{3}\rho k \delta_{ij} - \mu_t \left(\frac{\partial U_i}{\partial x_j} + \frac{\partial U_j}{\partial x_i}\right) \qquad [2.7]$$

The momentum equation [2.5] then reverts to a form analogous to equation [2.2]:

$$\rho \frac{DU_i}{Dt} = -\frac{\partial P}{\partial x_i} + \frac{\partial}{\partial x_j}\left[\mu_{eff}\left(\frac{\partial U_i}{\partial x_j} + \frac{\partial U_j}{\partial x_i}\right)\right] + F_i \qquad [2.8]$$

where $\mu_{eff} = \mu + \mu_t$. The turbulent eddy viscosity, μ_t, a scalar, is defined according to:

$$\mu_t = C_\mu \rho \frac{k^2}{\varepsilon} \qquad [2.9]$$

The turbulence kinetic energy and its rate of dissipation are determined from the following transport equations, modelled forms of the exact equations (Jones and Launder [1972]):

$$\rho \frac{Dk}{Dt} = \frac{\partial}{\partial x_i}\left(\frac{\mu_t}{\sigma_k}\frac{\partial k}{\partial x_i}\right) - \rho \overline{u_i u_j}\frac{\partial U_i}{\partial x_j} - \rho \varepsilon \qquad [2.10]$$

$$\rho \frac{D\varepsilon}{Dt} = \frac{\partial}{\partial x_i}\left(\frac{\mu_t}{\sigma_\varepsilon}\frac{\partial \varepsilon}{\partial x_i}\right) - \frac{\varepsilon}{k}C_1 \rho \overline{u_i u_j}\frac{\partial U_i}{\partial x_i} - C_2 \rho \frac{\varepsilon^2}{k} \qquad [2.11]$$

where C_μ, C_1, C_2, σ_k and σ_ε (in table 2.1) are empirical constants determined by calibration of the model against experiments in simpler flows (e.g. Rodi [1984]). These equations, [2.10] and [2.11], and the set of constants in table 2.1 are valid only for high turbulence Reynolds number, $R_t = \rho k^2/\mu\varepsilon$, and constitute the standard k-ε turbulence model.

TABLE 2.1 – Standard constants of the k-ε model

C_μ	C_1	C_2	σ_k	σ_ε
0.09	1.44	1.92	1.0	1.3

The double correlation $\rho\overline{u_i c}$ is approximated in the same manner as the Reynolds stress by a gradient transport assumption:

$$-\rho \overline{u_i c} = \Gamma_t \frac{\partial C}{\partial x_i} \qquad [2.12]$$

Leading to the eddy-diffusivity:

$$\Gamma_t = \frac{\mu_t}{\sigma_t} \qquad [2.13]$$

where, σ_t is designated as the turbulent Prandtl number. The modelled transport equation for the scalar quantity is then:

$$\rho \frac{DC}{Dt} = \frac{\partial}{\partial x_i}\left(\Gamma_{eff} \frac{\partial C}{\partial x_i}\right) + F_C \qquad [2.14]$$

where $\Gamma_{eff} = \Gamma + \Gamma_t$. This closes the set of equations formed by [2.4], [2.8], [2.10], [2.11] and [2.14], which can now be solved.

Turbulence modelling

Because for many aspects of the flow in a gas turbine combustor we may consider the flow to be largely driven by the pressure forces, it is usually argued (e.g. Green and Whitelaw [1983]; Coupland and Priddin [1987]) that no turbulence model of a level of closure higher than the k-ε model is necessary, at least to predict the mean motion characteristics. In the current work, the use of the k-ε model was used because at present, it still offers the best compromise between accuracy and computer requirements. The development of turbulence models was not an objective of the present work; but, in spite of that, let us briefly see what other options are available and review the main criticisms of the k-ε model; these remarks may then be borne in mind when we come to the comparisons between numerical and experimental results, in Chapter 5.

For a review of turbulence models based on the Reynolds average form of the fluid flow equations see Rodi [1984], and for a detailed account of the state of the art in

turbulence modelling before 1980 see the Proceedings of the Stanford Conference on Complex Flows (Kline, Cantwell and Lilley [1981]).

Turbulence models simpler than the k-ε model, zero or one-equation models (Hinze [1975], Reynolds [1976]) have performed well in boundary layer type flows, but are inadequate for recirculating flows because of the need to prescribe the characteristic turbulent scales. The k-ε model removes such a need and therefore has a wider range of applicability. However, it still suffers from some limitations, of which, in common to zero and one-equation models, the most often mentioned ones are: the assumption of a scalar (isotropic) eddy viscosity and a diffusive turbulent transport of the gradient type. This isotropy and alignment of the principal axis of the stress tensor and the mean rate of strain are the causes of the inherent inability of the model to predict secondary flows in ducts of non-circular cross-section (for example, Speziale [1987]) and the displacement of the location of the zero shear stress relative to the zero mean gradient in wall jets (e.g. Eskinazi and Erian [1969]; Hinze [1970]). Corrsin [1974] has reviewed the conditions under which gradient transport is valid; Sreenivasan, Tavoularis and Corrsin [1982] showed why the principle sometimes works well even in flows where such conditions are violated. These violations, though important, are sometimes restricted to a local region of the flow and do not preclude good results elsewhere in the domain.

Improvements of the k-ε model have been suggested, mainly through the alteration of the constants (in table 2.1) or the source term of the dissipation equation, to enable the application of the model or to improve its performance in, for instance, low turbulence Reynolds number regions (Jones and Launder [1972,1973], Bernard [1986]), curvature and swirling flows (Militzer, Nicoll and Alpay [1977], Launder, Priddin and Sharma [1977], Leschziner and Rodi [1981], Aupoix, Cousteix and Liandret [1983]), and flows with buoyancy (Gibson and Launder [1976]).

The Reynolds Stress Transport (RST) models (cf. Launder, Reece and Rodi [1975]) represent the level of closure immediately above the k-ε; transport equations are provided for each of the components of the Reynolds stress tensor, $\rho\overline{u_i u_j}$, and the scalar fluxes, $\rho\overline{u_i c}$, i.e. nine extra equations in general. The subsequent increased computer requirements, together with the problems arising due to the accuracy of the finite difference scheme, have hindered the development and application of these models to three dimensional combustor flows.

The algebraic stress type of models (ASM) is derived from the RST equations, either by dropping the convection and diffusion terms (Launder [1977]) or by replacing them by terms which do not involve stress gradients (Rodi [1972]). These models have a complexity only apparently between the RST and the k-ε; there are numerical difficulties associated with the nonlinear algebraic equations of the ASM

and these models are not a general realistic alternative to the k-ε model. Their use may be restricted to simpler flows or as a means of deriving more elaborate versions of the k-ε model, as, for instance, in Gibson and Launder [1976]. At an intermediate level of closure between the standard k-ε and the RST, probably the nonlinear k-ε of Speziale [1987] is now a more realistic alternative.

Deficiencies of the turbulence model are also made evident through the scalar field. In the momentum equation, the relative contribution of the turbulent diffusion may be reduced by the pressure gradient term, but no such compensating mechanism occurs in a conserved scalar equation. The correct prediction of the scalar field, i.e. the mixing process, is very important in the calculation of combustor flows; poor predictions may be a consequence of an inaccurate mixture fraction prediction rather than a failure of the combustion model (Jones and Whitelaw [1982]). It has often been argued that the turbulent transport of momentum and scalar quantities may occur through two different mechanisms (e.g. Hinze [1975]); however, the use of the analogy between the two has been of great usefulness for modelling purposes (Reynolds analogy). In the present model, this analogy is not used to its full extent; turbulent transport of momentum and scalars are both modelled by gradient diffusion (equations [2.9] and [2.12]), though with different coefficients. The ratio between their respective coefficients of diffusion, the turbulent Prandtl number, σ_t, is here assumed to be 0.9 and this is the value usually accepted as valid in boundary layer flows; values have been suggested in a range between 0.2 and 1.0 (Launder [1978]) and there is some uncertainty about what is the most appropriate value. The acceptance of lower turbulent Prandtl numbers for recirculating flows implies that the model as it stands tends to underpredict the levels of scalar mixing.

Comparison of equations [2.7] and [2.12] with the equations of transport of the Reynolds stresses, $\rho\overline{u_i u_j}$ (Bradshaw [1978]), and the turbulent fluxes, $\rho\overline{u_i c}$ (Launder [1978]), show the variety of phenomena neglected and lumped into such simple formulae. In an attempt to consider some of these phenomena, more elaborate definitions of σ_t have been derived (for example, Gibson and Launder [1976]) which, in accordance with experimental evidence (Antonia and Browne [1987]), result in σ_t being a function of location within the flow. In the three-dimensional flow inside a gas turbine combustor, the assumptions supporting such derivations are not valid and the use of turbulence models accounting for the individual components $\rho\overline{u_i c}$ appears to be the most consistent alternative, in spite of the likely computational cost.

Other approaches are available where the fluid flow equations are no longer used in the Reynolds averaged form, as, for instance, the direct (DS) and the large eddy simulation (LES) (cf. Rogallo and Moin [1984]). The direct, or full Navier-Stokes, simulation solves the fluid flow equations in their exact form (equations [2.1] to

[2.3]) and, as stated earlier, only low Reynolds number flows can be calculated. Large eddy simulation provides for modelling of the finer scales and this enables the calculation of more realistic flows. These methods, because of the computing requirements and Reynolds number limitations, have been used mainly in fundamental studies of turbulence and in the generation of turbulence data, difficult to achieve experimentally, to assist with the development of turbulence models of a lower level (see Hunt [1988]).

Turbulence models based on probability density functions, the PDF approach (Pope [1985]), and on the modelling of turbulence by vortex elements (Leonard [1985]) should also be mentioned. The former has become increasingly popular in the calculation of reacting flows; the vortex methods are particularly adequate in flows where vortex shedding phenomena are observed. More general applications of these models may be precluded by the complexity of their mathematical formulation (as in Pope [1975]) and programming, especially in three-dimensional flows.

More complex and elaborate turbulence models tend to be more general and, in principle, should be able to predict a wider variety of flows. But the question is, why have a complex model when in some regions simple models work as well as the most complex ones. This naturally leads to the concept of zonal modelling (Kline [1981]), where the flow domain is split into zones according to the type of turbulence models they require.

2.2.2 Finite Difference Discretisation

The following methodology for numerical solution of the governing equations has been incorporated into a computer program originally written by Jones [1975] and used in modified form for the predictions described elsewhere in this thesis. In all aspects, it is similar to that described in detail by Patankar [1980] and therefore only a brief description is given here.

All the transport equations above can be cast into the general form:

$$\rho \frac{\partial \phi}{\partial t} + \frac{\partial}{\partial x_i}(\rho U_i \phi) = \frac{\partial}{\partial x_i}\left(\Gamma_\phi \frac{\partial \phi}{\partial x_i}\right) + S^\phi \qquad [2.15]$$

transient term convection term gradient diffusion source term

where the diffusivity, Γ_ϕ, and the source term, S_ϕ, depend on the variable ϕ being considered. The source term can also accommodate terms from the original transport equation which do not fit into any of the other terms of the equation above.

The discretisation of equation [2.15] is accomplished using finite difference techniques, which are actually applied to its integral form (equation [2.16]) (i.e. the control volume approach, as described by Patankar [1980]). The equation to be discretised is, in steady formulation and using a cartesian system of coordinates in one dimension for simplicity:

$$(\rho_r\ U_r\ \phi_r - \rho_l\ U_l\ \phi_l) = (\Gamma_\phi \frac{d\phi}{dx}|_r - \Gamma_\phi \frac{d\phi}{dx}|_l) + S^\phi \qquad [2.16]$$

See Figure 2.1 for meaning of the various terms. The variables U_r and U_l are equivalent to U_R and U_P but this is a consequence of the use of staggered grids, where velocity and scalars are located in different locations in the grid, in a manner usually referenced as first used by Harlow and Welsh [1965]. The diffusion terms are always approximated by central differencing:

$$\frac{d\phi}{dx}|_r = \frac{\phi_R - \phi_P}{\Delta x_R} \qquad [2.17]$$

and the convective terms by either central differencing:

$$\phi_r = \frac{1}{2}(\phi_P + \phi_R) \qquad [2.18]$$

upwind differencing:

$$\phi_r = \phi_P \qquad \text{(for } U_r>0\text{)} \qquad [2.19]$$

or quadratic upwind differencing:

$$\phi_r = \frac{1}{2}(\phi_P + \phi_R) - \frac{1}{8}(\phi_L + \phi_R - 2\phi_P) \qquad \text{(for } U_r>0\text{)} \qquad [2.20]$$

The latter is called QUICK and has been suggested by Leonard [1979a]. In the three-dimensional calculations, central and upwind differencing were used together (the so-called hybrid differencing scheme), with the latter used for cells with a mesh Reynolds number, $Re(\Delta x_i) = |U_i|\ \Delta x_i/\Gamma$, greater than 2; in the two-dimensional calculations,

the combination of quadratic and upwind differencing could also be used, but the limiting mesh Reynolds number was previously selected for each variable and was kept as high as the convergence of the calculations allowed.

The final discretised form of equation [2.16], obtained by using the finite difference formulae above, is generalized to three-dimensional flows as follows:

$$A_P^{\phi}\,\phi_P = \sum_{nb} A_{nb}^{\phi}\,\phi_{nb} + S^{\phi} \qquad [2.21]$$

where the source term has been linearized, $S^{\phi} + S_p^{\phi}\,\phi_p$, and $A_p^{\phi} = \sum_{nb} A_{nb}^{\phi} - S_p^{\phi}$. The summation term extends over a number of neighbours which is a function of the dimension of the problem and the finite difference scheme used for discretisation. The latter may not be influential since, to reduce the number of diagonals of the matrix of coefficients A, the terms involving other terms than the immediate neighbours in each direction are usually explicitly discretised and lumped into the source term. Finally, when iterative methods are used for the solution of the equation above it is also under-relaxed:

$$\frac{1}{\alpha} A_P^{\phi}\,\phi_P = \sum_{nb} A_{nb}^{\phi}\,\phi_{nb} + S^{\phi} + \frac{1-\alpha}{\alpha} A_P^{\phi}\,\phi_P^0 \qquad [2.22]$$

The under-relaxation is also needed, because of the coupling and nonlinearities of the equations, to secure the convergence of the algorithm. In the current work, the well known tri-diagonal matrix algorithm (TDMA) was used to solve the algebraic equations with a number of iterations that depended on the variable ϕ. These iterations shall be designated by 'sweeps' in order to distinguish them from the iterations of the global algorithm, to be introduced later.

Numerical Accuracy

Assuming that ϕ and its derivatives are single valued, finite and continuous functions of x, then the value of ϕ at points P and R (Figure 2.1) is, by Taylor series analysis:

$$\phi_P = \phi_r - \Delta x_{Pr} \frac{d\phi}{dx}\Big|_r + \frac{1}{2!}(\Delta x_{Pr})^2 \frac{d^2\phi}{dx^2}\Big|_r - \frac{1}{3!}(\Delta x_{Pr})^3 \frac{d^3\phi}{dx^3}\Big|_r + \ldots \qquad [2.23]$$

$$\phi_R = \phi_r + \Delta x_{rR} \frac{d\phi}{dx}\Big|_r + \frac{1}{2!} (\Delta x_{rR})^2 \frac{d^2\phi}{dx^2}\Big|_r + \frac{1}{3!} (\Delta x_{rR})^3 \frac{d^3\phi}{dx^3}\Big|_r + \ldots \qquad [2.24]$$

At this stage, let us also assume that the grid is uniformly spaced (i.e. $\Delta X_{Pr}=\Delta X_{rR}=\Delta X/2$, where $\Delta X = \Delta X_L=\Delta X_R$). Then, it can be seen that equation [2.23] is identical to equation [2.19] if the derivative terms are neglected; also, by adding the two equations above and dividing by two, an equation similar to [2.18] is obtained if the terms of order $(\Delta X)^2$ and higher are neglected. The truncation error of the upwind and central are $O(\Delta X)$ and $O(\Delta X)^2$, respectively. This is a very simple analysis, it only sets the maximum possible global accuracy and shows that the finite difference equations (FDE) exist only as an asymptotic form (as ΔX goes to zero) of the partial differential equations (PDE); other factors, such as the treatment of the boundary conditions and the source terms, can reduce the global accuracy of the solutions (e.g. Blottner [1982]). The magnitude of the truncation error is usually referred to as the formal order of accuracy of the calculations. The QUICK formula [2.20] is derived by fitting a parabola through three upstream weighted nodes (Leonard [1979a]) and, according with Leonard's own definition, is 3rd order accurate. There are differences between this definition and the definition above based on the order of the truncated terms of the Taylor series; for our purpose here let us simply say that the QUICK scheme is at least as accurate as the central differencing scheme.

The use of the upwind scheme (the scheme with lowest accuracy) is justified only for stability reasons and its low accuracy has been a major cause of concern. The problem of the numerical accuracy evolves around the truncation error of the convective term and this subject has dominated recent literature in this field. There is a viewpoint which states that this low accuracy is the price to pay if one wishes to obtain solutions for a wide variety of situations on coarse meshes. Spalding [1972] has justified the upwind approach on the grounds that it is the asymptotic solution (high Reynolds number) of the one-dimensional convection-diffusion problem. Leonard [1979a,1979b] has strongly criticized these points of view and suggested a more accurate scheme, QUICK. However, this is not completely free from problems and, like every finite difference scheme of an order higher than the first (Roache [1972]), may fail to converge or give rise to physically unrealistic solutions, with spatial oscillations. There are two ways to remedy this: by reverting to lower order schemes (Chapman [1981]), or by refining the grid (Gresho and Lee [1979]).

The discussion above has concentrated on the increase of accuracy by including higher order terms into the finite difference approximations, but there are other strategies. The first truncated term of the upwind approximation is diffusive-like and

gives rise to solutions with too much diffusion (numerical diffusion). However, the effects of the truncation error are larger if the vector is not aligned with the grid lines (e.g. Wolfshtein [1968]; De Vahl Davis and Mallinson [1976]; Raithby [1976a]) and this is the argument supporting the derivation of the skew differencing schemes (Raithby [1976 b]), where the orientation of the velocity vector is taken into account.

Given the computer storage limitations, since the grid cannot be equally fine everywhere, the alternative is to concentrate it in regions of high gradients – a non-uniformly spaced grid. This reduces the formal order of accuracy of the central differencing scheme (and of any scheme of an order higher than 2), because the sum of the two first order terms in equations [2.23] and [2.24] is not zero. From a strictly theoretical analysis this seems to bring no benefits (Roache [1972], Rivas [1972], Crowder and Dalton [1971]). However, the gradient term may be reduced and the magnitude of the truncation terms may be lower, provided the ratio of the spacing between consecutive nodes is not much higher than 1 (Sundqvist and Veronis [1970]). The extension of this concept leads to the use of self-adapting grids, where the grid evolves during the calculation procedure as the variable field is updated (Thompson and Steger [1988]). Greater freedom in the arrangement of the grid is achieved by the use of more versatile coordinate systems, such as, for instance, the most recent curvi-linear non-orthogonal system, referred to in subsection 1.4.1.

Refining the grid is a relatively simple method to improve numerical accuracy, and this is valid, irrespective of the order of the scheme; halving the grid spacing reduces the truncation error of the upwind, central and upwind-quadratic schemes by a factor of 2, 4 and 8, respectively. (Note that the grid refinement becomes more effective as the order of the scheme increases.) Also, the accuracy of the other terms in the discretised equations (for instance, the source term) is improved. The normal practice is to compare the solutions obtained by progressively refined grids until the difference is found negligible – a grid independent solution. However, the computer storage poses a limit to this and, in some problems, solutions independent of the grid may currently not be possible.

The contribution of the truncated terms to the final solution can also be assessed by comparing their magnitude relative to the magnitude of the real terms in the transport equation. This can be made in two ways. The first is based on the ratio between the coefficients of numerical and physical viscosity, which, obviously, should be less than 1; formulae have been given for the numerical viscosity coefficient by Wolfshtein [1968], De Vahl Davis and Mallinson [1976] and Leschziner [1979] for two-dimensional flows, and Demuren [1985] for three-dimensional flows. The second method is to recalculate the convection terms using a finite difference scheme of an order higher than that used to obtain the solutions; this, reintroduced into the

equations gives rise to a residual term (the difference of the convection terms using two finite differences of different orders) which should be small compared with the remaining terms in the equation (McGuirk and Rodi [1978]). The two approaches above can also be used as criteria to guide the grid refinement. They are both not free from criticisms (Castro [1982]) and should be considered as only qualitative.

2.3 CALCULATION PROCEDURE

The procedure previously described may be used to solve all transport equations. The pressure, however, requires a special practice. For incompressible flows, the pressure correction approach has proved very successful and is also used in this work. The objective here is to examine several alternatives suggested to the SIMPLE algorithm in recent years (see review in subsection 1.4.3), and see whether they would be beneficial (reduction of the computing time) in the calculation of combustor-type flows. The derivation of SIMPLE and other algorithms (SIMPLEC, SIMPLER, PISO and AVPI) is presented here in its shortest and simplest form; it has been restricted to what was thought to be strictly necessary in the context of the present work. For more details and also lengthier introductions the reader should refer to the original works.

2.3.1 Alternative Formulations of the Pressure-Velocity Coupling

SIMPLE

The discretised momentum equation at the velocity node, U_P (see Figure 2.1), with the pressure gradient term extracted from the source term, is:

$$A_P^{U_P} U_P = \alpha_u \sum_{nb} A_{nb}^{U_P} U_{nb} + \alpha_u S^{U_P} + \alpha_u a\,(P_L - P_P) + (1 - \alpha_u)\, A_P^{U_P} U_P^0 \qquad [2.25]$$

where "a" is the cell area perpendicular to the velocity U_P, the area on which the pressure gradient acts. This variable is included here in order not to preclude the validity of the present derivation for two and three-dimensional situations, since in the strict context of a one-dimensional case "a" may be set equal to 1.

An equation similar to [2.25], but based on guessed velocity and pressure fields, U^* and P^*, is:

$$A_P^{U_P} U_P^* = \alpha_u \sum_{nb} A_{nb}^{U_P} U_{nb}^* + \alpha_u S^{U_P} + \alpha_u a\,(P_L^* - P_P^*) + \\ + (1 - \alpha_u)\, A_P^{U_P} U_P^0 \qquad [2.26]$$

By subtraction of the two above:

$$U_P' = U_P - U_P^* = \frac{\alpha_u}{A_P^{U_P}} \left(\sum_{nb} A_{nb}^{U_P} U_{nb} - \sum_{nb} A_{nb}^{U_P} U_{nb}^*\right) + \\ + \frac{\alpha_u a}{A_P^{U_P}} \left[(P_L - P_P) - (P_L^* - P_P^*)\right] \qquad [2.27]$$

and neglecting the first term on the right hand side (the difference between the summation terms), the velocity correction formula may be derived:

$$U_P' = \frac{\alpha_u a}{A_P^{U_P}} \left(P_L' - P_P'\right) \qquad [2.28]$$

where:

$$U = U^* + U' \qquad [2.29]$$

and:

$$P = P^* + P' \qquad [2.30]$$

Similar formulae can be derived for other velocities. Substituting all such relations for velocities which surround a given pressure node into the discretised continuity equation, the pressure correction equation becomes:

$$P_P' \left(\frac{a\,\alpha_u}{A_P^{U_P}} + \frac{a\,\alpha_u}{A_P^{U_R}}\right) - P_L' \left(\frac{a\,\alpha_u}{A_P^{U_P}}\right) - P_R' \left(\frac{a\,\alpha_u}{A_P^{U_R}}\right) = U_P^* - U_R^* \qquad [2.31]$$

The complete set of equations are thus solved in the following sequence:

make initial guesses for velocity and pressure fields
assemble coefficients of momentum equations [2.25]

solve momentum equations
assemble coefficients of pressure correction equation [2.31]
solve pressure correction equation
correct velocities (update velocity U by adding U' from [2.29]
correct pressure (update pressure P by adding P' from [2.31]
assemble coefficients of any other transport equation(s) affecting the flowfield
solve equation(s) above
convergence test

The test of convergence is usually based on a non-dimensional form of the term on the right hand side of equation [2.31]. This term represents the local imbalance in the continuity equation present in the current velocity field (mass source); it is zero under conditions of fully converged calculations. The neglect of the difference between the summation terms in deriving equation [2.27], leading to the velocity correction formula [2.28], is the major step in the derivation of the SIMPLE pressure correction equation and is thought to be the reason for slow convergence. Note that the momentum equations [2.25] and [2.26], from which the derivation started, contain terms involving U_R and U_L (in $\Sigma A_{nb} U_{nb}$) and, if this simplification had not been made, the final pressure correction equation, [2.31], would depend on more than the central node and its immediate neighbours. To avoid divergence of the calculations, because it is argued that this simplification causes an overprediction of the pressure, the under-relaxation of equation [2.30] is recommended (Patankar [1980]), i.e.

$$P = P^{*} + \alpha_p P' \qquad [2.32]$$

SIMPLEC

Van Doormaal and Raithby [1984] argue that it is not consistent to neglect the term:

$$\sum_{nb} A_{nb}^{U_P} U_{nb} - \sum_{nb} A_{nb}^{U_P} U_{nb}^{*}$$

(i.e. $\sum_{nb} A_{nb}^{U_P} U_{nb}'$) when a term of similar magnitude, the left hand side of [2.27], $A_P^{U_P} U_P'$, is retained, since $A_P^{U_P} \cong \sum_{nb} A_{nb}^{U_P}$. They have proposed that:

$$\sum_{nb} A_{nb}^{U_P} U'_P$$

be subtracted from both sides of equation [2.27]:

$$\left(\frac{A_P^{U_P}}{\alpha_u} - \sum_{nb} A_{nb}^{U_P}\right) U'_P = \sum_{nb} A_{nb}^{U_P} U'_{nb} - \sum_{nb} A_{nb}^{U_P} U'_P + a\,(P'_L - P'_P)$$

and only now is it, they say, justifiable to neglect the difference between the summation terms. The final velocity correction formula becomes:

$$U'_P = \frac{a\,(P'_L - P'_P)}{\frac{A_P^{U_P}}{\alpha_u} - \sum_{nb} A_{nb}^{U_P}} \qquad [2.33]$$

or because $A_P^{U_P} = \sum_{nb} A_{nb}^{U_P} - S_P^{U_P}$ it yields:

$$U'_P = \frac{\alpha_u\, a\,(P'_L - P'_P)}{\sum_{nb} A_{nb}^{U_P}\,(1 - \alpha_u) - S_P^{U_P}} \qquad [2.34]$$

This is the only difference between the SIMPLEC algorithm and the SIMPLE algorithm presented previously. The pressure correction equation of SIMPLEC has the same form as the pressure correction equations of SIMPLE, [2.31], but with re-defined coefficients.

SIMPLER

To circumvent the probable inaccuracy of the pressure correction equation as a means of evaluating the pressure, Patankar [1980] proposed the calculation of the pressure via another equation. This equation is derived by substituting the momentum equation [2.25] and a similar equation for U_R into the continuity equation; in our one-dimensional example, this yields:

$$P_P\left(\frac{a\alpha_u}{A_P}\Big|_{U_P} + \frac{a\alpha_u}{A_P}\Big|_{U_R}\right) - P_L\left(\frac{a\alpha_u}{A_P}\Big|_{U_P}\right) - P_R\left(\frac{a\alpha_u}{A_P}\Big|_{U_R}\right) =$$

$$= \alpha_u \sum_{nb} \frac{A_{nb} U_{nb}}{A_P}\Big|_{U_P} - \alpha_u \sum_{nb} \frac{A_{nb} U_{nb}}{A_P}\Big|_{U_R} + \alpha_u \frac{S}{A_P}\Big|_{U_P} - \alpha_u \frac{S}{A_P}\Big|_{U_R} \qquad [2.35]$$

The sequence of operations with this method includes the calculation of the pressure using the above equation before the calculation of the velocity field. Note that the only difference between this equation and the pressure correction equation [2.31] is the right hand side; the two equations lead to a similar matrix of coefficients. The SIMPLER algorithm therefore looks like:

make initial guesses for velocity and pressure fields
assemble and store coefficients of momentum equations [2.25]
assemble and store coefficients of pressure equation [2.31]
solve pressure equation [2.35]
solve momentum equations
calculate source term of pressure correction equation [2.31]
solve pressure correction equation [2.31]
correct velocities (update velocity U by adding U' from [2.28])
assemble coefficients of any other transport equation(s) affecting the flowfield
solve equation(s) above
convergence test

The introduction of an extra equation will increase the computational effort involved in one cycle of this algorithm, so that if an overall benefit is to be obtained, the convergence rate must improve by at least as much to compensate for this extra effort.

PISO

PISO (Issa [1986]) may follow directly from SIMPLE; it adds another step to the SIMPLE sequence of operations. The first pressure correction equation of PISO is identical to that used in SIMPLE, [2.31]. PISO, as SIMPLER, needs an extra pressure,

or better pressure correction equation, which is derived in the following manner. Given the momentum equations:

$$A_P^{U_P} U_P^{*} = \alpha_u \sum_{nb} A_{nb}^{U_P} U_{nb} + \alpha_u S^{U_P} + \alpha_u a\,(P_L^{*} - P_P^{*}) + (1-\alpha_u)\, A_P^{U_P} U_P$$

$$A_P^{U_P} U_P^{**} = \alpha_u \sum_{nb} A_{nb}^{U_P} U_{nb}^{*} + \alpha_u S^{U_P} + \alpha_u a\,(P_L^{**} - P_P^{**}) + (1-\alpha_u)\, A_P^{U_P} U_P^{0}$$

where the asterisks indicate variables calculated at different stages of the calculation; by subtraction and neglect of the difference between the source terms, the velocity correction formula is found:

$$U'' = U_P^{**} - U^{*} = \frac{\alpha_u \sum_{nb} A_{nb}^{U_P} (U_{nb}^{*} - U_{nb})}{A_P^{U_P}} + a \frac{\alpha_u}{A_P^{U_P}} (P_L'' - P_P'') \qquad [2.36]$$

where P"= P**-P*. Again, by continuity, but using the new velocity correction above, and because $U^{*} - U = U'$, the pressure correction equation becomes:

$$P_P' \left(\frac{a\,\alpha_u}{A_P^{U_P}} + \frac{a\,\alpha_u}{A_P^{U_R}}\right) - P_L' \left(\frac{a\,\alpha_u}{A_P^{U_P}}\right) - P_R' \left(\frac{a\,\alpha_u}{A_P^{U_R}}\right) =$$

$$= \frac{\alpha_u \sum_{nb} A_{nb}^{U_P} U_{nb}'}{A_P^{U_P}} - \frac{\alpha_u \sum_{nb} A_{nb}^{U_R} U_{nb}'}{A_P^{U_R}} + (U_P^{*} - U_R^{*}) \qquad [2.37]$$

This new equation and the corresponding corrector steps for velocity (equation [2.36]) and pressure are introduced in the SIMPLE sequence of operations after the correction of the pressure. The only difference between the equation above and both the pressure correction of SIMPLE, [2.31], (also the first pressure correction of this algorithm here) and the pressure equation of SIMPLER, [2.35], is in the source term. The equations [2.31], [2.35] and [2.37] all have a similar matrix of coefficients. The sequence of operations is the following:

make initial guesses for velocity and pressure
assemble and store coefficients of momentum equations [2.25]
solve momentum equations
assemble and store coefficients of first pressure correction equation [2.31]
solve first pressure correction equation
correct velocities (update velocity U by adding U' from [2.28])
correct pressure (update pressure P by adding P' from [2.31])
calculate source term of second pressure correction equation [2.37]
solve second pressure correction equation
correct velocities (update velocity U by adding U" from [2.36])
correct pressure (update pressure P by adding P" from [2.37])
assemble coefficients of any other transport equation(s) affecting the flowfield
solve equation(s) above
convergence test

AVPI

The AVPI algorithm (Jones [1984]) described here, differs from the previous ones in that it must be used within a time-dependent formulation. The momentum equations at two different instants of time ($t + \Delta t/2$ and $t + \Delta t$) may be written as:

$$\rho \Delta V \left(\frac{U_P^{t+\Delta t/2} - U_P^t}{\Delta t}\right) + A_P^{U_P} U_P^{t+\Delta t/2} = \sum_{nb} A_{nb}^{U_P} U_{nb}^{t+\Delta t/2} + S_U^{t+\Delta t/2} + a\,(P_L^t - P_P^t)$$

$$\rho \Delta V \left(\frac{U_P^{t+\Delta t} - U_P^t}{\Delta t}\right) + A_P^{U_P} U_P^{t+\Delta t/2} = \sum_{nb} A_{nb}^{U} U_{nb}^{t+\Delta t/2} + S_U^{t+\Delta t/2} + a\,(P_L^{t+\Delta t} - P_P^{t+\Delta t})$$

Subtracting the two equations above, the velocity correction formula becomes:

$$U_P^{t+\Delta t} = U_P^{t+\Delta t/2} + \frac{a\Delta t}{\rho \Delta V}(P_L' - P_P') \qquad [2.38]$$

$$P' = P^{t+\Delta t} - P^{\Delta t}$$

Again, the velocity correction formulae are substituted in the continuity equation to yield:

$$P'_P \left(\frac{a\ \Delta t}{\rho\ \Delta V} + \frac{a\ \Delta t}{\rho\ \Delta V}\right) - P'_L \left(\frac{a\ \Delta t}{\rho\ \Delta V}\right) - P'_R \left(\frac{a\ \Delta t}{\rho\ \Delta V}\right) = U_P^{t+\Delta t/2} - U_R^{t+\Delta t/2} \qquad [2.39]$$

The coefficients of this pressure correction equation do not depend on the coefficients of the momentum equation and this is a major difference. The sequence of operations is the same as in SIMPLE (apart from requiring a time-dependent formulation).

2.3.2 Details of the Calculation Procedure

The superior behaviour of any of the above pressure-velocity formulations relative to the others can only be revealed by comparative tests. The different formulations for the pressure-velocity coupling result from the belief that the pressure-velocity coupling carries the main responsibility for the rate of convergence. This may be true, especially in laminar flows, but other factors can also affect the rate of convergence. Before embarking on the actual tests of convergence, let us first briefly review the algorithms above and reveal subtle details of the calculation procedure, likely to affect not only the convergence of the calculations but also the selection of any of these algorithms as the most appropriate for the combustor flow calculations.

The sequence of operations presented together with the derivation of the various pressure correction equations shows what is called a global iterative cycle, or just iteration. The need for this iterative process is a consequence of the linearization of the coefficients. There are two basic steps for each discretised transport equation: the assembly of the coefficients and the solution of the algebraic equations using repeated applications of the TDMA method, mentioned earlier. The solution of the pressure correction equation(s) is(are) followed by the correction of the velocity, to establish a velocity field satisfying continuity, and updating of the pressure (except in SIMPLER).

Algorithms like PISO and SIMPLER, apart from the extra CPU time per iteration compared to the other three, also require extra storage, as a consequence of the need to use the coefficients of the momentum equations in later stages within the same global cycle. This extra storage requirement is ostensibly ignored by the literature reporting favourable comments on these algorithms. However, in the context

of our fully three dimensional combustor flow, storage has to be provided for four sets of coefficients (each containing eight three dimensional arrays of the same size as the total number of grid nodes) instead of only one set and this extra storage cannot be ignored when evaluating the relative merits of the various algorithms. In SIMPLE, SIMPLEC, SIMPLER and PISO, the coefficients of the pressure correction equation are assembled at the same time as the coefficients of each momentum equation, because they depend on the velocity; whereas in AVPI, because the coefficients of the pressure correction equation are only geometric functions, they may be assembled outside the global iterative cycle, and only once during the calculation, reducing the computing time per iteration. These details are features that can strongly influence the selection of the algorithm in any given problem.

The convergence of the calculations

If a solution exists, on simultaneous solution of the whole set of equations, the residual of all the equations should be negligible and there has to be some quantitative means of evaluating this. The main parameter used to assess the convergence of the calculations is the mass residual, i.e. the summation over the solution domain of the absolute values of the local mass continuity error (source term of the pressure correction equation). Residuals were also defined for the other equations, as below:

$$\phi_{res} = \frac{\sum_{nb} A^{\phi}_{nb}\,\phi_{nb} + S^{\phi} - A^{\phi}_{P}\phi_{P}}{\phi_{max} - \phi_{min}}\Bigg|_{max}$$

where ϕ_{max} and ϕ_{min} are the maximum and minimum values of ϕ in the field. The emphasis given to the mass residual results from the fact that if the pressure and velocity fields used to evaluate the coefficients are not solutions of the momentum equation, this produces a velocity field not satisfying continuity. The use of the mass residual as the exclusive criterion of convergence implies the acceptance that convergence can never occur through a sequence of steps satisfying continuity. The mass residual is appropriate to assess the convergence of both velocity and pressure fields but, in the case of a scalar variable, especially if it has a little influence on the momentum equations, it seems obvious that a fully converged solution can only be achieved after the velocity fields have been established.

The use of the difference between the variables at consecutive iterations as a criterion for convergence is not very reliable, because it may be merely implying a slow convergence. There are cases in the literature where the authors strongly under-

relax some variables to secure convergence; this practice must be carried out with some care, since it may result in apparently converged solutions. The most reliable technique is the observation of the convergence pattern (Roache [1972]) and this has been used initially as a means of establishing a sufficiently low mass residual to be used later as the convergence criterion.

Steady and unsteady formulations

The algorithms above have been derived assuming a steady-state formulation, but they can easily be extended to time-dependent problems. The discretised form of the transient term in equation [2.15], assuming a forward Euler integration in time, is:

$$\rho \frac{\partial \phi}{\partial t} = \frac{\rho \Delta V}{\Delta t} (\phi_P^{t+\Delta t} - \phi_P^t) \qquad [2.40]$$

For an explicit transient formulation, the analogue of equation [2.22] is:

$$\rho \frac{\Delta V}{\Delta t_{exp}} \phi_P^{t+\Delta t} = \sum_{nb} A_{nb}^{\phi} \phi_{nb}^t + S^{\phi t} + (\frac{\rho \Delta V}{\Delta t_{exp}} - A_P^{\phi}) \phi_P^t \qquad [2.41]$$

where, for stability reasons:

$$\rho \frac{\Delta V}{\Delta t_{exp}} \geq A_P^{\phi}$$

i.e.

$$\Delta t_{exp} \leq \frac{\rho \Delta V}{A_P^{\phi}} \qquad \text{or} \qquad \Delta t_{exp}^{max} = \frac{\rho \Delta V}{A_P^{\phi}} \qquad [2.42]$$

For an implicit transient formulation, the analogue of equation [2.22] is:

$$(\frac{\rho \Delta V}{\Delta t_{imp}} + A_P^{\phi}) \phi_P^{t+\Delta t} = \sum_{nb} A_{nb}^{\phi} \phi_{nb}^{t+\Delta t} + S^{\phi t} + \frac{\rho \Delta V}{\Delta t_{imp}} \phi_P^t \qquad [2.43]$$

This is the formulation usually preferred. The new velocity correction formulae derived on the basis of the equation above are:

For SIMPLE:

$$U'_P = \frac{a}{\frac{U_P}{A_P} + \frac{\rho \Delta V}{\Delta t_{imp}}} (P'_L - P'_P) \qquad [2.44]$$

and for SIMPLEC:

$$U'_P = \frac{a}{\frac{U_P}{S_P} + \frac{\rho \Delta V}{\Delta t_{imp}}} (P'_L - P'_P) \qquad [2.45]$$

The coefficients of the pressure and pressure correction equations of SIMPLER and PISO are the same as those used in the pressure correction equation of SIMPLE, as before.

Equation [2.43] is exactly identical to equation [2.22] if:

$$\frac{\rho \Delta V}{\Delta t_{imp}} = A_P^{\phi} \frac{1 - \alpha}{\alpha}$$

i.e., using [2.40]:

$$\Delta t_{imp} = \Delta t_{exp}^{max} \frac{\alpha}{1 - \alpha} \quad \text{or} \quad \alpha = \frac{1}{1 + \frac{\Delta t_{exp}^{max}}{\Delta t_{imp}}} \qquad [2.46]$$

The relationship above shows that the steady-state formulation is equivalent to an unsteady implicit formulation with a time-step equal to the maximum of the time-step of an unsteady explicit formulation multiplied by the factor $\alpha/(1-\alpha)$. The steady-state formulation is equivalent to an unsteady formulation where the time-step varies from one point to another (distorted time); the time-step, as can be seen from equation [2.42], depends on the dimensions of the finite difference cell and the local value of the velocity (the coefficient A_P contains terms depending on the velocity, originated from the convection term of the discretised momentum equation), which may also be changing from one global iteration to the next. The equivalence between steady and unsteady formulations also depends on the equation; solving the fluid flow equations in steady-state formulations is like advancing in time in a manner that differs from one

variable to another. This different speed of convergence of the variables can be questioned, since one of the variables may be converging at such a slow rate that the calculations are assumed as fully converged.

In heat conduction problems, distorted time techniques are very common, particularly the implicit unsteady formulation, because they remove the limitation of the maximum time-step, i.e. unconditionally stable. This is usually used as an argument to justify the utilization of the steady-state formulation also in fluid flow problems, and to abandon the explicit unsteady formulation on the grounds that the criterion of stability (equation [2.42]) is too restrictive. But equation [2.46] shows that, if advantage is to be taken from the use of steady-state relative to the unsteady explicit formulation, the under-relaxation factor has to be higher than 0.5 and this is in contrast to the normal practice, since $\alpha = 0.5$ is generally recommended and thought to be the optimum value (Patankar [1980]). A value of $\alpha = 1$ (infinite time-step) is equivalent to a calculation with only one iterative step, i.e. a direct calculation and no under-relaxation at all, but this is clearly not feasible.

The conclusion is that the computational superiority of the steady-state formulation relative to unsteady-state formulations cannot be taken for granted, especially when the under-relaxation factors are less than 0.5. Also, the correctness of the steady-state formulation may sometimes be questioned because it assumes the existence of a steady-state solution (Roache [1972]), an assumption that only experiments can confirm. Crocco [1965] argues that the steady-state formulation is a mathematical abstraction with no physical counterpart, since in nature, the steady-state exists only asymptotically and as a sequence of phenomena taking place simultaneously in time; here, these phenomena are still simultaneous, though represented by equations which have been split and are solved in a sequential procedure for computational convenience only

The nature of the pressure-velocity coupling

The nature of the pressure correction equation is Poisson-like and the factor multiplying the pressure gradient in the velocity correction formula can be seen as a 'diffusivity of pressure', Γ_p. For a given flow imbalance, the product of the pressure correction gradient across the cell multiplied by the diffusivity of the pressure is equal to the flow imbalance. Three basic proposals (in Table 2.2) can be identified among the five algorithms described previously.

The definition of Γ_p proposed by SIMPLEC in unsteady formulation and AVPI are similar if the source term is zero. SIMPLE, SIMPLER and PISO use the same Γ_p, which, because the terms in the denominator are positive quantities, is also the smallest, i.e. for an identical flow imbalance the pressure correction being generated

by these three algorithms is the highest. Because $\Sigma A_{nb} U_{nb}$ (and S_P^U at a lower extent) depends on the state of convergence, all the algorithms, except AVPI, propose a diffusivity varying as the calculation proceeds.

TABLE 2.2 – Coefficient of "Diffusivity for the Pressure" (Γ_p)

Algorithm	Steady-State	Unsteady State
SIMPLE SIMPLER PISO	$a/(\rho\,\Delta V/\Delta t + S_P^{U_P})$	$a\,/\,(A_P^{U_P} + \frac{\rho\Delta V}{\Delta t})$
SIMPLEC	$\alpha_u a\,/\,[\sum_{nb} A_{nb}^{U_P}(1-\alpha_u) + S_P^{U_P}]$	$\alpha_u a\,/(\sum_{nb} A_{nb}^{U_P} + S_P^{U_P})$
AVPI	------	$a\Delta t/\rho\Delta V$

The diffusivity of the pressure indicates the terms in the momentum equation through which the pressure correction and the momentum equations are actually linked: the Γ_p of SIMPLE, for instance, involves the totality of the terms, whereas in AVPI the link is made exclusively through the transient term. The former may be more exact but this does not necessarily imply a superior convergence of the algorithm, it may happen that these terms are also paths for transmission of instabilities (originating in other equations) to the pressure correction equation, which subsequently leads to deterioration of the pressure convergence and probably the convergence of the whole procedure.

Although the diffusivity coefficients are identical between SIMPLE, SIMPLER and PISO, the entire equation for P' or P" are different and this certainly influences performance. Among the various pressure and pressure correction equations, the pressure equation of SIMPLER, [2.35], is the most accurate (neither the A_{nb} terms nor the source term of the momentum equations have been neglected). The SIMPLER method contains in both the coefficients of the Poisson equation and the

right hand side contributions from both convective and diffusive effects. In the derivation of the pressure correction equations (except the 2nd pressure correction of PISO, [2.37]), the neglect of the difference between the summation terms transforms the right hand side into a mass balance emanating from convective effects only. The diffusivity however remains as in SIMPLER. This seems to be inconsistent and the pressure diffusivity should perhaps also only be influenced by convection.

It was mentioned earlier that the neglect of the summation terms $\Sigma A_{nb} U_{nb}$ was required for numerical convenience reasons. Taking the derivation of SIMPLE as an example, if this simplification had not been made, and each of the velocities appearing in the $\Sigma A_{nb} U_{nb}$ (in equations [2.25] and [2.26]) replaced by the corresponding momentum equation one would have ended up with a pressure correction equation involving all the pressure cells in the integration domain. This is how the pressure transfers the information and demonstrates its elliptic nature. In the present case, where the $\Sigma A_{nb} U_{nb}$ terms are discarded, the elliptic nature of the pressure still appears since a system of equations simultaneously involving all the cells is solved; however this "ellipticity" is reduced since the coupling between each pressure cell is made only through its closest neighbours and the pressure acquires a local character, rather than being extended over the whole integration domain. The pressure correction of PISO (equation [2.37]) improves this by calculating the $\Sigma A_{nb} U_{nb}$ terms, including them in the source term, but in an explicit fashion, again for numerical convenience. To summarize, we conclude that the neglect of the summation terms reduces the elliptic nature of the pressure, and coupling between the pressure cells, and transforms what would otherwise have been a difference between two Poisson equations for the pressure into a local requirement of conservation of mass emanating from convective effects only.

The under-relaxation factor (and the time-step)

Usually, under-relaxation is only said to be necessary to reduce the rate of updating the variables and secure convergence, due to the nonlinearity and coupling between the equations. This, immediately suggests that to speed up convergence, the under-relaxation factor should be as high as the convergence allows. However, higher under-relaxation factors may require more sweeps and this may result in increased computing time. The actual mechanism through which the under-relaxation works can be observed in the equation below (analogue to [2.22]).

$$A_P \phi_P = \alpha \left(\sum_{nb} A_{nb}^{\phi} \phi_{nb} + S^{\phi} \right) + (1 - \alpha)\, A_P^{\phi} \phi_P^0$$

The under-relaxation reduces the contribution of the neighbouring values, ϕ_{nb}: the domain of influence is restricted and the new value of ϕ_p tends to be more a function of the old and local $\overset{0}{\phi_p}$ than a function of its neighbouring values, as α decreases.

Recalling the previous derivation of the pressure correction equations, an interesting and important point èmerges, this time related to the pressure-velocity coupling. It can be seen that the validity of neglecting terms such as $\Sigma A_{nb} U_{nb}$ in the pressure correction equations is a function of the under-relaxation factor of the velocities, α_u; the approximate pressure correction equations tend to be more in "error" as α_u increases, since the relative weight of the neglected terms increases with α_u. Therefore, it is not surprising if algorithms with more accurate pressure correction formulations (as PISO and SIMPLER) can sustain higher values of α_u. Note that SIMPLER and PISO consider $\Sigma A_{nb} U_{nb}$, although in an explicit manner. A similar line of reasoning can be followed to conclude that the AVPI formulation is less in error at low Δt values. Patankar [1980] has recommended the under-relaxation of the pressure but the above arguments show that this may be needed only at high α_u, as an artifice to avoid the collapse of the pressure-velocity formulation. Algorithms such as SIMPLER and PISO will still need it, though at higher under-relaxation factors of the velocity. Further, it is expected that as α_u increases, the pressure will need to be more under-relaxed and this roughly agrees with the arguments of Van Doormaal and Raithby [1984] supporting the derivation of the SIMPLEC algorithm and the conclusion of Peric [1986] that in SIMPLE the best convergence is obtained using

$$\alpha_p = 1 - \alpha_u \qquad [2.48]$$

Note how the contribution of $\Sigma A_{nb} U_{nb}$ is reduced as α_u increases in the velocity correction formula of SIMPLEC (equation [2.34]) and this is why the need to under-relax the pressure in its updating stage in this algorithm is removed.

The discussion above has focussed on the difference between the summation terms of the momentum equations, but there are a variety of conditions where the difference between the source terms of the momentum equations may be significant and this simplification may also be responsible for a slow convergence. For instance, it has been mentioned that the source term may be used as a receptacle for other terms in the original partial differential equations. Some of these terms are, for example: the centrifugal forces of the momentum equations in polar coordinates, the extra diagonals of the matrix of coefficients generated by the QUICK differencing scheme or even the boundary conditions can also be introduced through the source term. The conditions above can also impair the accuracy of the pressure correction equation and the arguments used to justify the under-relaxation, if repeated here, lead to the conclusion

that even the second pressure correction of PISO is in "error" and under-relaxation of the pressure may still be required. These arguments contradict those presented in the original paper of PISO (Issa [1986]).

From a strictly numerical point of view and leaving aside the accuracy of the pressure-velocity formulation, it is a sufficient condition for convergence of the TDMA algorithm (Patankar [1980]) that:

$$|A_P| > \sum |A_{nb}|$$

i.e. for an under-relaxed equation:

$$|A_P| > \alpha \sum |A_{nb}|$$

and the condition for convergence of the TDMA becomes more true by reducing the under-relaxation factor. Also in the case of $A_P = \Sigma A_{nb}$, the need for $\alpha < 1$ is reinforced. The same arguments can be extended to the case of an implicit unsteady formulation, to show that the reduction of the time-step can be used as a means of re-establishing the diagonal dominance of the matrix of coefficients. Or better still, every argument under the present heading is expected to hold for unsteady formulations with the role of α played by the time-step, Δt.

The solver (TDMA)

In a single global iteration, a considerable portion of time is spent solving the equations. This time depends on the number of sweeps of the TDMA, which is a function of the level of accuracy required. This is the result of a compromise, because why solve the equations to a very high accuracy within a global cycle when the coefficients will be changed in the next cycle? A minimum level of accuracy (particularly in the pressure equations) may have to be achieved to secure convergence, but beyond that more accurate solutions will be unnecessary. The minimum level of accuracy seems to depend on the algorithm, since more elaborate pressure-velocity formulations appear to require more accurate intermediate solutions. For instance, Issa [1986] noticed that the success of PISO depended on the accuracy to which the pressure correction equations were solved, and Van Doormaal and Raithby [1984] attributed the problems of convergence with SIMPLER to the computer round-off. Further, if a minimum level of accuracy has to be achieved the number of sweeps required in TDMA will depend on how good the initial field is as a guess; this depends on the rate of updating of the

coefficients (i.e. the rate of updating of the variables) which is set in the first instance by the under-relaxation factors and as the under-relaxation factor increases, more sweeps are likely to be needed. The advantage of more efficient solvers may only show at high under-relaxation factors and with more elaborate pressure-velocity formulations, when the proportion of time spent solving the equations increases. In the present work, the actual level of minimum accuracy required was evaluated by first performing calculations with a variable number of sweeps in TDMA.

The influence of some parameters on the convergence of the calculations has ben discussed. The study of convergence by analytical means is impossible and this has been a qualitative discussion. The only way to confirm the trends and relationships mentioned above is via numerical experimentation, i.e. to change the parameters and see how they actually affect the convergence. This is the objective of the following section, which deals with one of the test cases used in the current work.

2.4 THE CONVERGENCE OF THE CALCULATION PROCEDURE (Case Study 1 - Two-Dimensional Flow Over an Obstacle)

The flow over an obstacle attached to a flat plate was selected as representative of re-circulating flows in general; the existence of a recirculation region with a separation point not dependent on the Reynolds number is one of the reasons why this geometry and the simpler backward facing step are the more common geometries used in studies of separated flows (see Simpson [1985] for a review). A second test case (three-dimensional) was also used to assess the performance of the various pressure-velocity formulations but this is included in the following chapter, Chapter 3.

This section is made up of three subsections. Subsection 2.4.1 specifies the test case, including the domain of integration, the numerical grid and the boundary conditions; the set of equations to be solved has been presented in Section 2.2. The presentation and discussion of the results are included in subsections 2.4.2 and 2.4.3, which deal with results obtained with the QUICK and the HYBRID schemes, respectively.

2.4.1 Solution Domain and Boundary Conditions

The flow conditions to be simulated are those corresponding to the experimental work of Crabb, Durão and Whitelaw [1981]. The domain of integration is shown in Figure 2.2. The distance downstream of the obstacle was such that the length of the recirculation region in the wake of the obstacle was not influenced by the boundary conditions used at the outlet section ($\partial\phi/\partial x = 0$). The inlet section was located at a position where the pressure coefficient along the bottom wall was not affected by the

presence of the obstacle; the precise location was based on the experiments of Good and Joubert [1968] in a similar flow.

Inlet and outlet boundary conditions

At the inlet, a boundary layer with a thickness of δ = 0.55 h was specified. The free stream values of mean longitudinal velocity and turbulence intensity were 18 ms^{-1} and 0.6%. The precise inlet conditions (see Table 2.3) follow from an assumption of a 1/7th power law for the boundary layer profile (Schlichting [1968]) and local equilibrium of the turbulence.

TABLE 2.3 – Boundary conditions at the inlet section

	$Y \leq \delta$	$Y > \delta$
U	$U_0 \left[\frac{Y}{\delta(\dot{x})}\right]^{1/7}$	U_0
V	$U_0 \left[\frac{Y^8}{\delta(\dot{x})}\right]^{1/7} \frac{1}{10\dot{x}}$	0
k	$\frac{l_m^2}{\sqrt{C_\mu}} \left[\frac{U_0}{7\,\delta(\dot{x})\;Y^6}\right]^{2/7}$	$\frac{3}{2} U_0^2 \left(\frac{\sqrt{\overline{uu}}}{U_0}\right)^2$
ε	$C_\mu^{3/4} \frac{k^{3/2}}{l_m}$	$\frac{k^{3/2}}{H}$

l_m = mixing length $\begin{cases} l_m = \kappa Y \quad , \quad Y \leq C_\mu \delta \\ l_m = C_\mu \delta \quad , \quad Y \geq C_\mu \delta \end{cases}$

$\dot{x}$ = longitudinal distance measured from the boundary layer origin:

$$\delta(\dot{x}) = 0.37\, \dot{x} \left(\frac{U_0 \dot{x}}{\nu}\right)^{-1/5}$$

A zero axial gradient was specified at the outlet section for all the variables.

Walls

For cells adjacent to the walls, the so-called wall function approach (Launder and Spalding [1974]) was used; this removed the need for very fine grids to resolve the high gradients of this region. Further, the version of the turbulence model used (see Section 2.2) does not account for the low turbulence Reynolds number characteristics of the wall regions. The diffusive flux of momentum in the direction perpendicular to the walls (i.e. the wall shear stress) is calculated via a modified form of the viscosity:

$$\tau_W = \mu_W^* \frac{U_P}{Y_P}$$

where:

$$\mu_W^* = \frac{\rho C_\mu^{1/4} k_P^{1/2} \kappa Y_P}{\ln\left(\frac{E Y_P C_\mu^{1/4} k_P^{1/2}}{\nu}\right)} \qquad [2.49]$$

This latter treatment assumes that the node adjacent to the wall is in the fully turbulent region (log-law region (Schlichting [1978]) of the boundary layer and the turbulence is in equilibrium. The constants E and κ were given values of 9.0 and 0.43 appropriate to smooth walls. The subscript P refers to the value of the variables in the node adjacent to the walls.

For the turbulence quantities k and ε, the wall function relations used were:

$$P_k = \frac{\rho k_P U_P C_\mu^{1/2}}{Y_P \ln\left(\frac{E Y_P C_\mu^{1/4} k_P^{1/2}}{\nu}\right)} \qquad [2.50]$$

and:

$$\varepsilon = \frac{C_\mu^{3/4} k_P^{3/2}}{\kappa Y_P} \qquad [2.51]$$

Equation [2.50] replaces the production term in the transport equation for k and the value of ε was set according to equation [2.51].

Since the obstacle protruded into the solution domain, all variables in cells covered by the obstacle were set to zero. Because of the staggering of the grid, the boundaries of the velocity cells do not lie along the limits of the obstacle (see Figure 2.3); a gap (the shaded area in Figure 2.3) exists along the vertical and top walls of

the obstacle in the case of U and V velocity cells, respectively. These gaps were accounted for by considering them as an increase of the area of the cells still inside the domain. The influence of this treatment was not assessed, but previous studies (e.g. Castro [1979], McDonald [1979]) reported that the neglect of this effect may lead to considerable errors, particularly near the corners of the obstacle.

Numerical grids

A grid of 25 x 22 grid nodes was used in the present calculations. As the majority of the grids included in this thesis, it was generated by the formula below, from Sundqvist and Veronis [1970]:

$$h_i = h_{i-1}\left[1 + \frac{\alpha}{L}\left(\frac{L - x_i}{L}\right)^{\beta} h_{i-1}\right] \qquad [2.52]$$

where h is the spacing between nodes, L is the distance along which the grid is distributed, x is the location of the node, and α and β are parameters to control the expansion of the grid. The use of this formula follows from the considerations about the use of non-uniformly spaced grids, in subsection 2.2.2; this equation was used because, unlike the common geometric expansion, it enabled the control of the maximum spacing between nodes.

2.4.2 Results with the Upwind Quadratic (QUICK) Scheme

Previous experience with the QUICK differencing scheme (Han, Humphrey and Launder [1986], and Papadimitriou [1986]) has shown that, in some cases, especially with coarse grids, convergence is not possible. Because of this, in the present calculations, QUICK was used only in the inner cells of the integration domain and, in the case of k and ε, only in cells with a Peclet number less than two; the upwind scheme was used in the rest of the domain. Also, to secure the convergence of the TDMA algorithm, the negative coefficients of the discretised transport equations using QUICK were written in an explicit form and stored in the source term. The possible implications of this technique on the convergence of the calculations has been referred to in the previous section.

Other numerical parameters of the calculations in this subsection were: a criterion of convergence based on a mass residual of 10^{-4}, a fixed number of sweeps of the TDMA algorithm [2 sweeps in the momentum, k and ε equations; 20 sweeps for all the pressure correction, or pressure, equations), and under-relaxation factors for k - ε and pressure fixed at 0.25 and 0.5. The high number of sweeps for the pressure equation was used to ensure a very accurate solution of the pressure at each iteration.

Figure 2.4 shows the predicted streamline pattern. The main feature is the presence of a large separated flow, in the wake of the obstacle,bounded by a curved shear layer, features found in many confined turbulent recirculating flows, including those observed in combustors.

Table 2.4 shows a sample set of results obtained under the conditions above.

TABLE 2.4 – Convergence tests with the Quadratic Upwind (QUICK) finite difference scheme - number of iterations

α_u,α_v	SIMPLE	SIMPLEC	SIMPLER	PISO	AVPI Δt[sec.]
0.4	268 (197)	291 (197)	273	——	0.0005 332
0.5	251 (183)	305 (187)	235	277	0.001 238
0.6	————	346 (178)	——	287	0.002 240
0.7	278 (165)	390 (171)	276	314	
CPU/Iteration	0.610	0.610	0.839	0.839	0.610

* Values within brackets are the number of iterations needed to obtain a pressure field similar to the final pressure field by less than 0.5%, whereas the other values correspond to a criterion of convergence based on a maximum mass residual of 10^{-4}.

The most important features of these results are:

1. The number of iterations needed to achieve convergence is very similar; according to some authors (see review in Chapter 1), differences by more than a factor of two were expected. There is a maximum difference of only 56 iterations between the optimum values of each algorithm (i.e. a variation of about 22% relative to an average value of 259).
2. Because a fixed number of sweeps was used, the total CPU time varies linearly with the number of iterations, and SIMPLER and PISO are the most expensive in terms of computing time.

A second convergence criterion (from Van Doormaal and Raithby [1984]) was also used here (the results within brackets in table 2.4). This criterion was less stringent than that based on the mass residual and calculations were assumed as converged in less iterations, but these results also underline the similarity between the number of iterations to reach convergence in all these algorithms.

Figure 2.5 shows the mass residual of the SIMPLE calculations as a function of the number of iterations. Sudden and large variations of the residual are seen to

occur quite late in the convergence pattern, when one might have expected a monotonic behaviour. These large variations were found to be caused by the switching between the two finite difference schemes (QUICK and upwind) in the ε equation, which subsequently affected the mass residual via the momentum equations. This pattern was removed by using the hybrid scheme in all equations (Figure 2.6). All further tests, in the following subsection, were performed under these conditions; the convergence of the various pressure convection algorithms was of main interest here and not the numerical accuracy of the predictions so the abandonment of QUICK in these tests was not crucial.

The use of an unsteady formulation can help but may not fully remove this behaviour, as can be seen in Figure 2.7b. Figure 2.7 shows the continuity error at three different stages of the AVPI algorithm for two values of Δt: after each of the momentum equations (the two curves at higher DSUM values) and after the velocity correction (the curve at the bottom). At the beginning of each time-step, or global iteration, (i.e. after the velocity correction), the continuity error is minimum (the bottom line) and then increases as the U and V momentum equations are solved until the new velocity correction step; this is how the calculations proceed, with the continuity error after the momentum equations being reduced until continuity can be satisfied at any stage of the algorithm. In Figure 2.7b with the lowest Δt (Δt = 0.001 sec), the three curves agree within the computer round-off error, but in Figure 2.7a (Δt = 0.002 sec) a small difference persists between the curves. This suggests that some inconsistency exists due to the splitting of the velocity and pressure; this inconsistency increases with the time-step and eventually results in divergence. Figure 2.8 is the extension of Figure 2.7a but with calculations in double precision; it shows that the level of the residuals at 2×10^{-8} in Figure 2.7 is the actual limit of accuracy of the computer in single precision.

A detailed analysis of graphs like the ones presented above should give some insight into the mechanisms of convergence and coupling between the equations. Further work in this direction was begun but was later discontinued because it deviated from the initial objective of testing the performance of alternative pressure-velocity formulations. This work is not reported here, but posed some interesting questions and is believed to be an area worthy of further research.

2.4.3 Results with the Hybrid Scheme - Comparison of PISO and SIMPLE

As mentioned above, further calculations were restricted to the hybrid scheme. There was interest in comparing the computational efficiency of both steady-state and unsteady formulations and, to reduce the number of cases tested, the algorithms

SIMPLER and SIMPLEC were not used further. PISO and SIMPLE were selected as representative of algorithms with one or two pressure equations, respectively.

PISO and SIMPLE in unsteady formulations

Figure 2.9 shows the results of PISO and SIMPLE in unsteady formulation. The pressure correction equations were solved with a variable number of sweeps until the residual was less than 10% of its initial value; a fixed number of sweeps (2) was used for all other equations. PISO enables higher time-steps before divergence occurs and, comparing the optimum values, it is faster than SIMPLE by 40%. The pressure was under-relaxed by 0.5 in both algorithms; this being the optimum value according to the results of Figure 2.10 performed at a constant Δt (see below).

It has been recommended (Issa [1986]) that the pressure correction equations be solved to a minimum tolerance of 10%, as above, to ensure that the coefficients of the discretised equations satisfy continuity and the calculations do not diverge. However, Figure 2.11 does not support these arguments. The top curve is the same as in Figure 2.9, obtained with a variable number of sweeps for the pressure to reduce the residual to a level below 10% of the initial residual, whereas the bottom curve corresponds to a calculation with only 2 sweeps for the pressure. In this case, though a few more iterations are required (see number of iterations near the lines), because the time for solving the pressure is substantially reduced, the overall CPU time is also reduced. These results also raise doubts on the need for more efficient methods to replace the TDMA algorithm for solving the pressure equation as a means of reducing the global computing time.

The following calculations, therefore, were all made with 2 sweeps for the pressure correction equations.

PISO and SIMPLE in steady-state formulations

Figure 2.12 shows how SIMPLE and PISO behave in steady-state formulation with varying under-relaxation factors in the transport equations. The under-relaxation factor for the pressure was 0.5. PISO can sustain higher values of α without diverging and is eventually 12% faster than SIMPLE. If all the under-relaxation factors are changed (including that for pressure (Figure 2.13)), the convergence of PISO is improved and PISO is 30% faster than SIMPLE. This value is very similar to the best obtained with unsteady formulations and this shows the equivalence between the two formulations also in terms of the computational efficiency. Results obtained with QUICK are also shown in the Figure 2.13 as an example of the restricted range of α where convergence can be obtained.

All the previous reported work (see review in Chapter 1) has tested the robustness of the algorithm by varying the under-relaxation factors, but whether with a fixed or varying under-relaxation of the pressure; is not usually mentioned. Here, the joint influence of the two under-relaxation parameters is shown in the form of contour maps (Figures 2.14 and 2.15). Tests were performed by changing the under-relaxation of the pressure (the horizontal scale) and the under-relaxation of all the other equations (the vertical scale) independently in steps of 0.1; the contours indicate the number of iterations needed to obtain convergence. It is evident in Figure 2.15, with SIMPLE tests , that as α_u increases, to secure faster convergence, the under-relaxation factor of the pressure has to decrease, this fully supports the arguments in subsection 2.3.2. Although not strictly following the relationship $\alpha_p = 1 - \alpha_u$, this is a good rule of thumb. In the case of PISO (Figures 2.14) there does not seem to be any obvious relationship between α_u and α_p and the area where divergence occurs is smaller which proves its higher robustness. Both algorithms, SIMPLE and PISO, required the under-relaxation of the pressure.

2.4.4 Conclusions

Calculations with the upwind quadratic scheme showed that, for the present problem SIMPLE, SIMPLEC, SIMPLER, PISO and AVPI all converged in a similar number of iterations.

In tests with the hybrid scheme, using PISO and SIMPLE, the steady and unsteady formulations were found to be equivalent in terms of computational efficiency. PISO is more robust than SIMPLE and can sustain both higher time-steps and under-relaxation factors; this suggests that the beneficial effect of the second pressure correction of PISO occurs only after SIMPLE has diverged. The advantages of PISO are shown only under these conditions and its best result was about 30% faster than SIMPLE. Previous claims of improvements of PISO relative to SIMPLE by a factor of 6, as in Benodekar, Goddard, Gosman and Issa [1984], may have resulted from non-optimization of the numerical parameters and should not be considered as representative.

In the region where both algorithms can converge, the number of iterations is identical. A minimum number of global iterations is needed at each time-step and the accuracy of the pressure correction equation alters this very little; updating of the coefficients is basically what is needed, and the nonlinearity and coupling of the equations are the main reasons for delayed convergence.

2.5 SUMMARY

The fundamentals of the mathematical models and numerical techniques to be used for the calculation of the non-reacting flow inside gas turbine combustors were introduced and accompanied by brief discussions of the limitations of both the turbulence model and the numerical procedure.

The calculation procedure was described, and the nature of the coupling between the continuity and momentum equations (pressure and velocity) discussed in detail. Various alternatives for the treatment of this coupling were discussed and their computational performance assessed via a case study: the two-dimensional flow over an obstacle attached to a flat plate. Results obtained with five different algorithms (SIMPLE, SIMPLEC, SIMPLER, PISO and AVPI) and a quadratic upwind finite difference scheme revealed that all the algorithms required a similar number of iterations to converge. More detailed tests, restricted only to PISO and SIMPLE, and the hybrid finite difference scheme, showed that PISO could sustain higher under-relaxation factors and time-steps before diverging; a maximum improvement of 30% in terms of CPU time relative to SIMPLE could then be achieved. Before concluding that the performance described here is generally applicable it requires confirmation in three-dimensional flows typical of those found in combustors; this is one of the topics of the following chapter.

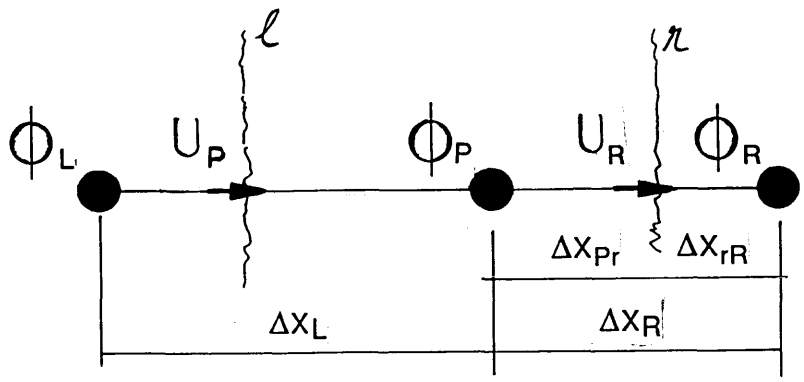


FIGURE 2.1 – Control volume for one dimension.

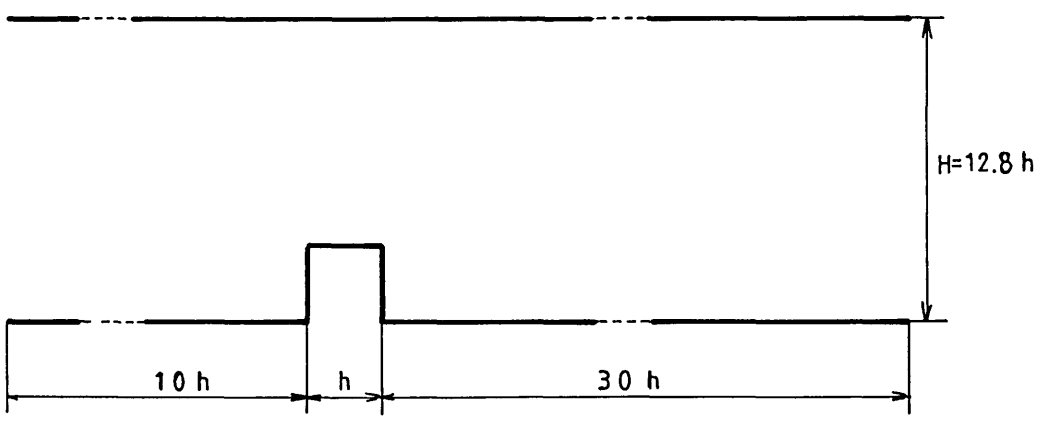


FIGURE 2.2 – Domain of Integration.

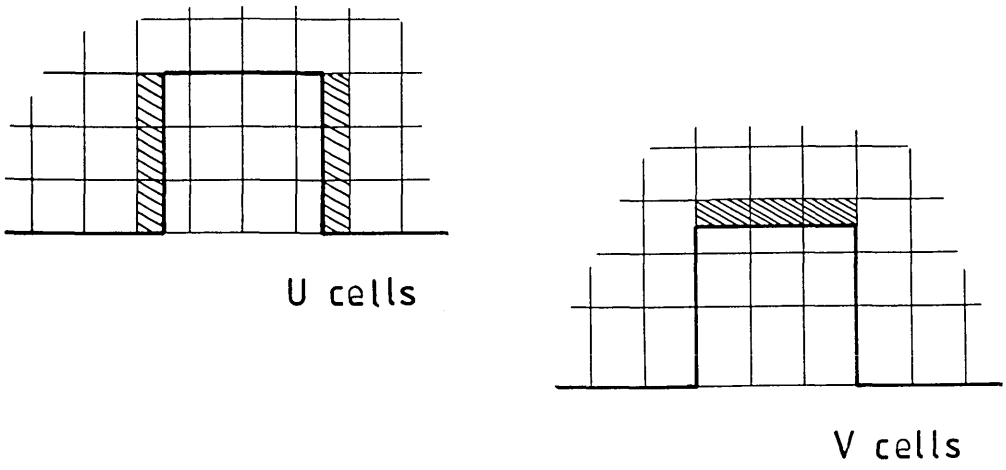


FIGURE 2.3 – Staggered cells around the obstacle.

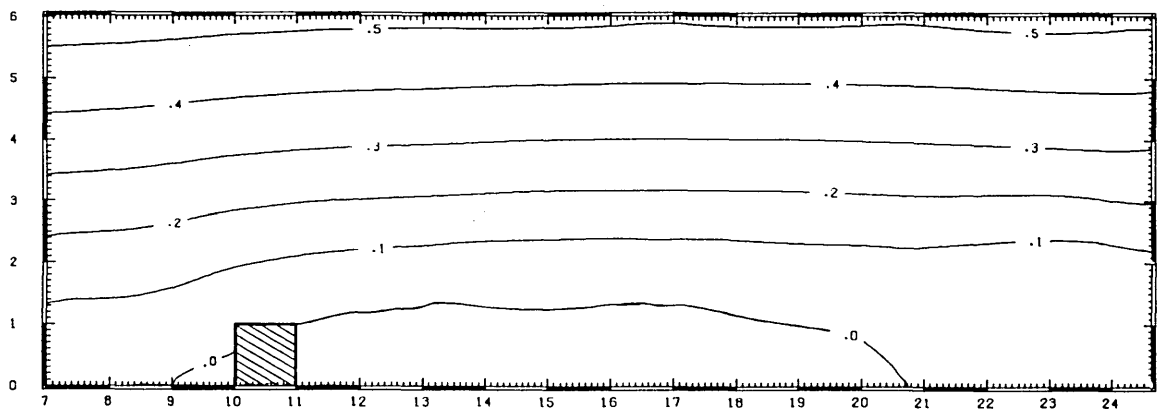


FIGURE 2.4 – Streamline pattern in the proximity of the obstacle.

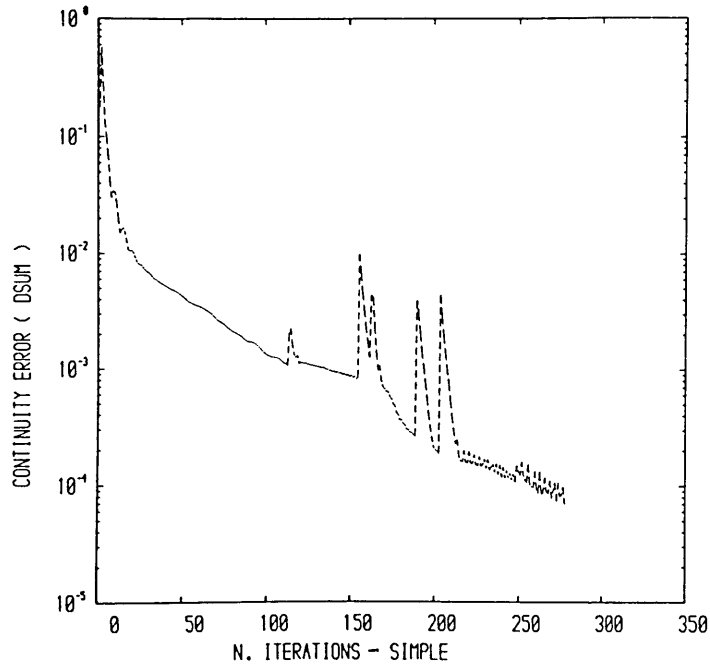


FIGURE 2.5 – Convergence behaviour of SIMPLE using QUICK difference scheme.

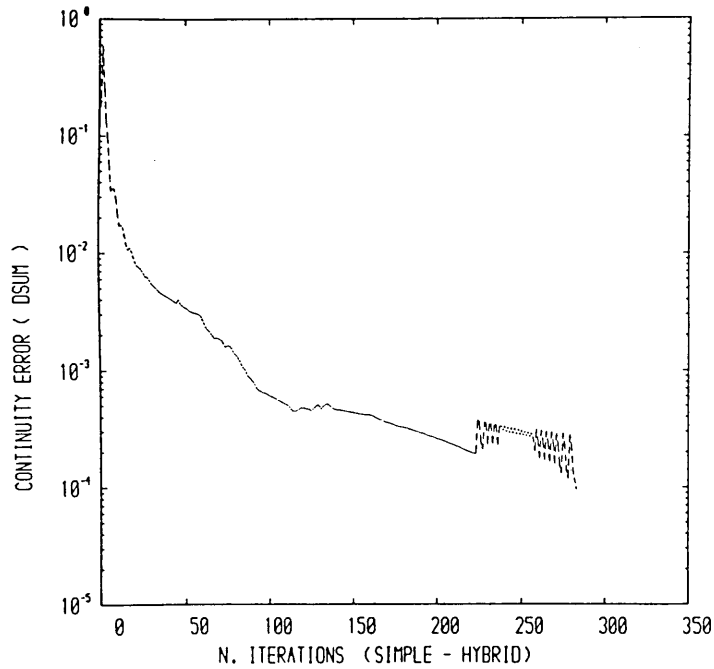


FIGURE 2.6 – Convergence behaviour of SIMPLE using hybrid difference scheme.

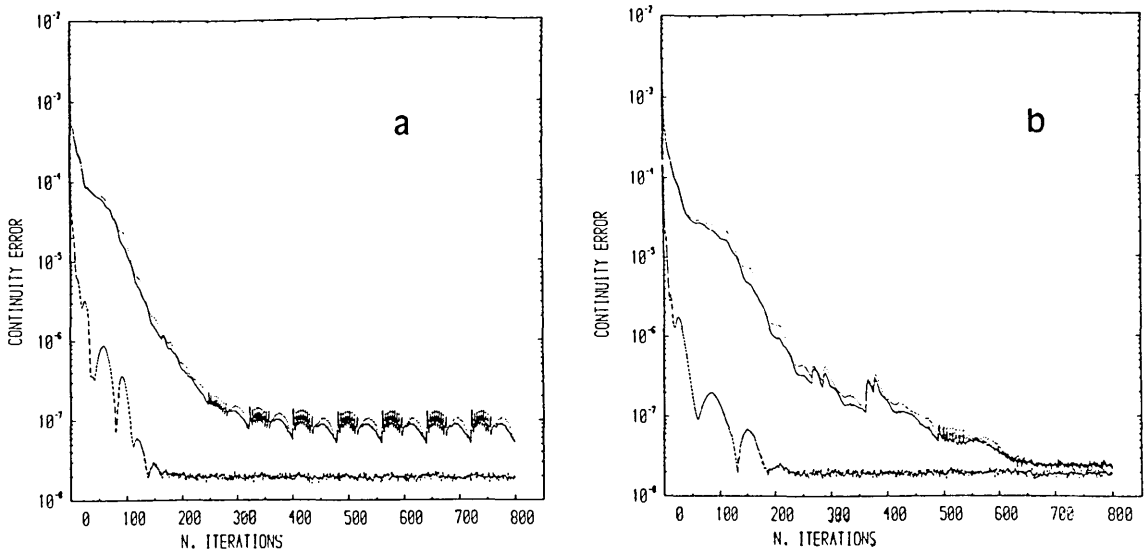


FIGURE 2.7 – Convergence behaviour of AVPI using QUICK difference scheme for two different time steps: a) Δt = 0.002 sec; b) Δt = 0.001 sec.

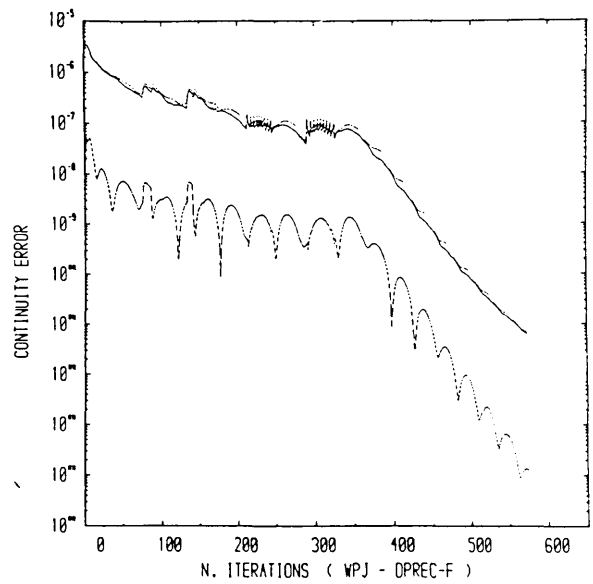


FIGURE 2.8 - Convergence behaviour of AVPI using QUICK difference scheme - calculations in double precision (Δt=0.001 sec) (vertical scale from 10^{-15} to 10^{-5})

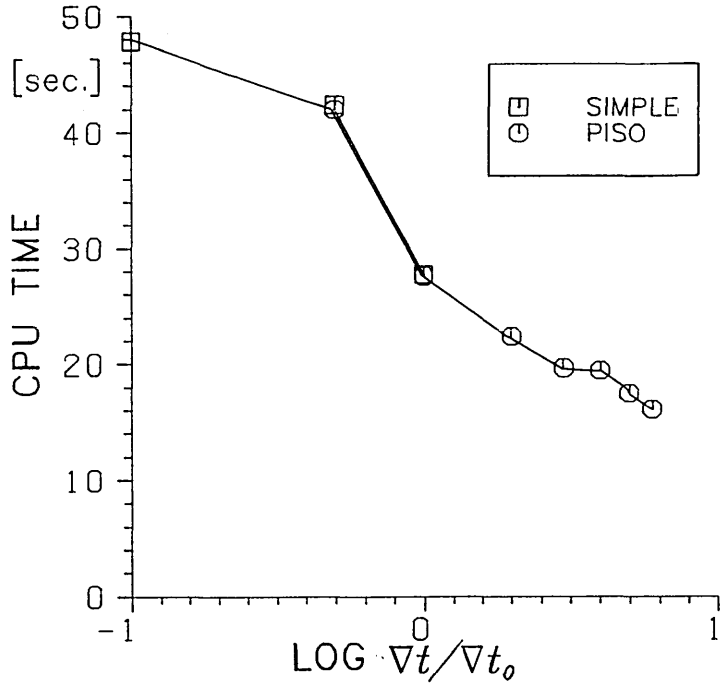


FIGURE 2.9 – SIMPLE and PISO in unsteady formulation with a criterion of convergence of the pressure of 10% (Δt_o = 0.001 sec).

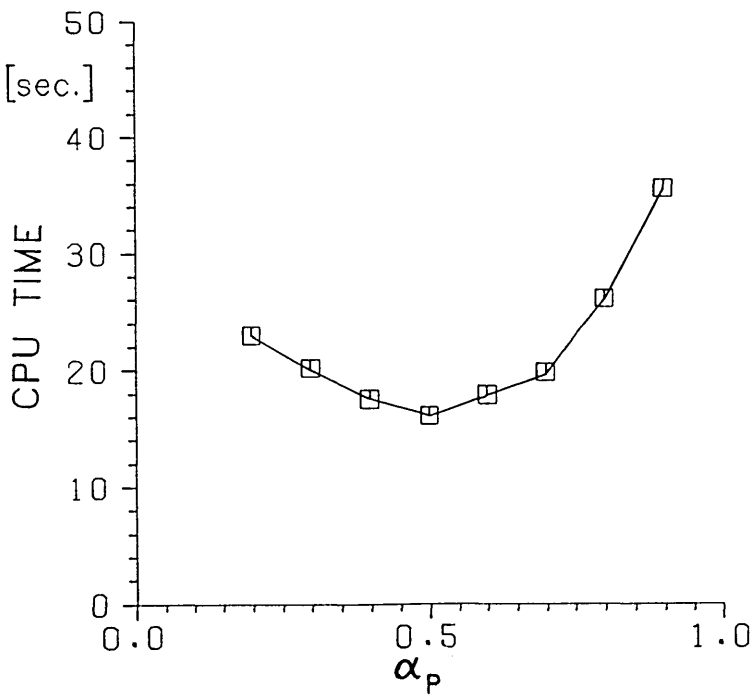


FIGURE 2.10 – Influence of the under-relaxation of the pressure in PISO unsteady formulation (Δt_o = 0.001 sec).

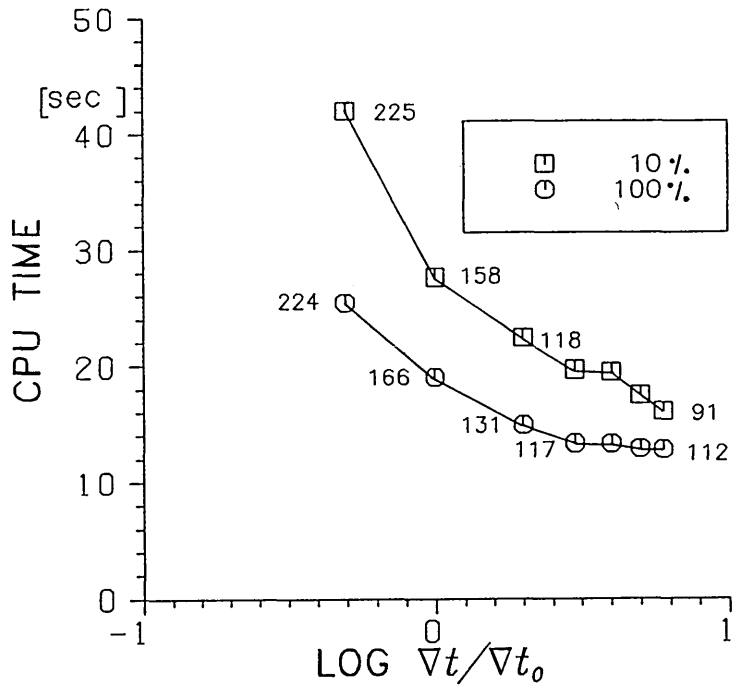


FIGURE 2.11 - Influence of the criterion of convergence of the pressure in PISO unsteady formulation (Δt_o = 0.001 sec) - number of iterations needed to reach convergence near the lines.

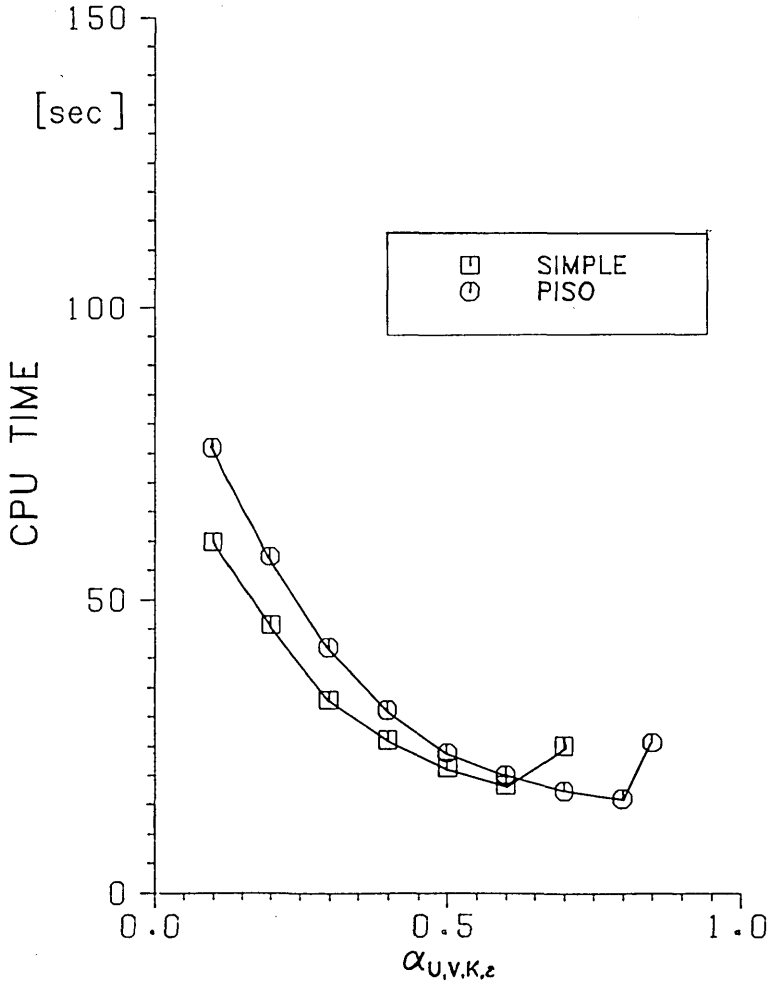


FIGURE 2.12 - The convergence of SIMPLE and PISO as a function of the under-relaxation factors (the under-relaxation for pressure was kept constant and equal to 0.5).

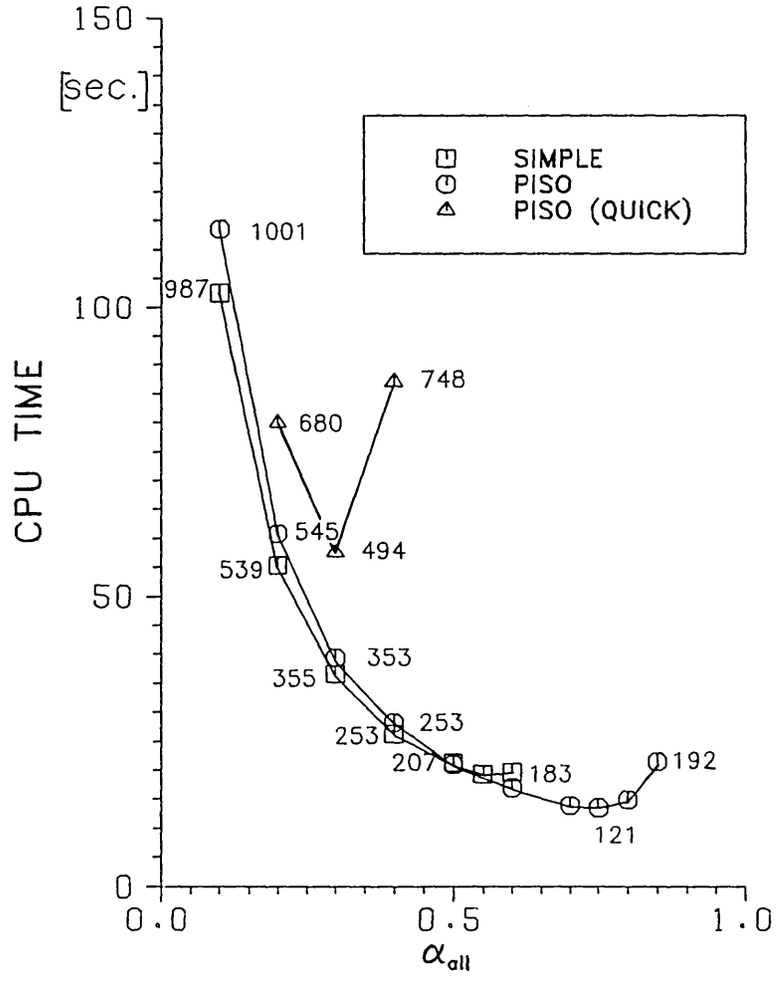


FIGURE 2.13 – Identical to Figure 2.12 but with the under-relaxation for pressure also being changed.

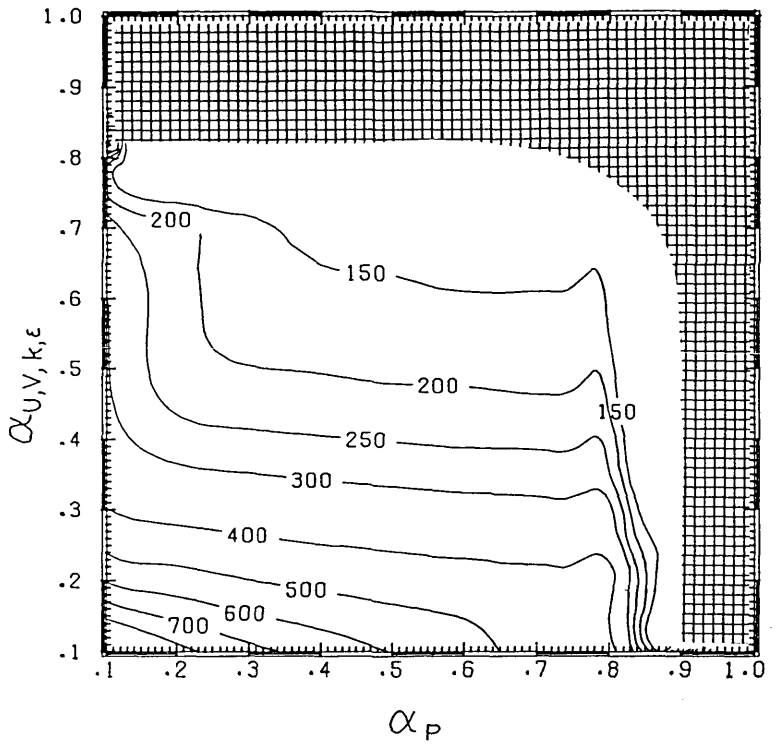


FIGURE 2.14 - Map of convergence of PISO - contours of identical number of iterations to reach convergence.

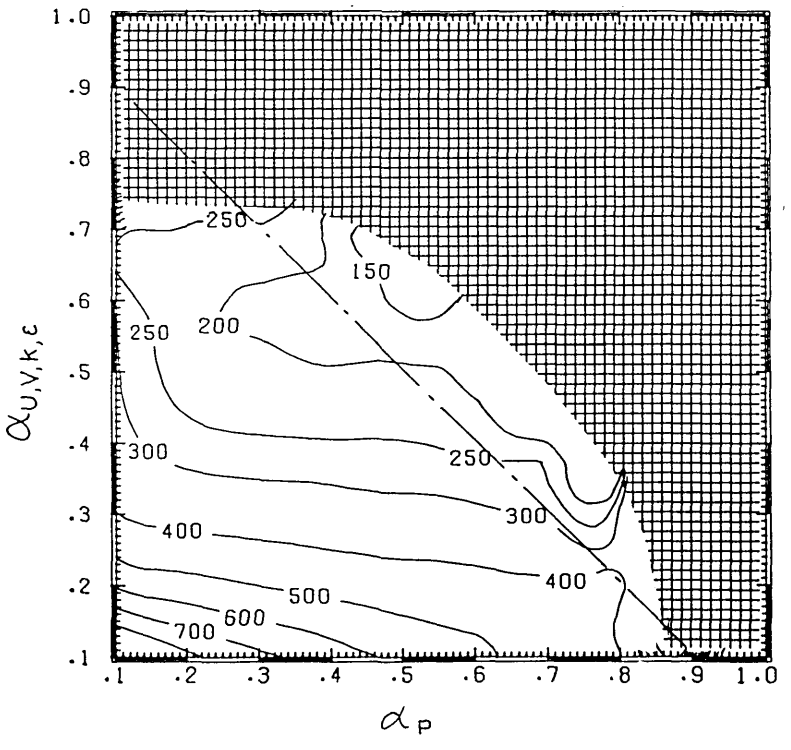


FIGURE 2.15 - Map of convergence of SIMPLE - contours of identical number of iterations to reach convergence.

CHAPTER 3
CALCULATIONS OF THE DILUTION SYSTEM IN AN ANNULAR COMBUSTOR GEOMETRY

3.1 INTRODUCTION

3.1.1 Objectives and Outline of the Chapter

The work in this chapter, the calculation of the flow in a dilution zone system, is a consequence of the previous studies of Koutmos [1985] and McGuirk [1984]. Koutmos observed, in his calculation of a can-type combustor flow, better results (compared with experiments) in the combustor primary zone than in the dilution zone; similarly, the results of preliminary calculations (McGuirk [1984]) of an isolated dilution zone system failed to show the correct location of the hot spots at the outlet section. An important question arises of whether there are some problems specific to the prediction of dilution zones; any successful calculation procedure clearly has to predict correctly the main features at the outlet of the combustor and this chapter addresses this important issue. A second objective of the study discussed here was to follow up the work presented in Chapter 2 on the relative performance of numerical algorithms for solution of the fluid flow equations. It is important that checks are made in realistic three-dimensional flows to ensure that the conclusions drawn from tests in a two-dimensional geometry are valid also for combustor type flows.

The mathematical model and the calculation procedure have been previously described (in Chapter 2) and in this chapter only the results of the calculations of the flow inside an annular dilution zone system are presented. The chapter is made up of two main sections. Section 3.2 includes the results of convergence tests using the SIMPLE, PISO and AVPI algorithms. Section 3.3 is more concerned with the physics of the problem and discusses the results of both constant and variable density calculations; some restricted comparisons with measurements are also made. The chapter ends with a short section, Section 3.4, containing the main conclusions.

The following subsection describes the geometry and the boundary conditions used.

3.1.2 Domain of integration

The experimental geometry (Shaw [1981]), Figure 3.1, consisted of an annular duct followed by a convergent nozzle. The annulus contained a total of 48 equally spaced directly opposed holes (equally divided between outer and inner wall). For numerical

simulation, a cylindrical polar system of coordinates was used with the longitudinal axis aligned with the engine axis, and depending on the boundary conditions, the domain of integration was extended over a circumferential sector of either 15° or 7.5°.

Holes and nozzle

The holes were approximated by cells of rectangular shape (see Figure 3.2). The fluid density for the cells inside the hole was multiplied by the ratio between the area of the hole and the total area of the cells inside the hole, to guarantee similar numerical and experimental flow rates. An initial procedure, where only the density of the cells on the edges of the hole was corrected, produced erroneous values in the region near the holes and was abandoned.

The sloped walls of the nozzle, like the holes, could not be followed by the present system of coordinates and were simulated in a castellated (staircase) fashion. In this approximation, the gaps between the velocity cells and the actual boundary of the staircase approximation, set by the scalar cells, have been neglected, contrary to subsection 2.4.1.

3.1.3 Boundary Conditions

The experiments of Shaw [1981] provided information on the flow rate and mean temperature of the flow in both annulus and hole flows (see Figure 3.3); this enabled the evaluation of the normal velocities. In the first predictions made, the other components of velocity were set to zero. The turbulence kinetic energy and its dissipation were set to 1.75×10^{-2} m^2s^{-2} and 7.694×10^{-3} m^2s^{-3}, respectively. For these conditions, a circumferential sector of 7.5° was used with symmetry conditions on the two extreme constant θ planes (case 1 in Table 3.1). The measurements of Shaw indicated, however, that the above conditions are probably too simplistic; in particular, the measurements showed an inclination of the jets with respect to the hole geometric axis. Averaging of the measurements of these jet angles leads to the values shown in Figure 3.3, which enabled the use of more accurate boundary conditions in the holes, with both axial and swirl velocities specified as well as the radial inflow component. In this case (cases 2 and 4 in Table 3.1), a 15° sector was needed, limited by the two longitudinal planes halfway between the jets; cyclic boundary conditions were now implemented on these planes. For both the above cases calculations were carried out assuming constant density. Cases 3 and 4 in Table 3.1 correspond to case 2 but now consider the variation of density.

The simplicity of the boundary conditions in the holes, with constant values specified in the hole surface for all the variables, contrasts with more elaborate treatments used in some calculations of jets in crossflow geometries (see review in

subsection 1.4.2 and the hole boundary conditions used in the case of the calculations of the flow inside a can-type combustor in Chapter 5), however in the present application this was considered as satisfactory, since the values were based as far as possible on experimental information.

TABLE 3.1 - Boundary conditions of the annular dilution system and momentum flux and velocity ratio between the jets and the annular flow

	Annulus	Inner Jet	Outer Jet		
Case	U V W	U V W	U V W	M_{ratio}	V_{ratio}
1	10.88 0 0	0 67.22 0	0 -75.53 0	42.7	6.5
	ρ=1.1774	ρ=1.1774	ρ=1.1774		
2	10.88 0 0	13.29 67.22 -0.90	20.93 -73.53 1.80	42.7	6.5
	ρ=1.1774	ρ=1.1774	ρ=1.1774		
3	32.42 0 0	0 90.84 0	0 90.19 0	18.6	2.8
	ρ=0.3871	ρ=0.8711	ρ=0.9599		
4	32.42 0 0	-17.96 90.84 -1.27	25.31 90.19 2.20	18.6	2.8
	ρ=0.3871	ρ=0.8711	ρ=0.9599		

• All runs with $k = 1.750 \times 10^{-2}$ m^2s^{-2} and $\varepsilon = 7.694 \times 10^{-3}$ m^2s^{-3}
$T_{annulus}$ = 900 K, T_{inner} = 363 K and T_{outer} = 400 K.
M_{ratio} - momentum flux ratio between the jets and the crossflow
V_{ratio} - velocity ratio between the jets and the crossflow

The cells adjacent to the plane walls were treated by the wall functions in the same manner as described in subsection 2.4.1. The boundary conditions in cells along the staircase approximation were zero convective and diffusive fluxes without using wall functions.

At the outlet section, a zero axial gradient was used as the boundary condition for all the variables and this led, relative to the experimental rig, to a plane extension duct at the nozzle exit to avoid the propagation of this 'artificial' boundary condition into the internal flow.

3.1.4 Numerical Meshes

Four numerical grids (Figure 3.4 and Table 3.2) were used. The grids were non-uniform along all the directions and were generated according to [2.52]. The coarsest grid, 17 × 11 × 6, was used to set up the boundary conditions, in the tests of convergence and later to illustrate the effects of insufficient numerical resolution. The two grids, 40 × 30 × 15 and 40 × 30 × 30, were the standard ones; the latter was used for calculations over a 15° sector to maintain a numerical resolution similar to the

case of calculations in a 7.5° sector. The finest grid, 70 × 40 × 25, occupied all the memory available on the computer hardware and was used only as a check on the numerical accuracy of the standard mesh predictions.

TABLE 3.2 - Numerical grids

N.	GRID SIZE [$N_Z \times N_R \times N_T$]	N. OF NODES	N. OF CELLS HOLES	N. OF CELLS NOZZLE†	N. OF CELLS %TOTAL	L/N_Z [mm]	R/N_R [mm]	T/N_T [degr]
1	17 × 11 × 6	1122	19	192	17	14.7	10.2	1.3
2	40 × 30 × 15	18000	121	2250	13	6.3	3.7	0.5
3	40 × 30 × 30	36000	228	4500	13	6.3	3.7	0.5
4	70 × 40 × 25	70000	282	9525	14	4.0	2.8	0.3

† - number of cells outside the domain
N_Z, N_R, N_T - number of nodes along the axial, radial and circumferential directions
L, R, T - dimensions of the integration domain along the three directions above

3.2 THE CONVERGENCE OF THE CALCULATION PROCEDURE (Case Study 2 - The Dilution System of an Annular-Type Combustor)

The conclusions drawn in Chapter 2 with respect to the convergence behaviour of the pressure correction algorithms, although important, emerged from a particular two-dimensional study. To ensure that they are in fact more general, a similar study of the convergence of the dilution zone calculations was also carried out.

3.2.1 Conditions of the Test and Presentation of Results

Three algorithms were used: SIMPLE, PISO and AVPI. The boundary conditions corresponded to case 1 in Table 3.1 and grid 1, in Table 3.2, was used.

The convergence criterion assumed the calculations as converged when the usual normalized mass source residual was less than 5×10^{-4}. The TDMA algorithm was used with five sweeps on the pressure correction equation(s) and two sweeps on all other equations. Preliminary tests showed that 5 sweeps were sufficient to reduce the residual of the pressure correction equation to negligible levels.

Discussion of the results is provided in three main parts. Subsection 3.2.2 compares PISO, SIMPLE and AVPI, and shows the influence of the under-relaxation factors and time step on the rate of convergence. Calculations with a more stringent convergence criterion are presented in subsection 3.2.3. Subsequently, because the convergence of the k and ε equations emerged as controlling the overall rate of convergence, tests were repeated in subsection 3.2.4 without solving the equations of

the turbulence model; a more comprehensive study of the three algorithms is then presented under these conditions, including unsteady formulation of SIMPLE and PISO for a direct comparison with AVPI.

3.2.2 The Convergence of the Complete Set of Equations

3.2.2.1 Relative performance of SIMPLE and PISO

The under-relaxation of all the variables

As a first test, the under-relaxation factors of all variables (α_{all}), including the pressure, were raised from 0.1 until divergence of the calculations occurred. These results are summarized in Figure 3.5. Let us first concentrate on the part of the curve for values of α_{all} higher than 0.3. For the same under-relaxation factor, both algorithms, SIMPLE and PISO, need a similar number of iterations to converge (see numbers near the lines in Figure 3.5) and, because of the extra pressure correction equation, PISO therefore takes longer to converge; its superiority is revealed only for under-relaxation factors above 0.65, when SIMPLE can no longer converge. Ultimately, PISO (α_{all} = 0.88) converges in half the number of iterations and in 68% of the CPU time of the best SIMPLE calculation (α_{all} = 0.65). The computing time for both algorithms is shown in Table 3.3.

TABLE 3.3 - CPU time per iteration (sec)

	Total	Assembling Coefficients	% Total	Solving Equations	%Total	Solving/ Assembling
PISO	0.322	3.997×10^{-2}	12.4	0.282	87.6	7.1
SIMPLE	0.253	3.497×10^{-2}	13.8	0.218	86.2	6.2

Note that more than 80% of the time is spent in solving the equations.

The total CPU time of SIMPLE and PISO is given by:

$$CPU_{SIMPLE} = 0.253\ N_S$$
$$CPU_{PISO} = 0.322\ N_P \qquad [3.1]$$

where N_s and N_p are the number of iterations in SIMPLE and PISO. The total CPU time is a linear function of the number of iterations and PISO can be faster than SIMPLE

only if the number of iterations, N_P, is less than 79% of the number of iterations of SIMPLE, N_S.

The convergence of the absolute sum of the mass residuals nondimensioned by the total inlet flow rate (DSUM) and the maximum mass residual (DMAX) are shown in Figure 3.6 for various values of α_{all}. There is a striking difference between the convergence of calculations with α_{all} higher than 0.4 and α_{all} equal to 0.1; the latter shows a fairly smooth decay of the residuals in contrast to the cases with α higher than 0.4, which display a spiky trend and a sudden drop of the residual in the last iterations. Identical behaviour is revealed by SIMPLE (Figure 3.7). The calculations with an under-relaxation factor of 0.2 did not converge in less than 6000 iterations and were stopped. There seems to be two different routes to convergence with a transition depending on the under-relaxation factor; this is evidenced either by the convergence pattern in Figures 3.6 and 3.7 or the number of iterations as a function of α_{all} in Figure 3.5. The convergence of the calculations with α_{all} lower than 0.3 will be readdressed in subsection 3.2.3.

The under-relaxation of the pressure

The above test is a little artificial since it is not usual to use the same under-relaxation factor for all variables, particularly for the pressure. Calculations were thus made by changing the under-relaxation factor of the pressure only; the relaxation of the other equations was kept constant and at its maximum according to the results above, i.e. α = 0.65 and α = 0.88 for SIMPLE and PISO, respectively. The effect of changing the under-relaxation of the pressure (Figure 3.8) is, however, minimal; in SIMPLE (neglecting the first two points at α_p = 0.1 and α_p = 0.2) there is a reduction of 3% on the CPU time, whereas PISO experiences a reduction of 14%. Both algorithms diverge for under-relaxation of the pressure above the under-relaxation of other equations. The condition [2.48] is therefore not confirmed in these tests.

The under-relaxation of the turbulence kinetic energy and its dissipation

Similar to the tests above, the under-relaxation of all variables was kept constant (0.65 and 0.88 for SIMPLE and PISO, respectively), while the under-relaxation of the turbulence quantities, k and ε, changed (Figure 3.9). The results for SIMPLE could be improved compared to the previous tests (Figure 3.5), where all the αs were changed simultaneously: a maximum value of 0.65 had been possible, but here by maintaining that value and increasing $\alpha_{k,\varepsilon}$ up to 0.80, SIMPLE could even be as fast as PISO, which, although converging in less iterations (551) and sustaining a higher under-relaxation

factor (0.88) required the same CPU time. As in the case when all the under-relaxation factors were changed, convergence could not be achieved when $\alpha_{k,\varepsilon} = 0.2$.

Figure 3.10 shows the rates of convergence of all the equations. There are three different figures for each run which include, from left to right: the convergence of the mass residuals, the velocity, and then the residual of the turbulence quantities. It can be seen that the two regimes of convergence previously noticed also exist here, controlled solely by the under-relaxation of the equations of the turbulence model. As $\alpha_{k,\varepsilon}$ is increased, the residuals of the turbulence kinetic energy and its dissipation also reach lower levels. It seems possible that the runs with lower under-relaxation factors were stopped before complete convergence of the turbulence field. This explains the lack of convergence at $\alpha_{all} = 0.2$ and why convergence is possible at $\alpha_{all} = 0.1$. The latter is like reducing the variations of the turbulence field so much that, because its influence on the velocity field is reduced, the velocity and pressure fields can converge - a phenomenon mentioned as possible in subsection 2.3.2. This shows how dangerous is the use of very low under-relaxation factors.

The results of Figures 3.5 and 3.9 are plotted on logarithmic scales in Figure 3.11. In the present case there is a very close linear relationship between the under-relaxation factor and the number of iterations to converge:

$$\log N_{ITER} = 2.66 - 1.93 \log \alpha$$

If the procedure is repeated in the case where all the under-relaxation factors are changed simultaneously, the same equation is obtained (the rate of decay is -1.94 rather than -1.93) and this is the best proof that the global convergence is set by the convergence of the turbulence kinetic energy and its dissipation. The conclusions here also agree with those of Correa and Shyy [1987] who found that the coupling between pressure and velocity was not a key factor in the overall convergence rate.

3.2.2.2 The performance of AVPI

The CPU time as a function of the time step with this algorithm is shown in Figure 3.12. A range of time steps covering three orders of magnitude was tried (Δt_0 was 0.001 sec). The curve of convergence is fairly flat, except when approaching divergence for $\Delta t > 0.001$; time steps below 10^{-5} sec were not tried because they were too small compared with the residence time (1000 times smaller). The number of runs may be insufficient, but, at least within this range, the curve of convergence does not suggest the existence of two different regimes, as in the case of SIMPLE and PISO. The fastest run converged in 541 iterations, 134 sec, and this is an improvement in CPU time of 20% and 27% relative to SIMPLE and PISO.

The trends of convergence for this algorithm (Figure 3.13) are much smoother and the erratic behaviour shown during the first iterations of SIMPLE and PISO was eliminated; a much better defined trend of convergence now exists right from the first iteration. The different formulation of the pressure correction in AVPI, where the 'coefficient of diffusion' of the pressure does not depend on the state of convergence, may have contributed to the elimination of the 'disorganized' convergence of the first iterations. The plot of the residuals of k and ε, as in the case of SIMPLE and PISO, show that the final solutions, although satisfying the mass residual, correspond to different levels of convergence of the turbulence quantities: lower residuals of k and ε are achieved as the time step increases (as in the case of SIMPLE and PISO, when the under-relaxation factors increase).

3.2.2.3 Conclusions

The main conclusions of this study are:

1 - If all the under-relaxation factors are changed simultaneously, PISO can sustain higher under-relaxation and is twice as fast as SIMPLE.
2 - The under-relaxation of the pressure should be as high as possible.
3 - The convergence is very dependent on the convergence of the turbulence field, and if the under-relaxation of the turbulence kinetic energy and its dissipation are changed while the others are kept constant, both algorithms, SIMPLE and PISO, reach convergence in similar CPU times.
4 - The best result is obtained with AVPI; this is about 20% faster than SIMPLE and PISO. The convergence of AVPI is much better behaved.

If the three algorithms are judged only in terms of the optimum CPU time, the order is: AVPI, PISO and SIMPLE. However, the differences are so small (less than 30%) that this order is irrelevant and other reasons may prevail. The value of these tests to assess the performance of the algorithms may be questioned, since the global rate of convergence is dominated by the convergence of k and ε and the level of the residuals of these quantities is not the same in all the runs; the criterion of convergence should be more stringent or the convergence of the turbulence quantities decoupled from the other variables.

3.2.3 The 'Exact' Solution of the Complete Set of Equations

The calculations of the previous section may have been stopped before the turbulence equations were fully converged; to examine this, calculations were repeated with all residuals brought down to the levels of round-off accuracy of the computer. The

history of convergence is shown in Figure 3.14 for all the algorithms being used. The common feature in these plots is the similarity between the trends of the residuals. Between SIMPLE and PISO, this occurs right from the first iteration, but, after the mass residual (DSUM) has reached a minimum level, all the curves have the same trend. They show that, regardless of the pressure correction equation, all algorithms follow a similar route of convergence. This last part of the curve, where DSUM, in AVPI for instance, after reaching 2×10^{-4}, goes up and down and only after attaining a constant level of 5×10^{-5}, could not be suspected from the previous calculations. The drop of the residuals, especially in SIMPLE and PISO, was so drastic that it was thought that a criterion of 5×10^{-4} would be stringent enough; with the exception of AVPI with $\Delta t = 0.002$ (Figure 3.13c), all the previous plots (in Figures 3.6, 3.7 and 3.10) did not show this last part of the curves. This calculation, referring back to Figure 3.12, is the one that took longer to converge and is already on the ascending part of the curve. Observing Figure 3.13c (AVPI, $\Delta t = 0.002$) in more detail, it can be seen that the same pattern is there but somehow the inflexion point of the DSUM curve (about iteration 800) did not satisfy the criterion DSUM $< 1 \times 10^{-4}$ and the calculations proceeded.

These plots illustrate the difficulty of selecting a single parameter representative of the convergence of the calculations and the need for monitoring the residuals of all the equations.

3.2.4 The Convergence of the Velocities and Pressure Isolated from the Turbulence Model Equations

The tests of convergence of the complete set of equations (velocities, pressure and turbulence model equations) may not evidence the superiority of different pressure-velocity formulation, and this is basically what the algorithms are all about. The following tests repeat the calculations of subsection 3.2.2 but without solving the equations for k and ε; the values of these quantities were obtained from a previous run converged to machine accuracy.

A global mass error of less than 5×10^{-5} (10 times smaller than in subsection 3.2.2) was set as the criterion of convergence. All the other conditions of the test were unaltered.

3.2.4.1 Relative performance of SIMPLE and PISO

The under-relaxation of the velocities and pressure

Figure 3.15, the analogue of Figure 3.5, shows the influence of the under-relaxation of the velocities and pressure. We observe now a monotonic trend, the CPU time decreases

as α increases, with no evidence of the two regime situation, and the CPU time has been reduced by a factor of about 10 relative to the results in Figure 3.5 as a consequence of starting the calculations with the final values of k and ε. When both converge, SIMPLE and PISO, as in the previous test, require an identical number of iterations and the rate of convergence (in Figure 3.16 on logarithmic scales) obeys the relationship:

$$\log N_{ITER} = 1.726 - 1.093 \log \alpha$$

A minimum of 53 iterations is needed on the assumption of a converged solution with α = 1.0. PISO gets closer to that limit and takes, with α = 0.80, 66 iterations to converge, but is slower than SIMPLE which needs 80 iterations for α = 0.65.

The convergence behaviour is now monotonic (Figure 3.17) and it is obvious that the wiggling behaviour observed in the previous tests in 3.2.2 was caused by the turbulence model equations.

The under-relaxation of the pressure

The influence of the under-relaxation of the pressure is shown in Figures 3.18. The conclusion is again that α_P should be as high as possible, similar to the previous tests. However, there are practical limits to this in the case of SIMPLE, whereas PISO still converges with α_P = 1.0, i.e. no under-relaxation. At low under-relaxation factors, the curve is characterized by a sudden increase of the number of iterations. The criterion $\alpha_P = 1 - \alpha_U$ as the relationship for optimum convergence does not hold. Since this is a two-variable (α_U, α_P) problem, as discussed in subsection 2.3.2, extensive tests were again made, in case of SIMPLE, for a complete range of values between 0.1 and 1.0. The results are presented on a convergence map (Figure 3.19) as before. The shaded area covers the combinations where divergence occurred and, below that area, two main regions limited by α_U = 0.5 seem to exist. In the region of α_U lower than 0.5, the number of iterations can be reduced by a factor of 3 by increasing the α_U from 0.1 to 0.5; whereas the α_P, which can even be equal to 1.0 (i.e. no under-relaxation of the pressure), hardly influences the convergence. For α_U higher than 0.5, the range of possible values of α_P is reduced: low α_P values cause a sudden increase of the number of iterations, for instance the combination (α_U = 0.8, α_P = 0.1) needed 550 iterations, and high α_P values lead to divergence; the upper limit of the α_P range is reduced as α_U increases. The best result was obtained with (α_U = 0.7, α_P = 0.6), but, if advantage has to be taken of under-relaxation above 0.5, a correct tuning of α_P has to be made. Recalling the analogy with the time-dependent formulation, in subsection 2.3.2, values of $\alpha > 0.5$ correspond to time steps higher than the maximum allowed by an explicit time-dependent formulation.

This need to reduce α_p as α_u is increased to secure convergence fully agrees with the arguments presented in subsection 2.3.2 under the heading " The under-relaxation factor (and the time step)" and with the results of the two dimensional test case.

3.2.4.2 Relative performance of SIMPLE and PISO (both in time-dependent formulation) and AVPI

An apparent superiority has been shown by AVPI in the previous sections, but, because AVPI uses a time-dependent formulation, for a correct appraisal of the three algorithms, SIMPLE and PISO were also used in unsteady formulation and compared with AVPI.

The range of time steps for which AVPI could satisfy the criterion of convergence was smaller (Figure 3.20) compared to the previous tests in Figure 3.12. This is an indication that the 'solution' of AVPI obtained at small time steps in subsection 3.2.2.2 were not representative and were probably also the result of slowing the convergence of k and ε as in the case of SIMPLE and PISO with $\alpha = 0.1$. The curves of convergence of SIMPLE and PISO are in Figure 3.21. The three algorithms need a similar number of iterations, or time steps, in the region where they all converge. However, comparing only the optimum results, AVPI is actually the worst; SIMPLE and PISO are faster by 30% and 70%, respectively. The difference is a consequence of the size of the time step they can sustain without diverging; PISO in its optimum needs only 52 iterations and thus gives the best result of all (note that this is also in excellent agreement with the minimum of 53 iterations predicted by extrapolation of the rate of convergence for the limit case of $\alpha = 1.0$ in subsection 3.2.4.1).

3.2.4.3 Summary

A tenfold reduction of the CPU time was obtained in the calculations, starting from the final fields of turbulence kinetic energy and its dissipation.

PISO sustained higher under-relaxation factors of the velocities but the number of iterations could not be lowered to levels where the higher CPU time per iteration was compensated and PISO was slower than SIMPLE.

The under-relaxation of the pressure in SIMPLE should be as high as possible but its influence is minimal, except if under-relaxation factors of the velocities higher than 0.5 are used.

The unsteady formulation was particularly advantageous for PISO when optimized. Although the best results of all were obtained by PISO in time-dependent formulation, it should not be taken as proof that this should be the preferred

combination. It is very unlikely that the optimization of the time step may always be made in a normal calculation and the use of steady-state formulation may still be preferred.

3.2.5 Conclusions of the Study of Convergence of the Calculation Procedure

To bring to an end the study of various pressure correction formulations in this chapter and in the previous chapter too, the main conclusions and recommendations of this study should be summarized.

1 - The computational efficiency of the algorithms SIMPLE, SIMPLEC, SIMPLER PISO and AVPI was assessed by performing calculations of two test cases, both turbulent and recirculating flows.

2 - Initial calculations using the five algorithms above and the QUICK differencing scheme showed that all the algorithms required a similar number of iterations to converge. This was thought to be a consequence of the treatment of the extra terms arising from the finite-difference discretisation and further calculations were performed using hybrid differencing scheme and restricted to three algorithms (SIMPLE, PISO and AVPI).

3 - No major differences continued to occur between the number of iterations and SIMPLE and PISO were even similar in terms of the convergence rate. Whenever both algorithms converged the plots of the residuals as a function of the number of iterations showed identical patterns.

4 - The convergence rate is dominated by the convergence of the turbulence quantities (k and ε) and the under-relaxation factors are the main parameters controlling convergence.

5 - The mechanism of convergence and coupling between the equations are such that all the under-relaxation factors, particularly those of the turbulence quantities should be as high as possible. In both SIMPLE and PISO, the under-relaxation factor of the pressure should be decreased as those of the velocities increase to avoid the breakdown of the pressure-velocity formulation. In PISO this need occurred for higher under-relaxation factors compared to SIMPLE.

6 - PISO, because of a stronger coupling between pressure and velocity sustained higher under-relaxation factors (or time steps) and under such circumstances could reach convergence in less iterations. However, because of the increased CPU time per iteration, this does not necessarily imply a reduced global CPU time. The increased robustness of PISO is obtained at the

expense of higher storage requirements and this should also be considered as an argument against this algorithm. This robustness may be more advantageous in the case of an increased number of coupled equations compared to the present one, where SIMPLE and AVPI fail to converge or require too small under-relaxation factors (or time steps).

7 - The AVPI algorithm showed a well behaved pattern of convergence due to the uncoupling of the turbulence quantities, the coefficients of the pressure correction equation being geometrical functions only. Advantage can be taken of this to reduce the CPU time per iteration.

8 - The probable advantages of algorithms like PISO, SIMPLER, SIMPLEC and AVPI, compared to the SIMPLE algorithm are not enough to recommend the alteration of presently available computer codes with the SIMPLE algorithm already incorporated. Strong arguments in favour of algorithms suggested as alternatives to SIMPLE are not supported by the present tests.

3.3 DISCUSSION OF RESULTS

3.3.1 Presentation of Results

Because of the complexity of the flow the numerical results are shown mainly as surface views. The velocity and scalar fields are illustrated by streakline and contour plots, respectively.

The computer program to plot the streaklines was originally written by Ho [1985]. The program basically tracks and plots the trajectory of particles released at selected locations in the flow. Because the velocity normal to the plane is not considered, the final result is similar to flow visualization obtained by illumination with a sheet of light (for instance, a water flow with particles in suspension) and the total tracking time here is analogous to the shutter speed of the camera (see subsection 4.1.4 for a discussion on flow visualization techniques). The contour plots were made by a software plotting package publicly available at the Imperial College Computer Centre (Dipple and Raby [1987]). The contours of a function are approximated on the basis of its local value and gradient calculated on a square mesh; because this approximation is made by piecewise quadratic functions with continuous differentiability across the boundaries of the elements of the mesh, the contours are piecewise continuous conical sections.

The presentation of the results forms three main subsections. The numerical accuracy is assessed first (subsection 3.3.2) by comparing the results obtained with grids of variable resolution to find the level of grid refinement needed. Subsection 3.3.3 discusses the results of the two basic sets of boundary conditions with

inclined and non-inclined jets, both assuming a constant density. The results in subsection 3.3.4 consider the variations of density as a local function of temperature. Finally, different turbulent Prandtl numbers are tried in an attempt to examine the sensitivity of the predicted results to the part of the turbulence model which directly affects scalar mixing.

The experimental values of the integral parameters of mixing, provided at the outlet section (Shaw [1981]), were used to assess the mathematical model. These parameters were defined as:

Overall temperature distribution factor (OTDF):

$$OTDF = \frac{T_{max} - T_{mean}}{T_{mean} - T_{jet}}$$

where T_{max} is the maximum temperature, T_{mean} is the mean exit temperature, and T_{jet} is the mean inlet temperature of the jets (the mass weighted average of the temperature of the two jets).

Radial temperature distribution factor (RTDF):

$$RTDF = \frac{T^{radial}_{max} - T_{mean}}{T_{mean} - T_{jet}}$$

where T^{radial}_{max} is the maximum circumferential mean temperature. This and the overall temperature distribution factor are the parameters most often used to characterize the mixing by combustor designers.

Mixedness parameter (h):

$$\eta = (1 - \frac{\sigma}{\sigma_{max}}) \times 100\%$$

Unmixedness parameter Ψ:

$$\psi = \frac{1}{2} \frac{\sigma}{\sigma_{max}} \frac{T_{annulus} - T_{jet}}{T_{mean} - T_{jet}}$$

where σ is the standard deviation, and $T_{annulus}$ is the mean inlet temperature of the annulus flow:

$$\sigma = \frac{\left[\sum_{i=1}^{N} (T - T_{mean})^2\right]^{1/2}}{N(T_{mean} - T_{jet})}$$

$$\sigma_{max} = (T_{jet} - T_{annulus}) \frac{\dot{m}_{jet}}{\dot{m}_{annulus} - \dot{m}_{jet}}$$

The transport equation for temperature used in the calculations in subsection 3.3.4 is identical to the equation used in subsection 3.3.3 for the transport of a passive scalar, Φ. In 3.3.3 the solution of the scalar equation could not feed back into the velocity equations, via the density whereas in 3.3.4, this was allowed to happen. In both cases the results are presented as contours, nondimensioned as follows: $\Phi^* = (\Phi - \Phi_{annulus})/(\Phi_{jet} - \Phi_{annulus})$ and $T^* = (T - T_{annulus})/(T_{jet} - T_{annulus})$, where the meaning of the subscripts is the same as above.

3.3.2 Constant Density Calculations

3.3.2.1 Grid resolution - numerical accuracy

Figures 3.22 to 3.24 show the streaklines along the streamwise direction in the two extreme θ planes: θ = 7.5°, the plane containing the axis of the holes (referred to below as the centre plane), and θ = 0°, halfway between the holes (referred to below as the mid plane). These figures include results from calculations using three numerical grids with different levels of refinement. The coarsest grid (grid 1 in Table 3.2) in Figure 3.22 shows, compared with Figure 3.23, higher numerical diffusion (smoother trajectory of the particles) and, because of the reduced number of nodes at mid height, is unable to capture the small recirculation zone upstream of the impingement region of the jets (see Figure 3.23). The coarsest grid is clearly unsuitable to calculate this flow.

The pattern in Figure 3.24 corresponds to the finest grid (grid 4 in Table 3.2) with 16 and 4 times more nodes than the grids used in the calculations of Figures 3.22 and 3.23, respectively. The longitudinal flow pattern (Figures 3.23 and 3.24) and the passive scalar fields (Figures 3.25 and 3.26) predicted by the two finer grids are very similar. Central differencing was used, in the case of the grid 70 × 40 × 25, over a large part of the integration domain: the higher Peclet numbers (above 10) are concentrated at the edges and upstream of the jets for the radial and axial directions,

respectively (Figure 3.27); similarity between the scalar fields of the two finer grids shows that the Peclet number distribution is similar in both grids.

The calculations in the finest grid required about 40 hours of CPU time to converge and this, considering also the small differences between the results of the two grids, discouraged any further calculations on this grid and led to the acceptance of the grid $40 \times 30 \times 15$ as accurate enough.

The calculations with inclined jets (case 2 in Table 3.1) were initially made on a grid of $40 \times 30 \times 15$, which reduced the numerical resolution along the angular direction, because the integration domain extended over a 15° instead of a 7.5° sector. The streaklines of this calculation (in Figure 3.28), have two salient features relative to the case with non-inclined jets (Figure 3.23): a steeper penetration of the bottom jet and, in its wake, a recirculation zone which extends over the whole sector (Figure 3.28b). The different trajectory of the jets is a consequence of their misalignment in the longitudinal plane (Figure 3.3), the bottom and top jets have upstream and downstream components, respectively; however, there seems to be no reason for the vortex in the wake of the bottom jet. To see whether this could be caused by the increased spacing between the nodes in the angular direction, calculations were made with non-inclined jets, symmetry boundary conditions, in a sector of 15°, twice of what was actually needed – a condition designated by double symmetry.

In the absence of effects caused by the grid distribution, both symmetry and double symmetry conditions should give strictly identical results. However, Figures 3.23 and 3.29 clearly indicate that they do not. The vortex in the wake of the bottom jet reappears in the case of double symmetry conditions and this leads to a more uniform distribution of the passive scalar, as can be seen by comparing Figures 3.30 and 3.25.

The transverse cross-sectional views for both conditions (Figures 3.31 and 3.32) provide an explanation for this phenomenon. Note that the cross-sectional views were magnified by 4 along the angular direction for the purposes of plotting and the 7.5° and 15° sectors, therefore, appear as 30° and 60° sectors. The striking feature of these figures is the region of streamwise vorticity in the upper half of the annulus created by the spanwise deflection of the jets. The particles were released at every angular location and it is clear that, in the case of double symmetry conditions (Figure 3.32), there are not enough grid lines to resolve the vortex formed between the mid plane and the edges of the bottom jet (compare Figures 3.31a and 3.32a, the cross-sectional view containing the axis of the holes). Further downstream, there is a tangential flow along the inner wall directed towards the centre plane, whose magnitude is reduced in the case of the double symmetry conditions (Figure 3.32b), where the particles mainly follow a radially outward trajectory. The magnitude of the azimuthal

component of velocity is generally lower over most of this plane and this is considered evidence of artificial diffusion, responsible for a higher decay rate of the secondary flows. Closer to the nozzle, the symmetry conditions, Figure 3.31c shows a radially outward flow, but this is reversed in the case of the double symmetry (Figure 3.32c) (this location corresponds to the downstream end of the jet wake).

As proof of the correctness of the program, observe the trajectory of the particles released on the axis of the holes (centre plane; Figure 3.32): all the particles follow an exact radial trajectory with no lateral deflection and the two halves of the figures are mirror images of each other. The boundary conditions at the longitudinal planes of symmetry consist of setting to zero the normal gradients of the scalar quantities and velocity components parallel to the plane; the component of velocity normal to the plane, the azimuthal component in the present case, is also set to zero. The existence of this boundary condition can equally be seen on the mid plane, the $\theta = 0°$ location, and there (Figures 3.32a and 3.32b) it is responsible in the upper half, for a sharper trajectory of the particles compared to Figure 3.31b. Near the inner wall, because the number of grid lines between the mid plane and the edges of the jet is small (only 2), the vortex is simply destroyed, the flow is mainly radial, because of the condition $W = 0$. The fluid which, by flowing around the base of the jet should fill the low pressure region in the wake of the bottom jet, is diverted to outer radial locations, forcing the jet fluid to be recirculated. This can be confirmed by the longitudinal contour plots through the relatively high scalar value of 0.5 in the wake of the jet (Figure 3.30 compared to the symmetry conditions (Figure 3.25)).

The trajectory of the particles near the edges of the sector is sharper, as opposed to what would be expected from a solution with higher numerical diffusion. The ability of the jets to penetrate deeper through the cross-stream in the double symmetry calculations corresponds to an increase of the jet to cross-stream momentum ratio. Referring back to the results of the coarsest grid, $17 \times 11 \times 6$ in Figure 3.22, the situation was the opposite: there, because the results are dominated by the numerical diffusion, the flow pattern in the longitudinal planes corresponds to a reduction of the jet to cross-stream momentum ratio and the effect of the longitudinal conditions of symmetry is not perceptible.

The main conclusions of this section are the proof that satisfactory accuracy can be achieved with grids of $40 \times 30 \times 15$ and $40 \times 30 \times 30$ to resolve the 7.5° and 15° sectors, respectively. The consequences of an insufficient number of nodes can show either through the inability of the grid to resolve small scale features of the flow or through the lower magnitude of the azimuthal component of velocity which, associated with the boundary conditions in the longitudinal planes of symmetry, may

lead to the appearance of spanwise vorticity in the wake of the jets and promote their coalescence.

3.3.2.2 Inclined and non-inclined jets

The main objective of this subsection is to discuss the flow in more detail and observe the differences between inclined and non-inclined jets (cases 1 and 2 in Table 3.1). Following the conclusions above, the calculations with inclined jets were made in a grid of 40 × 30 × 30.

The flow pattern in the longitudinal planes (Figure 3.33), resulting from calculations with inclined jets using the new grid of 40 × 30 × 30, confirms the steeper penetration of the inner jet and the vortex motion in the wake of the inner jet; this extends over the 15° of the sector, but is of a smaller size than that predicted by similar calculations on a coarser grid, 40 × 30 × 15 (Figure 3.28). The effect of this region is to produce a more uniform distribution of the passive scalar (Figure 3.34) compared with the case of non-inclined jets (Figure 3.25). This lateral coalescence of the neighbouring jets leading to an enlarged jet wake has been observed experimentally by for instance Crabb and Whitelaw [1979].

The highest values of turbulence kinetic energy (Figure 3.35) (associated with the regions of maximum strain rate) occur in the impingement region of the jets, in the downstream edge of the bottom jet and along the nozzle walls, especially at the downstream end. In this region, the simulation of the nozzle by steps may have contributed to the high values.

The cross-sectional views of the flow pattern produced by the inclined jets are shown in Figure 3.36. Broadly speaking, the figures are similar to the ones corresponding to the case of non-inclined jets (Figure 3.31). The non-perpendicular orientation of the jets is noticed by the impingement closer to the outer wall, as in the case of the longitudinal views, and the location of the centre of the top vortices biased anticlockwise and at a higher radial location. In the plane of the hole axis (Figure 3.36a), there is, in the case of the inclined jets, a more dominant radial trajectory of the particles. Further downstream, in Figure 3.36b, the tangential flow along the inner wall is stronger compared with the case of insufficient numerical resolution. This tangential motion along the inner wall is formed mainly by cross stream fluid. This penetrates between the jets in the regions near the walls (note the areas limited by the 0.1 contour in Figures 3.25b and 3.37b for symmetry conditions, or Figures 3.34b and 3.38a for inclined jets). It then flows around the jets and fills the wake region, being entrained by the jet fluid and following a radial trajectory along the axis of the jets. This explains why the low value contours, corresponding to the cross stream fluid, occur at a higher distance from the walls and in the longitudinal plane of

the holes (Figures 3.37 and 3.38). It is believed that the failure to resolve the sequence above was the reason why the preliminary calculations of McGuirk [1984] did not show the correct location of the fluid originating from the cross-stream at the outlet section.

The vortex motion in the upper half of the annulus should also appear in the lower half. This does not happen because: i) the smaller gap (pitch to diameter ratio) between jets on the inner wall, reducing the spanwise curvature of the jets and ii) the blockage effect caused by the nozzle, creating an upward motion of the flow over most of the inner half of the annulus. This can explain the fairly uniform concentration in the lower half (in Figure 3.37b and 3.37d) which is even more uniform in the case of inclined jets (Figure 3.38b and 3.38d).

At the outlet section (Figures 3.37d and 3.38d), the concentration contours show a pattern where the higher concentration fluid, originating from the jets, spreads along the inner wall and between the jets in the mid longitudinal plane, whereas the annulus fluid remains aligned with the holes.

The sensitivity of the results to a slight inclination of the jets, which in practice can be caused by manufacturing imperfections, is a proof of the accuracy of the calculations and an example of the role that computational fluid dynamics can play in the design of combustors. The appraisal of turbulence models on this type of geometry requires very detailed and accurate measurements of the inlet conditions (since small alterations of the boundary conditions may produce alterations of the flow higher than the ones caused by the modifications of the turbulence model). In the calculation of real combustor flows, the accuracy of the calculations is valid only under the assumption of some ideal boundary conditions and the need for more sophisticated turbulence models may be questioned.

3.3.3 Variable Density Calculations

In an attempt for a closer simulation of the experiments, the density was evaluated, at every point, from the equation of state of an ideal gas. The variations of density caused by the temperature were ignored in the previous calculations. The effect of fluctuations on mean density are still ignored.

The boundary conditions of the present calculations are included in Table 3.1, case 3. The normal velocities at every entry of the combustor were calculated using the air density corresponding to the temperature of the respective stream in order to maintain the same mass flow rate as the experiments. This also guarantees the same mass flow rate as in case 1 in Table 3.1 but leads to a momentum flux ratio between the jets and the crossflow of 18.6 compared to 42.7 in case of constant density calculations.

The longitudinal flow pattern is shown in Figure 3.39 and, relative to the previous calculation with constant density (Figure 3.23), the most important features are: the absence of the small recirculation zone upstream of the jets and the increased downstream bending of the jets. The latter can be seen in the transverse views (Figure 3.40) where a larger vortex structure is observed between the jets near the inner wall, Figure 3.40c compared to Figure 3.31c. The temperature contours (Figures 3.41 and 3.42) show a lower coalescence between the jets in comparison to the corresponding figures with constant density calculations (Figure 3.37); note, for instance, in Figure 3.42 b the predominantly vertical orientation of the contours between the jets at the mid longitudinal plane, and the isolated region of 0.6 at the outlet section (Figure 3.42 d). The pattern factor at the outlet section is 40.6%. In case of constant density calculations, the inclined jets gave rise to a more uniform distribution with a pattern factor of 36.2% as opposed to 47.1% for the case of perpendicular impingement, note however that the experimental value was 18.4% (Table 3.4).

3.3.3.2 Comparison with experiments. The turbulent Prandtl number

The final calculation (case 4 in Table 3.1) is the one that simulates most closely the experiments: the variation of the density with the temperature and the inclination of the jets have both been taken into account.

Figure 3.43 shows the streakline plots. There is hardly any difference between these views and Figure 3.39, the variable density case without inclined jets; the inclination of the jets was more important in the case of constant density (see subsection 3.3.2.2) which may be a consequence of the lower momentum flux ratio of the variable density calculations. The flow visualization, in Figure 3.44, although of poor quality, enables us to confirm the correct penetration of the jets and the absence of the small recirculation zone upstream of the impingement, predicted in the case of the constant density calculations. The cross-sectional views (Figure 3.45) show the effect of the anticlockwise swirl component introduced by the inclination of the jets: the vortices on the right hand side are larger and the flow pattern, similar to the case without inclined jets (Figure 3.40), is simply shifted towards the left.

The longitudinal radially averaged temperature contours are shown in a dimensional form in Figure 3.46. The larger pitch to diameter ratio of the top jets is evidenced by the higher temperatures near the outer wall and the absence of the protruding shape of the contour that, for instance in the region near the inner wall, enables us to identify the path of the jet. The central core of the flow is formed by colder air, mainly originating from the jets. The sequence in Figure 3.47 (the transverse contours) shows the process of formation of the two 'pockets' of higher

concentration (jet fluid, i.e. lower temperature) in the mid longitudinal planes, resulting from the splitting of the top jet before the merging of the two opposed jets has occurred (Figure 3.47c). For a comparison with the experimental values (Figure 3.48), the temperature at the outlet section is also plotted in a dimensional form (Figure 3.49): the underprediction of the diffusion is evident and the overall temperature distribution factor is 44.5%, whereas the experimental value is 18.4%.

Calculations were made with a lower turbulent Prandtl number (0.5), but even that was not enough (Figure 3.49b and Table 3.4). The pattern factor was reduced (35.8%), but is still too high by a factor of 2. The underprediction of the levels of mixing compared to the measurements is quantified through the mixing parameters in Table 3.4 and previously defined in subsection 3.3.1.

TABLE 3.4 – Integral parameters of mixing

		OTDF	RTDF	η	Ψ	T_{max}
Experimental		18.4	3.2	93.2	0.06	719
Variable Density	$\sigma_T = 0.9$	44.5	27.9	77.2	0.22	760
(Tilted)	$\sigma_T = 0.5$	35.8	19.2	81.6	0.18	740
Constant Density (Symmetry)		47.1	9.9	80.3	0.19	765

The overall shape of the distribution is not altered by a reduction of the turbulent Prandtl number (compare Figures 3.49a and 3.49b) and the range of temperatures shown by the calculations (between 560 and 740 K) is still too high compared to the measurements (between 650 and 719 K). There are also points of disagreement between the calculated and measured temperatures that suggest the existence of a different flow pattern. For instance, the lowest temperature near the outer wall shown by the measurements can only be caused by a stronger radial outward flow than predicted, which could be caused either by a stronger penetration of the bottom jet or an enhanced effect of the nozzle inner wall, promoting a stronger radially outward flow. This cannot be confirmed through the total pressure contours (in Figures 3.50 and 3.51) and detailed velocity measurements are required.

If the simple empirical formula below, from Lefebvre [1983], is used

$$OTDF = 1 - \exp\left[- 0.05 \frac{L}{\Delta D} \left(\frac{U_{jet}}{U_{ref}} \right)^2 \right]^{-1}$$

(where L and ΔD are the length and size of the annular gap; and U_{jet} and U_{ref} are the jet velocity and the mean velocity of the cross stream) the overprediction of the mixing parameters is even higher. In this case an OTDF of 76% is predicted. However, this may not be surprising since the effect of the nozzle has been ignored. This illustrates one of the main limitations of empirical correlations in the design of combustors and shows that the present calculations, although producing results different from the experimental values can perform better than empirical correlations.

3.3.4 Conclusions

The following conclusions can be drawn:

1 - The lack of numerical resolution along the circumferential direction causes an underprediction of the streamwise vorticity and could particularly influence the flow in the wake of the jets – this is relevant for any jet in crossflow geometry.

2 - The flow structure at the outlet section was mainly dominated by the outer jet, due to the radial location and steeper inclination of the inner wall of the nozzle.

3 - The effect of the inclination of the jets is almost negligible in variable density calculations because of the lower momentum flux ratio compared to the constant density case.

4 - The calculations evidence a lower level of diffusion relative to the measurements, which the reduction of the turbulent Prandtl number could not correct. The experimental temperature distribution suggests that the experimental flow pattern at the outlet section may differ from the calculated one.

3.4 SUMMARY

A numerical study of the non-reacting flow inside a dilution system of annular gas turbine combustor was presented in this chapter. This study comprised of two main parts. In the first part the relative performance of the algorithms SIMPLE, PISO and AVPI was evaluated. The second part assessed the capabilities of the model for the prediction of the overall parameters of mixing at the outlet section.

The performance tests showed that the overall convergence of the calculations was set by the convergence of the turbulence quantities. Algorithms like PISO, because allowing higher under-relaxation factors (or time steps) could under

such circumstances converge in less iterations but not necessarily in a reduced global CPU time because of the increased CPU time per iteration. There seems to be no reason to replace the SIMPLE algorithm by alternative algorithms in the calculation of gas-turbine combustor flows.

The agreement between experimental flow visualization along the centre plane and the streakline plots of the predicted flow, the use of accurate numerical grids and boundary conditions taking into account the misalignment of the jets, are reasons to believe that the mean flow pattern inside the dilution zone has been adequately predicted by the model. However, there is a consistent underprediction of the levels of mixing, leading to an OTDF twice as large as the experimental one (even after a reduction of the turbulent Prandtl number from 0.9 to 0.5). Differences between the shape of the numerical and experimental temperature contours at the outlet section suggested that a stronger penetration of the inner jet may exist in reality and this may have also contributed to an OTDF too high relative to the measurements. More accurate and detailed measurements, and not restricted to the outlet section are required.

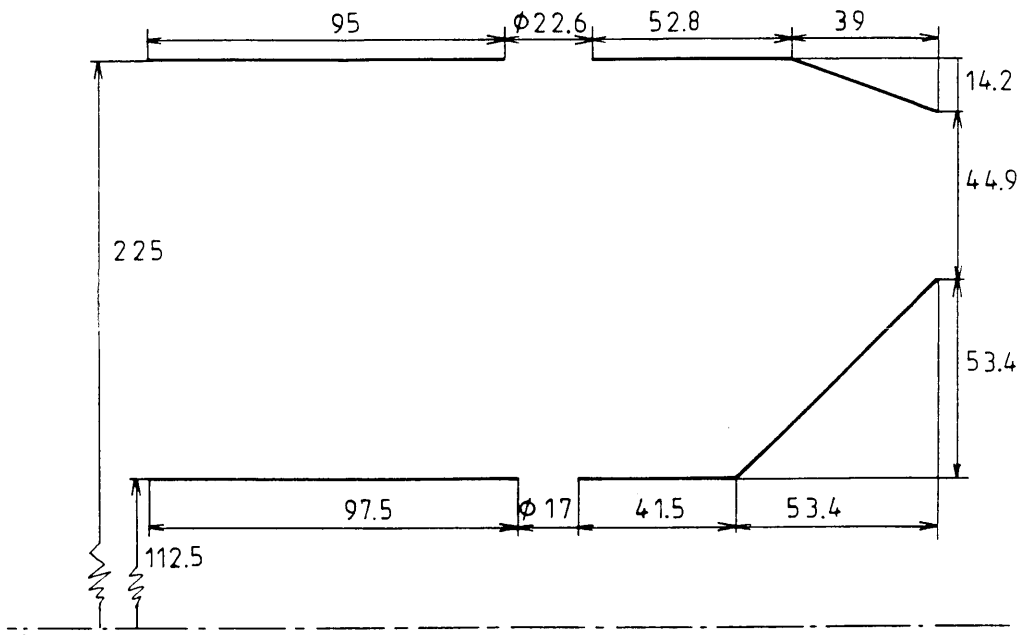


FIGURE 3.1 - Geometry of the annular dilution system (dimensions in mm).

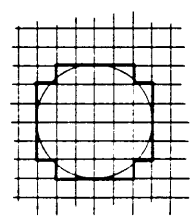


FIGURE 3.2 - Numerical simulation of the holes.

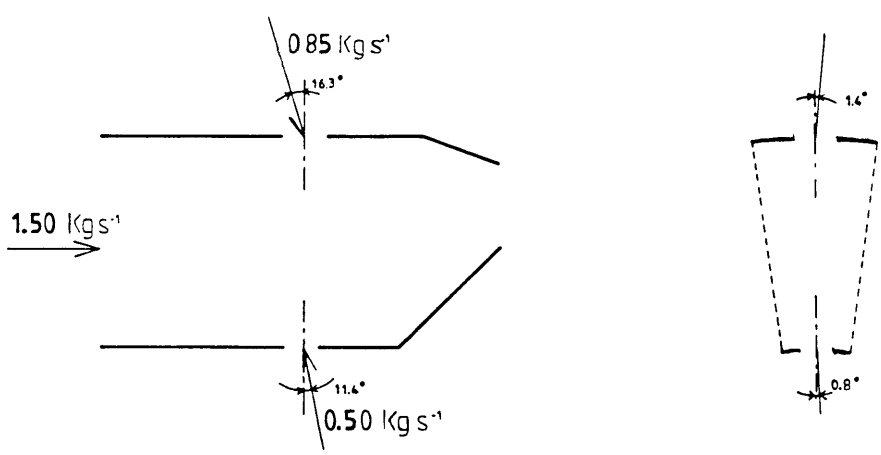


FIGURE 3.3 - Flow splits and inclination of the jets.

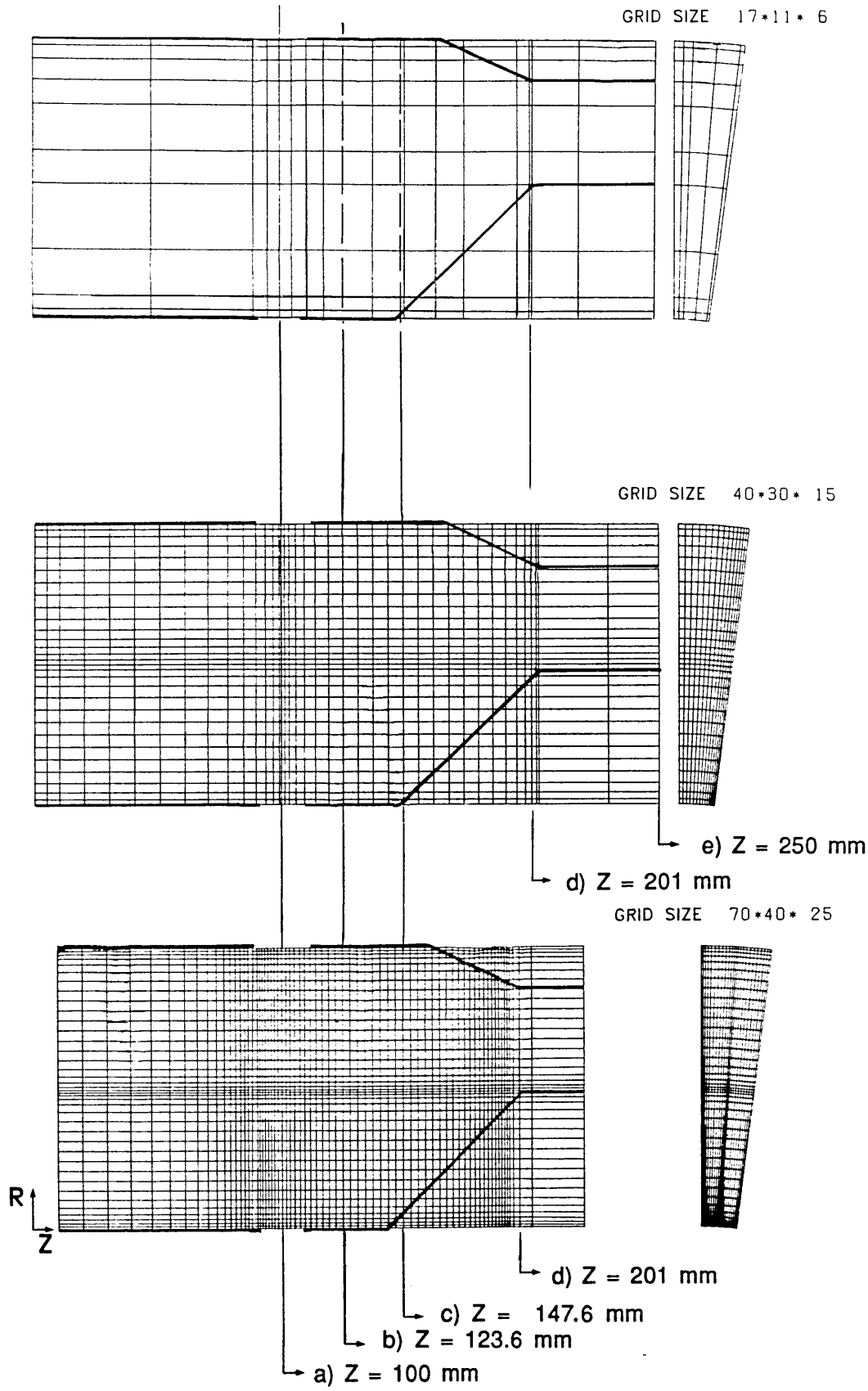


FIGURE 3.4 - Numerical meshes.

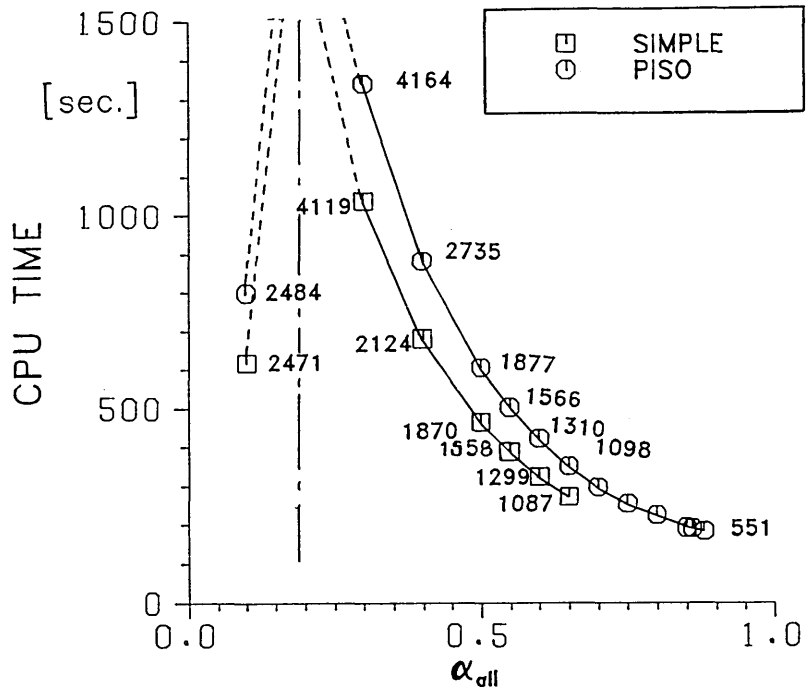


FIGURE 3.5 - Influence of the under-relaxation in PISO and SIMPLE (all under-relaxation factors changed simultaneously).

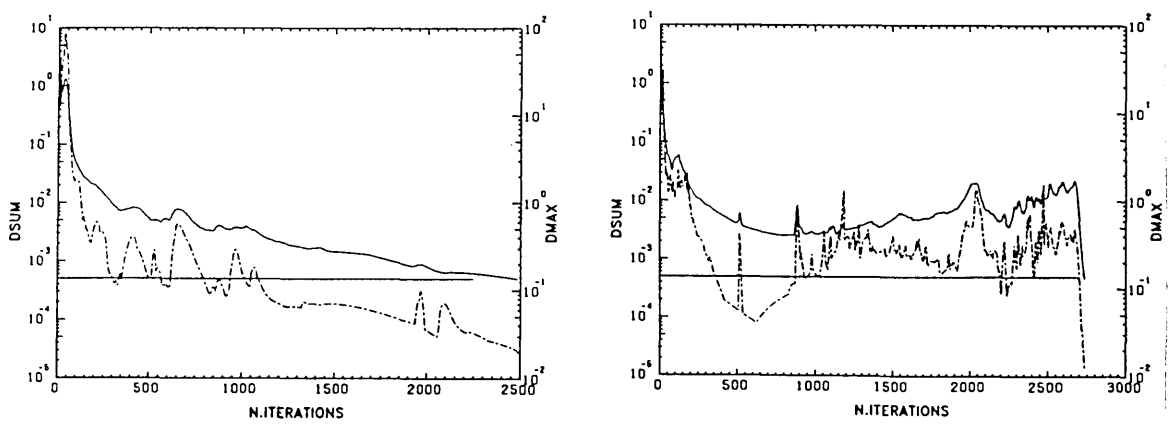


FIGURE 3.6 - The reduction of the mass residual in PISO for various under-relaxation factors (all under-relaxation factors changed simultaneously):
a) $\alpha_{all} = 0.1$ b) $\alpha_{all} = 0.4$.

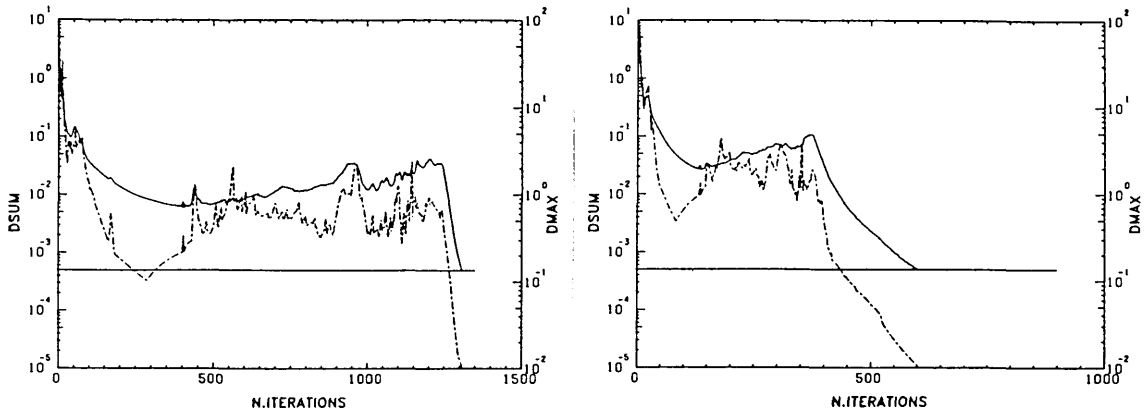


FIGURE 3.6 (continued)– The reduction of the mass residual in PISO for various under-relaxation factors (all under-relaxation factors changed simultaneously): c) $\alpha_{all} = 0.6$ d) $\alpha_{all} = 0.85$.

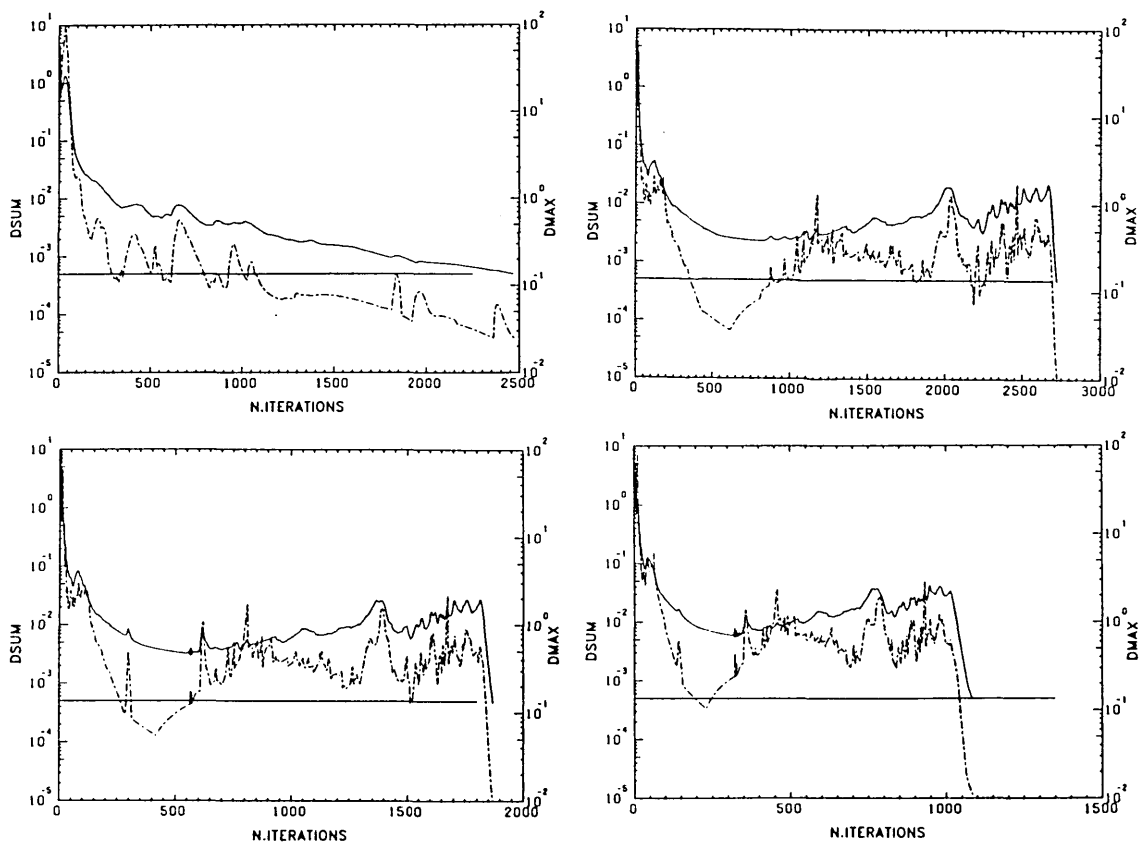


FIGURE 3.7 - The reduction of the mass residuals in SIMPLE for various under-relaxation factors (all under-relaxation factors changed simultaneously):
a) $\alpha_{all} = 0.1$ b) $\alpha_{all} = 0.4$ c) $\alpha_{all} = 0.5$ d) $\alpha_{all} = 0.65$.

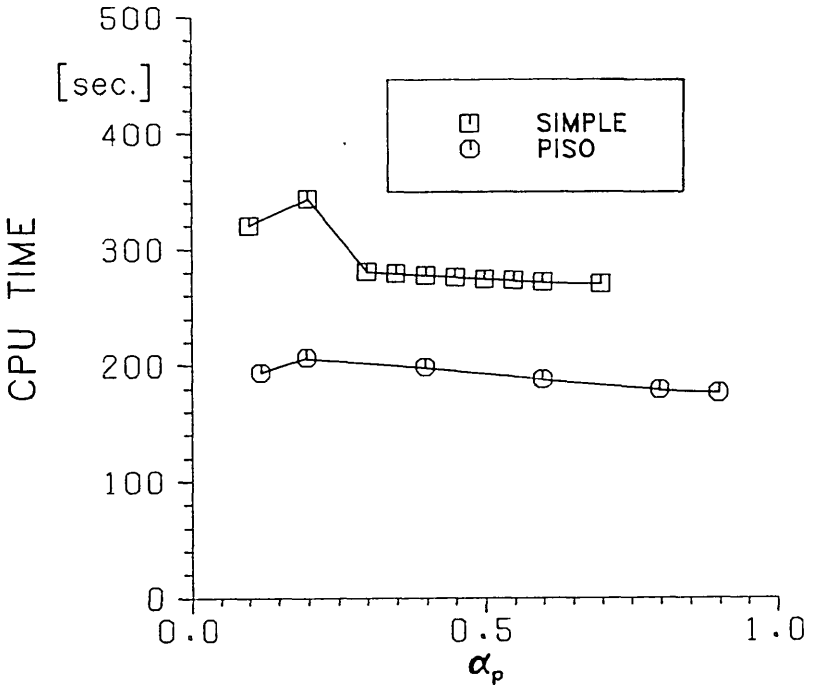


FIGURE 3.8 - Influence of the under-relaxation of the pressure in SIMPLE and PISO - α_p changed while $\alpha_{u,v,w,k,\varepsilon}$ were kept constant (0.65 for SIMPLE and 0.88 for PISO).

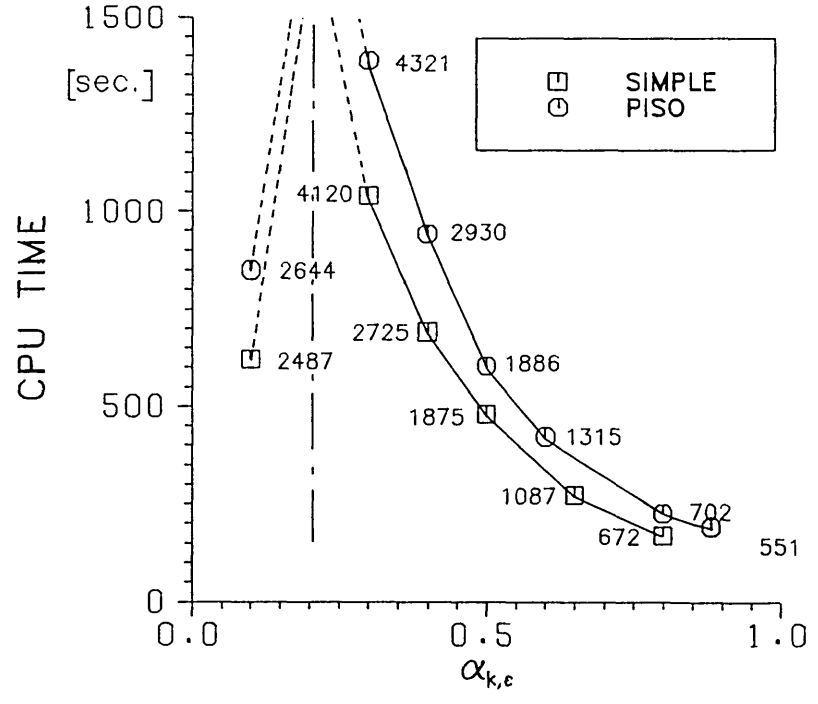


FIGURE 3.9 - Influence of the under-relaxation of the turbulence kinetic energy and its dissipation in SIMPLE and PISO - $\alpha_{k,\varepsilon}$ changed while $\alpha_{u,v,w,p}$ were kept constant (0.65 for SIMPLE and 0.88 for PISO).

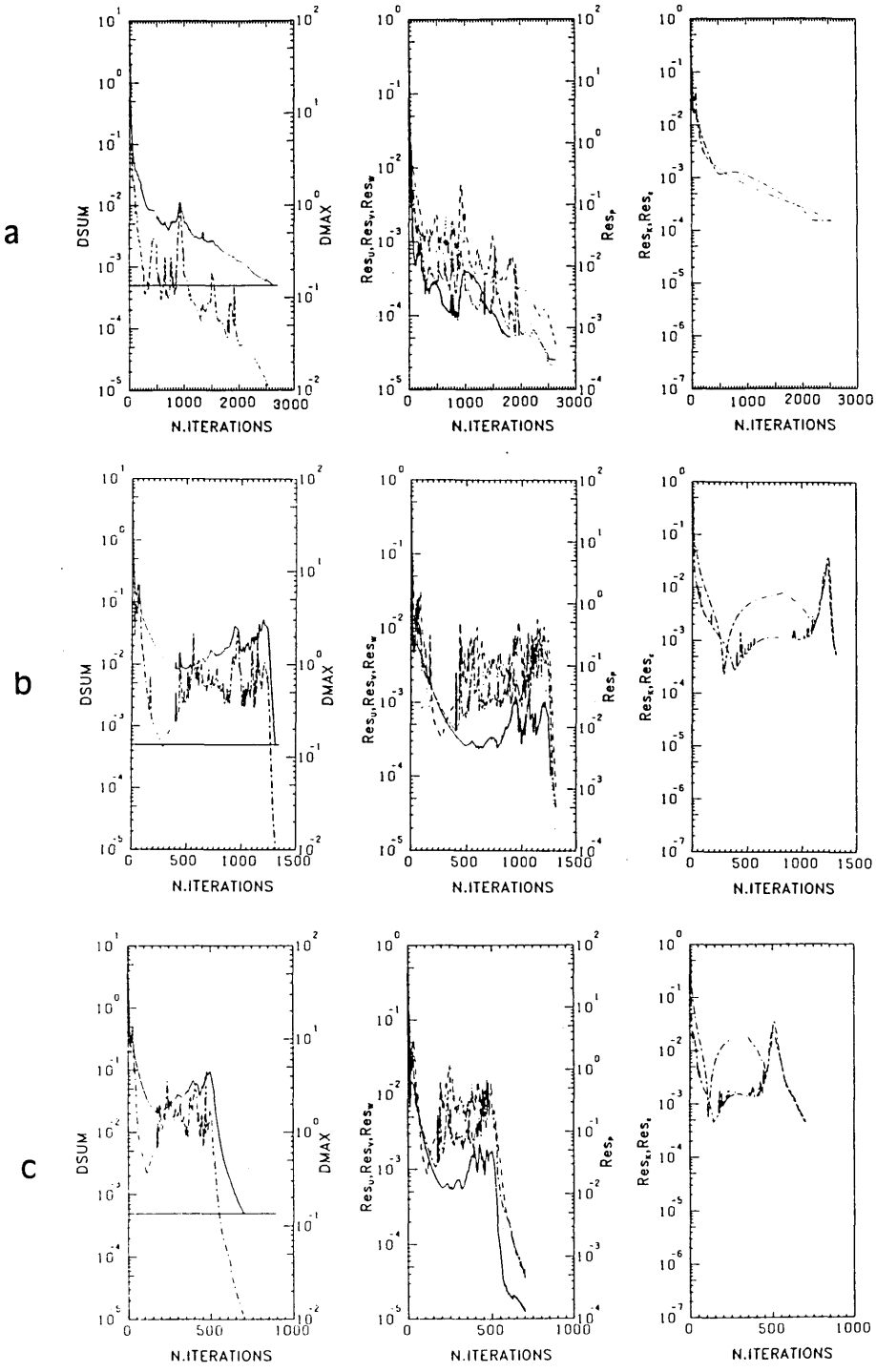


FIGURE 3.10 - The reduction of the residual of all the equations in SIMPLE and PISO for various under-relaxation factors of the turbulence kinetic energy and its dissipation- ($\alpha_{k,\varepsilon}$ changed while $\alpha_{u,v,w,p}$ were kept constant and equal to 0.88):

a) $\alpha_{k,\varepsilon} = 0.1$ b) $\alpha_{k,\varepsilon} = 0.6$ c) $\alpha_{k,\varepsilon} = 0.8$.

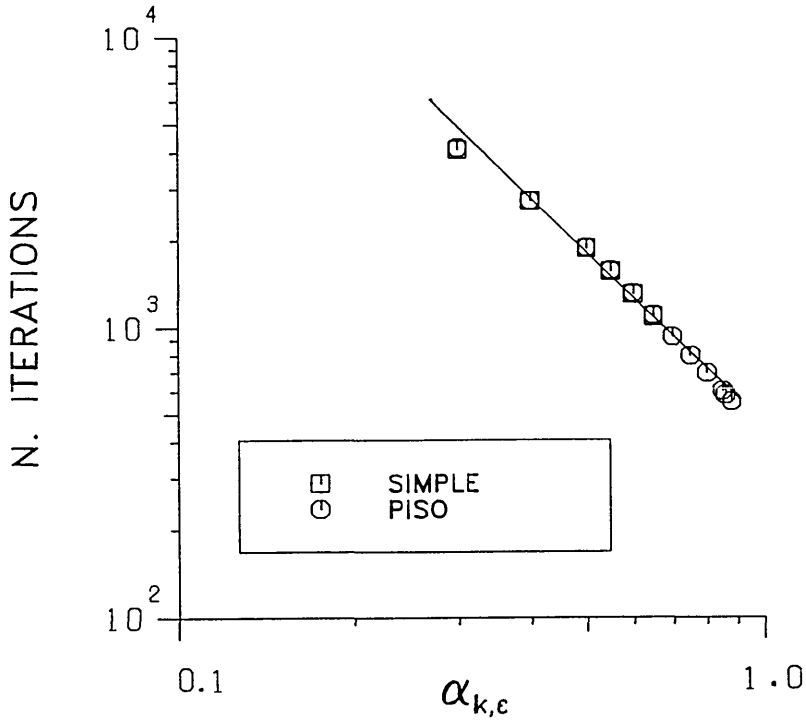


FIGURE 3.11 - Results from Figure 3.5 and Figure 3.9 plotted on logarithmic scales (the straight line was obtained by linear regression and obeys the relationship: $\log N_{iter} = 2.66 - 1.93 \log \alpha$).

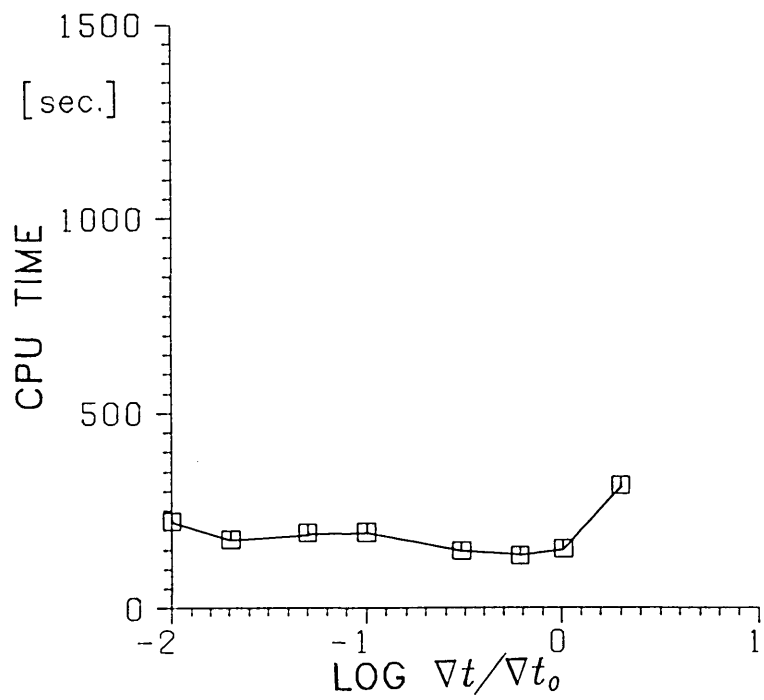


FIGURE 3.12 - Influence of the time step in AVPI (Δt_o = 0.001 sec).

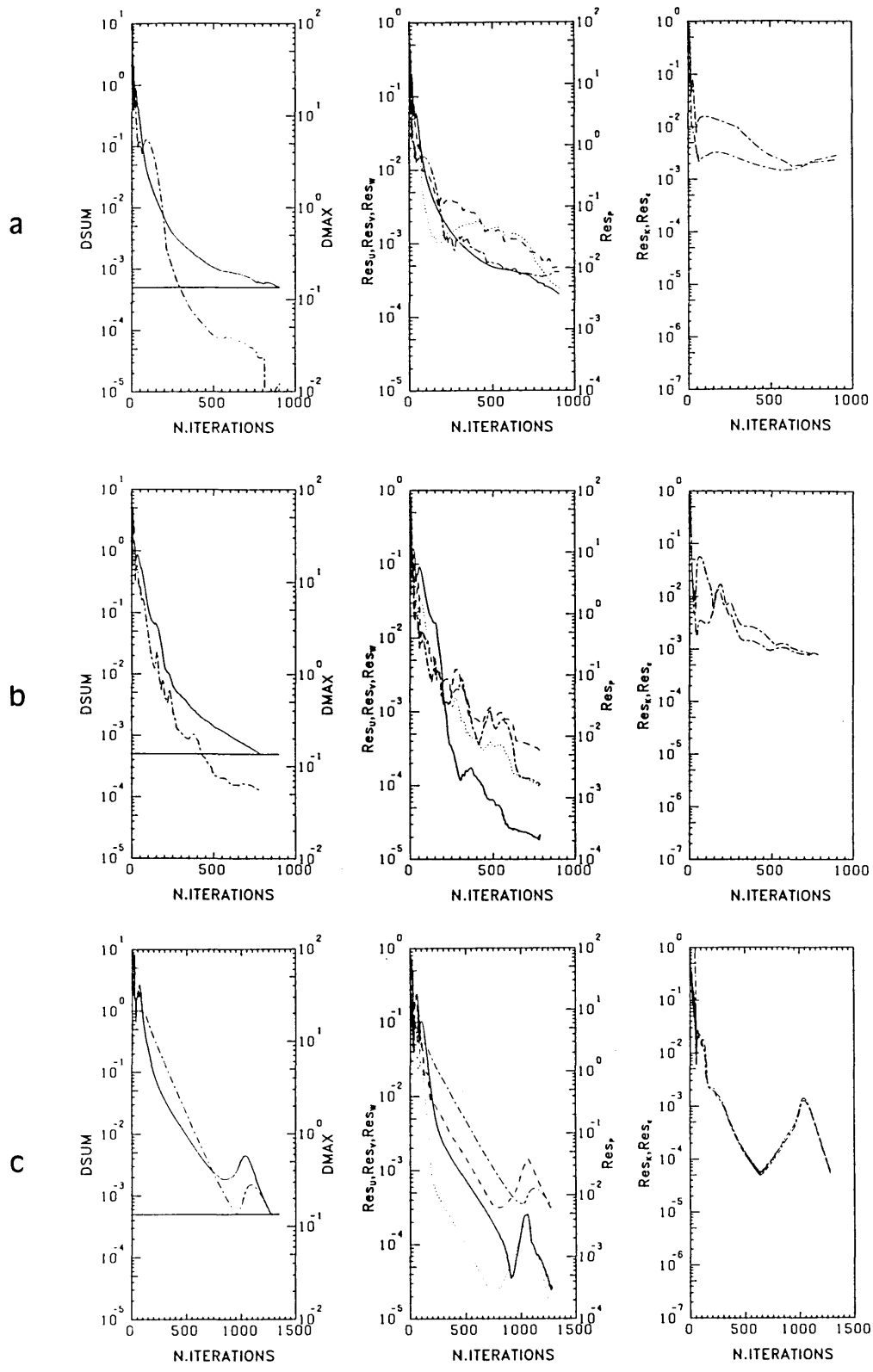


FIGURE 3.13 - The reduction of the residual of all the equations in AVPI for various time steps: a) Δt= 0.00001 sec b) Δt= 0.0001 sec c) Δt= 0.002 sec.

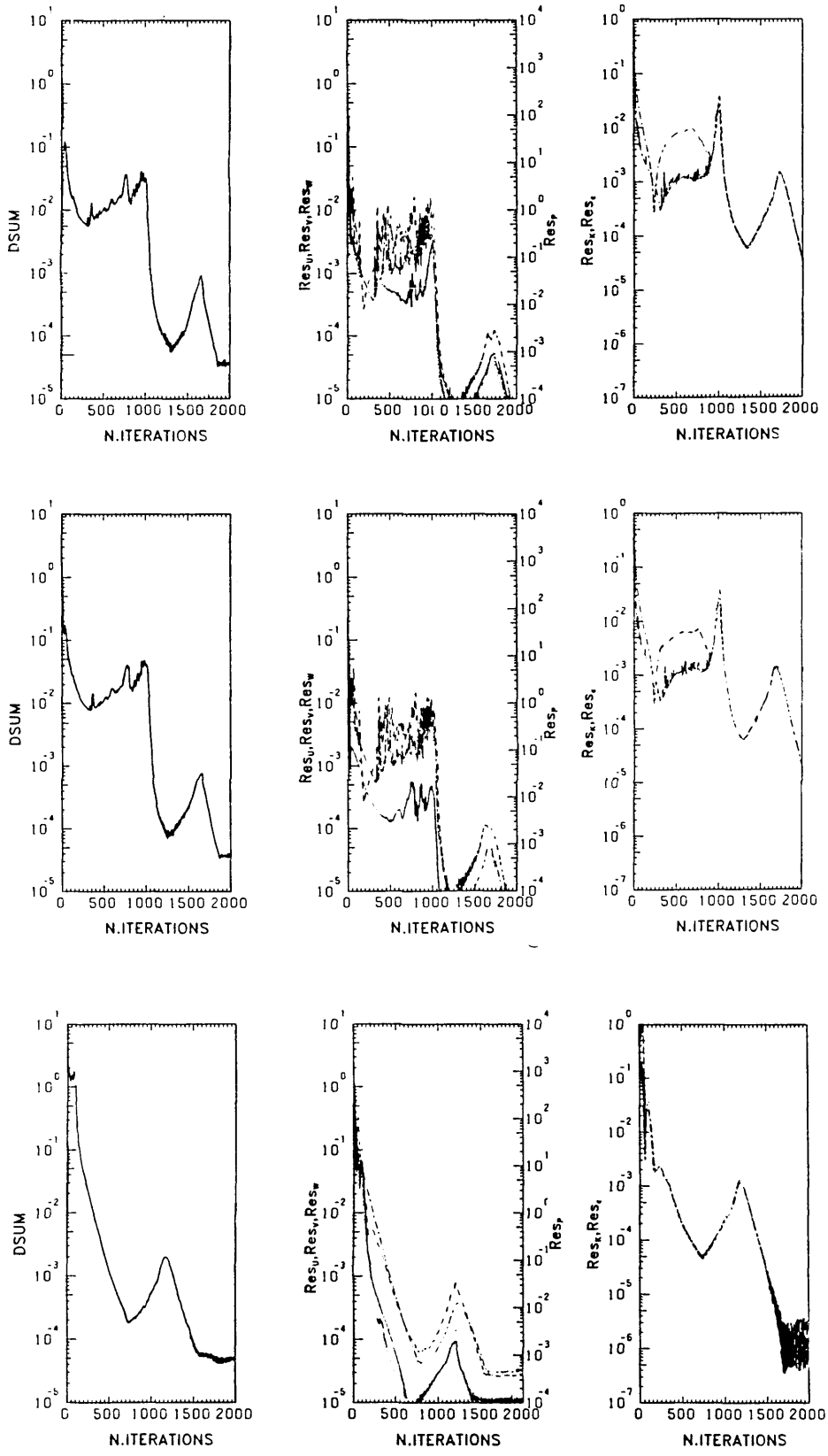


FIGURE 3.14 - The convergence of the calculations carried to the limits of machine accuracy: a) SIMPLE b) PISO c) AVPI.

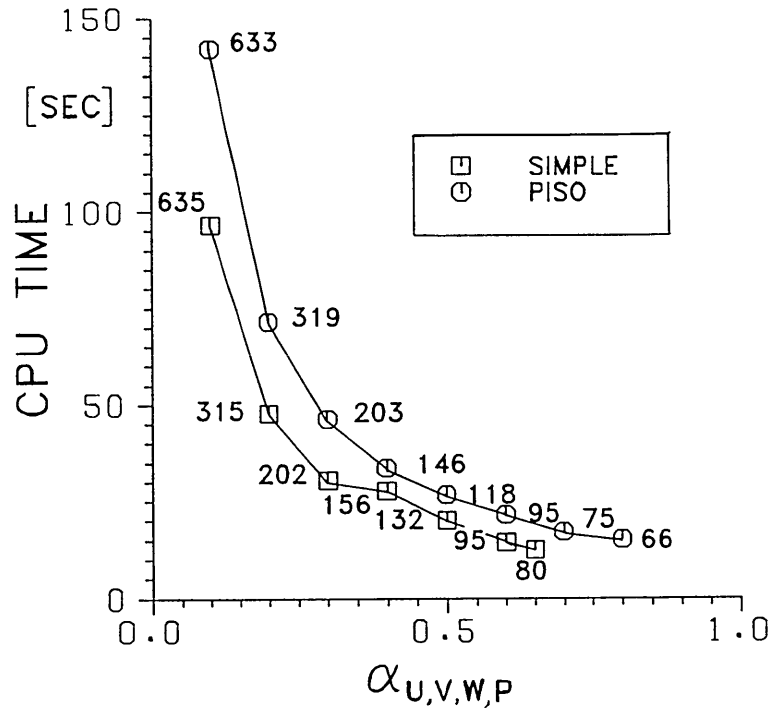


FIGURE 3.15 - Influence of the under-relaxation of the velocities and pressure in SIMPLE and PISO (k-ε fields obtained from a previous run converged to machine accuracy).

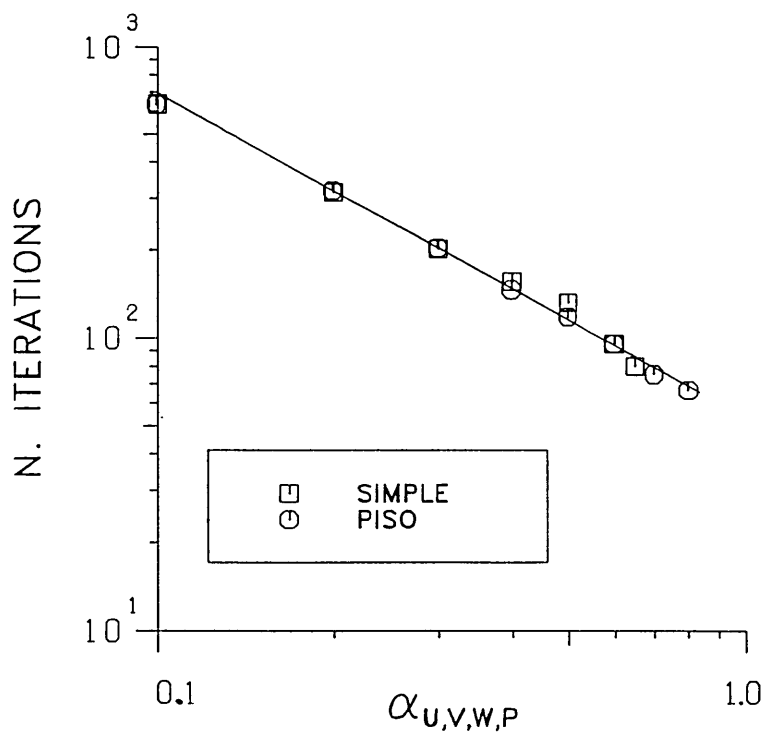


FIGURE 3.16 - Results from Figure 3.15 plotted on logarithmic scales (the straight line was obtained by linear regression and obeys the relationship: log N_{iter} = 1.73 - 1.10 log α).

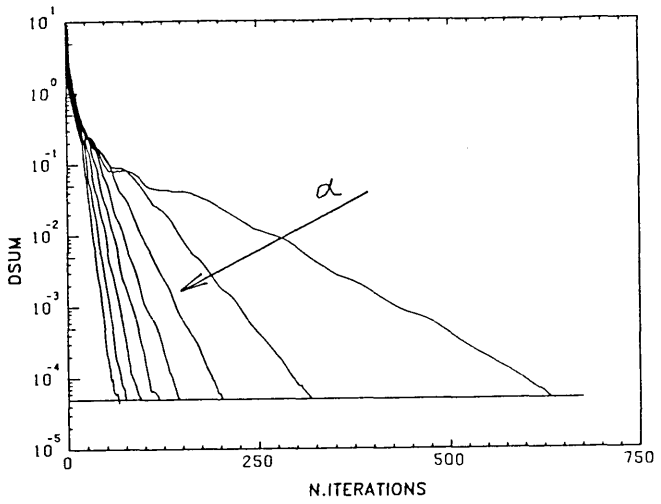


FIGURE 3.17 - The reduction of the mass residual (DSUM) in PISO for various under-relaxation factors $\alpha_{u,v,w,p}$ from 0.1 to 0.8 changed in steps of 0.1 (k-ε fields obtained from a previous run converged to machine accuracy)

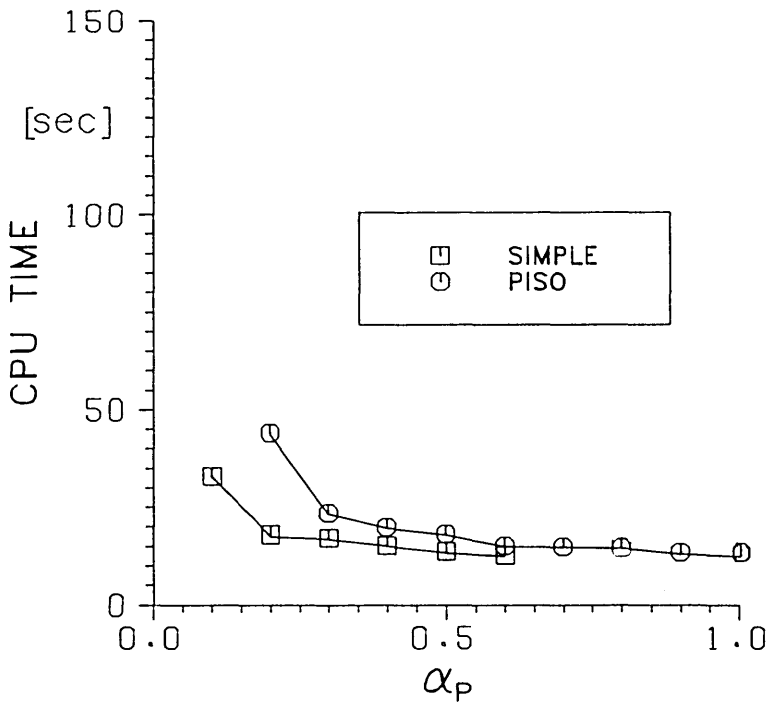


FIGURE 3.18 - Influence of the under-relaxation of the pressure in SIMPLE and PISO -α_p changed while $\alpha_{u,v,w}$ were kept constant (0.65 for SIMPLE and 0.88 for PISO, k-ε fields obtained from a previous run converged to machine accuracy).

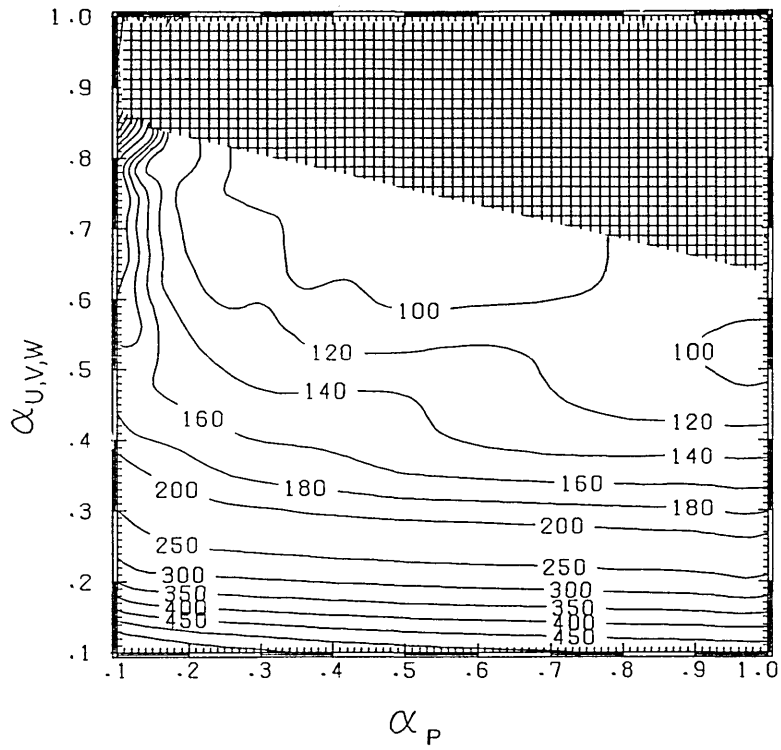


FIGURE 3.19 - Map of convergence of SIMPLE (k-ε fields obtained from a previous run converged to machine accuracy) - contours of number of iterations to reach convergence.

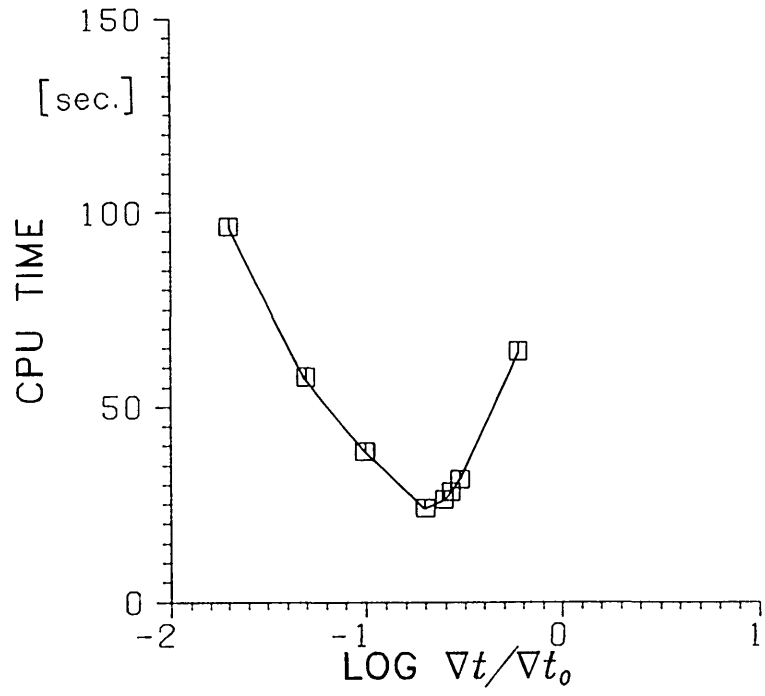


FIGURE 3.20 - Influence of the time step in AVPI (k-ε fields obtained from a previous run converged to machine accuracy).

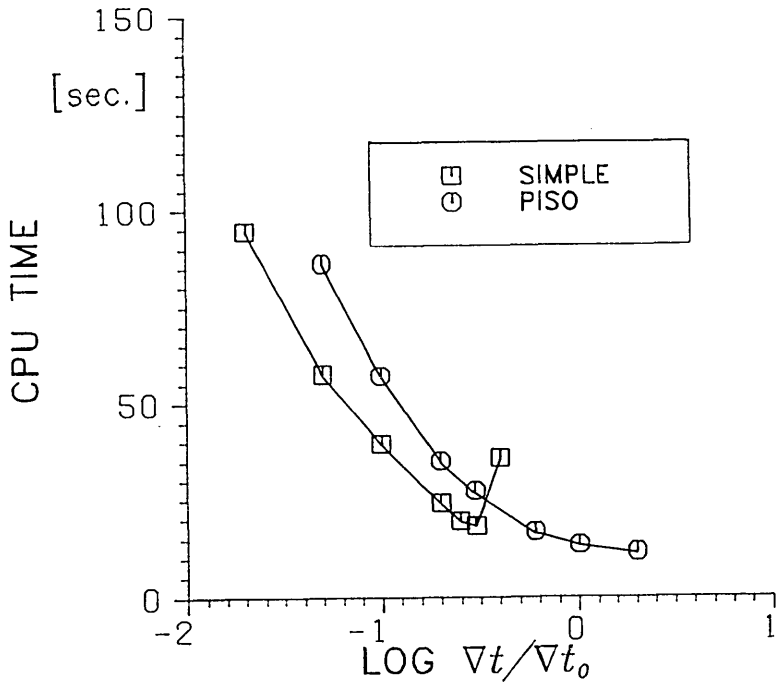


FIGURE 3.21 - Influence of the time step in SIMPLE and PISO (k-ε fields obtained from a previous run converged to machine accuracy).

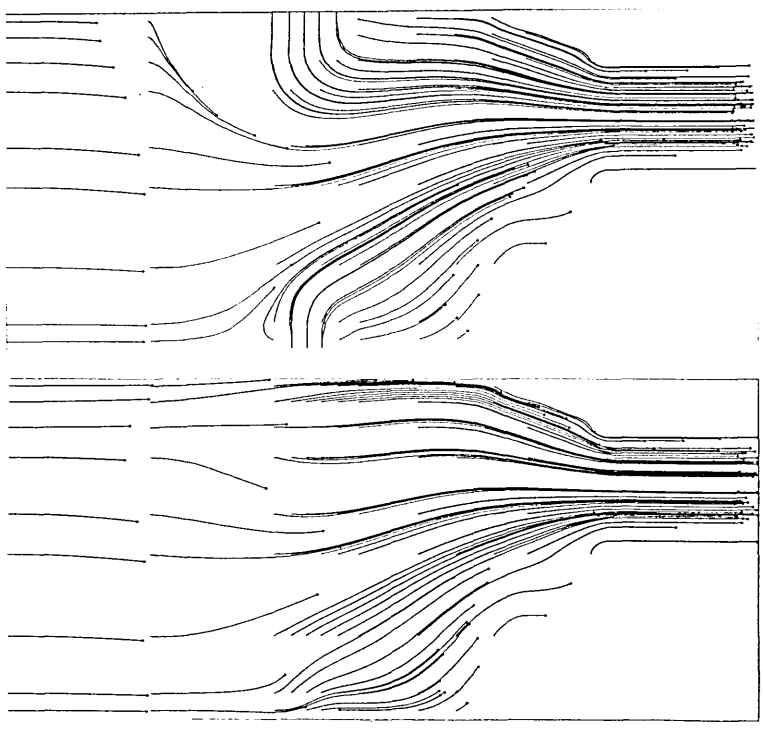


FIGURE 3.22 - Streakline plots: longitudinal views (grid 17 ×11 ×6) (case 1): a) centre plane b) mid plane.

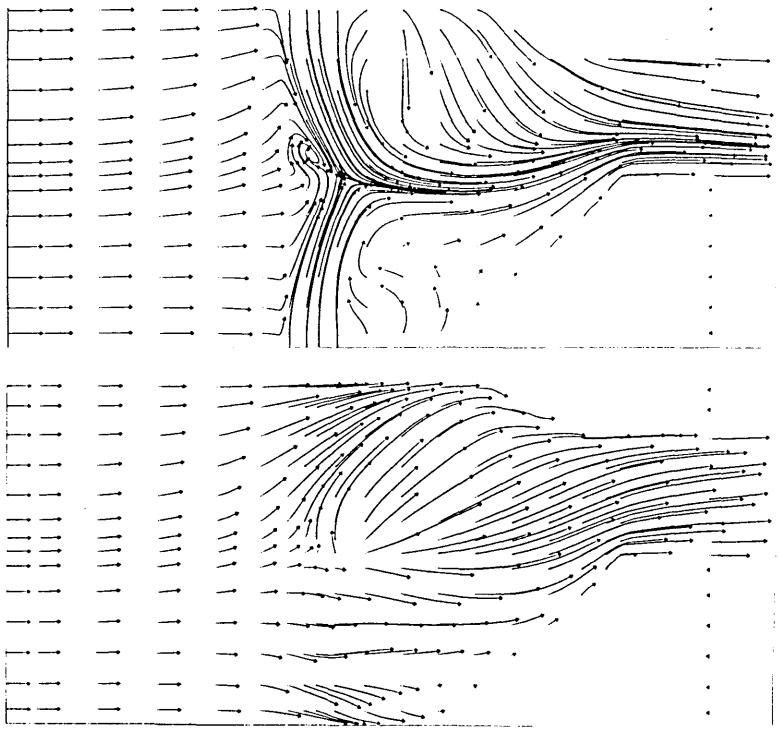


FIGURE 3.23 - Streakline plots: longitudinal views (grid 40 × 30 × 15) (case 1): a) centre plane b) mid plane.

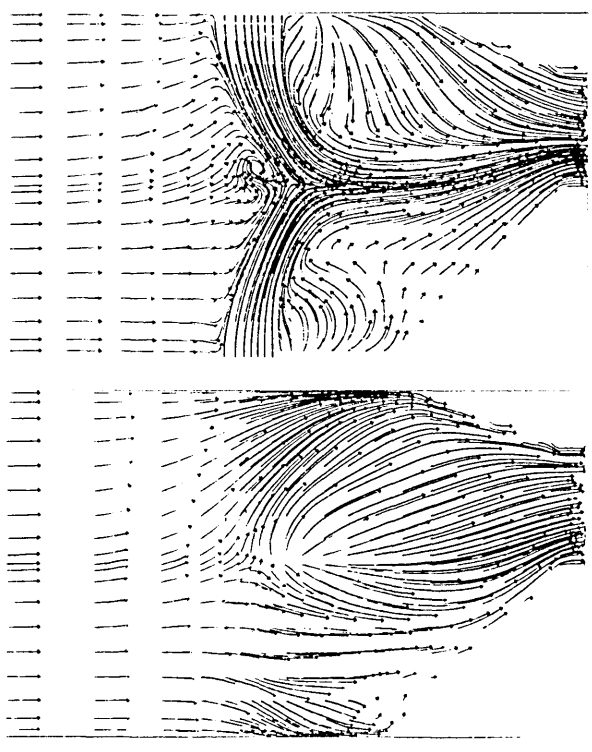


FIGURE 3.24 - Streakline plots: longitudinal views (grid 70 × 40 × 25) (case 1): a) centre plane b) mid plane.

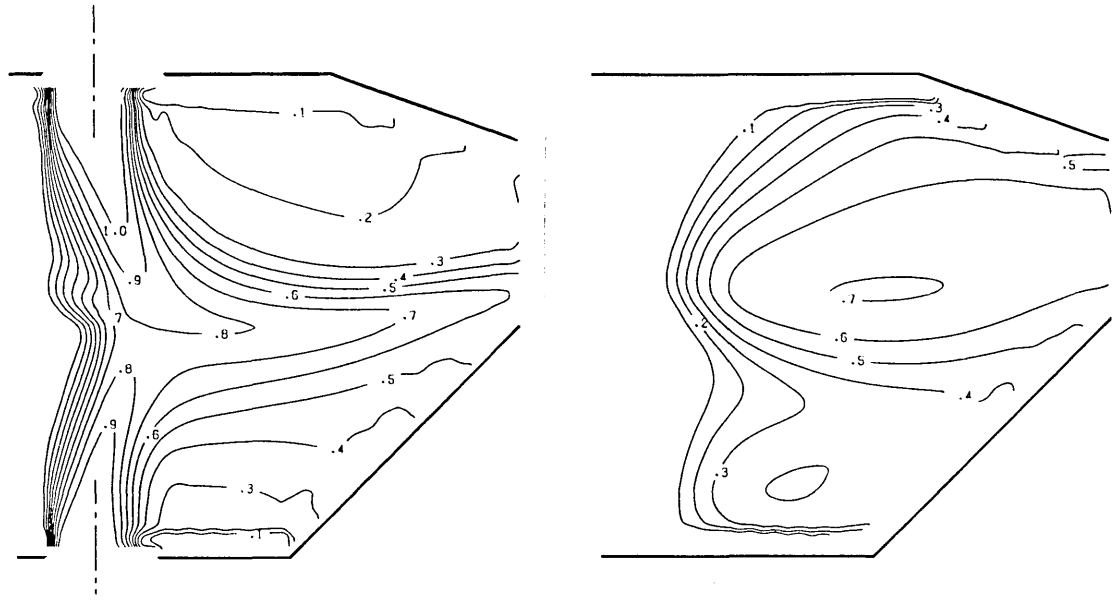


FIGURE 3.25 - Longitudinal contours of Φ^* (grid 40 × 30 × 15) (case 1):
a) centre plane b) mid plane.

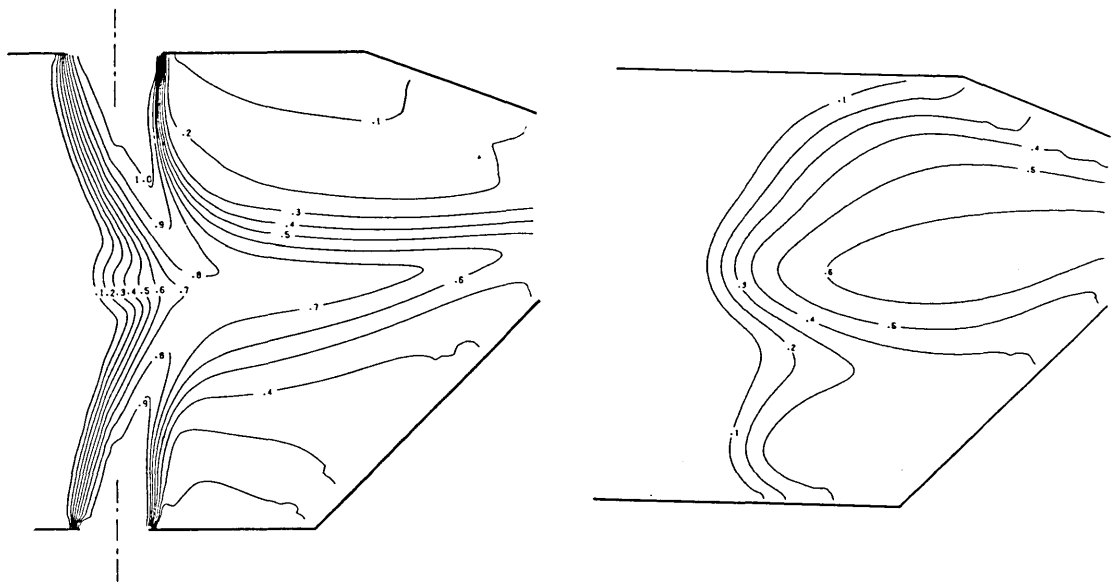
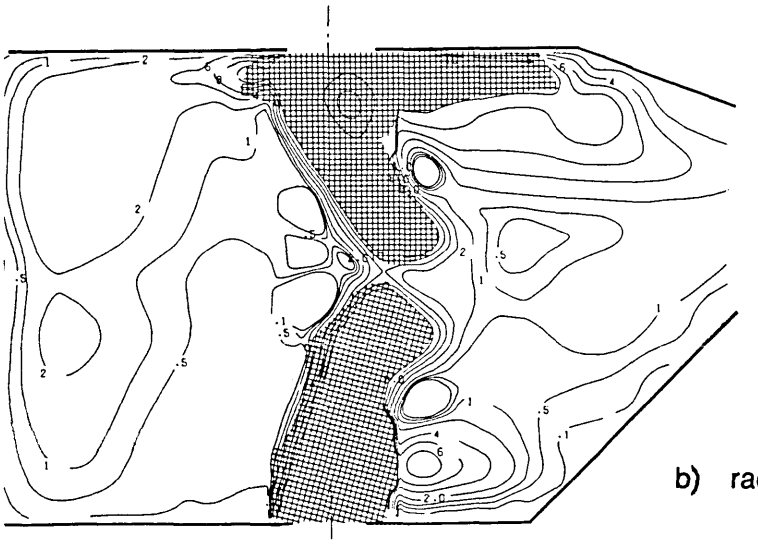
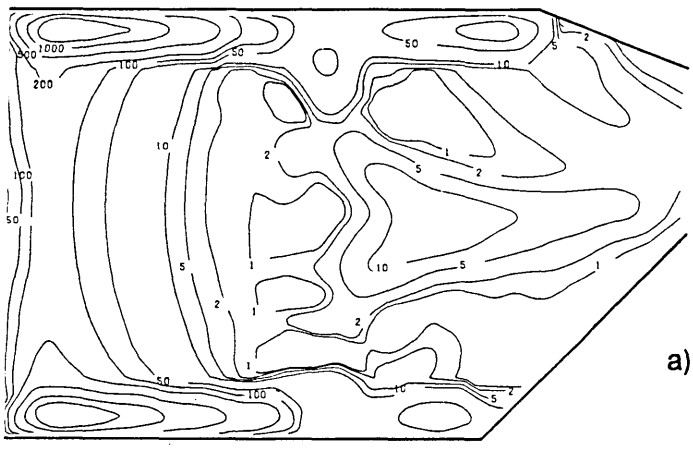


FIGURE 3.26 - Longitudinal contours of Φ^* (grid 70 × 40 × 25) (case 1):
a) centre plane b) mid plane.



b) radial direction



a) axial direction

FIGURE 3.27 - Peclet number contours on centre plane (grid 70 × 40 × 25) (case 1).

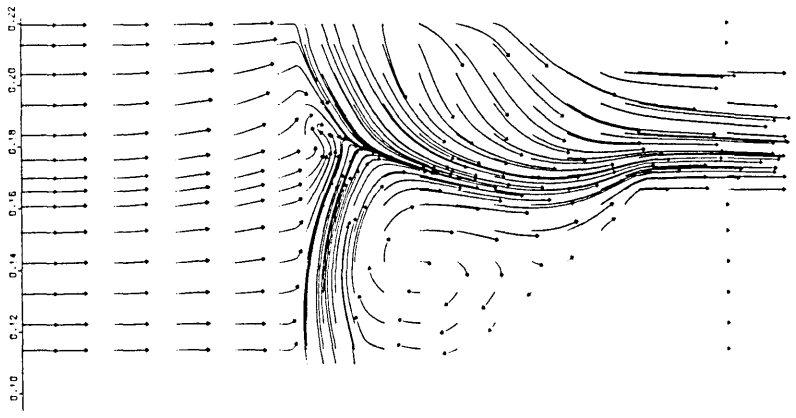


FIGURE 3.28 - Streakline plots: longitudinal views (grid 40 × 30 × 15)- inclined jets: a) centre plane

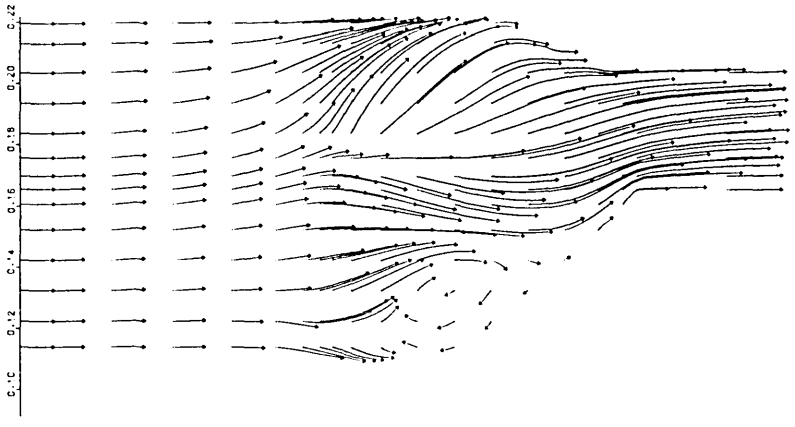


FIGURE 3.28 (continued)– Streakline plots: longitudinal views (grid 40 × 30 × 15)- inclined jets: b) mid plane.

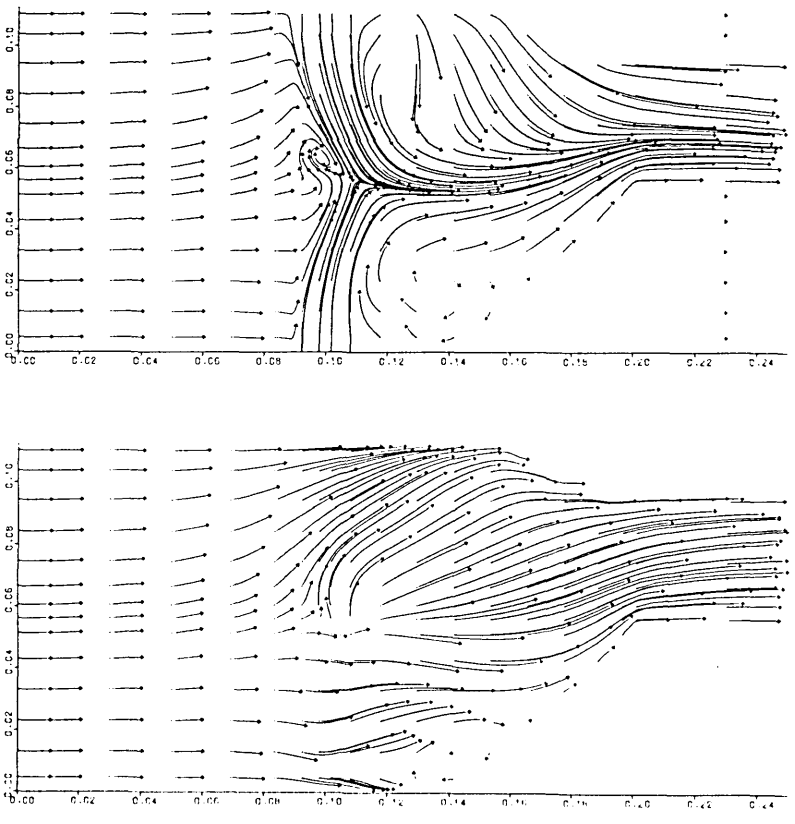


FIGURE 3.29 - Streakline plots: longitudinal views (grid 40 × 30 × 15)- double symmetry: a) centre plane b) mid plane.

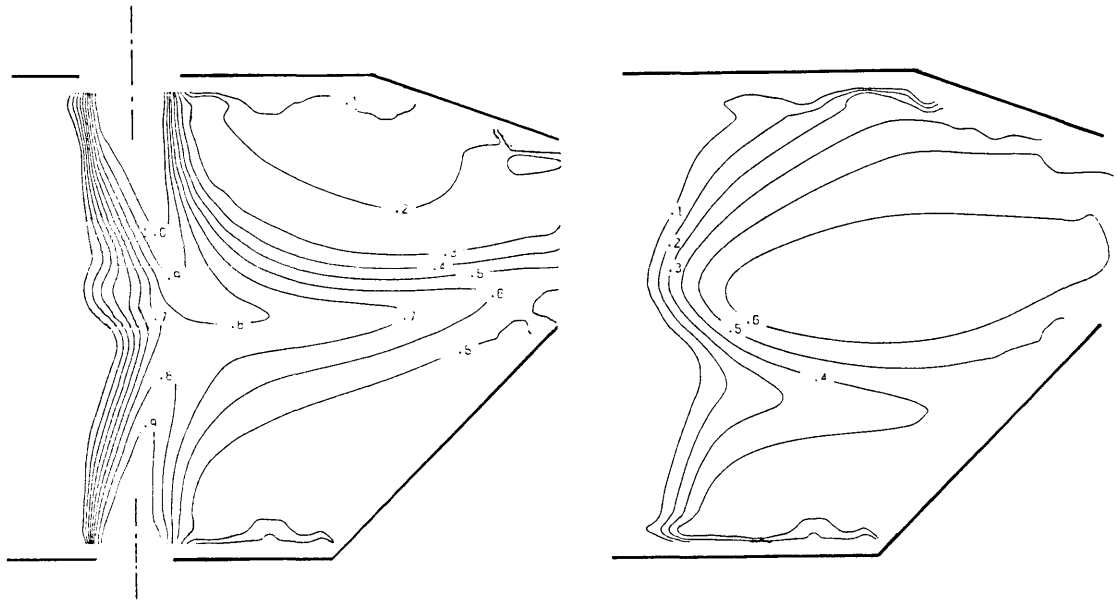


FIGURE 3.30 - Longitudinal contours of Φ (grid 40 x 30 x 15)- double symmetry: a) centre plane b) mid plane.

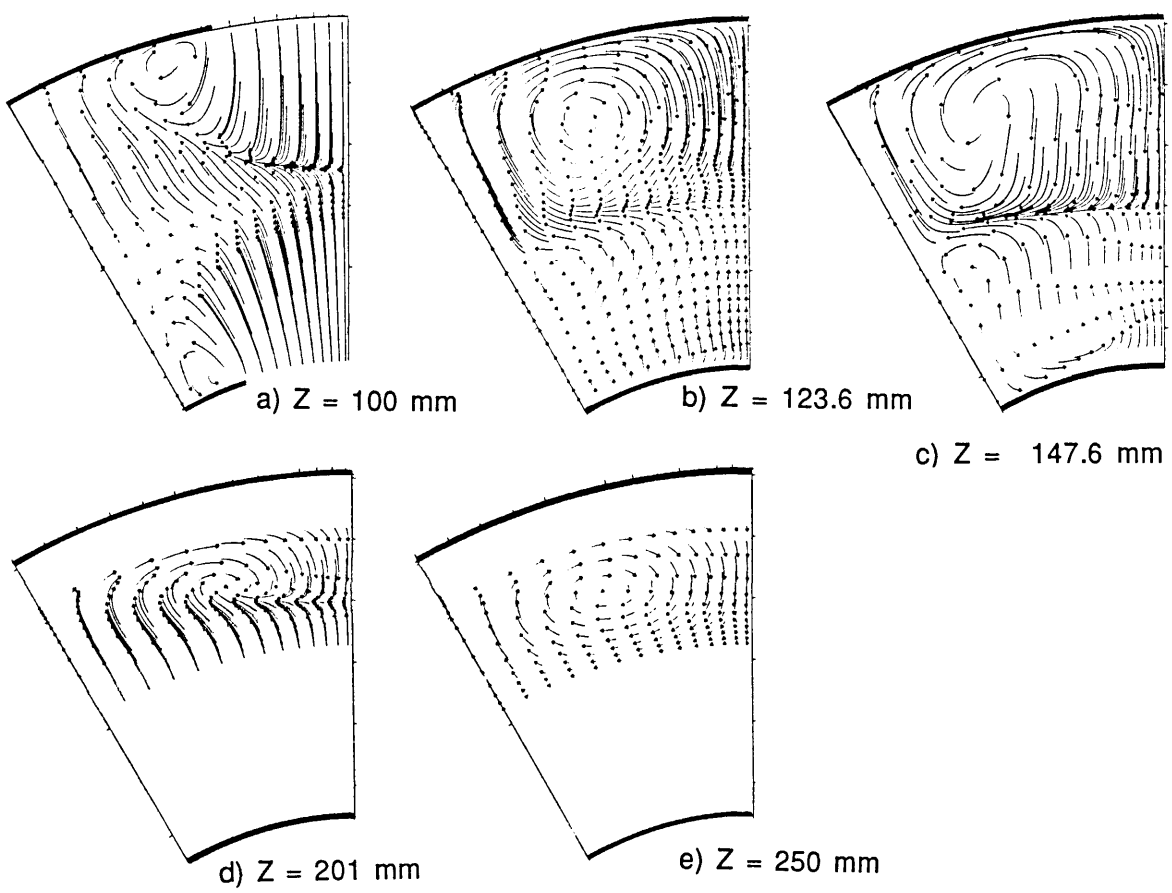


FIGURE 3.31 - Streakline plots: cross-sectional views (grid 40 x 30 x 15)- symmetry (case 1).

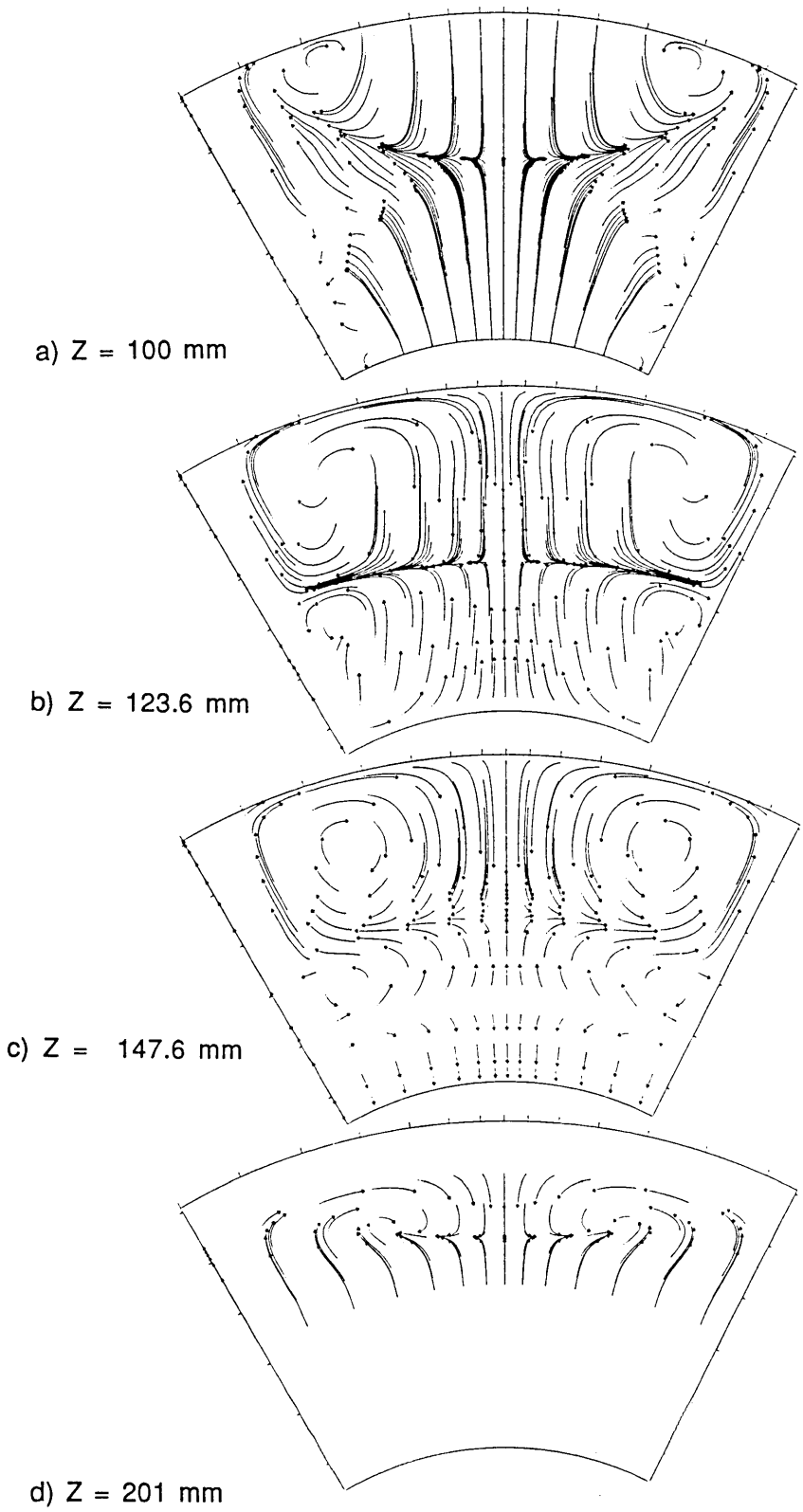


FIGURE 3.32 - Streakline plots: cross-sectional views (grid 40 × 30 × 15)- double symmetry.

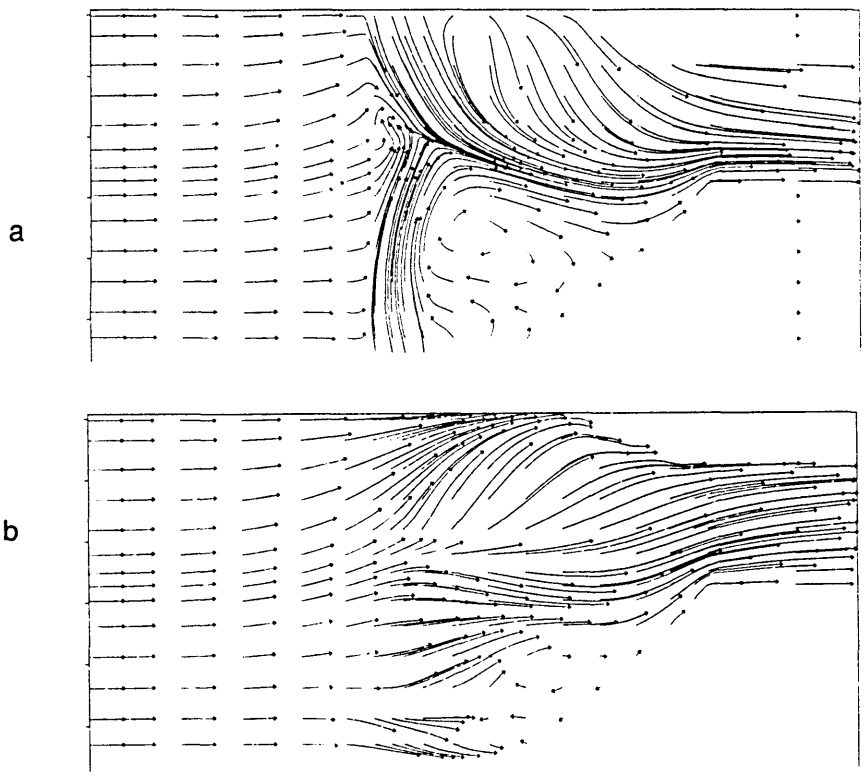
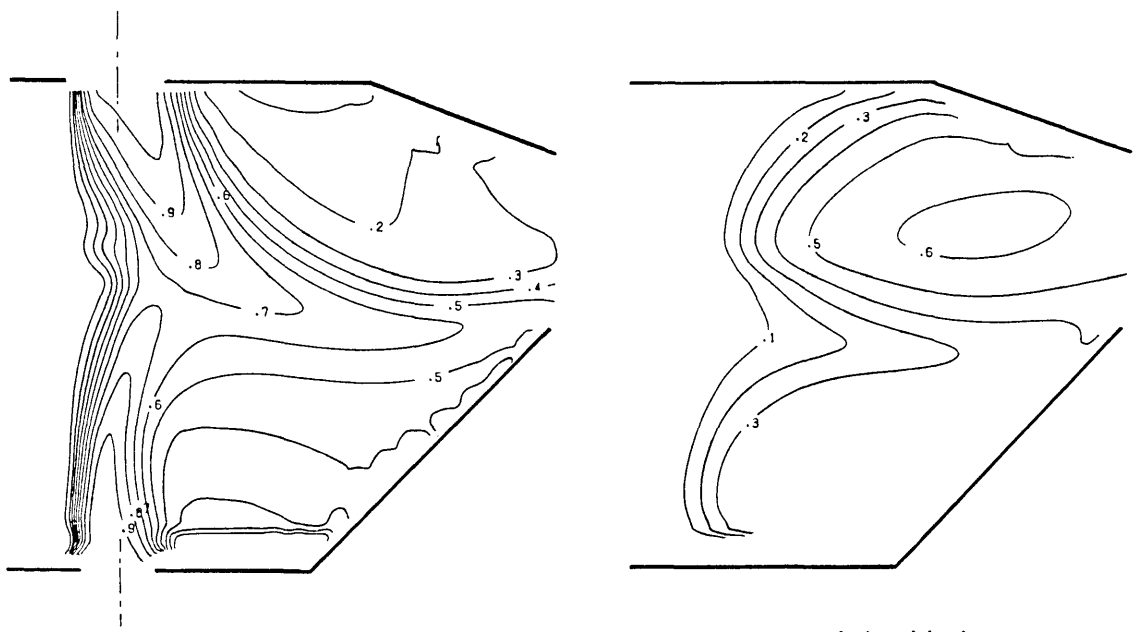


FIGURE 3.33 - Streakline plots: longitudinal views (grid 40 × 30 × 30)- inclined jets (case 2): a) centre plane b) mid plane.



a) centre plane b) mid plane.

FIGURE 3.34 - Longitudinal contours of Φ^* (grid 40 × 30 × 30)- inclined jets (case 2).

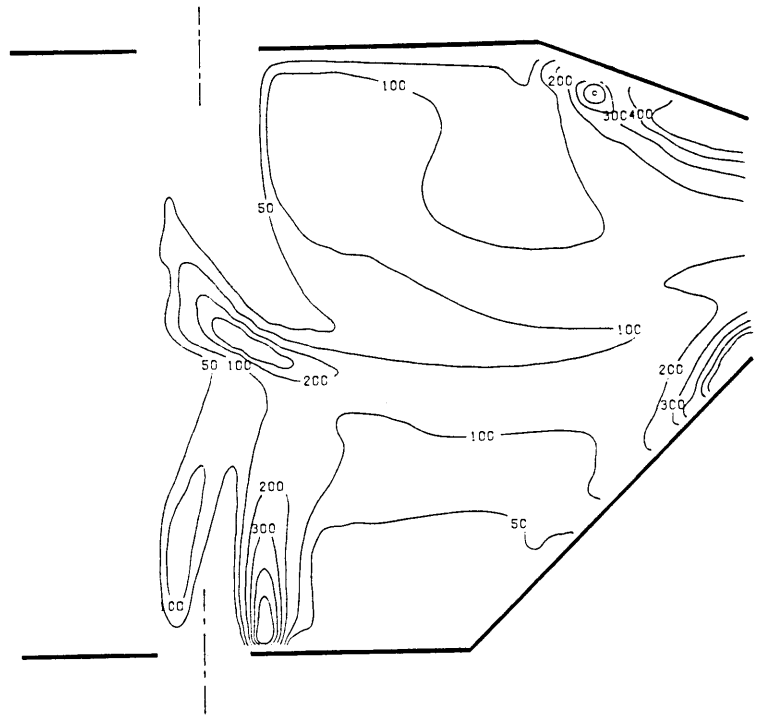


FIGURE 3.35 - Longitudinal contours of turbulence kinetic energy (grid 40 × 30 × 15) (case 1): centre plane

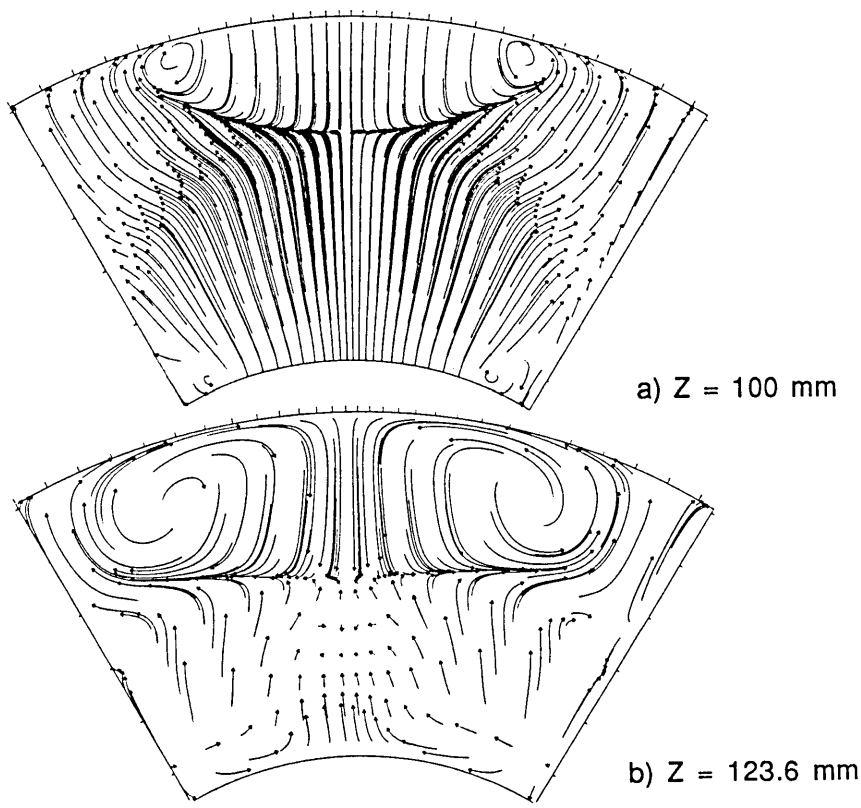
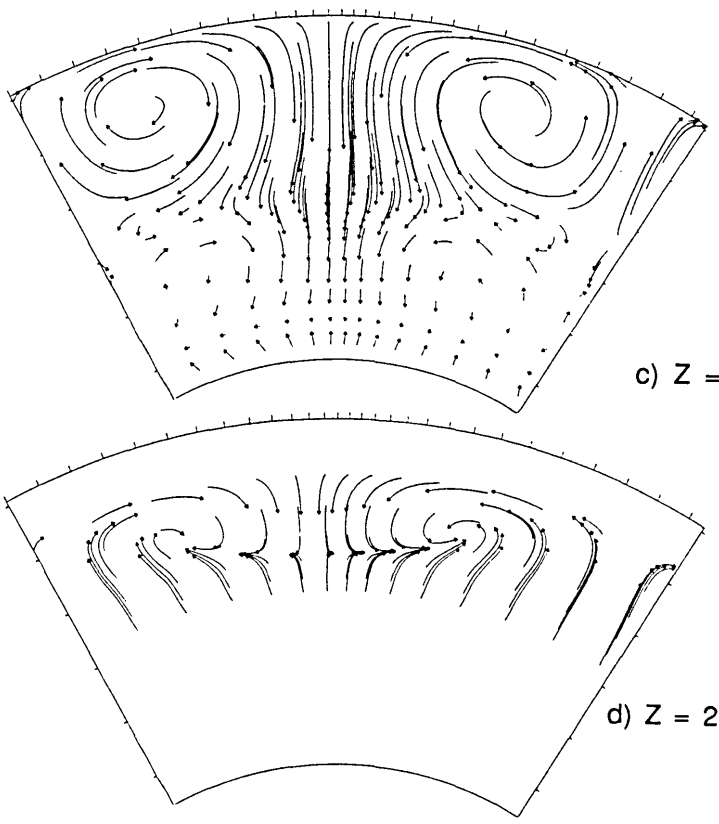


FIGURE 3.36 - Streakline plots: cross-sectional views (grid 40 × 30 × 30)- inclined jets (case 2).



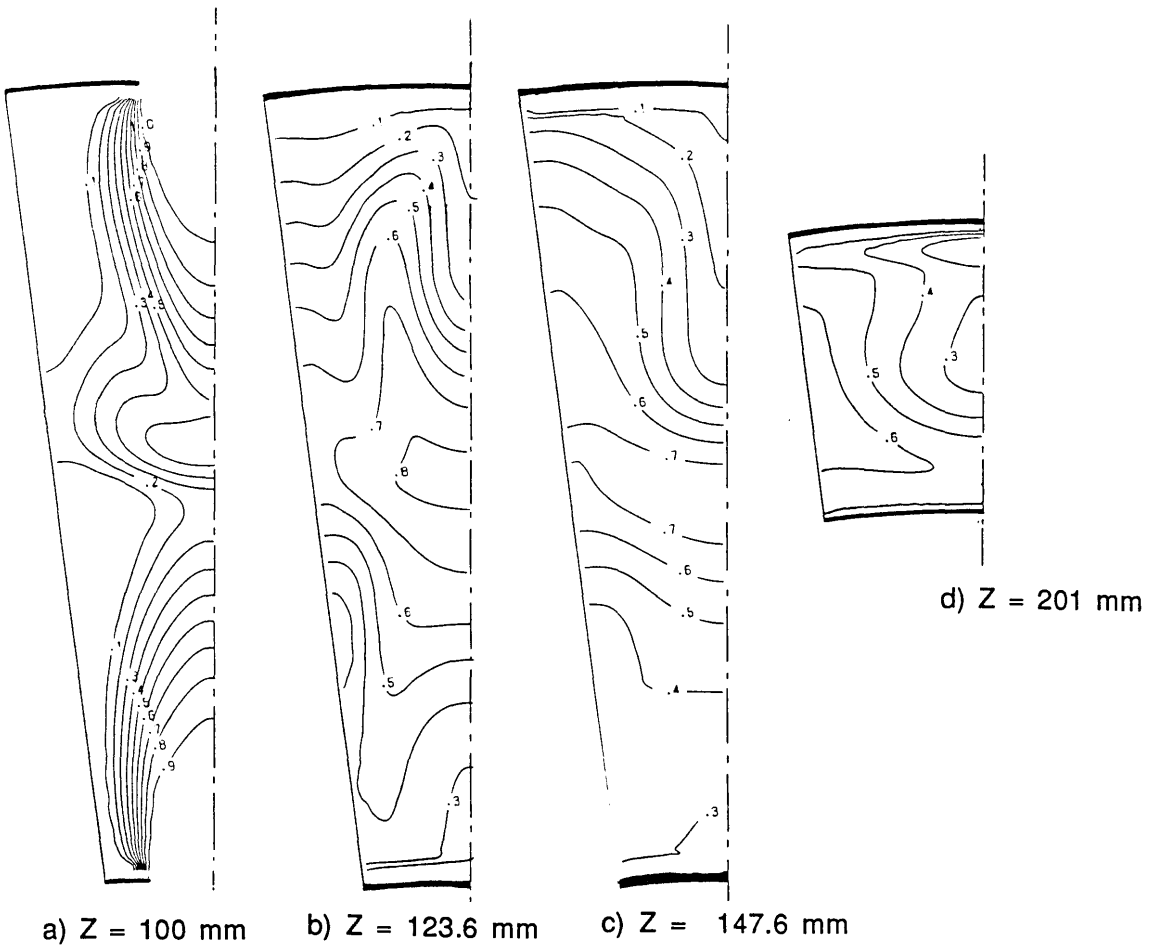
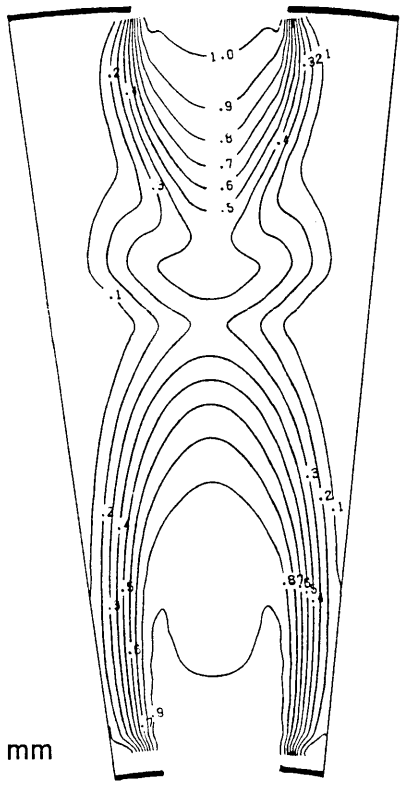
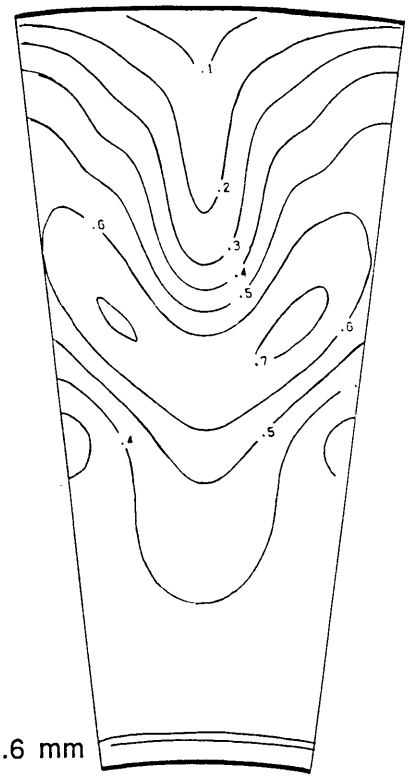


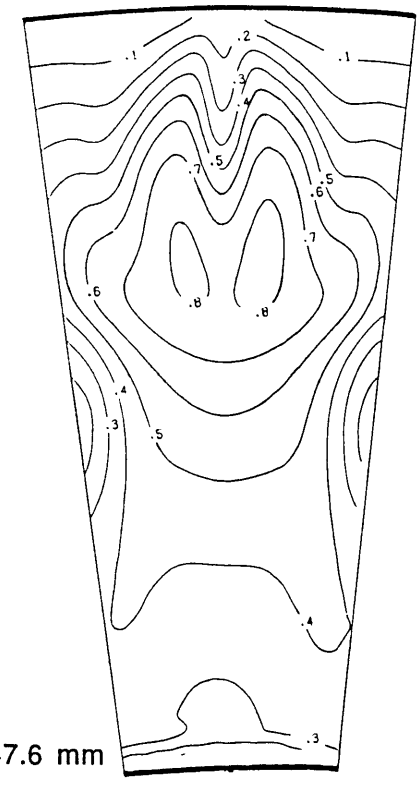
FIGURE 3.37 - Contours of Φ, cross-sectional views (grid 40 × 30 × 15) - symmetry (case 1).



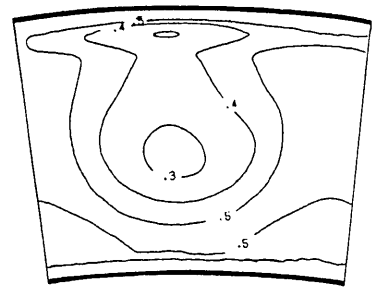
a) Z = 100 mm



b) Z = 123.6 mm



c) Z = 147.6 mm



d) Z = 201 mm

FIGURE 3.38 - Contours of Φ^*, cross-sectional views (grid 40 × 30 × 30) - inclined jets (case 2).

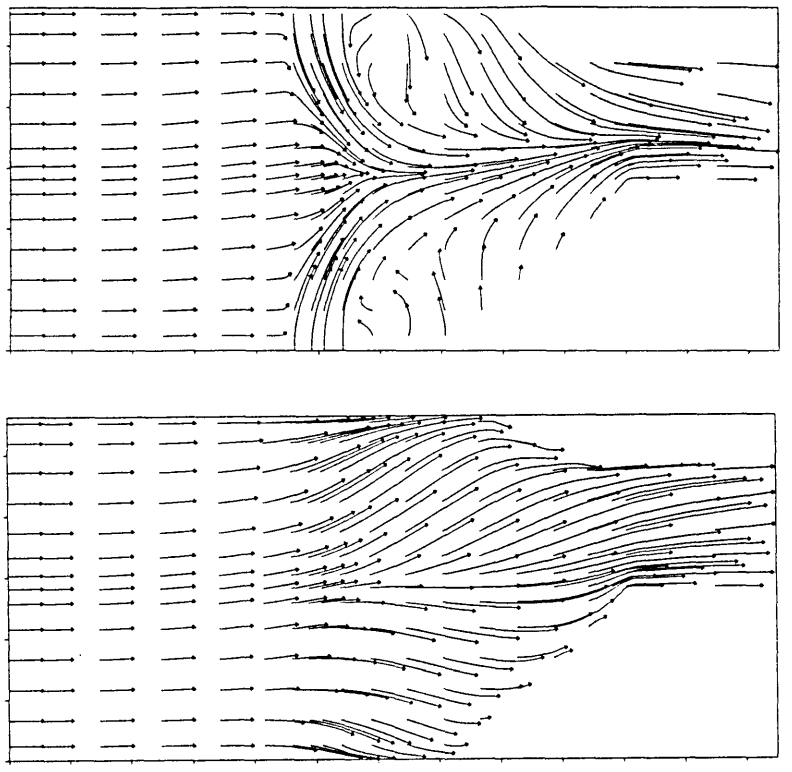


FIGURE 3.39 - Streakline plots: longitudinal views (grid 40 × 30 × 15)- variable density calculations (case 3): a) centre plane b) mid plane.

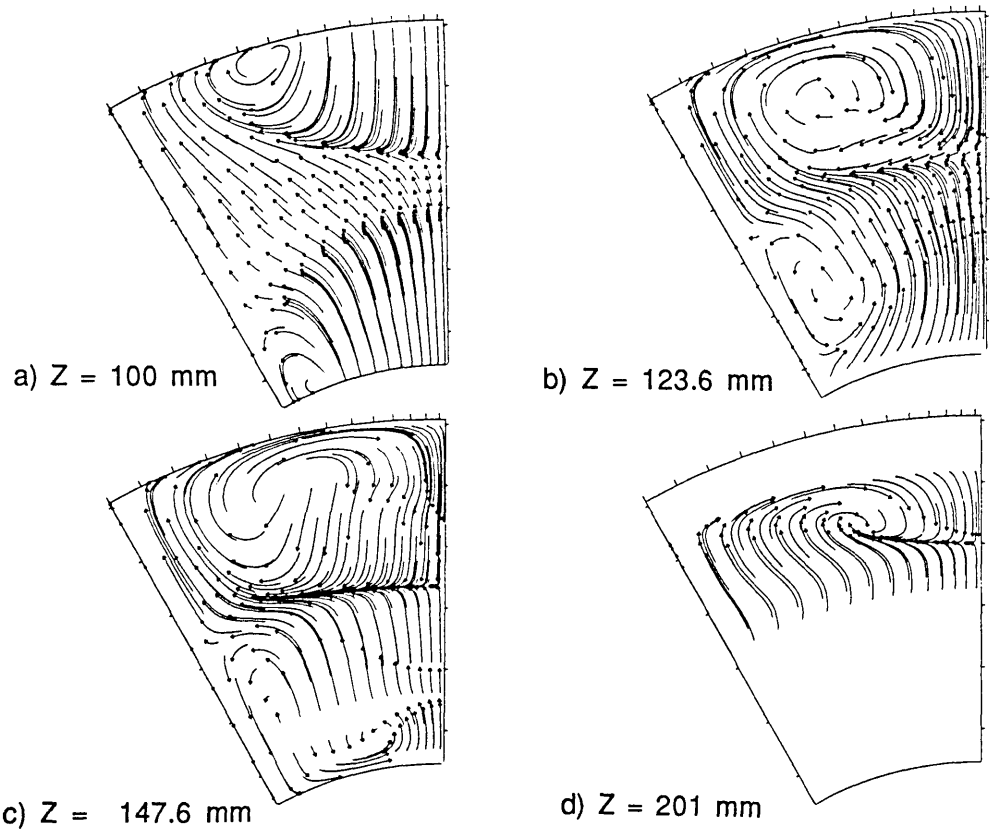


FIGURE 3.40 - Streakline plots: cross-sectional views (grid 40 × 30 × 15)- variable density calculations (case 3).

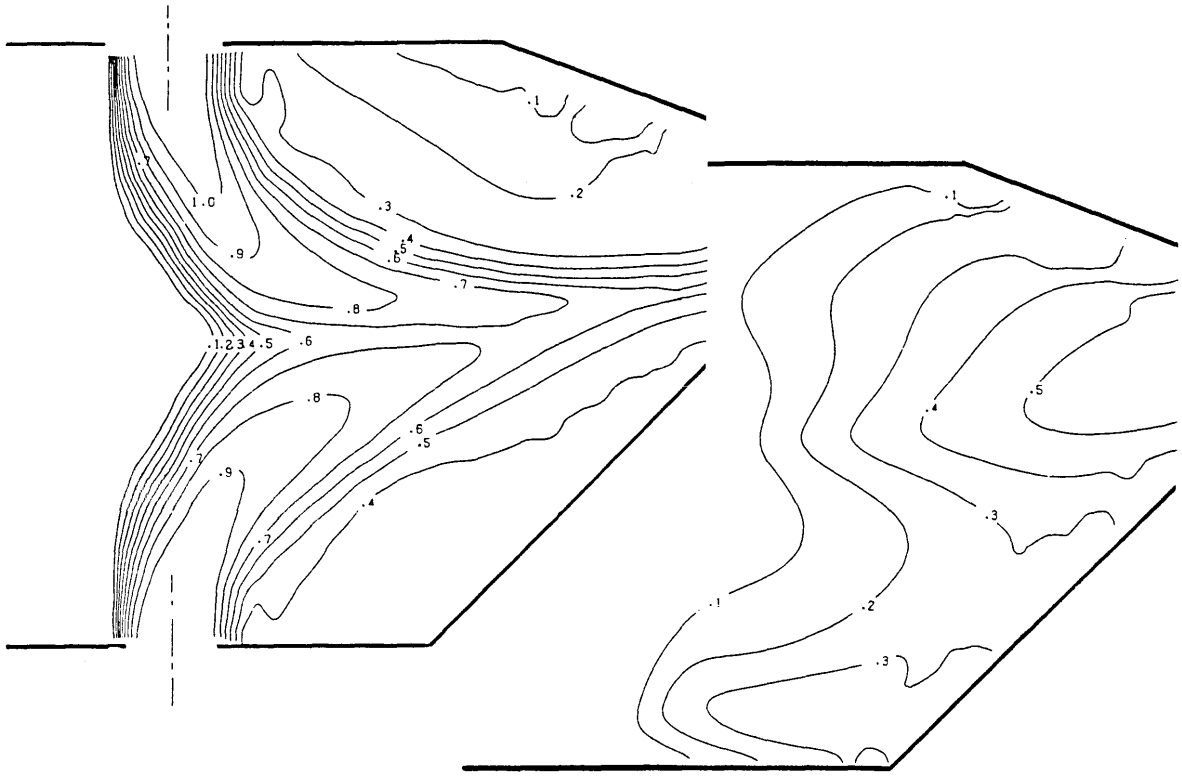


FIGURE 3.41 - Longitudinal contours of Φ^* (grid 40 × 30 × 15)- variable density calculations (case 4): a) centre plane b) mid plane.

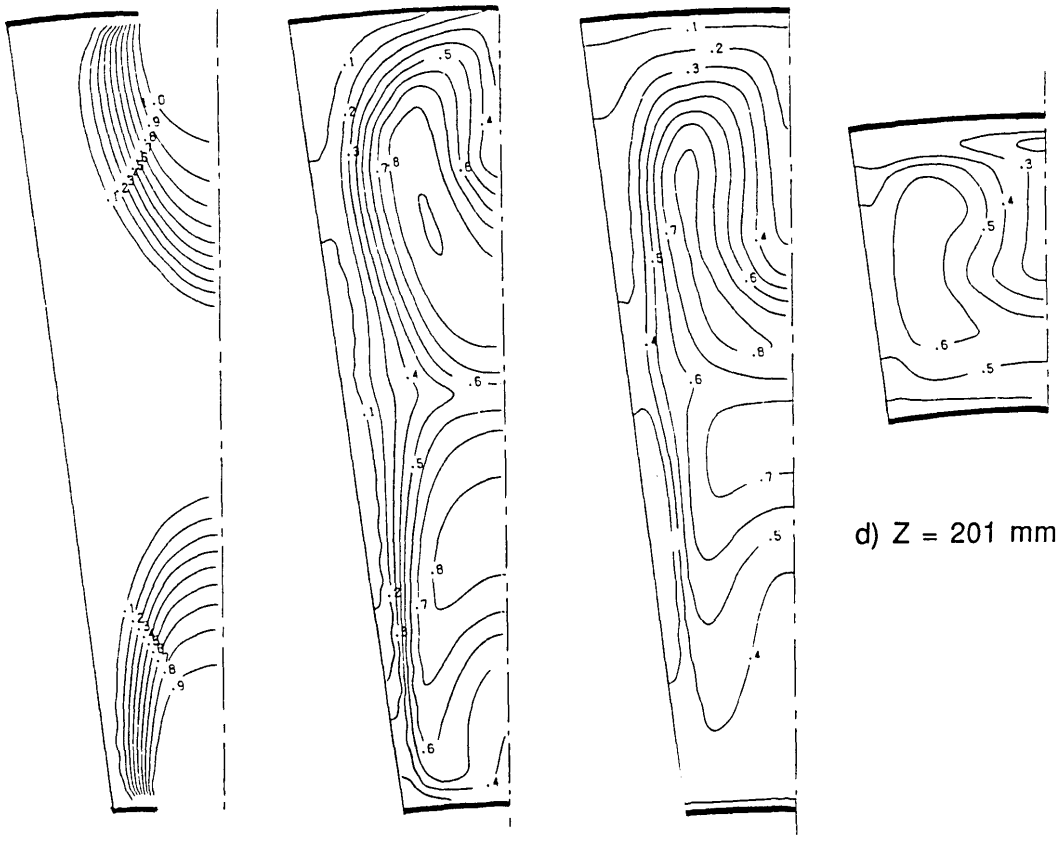


FIGURE 3.42 - Contours of T^*, cross-sectional views (grid 40 × 30 × 15) - variable density calculations (case 4).

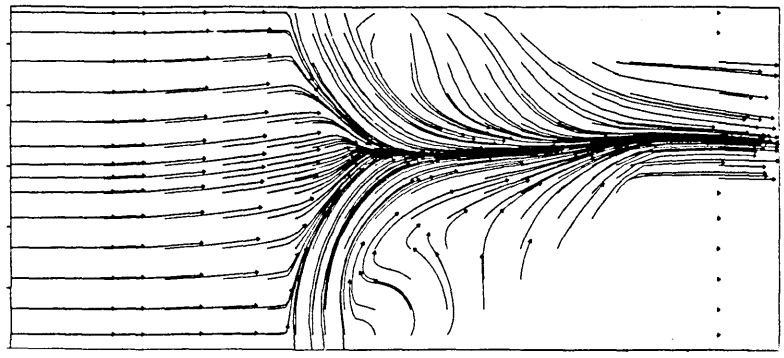


FIGURE 3.43 - Streakline plots: longitudinal views (grid 40 x 30 x 30)- variable density calculations, inclined jets (case 4): centre plane

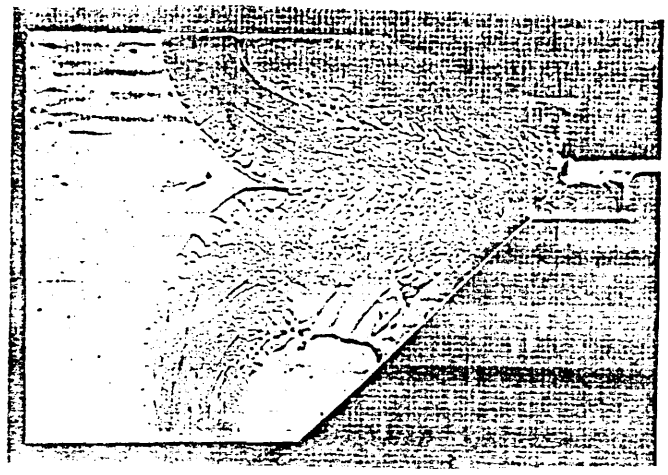
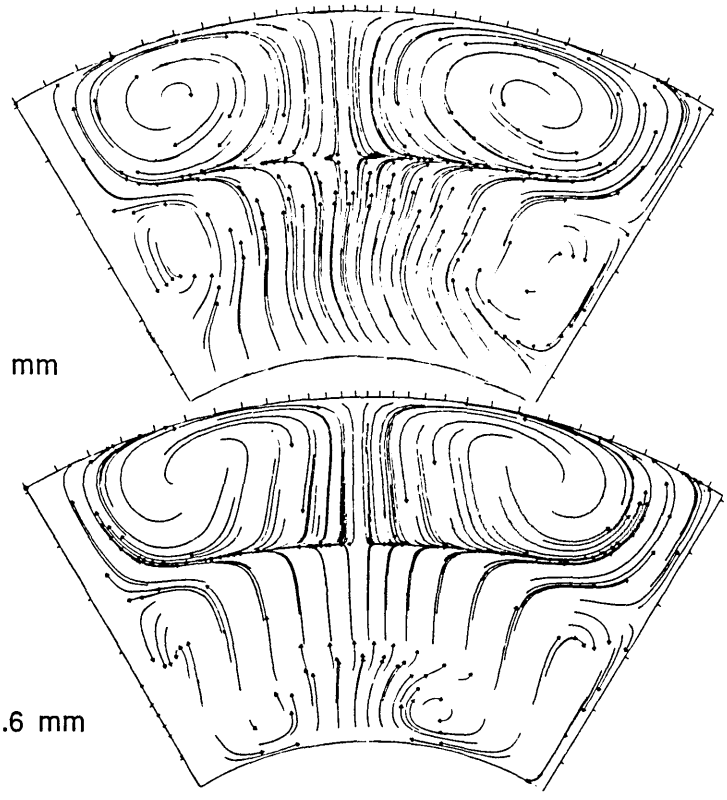


FIGURE 3.44 - Flow visualization (from Shaw [1981])



a) Z = 100 mm

b) Z = 123.6 mm

FIGURE 3.45 - Streakline plots: cross-sectional views (grid 40 x 30 x 30)- variable density calculations, inclined jets (case 4).

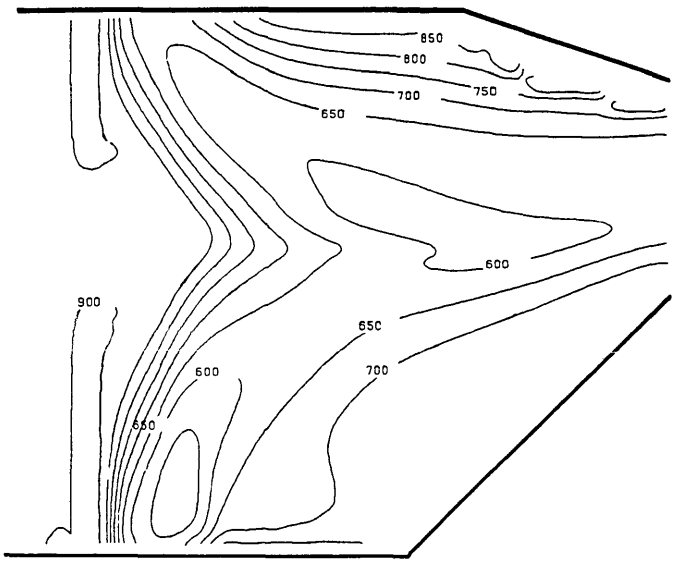
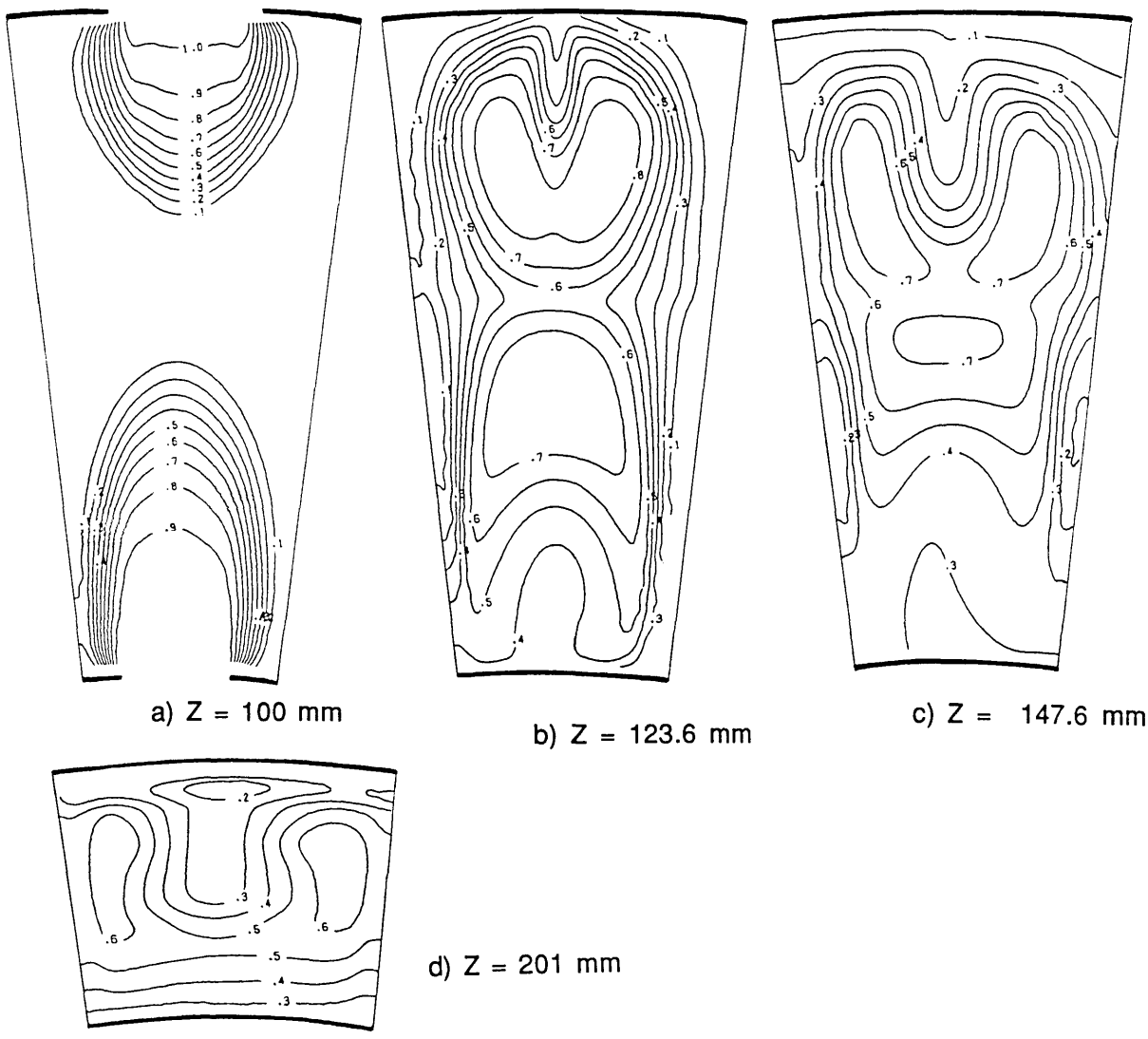


FIGURE 3.46 - Longitudinal radially averaged contours of mean radial temperature (grid 40 ×30 ×30)- variable density calculations, inclined jets (case 4).



a) Z = 100 mm

b) Z = 123.6 mm

c) Z = 147.6 mm

d) Z = 201 mm

FIGURE 3.47 - Contours of T^*, cross-sectional views (grid 40 × 30 × 30) - variable density calculations, inclined jets.

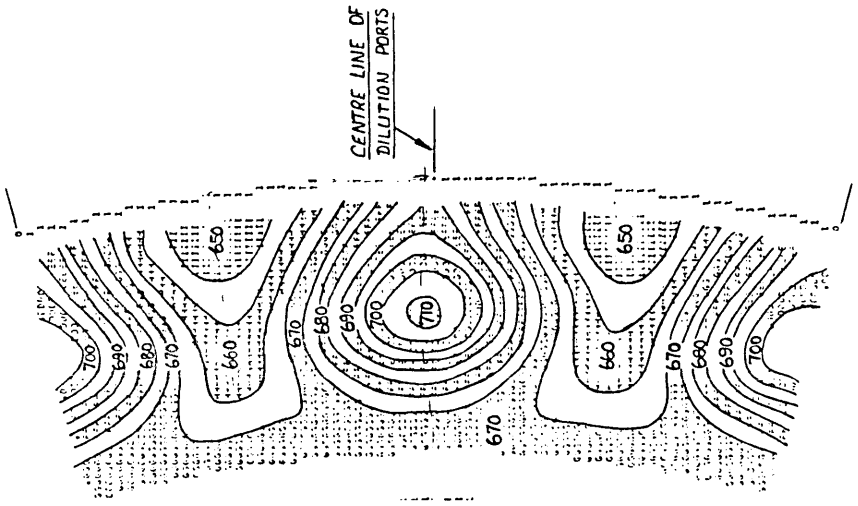


FIGURE 3.48 - Experimental temperature contours at the outlet section (from Shaw [1981]).



a) turbulent Prandtl number equal to 0.9 b) turbulent Prandtl number equal to 0.5.

FIGURE 3.49 - Temperature contours at the outlet section (grid 40 × 30 × 30) - variable density calculations, inclined jets (case 4).

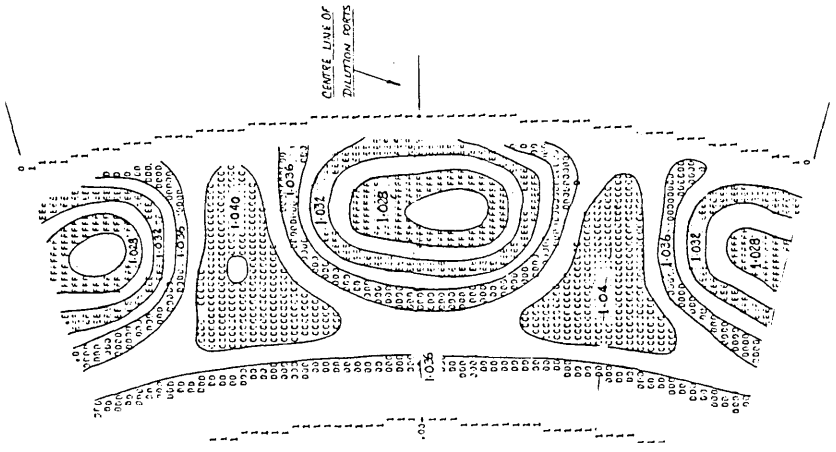


FIGURE 3.50 - Experimental total pressure contours at the outlet section (from Shaw [1981]).

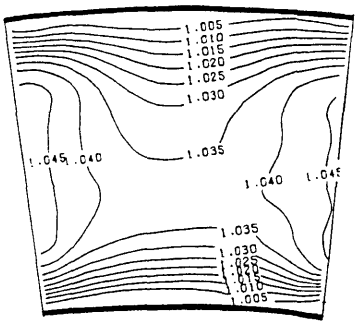


FIGURE 3.51 - Total pressure contours at the outlet section (grid 40 × 30 × 30) - variable density calculations, inclined jets (case 4), turbulent Prandtl number equal to 0.9.

CHAPTER 4
EXPERIMENTS IN A WATER MODEL OF A CAN-TYPE GAS TURBINE COMBUSTOR

4.1 INTRODUCTION

4.1.1 Objectives and Outline of the Chapter

The following chapter includes the main experimental contribution of the present work. The objective was the simulation, in a water model, of the internal flow pattern typical of a can-type gas turbine combustor and the generation of experimental data to assist the validation and development of mathematical models for such flows. Flow visualization and measurements of the physical variables of major importance, mean and fluctuating velocities, have been made. The use of water flow rather than air allows smaller model dimensions and lower velocities for similar Reynolds number, due to the higher viscosity of water. This choice facilitates flow visualization and, when using laser Doppler velocimetry (LDV) as in the present work, alleviates the seeding problems, since the naturally occurring particles in water are very efficient light scattering centres. The application of a non-intrusive technique, laser induced fluorescence (LIF), to measure the mean and fluctuating concentration was also initiated, but this is described in Appendix A.

This introductory section, Section 4.1, continues with a description of the water rig and geometry used, together with the experimental techniques and the corresponding error analysis. Before the measurements inside the model combustor are presented, two preliminary studies are described in Section 4.2: the first evaluates (experimentally) the swirl number of the swirler to be used in the combustor, the second describes the efforts made to ensure that the experimental conditions of the main experiment lead to a realistic simulation. The bulk of the results are then included in Section 4.3. Finally, the most important conclusions of the current chapter are summarized in Section 4.4.

4.1.2 Experimental Set Up and Geometry

The water rig, shown schematically in Figure 4.1, was operated either as a closed circuit, for velocity measurements, or as an open circuit, for concentration measurements and flow visualization; in the open circuit version, tank C discharged directly into the drain. The swirler flow was driven by the constant head tank B, while tank A fed the fuel injector, the primary holes and the dilution holes, all through

independent circuits. The maximum flow rates were set by the levels in tanks A and B with respect to tank C, but a higher fuel flow rate could be provided by pump 3 if desired. Pumps 1 and 2 fed tanks B and A, respectively. The circuit constituted by tank D and pump 4 was used for injection of dye through the fuel injector, for concentration measurements and fluid visualization studies. The four independent entry routes into the combustor were concentrically arranged and Figure 4.2 shows the dimensions of the various tubes. The outermost tube was surrounded at the measuring region by a plane walled box filled with water to minimize refraction of the laser beam.

The combustor model (Figure 4.2) was made up of three different parts: the head, the barrel and the nozzle, all machined from single plexiglass pieces of larger dimensions to guarantee high accuracy. The swirlers (Figure 4.3) and the fuel injector (Figure 4.4), a cone with 10 equally spaced holes of 1.7 mm diameter, were inserted at the centre of the hemispherical head. Two swirlers were used, both with 18 curved vanes but of different angles (30° and 45°) which provided swirl numbers of 0.46 and 0.56, respectively (see subsection 4.2.1). The barrel contained six 10 mm primary and six 20 mm dilution holes, 80 mm apart and staggered by half a pitch with respect to each other, but otherwise equally spaced around the cylindrical barrel; this could be terminated either by a circular to rectangular or by a conical nozzle.The conical nozzle was used to enable access for an intrusive optical probe used for mean concentration measurements (described in Appendix B). Velocity measurements upstream of the dilution holes indicated no differences between the two nozzles, as far as the internal flow patterns were concerned. The photographs in plate 1 provide a clearer view of the combustor model in the rig and assembled with the non-conical nozzle.

The present model is a plexiglass replica of a metal transply model used for combusting studies by Tse [1988] and differs from that used by Koutmos [1985] and Heitor and Whitelaw [1986] in number and size of dilution holes and swirler size. These changes have been made in order to simulate more closely the primary zone configuration of modern can combustor designs, such as found in the Rolls-Royce Tay engine. This required a reduction of the air fuel ratio (AFR) in the primary zone from 20 to 9, which results in a swirler flow of only some 7% of the total, compared to 25% in the model of Heitor and Whitelaw [1986]. The AFR of the primary zone is usually calculated according to

$$AFR_{PZ} = \frac{\dot{m}_{sw} + \dot{m}_{head} + 0.5\,\dot{m}_{p}}{\dot{m}_{fuel}}$$

Figure 4.5 shows values for these various inflow components, including: (i) flow splits typical of modern can combustors, (ii) the values chosen for the model

combustor of Tse [1988], and (iii) the corresponding values chosen for the water model. The reason behind these latter figures is given in subsection 4.2.2.

4.1.3 Measurement Techniques and Post-Processing of Data

The LDV arrangement

The LDV system, shown schematically in Figure 4.6, was operated in differential forward scatter mode. The fundamentals of this technique have been discussed in detail (e.g. Drain [1980]; Durst, Melling and Whitelaw [1981]) and only the characteristics and limitations of the present experimental arrangement are included here.

The emitting part of the optics consisted of a 15 mW He-Ne laser (Spectra Physics model 120S), a lens, L_1, of 150 mm focal length, a grating disc, G, and two lenses, L_2 and L_3, both with a focal length of 300 mm. The rotating grating module (the grating disc and its motor) and lenses L_2 and L_3 were all part of an integrated optical unit which, by rotation of the grating module, enabled the measurements of two perpendicular components of velocity without realignment. The lens L_1 was mounted on the laser head and focused the beam onto the grating disc. Focusing of the beam was necessary for two reasons: firstly, to ensure, after incidence upon the grating, split beams of circular cross-section; and, secondly, to guarantee that the waists of the two crossing beams emerging from L_3 coincide at the intersection region (Oldengarm, Krieken and Raterink [1976]). The radial grating (model type R-H, manufactured by Technisch Physische Dienst TNO-TH, Delft, The Netherlands) had an outer diameter of 35 mm and a total of 16384 etched line pairs in the first track. The shifting of the light was provided through the rotation of the disc, either clockwise or anti-clockwise, by a high speed brushless DC motor (Siemens 1AD 2001 0A); this could rotate at velocities between 1710 and 14500 rpm with a long term stability of 0.1% or short term stability of 0.6% rms, 0.3% rms and 0.1% rms at speeds of 1710, 3000 and 14500 rpm, respectively. According to the following equation:

$$f_s\,(\mathrm{Hz}) = 2\,p\,N\,f_r \qquad [4.1]$$

(where f_s is the frequency shift, p is the order of diffraction of the beams, N is the total number of line pairs, and f_r is the speed of rotation of the grating), frequency shifts were available through the first order diffracted beams from $\pm$ 0.944 MHz up to $\pm$ 7.9 MHz. The lens L_2 made parallel the two first order beams and finally lens L_3, with a focal length of 300 mm, formed the measuring volume by intersecting the two beams. A second L_3 lens with a longer focal length of 500 mm reduced the angle of intersection and allowed a complete radial traverse along the axis of the primary holes without interfering with the edges of the holes, but resulted in a reduced sensitivity,

an increased transfer constant, and a longer control volume; a lens of 200 mm focal length could not be used because of the short distance between the intersecting point and the optical unit. The spatial resolution of the system is set by the largest dimension of the control volume (George and Lumley [1973]) and an estimate of the Kolmogorov microscale length ($\eta = (\nu^3/\varepsilon)^{1/4}$, from Tennekes and Lumley [1972]) assuming $u=U_b$ ($\varepsilon = u^2/2Rc$) shows that its measurement is beyond the capabilities of the present system; λ, the Taylor microscale ($\lambda/\eta = 15^{1/4}\ R\lambda^{1/2}$) is just within the limitations of the system.

The receiving optics consisted of an imaging lens, L_4, of 200 mm focal length, which focused the scattered light onto the pinhole of a photomultiplier. The diameter of the beams at the intersection region is given by

$$b = \frac{4 \lambda f_1 f_3}{\pi b_0 f_2}$$

(where λ is the laser wavelength in vacuum; f_1, f_2 and f_3 are the focal lengths of the lenses L_1, L_2 and L_3, and b_0 is the diameter of the laser beam originating from the laser at $1/e^2$ intensity points), from which the length of the major and minor axes of the ellipsoidal control volume follows:

$$b_x = \frac{b}{\cos \alpha}$$

$$b_y = \frac{\eta b}{\sin \alpha}$$

where η is the refractive index of the water and α is the angle in air between the two intersecting laser beams. The measured half angle of intersection in air was 5.82° within ± 0.01°. The main characteristics of the LDV system are summarized in table 4.1.

The photomultiplier tube (E.M.I. 9558), was powered by a power supply (Brandenburg model 2475R), and its electric signal was high pass filtered by a Khron-Hite filter model 3200 and then analysed by a digital counter processing system. The counter was a model 2 counter, custom made in the Fluids Section, Imperial College (Heitor, Laker, Taylor and Vafidis [1984]), containing a 250 MHz clock and able to perform measurements over 8 or 16 cycles of frequencies from 31.25 KHz up to 15 MHz at a rate of one sample every 40 μs (i.e. a sampling frequency of 25 KHz). The remote control of the counter and processing of the data were made by an Apple IIe microcomputer which, through the minimum representable frequency in floating format of an 11-bit mantissa, set the minimum measurable frequency and the resolution of the system; this was always less than 0.1% of the measured frequency and varied from 30 Hz up to 4 KHz. The maximum measurable

frequency was set by the circuitry response of the counter and was well beyond the range of values of the present application. The statistical quantities were found from direct ensemble averaging over a maximum block size of 8064 individual samples, which required the total of the memory available (32 Kbytes)

TABLE 4.1 Characteristics of the Laser-Doppler anemometer

Characteristics of the beam originating from the He-Ne laser:	
Nominal power	15 mW
Wavelength in vacuum	632.8 nm
Diameter of $1/e^2$ intensity region	0.8 mm
Characteristics of the lenses (nominal focal lengths):	
Imaging lens from laser to grating (L_1)	150 mm
Collimating lens after grating (L_2)	300 mm
Imaging lens to form measuring volume (L_3)	300 mm
Imaging lens to collect scattered light (L_4)	200 mm
Characteristics of the measuring volume:	
Half-angle of intersection in air(measured)	5.82°
Half-angle of intersection in water(calculated)	4.37°
Minor axis of region within $1/e^2$ intensity, b_x in water (calculated)	0.152 mm
Major axis of region within $1/e^2$ intensity, b_y in water (calculated)	1.981 mm
Number of fringes (calculated)	48
Fringe spacing, d_f (calculated)	3.120 μm
Velocimeter transfer constant	0.321 MHz/(ms^{-1})
Shift frequency	0.944 MHz; 2.411 MHz

Spectral measurements were made with a Solartron/Schlumberger 1200 signal processor to which the analogue output of a frequency tracker/demodulator (Cambridge Consultants CC08 Processor) was input. The signal processor, with a frequency range from 0 up to 30 KHz, first digitised the signal and then produced the time series analysis by using FFT algorithms. Most of the signal occurred within a range of 4 Hz up to 1000 Hz, as was found through a previous sweep over the full range of the instrument; this was operated on a broadband analysis, log scale for

frequency, with a minimum value of 1 Hz. The sweeping time depended on the particular value of the frequency range being scanned and the spectral analysis was made with a fixed number of preselected averages. Spectral measurements were made to ascertain the turbulent nature of low frequency phenomena observed around the primary jet impingement. The inherent high frequency limitations of the LDV technique, affecting the measurement of the full turbulence spectra (e.g. George and Lumley [1973]; Buchave, George and Lumley [1979]) are irrelevant for the present purpose.

The optical set up was firmly attached to a manually operated traversing table. Figure 4.2 indicates the coordinate system used to describe the internal combustor flow, together with its orientation with respect to the vertical. The axial (Z direction), U, and azimuthal (θ direction), W, components were measured by moving the beams along a horizontal diameter with orthogonal rotation of the plane of the beams; the radial (R direction), V, component was measured with the beams oriented as for W (i.e. in a vertical plane) but moving along a vertical diameter. The measurements were made by moving the traversing table in steps of 2 mm or 1 mm and, because of refraction phenomena, the radial locations do not exactly coincide for all the normal stresses. The turbulence kinetic energy was found by linear interpolation between nodes; taking the location of U as datum points the values of W and V at the same datum locations were found by linear interpolation. The traversing table was positionable within ± 0.1 mm. However, the reference location was found by positioning the control volume on the wall and a displacement error of ± 1 mm can occur. Measurements at different angular locations (θ) were made by rotation of the whole combustor After rotation of the combustor a slight readjustment of the table was needed to re-establish the parallelism between the test section and the laser beam; the $\theta = 15°$ location precluded this adjustment, forcing reliance on the accuracy of the rotation of the flange, which was believed to be accurate within $\pm 1°$.

Corrections due to refraction effects (Bicen [1982]) were also made; corrections were needed to the location of the control volume and, in the case of the swirl component, also to the velocimeter transfer constant. These corrections did not exceed 1% in the case of profiles along the barrel or 2% for the combustor head. The low magnitude of these corrections, although corresponding to the worst situation (the locations close to the walls), is a consequence of the small thickness of the combustor wall compared to the diameter. Also because of refraction effects some measurements of radial velocity close to the walls were deleted on the grounds of unreliability.

Because of the low Doppler frequency characteristics of this flow, frequency light shifting was required (regardless of the need to resolve the directional ambiguity), due to the low frequency limitations of the counter system. The minimum

shift frequency available was 0.944 MHz and this centred the signal in a range of frequencies where the resolution of the counter was 0.49 KHz (0.0015 m/s) and the accuracy was 0.025%. The use of the shift requires its careful determination because of the low magnitude of the Doppler frequency, f_D, compared with the shifting frequency, f_s. The velocity is evaluated through the formula $U = cte(f_D - f_s)$, where cte is the transfer constant, and slight variations of the shift frequency may lead to drastic alterations of the mean velocity. This was particularly critical when measuring the velocities in the primary annulus where a deviation of 1% of the shift frequency could be responsible for a deviation of 30% on the velocity. A satisfactory and more accurate procedure was found by actually measuring the shift frequency, mean and rms, rather than using equation [4.1]. Higher shifting frequency, though increasing the relative magnitude of f_D and f_s even further and deteriorating the resolution of the counter, improves the short term stability of the grating. Two values of shift frequency were used: 0.944 MHz and 2.41 MHz. The latter was restricted to high turbulence locations which, unfortunately, were also locations of nearly zero velocity; nevertheless the resolution of the counter was always only 1.9 KHz and the accuracy 0.1%. At some stage, an attempt was made to use a frequency tracker (Cambridge Consultants CC08 Processor) but here the needs of higher dynamic response led to the use of the highest frequency range of the instrument, 16 MHz, with an inherent accuracy of $\pm$ 0.5%, 8 KHz (i.e. 0.25 m/s), and it was abandoned; similar problems have been reported by Founti, Vafidis and Whitelaw [1985].

The error associated with velocity-gradient broadening effects is of main concern in the measurements of rms values (Durst, Melling and Whitelaw [1981]). Gradient broadening can lead to overestimations of up to 5% in regions of very steep gradients, but, in most parts of the combustor, the maximum error in the rms values is less than 2% for the size of measuring volume used in the experiments. Other possible sources of error, e.g. velocity bias (McLaughlin and Tiedermann [1973] Edwards [1987]) were neglected; statistical errors due to finite sample size are considered below.

All the data were input to a CDC computer for post processing and plotting by a purpose written FORTRAN program. The following features and the refraction corrections mentioned above, have been incorporated into this program.

Larger sample sizes were needed to extend the total sampling time and obtain converged statistical values, especially in regions with a high energy content at low frequencies. This problem becomes particularly evident in the case of higher order moments presented in subsection 4.3.4. The program allowed an increase of sample size by merging the statistics of various data blocks (when available) corresponding to

a single location. For example, consider two data blocks of sample size M and N, respectively, taken at the same point.

Mean of separate blocks:

$$\bar{x}_M = \sum_{i=1}^{M} \frac{x_i}{M} \quad ; \quad \bar{x}_N = \sum_{j=1}^{N} \frac{x_j}{N}$$

The overall statistical parameters of merged blocks are:

mean

$$x_{MN} = \frac{1}{M+N} (\bar{x}_M M + \bar{x}_N N)$$

variance:

$$Var_{MN} = [(Var_N + \bar{x}_N^2) N + (Var_M + \bar{x}_M^2) M] / (M + N) -$$

$$- [(\bar{x}_M M + \bar{x}_N N) / (M + N)]^2$$

third order moment:

$$F3_{MN} = [(F3_M + 3\bar{x}_M Var_M + \bar{x}_M^3)M + (F3_N + 3\bar{x}_N Var_N + \bar{x}_N^3)N]/(M + N)$$

$$- \bar{x}_{MN}^3 - 3\bar{x}_{MN} Var_{MN}$$

fourth order moment:

$$F4_{MN} = [(F4_M + 6\bar{x}_M^2 Var_M + 4\bar{x}_M F3_M + \bar{x}_M^4) M +$$

$$+ (F4_N + 6\bar{x}_N^2 Var_N + 4\bar{x}_N F3_N + \bar{x}_N^4) N] / (M + N) -$$

$$- \bar{x}_{MN}^4 - 4\bar{x}_{MN} F3_{MN} - 6\bar{x}_{MN}^2 Var_{MN}$$

Although samples of any size could then be obtained, in practice, no more than four sets of 8064 samples (i.e. a maximum of 32256 individual samples) were taken, restricted to the regions around the primary jet impingement.

Statistical error analysis up to the 4th order moment

A statistical error analysis of the mean and rms measurements has been carried out, based on Yanta and Smith [1973]. It is important to note that this analysis is valid only under the assumption of Gaussian turbulence; in the present study, the measurements

of skewness and flatness provide a check on the validity of assumption. The absolute statistical error is:

$$\text{Mean:} \qquad \bar{U} = Z_c \frac{u'}{\sqrt{N}}$$

$$\text{Instantaneous:} \quad u' = Z_c \frac{u'}{\sqrt{2N}} \qquad [4.2]$$

where Z_c is a parameter known from the normal distribution and depends on the confidence level. In the case of the turbulence kinetic energy, it was assumed that the statistical error was the sum of the statistical errors of the three individual normal stresses. These errors are represented in the graphs with an error bar for a 99% confidence level and in all the cases but the turbulence energy the error bar is of a size smaller than the actual size of the symbols.

The data points of the mean and rms values were joined by straight lines; however, in the case of the higher order statistical moments, because of the scatter in the results, curve fitting was carried out before plotting. The numerical techniques used to perform the curve fitting and to evaluate the experimental random error involved in these quantities are presented below, since this has apparently not previously been used as a means of estimating the experimental error of higher order moments.

Firstly, since the measurements were made along the whole combustor diameter, in order to take advantage of the symmetry properties of the flow (i.e symmetric distributions of the flatness and skewness of the U component and anti-symmetric distribution of the skewness of the W and V components), data from the two halves of the combustor were first converted into a single half, thereby increasing the resolution. The curve fitting was performed in a domain $[0 \leq r/R_c<1]$, whereas the original data originated from a domain $[-1 < r/R_c<1]$. A polynomial curve was then fitted to the data points. Once the coefficients of the polynomial were found, the previously converted half could easily be recovered.

The polynomial was represented by a Chebyshev series form

$$f(x) = \frac{1}{2} a_0 T_0(x) + a_1 T_1(x) + a_2 T_2(x) + \ldots + a_k T_k(x)$$

(where $T_i(x)$ is the Chebyshev polynomial of the first kind of degree i).
With minimization of the l_2 norm,

$$l_2 = \sqrt{\sum_{i=1}^{N} [\, y_i - f(x_i)]^2}$$

a least squares fit could be performed; y_i is the experimental value, and $f(x_i)$ is the fitted value, either skewness or flatness. The use of the l_2 norm is consistent with the assumption that the distribution of the random error in y_i is normal; a practical advantage of the use of the l_2 norm as a criterion for minimization is the speed of calculation, this being a consequence of the linearity of the system of equations (Conte and Boor [1980]).

Within the same profile, an absolute accuracy was attributed to each point, depending on the size of the sample from which it was derived. If the variable to be fitted was the mean or the variance, the absolute accuracy would be proportional to $1/\sqrt{N}$ and $1/\sqrt{2N}$ respectively, according to the statistical error (equations [4.2]). In the absence of a similar analysis for the third and fourth order moments, the absolute error was considered to be some function of $1/\sqrt{N}$ and a weighting factor was attributed to each point. This weighting factor, W_i , was defined as $\sqrt{N_i}/\sqrt{N_{MAX}}$, where N_{MAX} is the biggest sample within the profile. The l_2 norm is then redefined as:

$$l_2 = \sqrt{\sum_{i=1}^{N} [y_i - f(x_i)]^2 \;\; W_i}$$

whose value the fitting subroutine minimized.

With the fitting points already known, the average experimental error of the whole profile could be estimated by comparison with the experimental values. Four possible definitions were used:

$$\sqrt{\sum_{i=1}^{N} [\, y_i - f(x_i)]^2 \;\; / \;\; N}$$

$$\sqrt{\sum_{i=1}^{N} \{\, [\, y_i - f(x_i)] \;/\; f(x_i) \,\}^2 \;\; / \;\; N} \qquad [4.3]$$

$$\sum_{i=1}^{N} ||y_i - f(x_i)||/N$$

$$\sum_{i=1}^{N} ||\frac{y_i - f(x_i)}{f(x_i)}||/N \qquad [4.4]$$

The first two, [4.3], are based on the root mean square of the distance between the fitted and the experimental value, defined either in absolute or in relative terms; the other two, [4.4], are alternative definitions where the average distance between the fitted and the experimental value was used as the definition of the error. Moffat [1988] has mentioned both of these approaches, especially the use of a mean deviation between experimental data and curve fitting, as very simple techniques which provide only an indication of the scatter of the results; the use of Moffat's alternative methodology has not been considered since it was uncovered only after completion of the present work. From the last two possible definitions, [4.4] (which lead to the highest value) the error is about 20% and 10% with a mean absolute error of around 0.1 and 0.2 for the skewness and the flatness, respectively. The values provided by the first two definitions seem to be unrealistically low. The error was evaluated using the totality of points in the profile; no experimental point was rejected on the basis of its distance from the fitting curve. In some cases, the relative errors of the skewness attain values greater than 100% , due to the proximity of the fitting curve to a zero value.

4.1.4 Flow Visualization

Various techniques are available for visualization in water flows, see Clayton and Massey [1967] or, more recently, Mueller [1983] and Merzkirch [1987]. The generation of hydrogen bubbles, certainly the most popular, gives results very similar to the injection of particles, with interrupted streaklines corresponding to the travel of a single particle, or bubble, along the plane of illumination. Neither of these two techniques was used in the present work to avoid alterations to the test section for the introduction of the electrodes and scratching of the plexiglass surfaces by the impact of the particles. Further their efficiency in highly turbulent flows is questionable, although good results, even quantitative ones, have been obtained under low velocity conditions (Ellis and Stefan [1986] and Schraub, Kline, Henry, Runstadler and Littell [1965]). In combustor flows the difficulties in obtaining good quality photographs has often led to the presentation of schematic views of the flow pattern based on

observation (e.g., Clarke, Gerrard and Holliday [1963], Coupland and Priddin [1987]).

For mixing studies, the injection of dyes is most appropriate since different colours, or different intensities of the same colour, are associated with different degrees of mixing and the path of the marked stream. Two types of dye can be found (conventional and fluorescent) and both were used in the present work. Conventional dyes were used initially to identify the mean trajectory of the primary and dilution jets and set the experimental conditions (see Section 4.2.2), whereas for a more detailed study of the mixing process, fluorescent dyes were selected instead. The principal disadvantage of conventional dyes (i.e. writing ink and other water soluble materials*) in recirculating flows is the loss of transparency caused by the accumulation of dye. Unless the injection of dye is made periodically or in regions of the flow where it is not recirculated, continuous observation of the flow is difficult. Fluorescent dyes do not suffer from this problem, since the absorption of light is much reduced. The flow never loses its transparency and because the dye only fluoresces when and where illuminated by the appropriate light wavelength, a much higher image definition, or spatial resolution, can be achieved compared to conventional dyes. Further advantages are that water containing fluorescent dye scatters light with an intensity proportional to the concentration of dye (see Appendix A), and at a different wavelength to the incident light and light scattered from regions of pure water and reflecting surfaces, i.e. frequency shift is present. If the concentration is high enough, the intensity of fluorescent light overshadows any other contribution, an intensity shift. Hence, the definition of the image can be further improved by eliminating the non-fluorescent contributions either by using an optical filter tuned with the fluorescent emission (frequency filtering) or by under-exposure of the photographic film (intensity filtering). The latter was preferred because frequency filtering also reduces the total amount of light and consequently the maximum shutter speed and frame rate possible. The physical processes behind the phenomena described above are described in Appendix A, in the context of the development of a non-intrusive technique for concentration measurements.

Photographic and visualization techniques

For conventional dye studies, a solution of nigrosine (BDH Chemicals Limited, Ref. C.I. 50420) diluted in water was injected through the fuel injector or through a small tube located at the centre of the primary and dilution holes. A 35 mm photographic

---

* Visualization by some dye-producing reaction or pH indicators (Merzkirch [1987]) may also be classified as a conventional dye, since they affect the entire flowfield and are not restricted to the region of illumination.

reflex camera, Minolta XM, with a zoom lens (Vivitar Series 1, 70 - 210 mm) was used; the camera was capable of shutter speeds up to 1/2000 sec. The illumination of the test section was made by spot lamps directed towards the regions of interest and orientated to reduce reflections upon the camera lens. Various colour reversal films and shutter speeds were tested. High shutter speeds of 1/1000 sec were made possible by using the maximum lens aperture (f = 2.8) and forced processing (at a rate of 1600 ASA) of a Kodak Ektachrome P800/1600 colour reversal film 5020. Two things resulted: the photographs were downgraded by the appearance of grain and, because the shutter speed was too high, the trajectory of the primary jets was not consistent, precluding the identification of a mean trajectory. Lower shutter speeds (1/60, 1/125) were preferred, together with more powerful light sources which allowed the use of films of lower sensitivity (Kodak Kodachrome 64 and Kodak Ektachrome 160 (tungsten)) and a smaller lens aperture (f = 8), resulting in pictures of higher quality. The photos in plate 1, accompanying the discussion in subsection 4.2.2, are black and white reproductions of slides obtained from the last two films.

For fluorescent dye studies, a solution of rhodamine B diluted in water to a concentration of 1.3 mg/l was injected through the fuel injector. The use of rhodamine B was a consequence of its use for concentration measurements (see Appendix A): for visualization purposes other fluorescent dyes may work as well. The illumination of the test section was provided by an argon-ion laser (Spectra Physics model 164, tuned at 514 mm and with a maximum power of 1.2W). A sheet of light was created by a cylindrical lens and the plane of light was either perpendicular to the axis of the combustor, for visualization of the cross-sectional planes, or parallel, for visualization of the longitudinal plane. In principle, any light source emitting within the absorption spectrum of the dye can be used but the laser offers some advantages due to the easy manipulation and creation of a very thin sheet of light.

Still and high speed photography were made. It is obvious that full advantage cannot be made of the films here, but some frames of the high speed film, in plate 5, are included; these were obtained by direct printing of some frames on photographic paper by the "Cibachrome" process. The photographic equipment was the same as above; two different films were used – Kodak Ektachrome 400 (daylight) colour reversal film, and a Kodak TMY black and white negative film. The cine camera was a Photec IV, model 164, 16 mm high speed motion camera (manufactured by Photonic Systems, Inc., USA); this is a rotating prism camera capable of speeds up to 20 000 frames per second in the configuration used where the standard 16 mm frame was split in two. A Mamiya-Sekor C lens (80 mm) with a maximum aperture of 2.8 was used throughout this work. Only one type of film was used – 7250 Eastman Ektachrome Video news film high speed (tungsten). The ability to film at high speeds depends, in

the first instance, on the amount of light available, the film sensitivity and the lens aperture. Without forced processing, 400 ASA, a maximum speed of 400 fps was possible when filming the cross-sectional views; the longitudinal views required forced processing at 1600 ASA , even at speeds of 200 fps, and this resulted in a slight deterioration of the image due to increased grain and blurring. It is worth noting that the ability to obtain good results at such relatively low frame rates of 200 and 400 fps is a consequence of the low velocities typical of water flows; higher velocities, as for instance in air flows would have required higher frame rates and, consequently, higher levels of illumination which could not be achieved under the present arrangement. This advantage and those already mentioned in the introductory subsection 4.1.1 reinforce the points made in Chapter 1 on the usefulness of water flow experiments in combustor studies.

A video film was also made but did not add new elements to the discussion, the quality of the image was poor compared to the still or high speed photography, and the ability to follow the fluctuations of the flow was diminished due to the low frame rate of 50 frames per second – 8 and 4 times lower than the high speed camera. The image recorded on the film is averaged during the time the shutter is open and this also sets a limit on the time resolution and spatial resolution, because a particle moving during that time will produce a blurred image which precludes the exact determination of its location. Spatial resolution (or definition of the image in photographic terms) is also set by the grain of the film which increases with the sensitivity and forced processing of the film, reducing spatial resolution. For video systems, the spatial resolution is set by the resolution of the screen. However, more sensitive films and forced processing allow higher shutter speeds, enabling higher frequency resolution (but only if there is enough light to impress the film). For a movie camera with a fully open shutter, the exposure duration is the inverse of the frame rate and, for a given amount of light, this set a limit on the highest frame rate possible. Arnold [1984] defends the use of the Hz as terminology as opposed to the "cumbersome frames per second" and this is certainly preferable, given the analogy between frame rate and sampling frequency; a movie film is like a digital system of data (image) acquisition with a sampling frequency of the frame rate. According to the Nyquist criterion (Bendat and Piersol [1986]) no phenomenon with a frequency higher than half the frequency of the film will be properly resolved.

4.1.5 Experimental Conditions

The experimental conditions under which the rig was used are summarized in Table 4.2. Case 1, the standard case, simulates the swirler/primary and dilution/cross flow ratios as in Tse's [1988] combusting experiment. A preliminary experiment to

confirm that these conditions provide a correct simulation of the flow pattern observed in the combusting experiment is presented in subsection 4.2.2. Case 2 differs from case 1 only in the type of swirler. Case 3 is similar to case 2 apart from the injection of "fuel". Water was injected through the fuel injector such that the ratio between the momentum flux of the swirler and the fuel injector flow was similar in both water and analogous combusting experiment. This condition, expressed in terms of mass flow rate, $\dot{m}$, reads (because the swirler and the fuel injector are geometrically similar in both rigs):

$$\frac{\dot{m}_{fuel}^{water}}{\dot{m}_{sw}^{water}} = \frac{\dot{m}_{fuel}^{air}}{\dot{m}_{sw}^{air}} \sqrt{\frac{\rho_{air}}{\rho_{fuel}}} \qquad [4.5]$$

Propane was the fuel used in the combusting experiment (Tse [1988]) ($\rho_{propane,T=310K}$ = 1.678 kg m^{-3}) and the ratio between the mass flow rates of the fuel injector and swirler under combusting and isothermal conditions should be proportional to the square root of the density ratio between air and propane (0.88). The swirler flow rate in the combusting experiment was 6.9 $\times$ 10^{-3} kg s^{-1}, and the maximum possible fuel flow rate in the water rig, 8.33 $\times$ 10^{-2} kg s^{-1}, corresponds to an air to fuel ratio, AFR_{PZ}, of 83. Lower AFR_{PZ} can be simulated only if the swirler flow rate is reduced and that is not possible without changing the ratio between the swirler and the primary flow. Case 4 examines the dilution flow and cases 5, 6 and 7 allow the effect of the swirler to be quantified. None of these cases will be covered as extensively as the standard case (e.g. no measurements of radial velocity have been made); the measurements were such as to allow the influence of the selected parameters to be assessed.

According to Bicen and Jones [1986], no significant Reynolds number dependence of the flow is expected at the values of Reynolds number (based on the combustor diameter and bulk velocity) of the present experiment. The swirler and fuel flow rates were monitored by rotameter and are accurate within $\pm$ 2%. The swirler rotameter was calibrated by integration of the velocity profiles inside the swirler entry tube. The fuel rotameter accuracy is that stated by the manufacturer, KDG Flowmeters. The primary and dilution flows, on the other hand, were found by integration of measured velocity profiles in the annular region of the corresponding supply tubes at some distance upstream of the combustor. No better than 10% accuracy could be achieved due to the uncertainty associated with the exact dimensions of the plexiglass tubes. The consequences of a 10% variation of the primary flow are examined further in Chapter 5.

TABLE 4.2 – Operating conditions of water rig

N.	θ	$\dot{m}_{sw}$	$\dot{m}_{fuel}$	$\dot{m}_{pr}$	$\dot{m}_{dil}$	$\dot{m}_{tot}$	U_{bulk}	Re_{bulk}	$\frac{\dot{m}_{fuel}}{\dot{m}_{sw}}$	$\frac{\dot{m}_{pr}}{\dot{m}_{sw}}$	$\frac{\dot{m}_{d}}{\dot{m}_{cross}}$
1	45°	0.543	-	1.04	1.60	3.19	0.741	4.896×10^4	0	1.92	1.01
		[17]	-	[33]	[50]						
2	30°	0.543	-	1.04	1.60	3.19	0.741	4.896×10^4	0	1.92	1.01
		[17]	-	[33]	[50]						
3	30°	0.543	0.083	1.04	1.60	3.27	0.760	5.023×10^4	0.153	1.92	0.96
		[17]	[2]	[32]	[49]						
		with fuel injection (AFR_{PZ}=83)									
4	45°	0.543	-	1.04	-	1.59	0.369	2.438×10^4	0	1.92	0
		[34]	-	[66]	-						
		without dilution flow									
5	–	-	-	1.04	1.60	2.64	0.615	4.062×10^4	0	∞	1.53
		-	-	[40]	[60]						
		without swirler flow									
6	30°	0.797	-	1.04	1.60	3.44	0.800	5.286×10^4	0	1.31	0.87
		[23]	-	[30]	[47]						
		higher swirler flow									
7	30°	0.543	-	-	-	0.543	0.126	5.286×10^4	0	0	0
		[100]	-	-	-						
		swirler flow only									

$[\dot{m}]$ = Kg/s; $[U_{bulk}]$ = m/s
mass flow rate as percentage of the total within brackets

$\dot{m}_{cross} = \dot{m}_{sw} + \dot{m}_{fuel} + \dot{m}_{pr}$

θ – swirler vane angle

4.2 TWO PRELIMINARY STUDIES

The two studies in this section preceded the main experiment described in Section 4.3. The first was necessary to evaluate the precise swirl number of the swirlers to be used in the combustor model. The second was the result of a need to check that a proper simulation of the flow pattern existing in the geometrically similar but burning combustor experiment of Tse [1988] had been achieved.

4.2.1 Swirl Number Evaluation - Assessment of the Axisymmetry of the Swirler Flow

The swirl number, S, is defined (cf. Beer and Chigier [1972], Gupta, Lilley and Syred [1984]) as the ratio between the axial flux of angular momentum and the axial flux of axial momentum divided by a characteristic radial dimension, R (the outer radius of the swirler was selected in the present study). This is the parameter most commonly used for characterisation of swirl flows and neglecting the turbulent stresses and pressure terms it may be written as:

$$S = \frac{\int_0^\infty \rho U W r^2 dr}{R \int_0^\infty \rho U^2 r \, dr} \qquad [4.6]$$

Alternatively, a more simplified version is possible, assuming constant radial profiles of U and W, where the swirl number becomes a function of geometrical parameters only:

$$S = \frac{2}{3} \frac{1 - (d_{int}/d_{ext})^3}{1 - (d_{int}/d_{ext})^2} \tan \Theta \qquad [4.7]$$

where θ is the vane angle, and d_{int} and d_{ext} the internal and external diameters of the swirler. Good results from the equation above are expected for low levels of swirl and moderate curvature of the vanes; a situation where the shape of the velocity profiles is almost constant over the radius and the efficiency of the vanes is close to 100%. In the present work, in order to find a more accurate value, velocity measurements were made allowing an experimental evaluation of the swirl number. Additional objectives of this preliminary study included i) the evaluation of the discharge coefficient and ii)

the assessment of the symmetry of the flow and the range of Reynolds number independence. The measurement of the discharge coefficient was made due to needs imposed only by the combusting experiment which used the same swirlers and will not be shown here; they have been previously reported (Bicen and Palma [1986]). The work of Tober [1988] showed significant angular variations of the velocity profiles at swirler exit and cast serious doubts on the ability of guide vane swirlers to generate axisymmetric flows, therefore this had to be confirmed for the present swirlers.

The rig described in detail in subsection 4.1.2 was used in a simplified version. Only the swirler feed system was used and the test section comprised a straight pipe extension of the swirler feed tube. The outer tube and the top of the trough surrounding it were removed, enabling the tube containing the swirler to be rotated, without the need to dismantle the test section; measurements could therefore be made at different angular locations relative to the swirler vanes.

The optical characteristics of the LDV set-up were given in Table 4.1. A different data acquisition system was used here: it consisted of a band pass filter and a counter, FS1 model, interfaced to an Apple microcomputer. A sample size of about 1000 individual samples was used throughout the experimental programme and statistical errors of about 2% in the mean and 4% in the turbulence intensity measurements were expected. The magnitudes of these errors are considered to be small and do not influence the conclusions reached on the basis of results presented in the following section. Refraction corrections were performed and the maximum correction was 3%. The bulk velocity and the internal diameter of the tube were used as the characteristic scales.

Results

Figure 4.7 shows the mean axial velocity one diameter downstream of the swirler. The maximum velocity is located at 2/3 of the radius with a relative difference of 8% between peaks on each side of the centreline. On the centreline, a slight negative velocity occurs. Further downstream (Figure 4.8), the symmetry of the flow has improved: two different orientations 120° apart relative to the vanes are shown, and the maximum difference between peaks, even involving profiles at two different orientations, gives rise to a deviation of only 5%. Measurements of the swirl component under similar conditions (Figure 4.9) show closely anti-symmetric behaviour and acceptable angular repeatability. Integration of the velocity profiles in previous figures, according to equation [4.6] led to a swirl number of 0.47, in very close agreement with the value of 0.46 predicted by equation [4.7]. The Reynolds number independence is confirmed by velocity measurements (Figure 4.10) for two Reynolds numbers, 16.7×10^3 and 25.5×10^3.

A similar test was performed for the 45° swirler. The measurements of mean axial and azimuthal velocities, two diameters downstream of the swirler, showed, as in the case of the 30° swirler, that where departures from symmetry occur, they were larger in the axial component (10% difference between peaks) than in the swirl component (0.2%). A swirl number of 0.56 was found from the integration of the velocity profiles, as opposed to 0.79, according to equation [4.7]. Different experimental and theoretical values were expected for a swirler with larger vane curvature, but a more complete assessment of why this can happen is possible from measurements in close proximity to the swirler. Because of the distribution of the vanes (not diametrically opposite), a complete traverse very close to the swirler would not necessarily be symmetric. Attention was restricted to half of the diameter and the middle of the vane passage. Figure 4.11 presents the axial and swirl component 3 mm downstream of the swirler and shows the existence of a constant W and a linear variation of axial velocity, except for a region very close to the wall and in the wake of the swirler hub. Equation [4.7] was derived on the basis of constant axial and azimuthal velocities. Also, the swirl number at this location was similar, within the experimental uncertainty, to the one corresponding to the further downstream stations, proving that the neglect of the turbulent stress and pressure terms in equation [4.6] was acceptable and that no swirl number increase occurred due to the expansion of the flow leaving the swirler.

To conclude, the velocity measurements in a straight pipe of the flow generated by the swirlers enabled the evaluation of the swirl number, 0.46 and 0.56, for the 30 and 45 degrees swirler, respectively. The symmetry of the flow was considered to be acceptable with maximum deviations of 10% on the maximum axial velocity.

4.2.2 Matching reacting and non-reacting conditions

This subsection discusses the experimental conditions resulting from the flow split shown in Figure 4.12. An extended version of this work has been reported by Bicen, McGuirk and Palma [1987].

In the first flow split considered (flow split 1) the flow through the swirler was initially fixed at around 7% (Figure 4.12a) of the total flow to correspond to that in Tse's [1988] combusting experiment (Figure 4.5b). The flow through the primary and dilution holes, fed from a common constant-head tank, divided according to the hole area ratio of 1:4. With this flow split, the swirler flow was exact and the primary/swirler flow ratio approximately comparable to that in the hot flow model, the dilution flow was necessarily high (around 75%) since no consideration was given to the wall cooling (transply) flow in the hot model, but its ratio to the

primary flow was the same as in the combusting experiment. The total mass flow rate resulted in a Reynolds numbers of 7.4×10^4 based on the combustor barrel diameter and total flow rate.

Velocity measurements were obtained by LDV as above, but the characteristics of the measuring volume were different and are given in Table 4.3, below.

TABLE 4.3 - Principal characteristics of the Laser-Doppler anemometer

Characteristics of the measuring volume:	
Half-angle of intersection in air(measured)	6.10°
Half-angle of intersection in water(calculated)	4.58°
Minor axis of region within $1/e^2$ intensity, b_x in water (calculated)	0.152 mm
Major axis of region within $1/e^2$ intensity, b_y in water (calculated)	1.981 mm
Number of fringes (calculated)	48
Fringe spacing, d_f (calculated)	3.167 μm
Velocimeter transfer constant	0.335 MHz/(ms^{-1})
Shift frequency	0.944 MHz; 2.411 MHz

No corrections to the velocity measurements due to refraction effects were made, but according to the analysis of Bicen [1982] the associated error is not likely to be more than 1% inside the barrel and 2% near the head of the combustor, as mentioned in Section 4.1.3. The statistical error in the mean velocity was of the order of 2% for the minimum sample size of 1000 used during the measurements and in the region where turbulence intensity was around 30%; the corresponding error for the rms value was about 4%.

Results

Measurements of mean axial and azimuthal velocities, U and W are shown at the mid-horizontal plane AA' of Figure 4.2; this plane passes through primary hole axes but is mid-way between the dilution holes. The results are provided in dimensional form and plotted as radial profiles and axial variations along the combustor centreline. In addition to the LDV measurement, flow visualization pictures are also included in order to illustrate the flow pattern prevailing inside the combustor.

Figure 4.13 shows the mean axial and azimuthal velocities 8 mm downstream of the swirler. This was the closest location to the swirler that could be measured. The central region of negative axial velocity corresponds to an azimuthal velocity close to zero. Most of the rotating fluid is transported near to the walls and rotates in an anticlockwise fashion, viewed from the swirler towards the exit nozzle. In what follows, the swirl velocity is displayed as positive (upward velocity) on the right hand side (looking downstream) and negative (downward velocity) on the left hand side of the centreline. A slight asymmetry about the centreline may be observed in the peak positive axial velocities, but this trend is much stronger in the swirl velocity component with maximum positive and negative velocities of 0.4 and -0.1 m/s, respectively. 42 mm further downstream, along the axis of the primary holes (Figure 4.14), the negative axial velocity has increased and the unbalanced trend of the swirl component still persists, although now much reduced. This trend, apart from casting serious doubts on the performance of the swirler/primary jet combination (which should produce symmetric U and anti-symmetric W profiles in this plane), makes this flow pattern unsuitable for computer code validation purposes: a calculation domain consisting of the complete combustor cross-section would be necessary, which would clearly stretch the capabilities of current computers.

The deviation from the cyclical repeatability of these measurements, particularly of the swirl component, suggests a poor swirler performance. The measurements in subsection 4.2.1 had, however, shown reasonable velocity profiles for the swirler operated in isolation. A test was therefore performed with the swirler flow switched off and the corresponding results are shown in Figures 4.15 and 4.16. Figure 4.15a shows that switching off the swirler flow leads to a slight weakening of the backflow near the head (central recirculation is now produced solely by the impinging primary jets), but, most surprisingly, Figure 4.15b indicates strong positive W velocities on both sides of the centreline. Superimposing an anti-symmetric swirl velocity on this profile would clearly lead to the profile observed in Figure 4.13b. Note that the W component should be identically zero on this plane for no input swirl momentum. Measurements of the W velocity further downstream at Z = 50 mm (Figure 4.16) confirmed the poor behaviour of the combustor under this flow split condition, since again a finite W component was measured without the swirler flow. This time, however, negative W velocities were obtained, suggesting an overpenetration of the primary jets in the upper half of the combustor.

The cause of the above problems was revealed when measurements were made further downstream at Z = 130 mm, corresponding to the position of the dilution hole plane. These show (Figure 4.17) that the large fraction of the total flow entering through these holes enables the dilution jets to impinge on each other and create a

strong backflow directed from the dilution zone towards the primary zone, as shown in Figure 4.17a. The close proximity of the nozzle downstream of these jets creates a strong upward velocity component which, after superimposing the swirl component, leads to a clearly non-anti-symmetric distribution (Figure 4.17b). These features are communicated upstream into the primary zone by the strong backflow; the extent of this is quantified in Figure 4.18 which shows the axial variation of the U velocity along the centreline. This then destroys the cyclical behaviour over the whole combustor, breaking down the cyclical nature of the primary flow pattern. Tests with the dilution jets blocked off confirmed these findings and resulted, as expected, in negligibly small W velocities in the primary zone under no swirler flow conditions.

The above measurements demonstrated that, for this combustor geometry at least, the basis of modelling used in flow split 1 was unsuitable. It was known from temperature measurements made in the same combustor geometry under burning conditions (Tse [1988]) that good cyclical repeatability was obtained, especially in the primary zone. It was clearly necessary to simulate the dilution jet penetration more accurately to prevent the strong jet impingement. This could only be achieved by a reduction of the dilution flow independently to the primary flow. This therefore required separate feed systems for the primary and dilution holes. Alterations to the initially available water rig (as in Koutmos [1985]) resulted in the final experimental set-up described in subsection 4.1.2. In the new flow split (case 1 in Table 4.2) the relative intensities between the jets and the cross flows is the same as in the hot model.

Immediate confirmation that these new conditions did not suffer from the backflow problems associated with the dilution jets was obtained using dye flow visualization, as shown in plate 1. The dilution jets bend noticeably downstream towards the nozzle with a radial penetration much reduced compared to that of the primary jets. The observed trajectories of both primary and dilution jets were found to be in close agreement with those inferred from the combusting flow temperature measurements of Tse [1988]. The measurements obtained under these conditions (flow case 1 in Table 4.2) were accepted as providing an adequate simulation and are fully described in the following section.

4.3 FLOW INSIDE A MODEL CAN-TYPE GAS TURBINE COMBUSTOR

The results below are now plotted in non-dimensional form; U_b is the bulk velocity inside the combustor for standard conditions (case 1) and R_C is the internal radius of the combustor. In the case of different experimental conditions (for instance, when blocking the swirler flow), the actual bulk velocity will be different, but to facilitate

comparisons between different conditions, it was not changed and a constant non-dimensional velocity of 0.741 m/s was used. Measurements were taken along a diameter of the combustor and are presented in that form to allow a check on the expected cyclical repeatability of the flow. The system of coordinates being used is included in Figure 4.2. Negative values of radial velocity, V, correspond to flow moving radially towards the centreline. The swirler flow rotates anti-clockwise, if viewed from the swirler towards the nozzle, and the same sign convention is adopted as in the previous subsection.

The skewness and flatness values generated by the fitted polynomials as described in subsection 4.1.3 were joined by spline curves and no attempt was made to avoid the fluctuations shown by the curves near the ends of the domain used for curve fitting (r/R_C = -1, 0 and +1). These fluctuations are known to be a characteristic of polynomial fitting and to become worse with the order of the polynomial. Here they are also due to two additional effects. Firstly, the reduction of the population size near the walls, reflecting an incomplete convergence of the higher order moments, and secondly a consequence of assuming anti-symmetric radial distributions for the skewness of the mean tangential component (Z = 50 mm, θ = 15°), an assumption that is not valid in the case of non-swirl flow. The four possible definitions of error in [4.3] and [4.4], together with the order of the polynomial, are shown on the top of every graph of the skewness and the flatness; the left hand values correspond to the skewness and the right hand ones to the flatness. The error values according to the first two definitions, in [4.3], are the left and right top ones, respectively. The degree of the polynomial was approximately $\sqrt{N}$, where N is the number of points of the profile; the final value resulted from the observation of the fitting curves for various values of N. In some cases an attempt was made to fit the flatness by a polynomial of one order above the polynomial used to fit the skewness data, which is consistent with turbulence models of gradient transport.

The results are presented in three subsections. Firstly, in subsection 4.3.1, the flow outside the combustor and in planes tangential to the surface of the holes is addressed. Subsection 4.3.2 deals with the flow pattern corresponding to the standard case; the flow is described starting from the swirler and moving towards the nozzle. The parametric study in subsection 4.3.3 shows how the flow is altered by changing the magnitude of parameters such as the Swirl number and the flow rates through the swirler, the primary or the dilution holes. Subsection 4.3.4 includes a study on the stability of the flow in particular in the region around the primary jets impingement; the discussion centres on the PDF distributions of velocity and higher order moments of the statistics. The effect of the simulated injection of fuel is quantified in subsection 4.3.5. The results end with the flow visualization study, in

4.3.6; photos and frames from the high speed film are used to illustrate the mixing process inside the combustor.

4.3.1 Flow in the External Annulus

In this section, the flow outside the combustor is addressed. Measurements in the annular gaps feeding the combustor are needed to evaluate the primary and dilution flow rates. Further, measurements in the plane of the primary and dilution holes should provide information to guide the boundary conditions for use in numerical calculations in chapter 5; a "guide" only is possible, because the flow in the entry planes of the combustor is strongly dependent on location and a detailed mapping of these planes is not possible, due to the interference of the laser beams with the hole edges. Only measurements with a refractive index-matching technique (Edwards and Dybbs [1984]) would circumvent this problem.

Figure 4.19 shows the measurements 65 mm upstream of the swirler in the annular gap feeding the primary holes. The primary flow rate was evaluated through the numerical integration of this profile; a primary flow rate of 1.044 kg/s was found which corresponds to a bulk velocity in the annulus of 0.117 m/s and a velocity through the primary holes of 2.215 m/s (i.e. a Reynolds number of 2×10^4 based on the diameter of the primary hole). Measurements with various swirler flow rates in the combustor led to differences in this profile well within the experimental uncertainty. Figure 4.20 shows measurements further downstream, between the outer tube of the primary annulus and the combustor barrel, 10 mm upstream of the primary holes axis and in a plane rotated by 30°. Measurements of the azimuthal velocity in these two locations, not presented here, showed zero mean values and turbulence intensities similar to the axial one.

Figure 4.21 shows the radial velocity (or the jet "axial" velocity in the coordinates of the hole) 3 mm above the outer surface of the combustor along a primary hole diameter; a steeper profile on the downstream edge of the hole is evidenced implying a slight inclination of the jet flow. This was the closest possible location to the inner surface of the combustor, i.e. the surface of the boundary conditions; the evaluation of the primary flow rate using these measurements is less accurate than using the measurements in the annulus because of the uncertainty of the area over which the numerical integration should be done and the asymmetry of the profile with respect to the axis of the hole. Measurements of the axial and azimuthal components were possible on the inner surface of the combustor and are presented in Figure 4.22. The axial velocity shows the confluence of the flow towards the centre of the hole; this is not however symmetric with respect to the axis of the hole. The edges of the jet, $r/R_H < 0.2$ and $r/R_H > 0.7$, show to what extent the cross flow disturbs the

jet profile in this region (there is a decay of the axial velocity and the swirl component increases to the values of the cross flow). The axial and azimuthal turbulence intensities are very similar and are, on average, twice the value of the radial component in Figure 4.21.

The dilution flow rate of 1.6 kg/s was found from an integration of measurements in the dilution annulus, 90 mm upstream of the axis of the dilution holes (Figure 4.23); the corresponding jet velocity is 0.849 m/s (i.e. a Reynolds number based on the hole diameter of 1.5×10^4).

At the plane of the dilution holes the radial velocity could be measured, because of the larger size of the holes, along the outer surface of the combustor (Figure 4.24) and shows slightly higher values on the downstream end of the hole due to the effect of the cross flow. The ratio between the dilution and the cross flow rate is 1, rather than 1.9 as the primary to cross flow ratio, and the effects of the cross flow are stronger in the dilution hole, as can be seen from the U and W measurements along the inner surface of the combustor (Figure 4.24b): the axial velocity is always positive (the jet is bent towards the nozzle) and reaches a maximum at $r/R_D = 0.25$, whereas the swirl component shows a monotonic distribution always decreasing downstream as the entry angle of the jet increases and the influence of the cross flow is reduced. The need for a different jet to cross flow ratio is a consequence of the different roles the primary and dilution jets play in the combustor: the role of the dilution jets is to decrease the bulk temperature and ensure an appropriate shape for the temperature profile at the inlet of the turbine. Consequently there is no need for such strong impingement as to cause upstream recirculation. This different distortion of the velocity profiles observed at the primary and dilution holes as a function of the jet to cross flow ratio is well known and has been referred to in subsection 1.4.2 in the context of previous work related to dilution zone studies.

4.3.2 Standard Case (45° Swirler)

Some features of the flow pattern inside the combustor have already been revealed. A brief overall picture is given at this point to provide a framework for presentation of the detailed measurements in this section. Schematic views of the flow based on observations (but not photographically documented for reasons discussed in subsection 4.1.4) are first described.

Figure 4.25 shows views in longitudinal planes containing the axis of the primary (a) and dilution holes (b). The primary and the dilution jets have different trajectories as shown in plate 1. The primary jets penetrate almost radially into the combustor and give rise to a toroidal central recirculation zone, zone A, in the head of the combustor. The main features of this region are set by the strength of the jets

relative to the cross flow. The swirler flow rate has been used to characterize the cross flow in the present work. Zone A is a prerequisite for stable combustion and, depending on the ratio between the two, the primary region is said to be driven either by the primary jets or by the swirler flow (Lefebvre [1983]). There are gas turbine combustor geometries without swirlers; however, all seem to have jets discharging through the combustor walls, probably because of the critical stability characteristics of swirling flows, either under isothermal conditions (e.g. Escudier and Zehnder [1982]) or under combusting conditions (e.g. Syred and Beer [1974]). A so-called precessing vortex core (PVC) in the case of gas-turbine combustor geometries can give rise to an undesirable central core of unmixed fluid throughout the combustor (Koutmos [1985]). Other regions with negative axial velocity are: zone B, near the combustor head, and zone C, in the wake of the primary jets. The former is a consequence of the sudden expansion of the flow leaving the swirler. Its size depends on the precise head geometry, but also the characteristics of both the swirler flow (higher swirl number may reduce it, e.g. So and Ahmed [1986]) and the primary flow (in the limit of no swirler flow this region does not exist and the central toroidal recirculation zone completely fills the combustor head, see latter). Region C is typical of flows involving jets in crossflow as in Chapter 3. Neither region B nor region C are requirements of design and region C is usually referred to as undesirable since it may provide an extra region for flame anchorage but now with damaging consequences on the combustor wall (Bhangu, Snape and Eardley [1983]).

The cross-sectional view in Figure 4.26a, shows the flow in the primary jet cross-sectional plane for a situation of low swirl momentum. There are two counter-rotating vortices between each pair of jets, i.e. a total of 12 vortices in the present case. Through the effect of the swirling flow these rotate and may eventually disappear, since one of these vortices rotates in a direction opposite to the rotation of the swirler flow. The dilution jets, Figure 4.26b on the basis of Plate 1 and measurements in the previous subsection are expected to bend according to the direction of the swirler flow (clockwise when viewed from downstream).

Recalling the introduction in Chapter 1, the flow modules mentioned as constituents of the combustor flow may now be identified. The variety of flow patterns that may be set up as the relative strength of these modules varies is the reason for the extreme complexity of the present flow. Flow visualization later in this section and calculations of the present flow in Chapter 5 will add some new points to the description above, but this is sufficient to provide a visual aid for understanding the following velocity measurements.

At Z = 8 mm (Figure 4.27) the influence of the swirler flow is evident from the positive values of the axial component of velocity for $r/R_C > 0.3$ and the two

peaks on the swirl component with values of 1.1; both axial and swirl turbulence intensity are fairly constant over the radius. The profiles further downstream, Z = 40 mm, 10 mm before the primary holes, are given for two circumferential planes, θ=0° (Figure 4.28) and θ=30° (Figure 4.29). A non-symmetric shape is observed in the mean radial component (Figure 4.28c), for which no explanation can be found; the negative radial velocity (flow moving towards the centreline) is due to the entrainment of the jet flow and sense of rotation of the central toroidal vortex. The region of negative axial velocity extends up to r/R_C = +0.7 (Figures 4.28a and 4.29a). Measurements along the centreline (Figure 4.30) show that this negative velocity prevails up to the impingement point of the primary jets with a maximum in the transition region between the head and the barrel of the combustor. At Z = 40 mm, the inner core of the flow is moving towards the swirler rotating in a solid body fashion up to mid radius (Figures 4.28b and 4.29b); the normal stresses show a feature typical of the region surrounding the primary jet impingement, i.e. the centreline values of the radial and azimuthal component are twice the axial component.

The high anisotropy of the flow is most evident at Z = 50 mm (Figures 4.31 to 4.33), where the absolute magnitude of the normal stresses is higher. Measurements of the radial velocity along the axis of the primary holes (Figure 4.31c) show a value of four times the bulk velocity with a linear deceleration between r/R_C = 0.5 and the centreline; the skewness is similar in shape to the previous location (10 mm upstream) in Figure 4.28c, but the flatness shows an inflexion point at mid radius, related to the deceleration of the jet, and increases up to a value of about 6 as the radial location increases and the distance to the primary holes decreases. No measurements of radial velocity were made for different flow conditions, but it is expected that the location of the inflexion point above is strongly dependent on the relative strength of the jet and cross flow.

In the case of the axial and swirl components at θ = 0° and the swirl component only at θ = 15° (still at Z=50 mm) a complete traverse was not possible due to interference of the laser beams with the edges of the holes. Little swirl motion has been imparted to the jets (Figure 4.31b) and a negative axial velocity on the centreline (Figure 4.31a) shows the upstream deflection of part of the jets. By comparing the profiles at θ = 0°, 15° and 30° (Figures 4.31a, 4.32a and 4.33a, respectively), one can see that only the region between the jets for $r/R_C > 0.7$ shows positive axial velocity; further, this is the only region where the rotation of the flow agrees with the rotation imparted by the swirler, showing that the swirler flow is mainly transported near the walls due to the blockage caused by the primary jet impingement. The swirl component in the inner region, $r/R_C < 0.7$, is dominated by the flow resulting from impingement and is strongly dependent on the angular location;

at θ = 15° (Figure 4.32b), the failure of the assumption of anti-symmetric profiles of skewness to calculate the fitting curves is evidenced by the wiggles near the centreline. The central region of low flatness values of the azimuthal component is wider in the planes not oriented with the axis of the holes; in some locations in these planes between the jets, bimodal PDF distributions of the swirl velocity were found (see Figure 4.33b) and the conditions leading to their formation are discussed in subsection 4.3.4.

Compared to the measurements along the axis of the primary holes, there is a dramatic decrease of the radial component at Z = 60 mm (Figure 4.34c) just one hole diameter further downstream; a maximum value of 0.3 was measured. Also, the turbulence levels of all components and the angular variations of the azimuthal component (Figures 4.34b 4.35b and 4.36b) are much reduced. The axial component reaches its maximum positive value on the centreline in this axial location (see also Figure 4.30) and becomes negative in the wake of the jets (Figure 4.34a), although not in the immediate vicinity of the wall; this is the region labelled as zone C in the introductory notes above.

Further downstream at Z = 70 mm, as the flow readjusts from the centreline towards the low pressure region behind the jets, the radial velocity becomes positive (Figure 4.37c) and the axial velocity increases near the wall (Figures 4.37a, 4.38a and 4.39a). The swirl component is nearly zero up to r/R_C = 0.4 at all three angular locations, and as the identity of each jet is lost, the turbulence approaches isotropy and all the flow seems to rotate via the effect of the enveloping swirler flow. All these characteristics are preserved until Z = 85 mm (see Figure 4.40).

Primary and dilution jets have different mass flow ratios compared with their respective cross flows (1.9 and 1, respectively) and this fact shows clearly in the velocity profiles. For instance, the centreline value of the axial component at the plane of the dilution jets (Figure 4.30) shows an acceleration of the flow due to the partial blockage caused by the dilution jets; no jet on jet impingement occurs, as was shown by the flow visualization in plate 1. Compare the measurements along the centreline under the present flow conditions, in Figure 4.30, with the measurements in Figure 4.19 under the initial flow conditions; Figure 4.30 provides quantitative evidence of the much improved dilution jet behaviour compared to the flow split initially attempted in section 4.2.2. The absence of any backflow region near the centreline is the expected feature of a well-behaved dilution jet system. Note that the dilution holes are not aligned with the primary holes and that the location θ = 30° corresponds to the axis of the dilution holes. The comparison between the two planes containing the dilution hole axis and midway between the hole axis, θ = 30° and θ = 0°, in Figures 4.41 and 4.42, shows that the cross flow accelerates near the wall as it goes

around the jets and that the swirl component is similar in both planes. The higher order moments show Gaussian characteristics for $r/R_C < 0.4$ with the exception of the skewness of the axial velocity which is positive in this region whereas it was zero in all the previous figures; this was observed under all the experimental conditions being measured (even in the absence of the dilution flow) and is believed to be caused by the longitudinal acceleration of the flow caused by the nozzle proximity. Virtually zero radial velocities were measured over the entire combustor diameter (Figure 4.42c) in the plane midway between the dilution jets.

4.3.3 Parametric Study

In the previous section, the results of the standard case with the 45° swirler were presented and the main features of the combustor flow introduced. Here, a study of the influence of some flow parameters is made by varying their relative strength:

- First, the effect of the swirl number is investigated (angular momentum changes, i.e. the study of the same flow with lower levels of rotation being imparted to it). These results correspond to case 2; the flow splits are the same as case 1 but the 30° swirler is used instead.

- Next, the effect of the primary to swirler flow ratio is altered by:
  (i) reducing the swirler flow to zero ($\dot{m}_{pr}/\dot{m}_{sw} = \infty$, case 5), i.e. the flow inside the combustor is set up only by the primary and the dilution jets; or
  (ii) increasing the swirler flow to the maximum possible in the present rig ($\dot{m}_{pr}/\dot{m}_{sw} = 1.31$, case 6) corresponding to a 30% decrease in primary to swirler flow ratio compared to case 2; or
  (iii) blocking both the primary and dilution holes ($\dot{m}_{pr}/\dot{m}_{sw}=0$, case 7, i.e. the flow inside the combustor is set by the swirler flow only

- Finally, the effect of the dilution to cross flow ratio is examined by blocking the dilution holes (case 4).

At Z = 40 mm, comparing Figures 4.28 and 4.43, little difference can be seen between the measurements with the 45° and the 30° swirler; this is proof that under the present flow split, the flow in the primary region is dominated by the primary jets. However, measurements in the absence of swirler flow, case 5, in Figure 4.44 show that the swirler flow has certainly contributed to an increased negative axial velocity between $r/R_C = 0.2$ and $r/R_C = 0.5$, which makes the profile shape wider and increases the backward flow rate; this is one of the advantages of the

swirler flow. It is interesting to note that the turbulence levels are practically unchanged when swirl is introduced.

In the case of no swirler flow the mean azimuthal component should be zero in the longitudinal planes aligned with the axis of the holes (θ = 0°) and midway between the axis of the holes (θ = 30°) for symmetry reasons. Figure 4.44b violates this condition in a region close to the centreline and this is believed to be related to a small misalignment of the jet impingement, as Figure 4.45b further downstream seems to show. This misalignment is attenuated for the 30° swirler (Figure 4.43b) and is certainly not visible in the case of the 45° swirler (Figure 4.28b). Similarly, with the 30° swirler, it does not show either for higher levels of swirler flow, (Figure 4.46b), or in the case of swirler flow only (Figure 4.47).

The sketches in Figure 4.26 of the cross sectional views of the mean flow pattern with six jets impinging on the centreline and two equal sized vortices between jets were idealized sketches. The location of the impingement point exactly on the centreline is difficult to achieve experimentally. Work made in the context of so-called side-dump ramjet combustors (e.g. Edelman and Harsha [1978], Nosseir and Behar [1986], Nosseir, Peled and Hildebrand [1987]) has shown that the jets tend to oscillate due to jet on jet impingement and this can give rise to an asymmetric mean flow pattern; the case of a stalled diffuser is another classical example of an asymmetric mean flow pattern generated by a symmetric geometry with apparently symmetric flow conditions. Sivasegaram and Whitelaw [1986] in a flow visualization study concluded that opposed jets in geometries without cross flow become more sensitive to small geometric or flow asymmetries. The above measurements indicate therefore another important role of the swirler flow under the present flow conditions, i.e. to help re-establish the symmetry of the mean flow pattern and reduce the sensitivity of the internal flow to small jet misalignement.

If we restrict our attention to the axial location Z = 50 mm, the plane containing the primary holes axis, Figures 4.45, 4.48, 4.46 and 4.47 show the influence of the swirler flow in an angular location midway between the jets, starting from no swirler flow (case 5), Figures 4.45, to the situation with swirler flow only (case 7) Figures 4.47. It becomes obvious that the high and unequal values of the normal stresses are due to the primary jet impingement; both axial and azimuthal turbulence intensities are higher if there is no swirler flow. Figure 4.47 (swirler flow only) shows similar and constant values of axial and azimuthal turbulence intensities across the combustor, whereas in Figure 4.45 (no swirler flow) the azimuthal turbulence intensity is 10 times higher than in the case of swirler flow only and is about two times higher than the axial turbulence intensity; these differences are reduced as the primary to swirler flow ratio decreases. A detailed discussion on the

influence of swirler flow on the shapes of velocity PDF and higher order moments is the subject of the following section. The profiles of axial velocity in these four figures all show a positive region for $r/R_C > 0.7$ but the negative centreline value in Figure 4.47a (swirler flow only) is known from measurements not included here to prevail throughout the combustor, whereas, in any of the other cases, the region of negative velocity is terminated by the primary jet impingement. The higher negative axial velocity on the centreline for the case with the highest swirler flow rate (Figure 4.46a) is due to the increased bending of the jets towards the nozzle and consequently an increase of the length of the toroidal vortex in the head of the combustor rather than any bending of the jets towards the swirler caused by the swirl motion. This was confirmed by flow visualization. As the primary flow rate decreases relative to the swirler flow, the jets, rather than impinging on each other, will tend to bend more and more towards the nozzle and follow a helical motion imparted by the swirling cross flow. As the ratio of the primary to swirler flow increases, the radial distribution of normal stresses and flatness becomes steeper near the centreline and, in the case of no swirler flow (Figure 4.46), no line can be fitted through the points with a high flatness value at mid radius unless the order of the polynomial is increased and wiggles appear. This steeper gradient can also be observed along the axis of the primary holes (Figure 4.49), but located closer to the centreline at $r/R_C = +0.3$. The negative axial velocity all across the combustor in the case of no swirler flow (Figure 4.49a) shows that the jets bend towards the combustor head but, nevertheless, with a lower integrated mass flow rate at this station compared to any of the cases with swirler flow.

Comparing measurements along the primary hole axis for the 45° and 30° swirlers (Figures 4.31 and 4.50, respectively), one can see that the only differences occur around the centreline where higher negative axial velocity and solid body rotation can be observed in the case of the 45° swirler.

Figure 4.51 (without swirler flow), 10 mm downstream of the primary jets and at an angular location rotated by 15° relative to the axis of the primary holes, should confirm the existence of the two counter-rotating vortices between the jets, but this was precluded by the low mean azimuthal velocity. The misalignment of the impingement mentioned above may also have changed the relative size of these vortices, in which case the 15° plane does not correspond to the centre of the vortices. However, the measurements with the 30° swirler (Figure 4.52b) do show the existence of the two counter rotating vortices between the jets very clearly; note the two peaks in the azimuthal velocity on each side of the centreline with a rotation opposite to the rotation of the swirling flow (the latter is restricted to the near wall regions), and in the same axial location of Figure 4.51, but at 0°, i.e. aligned with the primary hole axis. The

same trend exists at Z = 70 mm (Figure 4.53b) and Z = 85 mm (Figure 4.54b), although the strength of both mean swirl component and turbulence intensities reduce as the axial coordinate increases.

Figures at the same locations as above for the case of the 45° swirler (for instance Figures 4.34b and 4.37b) showed an identical pattern, but with the magnitude of the secondary flows around the centreline much reduced. These are created by the primary jet impingement and the higher levels of angular momentum imparted to the jets for a swirler with a higher Swirl number simply reduces the strength of the impingement. Previous work in gas turbine combustor geometries (e.g. Clarke, Gerrard and Holliday [1963], Lefebvre [1983]) or the studies related to the current work, e.g. Heitor and Whitelaw [1986] or Koutmos [1985], showed the intermediate region of the combustor more like a mass of fluid rotating in a vortex fashion upon which radial opposing jets penetrate and are compelled to follow a helical path. However the velocity measurements above show that this is not the case under the present conditions. The present flow should rather be viewed as a set of 12 similar sectors each of 30 degrees with a slightly rotating cross flow unable to impart much rotation to the jets and escaping in the gaps between them.

The swirl motion in the centre of the combustor is virtually zero at Z = 110 mm and the skewness of the axial velocity shows positive values on the centreline (Figure 4.56); a feature that can also be seen at Z = 130 mm, between the dilution holes, in Figure 4.57 and was already noticed in the case of the 45° swirler.

A more complete picture of the mean flow pattern can now be given on the basis of the results in the two previous subsections:

- the dilution jets do not penetrate as much as the primary jets and, due to blockage, only cause an acceleration of the cross flow in between the jets and along the centre of the combustor;
- the primary jet fluid dominates the centre of the combustor and most of the swirler flow is transported near the walls;
- for high primary to swirler flow ratios ($\dot{m}_{pr}/\dot{m}_{sw}$ = 1.92), two counter-rotating vortices are set up in between the jets, a motion that gradually disappears with distance from primary jet impingement;
- for lower primary to swirler flow ratios ($\dot{m}_{pr}/\dot{m}_{sw}$ = 1.31), a solid body rotation is shown in the centre of the combustor;
- for purely swirling flows with no jets a backward axial flow was set up throughout the combustor length;

4.3.4 PDFs and Higher Order Moments

PDFs of the axial and azimuthal components have been included in the figures presented so far, but only at selected locations, mainly around the primary jet impingement. The maximum block size of 8064 samples was used in all these distributions, where the horizontal axis, ranging from 0 to 5 MHz, represents the Doppler frequencies found and the vertical axis the probability associated with each frequency. The vertical line across each figure corresponds to the shift frequency, or zero mean velocity.

Figure 4.33b shows the PDFs of the azimuthal component of velocity in the mid longitudinal plane between the primary jets for the case of the 45° swirler (case 1). A bimodal shape is observed on both sides of the centreline. Other locations, although also possessing low flatness values, do not show this double peak structure so clearly. Further downstream in the combustor along the axis of the dilution holes, the PDF is far different (Figure 4.41b) and much more Gaussian shaped.

Distributions of probability with bimodal shape are associated with the coexistence of two phenomena of distinct frequencies, e.g. a low frequency phenomenon with superimposed high frequency turbulence. If this occurs inside combustors, there is cause for concern about the low frequency, intermittent, behaviour since it may affect the performance of the combustor, being a source of noise, flame instability and eventually also structural vibration. Further analysis of the data was undertaken in order to try to understand the reasons for the observed PDF shape.

A comparison between Figures 4.33b and 4.45b shows that the discrimination between the two modes of the PDF was enhanced on removal of the swirl flow. Moving from the centreline in Figure 4.45b (no swirler flow) towards the wall, there is a weakening of one of the peaks, accompanied by a smoothing and 'squeezing' of the distribution, leading to lower rms, turbulence levels and flatness values in excess of 3 for $r/R_C > 0.5$.

Figure 4.49b shows the results along the axis of the primary holes and, here, the distribution becomes flatter in a much narrower region near the centreline; this can also be seen on the radial profiles of F_W. Other locations, 10 mm upstream of the jets in Figure 4.44b or 10 mm downstream of the jets at an angular location rotated by 15° with respect to the axis of the combustor in Figure 4.51b, show no bimodal distributions. It is therefore clear that the bimodal distributions of the azimuthal component of velocity are restricted to the mid longitudinal plane between the primary jets, although flatness values of 2.2 and high W_{rms} values persist in a region around the primary jet impingement.

It is very likely that these distributions are related to the two contra-rotating vortices formed between the jets. Each peak is associated with a different jet (or vortex) and the reduced discrimination between the peaks and their eventual

merging as the distance from the jet axis increases is nothing but an indication of the rate of the mixing between the two jet streams. An increase of the swirler flow rate or the swirl number will reduce the penetration of the primary jets by simultaneously imparting rotation to the jets and forcing their downstream bending. This will reduce the strength of the vortices generated by the jet impingement and for low swirler flow rates will merely rotate the plane of the PDF bimodal shape; higher levels of swirl should give rise to different flow patterns. This influence of the swirler flow is not surprising since the observed instability is mainly an azimuthal instability which the swirler removes by imparting a preferred rotation to the cross flow.

To illustrate in more detail the influence of the primary to swirler flow ratio, attention shall be restricted to the diameter midway between the primary holes. Figure 4.48b shows a complete sequence of PDFs for the case of the 30° swirler (case 2). The general pattern is analogous to what had been found in the two previous conditions, the 45° swirler and no swirler flow; here, the two peaks are not as distinct as in the case of no swirler flow (Figure 4.45b) but are certainly more distinct than in the case of the 45° swirler (Figure 4.33b). Closer to the centreline, the distribution is nearly symmetric, as in the case of no swirler flow, but at locations corresponding to maxima points in the radial distribution of mean swirl velocity the shapes of the distribution are like mirror images of each other; anti-symmetrical images are a consequence of the swirler flow. This can prevail over a larger region if the swirler flow is increased to 0.797 kg/s (case 6). A complete traverse including the PDF of the axial component was made in this case and one can see (Figure 4.46b) a nearly symmetric distribution, becoming progressively more skewed towards the negative side, anticipating the change of sign of the mean velocity to occur at r/R_C = 0.65; a process consolidated closer to centreline with the distribution returning to symmetry but still with a flatness value below Gaussian. The width of the PDFs of the azimuthal component still increases towards the centreline, but to the lowest rms level of all the cases. The anti-symmetric shape of the distribution, mentioned above as typical of swirling flow, is evident and can also be observed in the radial profiles of the skewness. A flatness value below Gaussian can still be measured on the centreline but the radial distance over which this low value can spread is much restricted compared to any of the other experimental conditions with a lower swirler flow rate.

Once the location and probable cause of the bimodal behaviour had been confirmed, the question can be posed as to whether the low frequency contribution arises at a discrete frequency of the spectrum. Spectral measurements on the centreline at the primary jet impingement (Z = 50 mm) for the case of no swirler flow did not show any dominant frequency but a broad range of frequencies between 10 and 150 Hz with a maximum at about 60 Hz (Figure 4.58). The broad range nature of

the spectrum becomes more clear if the spectrum is taken over a longer sampling time (Figure 4.59) and removes any doubts about the turbulent nature of the phenomenon. For a swirler flow of 0.797 kg/s (case 6, $\dot{m}_{pr}/\dot{m}_{sw}$ = 1.31), the energy content of this range of frequencies is reduced (Figure 4.60), but a discrete frequency now appears at 10 Hz. This feature is not associated with the contra-rotating vortices as described above, since these weaken as the swirler flow rate increases, it is most likely associated with the precessing vortex core of the swirler flow, as observed by Koutmos [1985].

Implications for the jet impingement process

The arguments above are consistent with the present measurements in the sense that if the swirler flow increases, since this is mainly transported near the walls and between the jets, the between jet vortices will be weakened and the jets will be more stable. However, if the instability is associated with the interface between the vortices, why does it show only in the region around the centreline ? If one assumes that the jets penetrate into the combustor with negligible expansion, i.e. as a uniform inviscid column of fluid, it can be seen by simple geometrical relationships that the jets all meet at 10 mm from the centreline. This cylindrical region, concentric with the combustor axis, is precisely the region where bimodal distributions were detected and it is thus most likely that the bi-stable behaviour is a side-effect of the interactions between the jets themselves.

Because there is no region of constant velocity (in the coordinates of the jet), it is difficult to define a "developing region" for the present jets. Nevertheless, given that the turbulent structure of the jet edge shear layers in the "developing region" is characterized by large eddies, it is not surprising that, in the present case, the merger of the two jet flows is accompanied by very wide distributions of probability. Another conceptual model, equally appealing, is to think of the jet as a cylindrical bar under compression, showing transversal deformations. In this case the low frequencies would not only be caused by the merger of the shear layers of the jet but by vibration of the jet column. Both of these aspects, shear layer and jet column instability, are known in the literature (Becker and Massaro [1968] refer to the first reported studies in 1858 by Leconte). The shear layer type of instability shows as ripples on the surface of the jet and scales with the boundary layer thickness at the jet nozzle. The jet column instability is evidenced at low Reynolds number as sinusoidal oscillations of the jet, but for jet Reynolds numbers above 10^4 as in the range of the present work, it assumes the shape of axisymmetric vortex rings. The latter, although with a broad range frequency spectrum, peaks around a preferential frequency.

Crow and Champagne [1971], by externally exciting a round free jet, showed that every perturbation is linearly amplified until a saturation level is reached. This saturation reaches its maximum for a jet perturbation with a dimensionless frequency, Strouhal number ($St = (f\ D_{jet})/U_{jet}$) of 0.30 and occurs 3.7 diameters downstream with a wavelength of 2.38 jet diameters. In the present case, the 60 Hz of the frequency spectrum in Figure 4.58 if non-dimensionalised with the jet diameter, corresponds to a Strouhal number of 0.27, the distance between the hole and the centreline being the distance for maximum amplification found by Crow and Champagne, and the distance between the hole and the point where the bimodal starts being the wavelength of the most unstable mode of a free jet. The improved discrimination between the peaks of the bimodal PDF on the edges of the jet rather than on the centreline also agrees with the free jet characteristics because, as Crow and Champagne showed, the energy content of the amplified perturbations is higher in the jet shear layer.

Given the difference between the current geometry and the single jet experiment of Crow and Champagne, the agreement between the results is excellent and suggests that the stability characteristics of a free jet are not significantly altered by the impingement. The bimodal PDF on the centreline shows that the 'bi-stable' nature of a single jet is altered neither by impingement nor by the interaction between the six jets; there is no destructive interference and the whole system is organised around the most unstable mode of a free jet. This point has already been made by Crow and Champagne to justify the relevance of their experiment to unexcited jets ("... the structure of the big eddies can be expected to pull in around the mode at St = 0.30, which attains the highest possible amplitude under non-linear saturation..."). It has been further reinforced by Ho and Nosseir [1982]; they found that, if a plate is positioned in the potential core ($x/D_{jet} < 7.5$) of a high speed jet (Mach number > 0.7), the reflection of the pressure wave by the normally opposing plate provides the jet with its own source of excitation (positive feedback phenomenon). The resonance frequency is found to be such that an integer number of waves is contained in the distance between the jet and the plate, but again with a Strouhal number around 0.3. This model is also consistent with the present measurements because the increasing swirler flow, besides imparting rotation to the jets, also forces their bending and reduces the axial momentum. Irrespective of the physical model, the measurements clearly showed the existence of turbulent structures with a scale which invalidates assumptions inherent to gradient transport models.

It has been shown that by increasing the swirler flow strength with respect to the primary jets ($\dot{m}_{pr}/\dot{m}_{sw} = 1.92$), the jet impingement is made weaker and the flow acquires a more stable behaviour; however, if this process is "overdone", too high

swirler flow rates ($\dot{m}_{pr}/\dot{m}_{sw}$ = 1.31) also give rise to an instability, this time a single frequency attributed to a precessing vortex core. Geometrical alterations which may also lead to improved stability of the flow, now through the reduction of the momentum flux of the jet, include an increase in the number or size of the primary holes. Any procedure to improve the stability of the flow will lead to a lower level of turbulence intensity. This, in turn, will improve the mixing process and consequently the combustion efficiency of the combustor. Usually higher turbulence intensity is associated with higher mixing, but this may not be so in the present case where the high values of measured fluctuations are rather associated with the existence of large eddies whose scales are much bigger than would be desirable for an intimate mixing of fuel and air. For improved mixing, what is really needed is the break-up of these large eddies in the shortest time and space available. This argument may seem conceptually wrong because if the diffusivity due to turbulence is proportional to the rms amplitude of the velocity fluctuations times the characteristic length scale of the eddies (Tennekes and Lumley [1972]), the situation of no swirler flow is the most favourable. However, in the present case, the existence of high rms values and large length scales, especially on the centreline, is due to the convective transport of parcels of fluid (large eddies of a maximum size of the order of the primary jet diameter or combustor radius) which are not mixed with the cross flow. These eddies, in the case of increased swirler flow, no longer appear because their stretching and destruction has occurred due to the shear forces caused by the increased angular momentum and consequent acceleration of the process of decay. The description above will become clearer through the visualization study in subsection 4.3.6.

4.3.5 The Transport of Fuel

The fuel injector (Figure 4.5) is similar to the fuel injector used in the combusting experiment of Tse [1988]. The following measurements, made to quantify the effects of the fuel injection, correspond to case 3.

Figure 4.61 shows the measurements at Z = 8 mm with and without fuel injection. The present measurements were made as close to the fuel injector as possible. These measurements are likely to depend on the orientation relative to the injector holes and to the swirler vane passages, but no attempt was made to quantify this. In the case of fuel injection, there is an increase of the mean axial velocities, the maximum positive values are higher, the profile becomes steeper and the zero axial velocities occur nearer the centreline. This longitudinal acceleration of the flow, can also be observed in the mean swirl profile and especially in the turbulence intensities whose peaks are more evident and occur closer to the centreline; the axial acceleration of the flow is expected to contribute to a larger recirculation region attached to the

wall of the combustor just downstream of the swirler (zone B in Figure 4.25) and the two data points at r/R_C = -0.7 and -0.6 seem to confirm this. This region also exists in case of the 45° swirler but is already ended at the first measurement station.

The centreline measurements in Figure 4.62 show how small the differences are between the situation with and without fuel injection. At Z = 8 mm, the fuel injection increases the centreline negative axial velocity (as in Figure 4.61), but further downstream the opposite occurs; this seems to be similar to the effect seen in subsection 4.3.3, where it was shown that higher swirler flow rates reduce the centreline velocity. However, all these differences of an order of 3% may be too close to the experimental error to be considered as significant. Nevertheless, there does seem to be evidence that the fuel flow is rapidly entrained by the swirler flow and contributes (in regions corresponding to the swirler flow) to a global increase of the mean velocities, mainly the axial velocity, without noticeably altering the flow pattern in the case of no fuel injection. Differences between situations with and without fuel injection are noticed only near the fuel injector, and measurements even closer to the injector are not possible due to the head curvature. This is another region of the combustor where the use of refractive index matching techniques would be useful.

4.3.6 Flow Visualization and Mixing

The photographs to be presented include photos with various flow conditions and camera shutter speeds. The photographs at the longer exposure times (less than 1/125 sec) agree well with the image one would normally expect, given the present geometry and flow conditions. These photographs are usually of low quality with low definition (high image blurring) and a uniform light pattern over most of the combustor, giving the impression of a nearly uniform mixture. This effect is caused by too long an exposure, enabling the movement of the subject and the overshadowing of regions of lower light intensity by neighbouring regions of higher light intensity. Shorter exposure times revealed finer structures of the flow and produced some striking images. The cross-sectional views were illuminated by a sheet of laser light perpendicular to the combustor axis and the angle of observation of the camera was at 30° to the combustor axis, producing an ellipsoid shape with the major axis oriented along the vertical and emphasizing the trajectory of the two top and two bottom jets. The two opposing horizontal jets appear shorter because of the viewing angle. The view of the dilution holes is partially blocked by the metallic flange ending the primary annulus. The longitudinal views were obtained with a sheet of laser originating from below the test section and with the camera orthogonal to the plane of light. The photos are mounted such that different shutter speeds are shown along columns, whereas different flow conditions are shown along rows.

In the black and white photographs, plate 2, the white regions correspond to fluorescing dye (orange) and the black regions to pure water (green). The longitudinal views are shown in two sets, comprising the primary and the dilution holes. The vertical lines across the photographs were caused by blocking of the light by impurities accumulated on the bottom surface of the outer annulus and small air bubbles attached to the walls (these bubbles can be seen in the case of the dilution holes). Some attenuation of light also occurs from bottom to top and this effect, together with the blockage caused by air bubbles and impurities, is of extreme importance for quantitative applications of laser-induced fluorescence (see Appendix A).

Let us turn attention to the four photos of the primary zone first (the set of four photos on the top of plate 2). The top two exposures in the right column correspond to case 6 (i.e. with the highest swirler flow rate). In this case the penetration of the fuel jets has increased, due to the entrainment by the fluid originating from the swirler. The swirler flow itself is evidenced by the dark (green) region near the wall (region B in Figure 4.25). Other regions of similar low levels of concentration are the wake of the fuel injector and the entry of the primary jets. If the swirler flow is off (column on the left), the preferential transport of 'fuel' near the walls and the lower levels of mixing are clearer. Readdressing the coupling between turbulent stresses and mixing, it has been noted in subsection 4.3.4 that, although the turbulent stresses in the impingement region of the primary jets increase as the swirler flow rate decreases, overall rates of mixing decrease. This reduced mixing can be seen through: i) the central core of the flow, mainly formed by low concentration fluid emerging from the primary holes and ii) the bigger turbulent structures shown in the photos at higher shutter speeds; the photo at the higher shutter speed even shows the impact of the lateral jets on the centre plane as two craters.

The dilution jets, in the second set of photos, are staggered by half a pitch with respect to the primary jets and the vertical plane photographed here is midway between the dilution jets. Comparing swirler flow (right) with no swirler flow (left), in case of swirler flow the central core is much more uniform and the dilution jets show up as a region of pure water further downstream of the injection with a reduced radial penetration. If there is no swirler flow, they appear at inner radial locations after the expansion and merging of the neighbouring jets has occurred, and with different angles with respect to the crossflow. The photo at the top left shows a front of dyed fluid moving along the centre. This occurs due to the blockage caused by the dilution jets, forcing the dye moving along the wall to be driven towards the centre of the can and mixing with the fluid originating from the primary jets.

The colour plates are all cross section views. Plate 3 shows in the first row a plane close to the swirler and tangential to the tip of the fuel injector whereas the rest of the photos are in the plane containing the axis of the primary holes. Plate 4 is a view containing the dilution holes axis. Plate 5 are selected frames from the high speed film. The combustor is vertically oriented in these views and the direction of the flow is from the top to the bottom. Three columns are included this time; the first column corresponds to no swirler flow, the central column corresponds to case 1 and the column on the right corresponds to case 6, with the highest swirler flow rate.

In plate 3 moving along the first row the effect of the swirler flow in a transverse plane tangential to the tip of the fuel injector is shown. As the swirler flow rate increases (from left to right) the flow through the vanes draws a petal like pattern corresponding to alternate regions of lower and higher concentrate fluid.

In the plane of the primary jets the penetration is reduced as the swirler flow rate increases and this is accompanied by a more uniform colour pattern associated with more uniform mixing.

The views of the dilution jets are in plate 4. Only the under-exposed photos could resolve the finer structure of the flow. The photo in the bottom in case of no swirler flow (with the higher shutter speeds) is able to resolve a structure observed before in single jets issuing into stagnant surroundings, but this structure is most evident in frames obtained from the high speed film. These views, in plate 5, should be read from the top to bottom in order to follow the right sequence of events. Concentrating first on the views of the dilution jets on the right, and in the dilution jet shown on the right of the images, one can see that the jet progressively increases its penetration into the combustor and develops a mushroom shape at its front. The same shape is observed in the photo on the bottom left corner of plate 4. This reduction of the jet diameter is terminated later by the breakdown of the jet front end which develops into an isolated vortex ring later distorted and convected by the cross stream fluid. The jet is again at its lowest penetration into the combustor and this is the end of the cycle. Most surprisingly, the jet in the left hand side of the frames follows the same cycle but out of phase with the jet in the right; this was most evident from the projection of the films and showed that when one of the jets is moving radially inwards (and initiating the cycle) the neighbouring jet is on its return stage towards the wall. This cycle seems to occur at a constant frequency, judging from the projection of the films but no spectral analysis has been made in this region and this remains an unresolved question. However a rough estimate from these 30 frames shot at a frame rate of 200 Hz yields a frequency of the cycle at about 7 Hz.

There is nothing new about the structure observed at the front of the jet and the development of the two lateral vortices in the jet shear layer, creating the

appearance of a mushroom shape. Good pictures of the same phenomenon can be seen for instance in figure 1.8 of Hinze [1975] or in Chapter 5 of Van Dyke [1982] in case of single jets discharging into stagnant surroundings. The surprising and new thing here is the interaction and the apparent out of phase between the behaviour of two neighbouring jets. Spectral analysis in the plane of the dilution jets should be made in the future. The frames corresponding to the primary holes do not suggest the existence of a phenomenon similar to that observed in the dilution hole plane. A random pattern seems to prevail in agreement with the spectral analysis performed in subsection 4.3.4.

4.4 CONCLUSIONS

An experimental study of the flow inside a water model of a gas turbine combustor was presented in this chapter. The model was a geometrical replica of a combusting model intended to simulate can type combustors which are currently commercially available. It was found that for a good similarity between isothermal and combusting flow patterns the matching should be made in terms of the ratios between primary and swirler flow and between dilution and cross flow.

The flow inside the combustor was dominated by the primary jet impingement. The six primary opposed jets penetrate almost radially into the combustor, impinge on each other at the centreline and split giving rise to a toroidal recirculation zone in the head of the combustor.

The main characteristics of the region of impingement were:

A strong anisotropy of turbulence with an azimuthal component with a flatness value of around 2.2 and a normal stress twice as large as the axial normal stresses.

The anisotropy was characterized by the existence of large scales of turbulence (low frequency) revealed by flow visualization and bimodal PDFs in the plane between the jets.

Spectral analysis confirmed the turbulent nature of this low frequency which occurred in a broad range of frequencies between 10 Hz and 150 Hz with a maximum at 60 Hz. These are values in the range of frequencies found in single jets experiments and the origin of the phenomenon was attributed to the merger of the shear layers of neighbouring jets.

Improved levels of stability and mixing can be achieved if the swirler flow rate is increased but only to a level where it does not give

rise to a precessing vortex core in the centre of the combustor, otherwise a second type of dominant frequency begins to appear.

Because of the strong backflow created by the primary jet impingement the swirler flow was transported near the walls and between the primary jets throughout the combustor until the plane of the dilution jets. The swirler flow creates a small recirculation region near the combustor head.

The fuel flow, for the same reason as above did not disturb the flow pattern, was entrained by the swirler flow and followed a similar path.

The dilution jets penetrate less than the primary jets and did not impinge on each other.

Because staggered relative to the primary jets, the dilution jets blocked the upstream flow near the wall and force it to mix with the central core, mainly formed by the flow resulting from the primary jet impingement.

The penetration of neighbouring dilution jets occurred alternately and high speed film suggested a cyclic behaviour with a frequency of about 7 Hz.

Enormous differences were found between flows with and without the primary jets (swirler flow only) and this casts doubts on the usefulness of idealized geometries incorporating only swirler and/or coaxial jets to model the primary region of gas turbine combustors. Complete models such as that used in the current experiment are believed to be an absolute necessity.

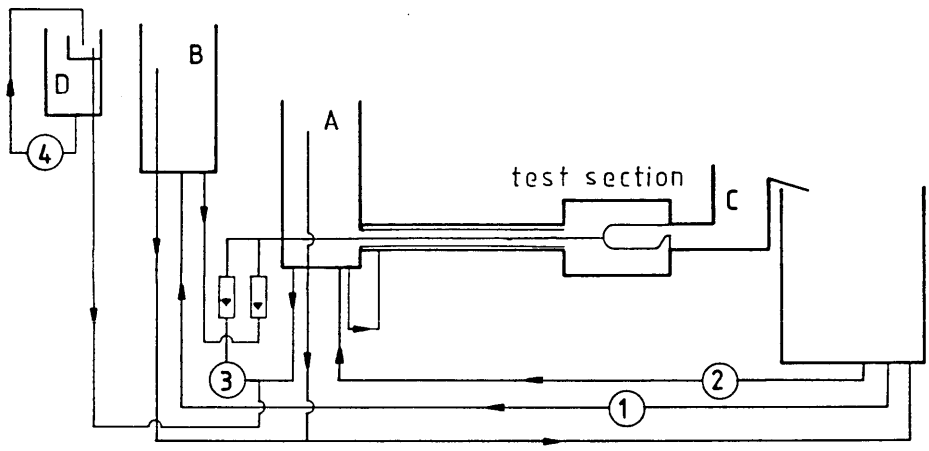


FIGURE 4.1 - Experimental rig.

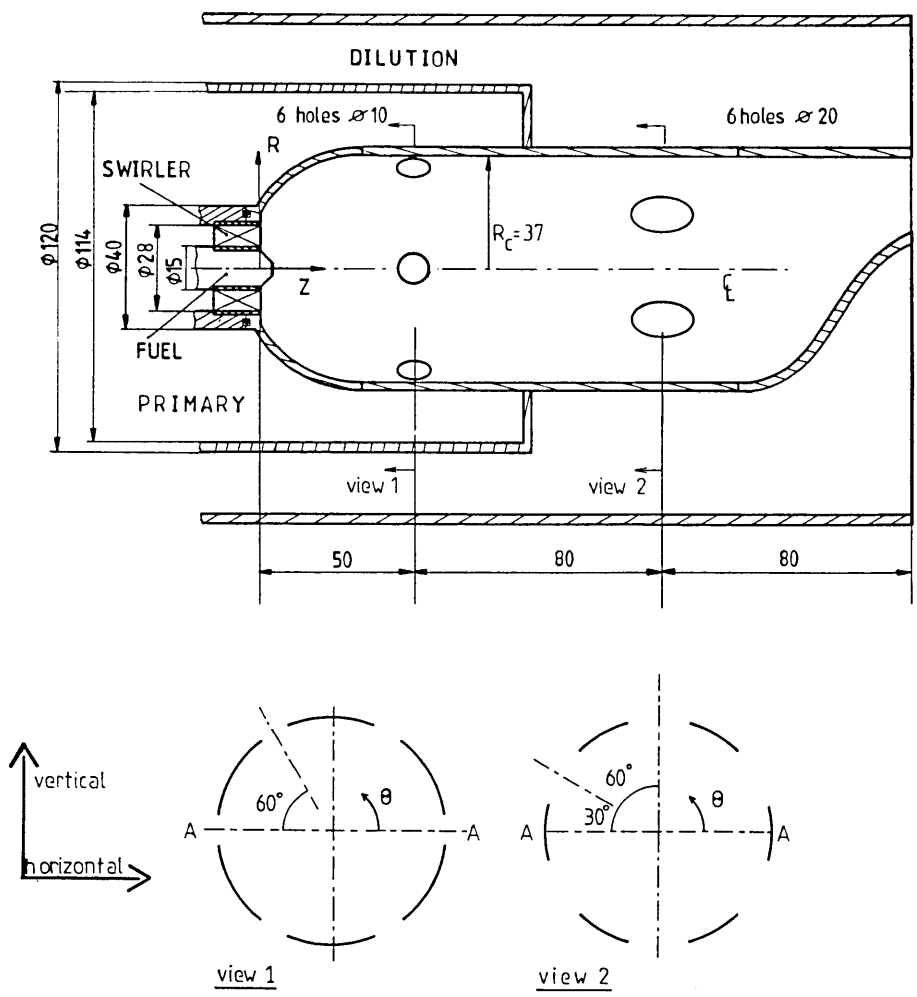
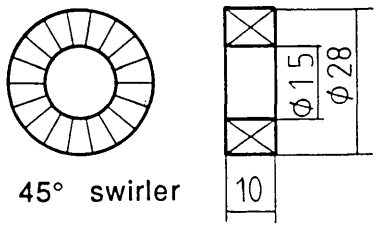


FIGURE 4.2 - Plexiglass combustor model.



SWIRLER NUMBER - 0.56

SWIRL NUMBER - 0.46

FIGURE 4.3 - Swirlers.

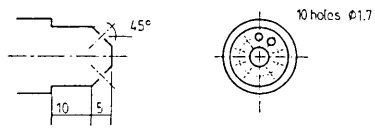
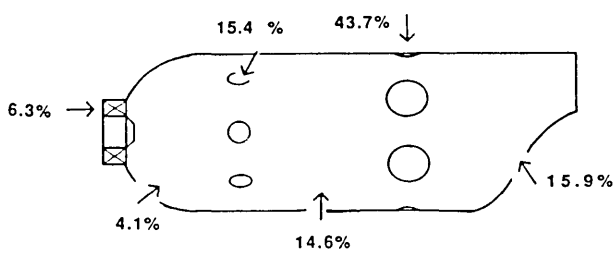
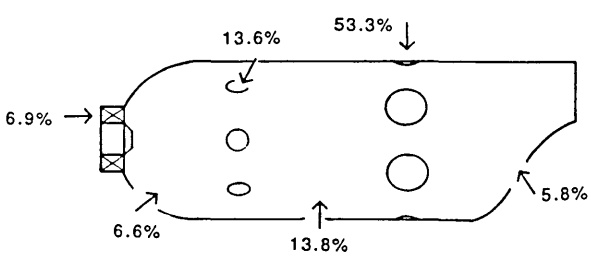


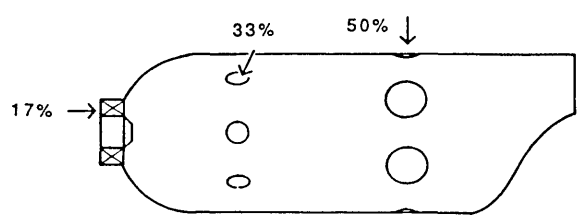
FIGURE 4.4 - Fuel injector.



a) real combustor



b) combusting experiment



c) water model experiment

FIGURE 4.5 - Flow splits found in engine and model combustors.

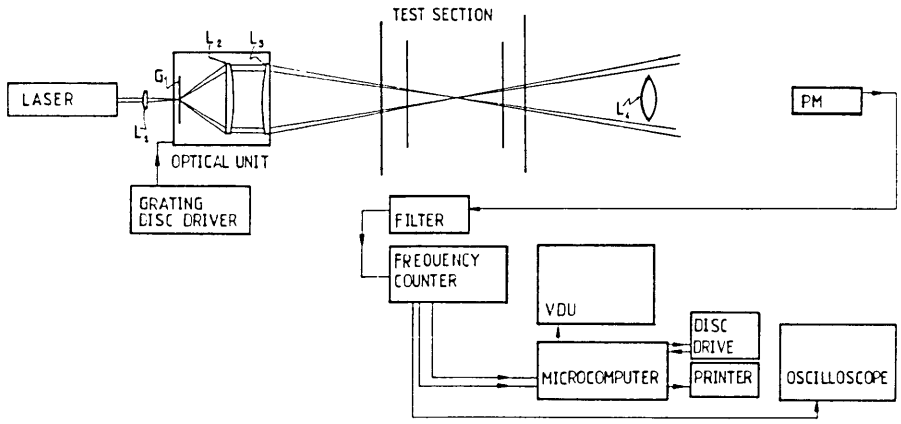


FIGURE 4.6 - Diagram of the LDV system.

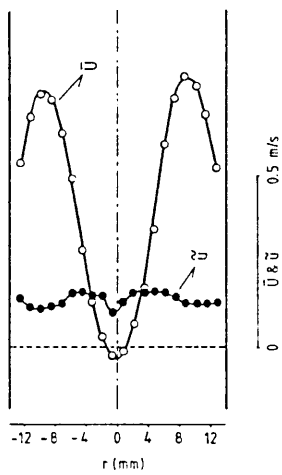


FIGURE 4.7 - Axial mean velocity and turbulence intensity profiles at Z/D=1 - 30 ° swirler.

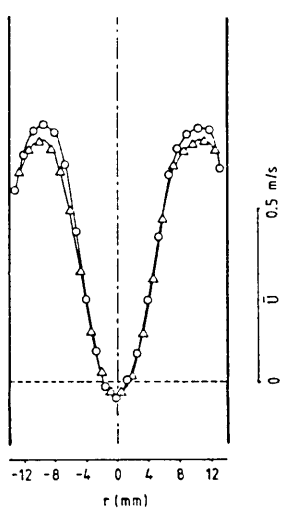


FIGURE 4.8 - Axial mean velocity profiles at Z/D=2 for two angular locations 120° apart - 30° swirler.

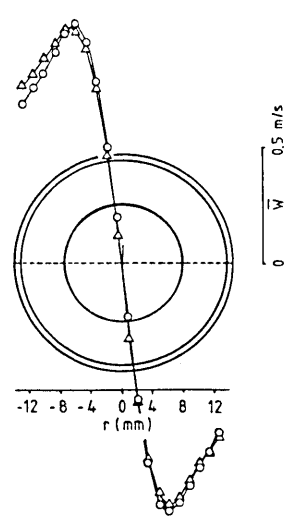


FIGURE 4.9 - Azimuthal mean velocity profiles at Z/D=2 for two angular locations 120° apart - 30° swirler.

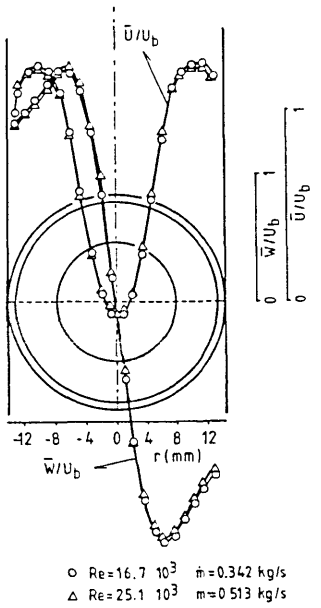


FIGURE 4.10 - Axial and azimuthal mean velocities at Z/D=2 for two Reynolds number - 30° swirler.

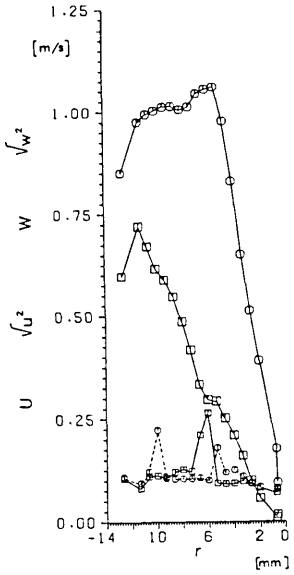


FIGURE 4.11 - Axial (□) and azimuthal (O) velocities at 3 mm downstream from the swirler and along the middle of the vane passage - 45° swirler.

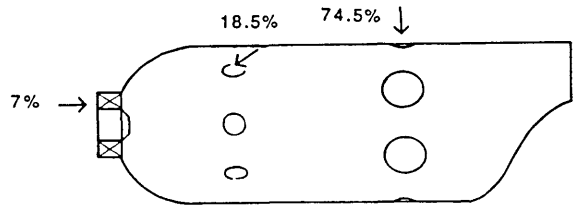


FIGURE 4.12 - Flow split (flow split 1) in a preliminary experiment to simulate the flow pattern of the combusting rig in the water rig.

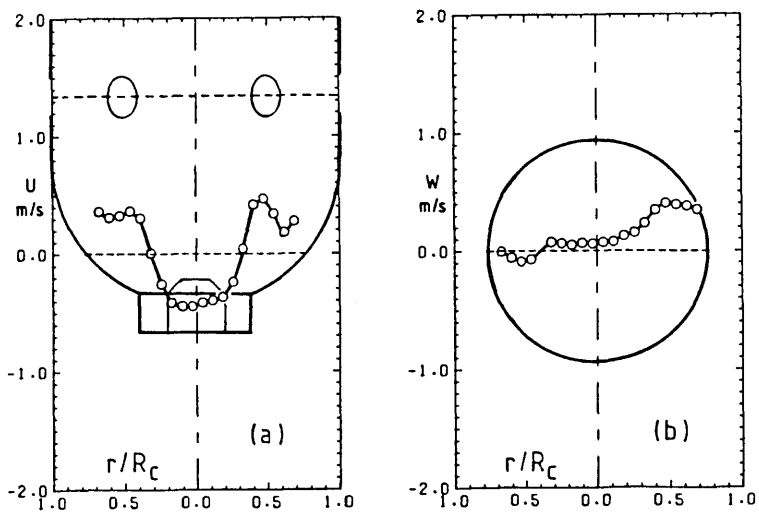


FIGURE 4.13 - Mean velocity profiles at Z = 8 mm, θ = 0° (flow split 1): a) axial component b) azimuthal component.

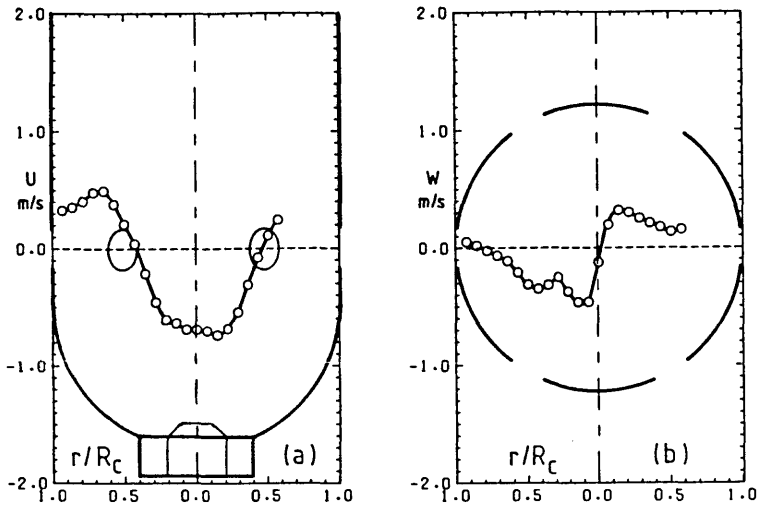


FIGURE 4.14 - Mean velocity profiles at Z = 50 mm, θ = 0° (flow split 1): a) axial component b) azimuthal component.

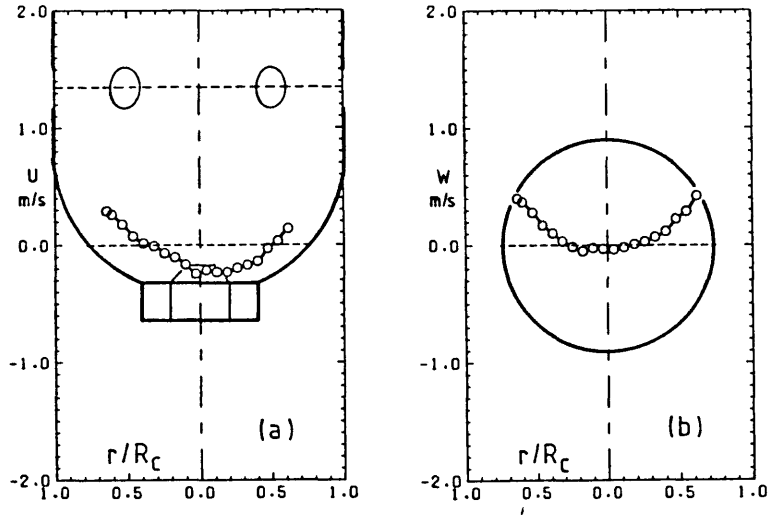


FIGURE 4.15 - Mean velocity profiles at Z = 8 mm, θ = 0° (flow split 1- no swirler flow): a) axial component b) azimuthal component.

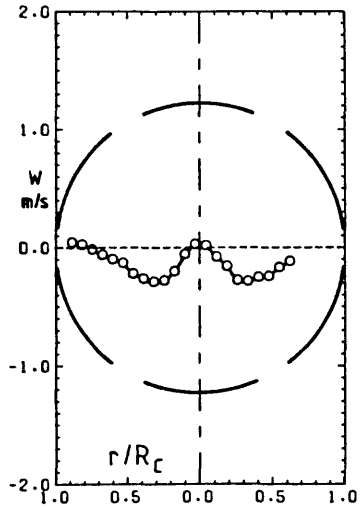


FIGURE 4.16 - Mean azimuthal velocity profile at Z = 8 mm, θ = 0° (flow split 1- no swirler flow).

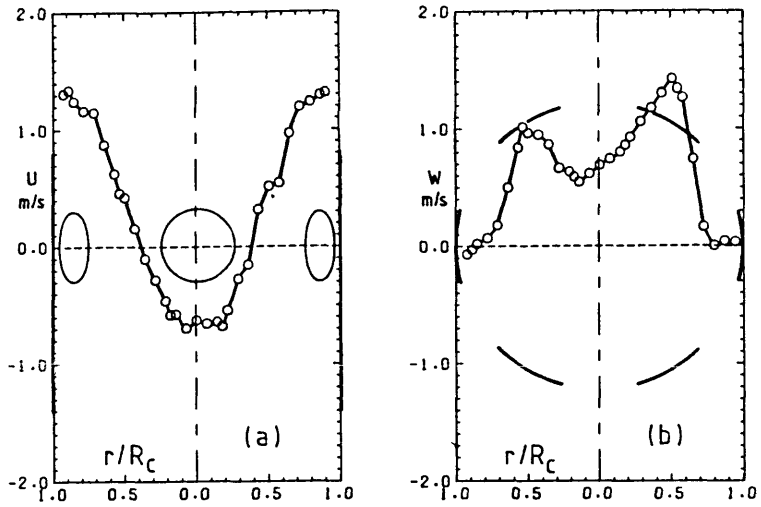


FIGURE 4.17 - Mean velocity profiles at Z = 130 mm, θ = 0° (flow split 1): a) axial component b) azimuthal component.

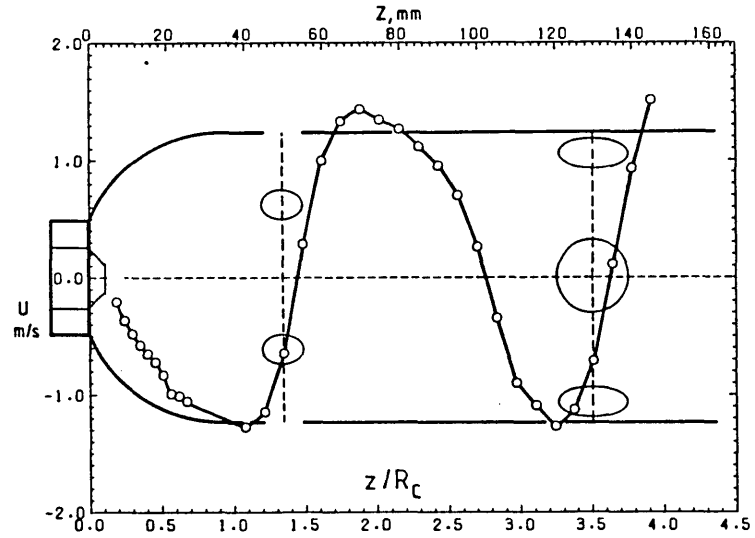
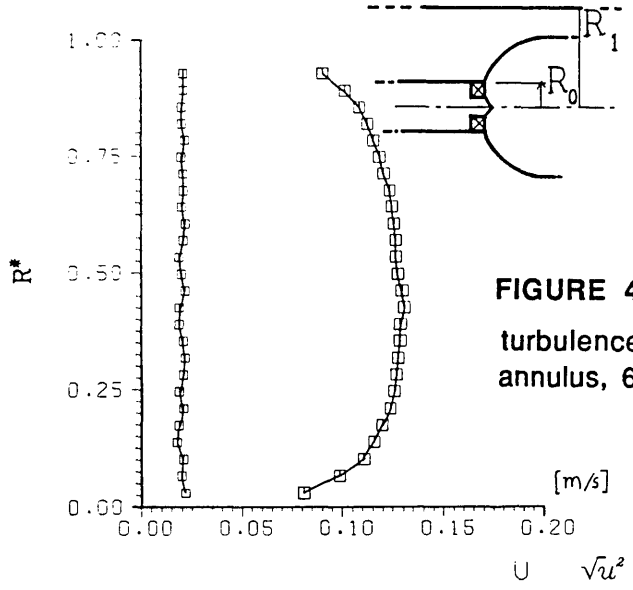


FIGURE 4.18 - Centreline values of mean axial velocity (flow split 1).



$$R^* = \frac{r - R_0}{R_1 - R_0}$$

FIGURE 4.19 - Axial mean velocity and turbulence intensity in the primary annulus, 65 mm upstream of the swirler.

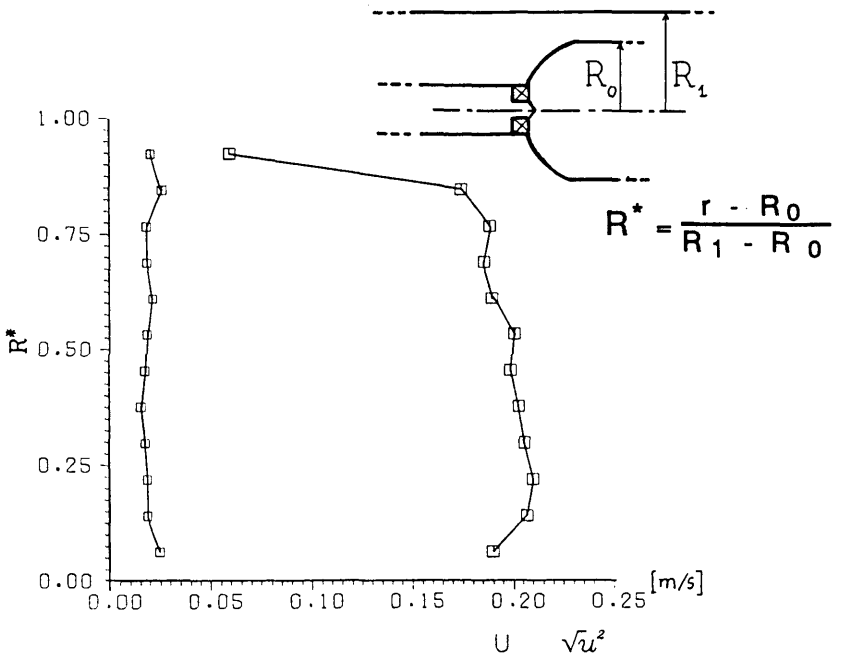


FIGURE 4.20 - Axial mean velocity and turbulence intensity in the primary annulus, 10 mm upstream of the primary holes and at $\theta = 30°$.

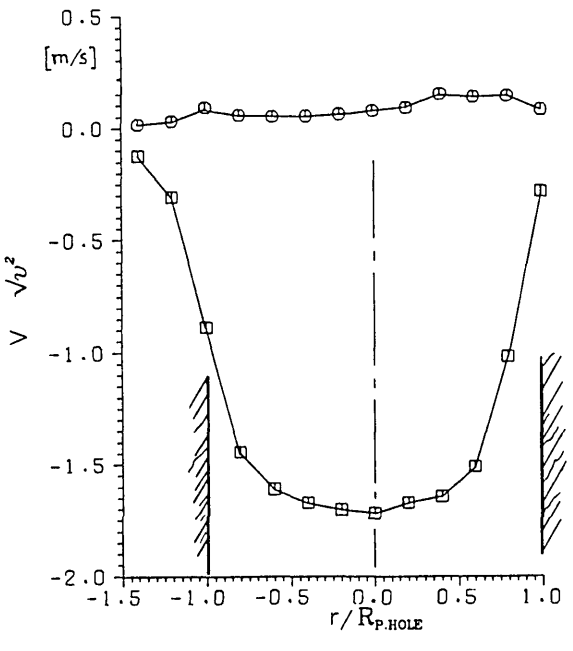


FIGURE 4.21 - Radial mean (▫) and turbulence (○)intensity 3 mm above the outer surface of the combustor along the primary hole diameter.

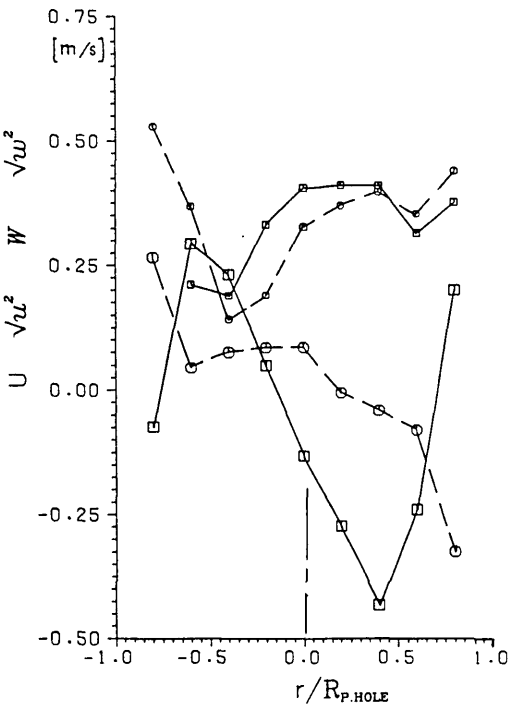


FIGURE 4.22 - Axial (▫) and azimuthal (○) components (mean and turbulence intensity) along the primary hole diameter in a plane tangential to the inner surface of the combustor.

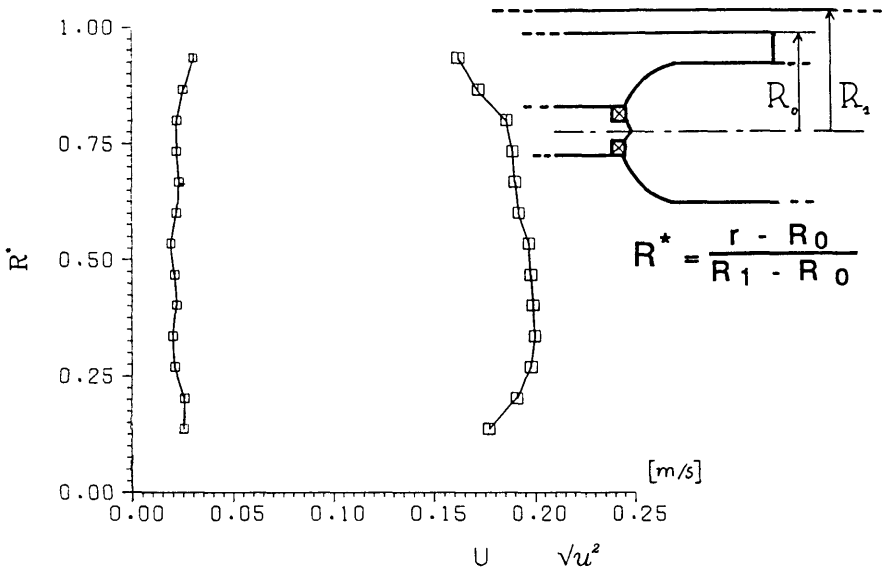


FIGURE 4.23 - Axial (□) mean velocity and turbulence intensity (□) in the dilution annulus 90 mm upstream of the dilution holes.

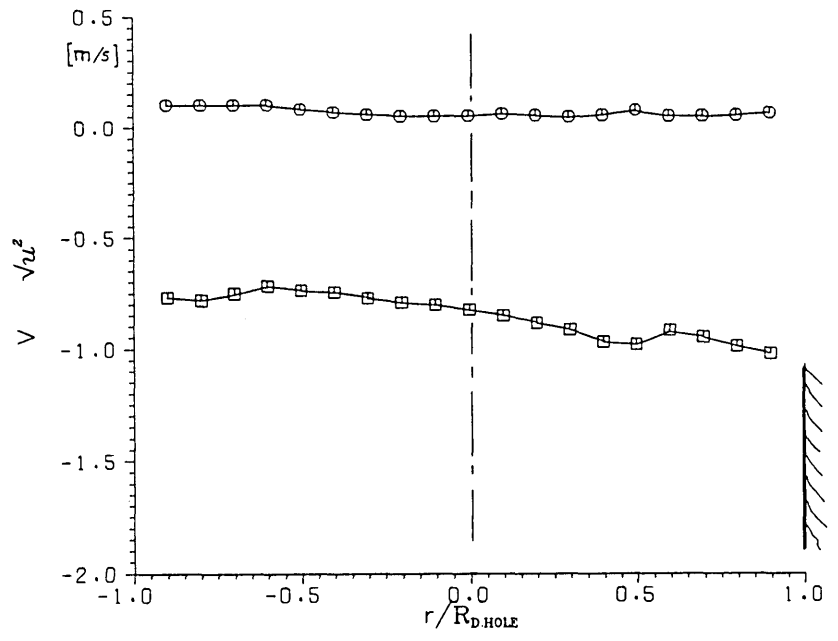


FIGURE 4.24a - Radial mean velocity (□) and turbulence intensity (○) along the dilution hole diameter in a plane tangential to the outer surface of the combustor.

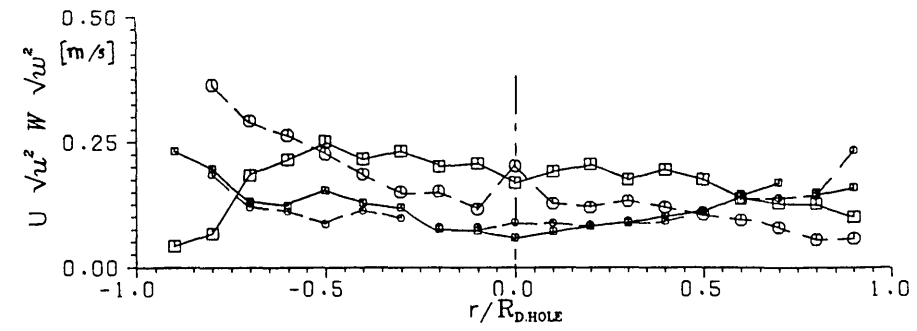


FIGURE 4.24b - Axial (□) and azimuthal (○) components (mean and turbulence intensity) along the dilution hole diameter in a plane tangential to the inner surface of the combustor.

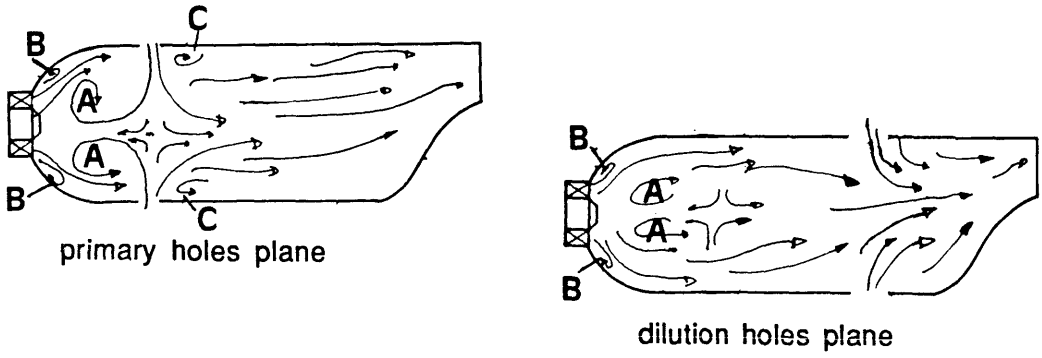


FIGURE 4.25 - Schematic longitudinal views of the flow pattern inside the combustor.



FIGURE 4.26 - Schematic cross-sectional views of the flow pattern inside the combustor.

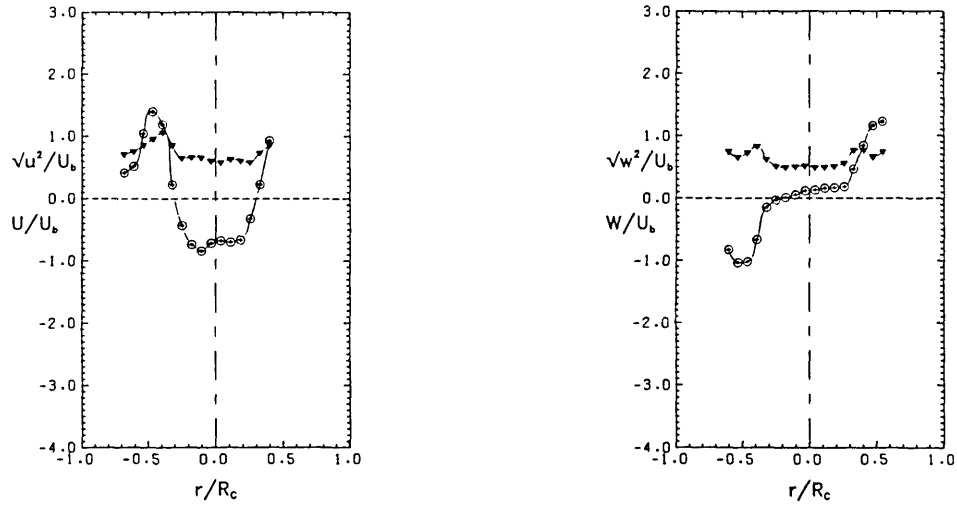


FIGURE 4.27 - Measurements at Z = 8 mm, θ = 0° (case 1).

○ **MEAN VELOCITY** (U/U_b, V/U_b, W/U_b)

▼ **TURBULENCE INTENSITY** ($\sqrt{u^2}/U_b$, $\sqrt{v^2}/U_b$, $\sqrt{w^2}/U_b$)

TURBULENCE KINETIC ENERGY ($\sqrt{k}\ /U_b$)

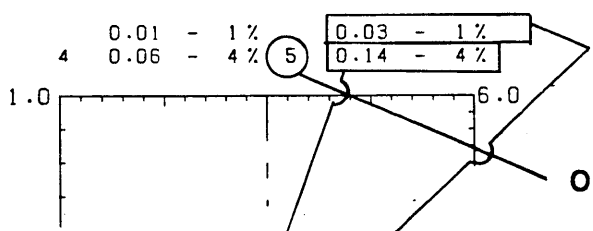
FLATNESS (F_u, F_v, F_w)

▲ **SKEWNESS** (S_u, S_v, S_w)

values on the left refer to the order of the polynomial used for fitting of the skewness values and evaluation of the experimental uncertainty according to equations [4.3] and [4.4]

values on the right are similar to those on the left but refer to the flatness

LEFT **RIGHT**



ORDER OF THE POLYNOMIAL

EXPERIMENTAL UNCERTAINTY ACCORDING TO [4.3]
the average root mean square of the distance between the fitted ($f(x_i)$) and experimental value (y_i) defined either in absolute terms (the value on the left) or in relative terms (the value on the right)

EXPERIMENTAL UNCERTAINTY ACCORDING TO [4.4]
the average distance between the fitted ($f(x_i)$) and experimental value (y_i) defined either in absolute terms (the value on the left) or in relative terms (the value on the right)

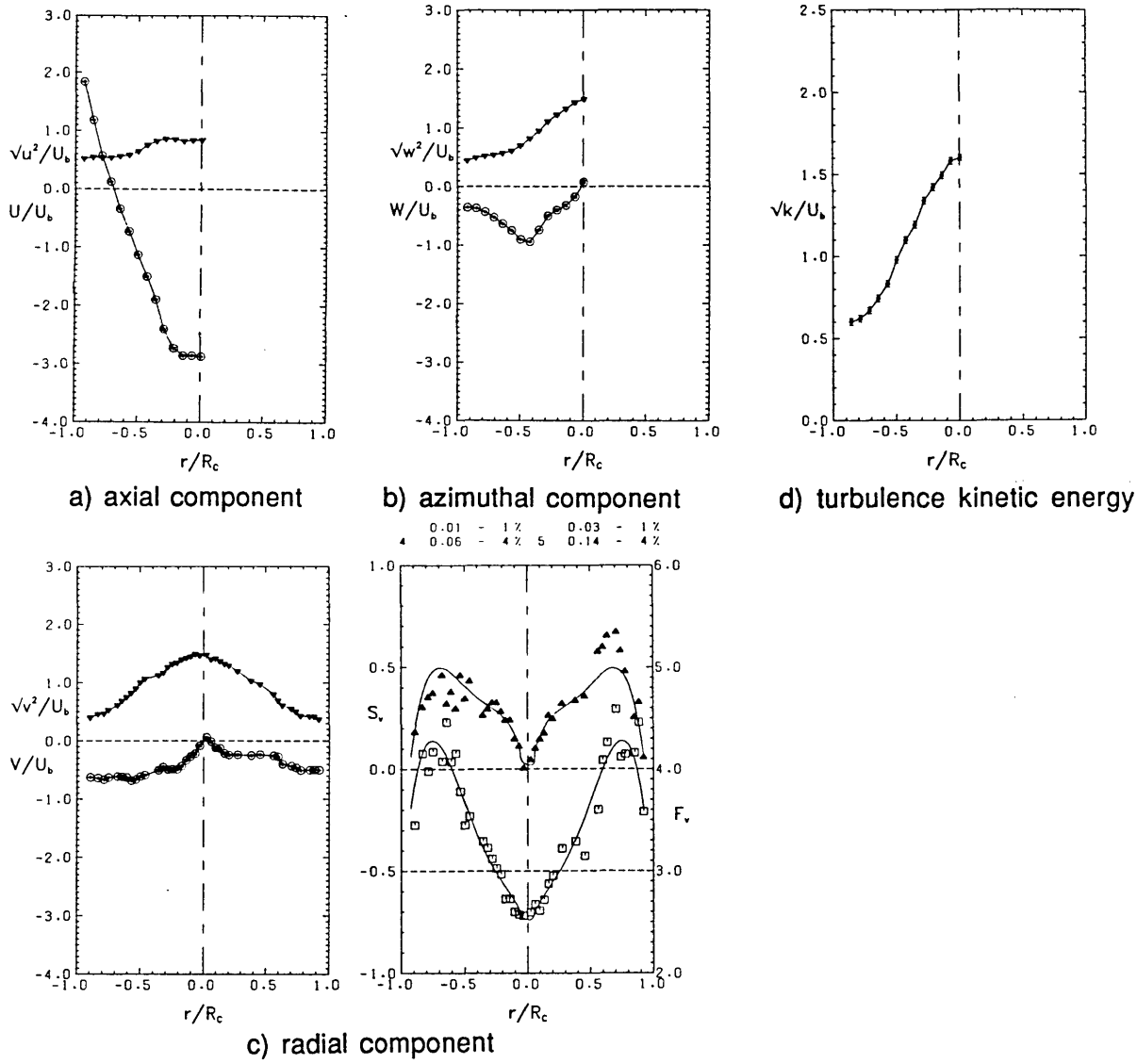


FIGURE 4.28 - Measurements at Z = 40 mm, θ = 0° (case 1).

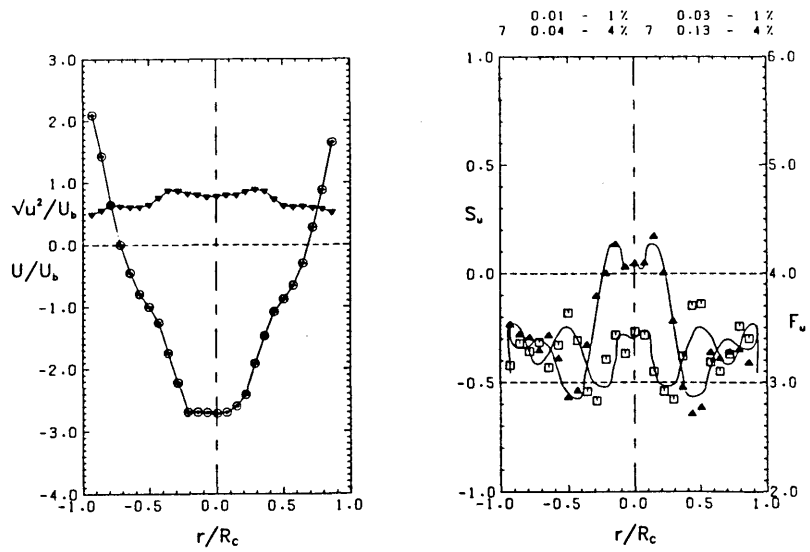
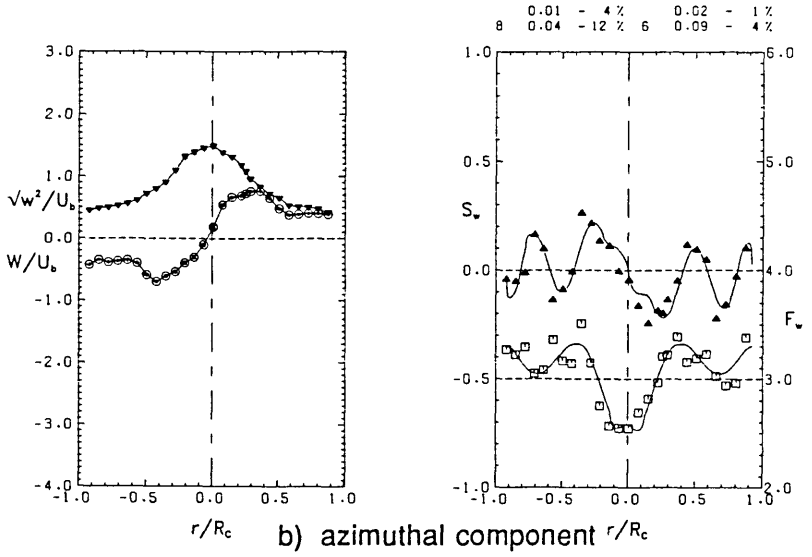


FIGURE 4.29 - Measurements at Z = 40 mm, θ = 30° (case 1).



b) azimuthal component

FIGURE 4.29 (continued)– Measurements at Z = 40 mm, θ = 30° (case 1).

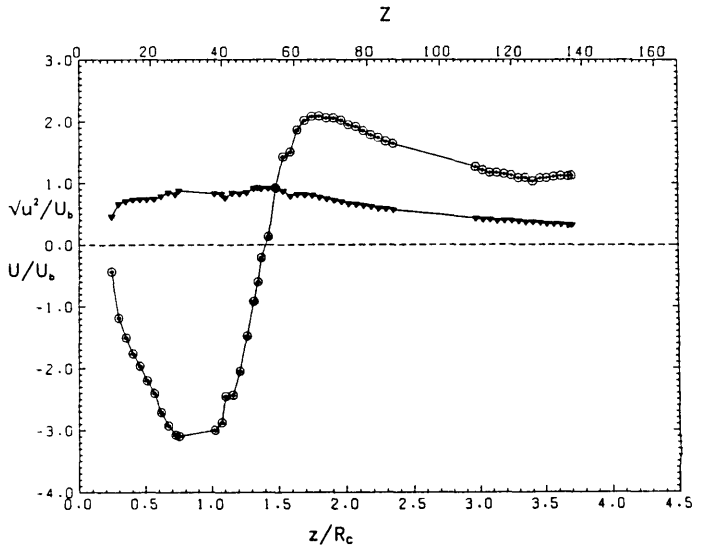
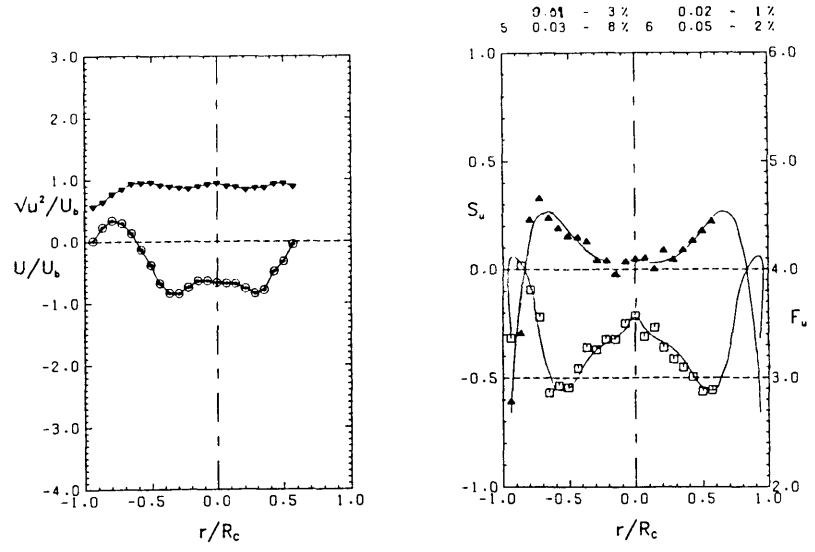


FIGURE 4.30 - Centreline mean axial velocity and turbulence intensity (case 1).



a) axial component

FIGURE 4.31 - Measurements at Z = 50 mm, θ = 0° (case 1).

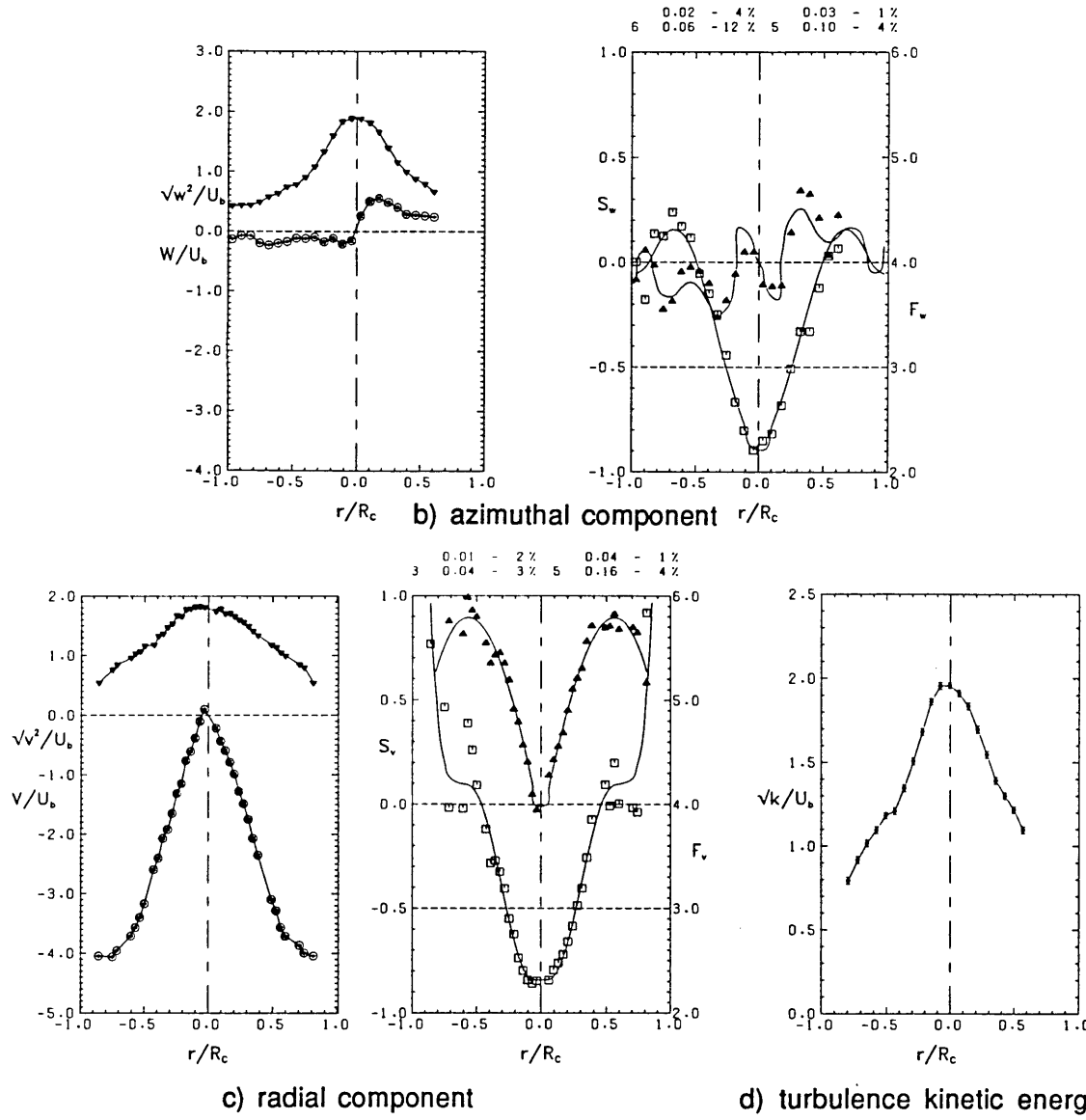


FIGURE 4.31 (continued)– Measurements at Z = 50 mm, θ = 0° (case 1).

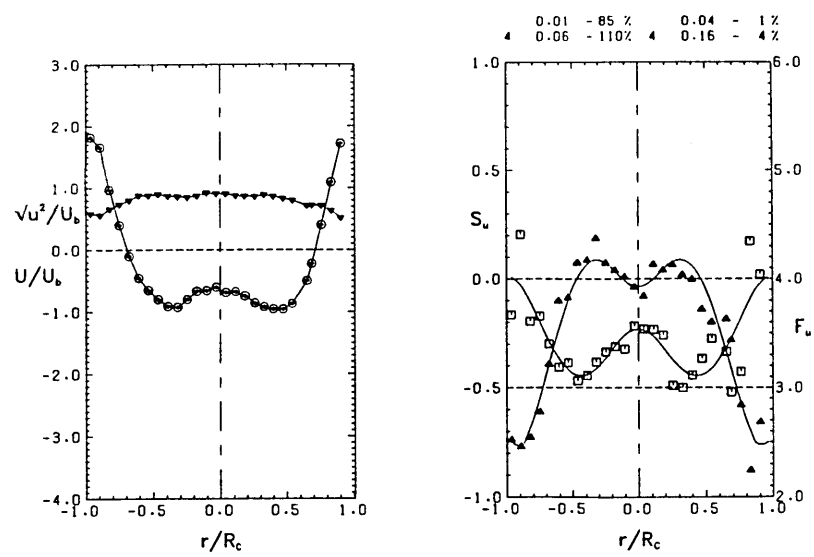
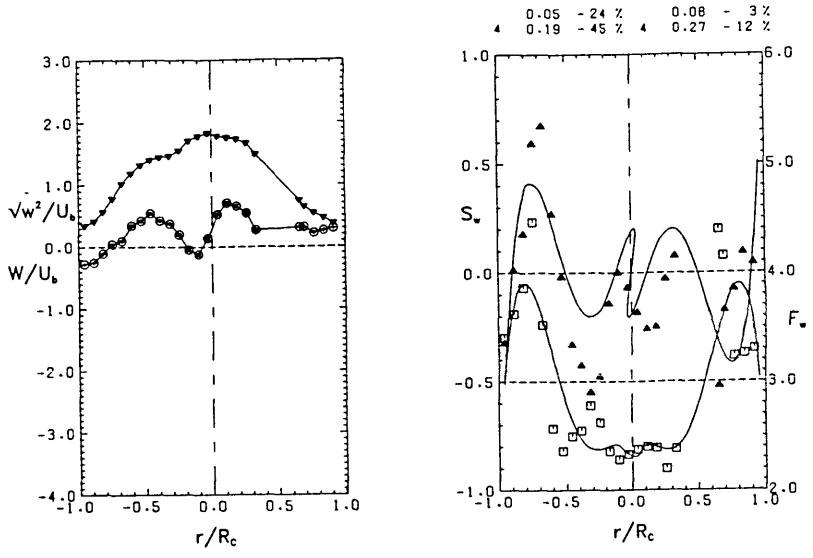
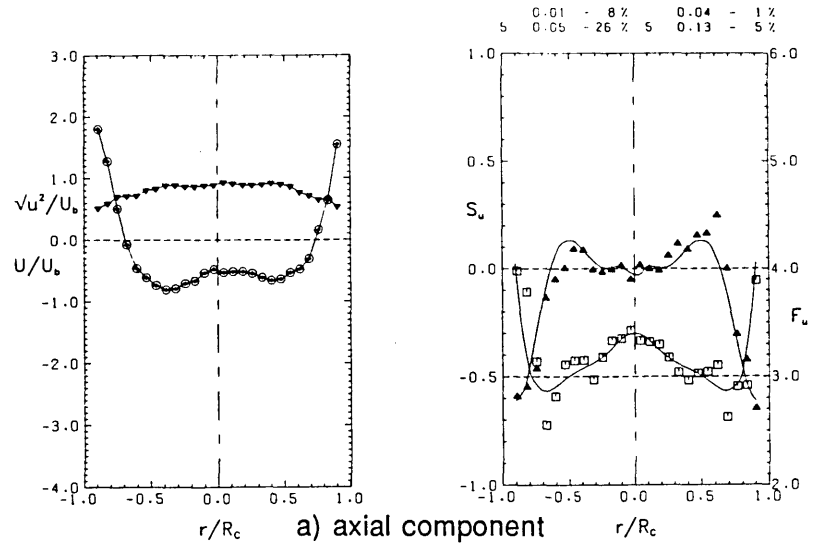


FIGURE 4.32 - Measurements at Z = 50 mm, θ = 15° (case 1).

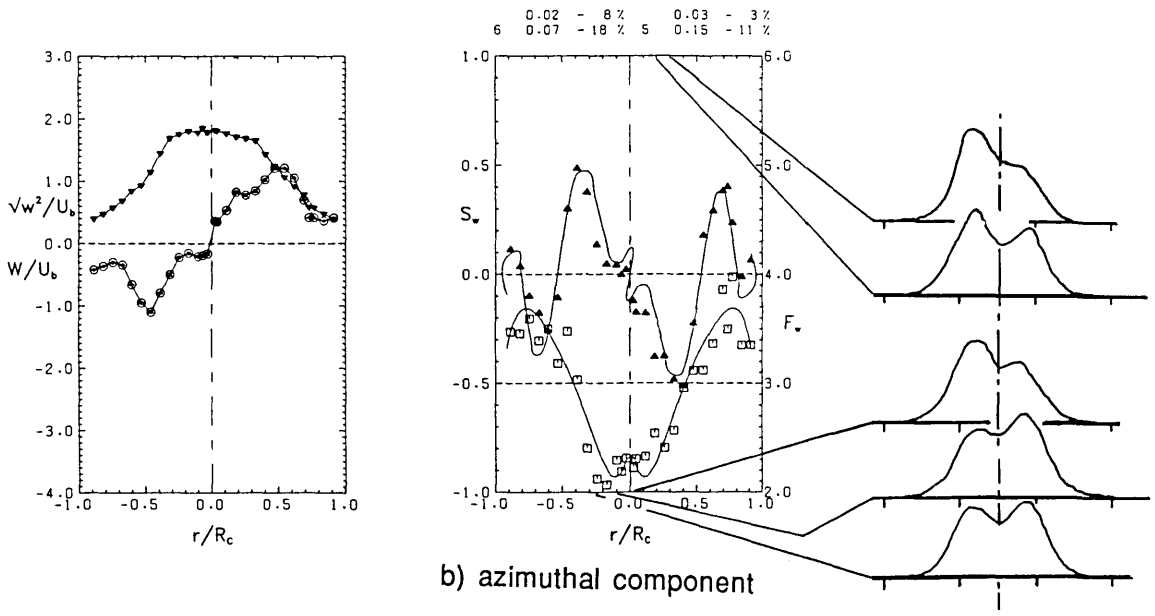


b) azimuthal component

FIGURE 4.32 (continued) - Measurements at Z = 50 mm, θ = 15° (case 1).



a) axial component



b) azimuthal component

FIGURE 4.33 - Measurements at Z = 50 mm, θ = 30° (case 1).

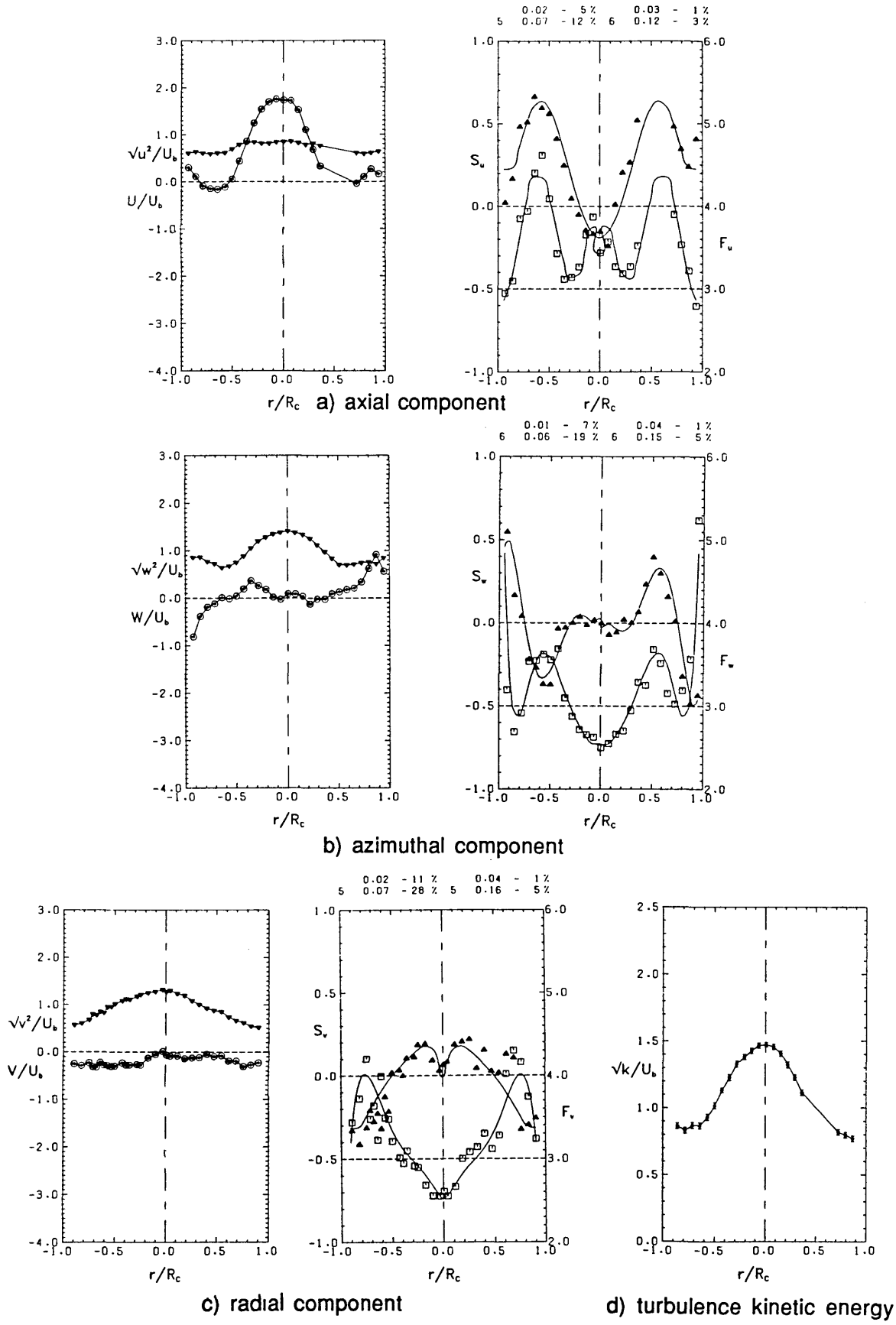
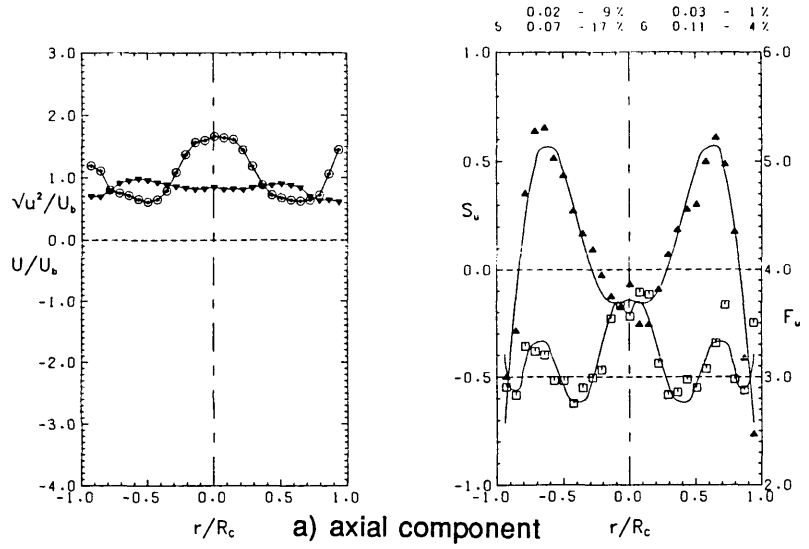
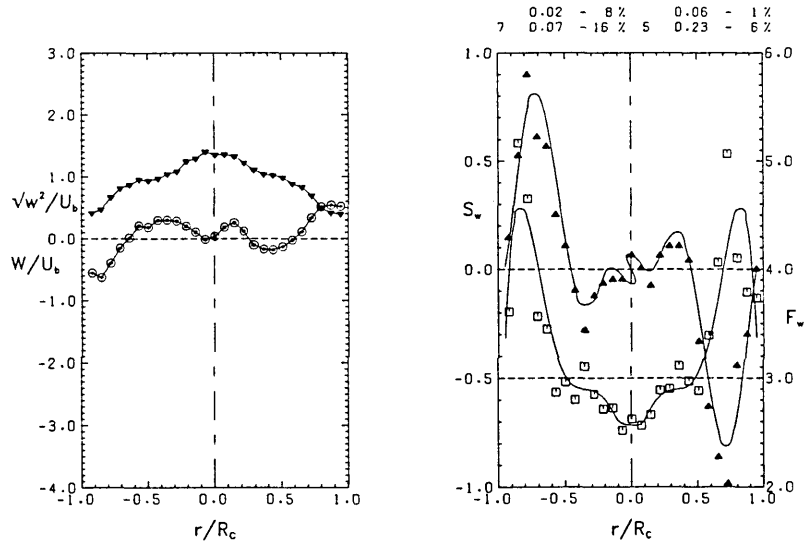


FIGURE 4.34 - Measurements at Z = 60 mm, θ = 0° (case 1).

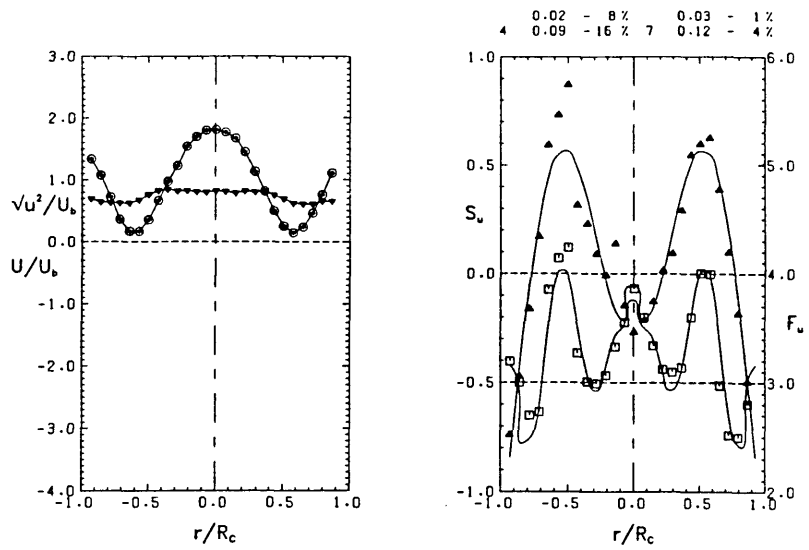


a) axial component



b) azimuthal component

FIGURE 4.35 - Measurements at Z = 60 mm, θ = 15° (case 1).



a) axial component

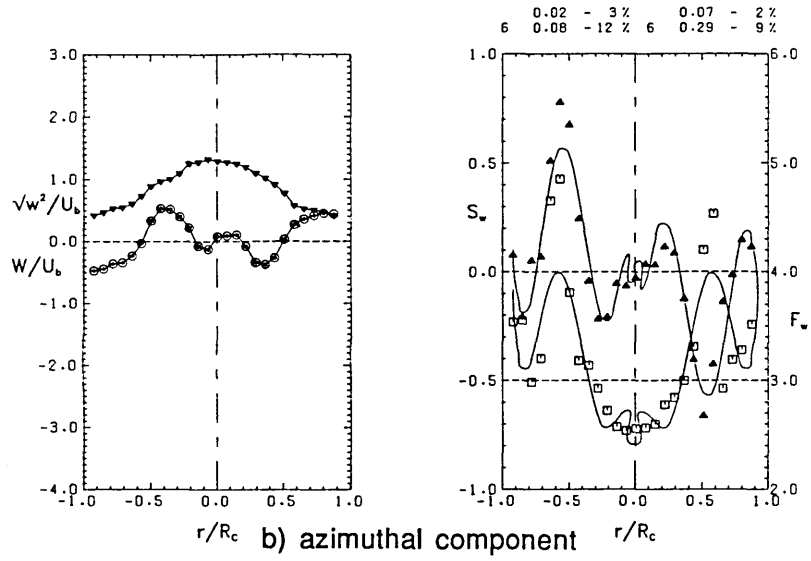
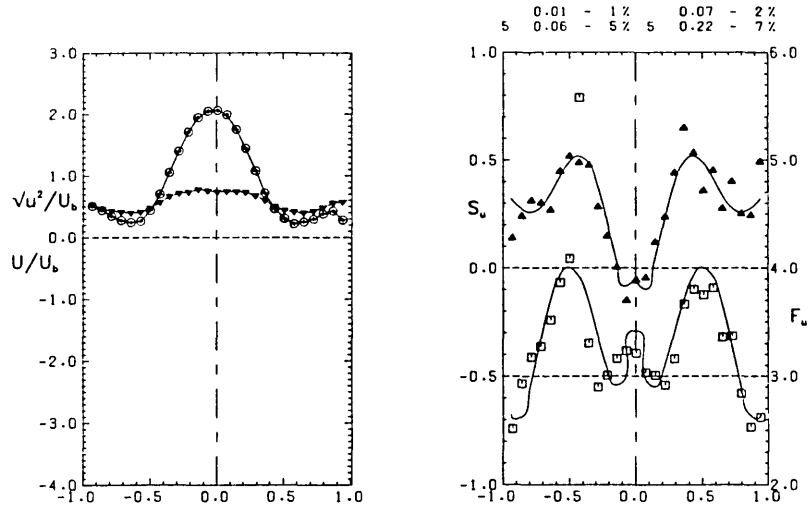
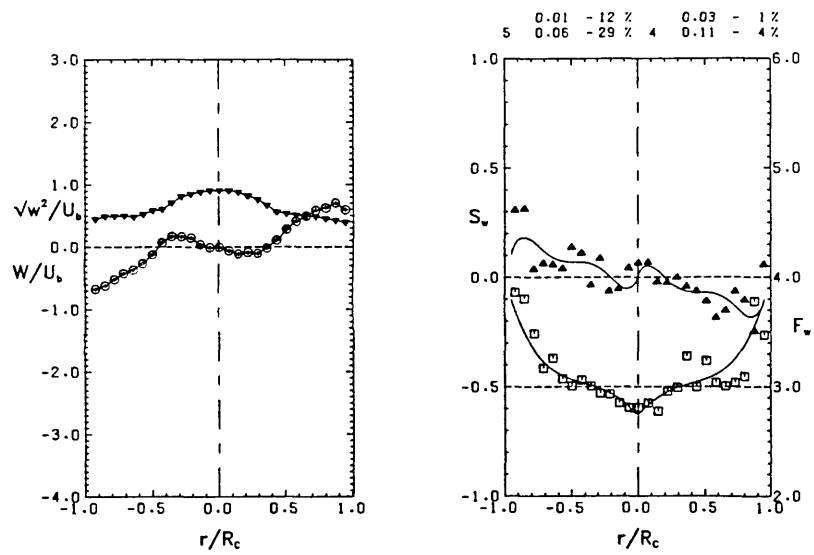
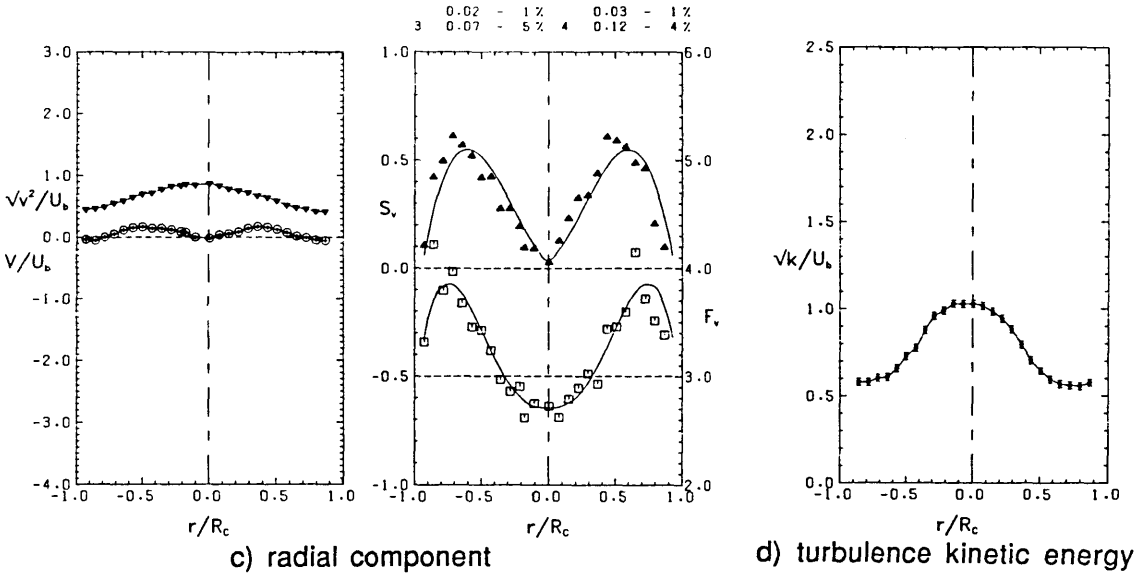


FIGURE 4.36 - Measurements at Z = 60 mm, θ = 30° (case 1):

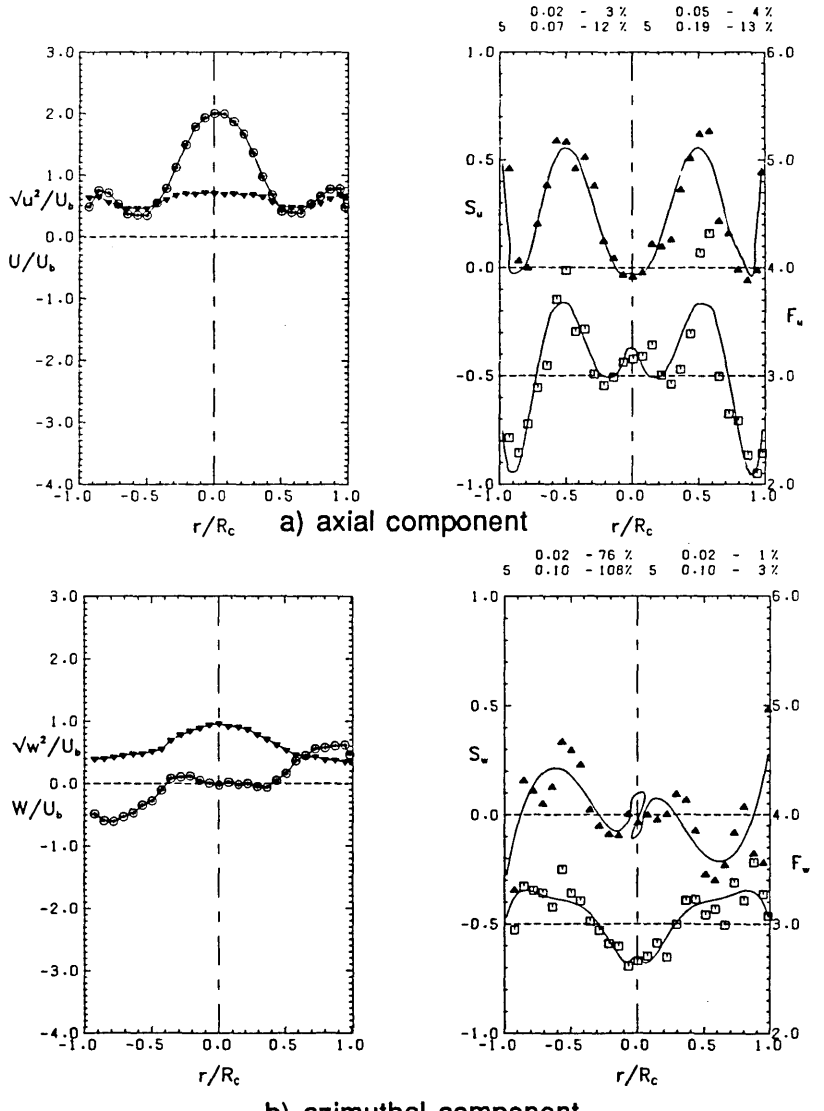






c) radial component d) turbulence kinetic energy

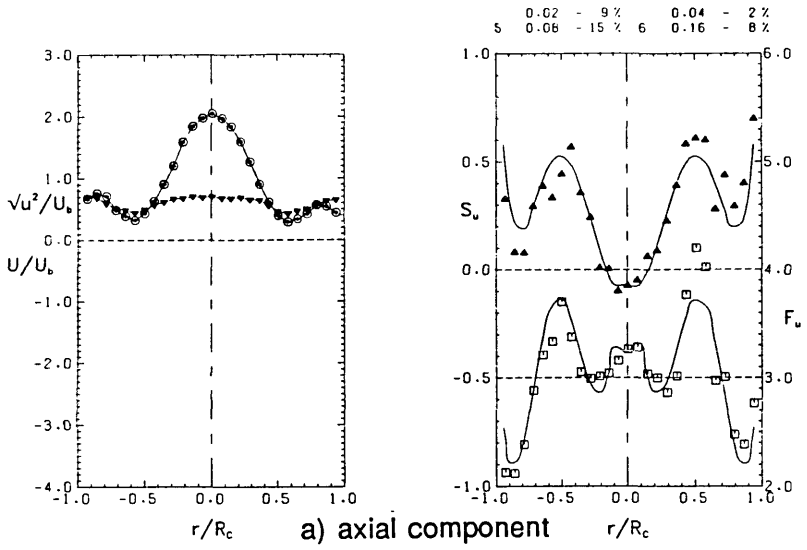
FIGURE 4.37 - Measurements at Z = 70 mm, θ = 0° (case 1).



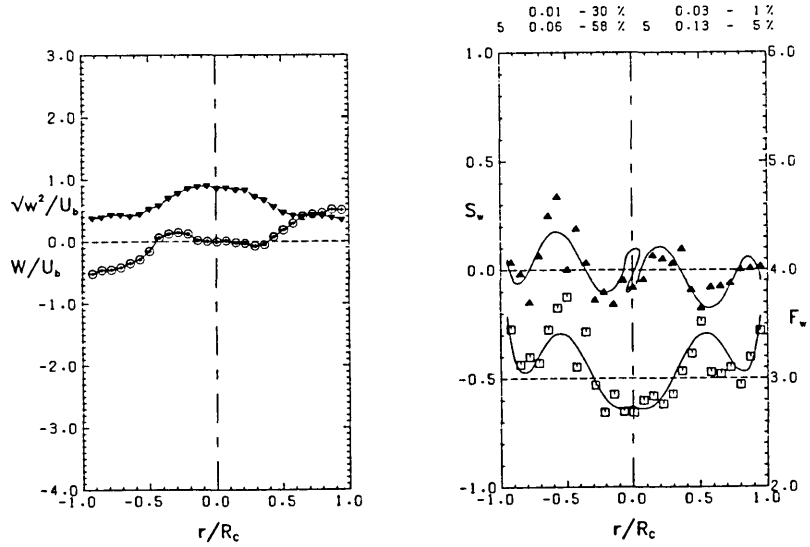
a) axial component

b) azimuthal component

FIGURE 4.38 - Measurements at Z = 70 mm, θ = 15° (case 1).

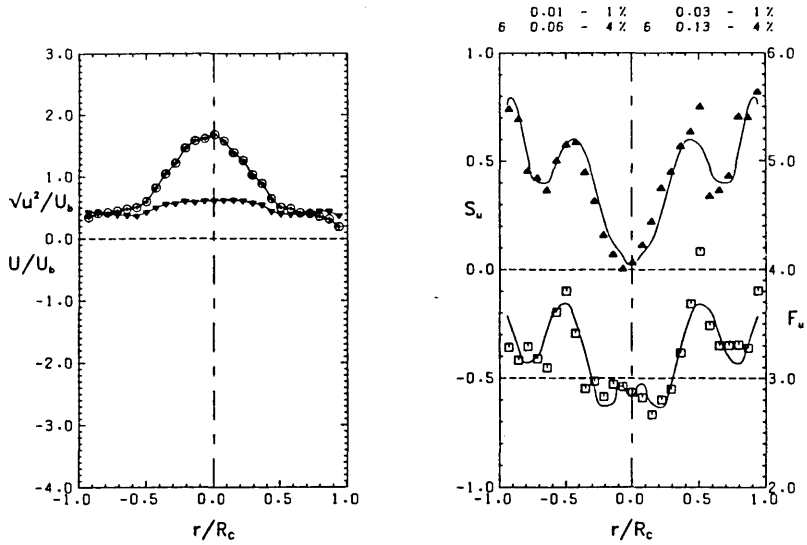


a) axial component



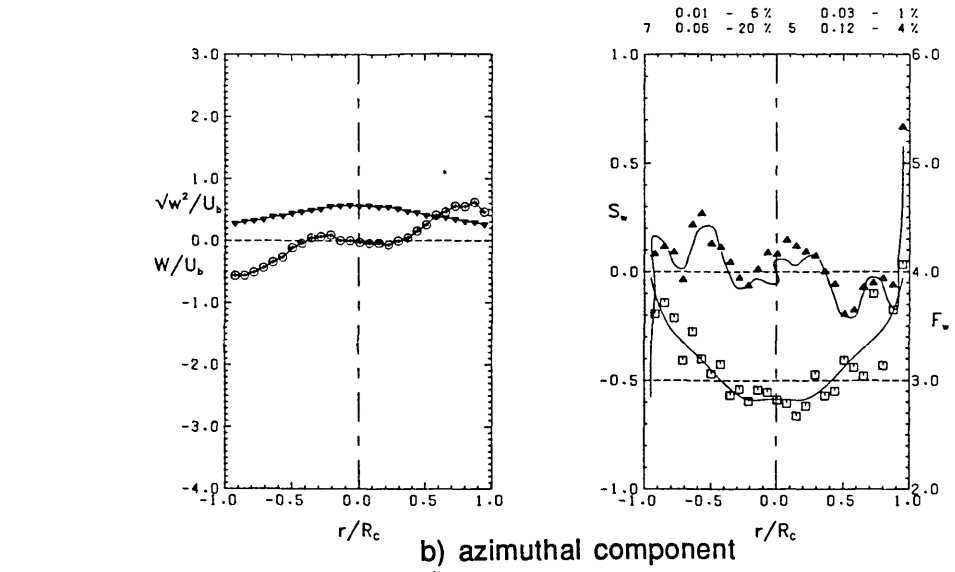
b) azimuthal component

FIGURE 4.39 - Measurements at Z = 70 mm, θ = 30° (case 1).

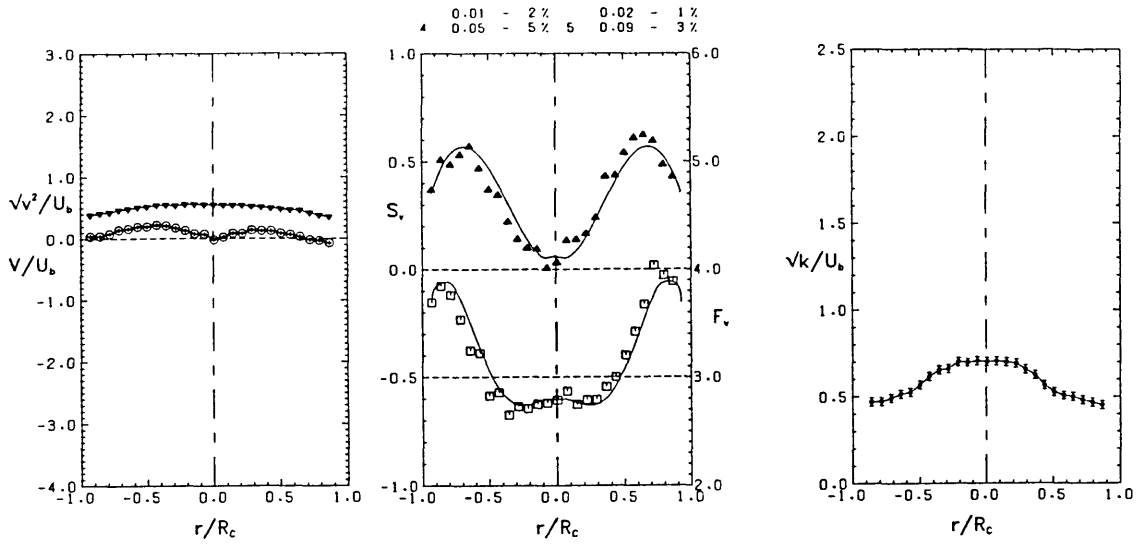


a) axial component

FIGURE 4.40 - Measurements at Z = 85 mm, θ = 0° (case 1).



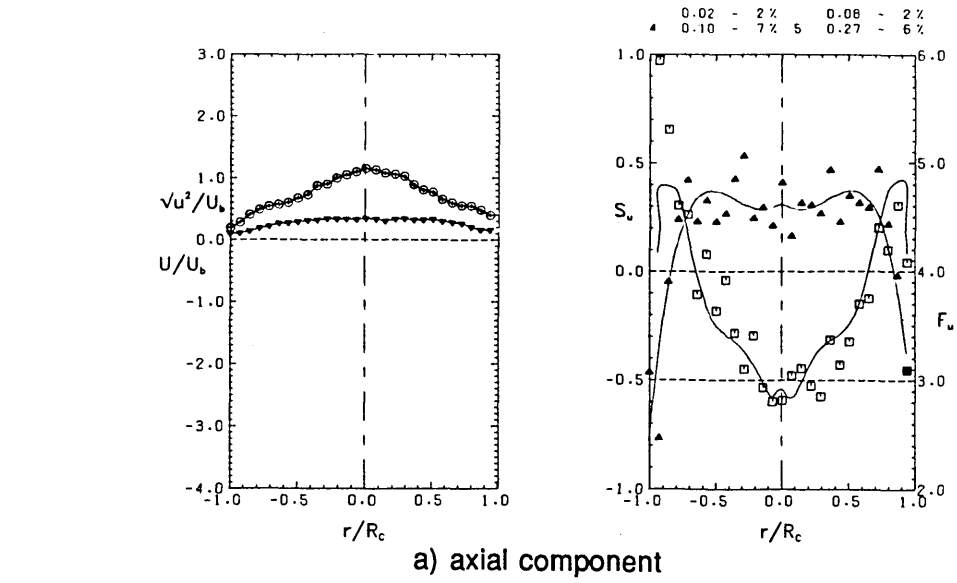
b) azimuthal component



c) radial component

d) turbulence kinetic energy

FIGURE 4.40 (continued) - Measurements at Z = 85 mm, θ = 0° (case 1):



a) axial component

FIGURE 4.41 - Measurements at Z = 130 mm, θ = 30° (case 1):

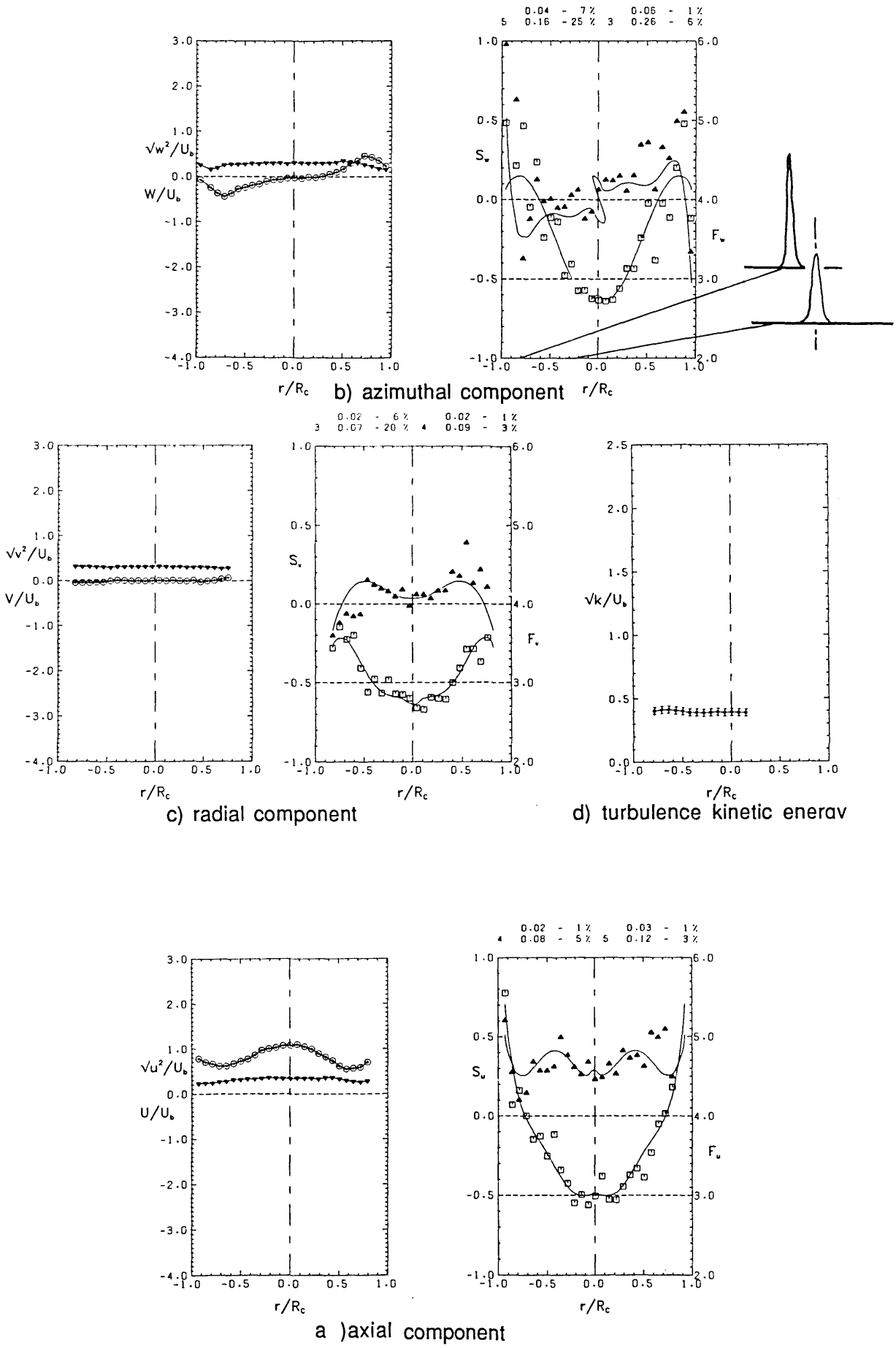
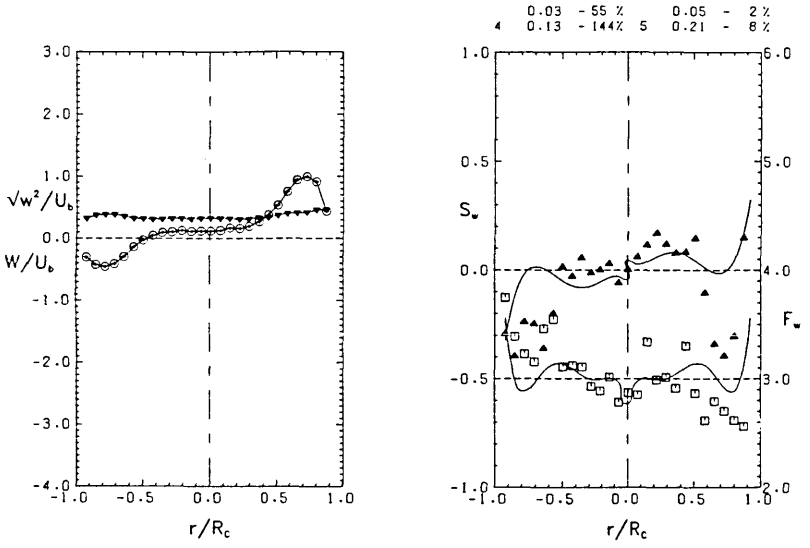
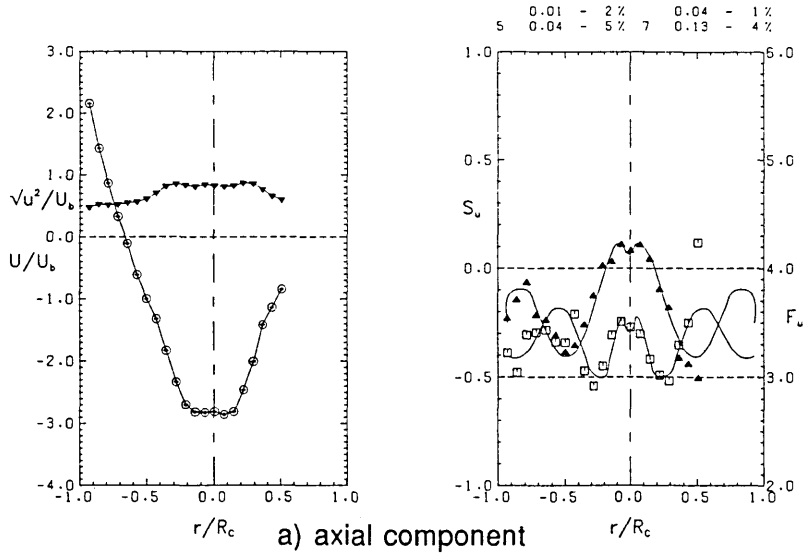


FIGURE 4.42 - Measurements at Z = 130 mm, θ = 0° (case 1).

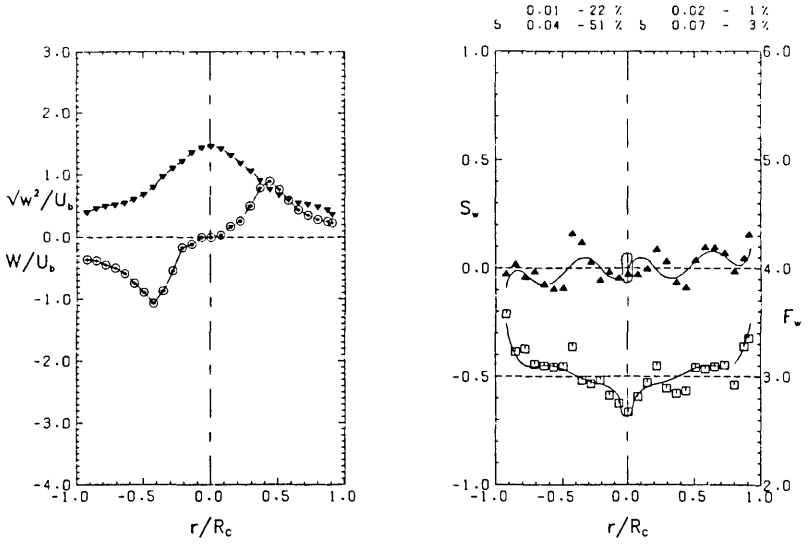


b) azimuthal component

FIGURE 4.42 (continued)– Measurements at Z = 130 mm, θ = 0° (case 1).



a) axial component



b) azimuthal component

FIGURE 4.43 - Measurements at Z = 40 mm, θ = 0° (case 2, conditions as in Figure 4.28 but with a 30° swirler).

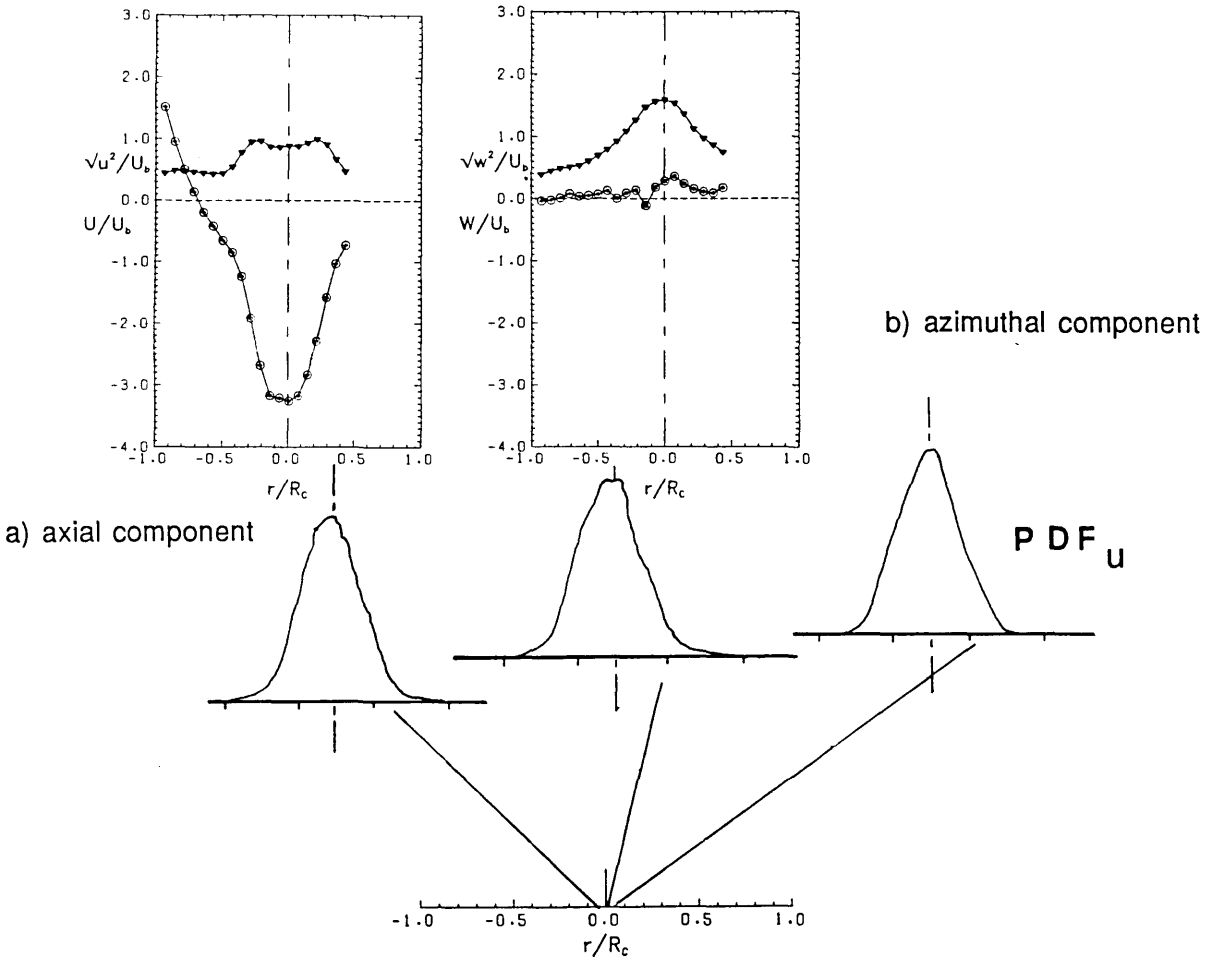


FIGURE 4.44 - Measurements at Z = 40 mm, θ = 0° (case 5, conditions as in Figure 4.28 but without swirler flow).

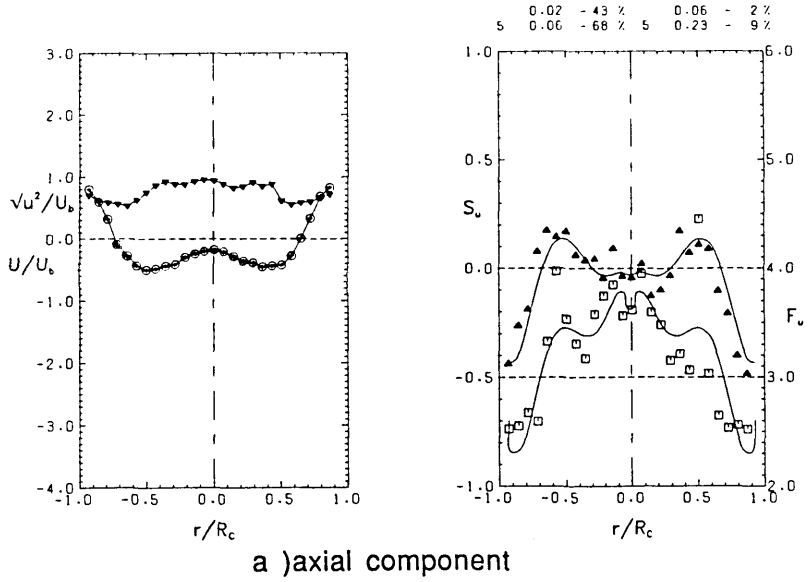


FIGURE 4.45 - Measurements at Z = 50 mm, θ = 30° (case 5, conditions as in Figure 4.33 but without swirler flow).

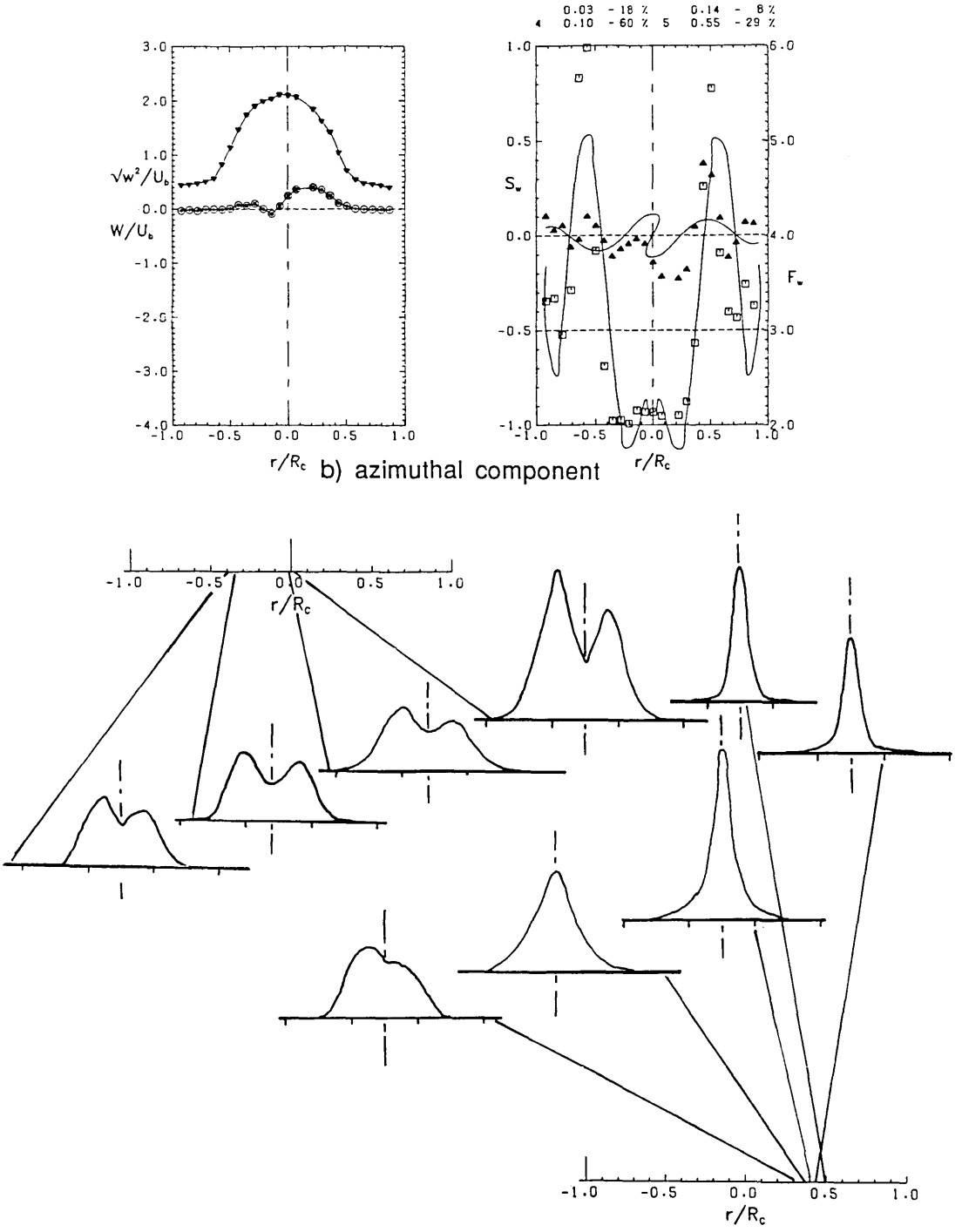


FIGURE 4.45 (continued)– Measurements at Z = 50 mm, θ = 30° (case 5, conditions as in Figure 4.33 but without swirler flow).

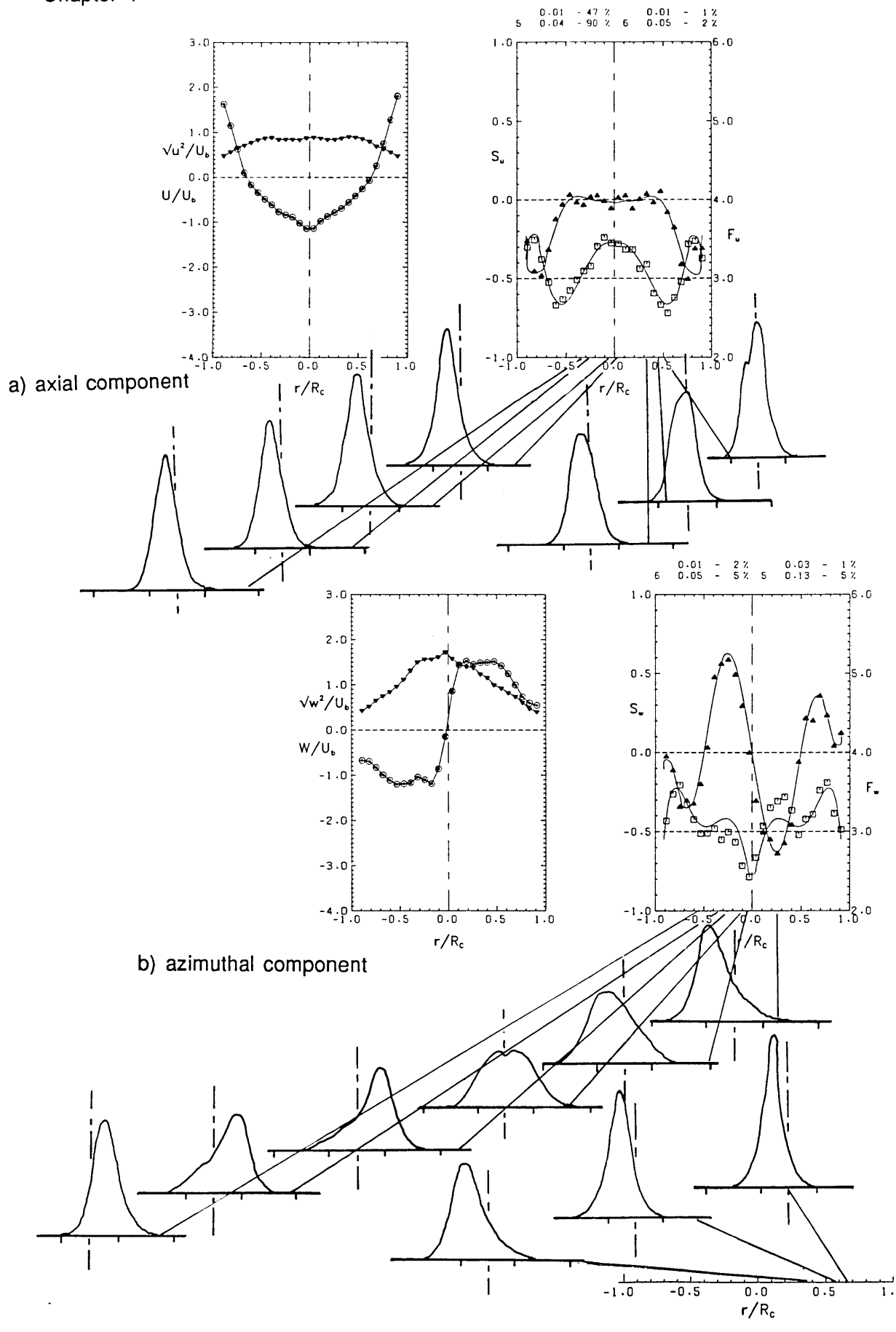


FIGURE 4.46 - Measurements at Z = 50 mm, θ = 30° (case 6, conditions as in Figure 4.33 but with higher swirler flow rate).

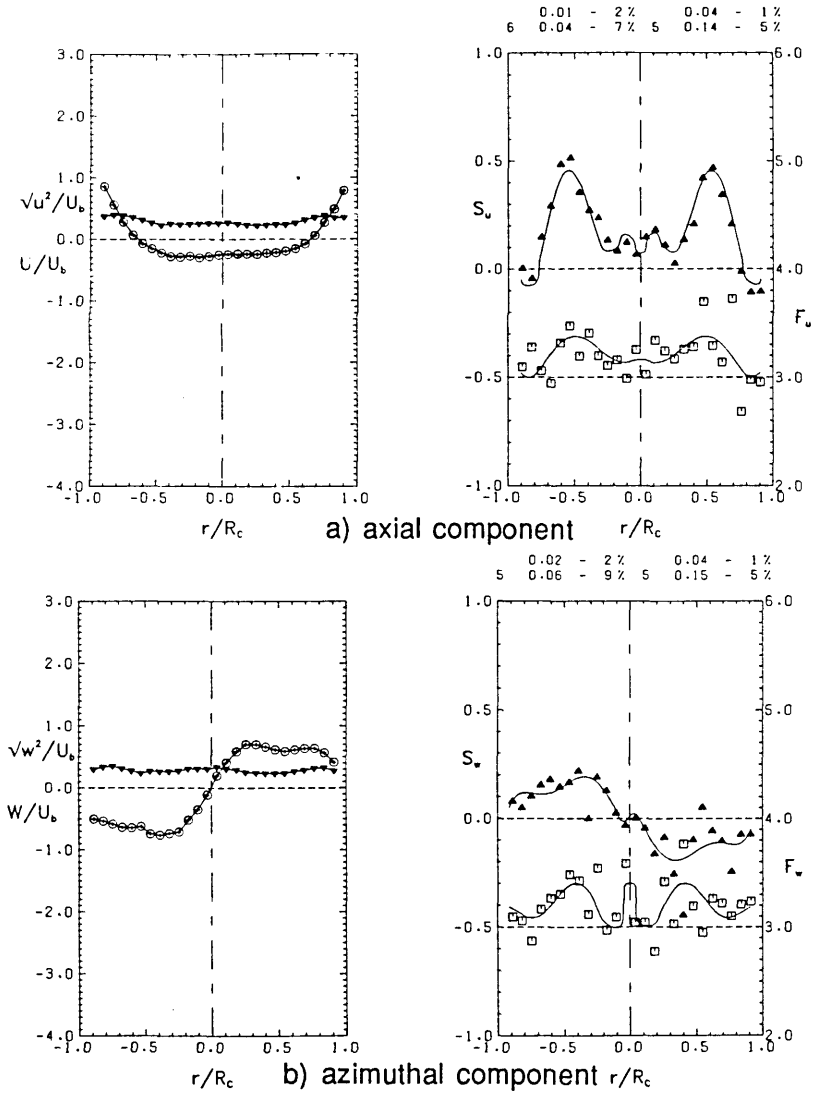


FIGURE 4.47 - Measurements at Z = 50 mm, θ = 30° (case 7, swirler flow only).

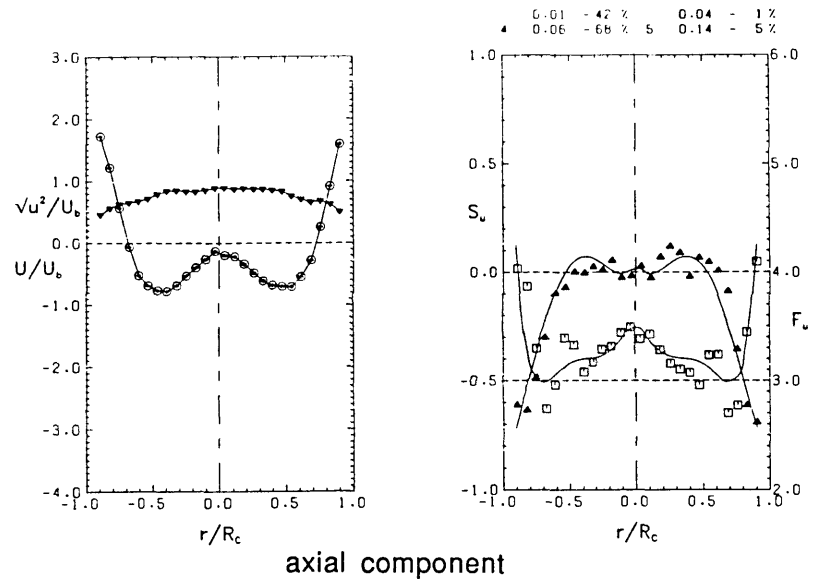


FIGURE 4.48 - Measurements at Z = 50 mm, θ = 30° (case 2, conditions as in Figure 4.33 but with a 30° swirler).

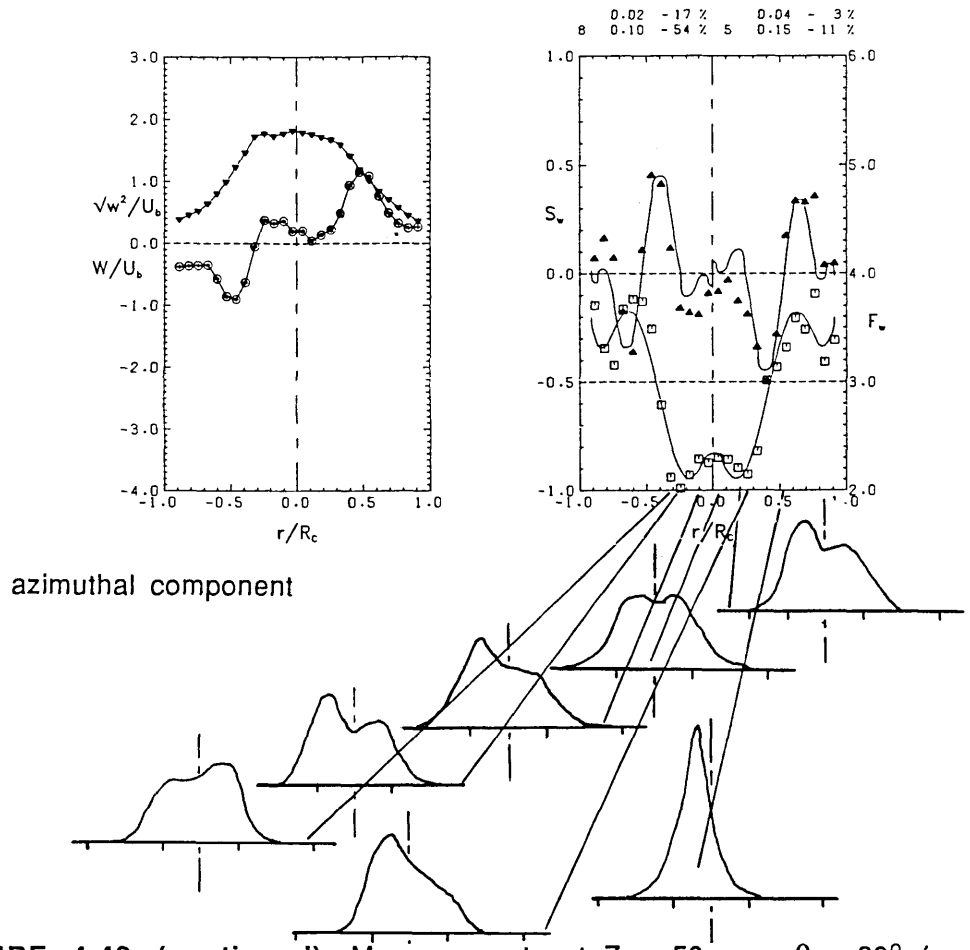
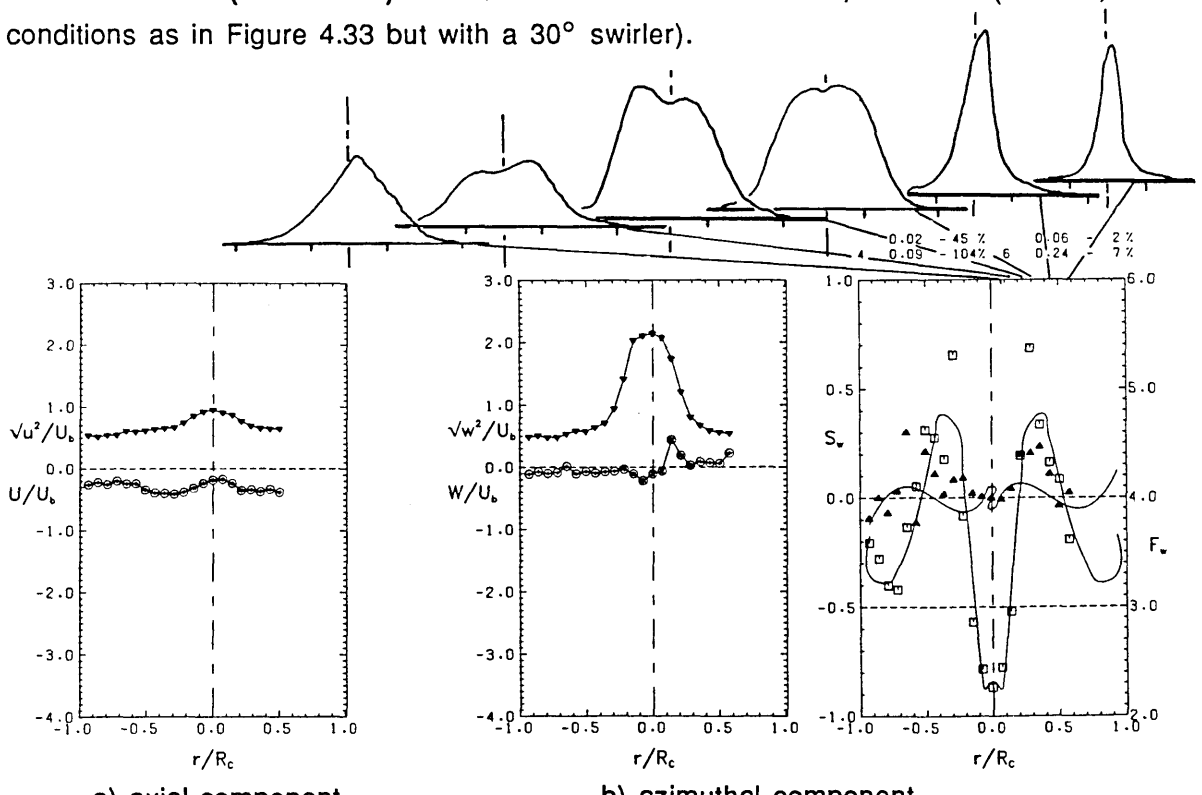


FIGURE 4.48 (continued)– Measurements at Z = 50 mm, θ = 30° (case 2, conditions as in Figure 4.33 but with a 30° swirler).



a) axial component b) azimuthal component

FIGURE 4.49 - Measurements at Z = 50 mm, θ = 0° (case 4, conditions as in Figure 4.31 but without swirler flow).

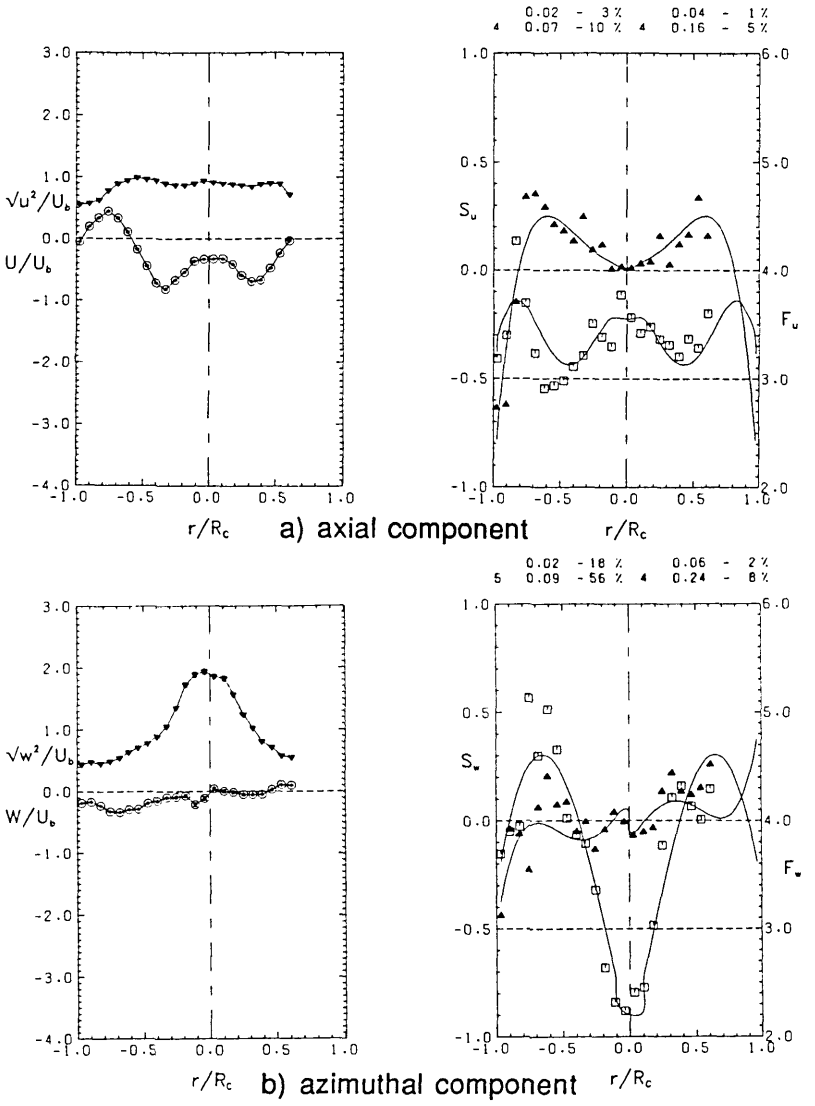


FIGURE 4.50 - Measurements at Z = 50 mm, θ = 0° (case 2, conditions as in Figure 4.31 but with a 30° swirler).

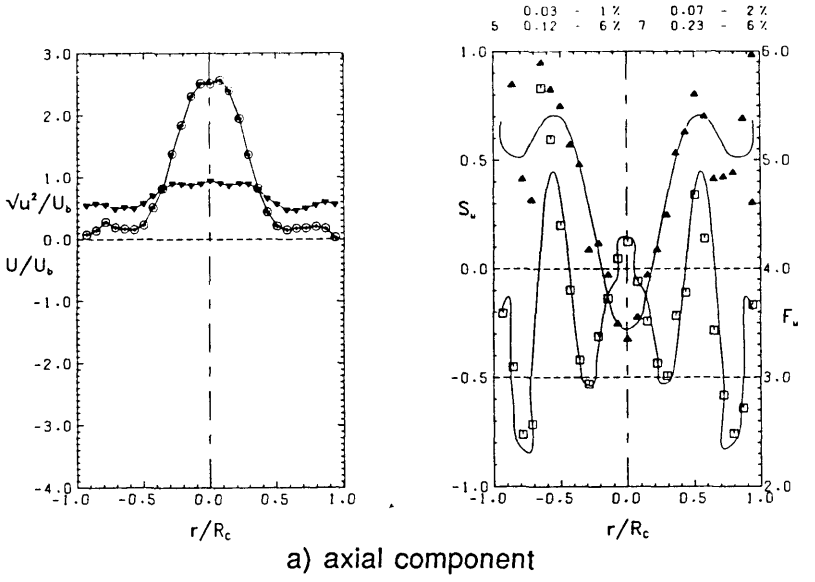


FIGURE 4.51 - Measurements at Z = 60 mm, θ = 15° (case 5, conditions as in Figure 4.35 but without swirler flow).

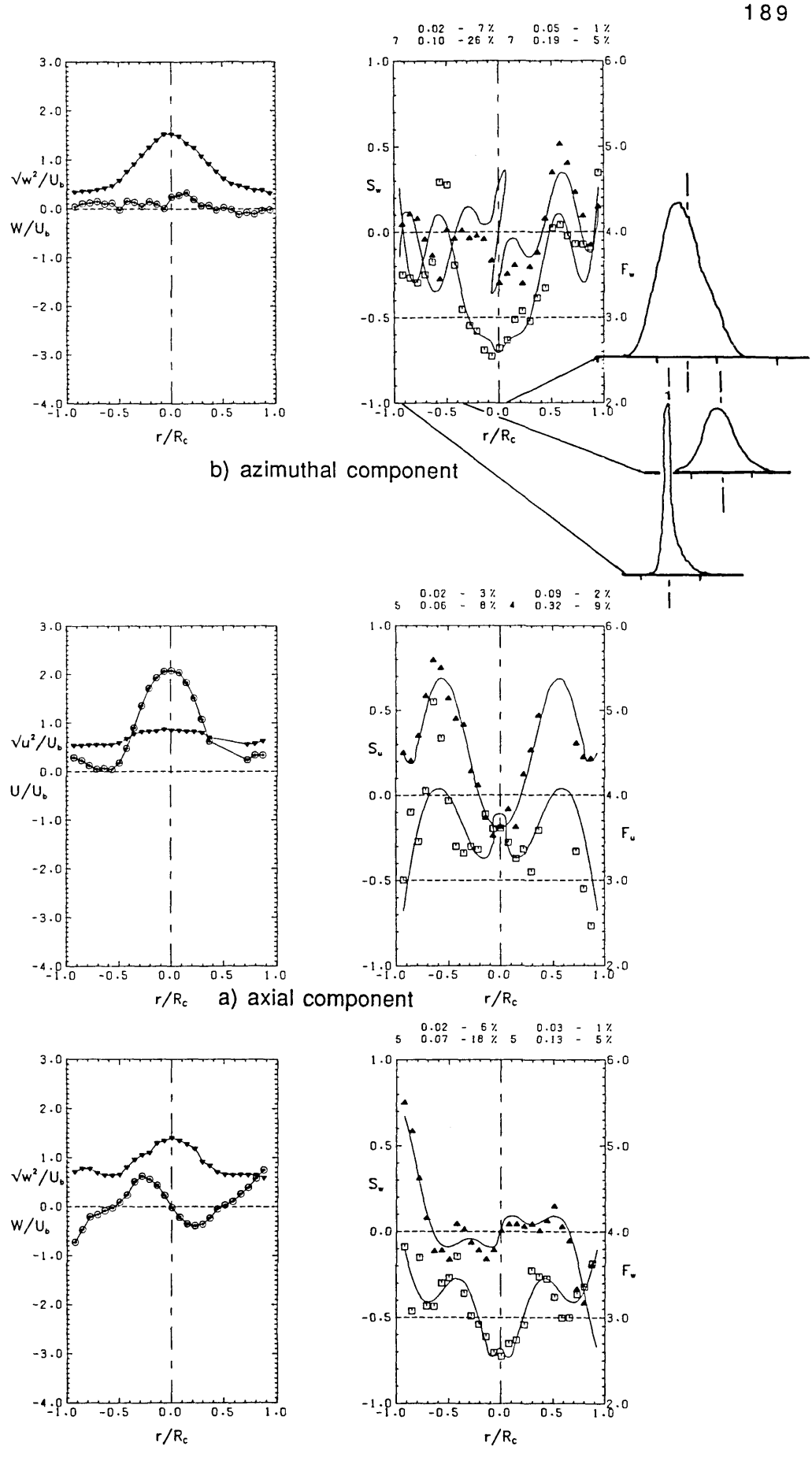


FIGURE 4.52 - Measurements at Z = 60 mm, θ = 0° (case 2, conditions as in Figure 4.34 but with a 30° swirler).

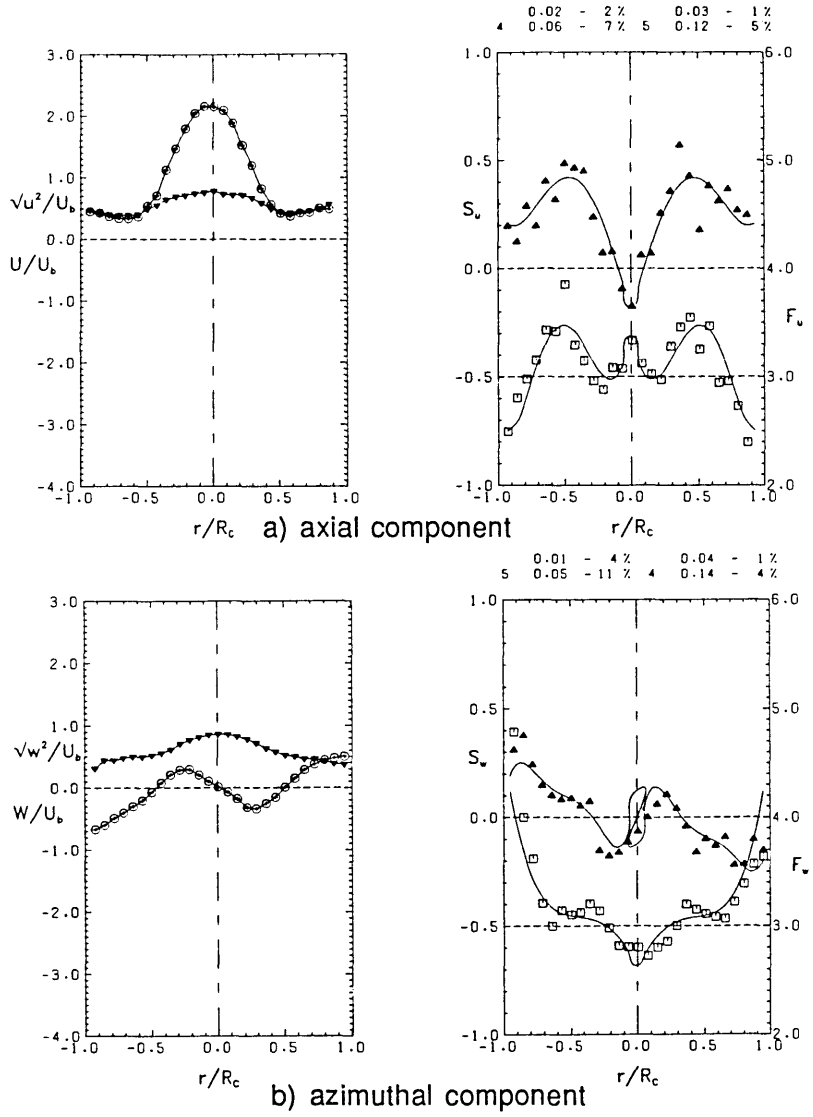


FIGURE 4.53 - Measurements at Z = 70 mm, θ = 0° (case 2, conditions as in Figure 4.37 but with a 30° swirler).

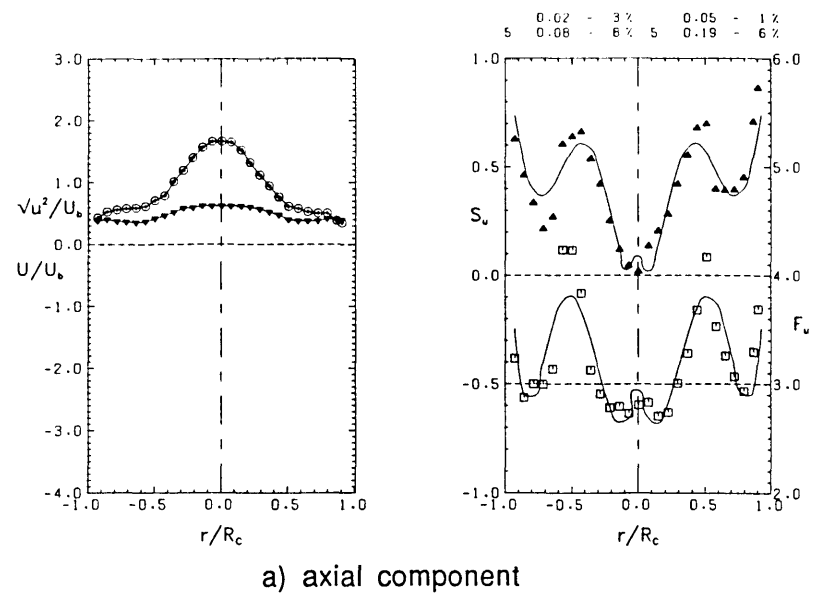


FIGURE 4.54 - Measurements at Z = 85 mm, θ = 0° (case 2, conditions as in Figure 4.40 but with a 30° swirler).

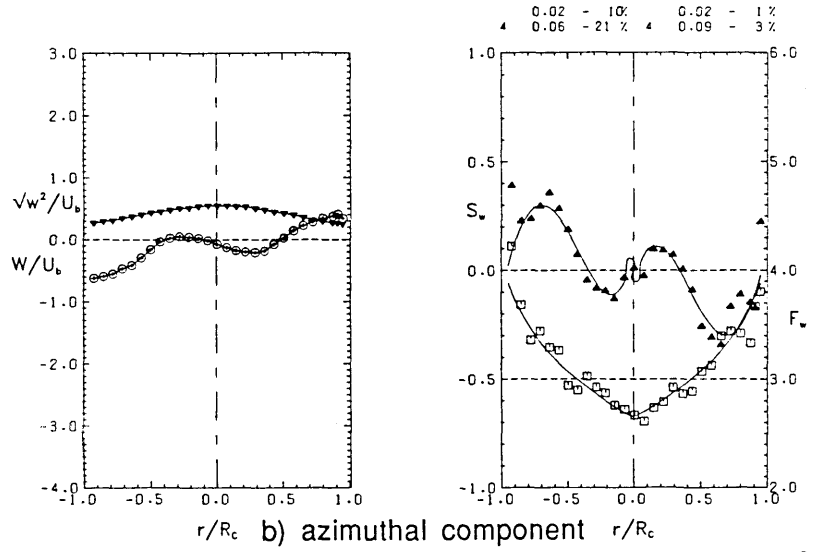


FIGURE 4.54 (continued)– Measurements at Z = 85 mm, θ = 0° (case 2, conditions as in Figure 4.40 but with a 30° swirler).

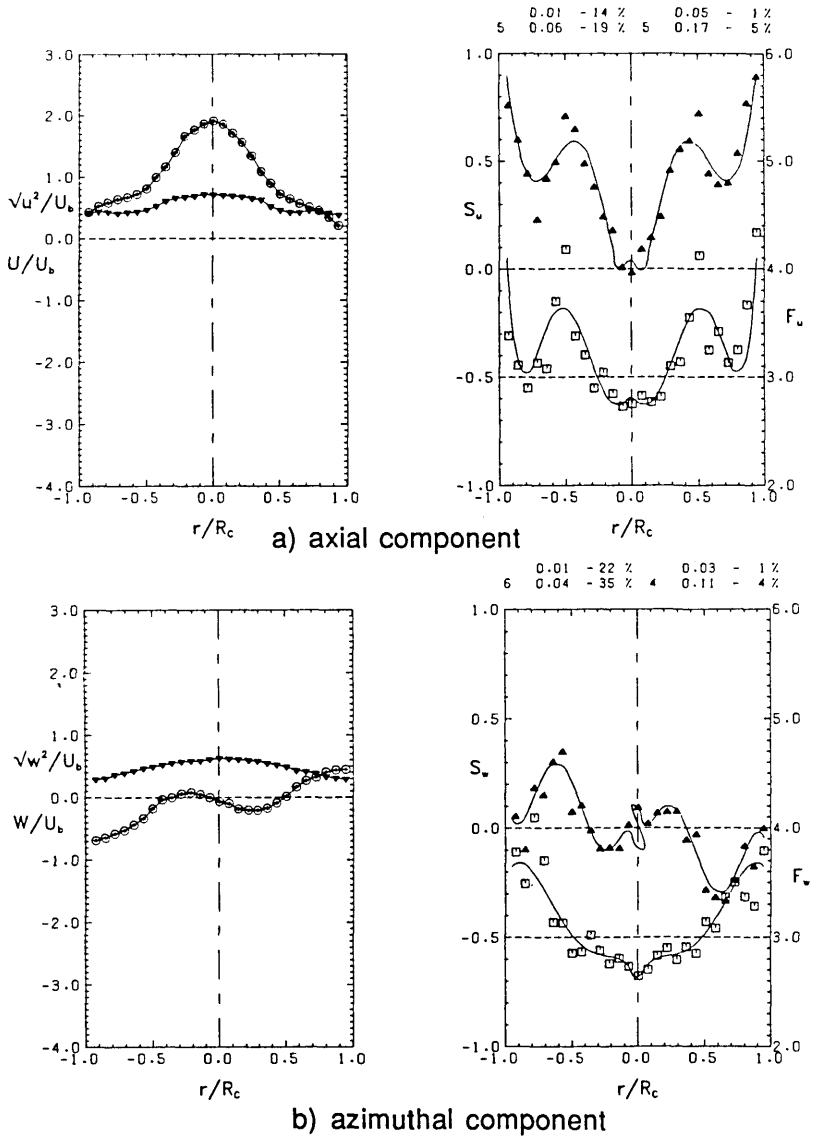


FIGURE 4.55 - Measurements at Z = 85 mm, θ = 0° (case 4, conditions as in Figure 4.40 but without dilution flow):

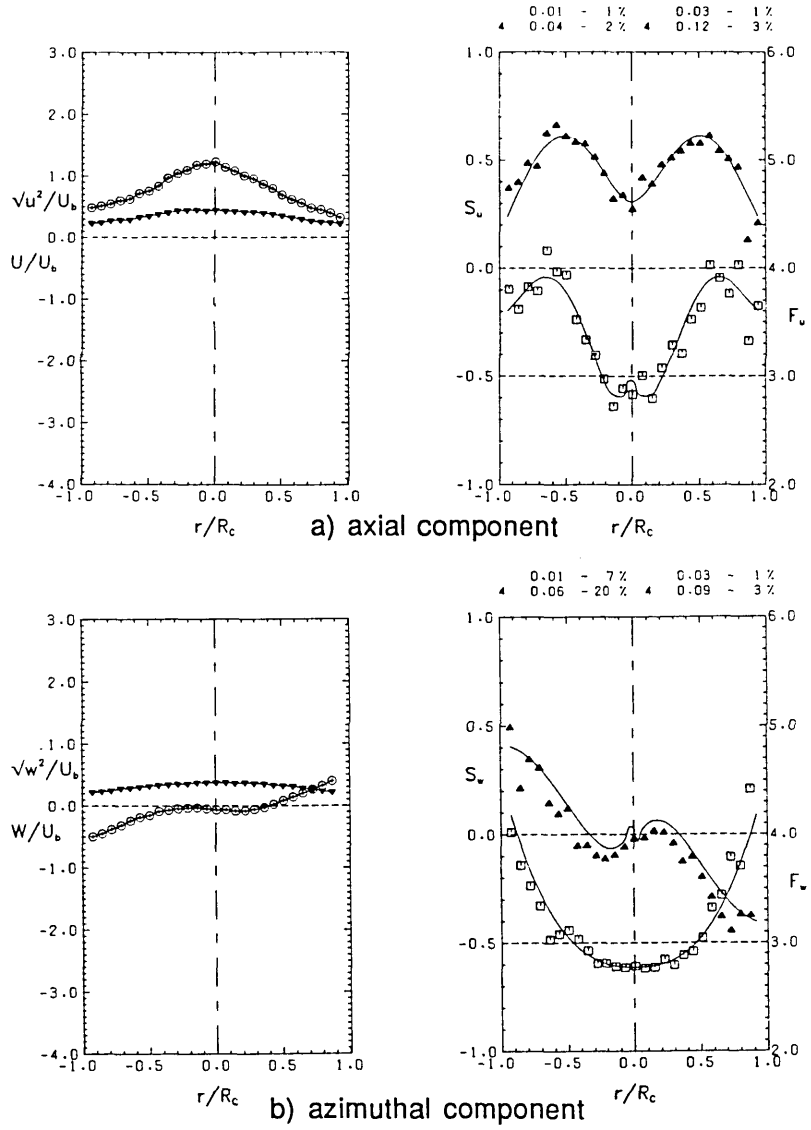


FIGURE 4.56 - Measurements at Z = 110 mm, θ = 0° (case 2, with a 30° swirler).

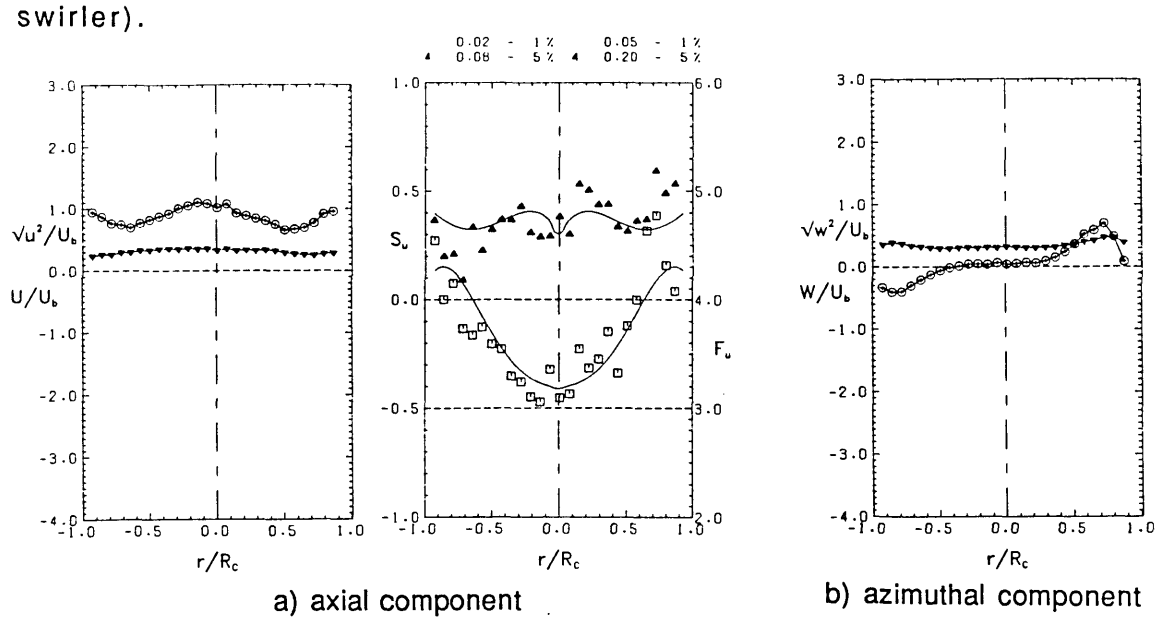


FIGURE 4.57 - Measurements at Z = 130 mm, θ = 0° (case 2, conditions as in Figure 4.42 but with a 30° swirler).

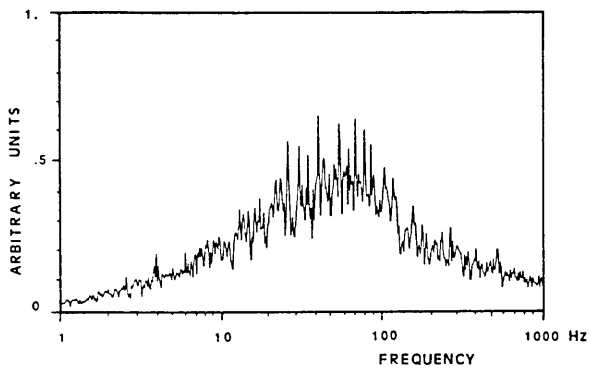


FIGURE 4.58 - Spectrum of the W component on the combustor centreline at Z = 50 mm (case 5).

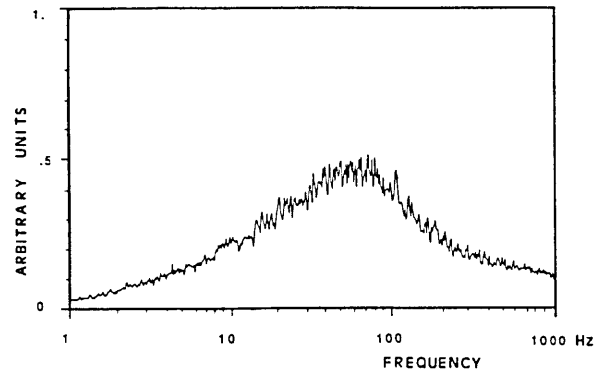


FIGURE 4.59 - Identical to Figure 4.58 but with a longer sampling time.

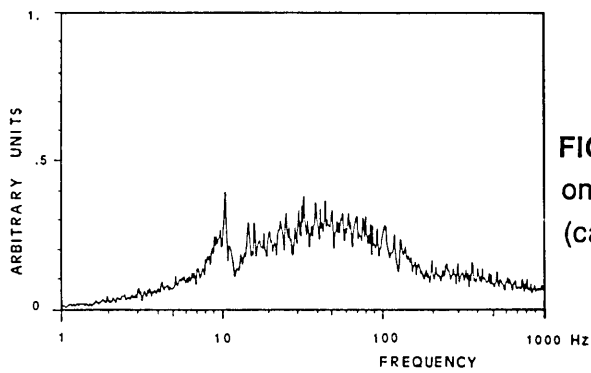
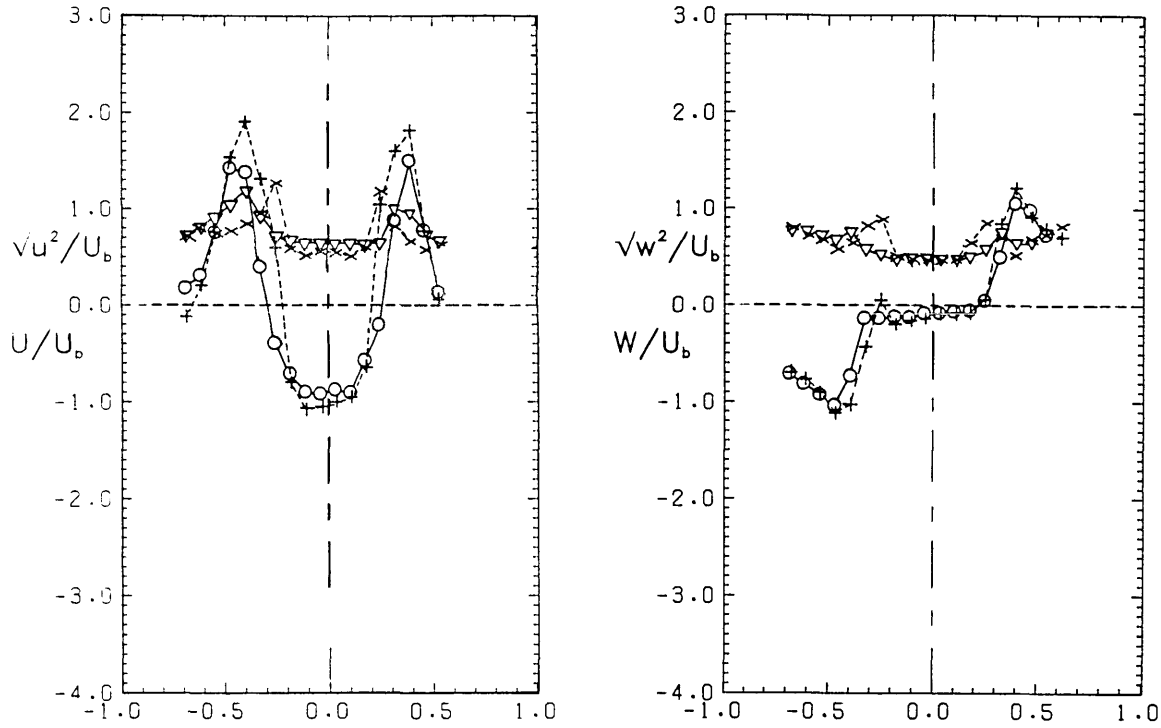


FIGURE 4.60 – Spectrum of the W component on the combustor centreline at Z = 50 mm (case 6, higher swirler flow rate)



a) axial component r/R_c b) azimuthal component r/R_c

FIGURE 4.61 - Measurements at Z = 8 mm, $\theta = 0°$ (case 2, conditions as in Figure 4.27 but with a 30° swirler and case 3, conditions as case 2 but with simulated injection of fuel).

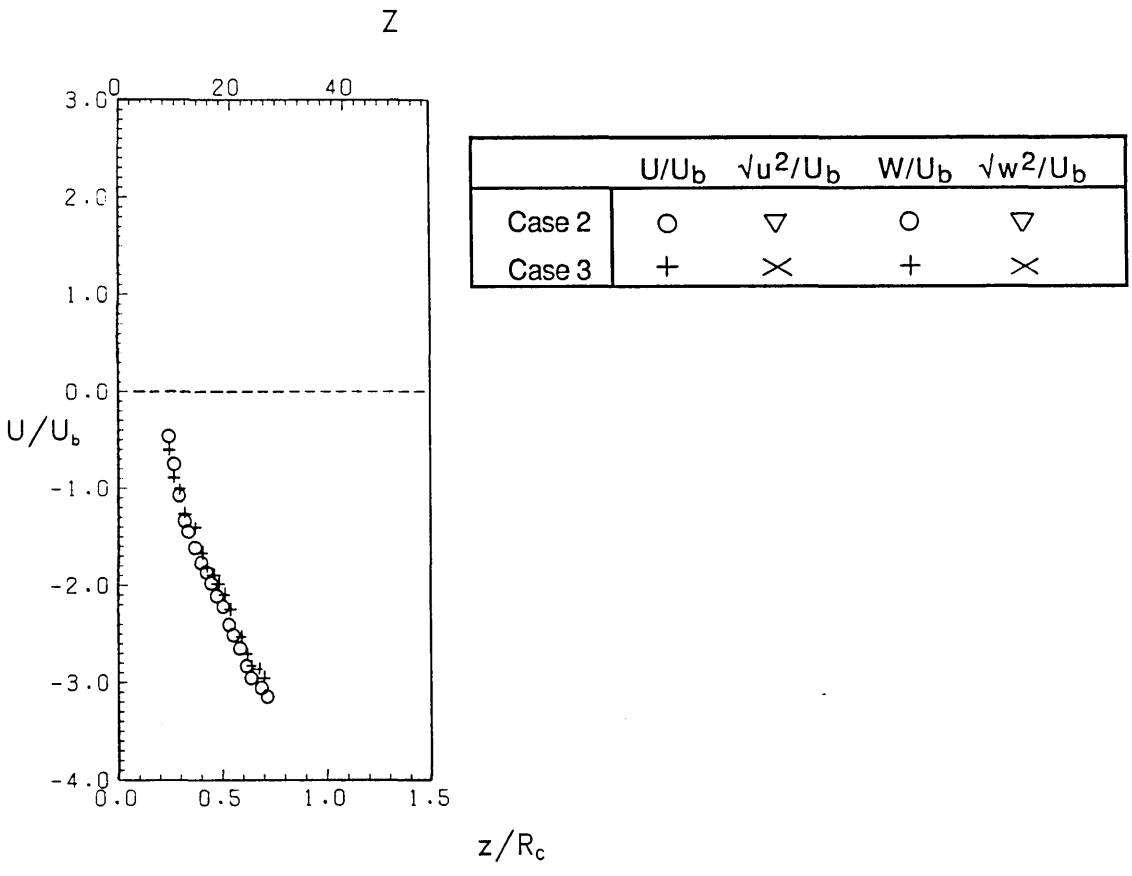


FIGURE 4.62 - Centreline values of mean axial component (case 2 and case 3, conditions as case 2 but with simulated injection of fuel).

CHAPTER 5
CALCULATION OF THE ISOTHERMAL FLOW INSIDE A GAS TURBINE COMBUSTOR

5.1 INTRODUCTION

5.1.1 Objectives and Outline of the Chapter

The main objective of this chapter is the appraisal of a mathematical model for the calculation of gas turbine combustor flows under isothermal conditions. The mathematical model has been introduced in Chapter 2 and a basis for this study is provided by the measurements of the flow inside a water model of a can-type combustor, presented in Chapter 4.

There are five sections in this chapter. This section, Section 5.1, introduces the domain of integration (subsection 5.1.2), the boundary conditions (subsection 5.1.3) and the numerical grids used in the present calculations (subsection 5.1.4). Section 5.2 discusses some questions arising from an initial set of calculations. Section 5.3 considers the use of and prediction sensitivity to alternative boundary conditions. Before conclusions may be drawn on the adequacy of the physical models, it is important that every aspect influencing the numerical accuracy of the results be addressed and the two sections above attempt to achieve this task. The actual validation of the k-ε turbulence model for this flow is made in Section 5.4, which includes comparisons with the flow cases studied in the experiments. The chapter ends with a summary of the conclusions in Section 5.5.

5.1.2 Domain of Integration

A cylindrical polar system of coordinates with the longitudinal direction aligned with the axis of the combustor was used. The calculations were restricted to a 60° sector of the flow inside the combustor and the length of the domain was set about one combustor radius downstream of the dilution holes. The annulus and the nozzle were not included, and the hemispherical head and the primary and dilution holes were approximated by rectangular castellations in the same manner as described in 3.1.2. Figure 5.1 shows the domain of integration and several mesh systems used in the present calculations.

The exclusion of the nozzle was partially because there was little interest in the flow at the combustor outlet in the present work, but also because it was known from the measurements that the presence of the nozzle was not felt upstream of the dilution holes. Further, calculations with the combustor nozzle would have had to cover

the entire 360° of the combustor, regardless of the existence of swirler flow or not, whereas neglecting the nozzle meant that a 60° sector could be used and when there was no swirler flow a small sector (only 30°) was used.

The crude representation of the combustor head and the primary and dilution holes is due to limitations of the present system of coordinates. These limitations are critical in the case of real combustor geometries and more flexible grid systems have been used (see review in subsection 1.4.1). In the current geometry, because less complicated, the limitations of a cylindrical polar system of coordinates are not expected to be as critical as in the calculations of real combustors; this aspect is readdressed in forthcoming sections.

5.1.3 Boundary Conditions

The boundary conditions described below are the simplest used in the current work and correspond to what has been used in the previous calculations of combustor flows by Green and Whitelaw [1983] and Koutmos [1985]. In the present work particular attention has been given to this aspect and the set of boundary conditions used in the final calculations will emerge only after the study in Section 5.3.

The swirler was simulated by an annular gap of the same height as the swirler vanes. The dimensions of this gap and the swirler flow rate, together with plug flow assumptions, set the axial velocity. The swirl velocity was then found from the integration of the swirl number definition, equation [4.6], also assuming a constant radial distribution; this guaranteed that experiments and calculations had the same swirl number. The swirl velocity calculated as the product of the axial velocity and the tangent of the vane angle is higher compared to the values derived from the swirl number definition, which were preferred, since they were based on measurements. The radial velocity was set to zero. The turbulence kinetic energy and its dissipation were found by assuming isotropic turbulence with a turbulence intensity of 13%, based on the measurements presented in subsection 4.2.1, and a typical eddy length equal to the height of the annular gap.

Axial and swirl velocities could be measured (subsection 4.3.1) in the plane of both primary and dilution holes. For these boundary conditions, the measurements were assumed constant over the hole. The radial velocity designated by V_{plug} followed from plug flow assumptions, given the hole diameter and the experimental flow rates. Turbulence kinetic energy and dissipation were again determined as above. A typical eddy length equal to the hole diameter was assumed, and the axial, radial and azimuthal turbulence intensities were, based on the measurements in subsection 4.3.1 (14%, 3% and 11% for the primary holes; 12%, 6%, and 6% for the dilution holes).

The boundary conditions at the combustor inlets are summarized in the table below.

TABLE 5.1 - Boundary conditions (45° swirler, case 1 of Table 4.2).

	Axial Velocity [ms^{-1}]	Swirl Velocity [ms^{-1}]	Radial Velocity [ms^{-1}]	Turbulence Kinetic Energy [m^2s^{-2}]	Dissipation [m^2s^{-3}]
Swirler	1.25	0.95	0.00	1.50×10^{-2}	3.06×10^{1}
Primary	0.00	0.08	2.22	1.24×10^{-1}	4.37
Dilution	0.20	0.00	0.85	1.12×10^{-2}	5.96×10^{-2}

A zero axial gradient was prescribed at the outlet section for all the variables.

The longitudinal side boundaries were planes of cyclic (periodic) or symmetry boundary conditions for swirling and no swirling flow, respectively. The wall regions were treated in the manner described in subsection 2.4.1.

5.1.4 Numerical Grids

The four numerical grids used in sections 5.2 and 5.3 are shown in Figure 5.1. A target value of about 35000 grid nodes was established on the basis of the dilution zone calculation in Chapter 3. A grid of this size occupied half of the computer memory available, allowing validation by significant refinement. The grid in the axial and radial directions was generated by using [2.52] and in such a way that a higher concentration of nodes occurred near the holes and the swirler. In the azimuthal direction, the grid was regular except around the axis of the holes and on the edges of the domain. The importance of the resolution in the circumferential direction has been established in Chapter 3 and, here, an average spacing of 3° between vertical planes was found acceptable. This resulted in a final mesh of 60 × 30 × 22 (axial, radial, circumferential), with 39600 nodes (Figure 5.1); this mesh is hereafter designated as the standard grid.

The coarsest grid, 33 × 17 × 13, with 7293 nodes was obtained from the standard grid by doubling the spacing between nodes, i.e. the truncation error of an upwind scheme would increase by a factor of 2. A refinement of the standard mesh was made by doubling the total number of nodes to 70 × 36 × 30 (75600 nodes), the maximum possible within the current limitations of computer memory. Finally, a fourth mesh of 46 × 24 × 20 (22080 nodes) is shown in Figure 5.1, resulting from a

50% reduction of the number of nodes of the finest grid in each direction. This reduction affected all the regions of the domain equally and was obtained by increasing the expansion ratios of [2.52]. The four grids are illustrated in Figure 5.2 and the first four entries in Table 5.2 summarize their characteristics. A more complete information about the resolution of each grid in Table 5.2 includes parameters such as the number of cells simulating the various combustor entries and the average spacing between nodes in every direction.

TABLE 5.2 Numerical grids

N.	GRID SIZE	N. OF	N. OF CELLS				L/N_Z	R/N_R	T/N_T
	$[N_Z \times N_R \times N_T]$	NODES	PRIM.	DIL.	HEAD†	SWIR.	[mm]	[mm]	[deg.]
1	33 × 17 × 13	7293	10	24	247	39	5.2	2.2	4.6
2	60 × 30 × 22	39600	40	79	1100	132	2.8	1.2	2.7
3	70 × 36 × 30	75600	67	100	2700	150	2.4	1.0	2.0
4	46 × 24 × 20	22080	21	61	580	120	3.7	1.5	3.0
5	60 × 53 × 22	69960	40	79	2420	88@	2.8	1.2	2.7
6	60 × 30 × 42	75600	60	145	2100	126@	2.8	0.7	1.4
7	96 × 30 × 22	63360	51	79	2728	66@	1.8	1.2	2.7
8	114 × 30 × 22	75240	51	100	2728	66@	1.5	1.2	2.7

† - number of cells outside the domain
@ - after reduction of the swirler size accounting for vane blockage
N_Z, N_R, N_T - number of nodes along the axial, radial and circumferential directions
L, R, T - dimensions of the integration domain along the three directions above

For validation of the final calculations , in Section 5.4, the two finest grids above (numbers 2 and 3) were retained and four other grids numbered from 5 to 8 were also used. These grids, shown in Figure 5.3, all originated from the standard grid following the methodology illustrated by the tree structure in Figure 5.4. Refinements were made in each direction by adding regularly spaced nodes to avoid the deterioration of the formal order of accuracy as discussed in subsection 2.2.2.

The emphasis given to the grid refinement in the present calculations results for several reasons. Firstly, due to the complexity of the flow: it is therefore even more important to avoid the situation experienced in Chapter 3, where simply because of an insufficient number of nodes the grid may be unable to resolve small flow structures. Secondly, when using the hybrid-differencing scheme very fine grids are needed to reduce the truncation error to negligible levels. Finally, because grid refinement was used as a means of assessing the numerical accuracy of the calculations rather than any of the methods mentioned in subsection 2.2.2.

In geometries similar to the present one (or more complicated), Coupland and Priddin [1987] used a grid of 58 × 21 × 29 (35322 nodes), although calculations with a finer grid (44330 nodes) showed some differences. Koutmos [1985] found a grid of 34 × 14 × 12 (5712 nodes) acceptable in comparison with finer ones, a level of refinement which Green and Whitelaw [1983] could not even reach because of the computer limitation at that time.

5.1.5 Presentation of the Results

The predicted results include the three components of velocity and turbulence kinetic energy; they are presented as radial and axial (centreline) profiles, streakline and contour plots. Experimental results are also shown, when available. Given the large amount of data to be scrutinized, an interactive plotting program was written, which could, in a single run, read and plot experimental and numerical results in any location in the combustor, irrespective of the grid distribution and size. The results of four numerical grids could be processed simultaneously (more than 10^6 values!) and plotted as radial and centreline distributions. The programs used for the streakline and contour plots were the same as used in Chapter 3.

5.2 PRELIMINARY CALCULATIONS: SOME FUNDAMENTAL QUESTIONS

In this section, the objective is: (i) to assess the convergence of the calculations, (ii) to assess the level of grid resolution needed to resolve the flow inside the combustor and (iii) to test an improved boundary condition in the primary hole. Each aspect is considered in separate subsections below.

5.2.1 The convergence pattern

Following the conclusions of the convergence studies in Chapters 2 and 3, special care was taken to ensure the convergence of the present calculations. Figure 5.5 shows the residuals of all the equations as a function of real time (the AVPI algorithm, described in subsection 2.3.1, was used in these calculations). The convergence pattern is shown for all the grids but the finest. It can be seen that the residuals reached levels close to machine round-off error; this is most evident in the plots corresponding to the grid 60 × 30 × 22, particularly through the residuals of k and ε.

The calculations on the two coarsest grids were accepted as converged when the nondimensional mass residual (DSUM) fell below 2×10^{-4}. It can be seen that, though the ratio between the total number of nodes of the two grids is 3, the total CPU time has increased by a ratio of 4.7. Calculations on finer grids were considered as converged only when the integrated flux of a passive scalar was the same (within 2%)

at every transverse cross section; this is a more stringent criterion (found necessary due to the slower convergence of the scalar field) and contributed even further to an increase of the total CPU time of the calculations on the finer grids. The fine grid solutions were produced by starting from previous runs and no attempt was made to quantify the total CPU time they required.

5.2.2 Results with four different grids

The following results were obtained with the boundary conditions exactly as in Table 5.1 and using the first four grids of Table 5.2.

A centreline plot is given in Figure 5.6. The maximum negative velocity is underpredicted by at least a factor of 2. For finer grids, as the positive peak increases, approaching the experimental value, worst results are obtained in the dilution region, Z = 130 mm, because the downstream decay rate is the same for all the grids. This does not affect the turbulence kinetic energy whose agreement is excellent in locations beyond Z = 80 mm, even for the coarsest grid, although the peak value at primary jet impingement is grossly underpredicted. From this figure there seems to be a need for even finer grids, at least in the primary region, where significant changes are still obtained.

Figure 5.7 shows the radial profiles at Z = 8 mm. As mentioned in Chapter 4, this is the nearest measured location to the swirler and, in the present calculations, there is a maximum of 6 grid lines upstream of the plane examined (only 4 in the case of the coarsest grid). The radial velocity (not measured) is the most sensitive to the grid refinement. The axial and azimuthal velocities are of similar magnitude compared with the measurements but are shifted towards the centreline; this persists for all finer grids.

The same features can be observed further downstream, Z = 40 mm, in Figure 5.8. The radial and azimuthal velocities are almost insensitive to the grid refinement, but for the axial velocity a better agreement with the measurements occurs as the grid is refined. In spite of this improvement, the values on the centreline and near the wall are still underpredicted by a factor of 2 and 3, respectively. In the case of the grids 33 × 17 × 13 and 60 × 30 × 22, the increase of the turbulence kinetic energy for $r/R_C > 0.5$ is neither confirmed by the measurements nor by the results of the other two grids. A greater confidence exists in the results of the finest mesh (70 × 36 × 30) and there the discrepancy between measurements and predictions increases towards the centreline; a location where the four meshes predict nearly the same value. The reason for the anomalous behaviour observed in grids 33 × 17 × 13 and 60 × 30 × 22 is the coarseness of the grid distribution in the region between the castellated head and the upstream edge of the hole.

The distribution of the turbulence kinetic energy predicted by the coarsest mesh at Z = 40 mm is still evident at Z = 50 mm (Figure 5.9) where a constant radial profile is shown. In terms of the shape, the finer grids produce better results, but quantitatively the agreement between predictions and measurements for is even worse than at the previous location. The predicted values of the finer grids show a higher radial velocity in the inner half of the combustor, but near the hole and for all grids this is always lower than the measured velocity. In this location (Z = 50 mm, θ = 0), because it is aligned with the axis of the primary holes, calculated and measured values should agree at r/R_c = 1 if the correct hole boundary conditions are being used. However, it is clear from Figure 5.9 that the radial velocity differs from the measurements by some 25%. This suggests that the simple boundary condition treatment outlined above is insufficient; some of the above discrepancies are undoubtedly related to this, and before making conclusive statements on grid dependence or more comprehensive comparisons with experiments attention is turned to this point in the following subsection.

5.2.3 The radial velocity boundary condition at the primary hole

A value of 10% has been quoted (subsection 4.1.5) as the experimental uncertainty in the primary flow rate. The first obvious test is to see whether an increase of the primary flow rate from 1.044 to 1.146 kg/s (the highest possible within the range of experimental uncertainty) can explain the differences between the measurements and the calculations of the radial velocity along the axis of the primary hole. Figures 5.10 and 5.11 show that the better agreement with the measurements is marginal, although in the right direction. The improvements affected mainly the regions around the centreline and the deficiencies noticed above, e.g. the centreline axial velocity upstream of the primary jets, were still present.

There are circumstances where a higher radial velocity on the primary hole may occur, without increasing the primary flow rate. We can recognize immediately that no attention has been given to the hole discharge coefficient and this can increase the radial velocity through the reduction of the effective area of the hole. In the present case, the availability of measurements of radial velocity just above the hole, Figure 4.21, allows this aspect to be quantified quite precisely. A new boundary condition was introduced where the shape of the experimental curve in Figure 4.21 was assumed to prevail in the plane of the hole. This shape was approximated by a piecewise linear approximation, symmetric relative to the axis of the hole, and then scaled to give the same primary flow rate as in the experiments. The radial velocity in each individual cell on the hole surface was then prescribed from these data rather than using a constant radial velocity as in table 5.1. All the other conditions were kept constant.

The results along the axis of the primary hole with this new boundary condition, designated V_{expt}, are shown in Figure 5.12: the agreement is excellent between calculated and measured values for the radial velocity. It can be seen that the change to this new boundary condition is much more effective in bringing the calculated values of the radial velocity closer to the experiments than the increase of the primary flow rate (also shown in the figure). The axial velocity did not change but the swirl velocity was slightly reduced and the turbulence kinetic energy increased, both trends leading to an improved agreement with measurements. Other locations, not shown, reinforced the appropriateness of this boundary condition. As in the case of the increased primary flow rate, the central part of the combustor is the most affected.

The discussion above agrees with the experimental results of Phipps [1981], who found that a jet with a peaked velocity profile penetrates deeper into the crossflow than a jet with a similar momentum flux but a constant velocity profile.

5.2.4 Conclusions

Two major conclusions emerged from these preliminary results on grids of variable density and using three boundary conditions for the primary hole. Firstly, that the primary region shows the larger discrepancies between numerical and experimental results; these discrepancies are reduced as the mesh is refined up to the limits of the computer memory available (≈ 7 Mbytes) and finer grids still seem to be needed. Secondly, that the details of the radial velocity profile in the primary hole were very important. An increase of the primary flow, within the experimental range of uncertainty using a plug flow profile did not explain the differences between measurements and calculations. The improvements obtained by using an improved boundary condition in the primary hole based on experimental data indicates a need to look more carefully at boundary conditions generally, and this is the subject of the following section.

5.3 BOUNDARY CONDITION STUDY

The previous section, apart from raising doubts on the grid independence of the current calculations, also called attention to the influence of the boundary conditions; definitive conclusion about the grid size cannot be made without first selecting the most appropriate set of boundary conditions and this is the objective of this section.

Various boundary conditions are possible due to the incomplete information provided by the measurements and limitations of the numerical model. This section discusses and presents the results of calculations using some of these boundary conditions: the swirler (subsection 5.3.2), the primary and dilution holes (subsection

5.3.3) and the fuel injector (subsection 5.3.4) were considered in sequence. A final set of boundary conditions emerged as optimum by comparison between the numerical and experimental data.

The previous calculations to assess the effect of various boundary conditions in the primary hole (in subsection 5.2.3) were made on the finest grid, 70 × 36 × 30. The results in subsection 5.2.2 had shown the need for this level of grid refinement. However, due to current computer limitations, it was not realistic to carry out an extensive study of the boundary conditions using this grid and it was decided to use a coarser one. First, it is demonstrated that this mesh is accurate enough for the present purpose.

5.3.1 Choice of Grid for Boundary Condition Study

Calculations similar to the ones presented in subsection 5.2.3 were repeated on the standard grid of 60 × 30 × 22. Figure 5.13 shows a sample of these results with the shape of the V profile in the primary hole taken from the measurements, as before designated by V_{expt}. The results of two other calculations using a radial plug flow, V_{plug}, and the V_{expt} condition, but in the finest grid of 70 × 36 × 30, are also included. It can be seen from the figures that both grids predict similar results for all the variables when the hole boundary condition based on the experiments is used, and differ markedly from the plug flow results. There is even an apparent superiority of the coarser grid which shows slightly higher (closer to the measurements) values of turbulence kinetic energy. This may be caused by a higher radial velocity near the hole evidenced by the coarser grid, as a consequence of a different area of the cells in the primary holes, and reinforces the need for an appropriate simulation of the hole.

From these tests, it appears that the standard mesh can certainly be used in a study of boundary conditions.

5.3.2 Swirler

The main objection to the boundary conditions for the swirler, discussed in subsection 5.1.3, is the simulation of the swirler by an annulus of the same inner and outer diameter as the real swirler, not accounting for the blockage of the flow caused by the swirler vanes. The cross-sectional area of the vanes is by no means negligible (41% of the total in the 45° swirler and 27% in the 30° swirler) and should be considered. As an attempt to compensate for this effect, the area of the annulus was reduced by the same amount as the area occupied by the vanes in the real swirler. This alteration was made in two ways: (i) by increasing the inner diameter and reducing the outer diameter by the same amount (method 1), and (ii) by increasing the inner diameter

only (method 2). Further area reductions would be needed if the discharge coefficient of the swirler were to be considered, but this was not done.

Constant radial distributions of axial and swirl velocities were assumed in subsection 5.1.3, but, in the absence of any experimental evidence, different combinations of the shape of the profiles seem to be equally valid. There are a total of 12 possible boundary conditions for the swirler if all these options (reduced or constant area and shape of the profiles, either uniform or linear) are combined, but not all of them are reasonable. The conditions accounting for vane blockage and linear profiles of axial velocity lead to a maximum axial velocity which is believed to be too high.

The large number of possible boundary conditions results also from the fact that different velocity profiles can exist with identical swirl number. This has been noticed before (e.g. Sloan, Smith and Smoot [1986]) and given the importance of the boundary conditions and the previous calculations of simple swirling flows made in the past, unanimity would be expected on what type of the boundary condition should be used at the outlet of the swirler. Sloan, Smith and Smoot [1986] collected a variety of formulae used by various authors to estimate the dissipation of the turbulence kinetic energy; however, even being a boundary condition of minor importance in confined swirling flows, this is the only boundary condition of which they mention a preferred formulation. Apart from Abujelala and Lilley [1983], no calculations of swirling flows could be found where the adequacy of the swirler boundary conditions had been tested. These authors strongly recommended the use of velocity profiles obtained from measurements. This recommendation could not be followed in the present calculations.

Constant or linear (radial) profiles of azimuthal velocity and blockage of the vanes (method 1)

Figure 5.14 shows the results of four boundary conditions: axial plug velocity and either constant or linear (solid body) swirl velocity combined with non-blockage or blockage (method 1) of the vanes. The boundary condition in the primary hole is a constant profile of radial velocity, V_{plug}. The blockage of the vanes (i.e. reduction of the annular gap) turns out to be the most important assumption of all due to the longitudinal acceleration of the flow and consequent increase of the turbulence kinetic energy. The solid body rotation affects the swirl component and shifts the profile towards the wall which is a desirable trend as was noticed in subsection 5.2.2. The solid body rotation profile is a characteristic to be maintained. The centreline plot in Figure 5.15 shows that the effect of the different swirler boundary conditions affects mainly the axial velocity and at locations $Z < 20$ mm, but is able, for options with a smaller annular gap, to reduce the positive and negative peaks of the axial velocity on

the centreline: contrary to what is desirable for a better agreement between calculations and experiments.

The location closer to the centreline of the calculated values of axial velocity, noticed above in 5.2.2, is not altered by these boundary conditions. Causes that can contribute to this behaviour are:

(i) These results were obtained with a V_{plug} boundary condition on the primary hole. The V_{expt} condition leading to higher negative axial velocities might shift the profiles towards the wall.
(ii) The use of method 1 for accounting for the vane blockage.
(iii) A zero radial velocity at the outlet of the swirler.
(iv) Reduction of the effective cross-section of the combustor due to the approximation of the head by castellations.
(v) The non-simulation of the conical shape of the fuel injector protruding from the swirler.

The effect of the first three causes is assessed below. Causes iv) and v), because they are limitations inherent to the present system of coordinates are addressed in subsection 5.4.1.

The effect of the boundary conditions on the primary hole

The results of three sets of boundary conditions are shown in Figures 5.16 and 5.17: (i) the reference case of constant radial and axial velocities, (ii) the case with constant axial, linear swirl velocity and area reduction using method 1, and (iii) as for (ii) but with a V_{expt} boundary condition in the primary hole. At Z = 8 mm, Figure 5.16, the latter condition reduces the maximum positive axial velocity. All the profiles are shifted radially outwards and, apart from the axial velocity, the maximum values are increased with the turbulence kinetic energy being nearly doubled for locations beyond $r/R_c > 0.4$. This figure shows that at Z = 8 mm the results are influenced by the boundary condition used in the primary hole and at Z = 40 mm, Figure 5.17, the effect of the swirler boundary condition is minimal.

The blockage of the vanes (method 2)

The area of the swirler annular gap was altered by increasing only its inner diameter, method 2. In terms of the increase of the maximum axial velocity, the effect is the same as method 1, since the reduction of area is similar but, here, the boundary conditions are set at an increased radial location.

The effect of this boundary condition is shown at Z = 8 mm in Figure 5.18. An increased radial shifting of the profiles is noticed in comparison with Figure 5.14. Lower axial velocities and turbulence kinetic energy occur on the centreline and a higher angular momentum is evident. It is difficult to justify the use of this boundary condition on the basis of an improved agreement with the measurements, but its use is preferred to method 1 on the grounds that the effectiveness of the vane blockage increases towards the centre of the swirler, as the spacing between the vanes is reduced.

The radial velocity

To test the influence of the radial velocity at the outlet of the swirler, a constant value of 0.4 times the axial velocity was selected.

The results in Figure 5.19 show that, in the previous calculations, the failure to predict the axial velocity near the wall is likely to be a consequence of a zero radial velocity. However, the better results near the wall, in the present calculation, were accompanied by a reduction of the peak value which suggests that this boundary condition should be accompanied by a further increase of the axial velocity at the swirler outlet, which would have been justifiable as an inclusion of the effect of the swirler discharge coefficient. However, this was not done. Without experimental results nearer to the swirler, it is not worthwhile to proceed with testing further combinations of boundary conditions for the swirler, also because the results above demonstrated that the swirler boundary conditions had a small influence on the predicted flow pattern. This however did not preclude the identification of a set of boundary conditions found to be more appropriate. The main conclusions are:

1. Good agreement with the measurements is possible at Z = 8 mm in the inner region of the profiles by using (i) a profile of the radial velocity in the primary hole taken from the measurements and (ii) the simulation of the swirler by an annular gap of the same area as the effective area of the swirler.
2. The region near the wall depends on the radial velocity at the outlet of the swirler.
3. The reduction of the size of the annular gap results in a slightly weaker primary jet impingement.
4. Swirler boundary conditions may be more critical under flow conditions with a higher swirler to primary flow ratio.

5.3.3 Primary and Dilution Holes

The results in subsection 5.2.3 clearly showed the inadequacy of a plug flow assumption as a boundary condition of the primary hole. Previous calculations and measurements of jets in crossflow have already shown that this is an unrealistic assumption, especially at momentum flux ratios between the jet and the crossflow of less than 1 (see review in subsection 1.4.2). The ideal would be to have a boundary condition based on the measurements, but, in case this is not possible, a more practical solution to account for the discharge coefficient is found by reducing the hole diameter, increasing the radial velocity. Coupland and Priddin [1987] used this approach and emphasized its importance.

Other alternatives are possible and were also tested in the current study, however, before describing them, let us re-iterate the alternatives already tested in subsection 5.2.3 and give them a number for later reference:

Condition 1: A plug flow profile and a hole of 10 mm diameter (the same diameter as the real hole). This has been designated by V_{plug} boundary condition.

Condition 2: A shape of the velocity profile taken from the measurements and scaled in order to give the prescribed primary flow rate. This condition has been referred to as the V_{expt} boundary condition.

Condition 3: Identical to condition 1 above, but with a higher primary flow rate still within the range of experimental uncertainty.

The results to be presented correspond to the following boundary conditions:

Condition 4: A plug flow profile, with the same velocity as the maximum velocity of condition 2 but a hole of 8.6 mm diameter.

Condition 5: A plug flow profile with the same velocity as the maximum velocity of condition 2, but with a hole of 10 mm diameter.

The maximum velocity found from the procedure used in condition 2 and then used as the plug flow velocity of condition 4 was 3 m/s, which, given the primary flow rate of 1.044 kg/s, resulted in a hole of 8.6 mm diameter, corresponding to a discharge coefficient of 0.74. The maximum value referred to by Lefebvre [1983] for a discharge coefficient is 0.6 and 0.84 for plain and plunged holes, respectively. In condition 5 because the hole diameter was not reduced, this resulted in a primary flow rate of 1.414 kg/s, outside the range of experimental uncertainty. Summarizing, conditions 1, 2 and 4 have the same primary flow rate (lower than conditions 3 and 5)

and conditions 2, 4 and 5 all have a similar radial velocity on the axis of the primary hole (higher than conditions 1 and 3). All the conditions above affect only the radial velocity, the other variables were kept constant across the hole surface and were as in Table 5.1.3. Here, the boundary conditions of the swirler were unaltered and corresponded to the set recommended in the previous section.

Reduction of hole diameter and increase in primary flow rate

The results of calculations with conditions 1, 2, 4 and 5 are discussed here.

At Z = 8 mm (Figure 5.20), the effect of the various primary hole boundary conditions relative to the reference case (condition 1), as seen above, is to decrease the maximum axial velocity and shift the profile towards the wall, more in agreement with the measurements. This, as discussed in subsection 5.3.2, can also be promoted by a non-zero radial velocity at the outlet of the swirler. In the present calculations, the radial velocity at the outlet of the swirler was zero. The turbulence kinetic energy near the centreline (Figure 5.20) is very sensitive to the specification of the radial velocity in the primary hole and increases by about 50% between conditions 1 and 5, increasing the difference from the experimental value.

It was concluded in subsection 5.2.2 that the inflection of the profile of turbulence kinetic energy for r/Rc > 0.5 at Z = 40 mm, θ = 0° (not in accord with the measurements) was due to the grid distribution. Here, Figure 5.21 where the results all correspond to the same grid, that behaviour is only observed in conditions 1 and 5, using a plug flow assumption for a primary hole of 10 mm diameter. Conditions 2 and 4, with the experimental shape of the profile and a reduced hole diameter, respectively, do not evidence this behaviour which shows that it also depends on the velocity distribution at the edges of the hole.

Along the axis of the primary holes (Figure 5.22), the radial velocity agrees with the measurements, except in condition 1. Higher values of the turbulence kinetic energy are predicted by changing from conditions 1 to 5, which improves the agreement with the measurements.

Apart from enabling the selection of a more realistic boundary condition the calculations above allowed the evaluation of how much and which regions in the combustor are likely to be affected by a variation of the primary flow rate. The calculations showed that the good agreement between the measurements and predictions of the radial velocity along the axis of the primary hole is not exclusive to a boundary condition based on the shape of the profile taken from the measurements. Different peak values of the radial velocity in the hole (either by different distributions or higher primary flow rates) affect mainly the central part of the combustor by promoting a stronger penetration of the jets. Conditions based on assumptions of plug

flow through a hole of diameter similar to the real diameter are not recommended. An artifice such as the reduction of the hole diameter by 14 % (C_D = 0.74) seems to be a good compromise in case no reasonable guess can be made about the shape of the profile.

The dilution flow rate

There are experimental uncertainties associated with the dilution flow rate also.

Results of calculations with and without dilution flow are shown. In terms of the centreline values of the axial velocity (Figure 5.23), the dilution jets cause an acceleration of the flow beyond Z = 120 mm, the location corresponding to the edges of the dilution holes. This fully agrees with the measurements discussed in subsection 4.3.3. The higher values of axial velocity predicted in the plane of the dilution jets are a genuine failure of the calculation rather than an incorrect specification of the dilution flow rate, which does not influence the upstream flow. The small influence of the dilution jets in the regions upstream also show the negligible effects of the outlet boundary condition with the axial gradient set to zero.

The need to specify the boundary conditions in the planes of the holes may be removed either through a single calculation where the domain of integration includes both the annulus and the combustor (e.g. Green and Whitelaw [1983]) or by two separate calculations with the holes as common boundaries. This solution may bring other problems. A similar difficulty has been encountered in predictions of the flow inside IC reciprocating engines and calculations comprising both the inlet manifold and the cylinder, though removing the need to prescribe the boundary conditions at the cylinder inlets became extremely dependent on the accuracy of the calculations in the manifold (Begleris [1986]).

5.3.4 The Injection of Fuel

Three of the boundary conditions considered for simulation of the fuel injection are included here. They all used point sources located in the first column of the grid to simulate the injection of fuel and differed only in the annular distribution of the fuel cells. These were located at the radial location of the holes in the real injector, between the combustor axis and the swirler. The sources of axial and radial momentum were similar to guarantee a 45° injection, as in the experiments. The azimuthal momentum source was set to zero. A value of 1.50×10^{-2} m^2s^{-2} (identical to the swirler) was assumed for the turbulence kinetic energy and the dissipation followed assuming an eddy size as the diameter of the fuel injector holes.

Option 1: The fuel cells were spread over a ring with an aperture of 60°.

The fuel injector contains a total of 10 holes. Therefore, in the integration domain (a 60° sector) there are 1 + 2/3 holes. These holes occupied half of the angular aperture of the sector and the next two options tried to account for the effect of a non-continuous arrangement of fuel cells (see Figure 5.24).

Option 2: The cells were restricted to a central annular ring with an angular aperture of 30°.

Option 3: The fuel cells were split into two sets of 15° angular aperture each and located on the edges of the calculation domain.

Neither of these boundary conditions simulated the conical shape of the fuel injector, but because the fuel cells are located in the first column of the grid they may produce an effect similar to the fuel injector, by protruding into the combustor. The effect of the fuel injector is assessed by a calculation with a castellated approximation of the injector in subsection 5.4.1.

5.3.5 Conclusions

The results of the calculations with various options of the velocity profiles in the combustor entries enabled, by comparison with the measurements, the choice of an optimum set of boundary conditions. The flow in the combustor, in the primary region in particular, is very dependent on the radial velocity specified in the primary hole.

The final set of boundary conditions for each combustor entry are:

Swirler: Axial plug flow, zero radial velocity and solid body rotation with the area of the annular gap simulating the swirler as the effective area of the swirler by increasing the hub radius.

Primary hole: Constant axial and azimuthal velocities, and radial velocity taken from the measurements.

Dilution hole: Constant values for all components of velocity. Calculations without dilution flow showed no upstream influence of the dilution jets.

Fuel injector: Point sources distributed along half of the angular aperture of the sector.

5.4 DISCUSSION OF RESULTS

The previous section showed the effects of various possible alternatives to the boundary conditions and enabled the selection of a set of boundary conditions by looking

at the results in some locations in the combustor. Here, a more detailed evaluation of the mathematical model is made by concentrating on other possible causes that may explain discrepancies between the numerical and experimental results, i.e. the turbulence model. This section starts (subsection 5.4.1) with the study of the influence of geometrical simplifications such as the castellated head and the holes of the combustor, and the shape of the fuel injector. The numerical accuracy is assessed (subsection 5.4.2) by grid refinement extended to the limits of the computer memory available and by evaluation of the mesh Peclet number. The actual discussion of the results and validation of the turbulence model is in subsections 5.4.3 to 5.4.5 and has been split into calculations of (i) combustor flow with swirler (subsection 5.4.3), (ii) combustor flows without swirler (subsection 5.4.4), and (iii) combustor flow with swirler and "fuel" injection (subsection 5.4.5).

5.4.1 The Importance of Some Geometrical Simplifications

Geometrical simplifications of the combustor shape that may have contributed to the predictions in the primary region were: (i) the castellated approximation of the hemispherical head and the primary and dilution holes, and (ii) the neglect of the fuel injector. The objective of this subsection is to see to what extent these simplifications may have affected the results. This can be made only approximately since for a complete assessment of these effects the results here should be compared against results obtained by a system of coordinates where these limitations are completely removed.

The castellated head may influence the results, for instance through the reduction of the effective area of the combustor cross-section. Three different locations of the castellated head were tried: (1) the length of the straight section (the combustor barrel) upstream of the primary hole was shorter than the real one by 3 mm; (2) the upstream barrel length was made the same as the real one; and (3) the castellations were set one cell radially outwards relative to case 2.

8 mm downstream of the swirler (Figure 5.25), the differences between these three options are very small: there is a slight increase of the radial velocity and turbulence kinetic energy. At Z = 40 mm (Figure 5.26), conditions 2 and 3 increase the negative axial velocity on the centreline and the positive axial velocity near the wall; the turbulence kinetic energy decreases instead and this agrees with Koutmos and McGuirk [1985], who found that a castellated approximation promotes turbulence through the extra roughness and retards the flow along the downstream flat walls. The centreline plot (Figure 5.27) shows that the better agreement in the primary region does not affect the downstream regions.

Figure 5.28 shows the effect of the area correction factors of the cells on the upstream edge of the primary hole: there is an increase of the turbulence kinetic

energy whereas the other variables are as before. It was noticed that the propagation of this effect to regions further away from the hole is a function of the grid distribution (subsection 5.2.2) and the shape of the radial velocity profile in the plane of the holes (subsection 5.3.3). Here, the effect is more localized; it does not affect the results along the hole axis but shows again on the downstream edge (Figure 5.29).

The injector protrudes about 5 mm from the surface of the swirler into the combustor and this has now been included. The results, in Figures 5.30 and 5.31, of calculations with a castellated approximation of the injector show that the region of influence of the injector at Z = 8 mm extends over a central region of radius r/R_c = 0.2 and axially along the centreline for locations at a distance less than 20 mm from the swirler.

These results show approximately what the improvements would be, had a more flexible grid system been used. However, none of the geometrical simplifications discussed above can explain the differences between calculations and experiments found in previous sections. The neglect of the injector shape and the area correction factor in cells in the holes cause localized effects of minor importance. The castellated approximation of the head can cause an underprediction of the axial velocity near the walls (and as a consequence also the underprediction of the negative axial velocity in the centreline) and the use of more versatile system of coordinates is encouraged. Given the regular shape of the combustor head the use of an orthogonal system seems to be appropriate. A non-orthogonal grid system (e.g. Shyy, Braaten and Sober [1987]), though more flexible, would increase the complexity and storage requirements of the program and does not seem to be necessary; this also because the present treatment of the holes appears to be satisfactory.

5.4.2 The Numerical Accuracy

Systematic grid refinement and the cell Peclet number distribution were used as means of assessing the numerical accuracy of the calculations on the standard grid, 60 × 30 × 22. The main characteristics of the grids used for this purpose have been described in subsection 5.1.4. The refinements were made starting from the standard grid and in each direction independently, because the computer storage limitations did not allow a uniform refinement in every direction. However, by proceeding this way the directions and areas where grid resolution was more important could be identified.

Systematic grid refinement: global and grid refinement in independent directions

There is no need to show the results of these calculations in their full extent. The major alterations were caused by the grid refinement in the axial direction. Refining

the grid along the angular direction (60 × 30 × 42) did not reveal any phenomena similar to those observed in Chapter 3.

The main differences between the results of the six grids occur on the centreline and are shown in Figure 5.32; the standard grid gave the same results as the grid refined along the angular direction (60 × 30 × 42) and the results of the two grids refined in the axial direction differed only in the region upstream of the primary holes. The turbulence kinetic energy of only one grid is plotted so as not to impair the clarity of the figure. The grid 96 × 30 × 22 produces better agreement with the experimental results in the primary region, relative to the standard mesh (Figure 5.32); this is a consequence of the higher radial velocity along the axis of the primary holes (Figure 5.33) where values even higher than the experimental ones are predicted. The improved agreement of the centreline velocity in the primary region (higher positive and negative peaks) results in values in excess of the experimental results further downstream, so that the better agreement in the primary region is obtained at the expense of the dilution region, since the decay rate (underpredicted by the calculations) is constant irrespective of the level of grid refinement. Calculations on the 114 × 30 × 22 grid (similar to 90 × 30 × 22, but with additional nodes in the axial direction between the jets) were made to see whether an increase in the number of nodes in the intermediate region altered the decay rate; the results were identical to those obtained in the grid 90 × 30 × 22. The results in subsection 5.2.3 and 5.3.3 with much coarser grids and different boundary conditions in the primary hole had exhibited the same behaviour and this is believed to be a limitation of the turbulence model.

Comparing Figures 5.32 and 5.6 one can see that the relative improvement introduced by the grid refinement has been reduced. These improvements are a function of the boundary conditions as could also have been concluded from the results in subsection 5.3.1. The use of a higher radial velocity in the primary hole, as in V_{expt} boundary condition leads to an increase of the turbulence kinetic energy and turbulent viscosity reducing the relative magnitude of numerical viscosity effects, therefore reducing the sensitivity of the results to grid refinement.

Peclet number

The Peclet number along the three coordinate directions was also evaluated for the transport of a passive scalar. It is shown as contour plots in the most significant planes in the combustor.

The Peclet number in the longitudinal direction, Pe_Z, in the centre and mid longitudinal planes (Figure 5.34) is generally low; the maximum value of about 10 is restricted to the dilution and wall regions. The use of central differencing occurs over a

significant part of the integration domain which includes the impingement region and the shear layer of the flow emerging from the swirler gap. The shaded areas in the figure are regions where switching to upwind differencing took place. Similar plots, but for the finer grid 70 × 36 × 30 (Figure 5.35), obviously show even larger regions of low Pe values.

The Peclet numbers in the radial, Pe_R, and angular, Pe_T, directions (Figure 5.36) are much lower than Pe_Z and this explains why the grid refinements in these two directions changed the results so little. Pe_R and Pe_T are less than 0.5 in most of the integration domain. Pe_T is greater than 2 only in a very narrow region near the wall, between the primary and dilution jets, and Pe_R in the combustor head and in the core of the primary and dilution jets.

The low Peclet numbers that have been found confirm that the predictions are relatively free from numerical diffusion and show that, within the current computer limitations, it is already possible to obtain accurate solutions of combustor flows. Suspicions often stated that numerically accurate solutions of three dimensional recirculating flows would not be possible (e.g. Jones and McGuirk [1979], Claus [1983]) probably need to be reassessed. In this case, the low Peclet numbers are not only a consequence of the fine grids being used, but also a consequence of the high levels of turbulence generated in the flow. The use of higher order differencing schemes in this flow seems unnecessary, at least if the use of an eddy viscosity model is to be retained.

Following the results of the grid refinement and the evaluation of the Peclet numbers (also after all the previous tests), it can be confidently stated the results of these tests confirmed the accuracy of the grid 60 × 30 × 22. Further reasons for the deficiencies of the calculations should be sought in the turbulence modelling.

5.4.3 Combustor Flow With Swirler

Comparisons between the numerical and experimental results are shown here in a greater detail than in previous sections.

Standard case (45° swirler)

The numerical results corresponding to case 1 of Table 4.2 are presented in Figures 5.37 to 5.52. Figures 5.37 and 5.38 show longitudinal and cross sectional views of the predicted flow pattern. These figures, if viewed together with the experimental flow visualization in subsection 4.3.6 and accompanied by the introductory text in subsection 4.3.2 give a very detailed and comprehensive picture of the mean flow pattern prevailing in the combustor under the present conditions. A description of the flow pattern seems unnecessary at this stage.

The largest discrepancies between the numerical and the experimental results occur in the region around primary jet impingement; the agreement in the furthest downstream and upstream stations (Figures 5.39 and 5.52) is excellent. In spite of the good agreement of the radial velocity along the axis of the primary holes (Figure 5.42), the calculations show a weaker toroidal vortex in the combustor head (Figures 5.40 and 5.41). Lower recirculated mass flow, i.e. lower axial velocities, and lower turbulence levels compared with the measurements are features of this region which extends about 20 mm downstream of the primary holes. The centreline plot in Figure 5.32 shows that a difference of 30% occurs between the maximum negative values of the axial velocity.

The underprediction of the axial velocity near the walls at Z = 40 mm, Figures 5.40 and 5.41 can either be caused by the castellated approximation of the combustor head, the wall functions or simply a consequence of the reduced backflow rate predicted by the calculations. This underprediction of the axial velocity near the walls affects all the downstream stations. The lower axial velocities near the wall and on the centreline are strongly related and improvements in one region influence the other as the tests in previous sections have showed.

At Z = 50 mm and halfway between the jets at θ = 30° (Figure 5.44), the minimum value of the axial velocity at mid radius and the maximum near the wall are not predicted, and this then affects the shape of the profile downstream of the jets (Figures 5.46 and 5.47). In the θ = 0° plane, the agreement improves as the distance from the primary holes increases (Figures 5.45, 5.48, 5.51 and 5.52). The correct shape of the turbulence kinetic energy distribution is shown across the combustor, although with underpredicted levels except at the further downstream stations where good agreement is achieved in the regions around the centreline.

The good agreement obtained for the axial velocity in the intermediate locations Z = 70 mm and Z = 85 mm, in Figures 5.48 to 5.51, is somewhat fortuitous and corresponds to the region where, in the centreline plots (Figure 5.32), the experimental and numerical curve cross each other. This level of agreement is never obtained in the azimuthal component of velocity.

The calculations, by underpredicting the strength of the toroidal vortex in the combustor head, overpredict the strength of the swirler flow and show the central core usually rotating as the swirling flow. Features exhibited in the measurements and strongly connected to the primary jets, are not shown so obviously by the calculations; this becomes clear in the azimuthal velocity around the centreline, in the intermediate stations. Only in Figure 5.43, at the plane of the primary holes halfway between the jets do the calculations show the positive values of the azimuthal velocity. The downstream stations fail to show the correct shape of the azimuthal velocity profile and

evidence higher levels of radial diffusion compared with the measurements. The high values of W in regions around the centreline in the downstream stations are then responsible for the lower values predicted near the combustor walls. This dominance of the swirler flow partly explains why lower levels of turbulence are predicted in the impingement region; as the measurements showed, higher levels of swirler reduce the turbulence intensity in the centre of the combustor.

Calculations without swirler flow predicted higher values of turbulence kinetic energy and stronger backflow but never as high as the measured values with swirler flow. The boundary conditions tests showed that better results could be obtained as the distribution of the radial velocity along the axis of the primary holes approached the measured values; this dependence of the turbulence kinetic energy on the radial gradient of the radial velocity is expected to be extended to a dependence also on the axial gradient of the axial velocity along the centreline, which the calculations largely underpredict and may explain the lower levels of turbulence. The existence of other mechanisms contributing to the high experimental values of turbulence, and not accounted for by the present turbulence model, should not be fully discarded. The contribution that may have occurred due to the low frequencies associated with the jet shear layer instability, discussed in Chapter 4 are not supposed to be accounted for by the turbulence model. The characteristic time (1/60 Hz, i.e 0.017 sec) and length scale of the phenomenon above are higher than the time step (Δt = 0.004 sec) and the average dimensions of the grid cells at the primary jet impingement (about 2 mm) and the present mathematical model in principle should be able to predict such phenomenon. This, however may have been precluded by the symmetry (cyclic) boundary conditions of the present calculations; full three-dimensional calculations, covering the whole 360° of the combustor may be needed since instantaneously the assumptions of symmetry are not valid.

The contour plots in Figure 5.53 and 5.54 give an overview of the turbulence kinetic energy field. The maximum values exist around the primary jet, especially near the impingement point and in the upstream shear layer of the jet. Note also the order of magnitude difference between these and the values near the walls, a difference that the measurements do not confirm. The calculations consistently show lower values of turbulence kinetic energy near the walls, even in regions (e.g. Z = 85 mm, Figure 5.51) where good agreement of the axial velocity is obtained, which suggests that these lower values may be a consequence of the azimuthal velocity whose magnitude near the walls is also underpredicted.

In general, the calculations show a higher level of diffusion compared with the measurements. This is known to be a typical feature of the k-ε model in recirculating flows, whose variants usually involve a reduction of the eddy viscosity

(e.g. Leschziner and Rodi [1981]) either through the alteration of the constant $C\mu$ or the inclusion of extra terms in the equation of dissipation of the turbulence kinetic energy.

The calculations obtained with the 30 degree swirler under similar experimental conditions (case 2 of Table 4.2) evidenced identical features and are not worth including. Results with the 30 degree swirler but a higher swirler flow rate are shown below.

Higher swirler flow rate (30° swirler)

Calculations with an increased swirler flow rate (primary to swirler flow ratio of 1.31, case 6 in Table 4.2) were made. Figure 5.55 shows the flow pattern in the centre and mid longitudinal planes; the swirler flow penetrates axially deep into the primary zone, rather than being restricted to the region near the wall by the toroidal vortex resulting from primary jet impingement (as in Figure 5.37, corresponding to a primary to swirler flow ratio of 1.92). Three vortices can be identified in the combustor head: a large one with an anticlockwise rotation, which can be understood as an enlarged version of the region identified as B in Figure 4.25; two smaller vortices trapped below the swirler flow stream, one in the wake of the swirler hub and the other closer to the primary hole axis. Both seem to be part of a larger vortex limited by the shear layer of the swirler flow and the combustor centreline. (A much smaller vortex structure exists on the upstream edge of the primary holes near the wall but the number of 'particles' released in this region is not enough to resolve it.) The longitudinal views in the planes between and including the jets, show the axisymmetry of the flow pattern in much of the combustor head implying that the flow is now dominated by the swirler rather than the primary jet flow.

Cross-sectional views in the plane of the primary hole axis, viewing the flow from the downstream end towards the swirler are shown in Figure 5.56b; two vortices can be seen, one on each side of the jet. The swirler flow rotates clockwise and the vortex on the right hand side, being on the low pressure side of the jet, is larger and can even rotate in a direction opposite to the swirler flow; compare this with Figure 5.55a, 10 mm upstream of the jets. In the plane of the dilution hole axis (Figure 5.55c), there is a structure similar to the one observed in the plane of the primary holes, although it is not so clear because of the increased bending of the jets.

The restricted measurements of axial and azimuthal velocities, at only one station between the primary jets (Figure 5.57) are not enough to confirm or deny the existence of this flow pattern. The acceleration of the flow on the centreline, relative to the standard situation, was thought in Chapter 4 to be caused only by a downstream shift of the impingement point and a longer primary vortex; no major alteration of the

flow pattern was expected. However, given the level of agreement between the calculated and experimental results in the previous subsection, the pattern shown above is believed to be generally correct. Here, the swirler boundary conditions are likely to be more critical than in the previous case and the radial velocity at the outlet of the swirler, for instance, may have to be specified. If the underprediction of the negative axial velocity on the centreline is repeated here, then the impingement of the swirler flow on the combustor wall in reality occurs further upstream and the recirculation region near the centreline is larger at the expense of a reduction of the upper vortex near the wall. The flow pattern being predicted may actually happen for higher swirler flow rates, if the tendency to overpredict the strength of the swirler flow also persists.

The swirler flow rate was, in this calculation, 30% of the total flow and this is similar to the experimental conditions of Heitor and Whitelaw [1986] and Bicen and Jones [1986]. The pattern predicted here is likely to be similar to that in existence in their experiments; note, for instance, the radial distribution of turbulence kinetic energy in Heitor and Whitelaw [1986] with a peak at mid radius, which, according to the present calculations (Figure 5.58), seems to be associated with the impingement of the swirler "jet" on the primary jet (Figure 5.55). Their maximum turbulence kinetic energy on the centreline is associated with the precessing vortex core of the swirler flow and obviously cannot be predicted by the present calculations. Also, the striking and unexplained influence of the fuel flow rate upon the axial velocity on the axis of the primary holes in Bicen and Jones [1986] may be explained through the contribution of the fuel to increase the swirler flow rate and the vortex near the centreline in the plane of the primary holes.

5.4.4 Combustor Flow Without Swirl

Following the measurements without swirler flow presented in the previous chapter, calculations were also made to assess the performance of the turbulence model in the absence of swirler flow. Two calculations were made: (1) with no flow through the annular gap simulating the swirler (both the azimuthal and axial velocities were set to zero) and (2) with only the azimuthal velocity set to zero. The domain of integration was halved, a 30° sector limited by longitudinal planes of symmetry was used. The number of nodes in the azimuthal direction was also halved (a grid of $60 \times 30 \times 11$) to maintain a similar grid resolution.

Figures 5.59 and 5.60 show the longitudinal streakline plots for the two flow conditions mentioned above. In condition 1, Figures 5.59, there is a single vortex in the head, which is set exclusively by the primary jet impingement. With flow through the annular gap simulating the swirler (Figure 5.60) region B, in the upper

left corner, can be seen; the size of this region is larger than in case of swirling flow and agrees with the introductory remarks in subsection 4.3.2.

In the intermediate region there is another toroidal vortex (Figure 5.59), which is eliminated if there is flow through the swirler, either without (Figures 5.60) or with swirl component (Figures 5.37). This is simply because this flow increases the axial momentum near the walls, downstream of the primary jets. The measurements confirm the existence of this structure, but it is somehow smaller as can be concluded from comparison with measured axial velocities at Z = 85 mm in Figure 5.65. This is a consequence of a lower predicted recirculated flow rate, as the measurements and calculations 10 mm upstream of the primary jets show (Figure 5.61). In realistic combustor geometries, the probability of this structure occurring is reduced by including extra holes (smaller) between the primary and dilution holes. Further downstream, in the wake of the dilution jets (Figures 5.59 and 5.60), a similar phenomenon re-occurs and is eliminated only if there is swirling flow (Figure 5.37).

The cross-sectional views in the plane of the primary holes (Figure 5.67) show the vortex generated by the impingement of the jets and restricted to the outer region of the combustor. The jet is slightly wider in the case of the injection of fluid through the annular gap of the swirler. Note the differences between the flow pattern here ($\dot{m}_p/\dot{m}_{sw} = \infty$) and the flow pattern obtained with conditions from case 1, ($\dot{m}_p/\dot{m}_{sw} = 1.92$) (Figure 5.38a), and case 6 (Figure 5.56b) with a decreased primary to swirler flow ratio ($\dot{m}_p/\dot{m}_{sw} = 1.31$). Recalling the discussion on the bimodal PDFs of W velocity (in subsection 4.3.4), it can be seen in Figure 5.67a that the inner radial half of the combustor corresponds to the merger of the two neighbouring jets, rather than to the boundary of the two vortices formed between the jets (these vortices are actually restricted to the outer half of the combustor, where there was no evidence of bimodal PDFs). The arguments presented in subsection 4.3.4 (under the heading " Implications for the jet impingement process") are consistent with these streakline views.

Quantitative differences between the flow conditions (1) and (2) are better seen in Figures 5.60 to 5.65. The main differences occur near the wall where the extra swirler flow shows either by increasing the axial velocity, upstream of the dilution jets, or near the centreline downstream of the dilution jets (Figure 5.66). The higher negative centreline velocity in Z = 50 mm (Figure 5.62) is caused by a slight downstream bending of the primary jets.

In general, the level of agreement between the experimental and numerical results is the same as in the previous situation with swirling flow; for instance, the underprediction of the axial velocity and turbulence kinetic energy on the centreline

(Figures 5.66). The comments made above are also valid for this condition and show that the deficiencies of the turbulence model are associated with the prediction of the impingement region irrespective of the existence of swirler flow. The poor performance of the model in the intermediate region appears to be more a consequence of the poor results upstream in the combustor and the use of higher order closure turbulence models, though perhaps necessary to improve the predictions in the primary region may not be needed for the downstream regions.

5.4.5 The Transport of Fuel

Figures 5.68 to 5.70 include the results of the simulation of fuel injection. The flow conditions correspond to case 3 in Table 4.2. Figures 5.68 and 5.69 show the radial profiles at two angular locations. Apart from a small lump near the centreline where there is the reverse of the relative position between conditions 2 and 3, consequence of the orientation relative to the fuel cells, there are no major differences between the various geometrical arrangements of the fuel cells. The centreline plot (Figure 5.70) agrees with the measurements in the case of conditions 3 and 4; the measurements also showed this reverse of the relative position of the curves with and without injection. Beyond Z = 30 mm, there is no influence of the fuel injection on the centreline.

The transport of fuel near the combustor walls was noticed in the flow visualization study (subsection 4.3.6) and is illustrated here also by the contour plots of mixture fraction (values in per cent) in Figures 5.72 to 5.76. Values of fuel fraction above 10% occur only within the first 10 mm of the combustor (Figure 5.72). The effect of the geometrical arrangement of the fuel cells is evident 8 mm downstream of the swirler (compare Figures 5.72, 5.73 and 5.74), but, at 30 mm, the axisymmetry of the flow is re-established and the three arrangements of the fuel cells give identical results. The fuel jet, unable to penetrate the recirculated flow created by the primary jet impingement, mixes with the swirler flow and escapes between the primary jets, being transported near the wall with reduced mixing with the central core of the flow, formed mainly by primary jet fluid. In the dilution region, the jets, because of their weaker penetration drive the fuel towards the centreline (Figure 5.71). This was also the picture built on the basis of the flow visualization study, which supports the calculations. However, this particular pattern is a consequence of the primary to swirler flow ratio and is by no means the only one possible in gas turbine combustors; the calculations of Coupland and Priddin [1987] show, for instance and the experimental results of Bicen and Jones [1986] suggest, that the fuel can mix with the central core (swirler flow) throughout the combustor.

Scalar mixing – the turbulent Prandtl number

Predictions have been carried out with various values of turbulent Prandtl number. Calculations with values of 0.7 and 0.4 show, as expected, smoother distributions as the turbulent Prandtl number is reduced. In the plane of the primary jets, Z = 50 mm in Figures 5.73, 5.75 and 5.76, it appears, due to the increased diffusion, as if the penetration of the primary jet has been reduced, as opposed to a higher penetration of the fuelled fluid between the jets, leading to higher values of the fuel fraction on the centreline. This agrees with the restricted set of measurements made with an intrusive concentration probe, in Appendix B, and may support the use of a turbulent Prandtl number lower than 0.9, as has been suggested by various authors (see remarks in Chapter 2). The need to increase the diffusion of a passive scalar for better agreement with the measurements, contrasts with another common suggestion to reduce the value of the constant C_μ in the model which contributes to the reduction of the diffusion of momentum. A more detailed study of the concentration field inside the combustor should await detailed measurements, depending on the development of the techniques described in Appendices A and B.

5.5 CONCLUSIONS

Discrepancies between the numerical and experimental results were found to be due to numerical or turbulence modelling reasons.

From a numerical point of view, the main conclusions of this chapter are:

1. Fine numerical grids are needed to resolve the flow in the combustor. The level of refinement depends to some extent on the boundary conditions and, provided the correct boundary conditions are specified, grids of about 30000 nodes offer a good compromise between accuracy and computer run time.
2. In the limits of computer memory available (about 7 Mbytes), solutions are possible with central differencing scheme in a substantial part of the integration domain, demonstrating that numerically accurate solutions are possible in a flow of engineering interest.
3. The grid resolution is most critical in the axial direction, especially in the combustor head.
4. Of the boundary conditions, the radial velocity in the primary hole is determinant and can influence the flow pattern in all of the combustor.

5. Other boundary conditions at different entries of the combustor may be equally or more important in the case of different flow splits.

From a turbulence modelling point of view:

1. The calculated results exhibit, in general, higher levels of diffusion, which show, for instance, in the axial centreline velocity through the underprediction (30%) of the maximum negative value and a decay rate lower than measured.
2. No qualitative agreement with the azimuthal velocity in the region downstream of the primary jets could be achieved.

From a design point of view:

1. The model gives acceptably good results and proved to be a very powerful design tool, especially if one is interested mainly in qualitative answers. For higher confidence on the results under flow conditions differing from the present ones a cautious use of the model is recommended and at least, tests of sensitivity to the boundary conditions should be performed.

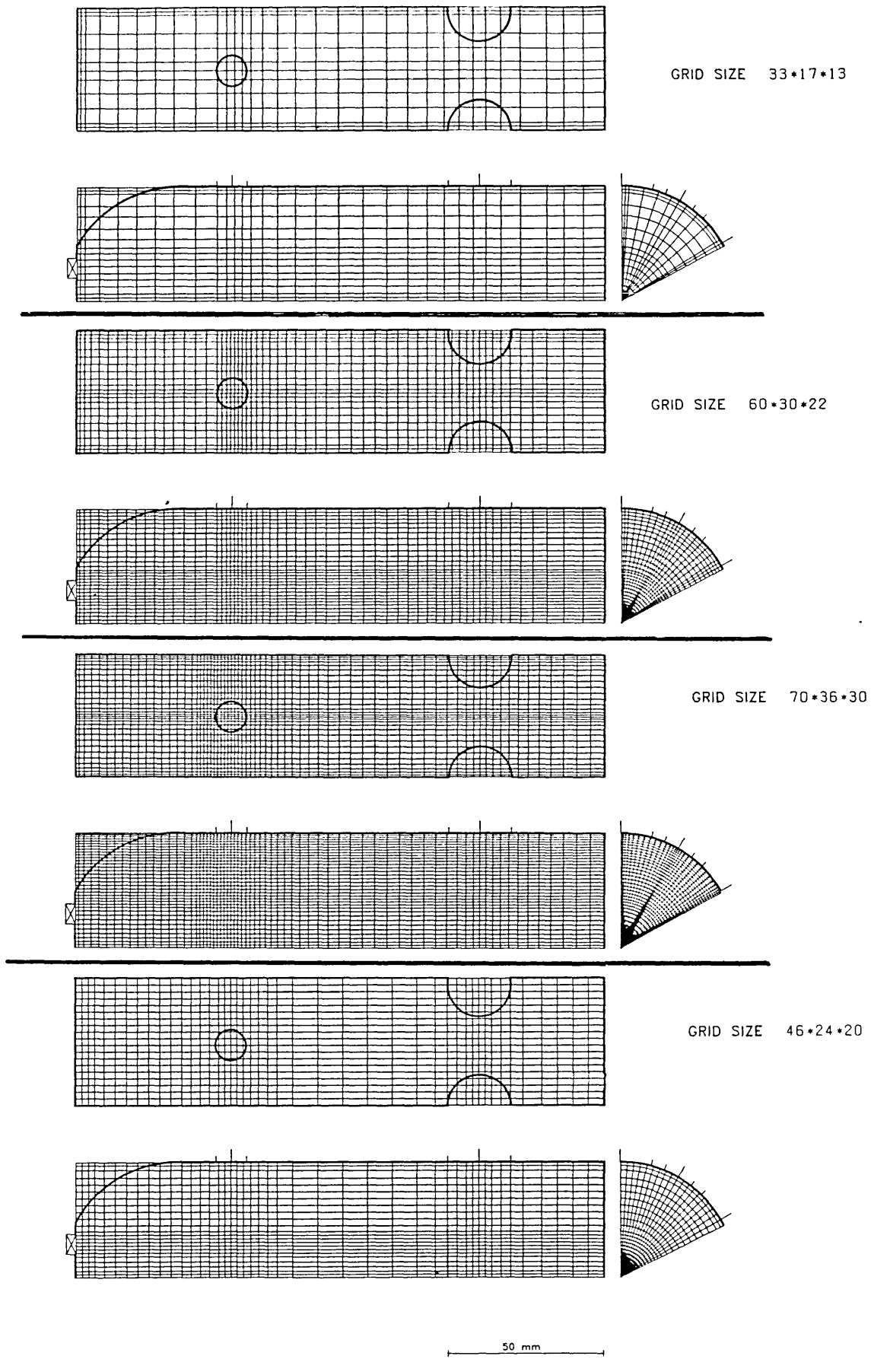


FIGURE 5.1 - Numerical grids used in preliminary calculations (grids n. 1, 2, 3 and 4).

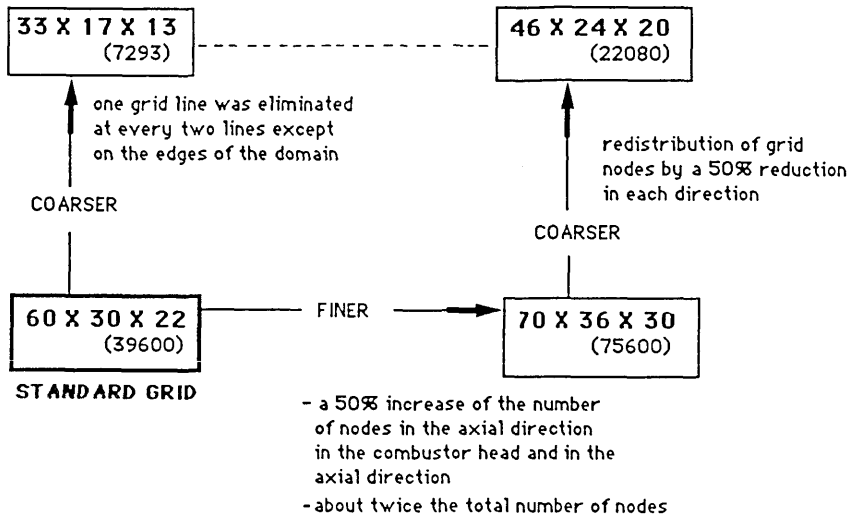
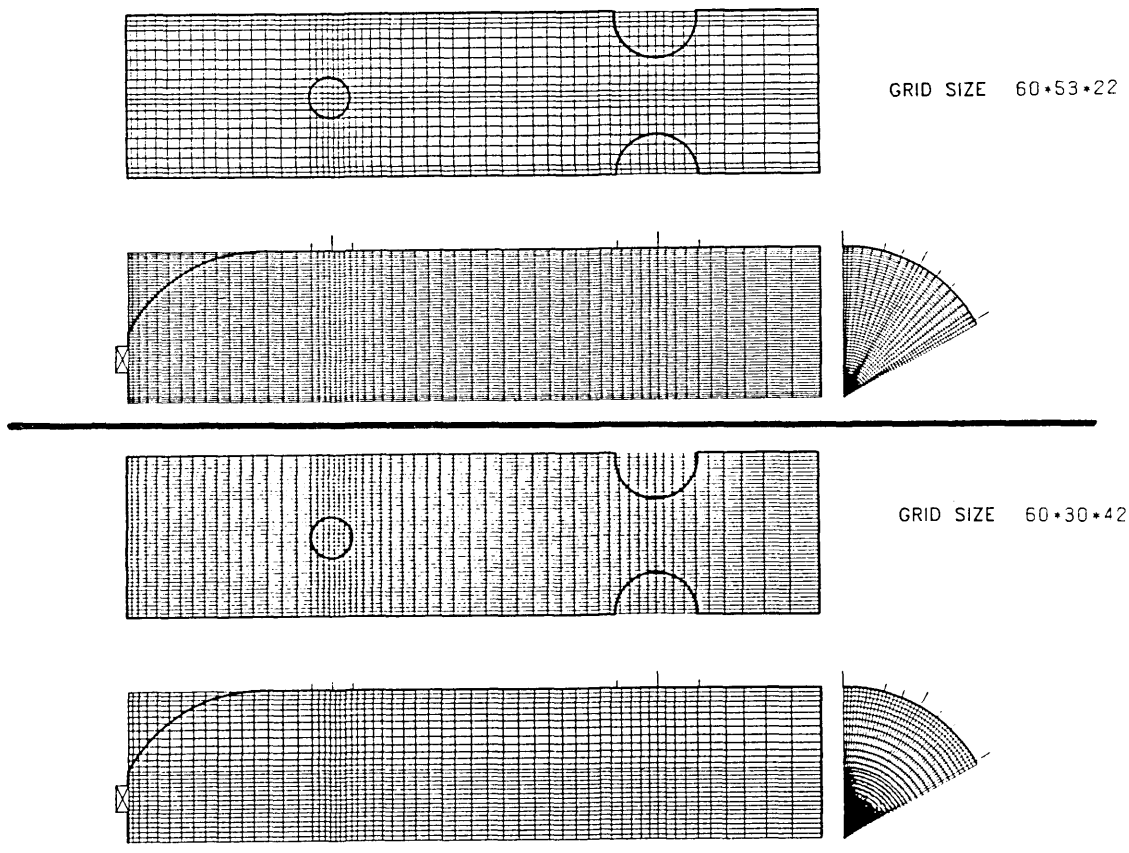


FIGURE 5.2 - The relationship between the numerical grids used in preliminary calculations (total number of nodes within brackets).



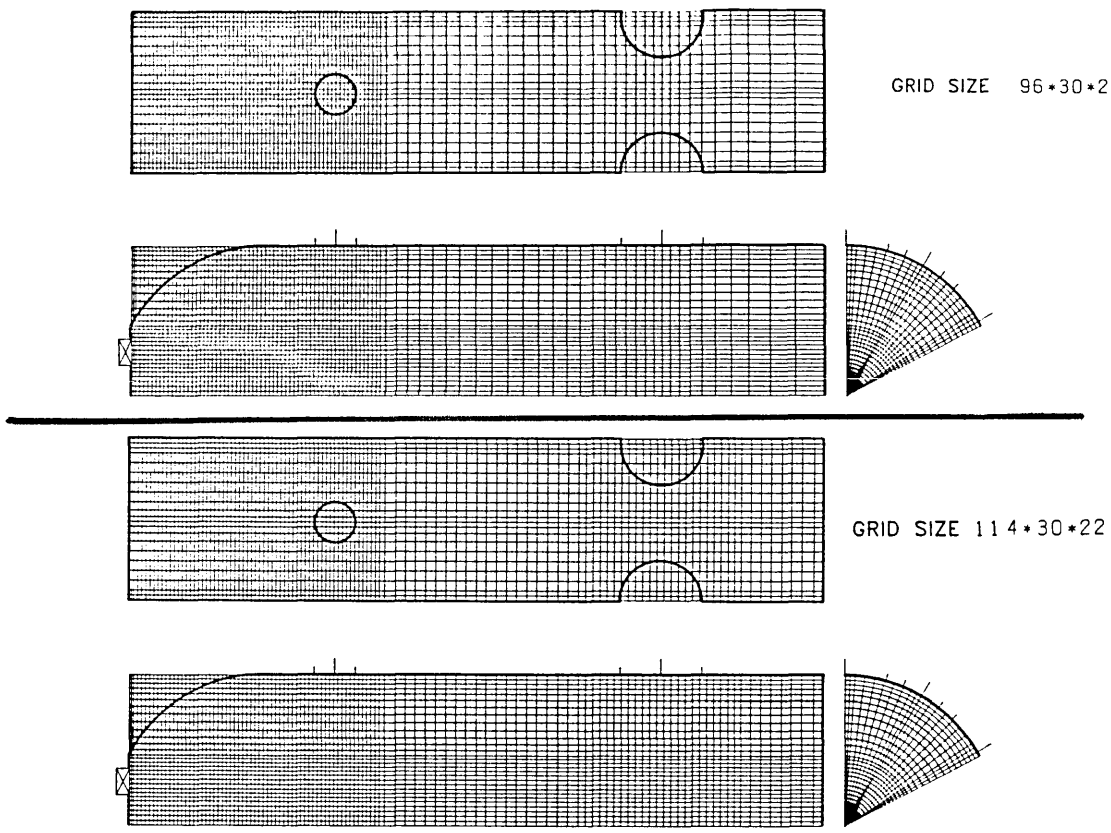


FIGURE 5.3 - Numerical grids used in the final set of calculations (grids n. 5, 6, 7 and 8).

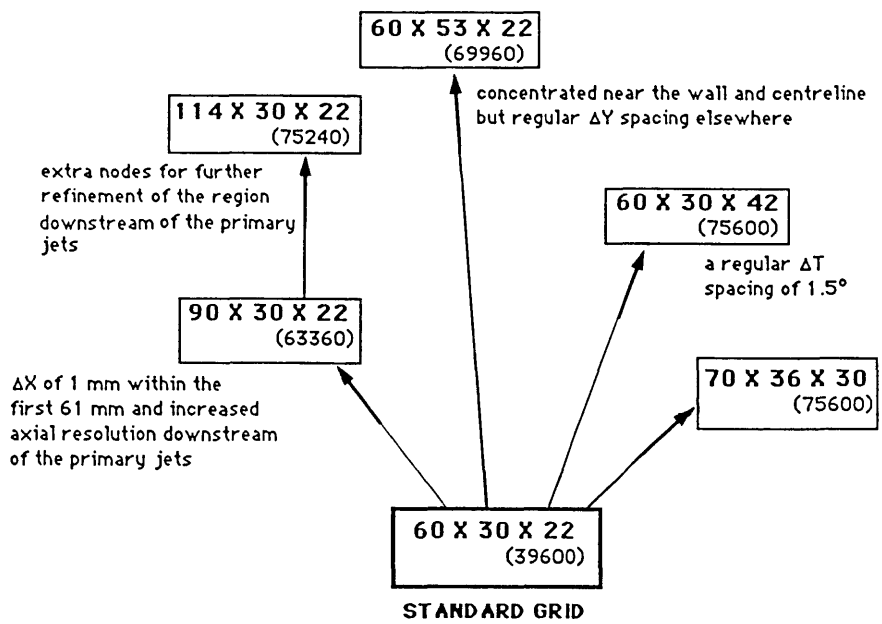


FIGURE 5.4 - The relationship between the numerical grids used in the final set of calculations (total number of nodes within brackets).

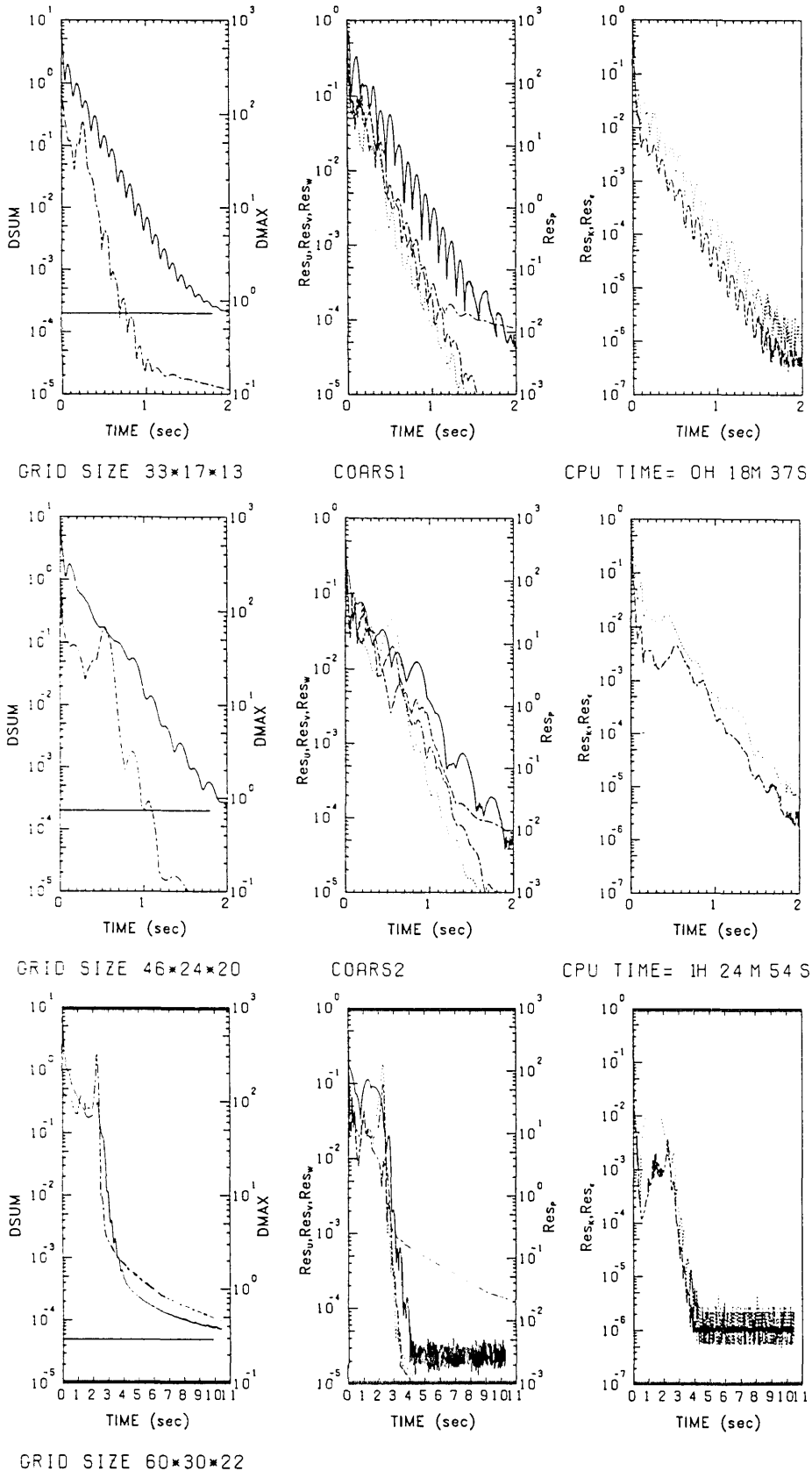


FIGURE 5.5 - The convergence pattern of the calculations using three different grids.

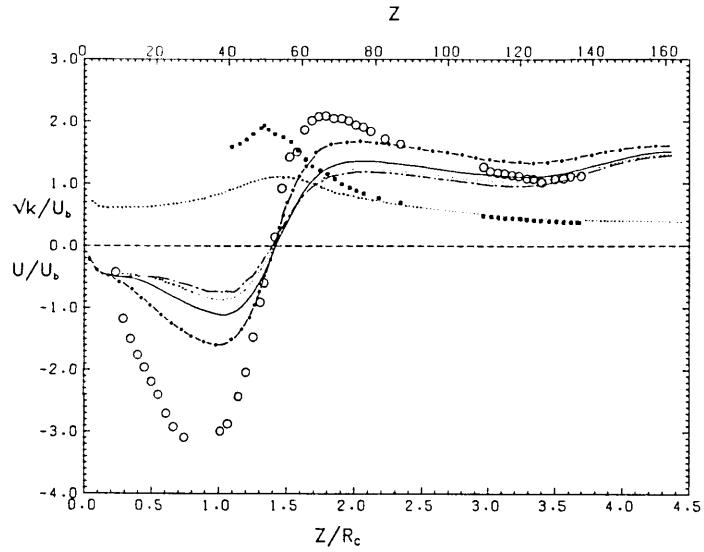


FIGURE 5.6 - Axial velocity and turbulence kinetic energy along the combustor centreline using four different grids: —·—·— grid 33 ×17 ×13 ---------- grid 46 ×24 ×20 ——— grid 60 ×30 ×22 —·—·— grid 70 ×36 ×30.

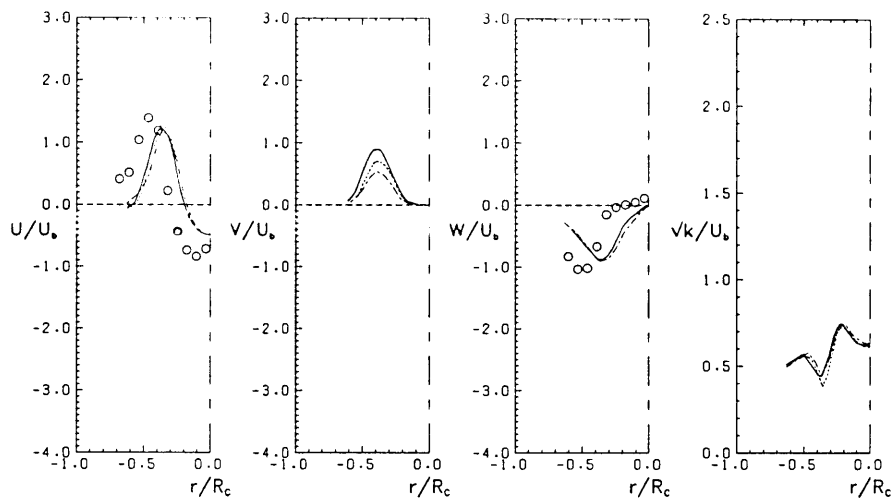


FIGURE 5.7 - Results at Z = 8 mm, θ = 0° using four different grids - key as in Figure 5.6.

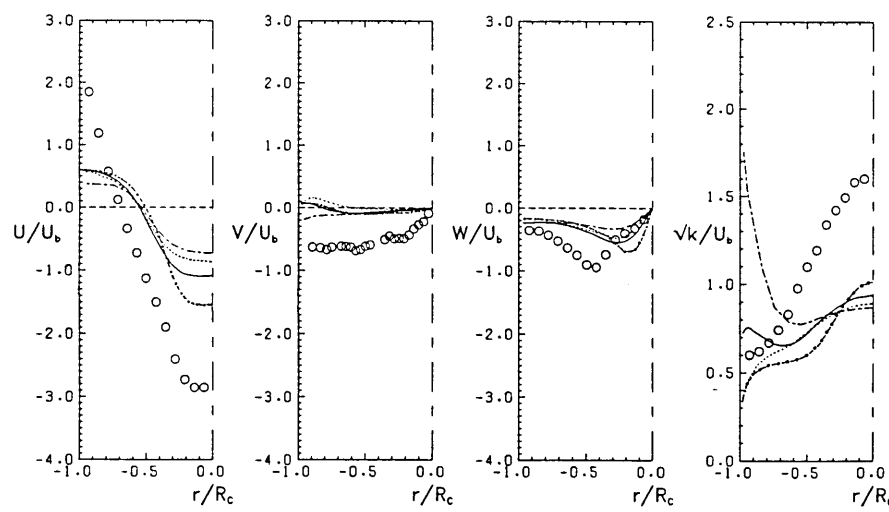


FIGURE 5.8 - Results at Z = 40 mm, θ = 0° using four different grids - key as in Figure 5.6.

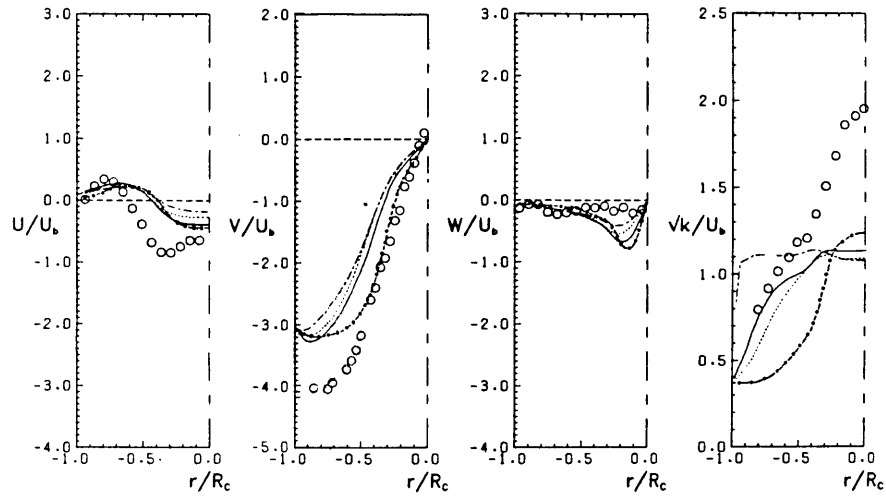


FIGURE 5.9 - Results at Z = 50 mm, θ = 0° using four different grids - key as in Figure 5.6.

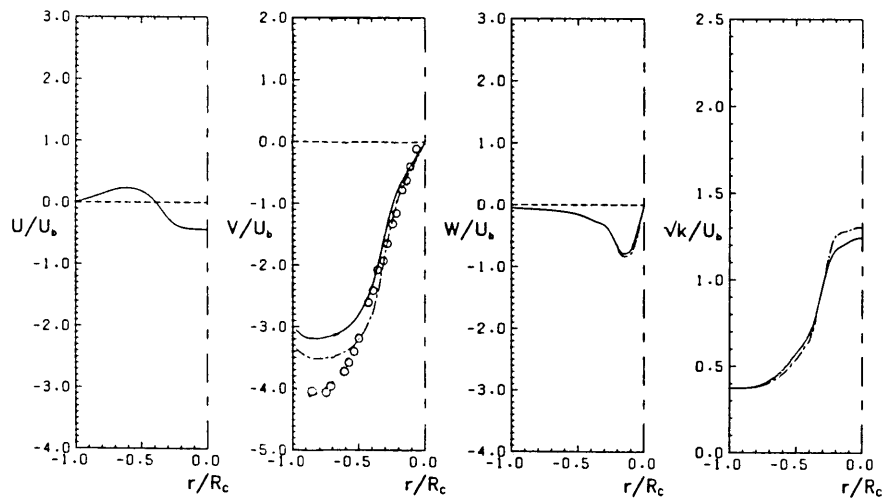


FIGURE 5.10 - Results at Z = 50 mm, θ = 0° using two primary flow rates:

——— $\dot{m}_p$ = 1.044 kg/s — - —·— - $\dot{m}_p$ = 1.146 kg/s.

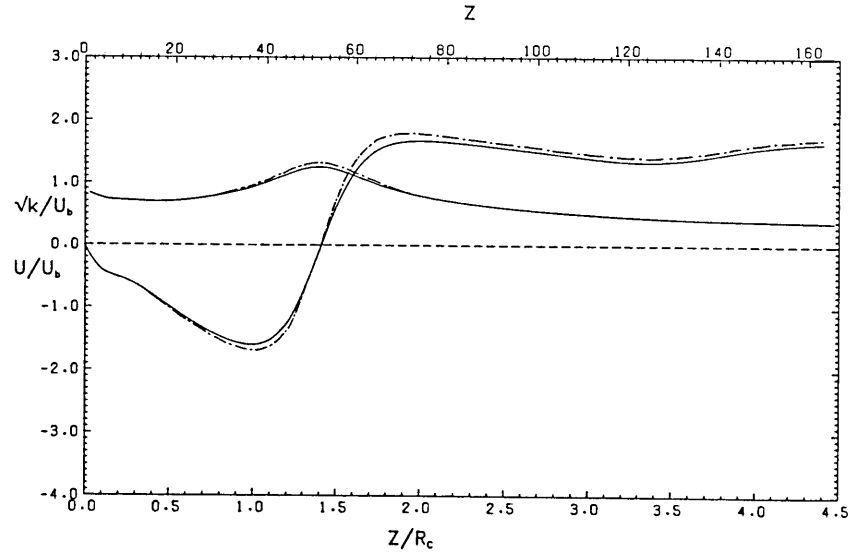


FIGURE 5.11 - Axial velocity and turbulence kinetic energy along the combustor centreline for two primary flow rates:

——— $\dot{m}_p$ = 1.044 kg/s —·—·— $\dot{m}_p$ = 1.146 kg/s.

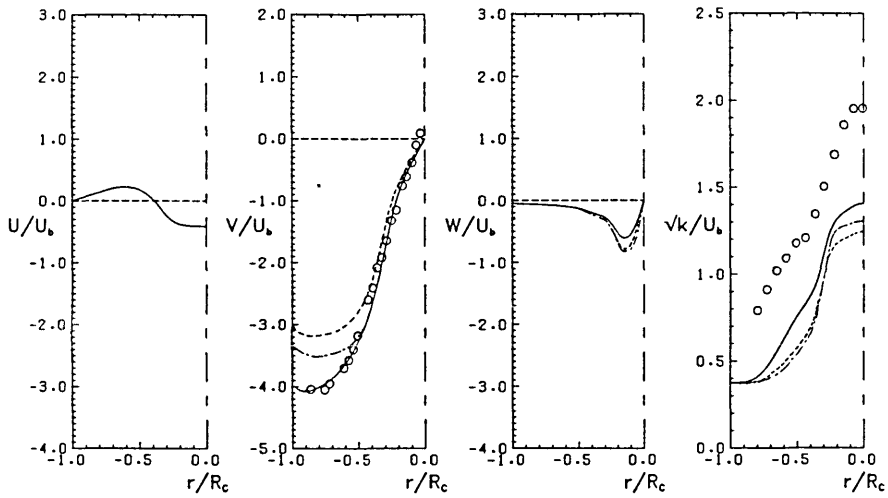


FIGURE 5.12 - Results at Z = 50 mm, θ = 0° using three alternative boundary conditions for the radial velocity on the primary hole: ------ V_{plug} ($\dot{m}_p$ = 1.044 kg/s ——— V_{expt} ($\dot{m}_p$ = 1.044 kg/s) —·—·—·— V_{plug} ($\dot{m}_p$ = 1.146 kg/s

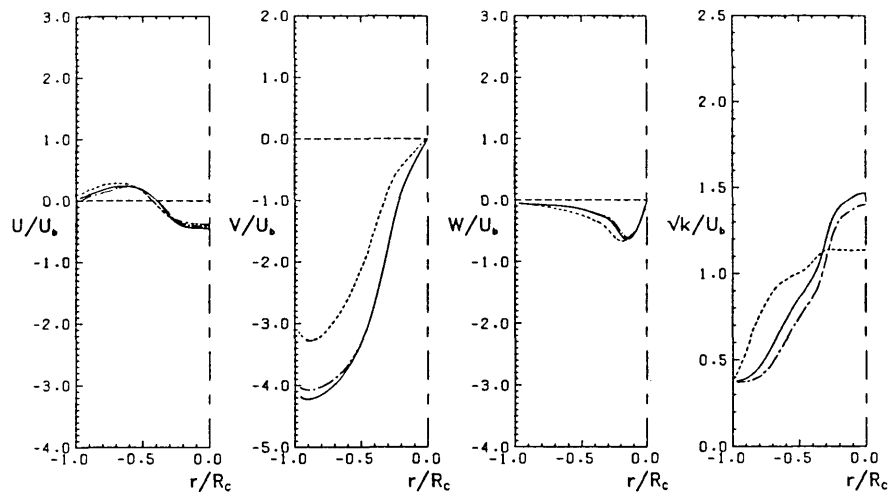


FIGURE 5.13 - Results at Z = 50 mm, θ = 0°, using three alternative boundary conditions for the radial velocity on the primary hole:
---------- V_{plug} (grid 60 ×30 × 22) —·—·— V_{expt} (grid 70 ×36 × 30)
——— V_{expt} (grid 60 ×30 × 22).

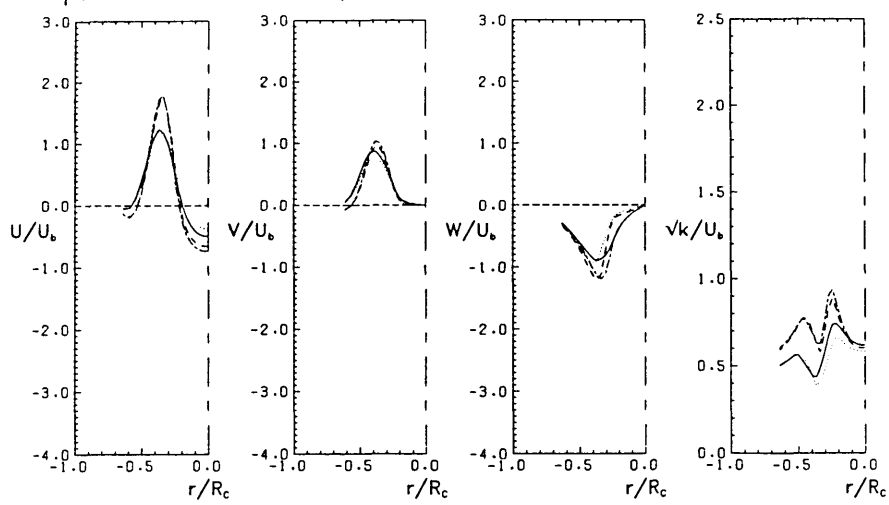


FIGURE 5.14 - Results at Z = 8 mm, θ = 0° using four alternative boundary conditions for the swirler: ——— U_{plug}, W_{cte}; ---------- U_{plug}, $W_{solid\ body}$;
—·—·— U_{plug}, W_{cte} + vane blockage(method 1);
– – – – – – – U_{plug}, $W_{solid\ body}$ + vane blockage(method 1).

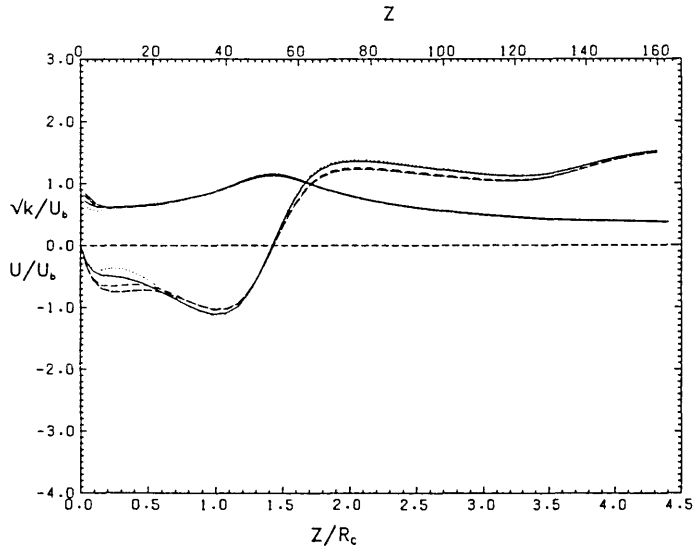


FIGURE 5.15 - Axial velocity and turbulence kinetic energy along the combustor centreline with four alternative boundary conditions for the swirler - key as in Figure 5.14.

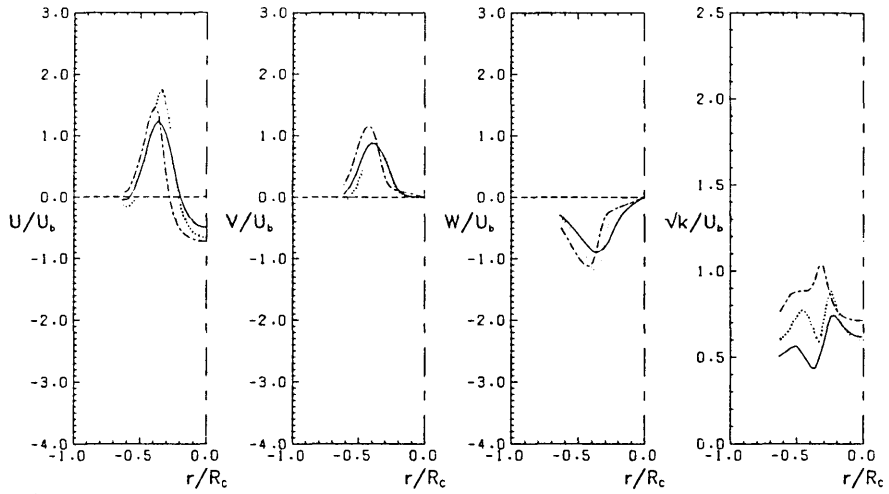


FIGURE 5.16 - Results at Z = 8 mm, θ = 0° using two alternative boundary conditions for the swirler and two alternative boundary conditions for the primary hole: ——— U_{plug}, W_{cte};
- - - - - - - - - - - - U_{plug}, $W_{solid\ body}$ + V_{plug} in primary hole;
— · — · — · — U_{plug}, $W_{solid\ body}$ + V_{expt} in primary hole.

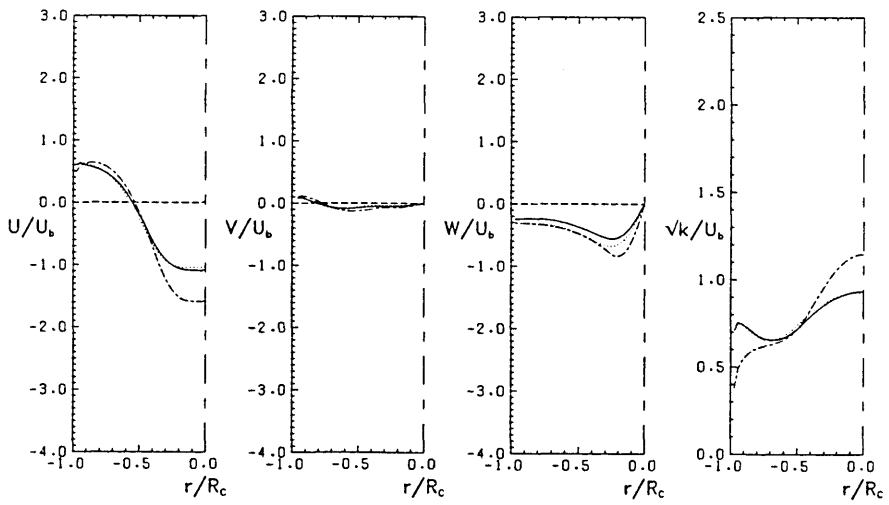


FIGURE 5.17 - As above but at Z = 40 mm, θ = 0°.

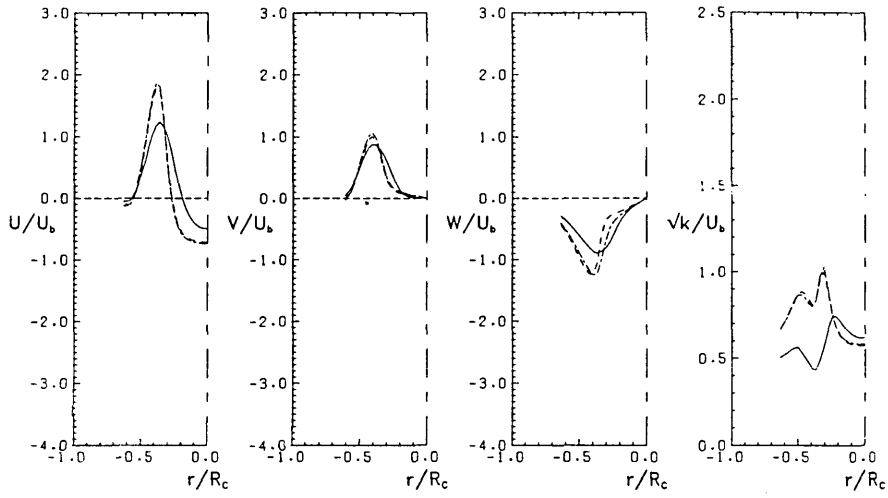


FIGURE 5.18 - Results at Z = 8 mm , θ = 0° using three alternative boundary conditions for the swirler: ——— U_{plug}, W_{cte};
—·—·— U_{plug}, W_{cte} + vane blockage(method 2);
- - - - - - - - U_{plug}, $W_{solid\ body}$ + vane blockage(method 2).

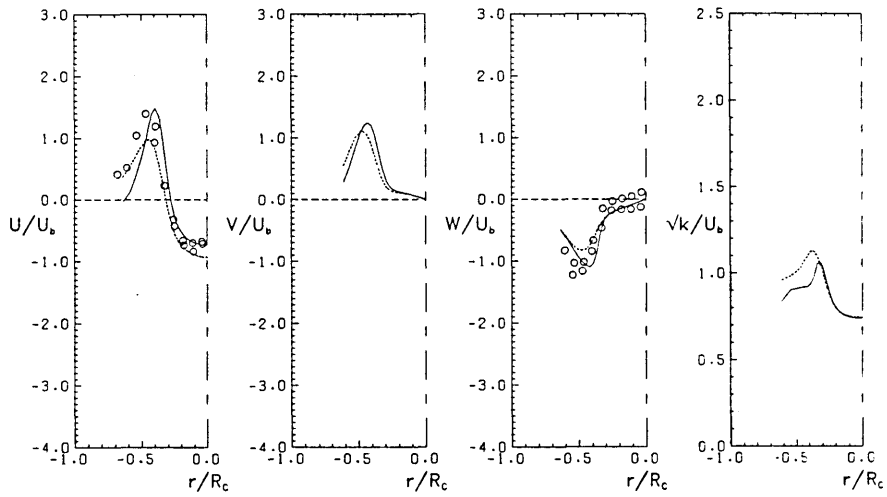


FIGURE 5.19 - The influence of the radial velocity at the outlet of the swirler. Results at Z = 8 mm , θ = 0°: ——— U_{plug}, $W_{solid\ body}$ + vane blockage(method 2)+ V_{expt}
--------- similar conditions, but with V=0.4 U at the swirler outlet also.

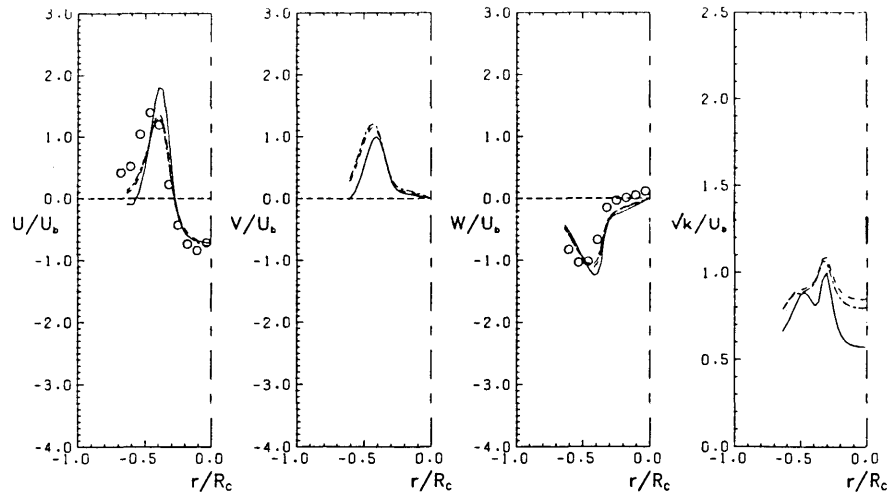


FIGURE 5.20 - Results at Z = 8 mm , θ = 0° using four alternative boundary conditions for the radial velocity in the primary hole:
——— V_{plug} ($\dot{m}_p$ = 1.044 kg/s - condition 1) - - - - - - - V_{expt} ($\dot{m}_p$ = 1.044 kg/s - condition 2)
—·—·—·— V_{plug} but smaller hole ($\dot{m}_p$ = 1.044 kg/s - condition 4)
— — — — V_{plug} ($\dot{m}_p$ = 1.414 kg/s - condition 5)

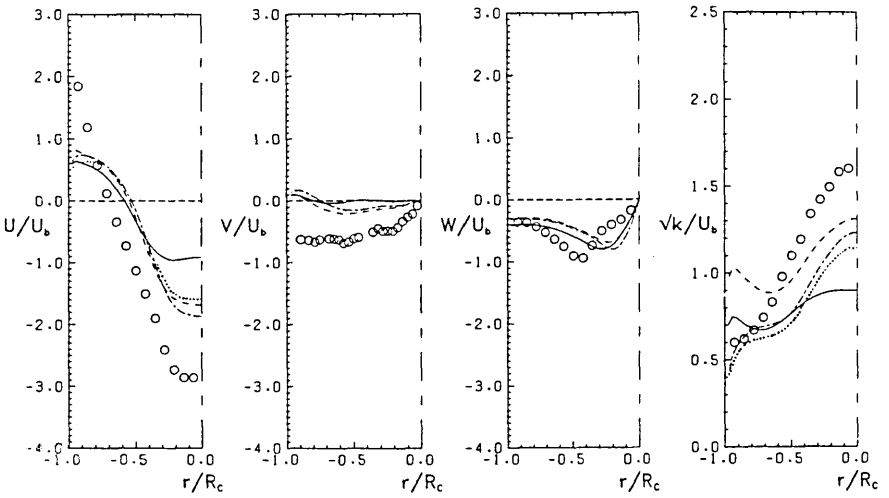


FIGURE 5.21 - Identical to Figure 5.20, but at Z = 40 mm, θ = 0°.

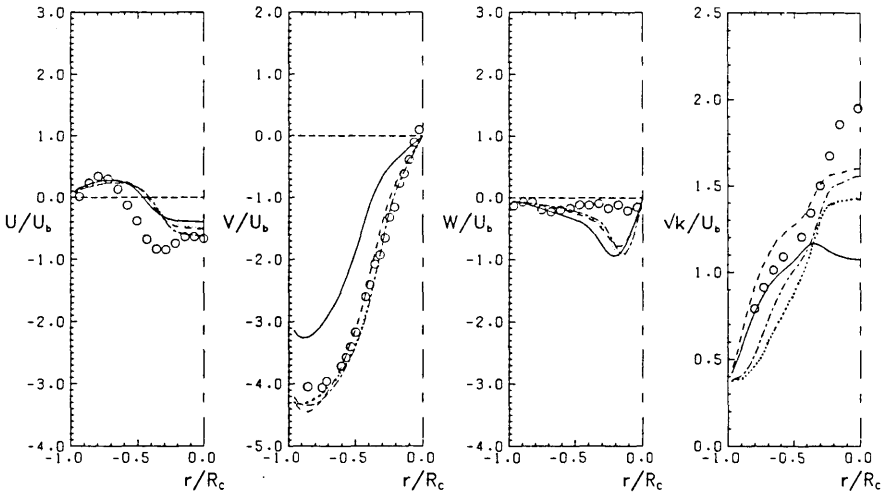


FIGURE 5.22 - Identical to Figure 5.20, but at Z = 50 mm, θ = 0°.

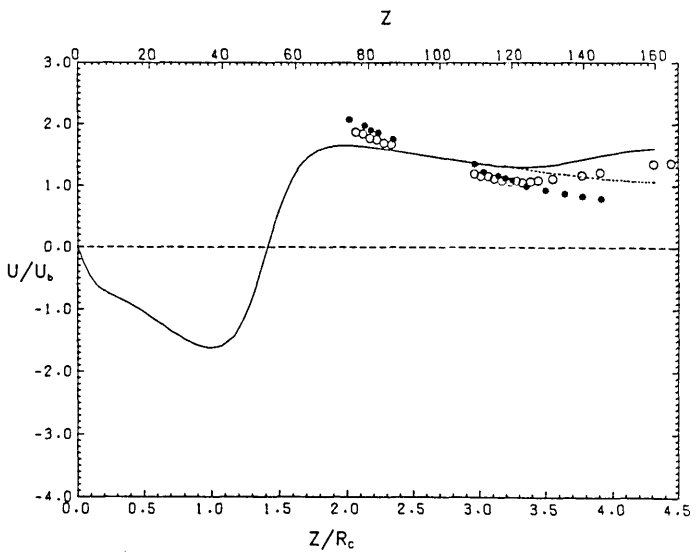


FIGURE 5.23 - Axial velocity along the combustor centreline with and without dilution flow: ○ —— with dilution flow ● ------ without dilution flow.

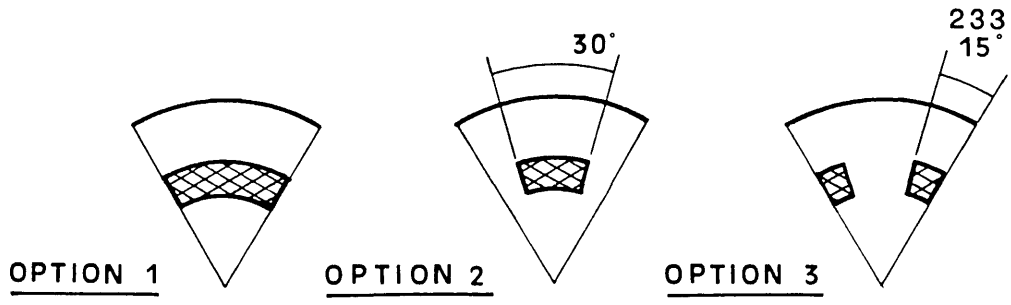


FIGURE 5.24 - Arrangement of cells simulating the injection of fuel.

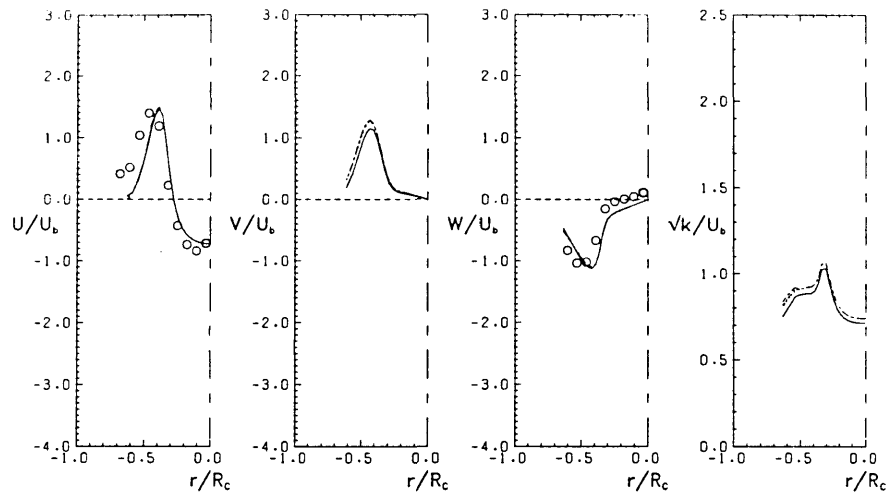


FIGURE 5.25 - Results from calculations with three different castellations to simulate the hemispherical head of the combustor:
——— case 1 ---------- case 2 —— - —— - —— case 3

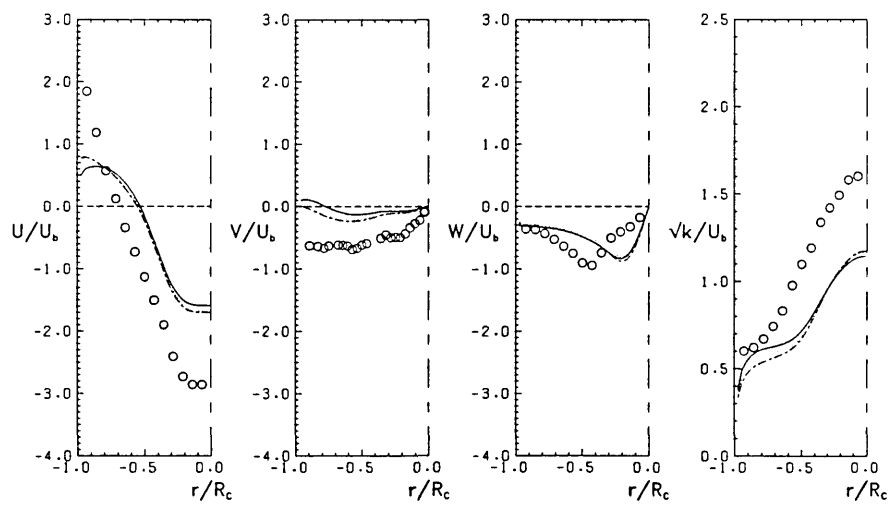


FIGURE 5.26 - Similar to Figure 5.25 but at Z = 40 mm, θ = 0°.

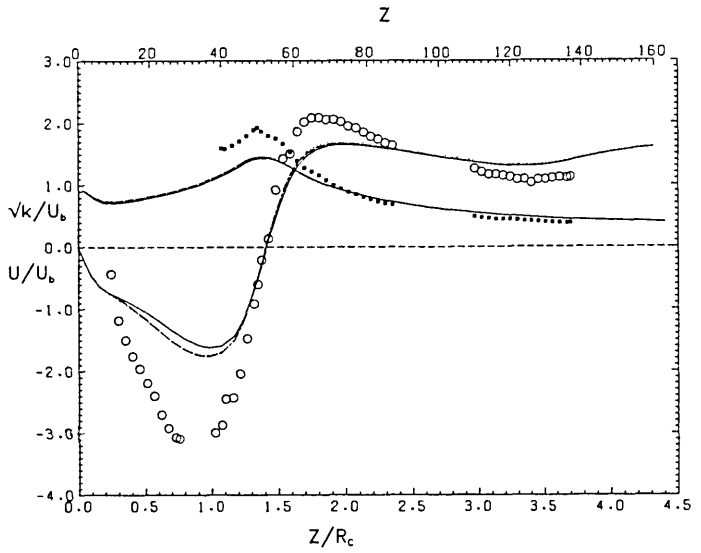


FIGURE 5.27 - Axial velocity and turbulence kinetic energy along the combustor centreline - see key in Figure 5.25.

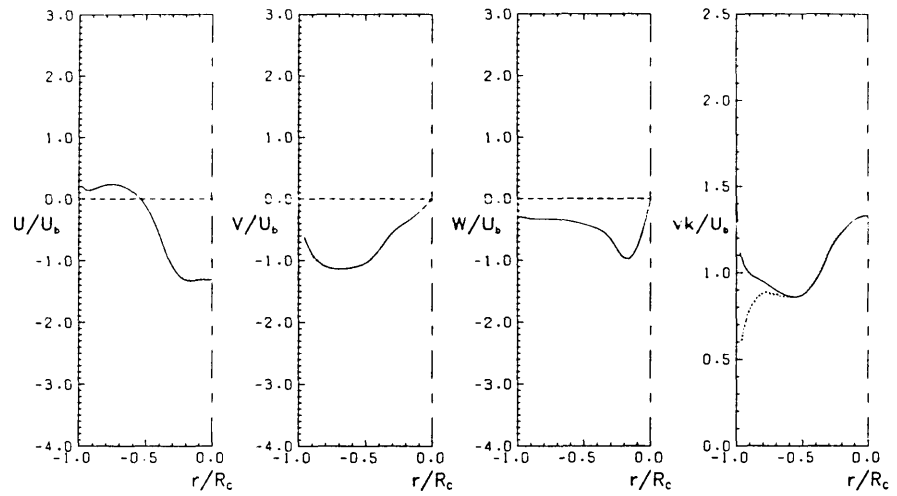


FIGURE 5.28 - Results from calculations with and without area correction factors for the primary holes:
——— with correction factors; ---------- without correction factors.

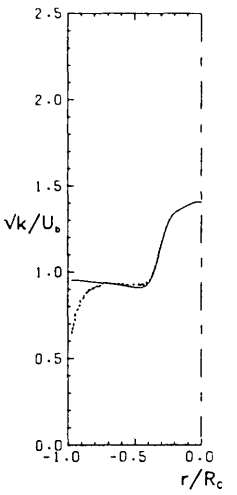


FIGURE 5.29 - Similar to Figure 5.28 but at Z = 55 mm, θ = 0°.

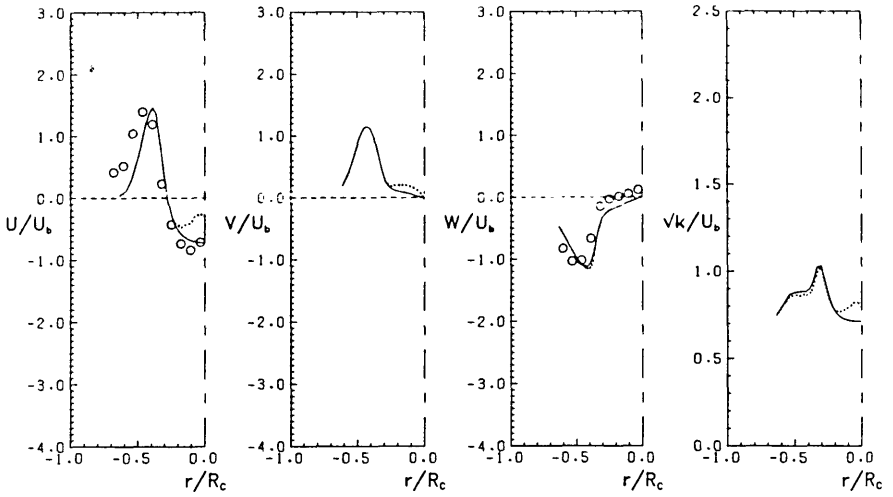


FIGURE 5.30 - Results from calculations with and without a castellated approximation of the fuel injector shape at Z = 8 mm, θ = 0°:
-------- with castellations; ——— without castellations.

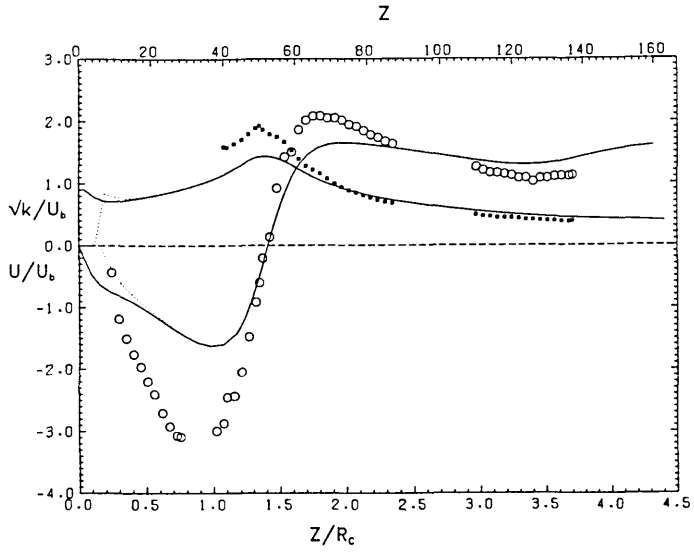


FIGURE 5.31 - Axial velocity and turbulence kinetic energy along the combustor centreline - see key in Figure 5.30.

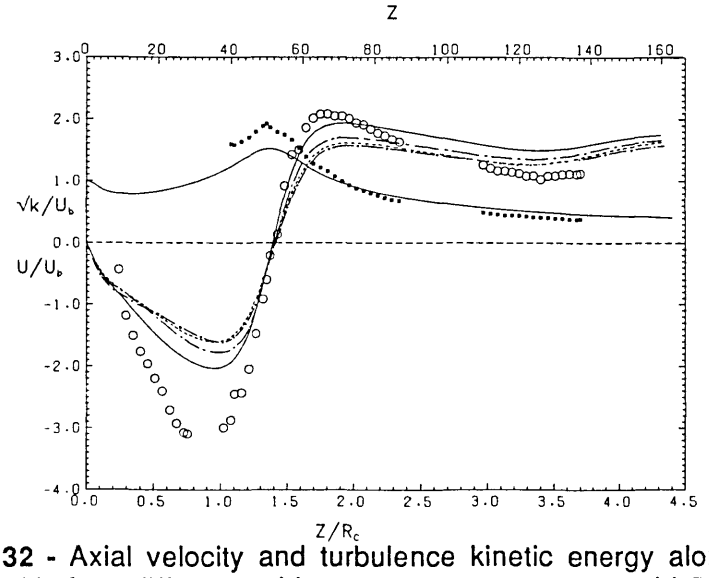


FIGURE 5.32 - Axial velocity and turbulence kinetic energy along the combustor centreline with four different grids: —·—·— grid 70 × 36 × 30: – – – – – grid 60 × 53 × 22; —— grid 96 × 30 × 22; —·—·— grid 60 × 30 × 42.

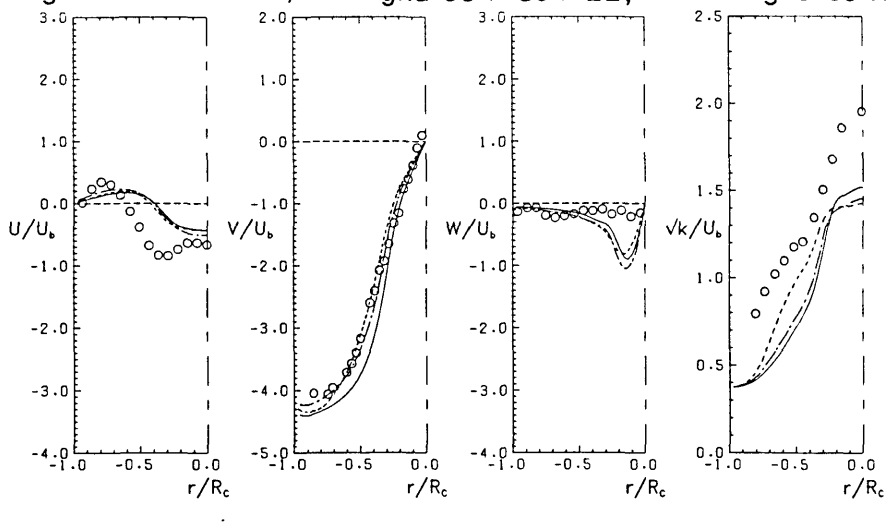


FIGURE 5.33 - As in Figure 5.32, but at Z = 50 mm θ = 0°.

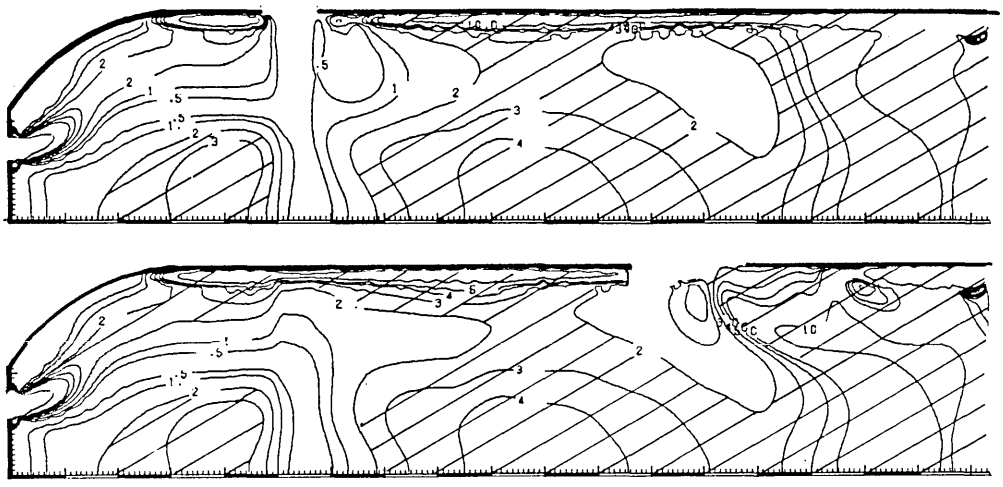


FIGURE 5.34 - Peclet number along the axial direction (Pe_Z) in the longitudinal plane (grid 60 × 30 × 22).

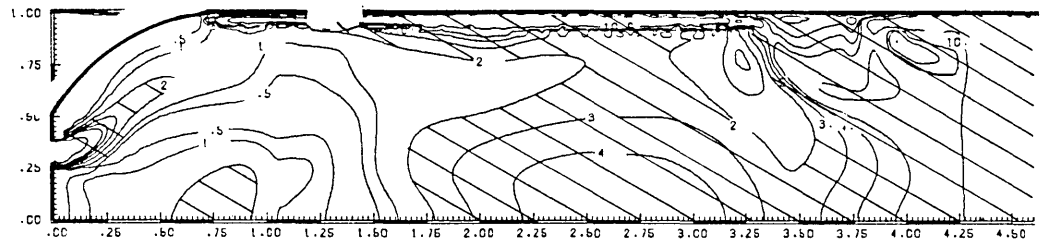


FIGURE 5.35 - Peclet number along the axial direction (Pe_Z) in the longitudinal plane containing the axis of the primary hole (grid 70 × 36 × 30).

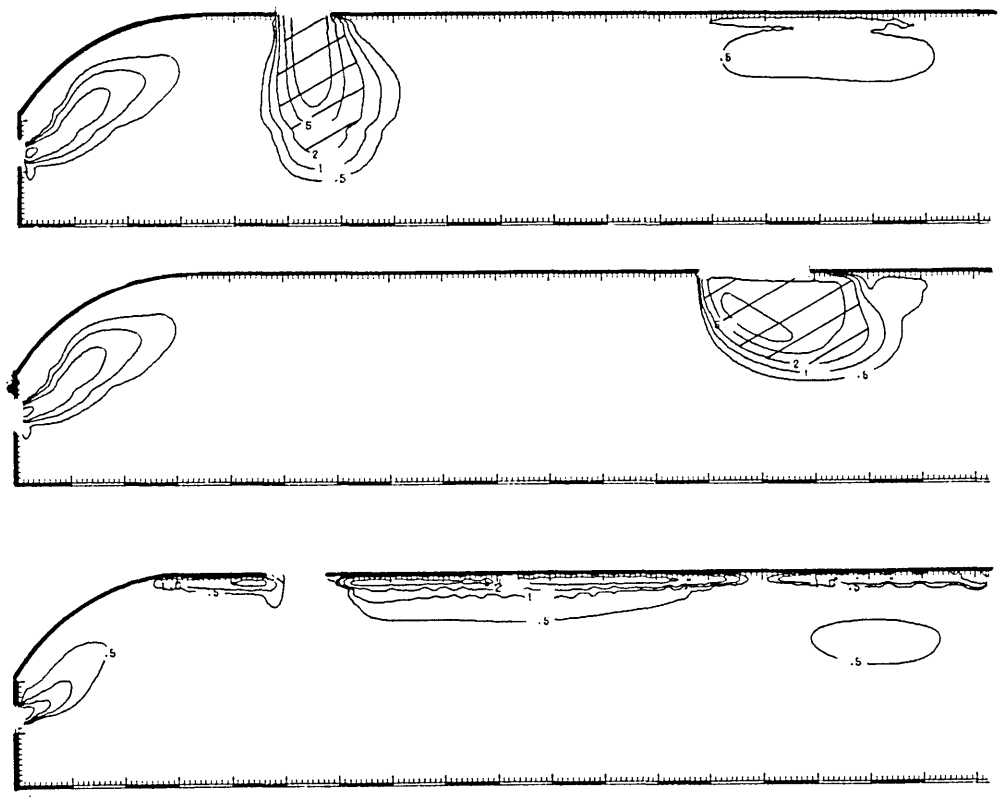


FIGURE 5.36 - Peclet numbers along the radial (Pe_R)and angular (Pe_T) directions in the longitudinal plane containing the axis of the holes (grid 60 × 30 × 22).

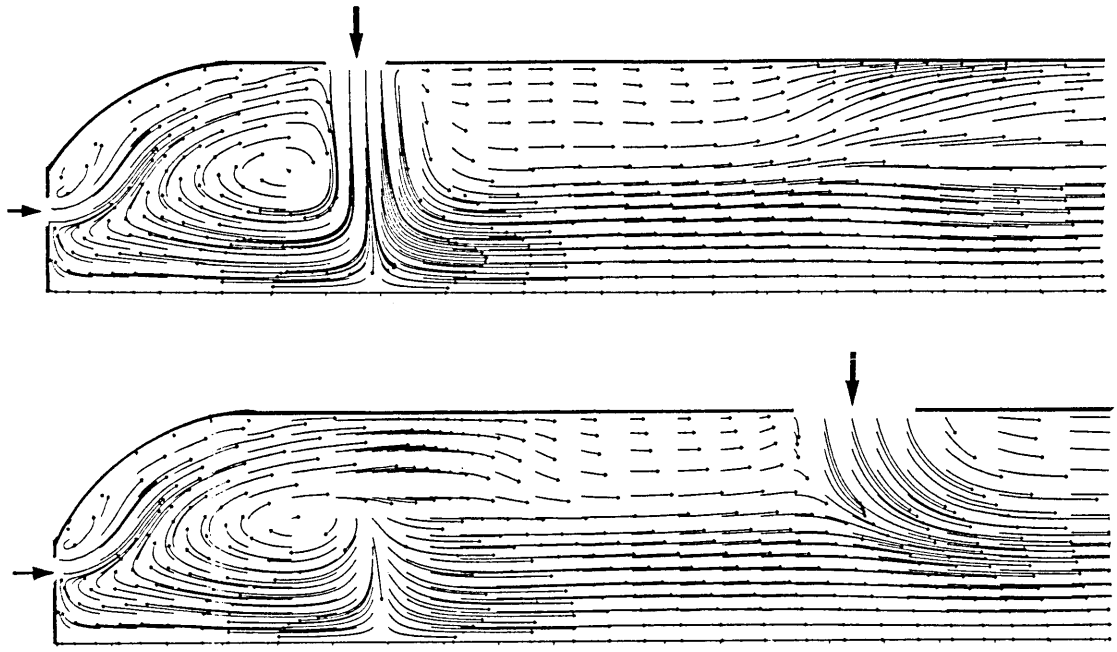


FIGURE 5.37 - Streakline plots corresponding to case 1 - views in the longitudinal planes containing the axis of the holes.

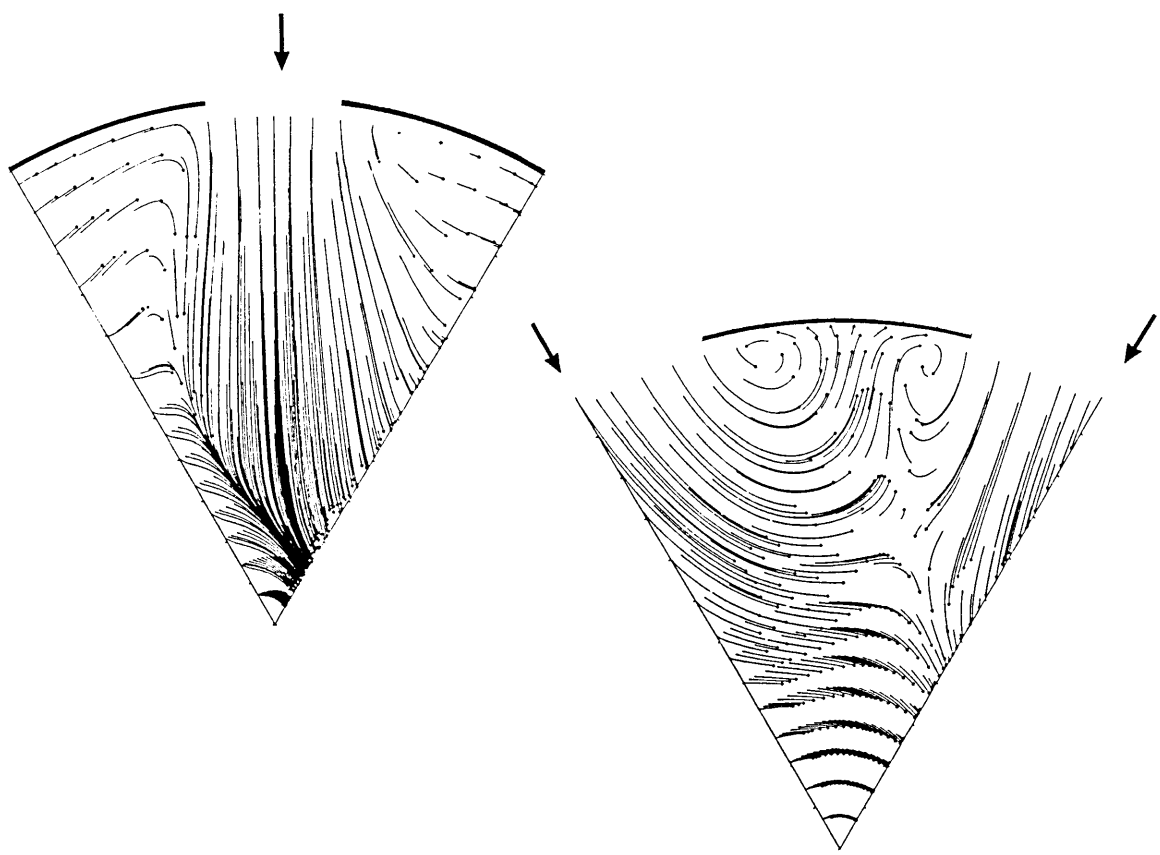


FIGURE 5.38 - As in Figure 5.37, but views in the cross-sectional planes containing the axis of the primary and dilution holes.

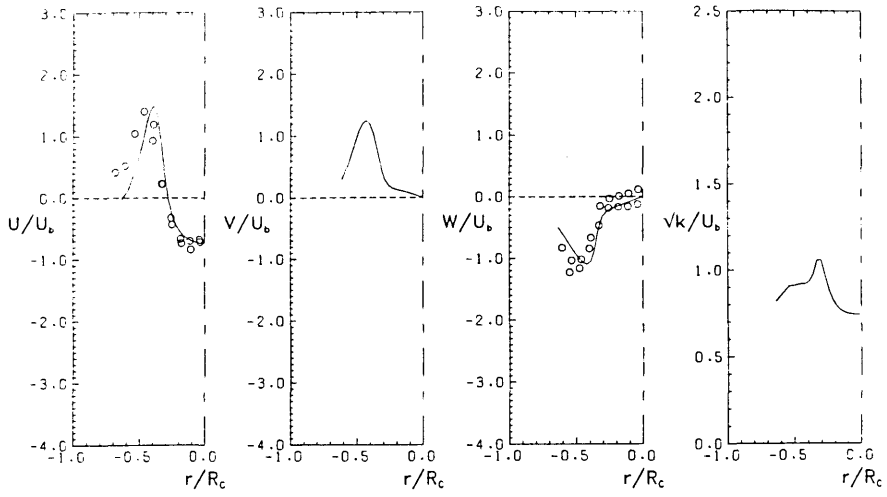


FIGURE 5.39 - Results corresponding to case 1 at Z = 8 mm, θ = 0°.

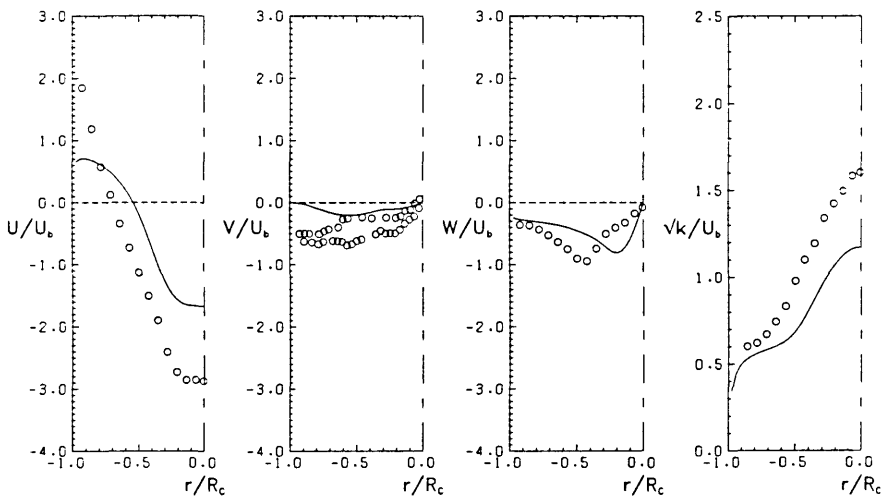


FIGURE 5.40 - Results corresponding to case 1 at Z = 40 mm, θ = 0°.

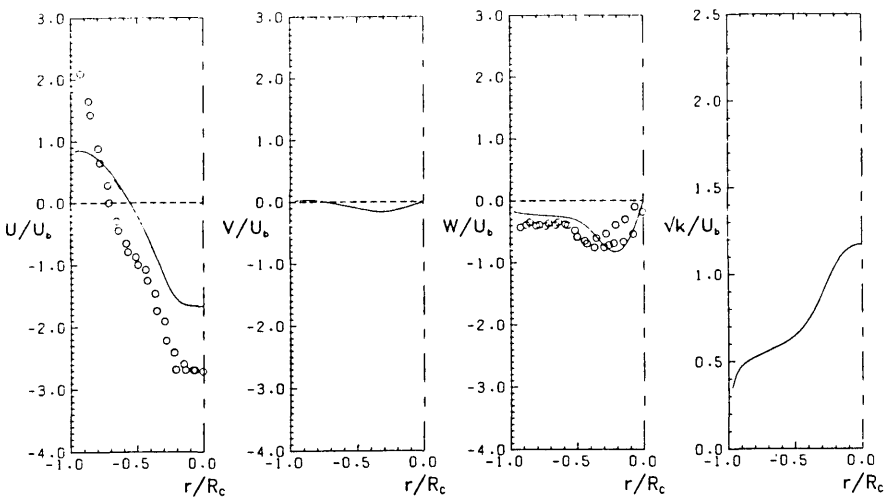


FIGURE 5.41 - Results corresponding to case 1 at Z = 40 mm, θ = 30°.

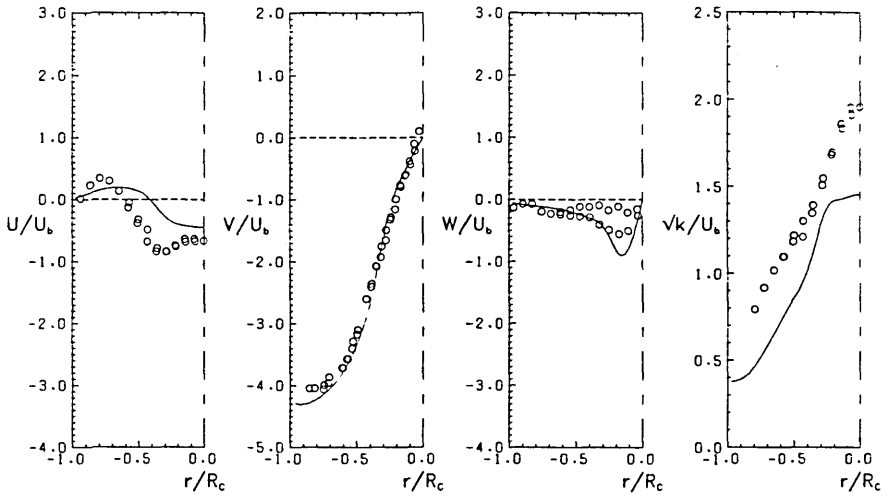


FIGURE 5.42 - Results corresponding to case 1 at Z = 50 mm, θ = 0°.

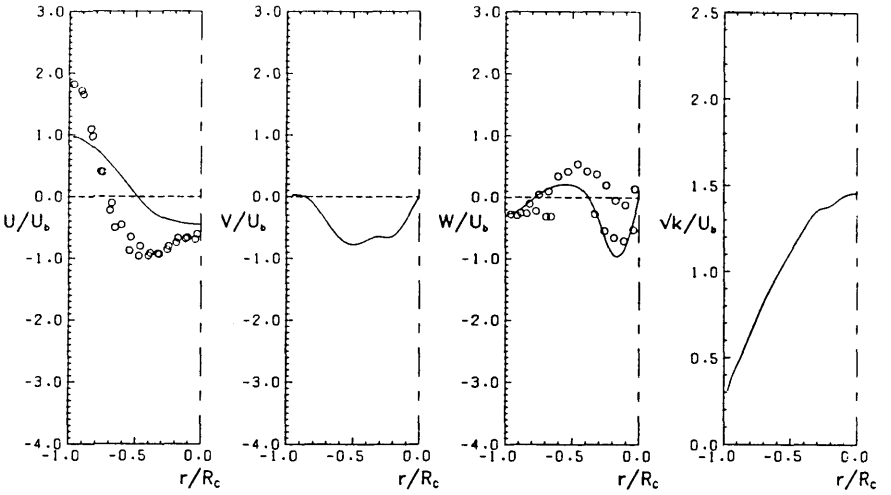


FIGURE 5.43 - Results corresponding to case 1 at Z = 50 mm, θ = 15°.

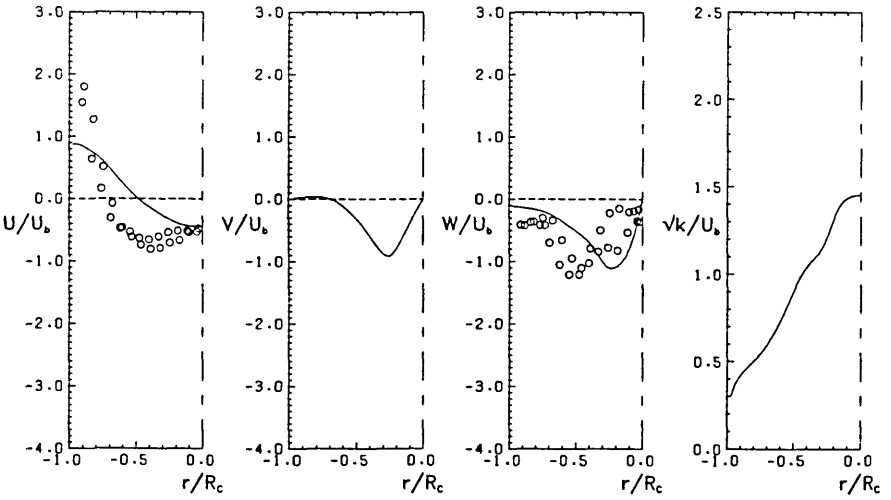


FIGURE 5.44 - Results corresponding to case 1 at Z = 50 mm, θ = 30°.

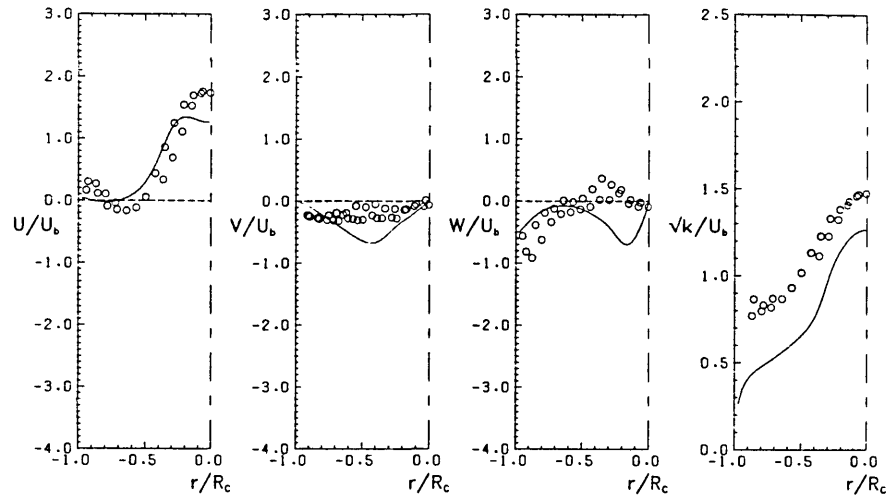


FIGURE 5.45 - Results corresponding to case 1 at Z = 60 mm, θ = 0°.

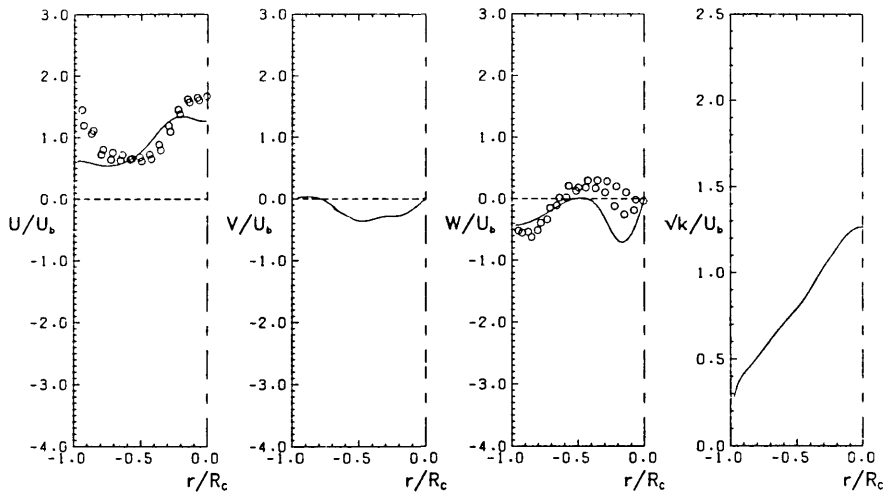


FIGURE 5.46 - Results corresponding to case 1 at Z = 60 mm, θ = 15°.

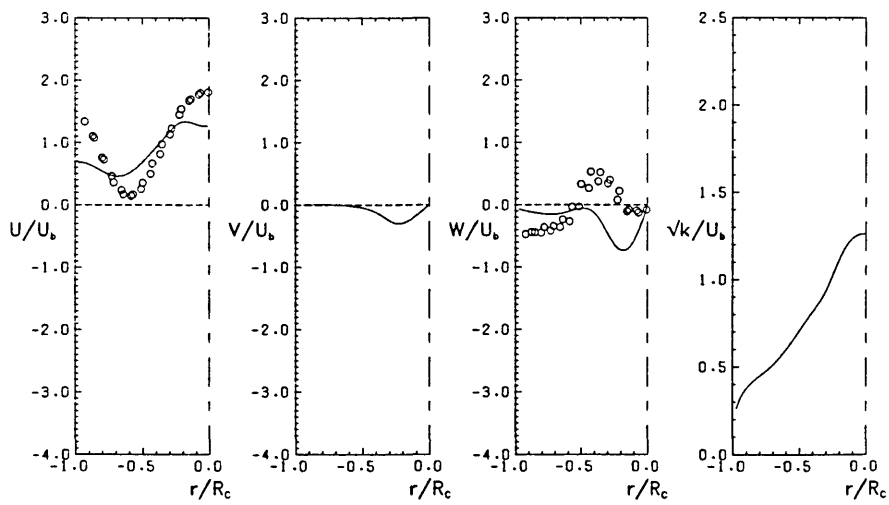


FIGURE 5.47 - Results corresponding to case 1 at Z = 60 mm, θ = 30°.

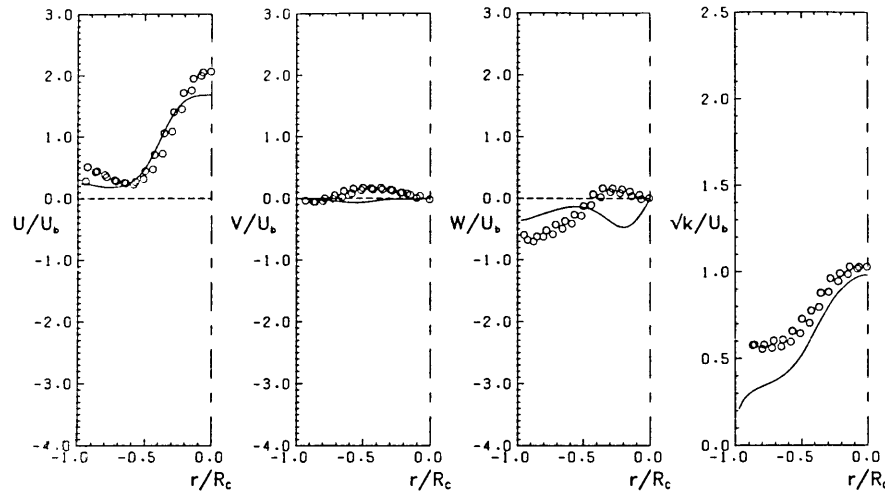


FIGURE 5.48 - Results corresponding to case 1 at Z = 70 mm, θ = 0°.

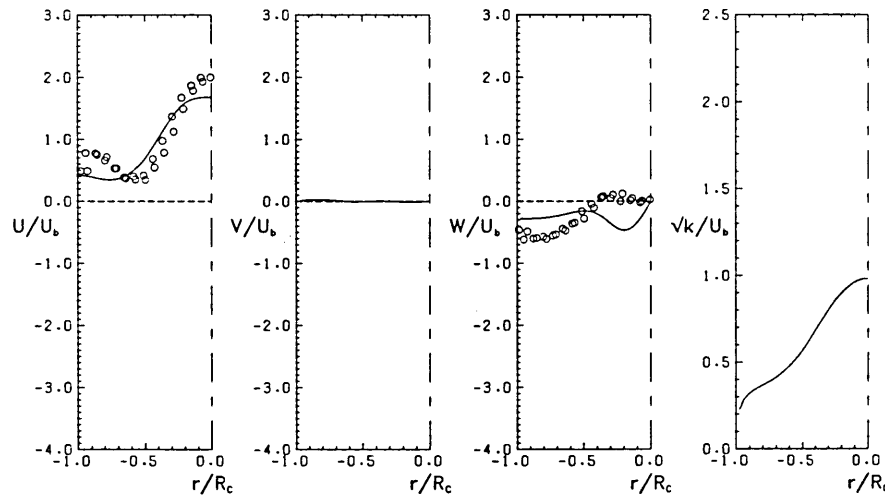


FIGURE 5.49 - Results corresponding to case 1 at Z = 70 mm, θ = 15°.

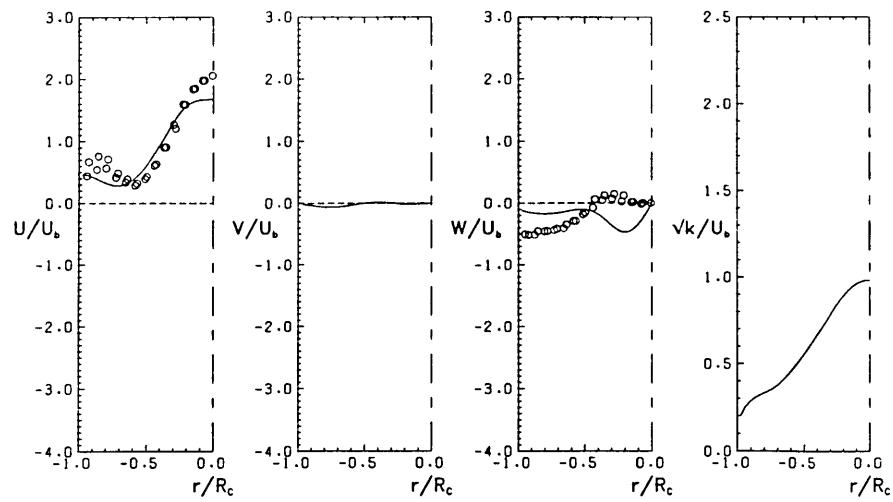


FIGURE 5.50 - Results corresponding to case 1 at Z = 70 mm, θ = 30°.

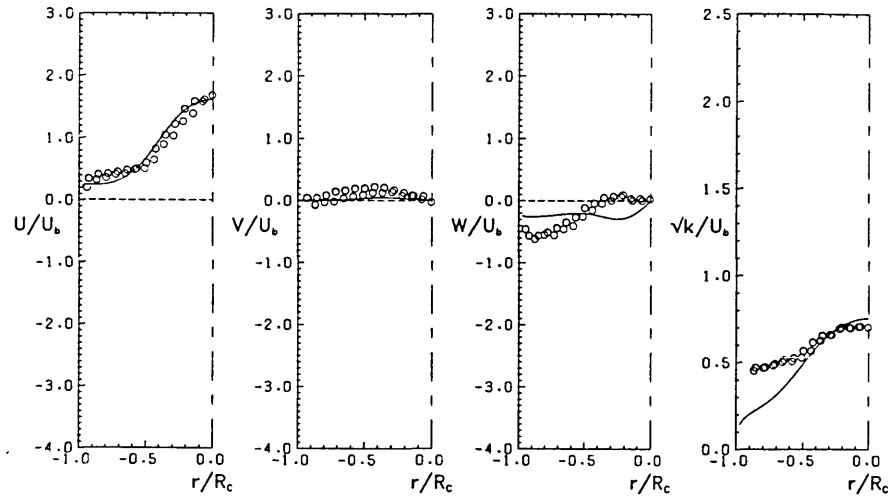


FIGURE 5.51 - Results corresponding to case 1 at Z = 85 mm, θ = 0°.

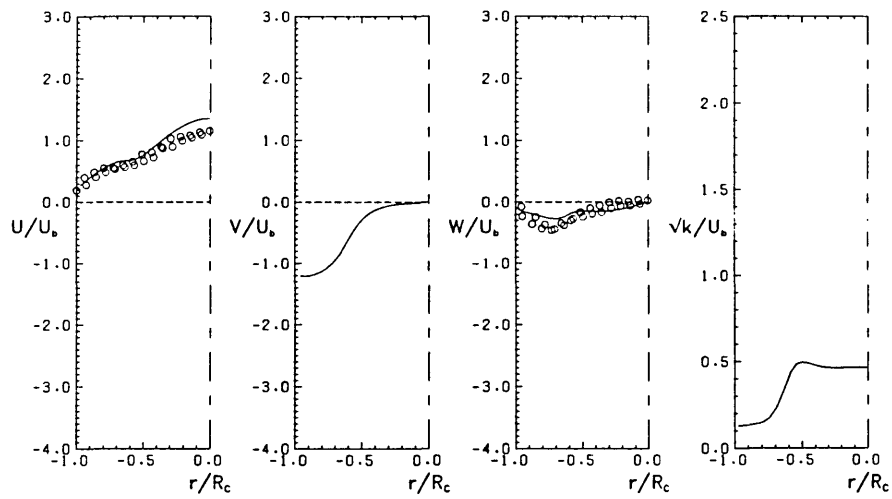


FIGURE 5.52 - Results corresponding to case 1 at Z = 130 mm, θ = 30°.

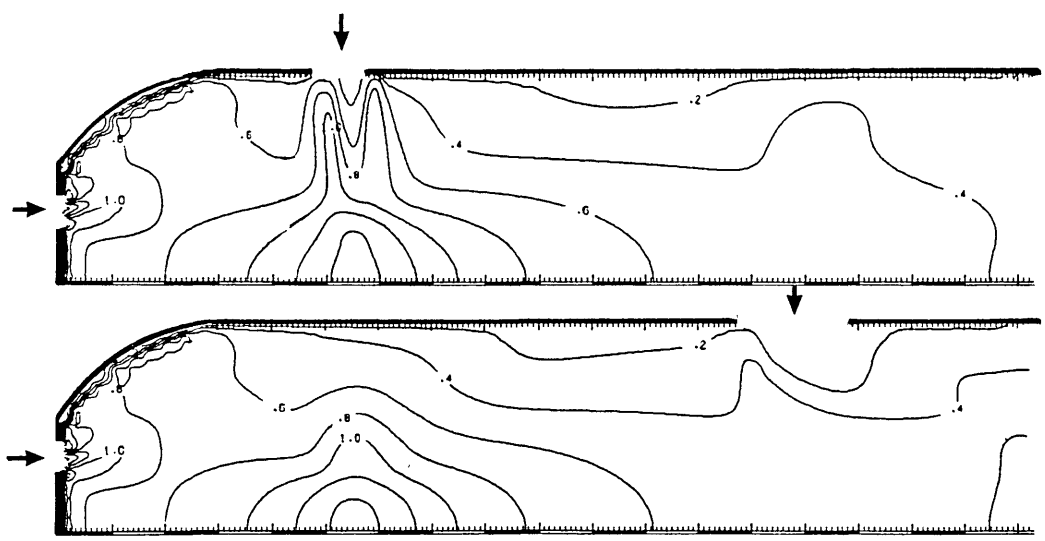


FIGURE 5.53 - Contour plots of turbulence kinetic energy ($\sqrt{k}/U_b$) in the longitudinal planes containing the axis of the holes.

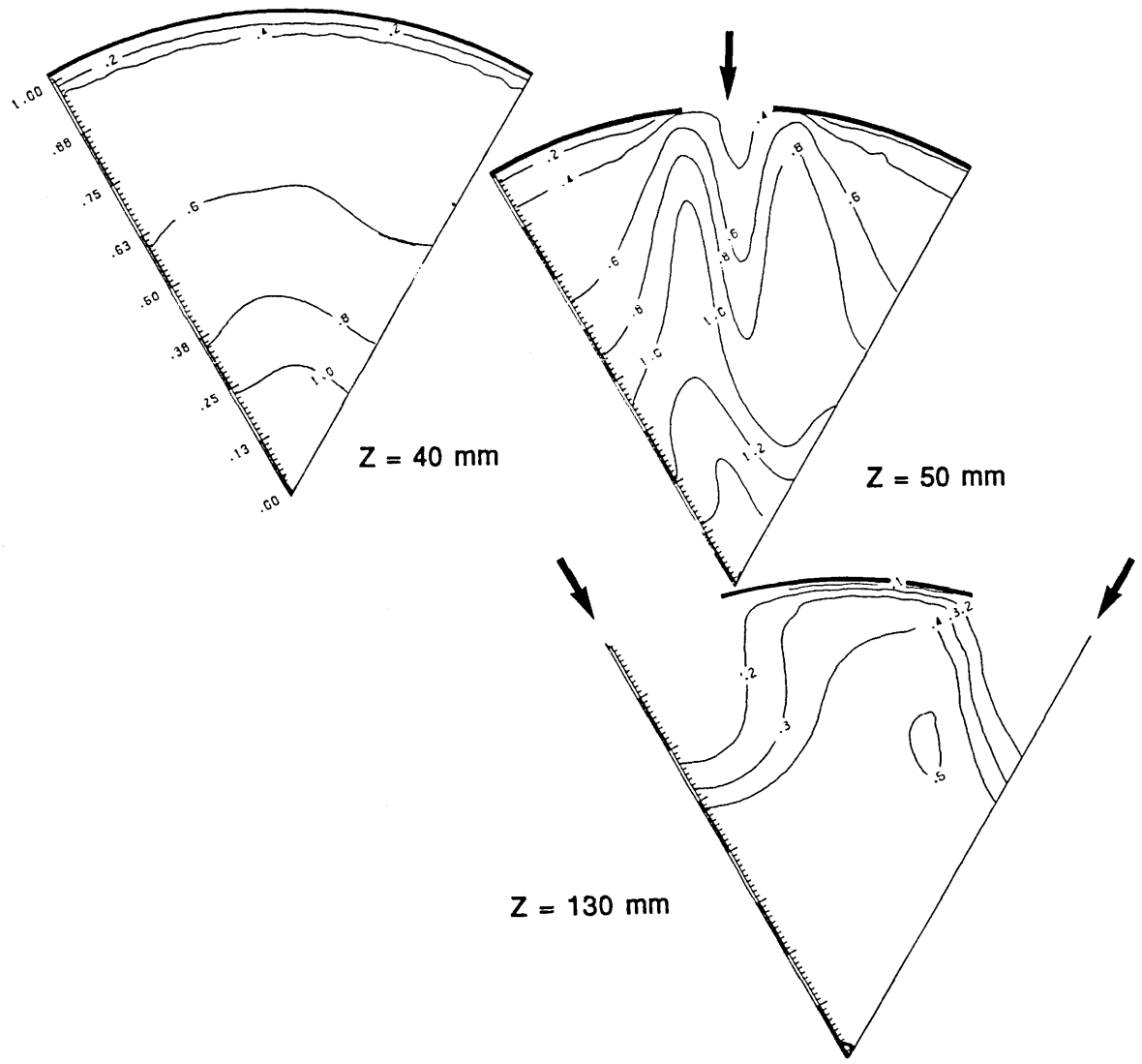


FIGURE 5.54 - Contour plots of turbulence kinetic energy ($\sqrt{k}/U_b$) in the transverse cross-sectional planes.

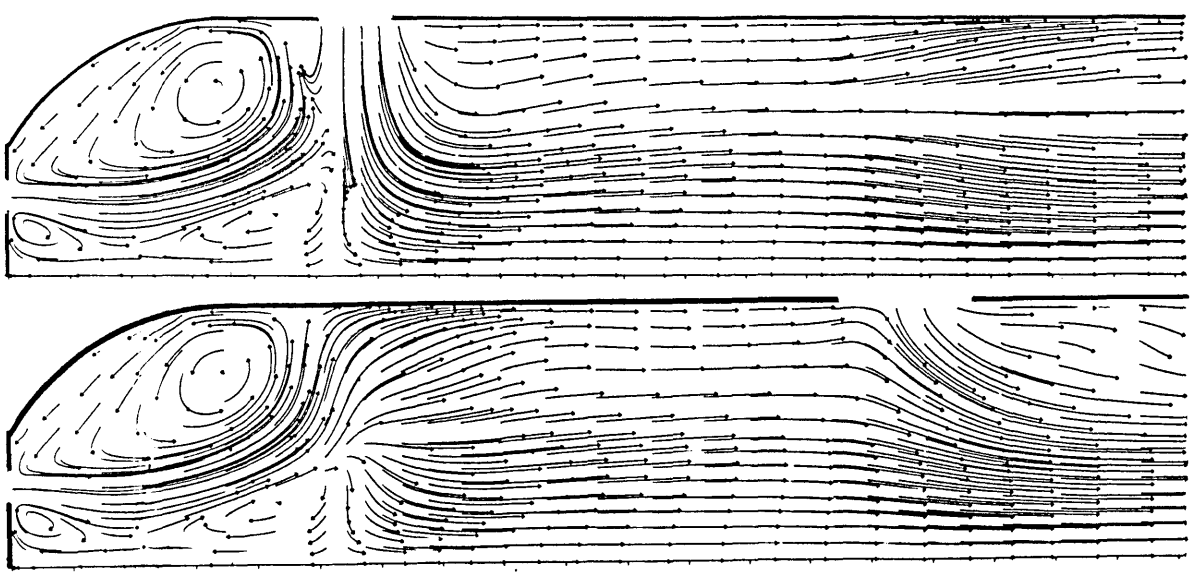


FIGURE 5.55 - Streakline plots corresponding to case 6 - views in the longitudinal planes containing the axis of the holes.

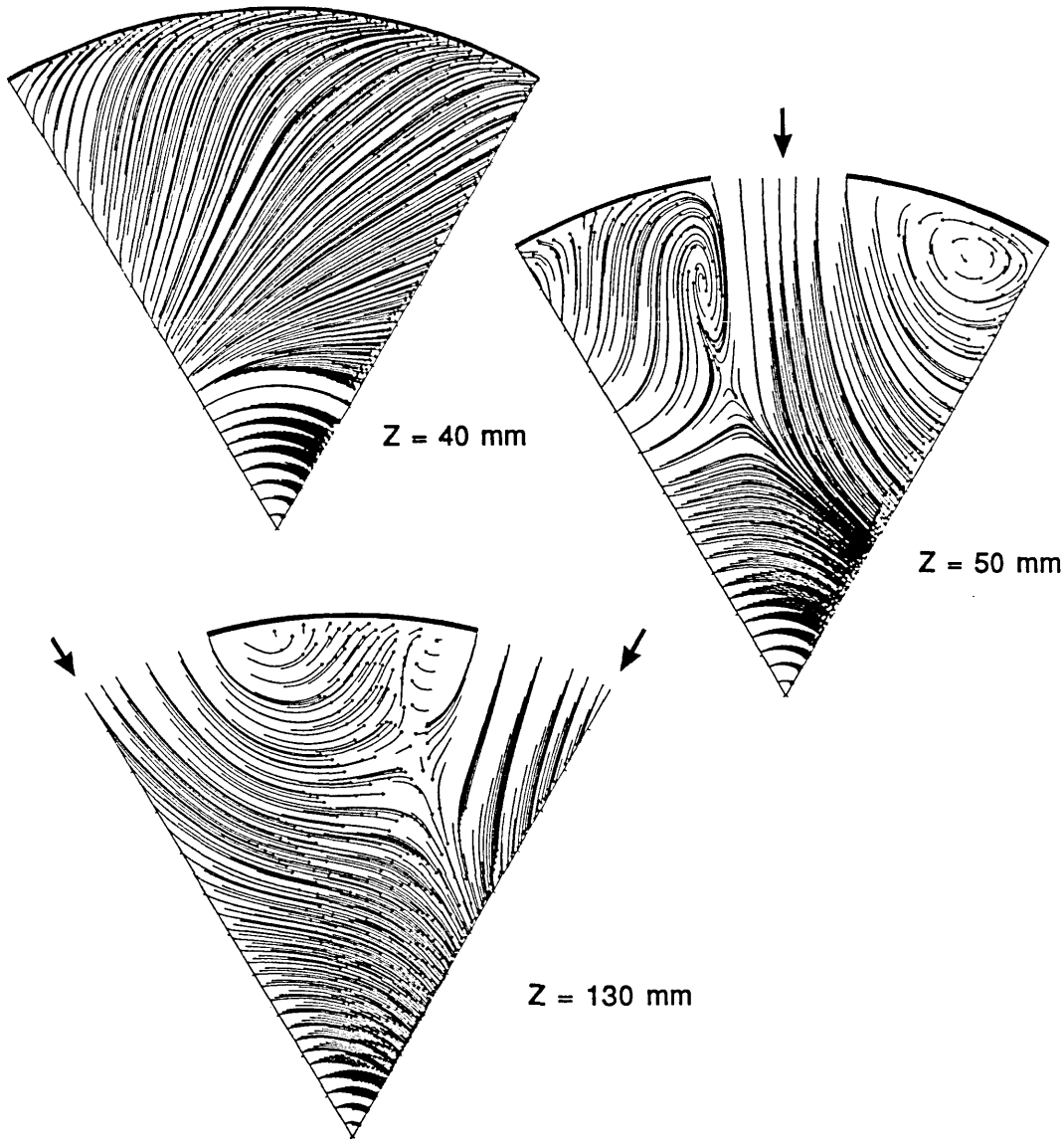


FIGURE 5.56 - As in Figure 5.55 but views in the cross-sectional planes.

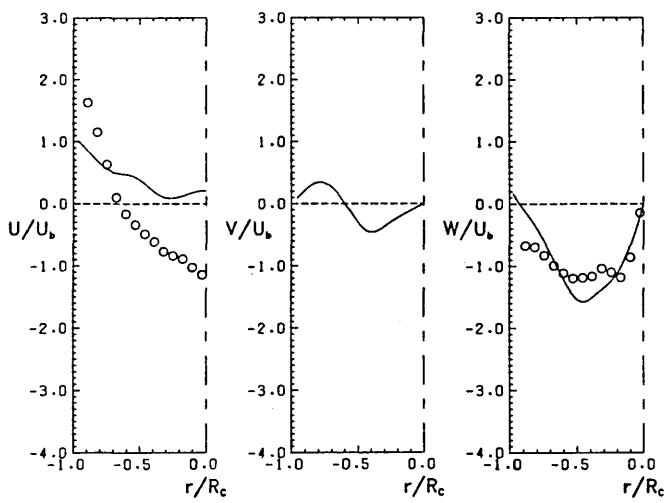


FIGURE 5.57 - Results corresponding to case 6 at Z = 50 θ = 30°.

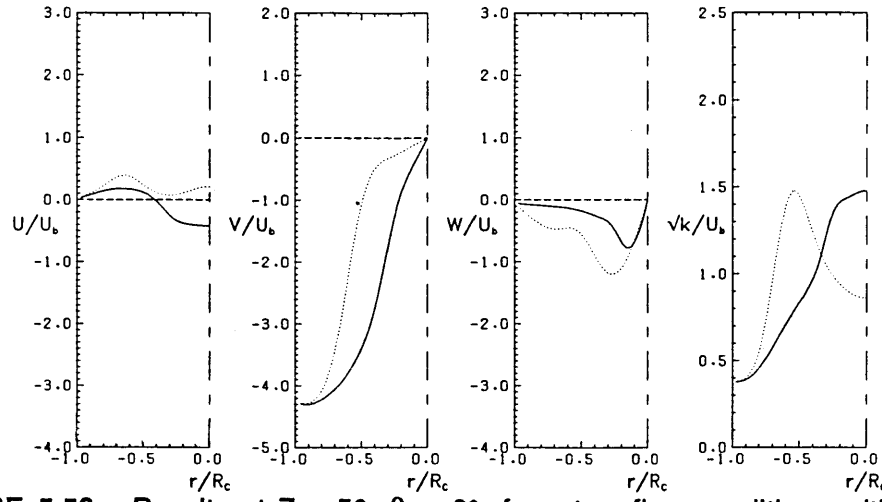


FIGURE 5.58 - Results at Z = 50, θ = 0°, from two flow conditions with different primary to swirler flow ratio:
———— case 1 - $\dot{m}_p/\dot{m}_s$ = 1.92 ---------- case 6 - $\dot{m}_p/\dot{m}_s$ = 1.31.

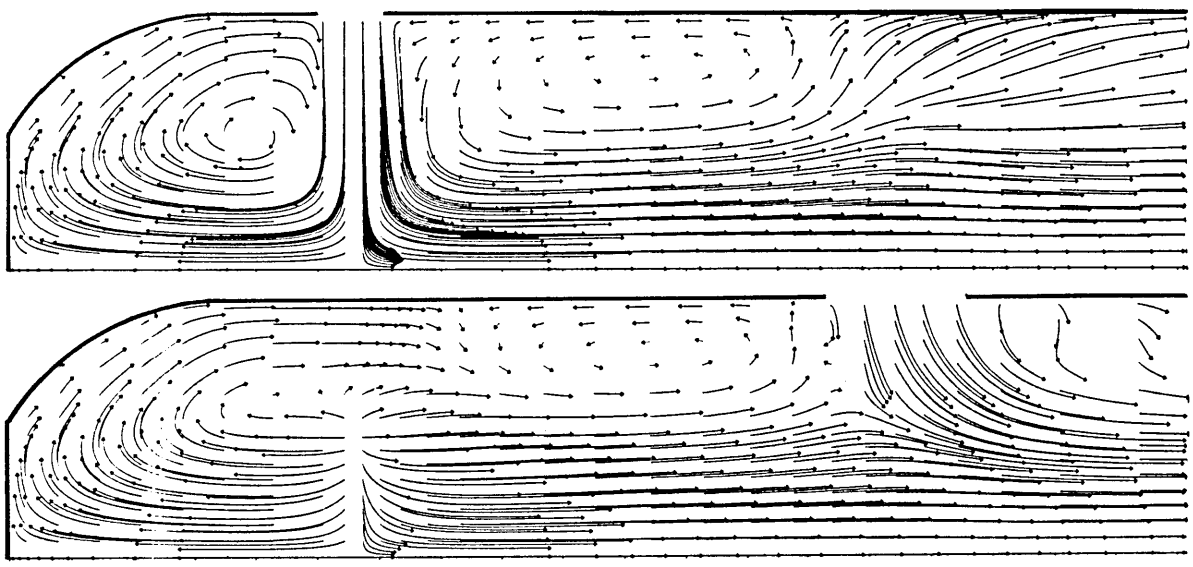


FIGURE 5.59 - Streakline plots corresponding to case 5 (without swirler flow) - views in the longitudinal planes containing the axis of the holes.

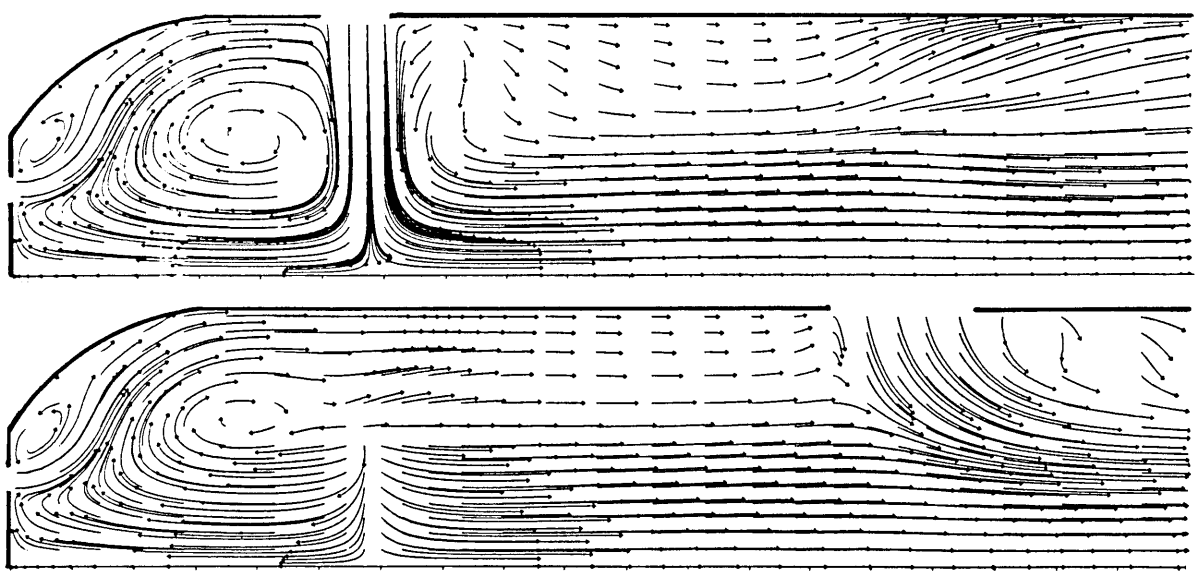


FIGURE 5.60 - Streakline plots from calculations with flow through the swirler gap without swirl component of velocity - views in the longitudinal planes containing the axis of the holes.

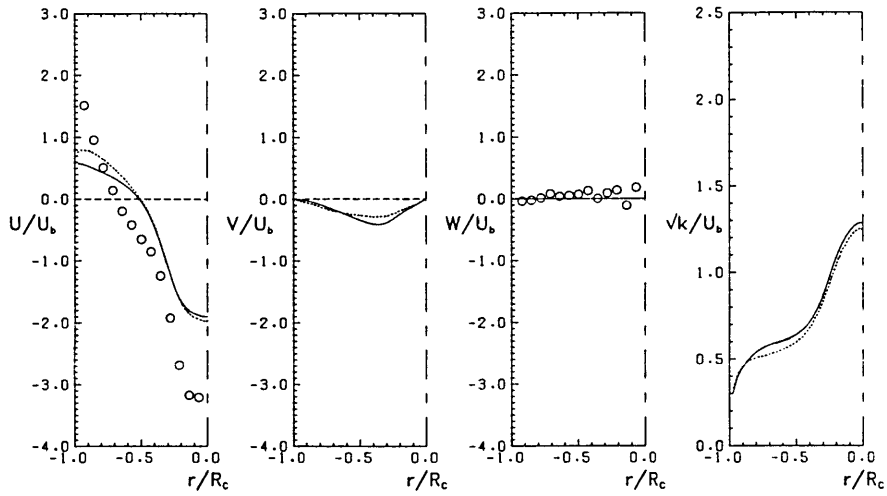


FIGURE 5.61 - Experimental data from case 5 (without swirler flow). Numerical results from calculations without swirler flow (————) and flow through the swirler gap with no azimuthal component of velocity (- - - - - - - - - - - -).

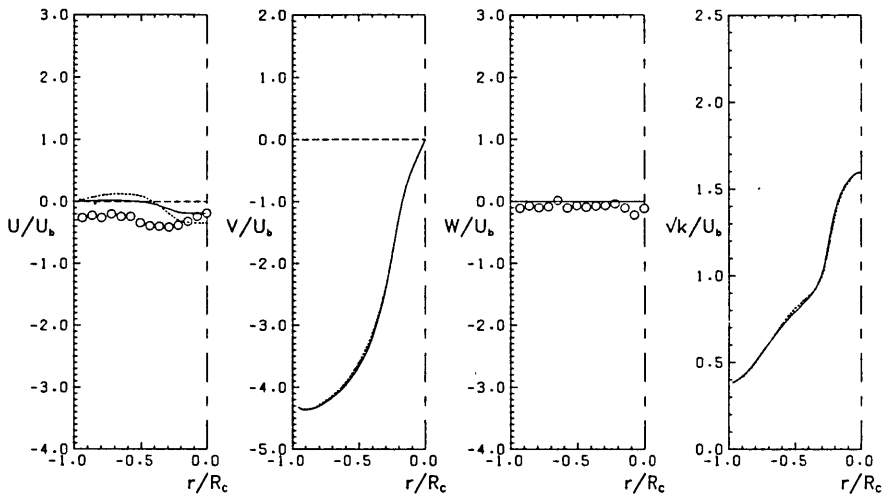


FIGURE 5.62 - Results at Z = 50, θ = 0°, corresponding to case 5.

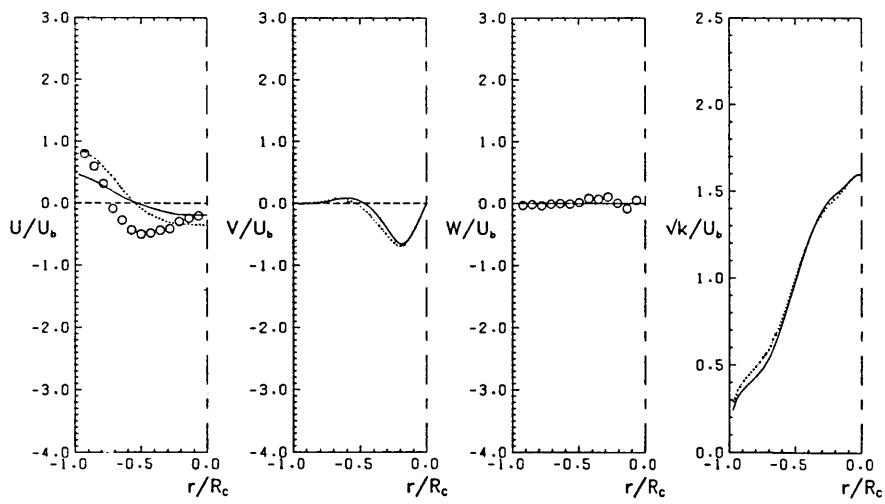


FIGURE 5.63 - Results at Z = 50, θ = 30°, corresponding to case 5.

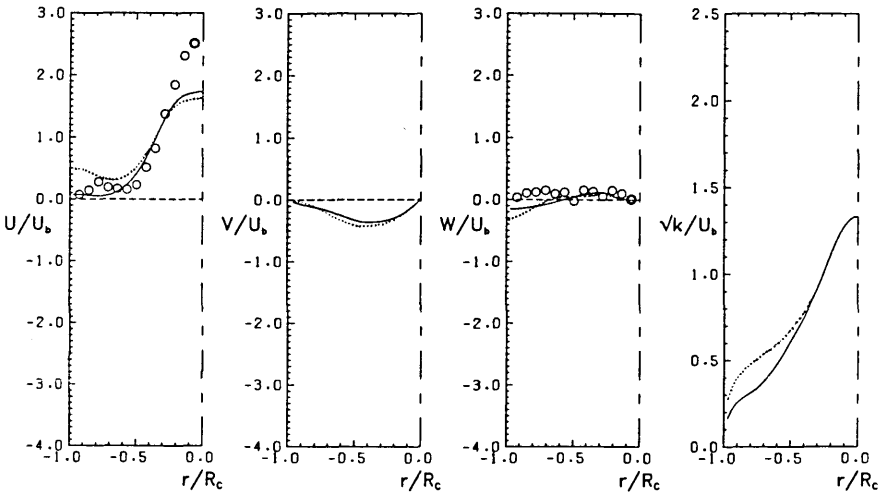


FIGURE 5.64 - Results at Z = 60, θ = 15°, corresponding to case 5.

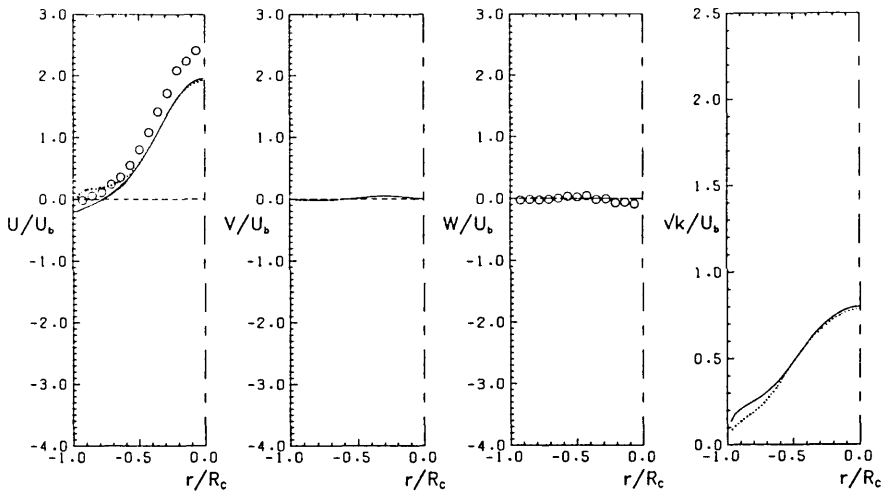


FIGURE 5.65 - Results at Z = 85, θ = 0°, corresponding to case 5.

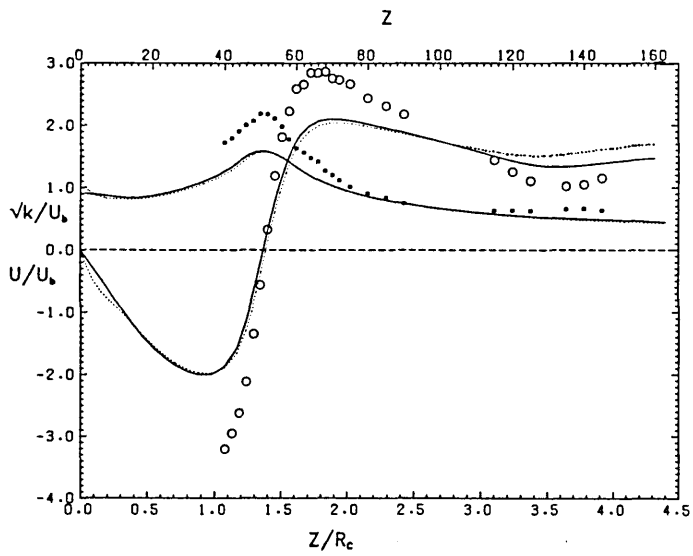


FIGURE 5.66 - As in 5.61 to 5.65 but along the combustor centreline.

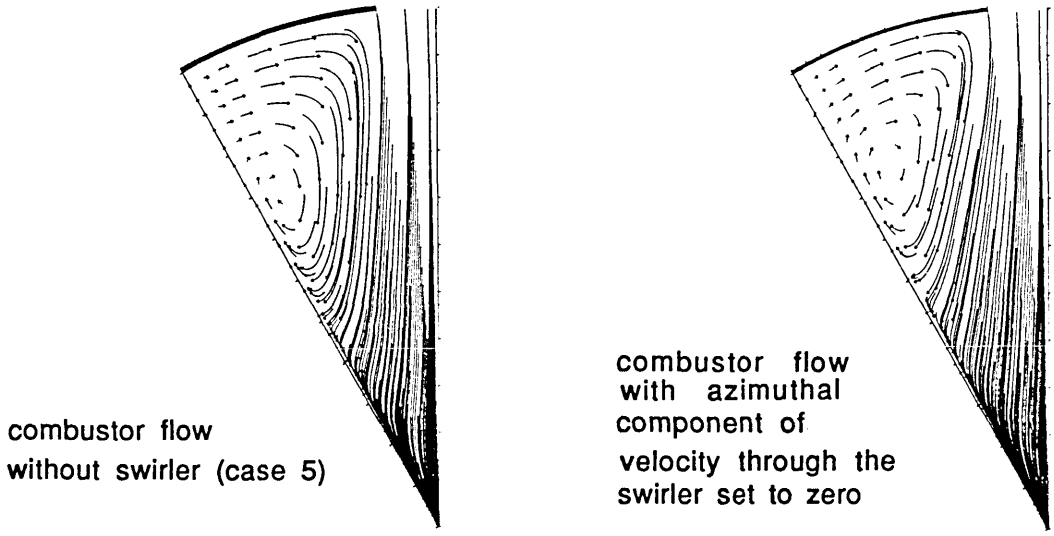


FIGURE 5.67 - Streakline plots from calculations in the planes containing the axis of the primary hole.

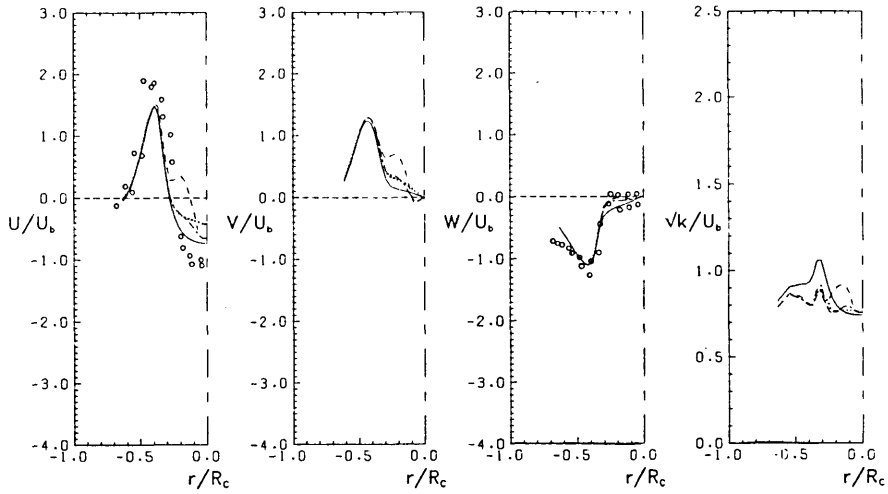


FIGURE 5.68 - Results at Z = 8, θ = 15°, corresponding to case 3 (with simulation of fuel injection).

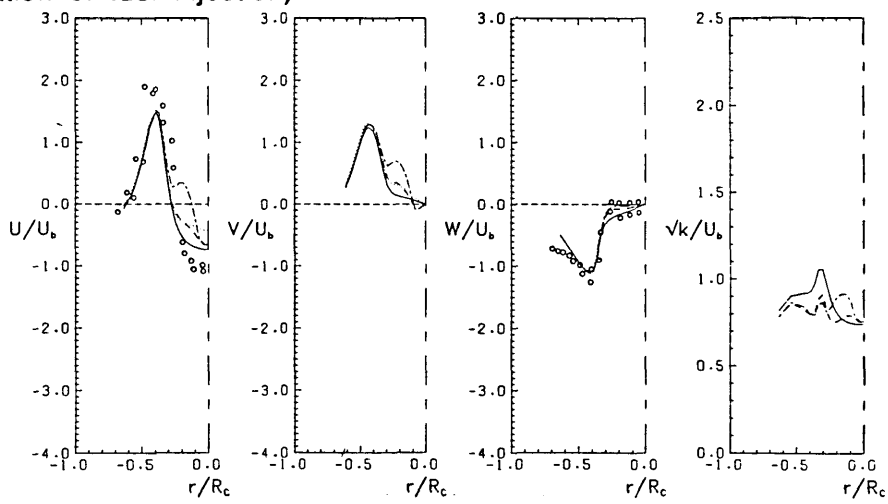


FIGURE 5.69 - As in Figure 5.68 but at Z = 8, θ = 30°:
——— no fuel injection
····· option 1 —·—·— option 2 — — — — — option 3.

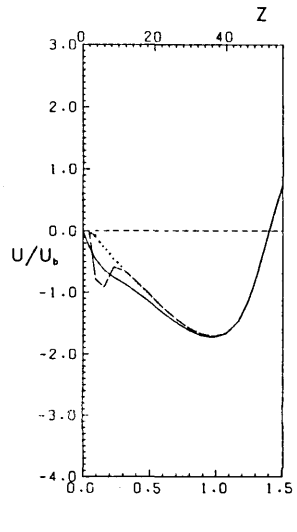


FIGURE 5.70 - As in Figure 5.65 but along the centreline.

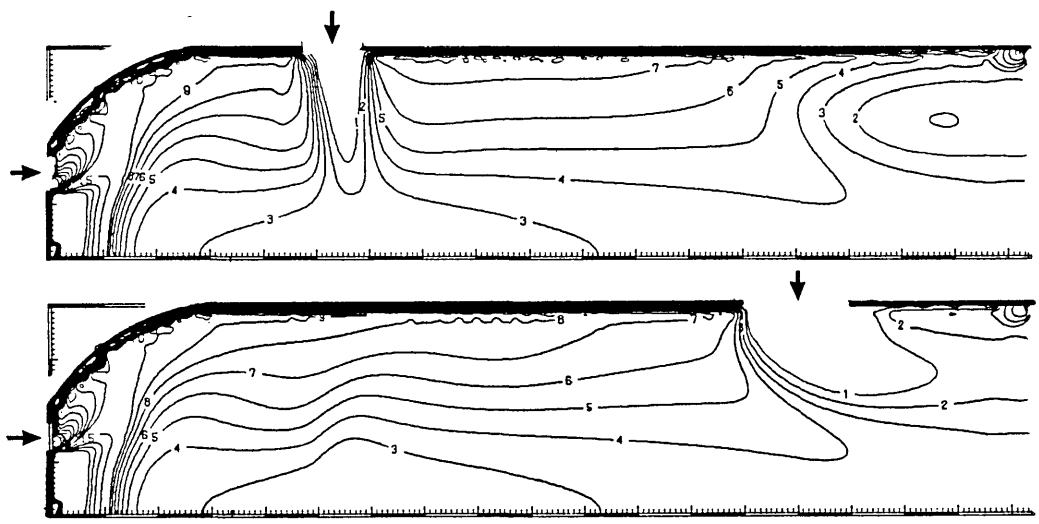


FIGURE 5.71 - Fuel fraction field in the longitudinal planes (option 1).

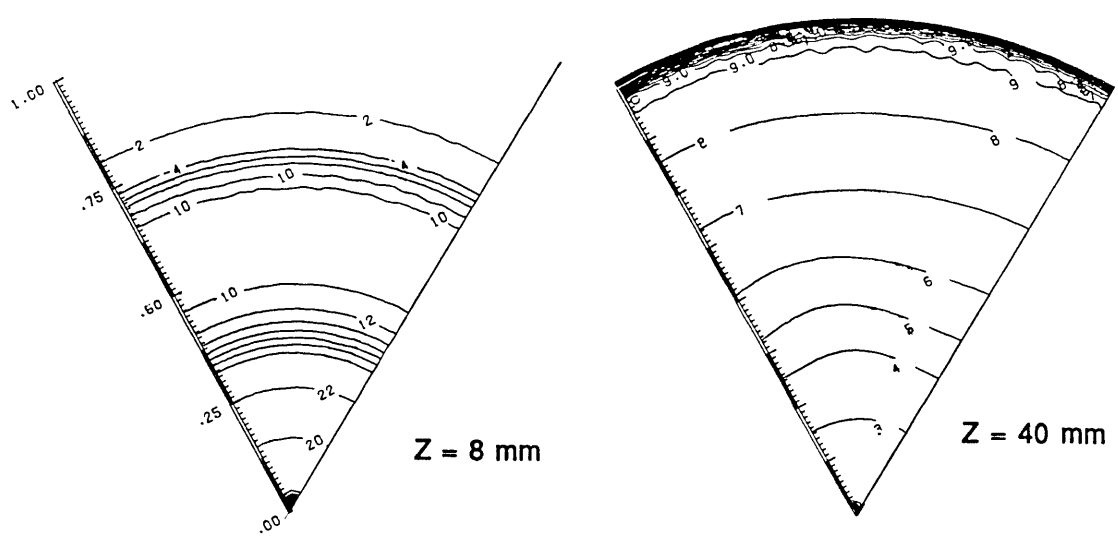


FIGURE 5.72 - As in Figure 5.69 but cross-sectional views.

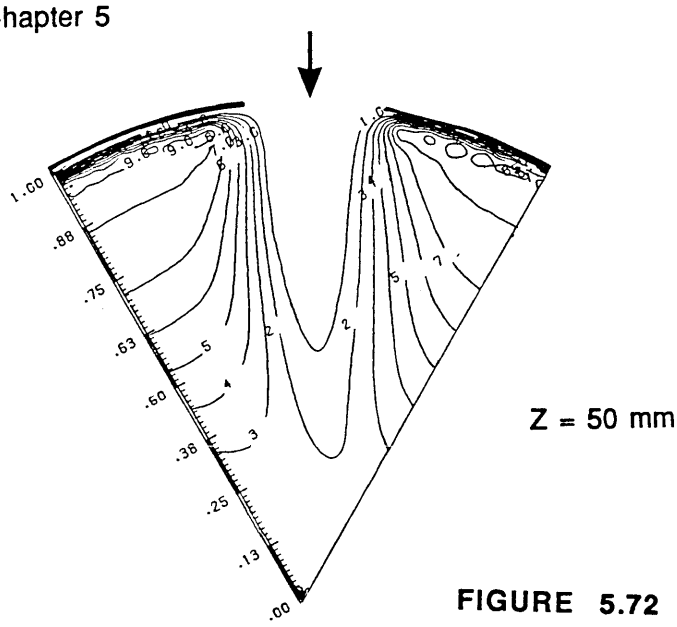


FIGURE 5.72 (continued).

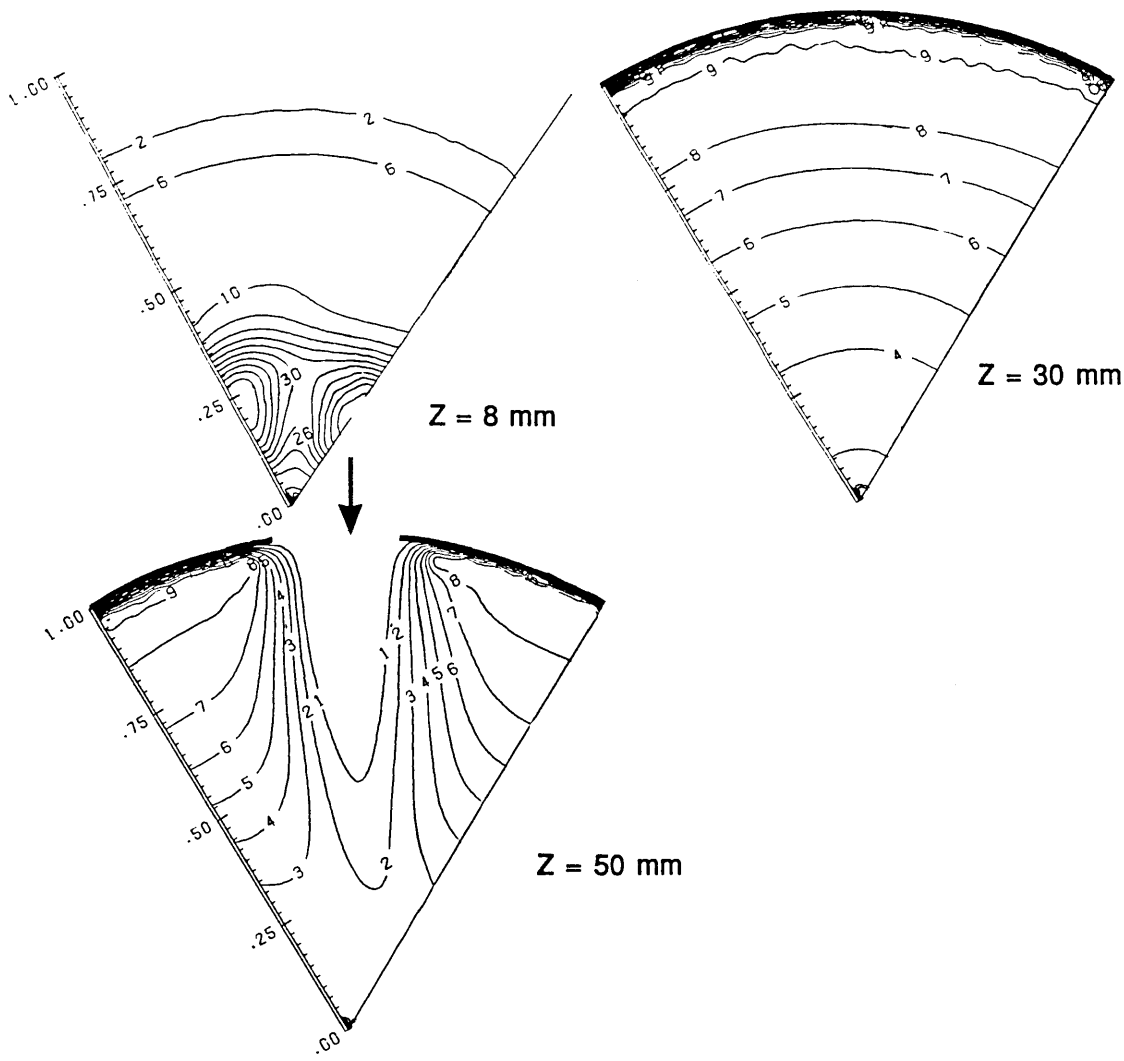


FIGURE 5.73 - Fuel fraction field in the cross sectional planes (option 2).

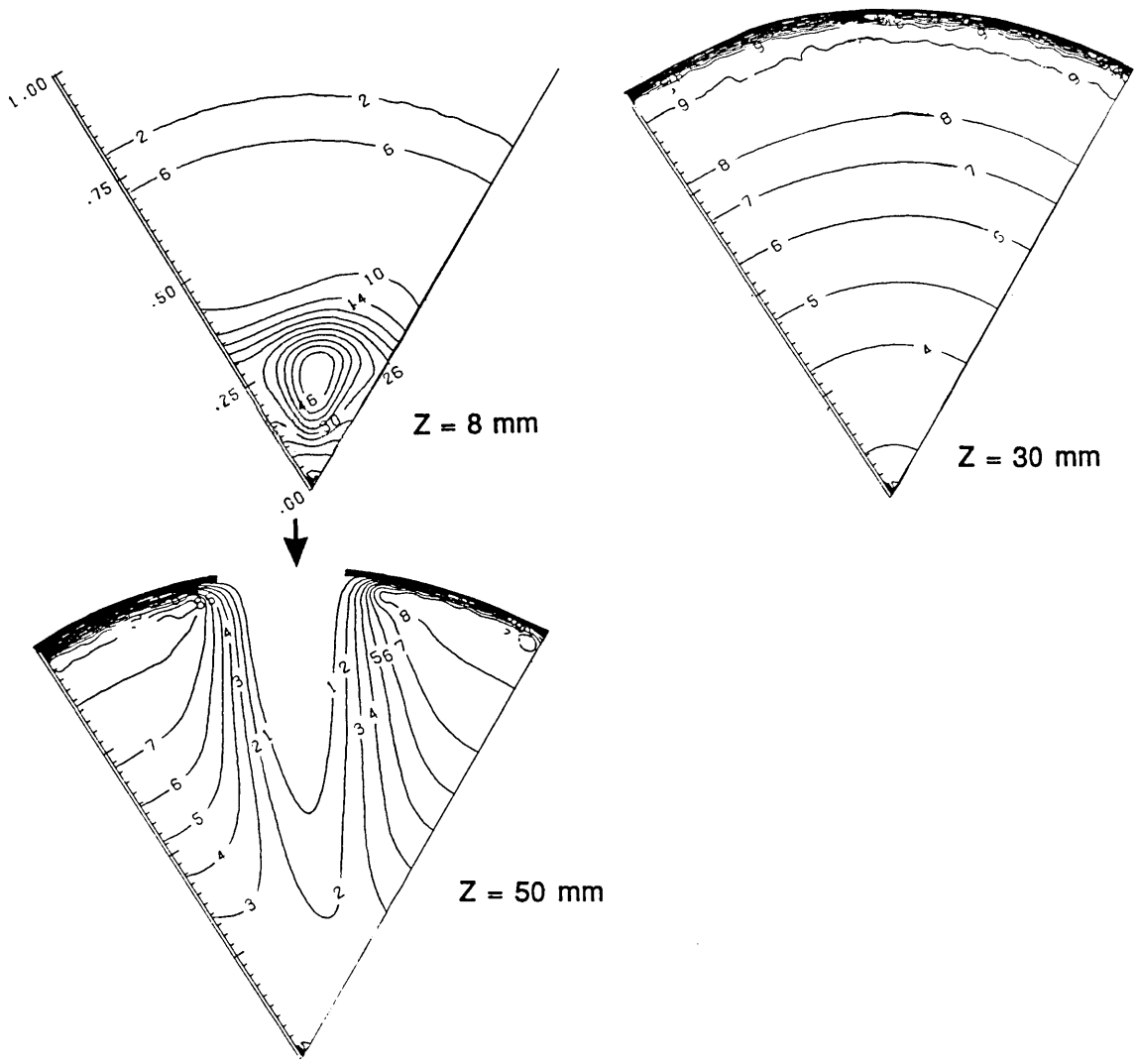


FIGURE 5.74 - Fuel fraction field in the cross sectional planes (option 3).

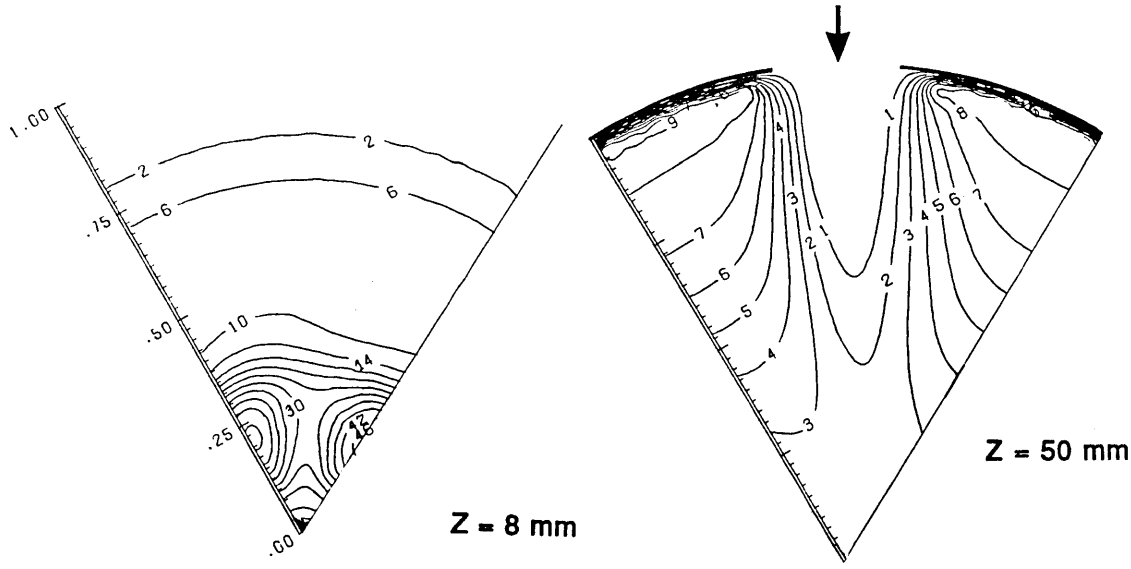


FIGURE 5.75 - As in Figure 5.73 but for a turbulent Prandtl number of 0.7.

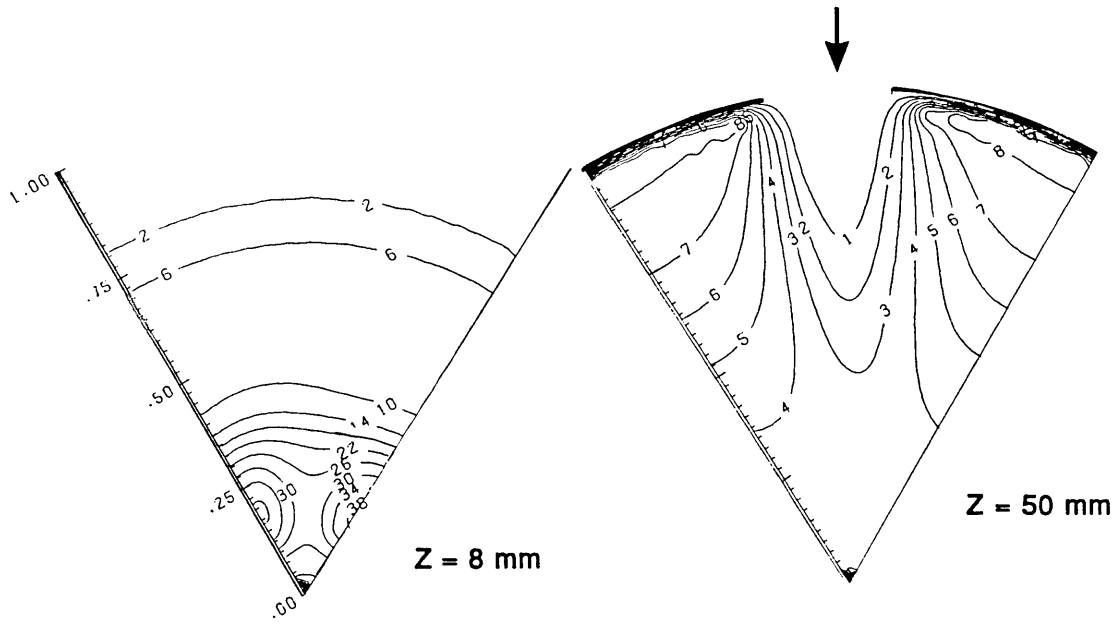


FIGURE 5.76 - As in Figure 5.73 but for a turbulent Prandtl number of 0.4.

CHAPTER 6
CLOSURE

The objective of this chapter is to summarize the main conclusions of the present work and provide suggestions for future work.

6.1 CONCLUSIONS

Experimental

The experimental work demonstrated firstly that a flow pattern similar to that inferred from temperature measurements inside a similar but combusting rig could be obtained under isothermal conditions, provided the ratio between the primary and the swirler flow and the ratio between the dilution and the cross flow were similar in both experiments. The bulk of the velocity measurements were then obtained under these conditions. These measurements showed that the flow in the primary region was mainly set by the impingement of the primary jets. The swirler flow was restricted to the region near the outer wall of the combustor and the region between the primary jets.

The primary jet impingement gave rise to a region of high anisotropy of turbulence where the azimuthal normal stress was twice as large as the axial normal stress. Other characteristics of the azimuthal velocity in this region included a flatness value of around 2.2 and the existence of bimodal PDFs between the primary holes attributed to the merging of the jet shear layers. Spectral analysis confirmed the turbulent nature of this phenomenon with a broad range of frequencies between 10 Hz and 150 Hz with a maximum at 60 Hz.

Flow visualization using high speed photography and laser induced fluorescence revealed the presence of large turbulent eddies originating from the jet flow, which were most evident in case of combustor flow without swirl. The breaking up of these eddies increased with the distance from the primary jets. The flow visualization also supported the statement that, in case of no swirl flow the higher turbulence intensity measured in the region of impingement corresponds to lower mixing compared to the case with swirl flow .

Although the laser induced fluorescence has proven to be excellent for flow visualization purposes, a feasibility study of this technique for measurements of concentration evidenced some difficulties to be overcome in future work. Rhodamine B

was selected as the most appropriate dye for quantitative applications of the laser induced fluorescence on the basis of its characteristics of stability.

Numerical

The performance tests of the several pressure-velocity coupling algorithms showed that the overall convergence of the calculation procedure is dominated by the convergence of the turbulence model equations. More elaborate pressure velocity formulations, e.g. PISO, are beneficial mainly because they allow the use of higher under-relaxation factors and under such circumstances convergence can be achieved in less iterations but not necessarily less CPU time. The higher robustness of this type of algorithms may be more important in situations with an increased number of equations; however under the present conditions the replacement of algorithms with only one pressure correction equation (e.g. SIMPLE) is not recommended.

A large proportion of the CPU time per iteration is spent solving the set of simultaneous linear equations. Reduction of the global CPU time was obtained by reducing the number of sweeps in TDMA, i.e. solving the equations to a less stringent criterion of convergence. This would sometimes result in a higher number of global iterations but the global computing time was still reduced. This showed that the coupling and the nonlinearity between the equations is the factor delaying convergence, not the accuracy to which the equations are solved at each global iteration. The usefulness or the need for better algebraic solver techniques as a means of reducing the computing time is thus questionable, since they will always be more time consuming than the simple TDMA, used in the present tests.

The calculations of the flow inside the water model showed that the boundary conditions in the plane of the primary holes were determinant, particularly the radial velocity. The fine grid calculations led to the use of central differencing in a large proportion of the integration domain and a study could be made of the effect of the boundary conditions and other geometrical simplifications imposed by the use of a cylindrical polar system of coordinates. The remaining discrepancies between the numerical and experimental results are believed to be caused by deficiencies inherent to the turbulence model k-ε. These were, in summary, an underprediction of the levels of turbulence in the primary region and a solid body rotation type of flow throughout the combustor. The high levels of diffusion of momentum observed through the smoother velocity profiles compared to the measurements contrasts with the lower diffusion observed in the calculations of the dilution zone system of the annular combustor. In this case the overall temperature pattern factor at the outlet of the combustor was underpredicted by 100%, even with a reduction of the turbulent Prandtl number from 0.9 to 0.5.

The real possibility of obtaining numerically accurate solutions of gas turbine combustor like flows is a major conclusion of the present work and opens the way to further development and calculations with more elaborate turbulence models.

6.2 SUGGESTIONS FOR FUTURE WORK

Numerical

Efforts should be made towards the development of a more accurate modelling of the mixing processes inside the combustor. This can only be achieved using a higher order turbulence closure, i.e. Reynolds stress and scalar flux modelling, which may also be the right direction to move given the difficulties of predicting the primary region set by the primary jet impingement. This should be preceded by real time dependent calculations involving the whole 360° of the combustor to asses the validity of the symmetry boundary conditions and ascertain the probable capability of the present mathematical model to predict the jet impingement behaviour.

The higher complexity of the turbulence model and probably the extension of the integration domain to include the annular flow will cause an increase of the storage requirements and may deteriorate the spatial resolution relatively to that achieved in the present calculations. This, however may be alleviated by calculating the combustor flow in separate modules where the system of coordinates and the turbulence model may vary according to the region to be resolved. Such approach is not possible in case of the time dependent calculations mentioned above and this may reduce the spatial resolution of the grid to a level where the jet behaviour cannot be resolved.

Reductions of the computing time involved in the calculation of combustor flows may occur through algorithms providing a stronger coupling between the complete set of equations (momentum, pressure and turbulence model), not only between the pressure and the velocity, and probably enabling a more frequent update of the coefficients or even the abandonment of their linearization, which are ultimately responsible for the convergence of the calculations. The current knowledge and numerical techniques are based on calculations with a single equation of transport (not a set of coupled transport equations). If more efficient numerical techniques to solve the fluid flow equations have to be found, a fundamental study of the relationships between the equations has to be made. This of course can only be made by numerical experimentation and the conclusions may be restricted to the test case selected. Although such study is needed it is however very unlikely to bring, at least in a short term basis more benefits than the rewriting of the available software for calculations

in parallel computing machines. This undoubtedly has to happen at some stage to follow the present trends of computer hardware development.

Experimental

On the experimental side the water rig should be redesigned with provision for monitoring of each flow entry to the combustor and a new injection system enabling the injection of very small amounts of dye as required for the laser induced fluorescence technique. The calculations showed the importance of the boundary conditions, particularly in the inlet plane of the primary jets, and to enable measurements in these planes and also measurements of shear stresses the new rig should be designed by keeping in mind the possible future use of a refractive index matching technique.

There seems to be no detailed experimental study able to assist the development and test of scalar flux models in gas-turbine combustor geometries and an experimental program should be undertaken for which the development of the techniques for measuring concentration initiated in the current work should also be continued. A simpler geometry compared to the combustor used in the present work should be used for development of these techniques.

As mentioned in the Introduction in Chapter 1, developments are needed in many areas for an increased understanding of the phenomena occurring inside gas turbine combustors. The aspects mentioned above suggest some of the possible directions to be followed.

APPENDIX A
A FEASIBILITY STUDY OF LASER-INDUCED FLUORESCENCE (LIF)

A.1 INTRODUCTION

The main objective of this appendix is to describe the present status of development of the laser induced fluorescence (LIF) technique and to assess its potential for scalar field measurements in water model combustor flows. Preliminary results using this technique were obtained in a very simple configuration which enabled identification of not only the potential, but also the main difficulties of using LIF. These difficulties were then confirmed in an attempt to use the technique in the combustor model; the completion of this feasibility study allowed suggestions to be made for the development of the system to enable its future application to combustor flows.

The appendix contains five main sections. Firstly, in Sections A.2 and A.3, a brief review of the previous related work and basic principles of fluorescence is made. Section A.4 discuss the experimental results, followed by the conclusions and recommendations for future work in Section A.5.

A.2 REVIEW OF PREVIOUS WORK

Measurements of concentration by induced fluorescence effects is a common technique in the analytical chemistry field, where it is referred to as fluorescence spectroscopy. For an introduction to the physics of the technique, several textbooks are available: Parker [1968] deals with photoluminescence in general, and Guilbault [1973] and, more recently, Lakowicz [1983] deal with fluorescence only. For a collection of experimental procedures, see Miller [1981]. In the fluid mechanics context, the first quantitative application of this technique was presented by Owen [1976], who measured the concentration and velocity of two coaxial jets discharging into a sudden expansion; this flow was also studied by Johnson and Bennett [1981]. Roback and Johnson [1983] used a similar geometry but with an outer swirling jet. In all of these works, laser-induced fluorescence is presented as a relatively simple technique and no considerations were given to complications due to effects such as undesirable light absorption or curved surfaces. Durst and Schmitt [1984] were the first to address these experimental difficulties and discuss the need to match laser power and dye concentration. Other works include Dimotakis, Miake-Lye and Papantoniou [1983], Koochesfahani and Dimotakis [1985] and Papanicolaou and List [1984]. From the

various works mentioned, no unanimous choice has emerged on which dye is most appropriate, nor at what range of concentration a particular dye should be used. The question of selecting a dye seems to have been largely ignored except by Stevenson, Santos and Mettler [1976], who made some tests on the relative fluorescence intensity and stability of various combinations of dye and solvent. Fluorescein is the most commonly used dye, but Owen [1976], Johnson and Bennett [1981] and Durst and Schmitt [1984] have used it in absolute concentrations of 0.4 mg/l, 2 mg/l and 0.001 mg/l, respectively. In terms of optical considerations, Durst and Schmitt [1984] considered the absorption of light across the test section caused by fluorescence and introduced a second photomultiplier to monitor this, while all the others seem to have ignored this problem. Clearly, the absorption of incident light is a function of the optical path length and transmissivity of the medium, but if corrections due to absorption have to be made because of high concentrations of fluorescent material, then the characteristics of the fluorescence technique, and its main advantage (the linear response of intensity of fluorescent light to concentration) relative to any absorption-based technique, is lost. Also, all the books on fluorescence spectrometry quoted above, point out that it is always possible to bring the levels of concentration to values where the absorption can be made negligible. Disagreement on the levels of concentration is expected, given the differences in geometries, instrumentation and instrument settings. Usually, the laser power used, efficiency of the optics and voltage of the photomultiplier supply are never mentioned and, as shown below these are very important determinants of the signal intensity.

A.3 BASIC PRINCIPLES OF FLUORESCENCE

The fluorescence phenomenon involves a molecular process with a transition between different electronic states and is a non-elastic process: the frequency of the emitted light is different from the frequency of the absorbed light. Photoluminescence phenomena are classified into three different types: fluorescence, phosphorescence and delayed fluorescence. The energy diagram, in Figure A.1, provides the basis for a differentiation of these three.

The electronic state of an electron is defined by its spin, S, which is +1/2 or -1/2, and the orbital momentum of a given electronic state is defined by: M=2S+1, where M is the multiplicity. For an electronic state with two paired electrons (spins of +1/2 and -1/2), the multiplicity is 1: a singlet state. For an electronic state with two unpaired electrons (e.g. spins of +1/2 and +1/2), the multiplicity is 3: a triplet state, T.

If the molecule is excited by a photon of light, a transition with absorption of light energy can occur from the singlet ground state, S_0, the highly populated state, to any of the various vibrational levels associated with any of the singlet excited electronic states (transition from the ground to a triplet state is, from a quantum mechanics point of view, 'forbidden' or highly improbable). Once in a higher energy level, the molecule will tend to reduce its energy by internal conversion, moving to lower energetic states in the same singlet state: a radiationless process with a lifetime of about 10^{-12} s and less than necessary for a return to the ground state again. The time between the excitation of the molecule and the return to the ground state is called the fluorescence lifetime and is of the order of 10^{-8} s. This return to the ground state S_0 is accompanied by a radiation process -**fluorescence** -, which occurs at longer wavelengths due to the absorption of energy in the transition between the different vibrational levels: an inelastic phenomenon. The type of fluorescence described above is the so-called Stokes fluorescence; two other types can occur where the emitted light can either be of the same wavelength as the absorbed light (resonance fluorescence) or even lower (anti-Stokes fluorescence). Neither of these two occurs in liquid solutions and shall be ignored; in the text, fluorescence refers to Stokes fluorescence.

Transition to states of lower energy can also occur via a reversal of the electron spin, a radiationless process, from a singlet to a triplet state of lower energy (inter-system crossing) and then to the ground state. Triplet states can be populated in this way; only by electrons coming from higher energy levels. This phenomenon, with a transition time of 10^{-4} s, is called **phosphorescence** and is possible with substances involved in a rigid medium. If the molecule acquires some extra energy, a transition from a triplet to the ground state via a higher energetic singlet state can happen and is called **delayed fluorescence**. Its lifetime is of the same order of magnitude of the phosphorescence lifetime (10^{-4} s) and can be incorrectly assumed as such.

The properties discussed above can be observed in Figure A.2, where the emission and absorption spectra of various fluorescent substances are shown. The shift of the emission spectrum to longer wavelengths (Stokes shift) is due to the transition within the various vibrational levels of the singlet excited state prior to the fluorescence. The mirror image of the emission spectrum occurs because each absorption band to the first electronic state will have a corresponding emission, or fluorescence, band. The different intensities of the spectrum at different wavelengths, its shape, the length of the overlapping region, the location and number of peaks, etc., depend on the substance and are some of the reasons why this technique is so common in chemical analysis. The highest quantum efficiency,Φ , defined as the ratio between the total of emitted energy and the total of absorbed energy, occurs for a wavelength equal

to the peak of the absorption spectrum; it is a property of the substance and is always less than 1 due to the Stokes shift.

The basic equation defining the relationship between fluorescence intensity, I_f, and liquid dye concentration, c, is (e.g. Guilbault [1973]):

$$I_f = \Phi I_0 (1 - e^{-\varepsilon b c}) \qquad [A1]$$

where I_0 is the incident radiation power, ε is the molar absorptivity and b is the absorption path length. The equation above, in terms of c assumes a form usually designated as the Beer-Lambert law:

$$c = \frac{1}{b\varepsilon} \ln \left(1 - \frac{I_f}{\Phi I_0}\right)$$

For very dilute concentrations, only the first two terms of the power series expansion of the exponential are retained and equation [A.1] reduces to:

$$I_f = 2.3 \; \Phi I_0 \varepsilon b c$$

and shows one of the main advantages of the fluorescence-based techniques: a linear response to concentration for constant light sources. Guilbault [1973] states that, for a linear response of fluorescence with respect to concentration, no more than 5% of the exciting light should be absorbed. The absorption of light increases with the concentration and, depending on the dye properties, with the extent of the respective overlapping tails of the spectra. However, other factors in addition to high concentration can also affect the linear response and require some careful experimental procedures. Reduction of the intensity of fluorescence is referred to as 'quenching' and can also occur because of, for instance, temperature increase, or chemical or photochemical decomposition. The last is of major concern and can be avoided by using lower intensities of light, longer wavelengths (less energetic photons) for excitation, and reducing the time of exposure of the solution to exciting light.

A.4 EXPERIMENTAL RESULTS

The results are presented under two headings. In the first a fluorescent dye is selected from a set of three on the basis of characteristics such as, for instance the stability of the solution. In the second the results in the combustor model are reported.

Selection of the Fluorescent Dye

A variety of fluorescent substances is available (Berlman [1971]) but not all are of interest to the present application. The selection must be made according to considerations such as:

- soluble in water
- availability and cost
- absorption and emission spectra in the range of wavelengths measurable by the instrumentation available
- low toxicity
- a relatively high quantum efficiency to provide a high signal to noise ratio
- a large Stokes shift to decrease the overlap between the absorption and emission spectrum
- minimal susceptibility to environmental factors (oxygen, concentration, temperature) affecting the quantum efficiency, quenching

Three of the most common fluorescent dyes were used in the present study: fluorescein, rhodamine B and rhodamine 6G. Table A.1 summarises the characteristics of the three dyes - fluorescein, rhodamine 6G and rhodamine B - whose spectra have previously been shown in Figure A.2

TABLE A.1 Spectral Characteristics of Fluorescein, Rhodamine B and Rhodamine 6G

	Absorption Spectrum			Emission Spectrum			Extent of the	
	Lower	Upper	Max	Lower	Upper	Max	Stokes Shift	Overlapping Region
Fluorescein	430	520	490	490	600	510	20	30
Rhodamine B	460	590	550	550	680	590	40	40
Rhodamine 6G	460	560	530	540	660	560	30	20

* wavelength above in nanometer

Fluorescein: Chemical formula = $C_{20}H_{10}O_5N_2$. Available from Fison under the trade name of Fluorescein Sodium, Ref. F/1300.

Rhodamine B: Chemical formula = $C_{28}H_{31}N_2O_3Cl$. Available from BDH under the same trade name, Ref. CI.45170.

Rhodamine 6G: Chemical formula not known. Available from BDH under the same trade name, Ref. CI.45160.

The main objectives of this study were to assess the stability of the mixtures, to find suitable operating ranges of the instrumentation (laser power, PM voltage, etc.) and to identify the range of concentration where linear response could be found. Only one dye should be considered for later use.

The experimental set-up used in these preliminary studies is shown in Figure A.3. An argon-ion laser (Spectra Physics model 164) and a photomultiplier (DISA-RCA-4526) were used as source and light detector, respectively. The laser was operated in light mode at 488 nm or 514 nm, depending on the dye under investigation (fluorescein 483 nm, and rhodamine B and 6G 514 nm). Both wavelengths are still within the absorption spectra of the three dyes, and the tuning of the laser light according to the dye was made only for a higher quantum efficiency. The linear response of the photomultiplier to intensity of light was previously confirmed for a range of 0.10 to 0.42 W of laser power, at a constant power supply voltage, and a signal level between 20 and 86 mV. The focusing optics consisted of a polariser and a bi-convex lens of 500 mm focal length which decreased the radius of the beam from 1.5 mm to 0.2 mm. Before collection, the light was filtered by a sharp cut-off filter (Melles Griot OG590) in the case of rhodamine B and rhodamine 6G, or by a band pass filter (Melles Griot 03 FIX044) in the case of the fluorescein. The signal from the photomultiplier, powered by a power supply Brandenburg (model 2475R) was fed to a voltmeter (Thurbly, model 1905A) and viewed in an oscilloscope.

Concentrate solutions were prepared in a proportion of 0.1 g per 1 litre of tap water, and then progressively diluted by the addition of water. The solution was contained in a cubic vessel (150 × 150 × 150 mm) with glass walls of 5 mm thickness and traversed by a single laser beam (Figure A.3) at the mid-width of the vessel. The light was collected at 90° and the vessel moved along the beam to avoid refocusing of the photomultiplier.

Initial measurements showed poor repeatability with significant scattering; this was reduced by stirring the solution while measuring, but repeated measurements of the same sample showed a consistent decrease of signal level and this cast doubts on the stability of the solution. Figure A.4 shows the intensity of the signal over a total of 95 min, from a solution of fluorescein at a concentration of 0.04 mg/l for a laser power of 0.2 and 0.4 W. Higher laser power increases the rate of deterioration of the sample, although it is desirable to reduce the electronic shot noise of the photomultiplier (e.g. Becker [1977]). This reduction of the fluorescence intensity could actually be seen by simple observation of a still solution crossed by a laser beam: spots of lower intensity of light along the beam were evident, which, after illumination of the vessel with a plane of light, were revealed to be thin sheets whose cause could either be insolubility or photo-decomposition. Miller [1981] says that the rate of

photo-decomposition may be reduced if the solution is stirred during the measurements and this explains the relative improvement found by stirring the solution. However, according to Durst and Schmitt [1984], for a calculated beam waist diameter of 218 μm, the maximum permissible concentrations to avoid photo-decomposition were 22 and 44 mg/l for 0.2 and 0.4 W, respectively. The concentration in Figure A.4 is at least 55 times lower than the limit value recommended by Durst and Schmitt. The methodology followed by these authors (monitoring of the distortion of the Gaussian radial profile of the laser beam) does not correspond to the most obvious nor the most common practice in photo-decomposition measurements (to measure the rate of decay of the fluorescence intensity (Miller [1981]). Also according to Miller and in contrast to Durst and Schmitt, the effect of photodecomposition is much less in concentrated than in dilute solutions; what the latter designated by photochemical decomposition is perhaps some other phenomenon. For instance, Stevenson, Santos and Mettler [1976] noted that, although fluorescein could easily be dissolved in water, it required the addition of a liquid detergent to reduce the tendency of binding of the fluorescein molecules (dimerisation) and consequent reduction of the fluorescence intensity (quenching). Johnson and Bennet [1981] used alcohol for no stated reason and Durst and Schmitt [1984] did not use any additive. No attempts were made to find a conclusive explanation for this behaviour; it is likely to be caused by chemical phenomena which are beyond the scope of the present work. Further, the fluorescein dyes used by other workers were slightly different in composition:

Durst and Schmitt	$C_{20}H_{10}O_5$
Johnson and Bennet	$C_{20}H_{10}O_5Na_2$
The present work	$C_{20}H_{10}O_5N_2$

and this probably explains why this behaviour has not been reported.

A further reason for neglecting these effects is that the behaviour of solutions of rhodamine B and rhodamine 6G was found to be stable (Figure A.5), and rhodamine B was the dye finally selected (also because of its low price).

As the concentration of rhodamine B is reduced (Figure A.6), one can see how the intensity of the signal becomes independent of the optical path length, reaching a situation where no absorption occurs at a concentration of 0.08 mg/l. At 0.32 mg/l, a reduction of 20% is evidenced. Figure A.7 shows a set of measurements for concentrations between 0.0018 mg/l and 0.005 mg/l to demonstrate the absence of absorption, and Figure A.8 shows the linear relationship between concentration and fluorescence intensity for this range of concentrations and laser power.

Difficulties of Using the Technique in the Combustor Model

Following the selection of the dye, calibration tests were made with an experimental arrangement more adequate for experiments in the water rig.

An argon-ion laser (Spectra Physics model 164) was used as the light source. The laser with a small optical unit attached to its head provided a beam of light of 514.5 nm with a mean and rms power stability of 0.5% and 0.2%, respectively. The optical unit consisted of a 3× beam expander, a polariser and a focusing lens with a focal length of 200 mm. The collecting optics, oriented at 90° to the laser beam, comprised a focusing lens of 150 mm focal length, an optical high pass filter (Melles Griot OG590), two slits on the top of each other to form a rectangular window of 1 mm by 0.1 mm, and a lens with a focal length of 25.4 mm to image the slit onto the pinhole (50 μm diameter) of a photomultiplier. For a higher photon amplification, the photomultiplier (EMI 9816B, S20 cathode) consisted of 14 dynodes; a Brandenburg power supply (model 2475-R) was used. The electric signal was filtered by a Kron-Hite filter (model 3200) amplified 50× and digitised. An Apple IIe micro-computer sampled the data at a frequency of 25 KHz and processed it in blocks of a maximum size of 1280 values. The instrumentation used here, with the exception of the optical filter, was developed for Rayleigh scattering measurements and, for more details, refer to Arcoumanis and Laker [1984].

The use of instrumentation different from the previous section required the repetition of some static calibration tests already performed, but now with only one dye: rhodamine B. A concentrate solution of 0.1 g (± 0.00001g) of rhodamine B in 0.5 l of water was first prepared. Figure A.9 shows the result of one of these tests where the amount of dye in 2 litres of tap water was increased by successive addition of 0.1 ml of the concentrate solution above. The laser power and photomultiplier supply voltage were set at 0.8 W and 1000 V, respectively. An excellent linear increase of the signal intensity with concentration is shown. The first attempts to repeat the results of this very simple test showed differences of an order of 20% and considerable care was needed in the preparation of the solutions before repeatability of the calibration curves could be achieved within 5%.

Figure A.10 shows the response to different laser powers. The straight lines have been found by linear regression. The decreased slope of the lines is noted as the laser power is reduced; this slope should decrease in the same ratio as the laser power if the fluorescent intensity is proportional to the incident light intensity. Locally, the fluorescent intensity should also fall to zero in the case of zero concentration, but all the curves originate from a single value of about 200 mV - the background light intensity. The use of lower laser power reduces the sensitivity of the system and, for

this range of concentrations, does not take advantage of the full 5.12 V scale of the micro-computer. The highest laser intensity should be used. Figure A.11 shows the influence of the photomultiplier voltage supply. The intensity of the signal is shown to increase with the photomultiplier voltage and advantage can also be taken of this in case of low laser power available.

One of the objectives of the optical unit in front of the laser is to reduce the radius of the laser beam and increase the spatial resolution and intensity of the incident light. From Gaussian optics, it is known that the minimum beam radius occurs at the focal point of the lens, if the light travels in a medium with a constant refractive index and the lens is free from aberrations. This approximately sets the distance between the front lens, L, and the axis of the light collecting system. Finer adjustment is obviously needed. In the present situation, the light emerging from the laser travels through three media, all of different refractive index, and the location of the beam waist depends on the distance between the vessel and the lens, L. If one considers a very simple situation illustrated in Figure A.12 where the light beam focused by a lens of nominal focal length, f, crosses two media of refractive indices, n_1 and n_2, with an angle α_1 at the interface ($n_1 \sin\alpha_1 = n_2 \sin\alpha_2$) of negligible thickness. The angle α_1 is the angle of convergence of the beam, which is altered to α_2 as the beam goes across the interface, and the deviation of the effective focal length of the lens is given by:

$$\Delta f = d_0 \left(1 - \frac{l}{f}\right) \frac{\sin \alpha_2 - \sin \alpha_1}{\sin \alpha_2 \sin \alpha_1}$$

Where l is the distance between the interface and the lens L and d_0 is the beam diameter. The equation above shows that there is no deviation in the case of only one medium ($n_1 = n_2$) and, if the refractive indices are different, the deviation depends on the distance between the lens and the interface and increases as the focal length of the lens decreases.

In the case of the combustor geometry, if the laser is moved along the combustor axis, the number of interfaces (Perspex walls) crossed by the laser beam depends on the axial location; if the laser moves towards the combustor, for a radial traverse, the distance between the laser and the model changes. In either of these situations, light will be collected from a point on the beam other than the waist, if the photomultiplier is not readjusted. However, that readjustment may result in collecting light from somewhere else in the flow, still along the beam. In geometries with curved surfaces and single beam arrangements due to refraction effects, it is impossible to be sure from where the light is being collected since there is no reference point along the

beam. In LDV measurements, because the signal is only originated from the control volume, this problem is alleviated and the question is to know the location of the control volume. A cross beam configuration should be preferred in geometries with curved surface since the crossing of the beams provides a spot of much higher light intensity with respect to which the collecting optics can be readjusted. Even better is a backward scattering unit: fluorescent emission, unlike Rayleigh scattering, is not directional dependent and the refocusing of the collecting optics is not needed since the focusing and collecting lenses are the same. Johnson and Bennett [1981] used this arrangement.

Figure A.13 shows the centreline values of two sets of measurements (curves A and B), corresponding to the flow conditions as in case 3 of Table 4.2. For the reasons described above, only measurements along the centreline of the combustor were made. The dye was injected through the fuel injector with a concentration of 1.3 mg/l of water. This concentration was such that after mixing with the swirler and the primary jet flow the levels of dye concentration were similar to those for which the system had been previously calibrated. The trend of curve A indicates a sudden drop in the first 20 mm with a kink about the primary jet impingement point and slow recovery afterwards. Similar measurements with initial higher concentration of the dye showed complete random patterns; measurements made at the same location, without touching the optics, showed values different by a factor of six or seven and this was attributed to the injection system. An attempt to reproduce the results of curve A, in Figure A.13, a couple of days later with realignment of the optical system resulted in curve B.

A.5 CONCLUSIONS

Some of the experimental difficulties encountered with this technique are common to all intensity-based techniques (Becker [1977]) where the extreme sensitivity, if advantageous in some circumstances, usually requires a very close monitoring of the experimental conditions. Special attention is needed to make sure of the stability of the solution, and photomultiplier and laser power supplies. Localised imperfections in surfaces, incomplete focusing of the optical system, ambient factors (e.g. temperature and artificial illumination), attenuation of the laser beam and drift of the electronics can be other sources of error. A discussion of these sources of error is premature, but their importance should be assessed in future applications of LIF; the works by Becker [1977], Becker, Hottel and Williams [1967] and Shaughnessy and Morton [1977] in the context of measurements of concentration by Mie sccatering provide a detailed discussion on this type of errors of relevance to the present technique too.

It is clear that, although some confidence could be achieved in static applications of laser induced fluorescence, its use in the presently available water rig is impossible: the rig requires more accurate methods to control and monitor the various flows and provide a fuel injector flow with constant concentration. Also, the LIF itself needs further development, for preference in much simpler flows where the levels of uncertainty can be assessed. The main conclusions of this work were:

- No satisfactory stability of solutions of fluorescein could be found and its future use was abandoned in favour of rhodamine B.
- A linear response of fluorescence to the incident light is possible for concentrations of rhodamine B less than 0.08 mg/l.
- Special care is needed to guarantee repeatability of measurements.

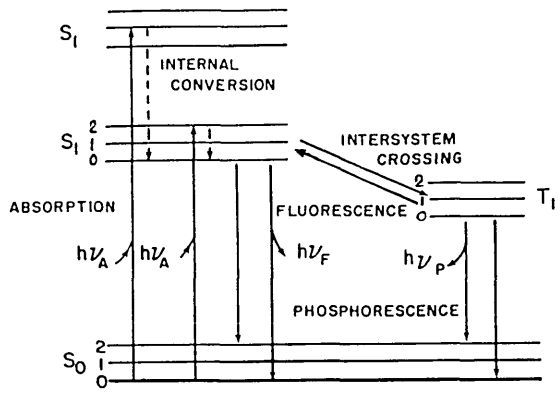


FIGURE A1-Energy diagram of photoluminiscence phenomena (from "*Principles of Fluorescence Spectroscopy*" by Lakowicz [1983]) -S_0: ground electronic state; S_1: first excited singlet state; T_1: first excited triplet state.

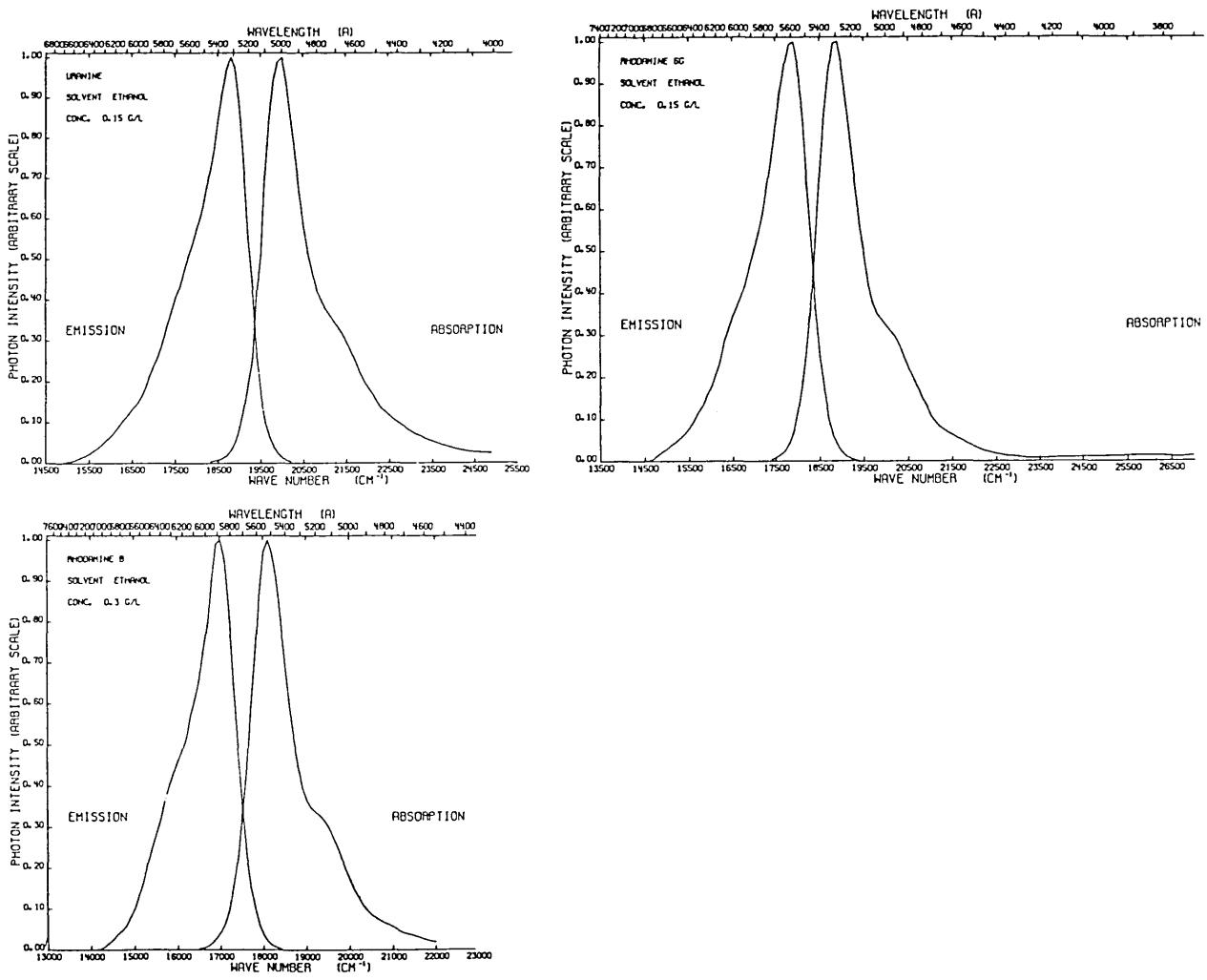


FIGURE A2-Spectra of three fluorescent sub stances: uranine, rhodamine 6G, rhodamine B (from " *Handbook of Fluorescence Spectra of Aromatic Molecules (2nd edition)*" by Berlman [1971]).

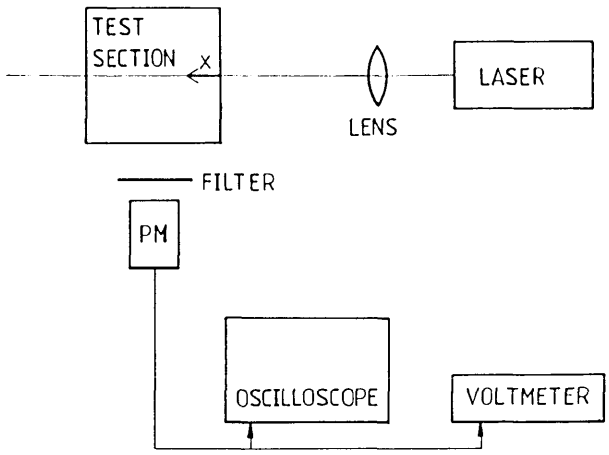


FIGURE A3-Experimental set-up used to assess the main characteristics of the dyes.

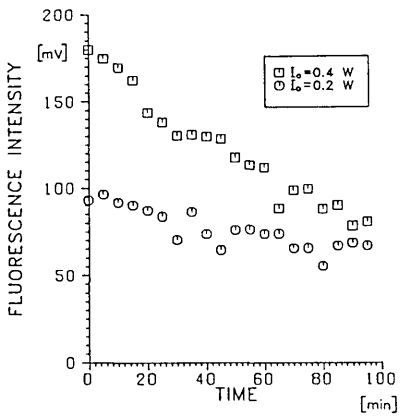


FIGURE A4-Intensity of fluorescence versus time for fluorescein at a concentration of 40 $X10^{-3}$ mg/l.

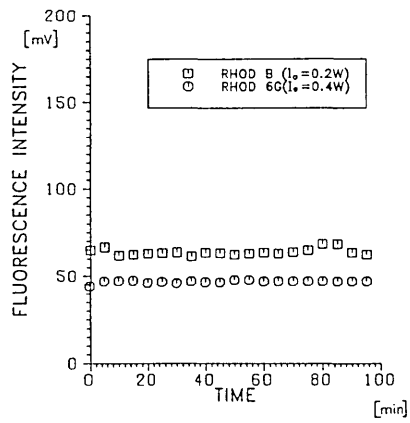


FIGURE A5-Intensity of fluorescence versus time for rhodamine B and rhodamine 6G at a concentration of 40 $X10^{-3}$ mg/l.

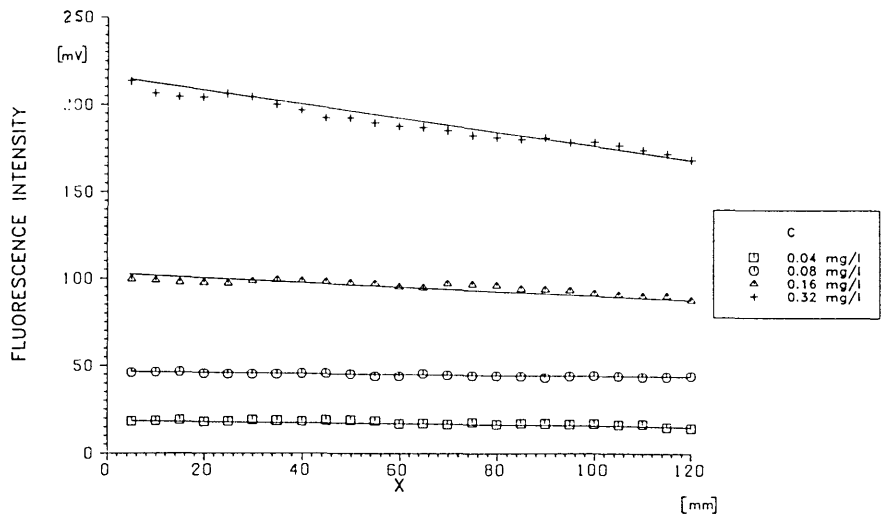


FIGURE A.6-Intensity of fluorescence versus distance for different concentrations of rhodamine B.

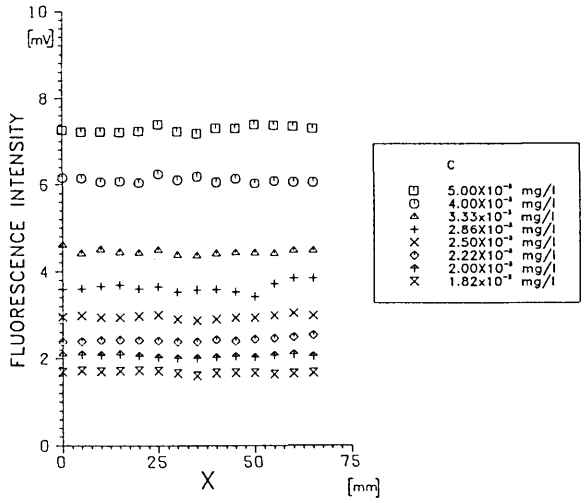


FIGURE A.7-Intensity of fluorescence versus distance for low concentrations of rhodamine B.

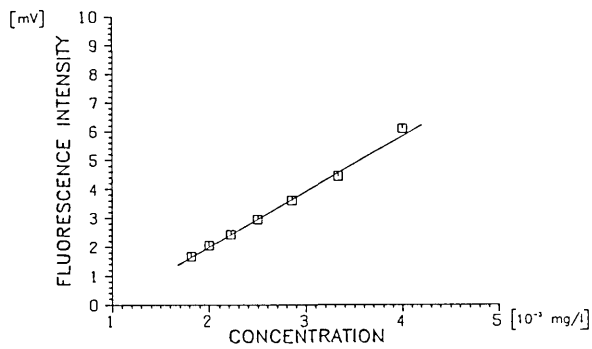


FIGURE A.8-Intensity of fluorescence versus concentration of rhodamine B.

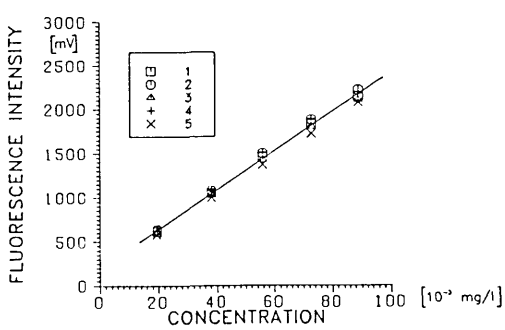


FIGURE A.9-Intensity of fluorescence versus concentration of rhodamine B (2nd experimental arrangement).

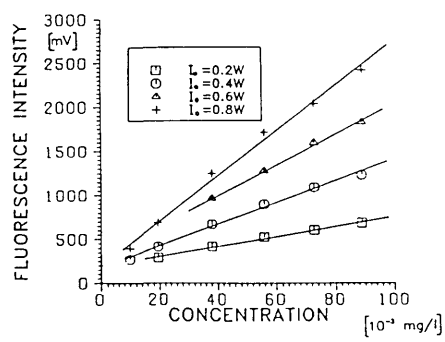


FIGURE A.10-Intensity of fluorescence as a function of laser power and concentration of rhodamine B (2nd experimental arrangement).

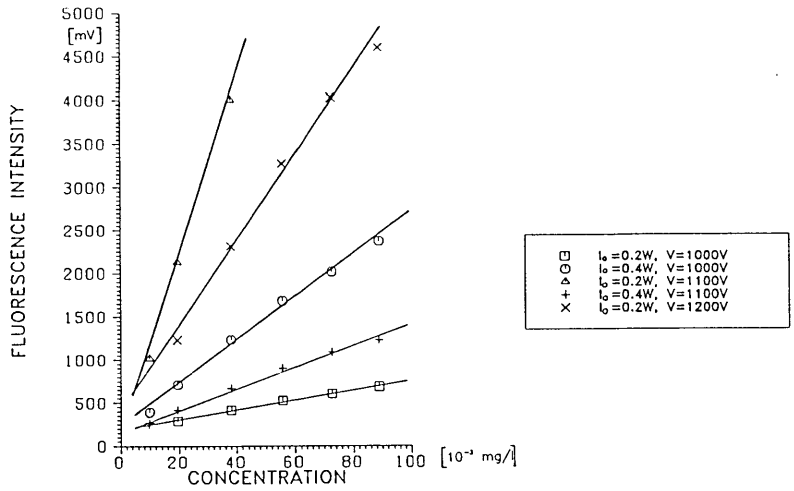


FIGURE A.11-Intensity of fluorescence as a function of laser power, concentration and photomultiplier voltage supply.

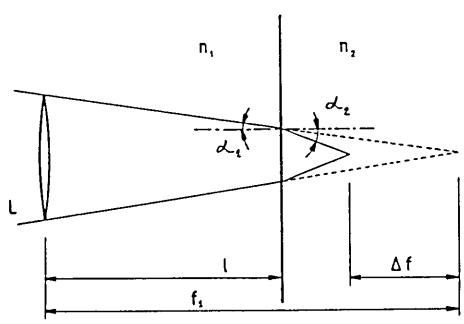


FIGURE A.12-The location of the beam waist.

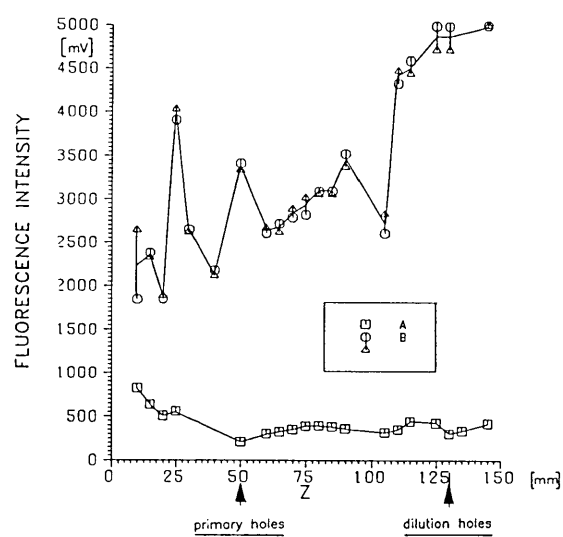


FIGURE A.13-Fluorescence intensity along the centreline of the model combustor.

APPENDIX B
THE LUCAS DYE TRACER TECHNIQUE

Lucas Aerospace Limited has developed an intrusive optical probe, designated here as the 'Lucas dye tracer technique', for mixing studies inside water models of combustor geometries (Stevens [1985]). As in all probe based measurements, flow disturbance is a constant worry, consequently the probe used in this work is a copy of the Lucas probe but in a smaller size; its redesign was undertaken by Shalloe [1987] and only the main characteristics of the probe and data acquisition system will be described here.

The probe, shown in Figure B.1, consists basically of a diode emitting near infrared wavelength light(Ref. TIL24, Texas Instruments) in one end of a metallic tube and a sensor (Ref. LS600, Texas Instruments) in the opposite end with a slot between them. The amount of light reaching the sensor depends on the absorption of the emitted light over the slot. This is determined by the local concentration of dyed water present in the slot at any instant of time. Dyed water of fixed concentration was injected into the combustor as "fuel" and was diluted by the undyed water entering the combustor through the swirler and the primary and dilution holes. The relationship between light intensity and concentration of dye is found by calibration of the probe in solutions of a known concentration. The probe, which could be moved in any direction, was introduced from the downstream end of the combustor with the slot facing the axial flow direction. The electronic signal from the light sensor was amplified and digitised through an A/D converter which was interfaced to a BBC micro-computer. This sampled the data at a maximum frequency of 200 Hz and processed it. The dye used was Pelikan drawing ink but any other material soluble in water and containing carbon particles (responsible for the infrared absorption) can be used. Figure B.2 shows the calibration curve with a working range between 100 and 1000 ppm of dye in water, i.e. a factor of 10 between the lowest and highest measurable value. Two types of Pelikan ink (drawing and Indian inks) give slightly different calibration curves and both are shown in Figure B.2 The principal problem encountered was the sealing of the electronic components and corresponding circuits inside the probe. Initial prototypes could not even resist the calibration tests. Various methods of fabrication were tried, but immersion of the probe in water for long periods was difficult and the only measurements made follow below.

The measurements shown in Figure B.3 correspond to four angular locations 50 mm downstream of the swirler, i.e. the plane of the primary hole axis. Pelikan drawing ink mixed with water to a concentration of 2000 ppm was injected through the fuel injector and the results are presented normalized by this maximum concentration to represent the fuel fraction. The trend is correct and shows a decrease of the concentration of fuel towards the centreline at angular locations not aligned with the hole axis. All four angular profiles converge to a single value on the centreline, as they should. The results from numerical calculations (described in Chapter 5) in Figure B.3 agree with the measurements in terms of shapes and trends, although the value of the centreline is underpredicted. However, detailed comparisons between predictions and measurements must wait for further development and evaluation of the technique.

Finally, there seems to be no advantage in the inclusion of the electronic components in the probe itself: this poses severe problems of sealing against water ingress and is an obstacle to miniaturization of the probe which increases the blockage and perturbation of the flow. Furthermore, it is doubtful that this technique can give more accurate results than the suction probes used in reacting flows. A new design is proposed with the electronic elements not immersed in water and samples of water collected through a small pitot tube. The development of this technique should be pursued simultaneously with the LIF technique described in the previous Appendix to provide a cross-check between the two.

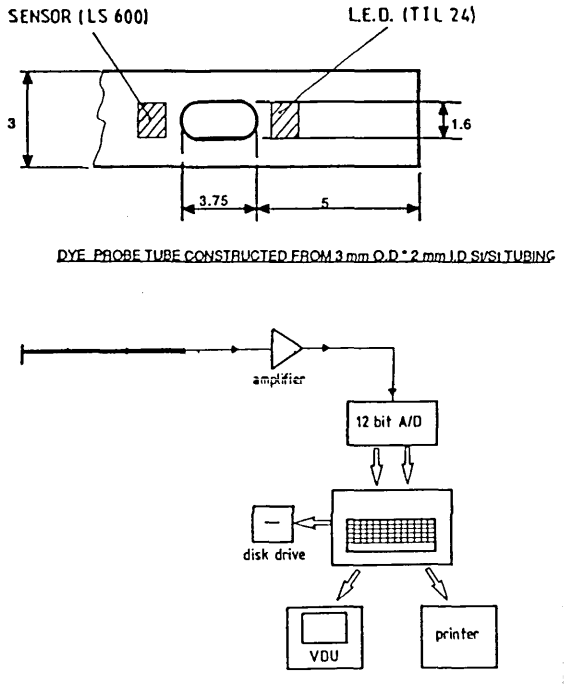


FIGURE B1-Dye trace probe and data acquisition system.

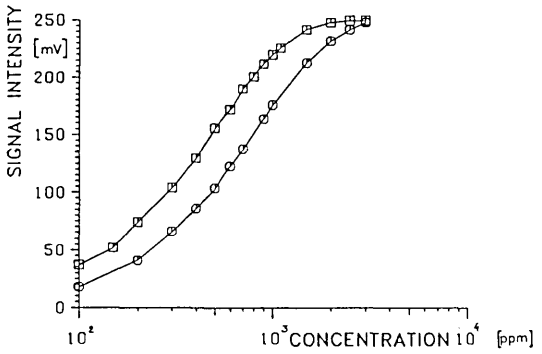


FIGURE B2-Calibration curve (□ - drawing ink; ⊙ - indian ink).

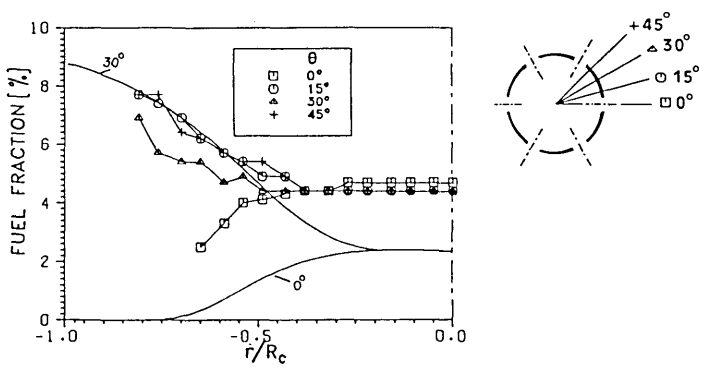


FIGURE B3-Radial profiles of fuel fraction at the primary hole plane (lines from numerical calculations reported in Chapter 5).

REFERENCES

ABUJELALA, M. T. and LILLEY, D.G. [1983]. 'Confined swirling flow predictions'. AIAA paper No. 83-0316.

AHMED, S.A., and SO, R.M.C. [1987]. 'Characteristics of air jets discharging normally into a swirling crossflow'. AIAA Journal, **25**, 429-435.

ANDREOPOULOS, J. [1982]. 'Measurements in a jet-pipe flow issuing perpendicularly into a cross-stream'. Journal of Fluids Engineering, **104**, 493-499.

ANDREOPOULOS, J., and RODI, W. [1984]. 'Experimental investigation of jets in crossflow'. Journal of Fluid Mechanics, **138**, 93-127.

ANTONIA, R.A., and BROWNE, L.W.B. [1987]. 'Conventional and conditional Prandtl number in a turbulent plane wake'. International Journal of Heat and Mass Transfer, **30**, 2023-2029.

ARCOUMANIS, C., and LAKER, J. [1984]. 'A laser Rayleigh scattering system for scalar transport studies'. Imperial College, Fluids Section Report FS/84/1, London.

ARNOLD, C.R. [1984]. 'Analysis using film'. In Chapter 10 of '*Photography for the Scientist*', 2nd edition (edited by R.A. Morton), Academic Press, London.

ATKINSON, K.N., KHAN, Z.A., and WHITELAW, J.H. [1982]. 'Experimental investigation of opposed jets discharging normally into a cross-stream'. Journal of Fluid Mechanics, **115**, 493-504.

AUPOIX, B., COUSTEIX, J., and LIANDRET, J. [1983]. 'Effects of rotation on isotropic turbulence'. *Proceedings of the 4th Symposium on Turbulent Shear Flows*, Karlsruhe.

BAHR, D.W. [1987]. 'Technology for the design of high temperature rise combustors'. Journal of Propulsion, **3**, 179-186.

BECKER, H.A. [1977]. 'Mixing, concentration fluctuations, and marker nephelometry'. In '*Studies in Convection*' (edited by B.E. Launder), Academic Press, London, **2**, 45-139.

BECKER, H.A., HOTTEL, H.C., and WILLIAMS, G.C. [1967]. 'On the light-scatter technique for the study of turbulence and mixing'. Journal of Fluid Mechanics, **30**, 259-284.

BECKER, H.A. and MASSARO, T.A. [1968]. 'Vortex evolution in a round jet'. Journal of Fluid Mechanics, **31**, 435-448.

BEER, J.M., and CHIGIER, N.A. [1972]. '*Combustion Aerodynamics*'. Applied Science Publishers, London.

BEGLERIS, P. [1986]. '*Three-dimensional flow predictions in motored diesel engines*'. PhD Thesis, University of London.

BENDAT, J.S., and PIERSOL, A.G. [1986]. '*Random Data - Analysis and Measurement Procedures*', 2nd edition (revised and expanded), John Wiley and Sons, New York.

BENODEKAR, R.W., GODDARD, A.J.H., GOSMAN, A.D., and ISSA, R.I. [1983]. 'Numerical prediction of turbulent flow over surface mounted ribs'. ASME Paper 83-FE-13.

BERLMAN, I.B. [1971]. '*Handbook of Fluorescence Spectra of Aromatic Molecules*', 2nd edition, Academic Press, New York.

BERNARD, P.S. [1986]. 'Limitations of the near-wall k-ε turbulence model'. AIAA Journal, **24**, 619-622.

BHANGU, J.K., SNAPE, D.M., and EARDLEY, B.R. [1983]. 'The design and development of a low emissions transply combustor for the civil SPEY engine'. AGARD-CP353, Paper No. 23.

BICEN, A.F. [1982]. 'Refraction correction for LDA measurements in flows with curved optical boundaries'. TSI Quarterly, **8**, 10-12.

BICEN, A.F., and JONES, W.P. [1986]. 'Velocity characteristics of isothermal and combusting flows'. Combustion Science and Technology, **49**, 1-15.

BICEN, A.F., and PALMA, J.M.L.M. [1986]. 'Flow characteristics of swirlers of a model TAY combustor'. Imperial College, Fluids Section Report FS/86/36, London.

BICEN, A.F., McGUIRK, J.J., and PALMA, J.M.L.M. [1988]. 'Modelling gas-turbine combustor flow fields in isothermal flow experiments'. To be submitted for publication.

BLOTTNER, F.G. [1982]. 'Influence of boundary approximations and conditions of finite-difference solutions'. Journal of Computational Physics, **48**, 246-269.

BRADSHAW, P. [1978]. '*Turbulence*', 2nd edition, Springer-Verlag, Berlin.

BREIDENTHAL, R.E., TONG, K.-O., WONG, G.S., HAMERQUIST, R., and LANDRY, P. [1986]. 'Turbulent mixing in two-dimensional ducts with transverse jets'. AIAA Journal, **24**, 1867-1869.

BRUCE, T.W., MONGIA, H.C., and REYNOLDS, R.S. [1979]. '*Combustor Design Criteria Validation. Vol. 1 - Element Tests and Model Validation*', USARTL-TR-78-55A.

BUCHAVE, P., GEORGE, W.K., and LUMLEY, J.L. [1979]. 'The measurement of turbulence with the laser-Doppler anemometer'. Annual Review of Fluid Mechanics, **11**, 443-503.

BURRUS, D.L., SHYY, W., and BRAATEN, M.E. [1987]. 'Numerical models for analytical predictions of combustor aerothermal performance characteristics'. AGARD-CP422, Paper No. 25.

CAMERON, C.D., BROUWER, J., WOOD, C.P., and SAMUELSEN, G.S. [1988]. 'A detailed characterization of the velocity and thermal fields in a model can combustor with wall jet injection'. ASME Paper 88-GT-26.

CASTRO, I.P. [1979]. 'Numerical difficulties in the calculation of complex turbulent flows'. In '*Turbulent Shear Flows I*' (edited by F.Durst, B.E.Launder, F.W.Schmidt and J.H.Whitelaw), Springer-Verlag, Berlin, 220-236.

CASTRO, I.P. [1982]. Introductory remarks to Part III - Recirculating Flows. In '*Turbulent Shear Flows III*' (edited by J.S.Bradbury, F.Durst, B.E.Launder, F.W.Schmidt and J.H.Whitelaw), Springer-Verlag, Berlin, 157-161.

CHLEBOUN, P.V., CRAIG, P.J., SEBBOWA, F.B., and SHEPPARD, C.G.W. [1982]. 'A study of transverse turbulent jets in a crossflow'. Combustion Science and Technology, **29**, 107-111.

CHAPMAN, M. [1981]. 'FRAM - nonlinear damping algorithms for the continuity equation'. Journal of Computational Physics, **44**, 84-103.

CHORIN, A.J. [1967]. 'A numerical method for solving incompressible viscous flow problems'. Journal of Computational Physics, **2**, 12-26.

CLARKE, A.E., GERRARD, A.J., and HOLLIDAY, L.A. [1963]. 'Some experiments in gas turbine combustion chamber practice using water flow visualization techniques'. *Proceedings of the 9th International Symposium on Combustion*, 878-891.

CLAUS, R.W. [1983]. 'Analytical calculation of a single jet in crossflow and comparison with experiment'. AIAA Paper.

CONNELL, S.D., and STOW, P. [1986]. 'The pressure correction method'. Computer and Fluids, **14**, 1-10.

CONTE, S.M., and de BOOR, C. [1980]. '*Elementary Numerical Analysis*', 3rd edition, McGraw-Hill, New York.

CORREA, S.M., and SHYY, W. [1987]. 'Computational models and methods for continuous gaseous turbulent combustion'. Progress in Energy and Combustion Science, **13**, 249-292.

CORRSIN, S. [1974]. 'Limitations of gradient transport models in random walks and in turbulence'. Advances in Geophysics, **18A**, 25-60.

COUPLAND, J., and PRIDDIN, C.H. [1987]. 'Modelling the flow and combustion in a production gas turbine combustor'. In '*Turbulent Shear Flows V*' (edited by F.Durst, B.E.Launder, F.W.Schmidt and J.H.Whitelaw), Springer-Verlag, Berlin, 310-323.

COX, Jr., G.B. [1976]. 'Multiple jet correlations for gas turbine engine combustor design'. Journal of Engineering for Power, **98**, 265-273.

CRABB, D., and WHITELAW, J.H. [1979]. 'The influence of geometric asymmetry on the flow downstream of row of jets discharging normally into a free stream'. Journal of Heat Transfer, **101**, 183-185.

CRABB, D., DURÃO, D.F.G., and WHITELAW, J.H. [1981]. 'Velocity characteristics in the vicinity of a two-dimensional rib'. *Proceedings of the 3rd Symposium on Turbulent Shear Flows*, 16.5-16.10.

CRABB, D., DURÃO, D.F.G., and WHITELAW, J.H. [1987]. 'A round jet normal to a crossflow'. Journal of Fluids Engineering, **103**, 142-153.

CROCCO, L. [1965]. 'A suggestion for the numerical solution of the steady Navier-Stokes equation'. AIAA Journal, **3**, 1824-1832.

CROWDER, H.J. and DALTON, C. [1971]. 'Errors in the use of nonuniform mesh systems'. Journal of Computational Physics, **7**, 32-45.

CROW, S.C. and CHAMPAGNE, F.H. [1971]. 'Orderly jet structure in jet turbulence'. Journal of Fluid Mechanics, **48**, 547-591.

DEMUREN, A.O. [1983]. 'Numerical calculations of steady three-dimensional turbulent jets in crossflow'. Computer Methods in Applied Mechanics and Engineering, **37**, 309-328.

DEMUREN, A.O. [1985]. 'False diffusion in three-dimensional flow calculations'. Computer and Fluids, **13**, 411-419.

DEMUREN, A.O. [1986]. 'Modelling turbulent jets in crossflow'. In '*Encyclopaedia of Fluid Mechanics*' (edited by N.P. Cheremisinoff), Gulf Publishing Company, New York, **2**, 430-465.

DIMOTAKIS, P.E., MIAKE-LYE, R.C., and PAPANTONIOU, D. [1983]. 'Structure and dynamics of round turbulent jets'. Physics of Fluids, **26**, 3185-3192.

DIPPLE, G., and RABY, R. [1987]. 'TILE, SOLID and CONICON - software for data in the plane'. ICCC Bulletin No. 4.22/7.

DRAIN, L.E. [1980]. '*The Laser Doppler Technique*', John Wiley and Sons, New York.

DURST, F., MELLING, A., and WHITELAW, J.H. [1981]. '*Principles and Practice of Laser-Doppler Anemometry*', 2nd edition, Academic Press, London.

DURST, F., and SCHMITT, F. [1984]. 'Joint laser-Doppler/laser-induced-fluorescence measurements in a turbulent jet'. *Proceedings of the 2nd Symposium on Applications of Laser Anemometry to Fluid Mechanics*, Lisbon, Paper No. 8.5.

ECKBRETH, A.C. [1987]. '*Laser Diagnostics for Temperature and Species*', Abacus Press, Tunbridge Wells, England.

EDELMAN, R.B. and HARSHA, P.T. [1978]. 'Laminar and turbulent gas dynamics in combustors - current status'. Progress in Energy and Combustion Science, **4**, 1-62.

EDWARDS, R.V. [1987]. 'Report of the special panel on statistical particle bias problems in laser anemometry'. Journal of Fluids Engineering, **109**, 89-93.

EDWARDS, R.V., and DYBBS, A. [1984]. 'Refractive index matching for velocity measurements in complex geometries'. TSI Quarterly, **10**, 3-11.

ELLIS, C.R., AND STEFAN, H.G. [1986]. Development of hydrogen bubble velocity meter'. Journal of Hydraulic Engineering, **112**, 59-64.

ESCUDIER, M.P., and ZEHNDER, N. [1982]. 'Vortex-flow regimes'. Journal of Fluid Mechanics, **115**, 105-121.

ESKINAZI, S., and ERIAN, F.F. [1969]. 'Energy reversal in turbulent flows'. Physics of Fluids, **12**, 1988-1998.

FOUNTI, M., VAFIDIS, C., and WHITELAW, J.H. [1985]. 'Shell-side distributions and the influence of inlet conditions in a model of a disc and doughnut heat exchanger'. Experiments in Fluids, **3**, 293-300.

GALPIN, P.F., van DOORMAAL, J.P., and RAITHBY, G.D. [1985]. 'Solution of the incompressible mass and momentum equations by application of a coupled equation line solver'. International Journal for Numerical Methods in Fluids, **5**, 1-11.

GALPIN, P.F., and RAITHBY, G.D. [1986]. 'Numerical solution of problems in incompressible fluid flow: treatment of the temperature-velocity coupling'. Numerical Heat Transfer, **10**, 105-129.

GEORGE, W.K., and LUMLEY, J.L. [1973]. 'The laser-Doppler velocimeter and its application to the measurement of turbulence'. Journal of Fluid Mechanics, **60**, 321-362.

GIBSON, M.M., and LAUNDER, B.E. [1976]. 'On the calculation of horizontal turbulent, free shear flows under gravitational influence'. Journal of Heat Transfer, **90C**, 81-87.

GIBSON, M.M., and LAUNDER, B.E. [1978]. 'Ground effects on pressure fluctuations in the atmospheric boundary layer'. Journal of Fluid Mechanics, **86**, 491-511.

GOLDSTEIN, R.J., LAU, K.Y., and LEUNG, C.C. [1983]. 'Velocity and turbulence measurements in combustion systems'. Experiments in Fluids, **1**, 93-99.

GOOD, M.C., and JOUBERT, P.N. [1968]. 'The form drag of two-dimensional bluff-plates immersed in turbulent boundary layers'. Journal of Fluid Mechanics, **31**, 547-582.

GOSMAN, A.D., and IDERIAH, F.J.K. [1976]. 'TEACH-2E: a general computer program for two-dimensional, turbulent recirculating flows'. Imperial College, internal report.

GREEN, A.S., and WHITELAW, J.H. [1983]. 'Isothermal models of gas-turbine combustors'. Journal of Fluid Mechanics, **126**, 399-412.

GRESHO, P.M., and LEE, R.C. [1981]. 'Don't suppress the wiggles - they're telling you something!'. Computer and Fluids, **9**, 223-253.

GUILBAULT, G.C. [1973]. '*Practical Fluorescence*', Marcel Dekker, New York.

GUPTA, A.K., LILLEY, D.G., and SYRED, N. [1984]. '*Swirl Flows*', Abacus Press, Tunbridge Wells, England.

GUPTA, A.K., and LILLEY, D.G. [1985]. '*Flowfield Modelling and Diagnostics*', Abacus Press, Tunbridge Wells, England.

HAN, T., HUMPHREY, J.A.C., and LAUNDER, B.E. [1981]. 'A comparison of hybrid and quadratic-upstream differencing in high Reynolds number elliptic flows'. Computer Methods in Applied Mechanics and Engineering, **29**, 81-95.

HARLOW, F.H., and WELCH, J.E. [1965]. 'Numerical calculation of time-dependent viscous incompressible flow of fluid with free surface'. The Physics of Fluids, **8**, 2182-2189.

HARLOW, F.H., and AMSDEN, A.A. [1971]. 'A numerical fluid dynamics calculation method for all flow speeds'. Journal of Computational Physics, **8**, 197-213.

HEITOR, M.V., LAKER, J.R., TAYLOR, A.M.K.P., and VAFIDIS, C. [1984]. 'Instruction manual for the FS 'model 2' Doppler-frequency counter'. Imperial College, Fluids Section Report FS/84/10.

HEITOR, M.V., and WHITELAW, J.H. [1986]. 'Velocity, temperature, and species characteristics of the flow in a gas-turbine combustor'. Combustion and Flame, **64**, 1-32.

HINZE, J.O. [1975]. '*Turbulence*', 2nd edition, McGraw-Hill, New York.

HO, C.-M. and NOSSEIR, N.S. [1981]. 'Dynamics of an impinging jet. Part 1. The feedback phenomenon', Journal of Fluid Mechanics, **105**, 119-142.

HO, P.Y. [1985]. 'Simulation of the flow pattern of a combustion chamber'. 3M Project, Imperial College, Mechanical Engineering Department, London.

HOLDEMAN, J.D., and WALKER, R.E. [1977]. 'Mixing of a row of jets with a confined crossflow'. AIAA Journal, **15**, 243-249.

HOLDEMAN, J.D., SRINIVASAN, R., and BERENFELD, A. [1984]. 'Experiments in dilution jet mixing'. AIAA Journal, **22**, 1436-1443.

HUNT, J.C.R. [1988]. 'Studying turbulence using direct numerical simulation. 1987 Center for Turbulence Research, NASA Ames/Stanford Summer Programme', Journal of Fluid Mechanics, **190**, 375-392.

IKEDA, Y., NAKAHJIMA, T., MATSUMOTO, R., YAMAZAKI, T., and HORIKAWA, N. [1987]. 'Flow characteristics of mixing process of dilution air in a premixing gas turbine combustor'. International Gas Turbine Congress, III33-III39.

ISSA, R.I. [1986]. 'Solution of the implicitly discretized fluid flow equations by operator splitting'. Journal of Computational Physics, **62**, 40-65.

ISSA, R.I., GOSMAN, A.D., and WATKINS, A.P. [1986]. 'The computation of compressible and incompressible recirculating flows by a non-iterative implicit scheme'. Journal of Computational Physics, **62**, 66-82.

JANG, D.S., JETLI, R., and ACHARYA, S. [1986]. 'Comparison of the PISO, SIMPLER and SIMPLEC algorithms for the treatment of the pressure-velocity coupling in steady flow problems'. Numerical Heat Transfer, **10**, 209-228.

JOHNSON, B.V., and BENNET, J.C. [1981]. 'Mass and momentum transport experiments with confined coaxial jets'. NASA-CR-165574 and WTRC Report RB1-915540-9.

JONES, R.E. [1978]. 'Gas turbine emissions - problems, progress and future'. Progress in Energy and Combustion Science, **4**, 73-113.

JONES, W.P. [1975]. 'PACE: a computer program for solving three-dimensional flow problems'. Rolls-Royce Internal Report.

JONES, W.P. [1980]. 'Models for turbulent flows with variable density and combustion'. In '*Prediction Methods for Turbulent Flows*' (edited by W. Kollmann), Hemisphere Publishing Corporation, New York, 379-421.

JONES, W.P. [1984]. 'private communication'.

JONES, W.P., CLIFFORD, W.C., PRIDDIN, C.H., and CHAIR, R. [1977]. 'A comparison between predicted and measured species concentration and velocities in a research combustor'. AGARD-CP229, Paper No. 40.

JONES, W.P., and LAUNDER, B.E. [1972]. 'The prediction of laminarisation with a two-equation turbulence model'. International Journal of Heat and Mass Transfer, **15**, 301-314.

JONES, W.P., and LAUNDER, B.E. [1973]. 'The calculation of low Reynolds number phenomena with a two-equation model of turbulence'. International Journal of Heat and Mass Transfer, **16**, 1119-1130.

JONES, W.P., and PRIDDIN, C.H. [1978]. 'Predictions of the flow field and local gas composition in gas turbine combustors'. *Proceedings of the 17th International Symposium on Combustion*, 399-409.

JONES, W.P., and McGUIRK, J.J. [1979]. 'Computation of a round turbulent jet discharging into a confined crossflow'. In '*Turbulent Shear Flows II*' (edited by J.S.Bradbury, F.Durst, B.E.Launder, F.W.Schmidt and J.H.Whitelaw), Springer-Verlag, Berlin, 233-245.

JONES, W.P., and McGUIRK, J.J. [1979]. 'Mathematical modelling of gas-turbine combustion chambers'. AGARD-CP275, Paper No. 4.

JONES, W.P., and WHITELAW, J.H. [1982]. 'Calculation methods for reacting turbulent flows: a review'. Combustion and Flame, **48**, 1-26.

KHAN, Z.A., and WHITELAW, J.H. [1980]. 'Vector and scalar characteristics of opposing jets discharging normally into a cross-stream'. International Journal of Heat and Mass Transfer, **23**, 1673-1677.

KHAN, Z.A., McGUIRK, J.J., and WHITELAW, J.H. [1981]. 'A row of jets in a crossflow'. AGARD-CP308, Paper No. 10.

KLINE, S.J., CANTWELL, B.J. and LILLEY, G.M. (editors) [1981]. '*Proceedings of 1980-81 AFOSR-HTTM-Stanford Conference on Complex Turbulent Flows*'.

KLINE, S.J. [1981]. 'Universal or zonal modelling - the road ahead'. *Proceedings of 1980-81 AFOSR-HTTM-Stanford Conference on Complex Turbulent Flows*', **2**, 991-1015.

KOOCHESFAHANI, M.M., and DIMOTAKIS, P.E. [1985]. 'Laser-induced fluorescence measurements of mixed fluid concentration in a liquid plane shear layer'. AIAA Journal, **23**, 1700-1707.

KOUTMOS, P. [1985]. '*An isothermal study of gas turbine combustor flows*'. PhD Thesis, University of London.

LAKOWICZ, J.R. [1983]. '*Principles of Fluorescence Spectroscopy*', Plenum Press, New York.

LATIMER, B.R., and POLLARD, A. [1985]. 'Comparison of pressure-velocity coupling solution algorithms'. Numerical Heat Transfer, **8**, 635-652.

LAUNDER, B.E. [1971]. 'An improved algebraic modelling of the Reynolds stresses'. Imperial College Report TM/TN/A/9.

LAUNDER, B.E. [1978]. 'Heat and mass transport'. In '*Turbulence*', 2nd edition (edited by P. Bradshaw), Springer-Verlag, Berlin, 231-287.

LAUNDER, B.E., and SPALDING D.B. [1974]. 'The numerical computation of turbulent flows'. Computer Methods in Applied Mechanics and Engineering, **3**, 269-289.

LAUNDER, B.E., REECE, G.J., and RODI, W. [1975]. 'Progress in the development of a Reynolds stress turbulence closure'. Journal of Fluid Mechanics, **68**, 537-566.

LAUNDER, B.E., PRIDDIN, C.M., and SHARMA, B.I. [1977]. 'The calculation of turbulent boundary layers on spinning and curved surfaces'. Journal of Fluids Engineering, **99**, 231-239.

LEFEBVRE, A.H. [1965]. 'Progress and problems in gas-turbine combustion'. *Proceedings of the 10th International Symposium on Combustion*, 1129-1137.

LEFEBVRE, A.H. [1983]. '*Gas Turbine Combustion*', McGraw-Hill, New York.

LEONARD, A. [1985]. 'Computing three-dimensional incompressible flows with vortex elements'. Annual Review of Fluid Mechanics, **17**, 523-559.

LEONARD, B.P. [1979a]. 'A stable and accurate convective modelling procedure based on quadratic upstream interpolation'. Computer Methods in Applied Mechanics and Engineering, **19**, 59-98.

LEONARD, B.P. [1979b]. 'A survey of finite differences of opinion on numerical muddling of the incomprehensible defective confusion equation'. In '*Finite Element Methods for Convection Dominated Flows*' (edited by T.J.R. Hughes), AMD, **34** (ASME).

LESCHZINER, M.A. [1979]. 'A comparison between three finite-difference schemes for the computation of steady-state recirculating flows'. Report No. SFB 80/T/146, SFB 80, University of Karlsruhe, West Germany.

LESCHZINER, M.A., and RODI, W. [1981]. 'Calculation of annular and twin parallel jets using various discretization schemes and turbulence-model variations'. Journal of Fluids Engineering, **103**, 352-360.

LIBBY, P.A., and WILLIAMS, F.A. (editors) [1980]. '*Turbulent Reacting Flows*', Springer-Verlag, Berlin.

MANNERS, A.P. [1988]. '*The calculation of the flows in gas turbine combustion*'. PhD Thesis, University of London.

MARQUIS, A.J. [1986]. '*The application of high order convection approximations and second order turbulence closures to recirculating flows*'. PhD Thesis, University of London.

McDONALD, H. [1979]. 'Combustion modelling in two and three dimensions - some numerical considerations'. Progress in Energy and Combustion Science, **5**, 97-122.

McGUIRK, J.J. [1984]. 'private communication'.

McGUIRK, J.J., and RODI, W. [1978]. 'A depth-averaged mathematical model for the near field of side discharges into open-channel flow'. Journal of Fluid Mechanics, **86**, 761-781.

McLAUGHLIN, D.K., and TIEDERMANN, W.G. [1973]. 'Biasing correction for individual realizations of laser anemometer measurements in turbulent flow'. The Physics of Fluids, **16**, 2082-2088.

MERZKIRCH, W. [1987]. '*Flow Visualization*', 2nd edition, Academic Press, New York.

MILITZER, J., NICOLL, W.B., and ALPAY, S.A. [1977]. 'Some observations on the numerical calculation of the recirculation region of twin parallel symmetric jet flow', *Proceedings of the 1st Symposium on Turbulent Shear Flows*, Pennsylvania.

MILLER, J.N. (editor) [1981]. '*Standards in Fluorescence Spectrometry*', Chapman and Hall, London.

MOFFAT, R.J. [1986]. 'Describing the uncertainties in experimental results'. Experimental Thermal and Fluid Science, **1**, 3-17.

MONGIA, H. [1987]. 'A status report on gas turbine combustion modelling', AGARD-CP422, Paper No. 26.

MONGIA, H., REYNOLDS, R., COLEMAN, E., and BRUCE, T. [1979]. 'Combustor Design Criteria Validation. Vol. II - Development Testing of Two Full-Scale Annular Gas Turbine Combustors'. USARTL-TR-78-55B.

MONGIA, H., and REIDER, S.B. [1985]. 'ALLISON combustion research and development activities'. AIAA Paper 85-1402.

MUELLER, T.J. [1983]. 'Flow visualization by direct injection'. In Chapter 7 of '*Fluid Mechanics Measurements*' (edited by R.J. Goldstein), Hemisphere Publishing Corporation, Washington, D.C.

NOSSEIR, N.S. and BEHAR, S. [1986]. 'Characteristics of jet impingement in a side-dump combustor'. AIAA Journal, **24**, 1753-1757.

NOSSEIR, N.S., PELED, U. and HILDEBRAND, G. [1987]. 'Pressure field generated by jet-on-jet impingement'. AIAA Journal, **25**, 1312-1317.

ODGERS, J., and KRETSCHMER, D. [1986]. '*Gas Turbine Fuels and Their Influence on Combustion*', Abacus Press, Tunbridge Wells, England.

OLDENGARM, J., van KRIEKEN, A.H., and RATERINK, H.J. [1976]. 'Development of a rotating grating and its use in laser velocimetry'. *Proceedings of the ISL/AGARD Workshop on Laser Anemometry*, 603-615.

OWEN, F.R. [1976]. 'Simultaneous laser measurements of instantaneous velocity and concentration in turbulent mixing flows'. AGARD-CP193, Paper No. 27.

PAPADIMITRIOU, C. [1986].'*The prediction of turbulent stably-stratified buoyant flows*'. PhD Thesis, University of London.

PAPANICOLAOU, P.N., and LIST, E.J. [1984]. 'Turbulent mass and momentum transport in round vertical turbulent buoyancy'. *Proceedings of the 2nd Symposium on Applications of Laser Anemometry to Fluid Mechanics*, Lisbon, Paper No. 7.4.

PARKER, C.A. [1968]. '*Photoluminescence of Solutions*', Elsevier Publishing Company, Amsterdam.

PATANKAR, S.V. [1980]. '*Numerical Heat Transfer and Fluid Flow*', Hemisphere Publishing, Washington, D.C.

PATANKAR, S.V. [1985]. 'A calculation procedure for two-dimensional elliptic situations'. Numerical Heat Transfer, **14**, 409-425.

PATANKAR, S.V., and SPALDING, D.B. [1972]. 'A calculation procedure for heat, mass and momentum transfer in three-dimensional parabolic flows'. International Journal of Heat and Mass Transfer, **15**, 1787-1806.

PELED, A. [1987]. 'The next computer revolution'. Scientific American, **257**(4), 34-44.

PERIC, M. [1985]. '*A finite volume method for the prediction of three-dimensional fluid flow in complex ducts*'. PhD Thesis, University of London.

PHIPPS, R.S.B. [1981].'*The behaviour of jets with a variable density profile in a crossflow*. PhD Thesis, University of Bristol.

POPE, S. [1985]. 'PDF methods for turbulent reactive flows'. Progress in Energy and Combustion Science, **11**, 119-192.

PRIDDIN, C.H., and COUPLAND, J. [1986]. 'Impact of numerical methods on gas turbine combustor design and development'. In '*Calculations of Turbulent Reactive Flows*' (edited by R.M.C. So, J.H. Whitelaw and H.C. Mongia), ASME Winter Annual Meeting, AMD-81, 335-348.

RAITHBY, G.D. [1976a]. 'A critical evaluation of upstream differencing applied to problems involving fluid flow'. Computer Methods in Applied Mechanics and Engineering, **9**, 75-103.

RAITHBY, G.D. [1976b]. 'Skew upwind differencing schemes for problems involving fluid flow' Computer Methods in Applied Mechanics and Engineering, **9**, 151-162.

RAITHBY, G.D., and SCHNEIDER, G.E. [1979]. 'Numerical solution of problems in incompressible fluid flow: treatment of the velocity pressure coupling'. Numerical Heat Transfer, **2**, 417-440.

REYNOLDS, W.C. [1976]. 'Computation of turbulent flows'. Annual Review of Fluid Mechanics, **8**, 183-208.

RIVAS, E.K. [1972]. 'On the use of nonuniform grids in finite-difference equations'. Journal of Computational Physics, **10**, 202-210.

ROACHE, P.J. [1972]. '*Computational Fluid Dynamics*', Hermosa Publishers, Albuquerque.

ROBACK, R., and JOHNSON, B.V. [1983]. 'Mass and momentum turbulent transport experiments with confined swirling coaxial jets'. NASA-CR-168252.

RODI, W. [1972]. '*The Prediction of Free Turbulent Boundary Layers by Use of a Two-Equation Model of Turbulence*'. PhD Thesis, University of London.

RODI, W. [1984]. '*Turbulence models and their application in hydraulics - a state of the art review*', 2nd edition, International Association for Hydraulic Research, Delft.

ROGALLO, R.S., and MOIN, P. [1984]. 'Numerical simulation of turbulent flows'. Annual Review of Fluid Mechanics, **16**, 99-137.

SAFFMAN, P.G. [1978]. 'Problems and progress in the theory of turbulence'. In '*Lecture Notes in Physics*', Springer-Verlag, Berlin,**78**, 273-306.

SCHLICHTING, H. [1968]. '*Boundary-Layer Theory*', 6th edition, McGraw-Hill, New York.

SCHRAUB, F.A., KLINE, S.J., HENRY, J. RUNSTADLER, Jr., P.W., and LITTELL, A. [1965]. 'Use of hydrogen bubbles for quantitative determination of time-dependent velocity fields in low-speed water flows'. Journal of Basic Engineering, **87**, 429-444.

SERAG-ELDIN, M.A., and SPALDING, D.B. [1979]. 'Computations of three-dimensional gas-turbine combustion chamber flows'. Journal of Engineering for Power, **101**, 326-336.

SHALLOE, D. [1987]. 'The design, calibration and testing of a technique for dye-trace measurement in a can-type gas turbine combustion chamber'. 3M Project, Imperial College, Mechanical Engineering Department, London.

SHAUGHNESSY, E.J., and MORTON, J.B. [1977]. 'Laser light-scattering measurements of particle concentration in a turbulent jet'. Journal of Fluid Mechanics, **80**, 129-148.

SHAW, D.F. [1981]. 'An investigation into the factors affecting randomness in combustor exit temperature distribution'. Rolls-Royce Report PD2181.

SHYY, W., CORREA, S.M., and BRAATEN, M.E. [1986]. 'Computational models for gas-turbine combustors'. In '*Calculations of Turbulent Reactive Flows*' (edited by R.M.C. So, J.H. Whitelaw and M.C. Mongia), ASME Winter Annual Meeting, AMD-81, 141-183.

SHYY, W., BRAATEN, M.E., and SOBER, J.S. [1987]. 'A three-dimensional grid generation method for gas-turbine combustor flow computations'. AIAA Paper No. 87-0204.

SIMPSON, R.L. [1985]. '*Two-Dimensional Turbulent Separated Flow*', AGARDograph No. 287, **1**.

SIVASEGARAM, S., and WHITELAW, J.H. [1986]. 'Flow characteristics of opposing rows of jets in a confined space'. Proceedings of the Institution of Mechanical Engineers, **200**(C1), 71-75.

SLOAN, D.G., SMITH, P.J., and SMOOT, L.D. [1986]. 'Modelling of swirl in turbulent flow systems'. Progress in Energy and Combustion Science, **12**, 163-250.

SO, R.M.C., and AHMED, S.A. [1986]. 'Effects of rotation on the flow through an axisymmetric dump combustor'. *Proceedings of the 3rd International Symposium on Applications of Laser Anemometry to Fluid Mechanics*, Lisbon. Paper No. 1.1.

SPALDING, D.B. [1963]. 'The art of partial modelling'. *Proceedings of the 9th International Symposium on Combustion*, 833-843.

SPALDING, D.B. [1972]. 'A novel finite-difference formulation for differential expressions involving both first and second derivations'. International Journal of Numerical Methods in Engineering, **4**, 551-559.

SPEZIALE, C.G. [1987]. 'On nonlinear k-l and k-ε models of turbulence'. Journal of Fluid Mechanics, **178**, 459-475.

SREENIVASAN, K.R., TAVOULARIS, S., and CORRSIN, S. [1982]. 'A test of gradient transport and its generalizations'. In '*Turbulent Shear Flows III*', (edited by F.Durst, B.E.Launder, F.W.Schmidt and J.H.Whitelaw) Springer-Verlag, Berlin, 96-112.

SRINIVASAN, R., REYNOLDS, R., BALL, I., BERRY, R., JOHNSON, K., and MONGIA, H.C. [1983]. 'Aerothermal modelling program. Phase I - Final report'. NASA CR-168243, GARRET 21-4742-2.

STEVENS, A.J. [1986]. 'Dye mixing studies on 3rd arrangement of R.A.E. axi-symmetric combustor'. Lucas Aerospace Report No. B49-704.

STEVENSON, W.H., SANTOS, R., and METTLER, S.C. [1976]. 'Fringe mode fluorescence velocimetry'. AGARD-CP193, Paper No. 20.

STURGESS, G.J. [1984]. 'Stationary state computational fluid dynamics for aero-propulsion devices'. CPIA Publication 401, Computational Methods, JPM, Specialist Session (edited by Karen L. Strange).

STURGESS, G.J. [1986]. 'Calculations of aerospace propulsion combustors: a view from industry'. In '*Calculation of Turbulent Reactive Flows*' (edited by R.M.C. So, J.H. Whitelaw and H.C. Mongia), ASME Winter Annual Meeting, AMD-81, 185-231.

STURGESS, G.J., SYED, S.A., and SEPULVEDA, D. [1981]. 'Application of numerical modelling to gas turbine combustor development problems'. In 'Fluid Mechanics of Combustion Systems' (edited by T. Morel), ASME Winter Annual Meeting.

SUGIYAMA, Y., and USAMI, Y. [1979]. 'Experiments on the flow in and around jets directed normal to a crossflow'. Bulletin of the JSME, **22**, 1736-1745.

SUNDQVIST, H., and VERONIS, G. [1970]. 'A simple finite-difference grid with non-constant intervals'. Tellus, **22**, 26-31.

SYED, S.A., and CHIAPPETTA, L. [1985]. 'Finite-difference methods for numerical diffusion in TEACH-type calculations'. AIAA Paper No. 85-0057.

SYED, S.A., AND STURGESS, G.J. [1980]. 'Validation studies of turbulence and combustion models for aircraft gas turbine combustors'. In '*Momentum and Heat Transfer Processes in Recirculating Flows*' (edited by B.E. Launder and J.A.C. Humphrey), ASME Winter Annual Meeting

SYRED, N., and BEER, J.H. [1974]. 'Combustion in swirling flows: a review'. Combustion and Flame, **23**, 143-201.

SWITHENBANK, J., TURAN, A. and FELTON, P.G. [1978]. 'Three-dimensional two-phase modelling of gas-turbine combustors' in '*Gas Turbine Combustor Design Problems*', edited by A.H.Lefebvre, Hemisphere Publishing, Washington, D.C., 249-314.

TENNEKES, H., and LUMLEY, J.L. [1972]. '*A First Course in Turbulence*', MIT Press, Cambridge, Massachusetts.

THOMSON, J.F., and STEGER, J.C. [1988]. '*Three-Dimensional Grid Generation for Complex Configurations - Recent Program*'. AGARDograph No. 309 (edited by H. Yoshihara).

TOBER, A. [1988]. PhD Thesis, University of London (in preparation).

TSE, D. [1988]. '*Flow and combustion characteristics of model annular and can-type combustors*'. PhD Thesis, University of London.

VAHL DAVIS, G., and MALLINSON, G.D. [1976]. 'An evaluation of upwind and central difference approximations by a study of recirculating flow'. Computer and Fluids, **4**, 29-43.

van DOORMAAL, J.P., and RAITHBY, G.D. [1984]. 'Enhancements of the SIMPLE method for predicting incompressible fluid flows'. Numerical Heat Transfer, **17**, 147-163.

van DOORMAAL, J.P., and RAITHBY, G.D. [1985]. 'An evaluation of the segregated approach for predicting incompressible fluid flows'. ASME Paper 85-HT-9, presented at the National Heat Transfer Conference, Denver, Colorado, 4-7 August.

van DYKE, M. [1982]. *'An Album of Fluid Motion'*. Parabolic Press, Stanford.

VANKA, S. P. [1985]. 'Block-implicit calculation of steady turbulent recirculating flows'. International Journal of Heat and Mass Transfer, **28**, 2093-2103.

WHITE, A.J. |[1980]. 'The prediction of the flow and heat transfer in the vicinity of a jet in crossflow'. ASME Paper No. 80-WA/HT-26.

WILD, P.N., BOYSAN, F., SWITHENBANK, J., and LU, X. [1987]. 'Three-dimensional gas turbine combustor modelling'. AGARD-CP422, Paper No. 27.

WILKES, N.S., THOMPSON, C.P., HIGHTLEY, J.R., JONES, I.P., and BURNS, A.D. [1986]. 'On the numerical solution of three-dimensional incompressible flow problems'. In *'Numerical Methods for Fluid Dynamics II'* (edited by K.W. Morton and M.J. Baines), Clarendon Press, Oxford, 499-511.

WITTIG, S.C.K., EL BAHAR, O.M.F., and NOLL, B.E. [1984]. 'Temperature profile development in turbulent mixing of coolant jets with a confined hot crossflow'. Journal of Engineering for Gas Turbines and Power, **106**, 193-197.

WITTIG, S.C.K., BAUER, H.J., and NOLL, B.E. [1987]. 'On the application of finite-difference techniques for the computation of the flow field in gas turbine combustors with complex geometries'. AGARD-CP422, Paper No. 28.

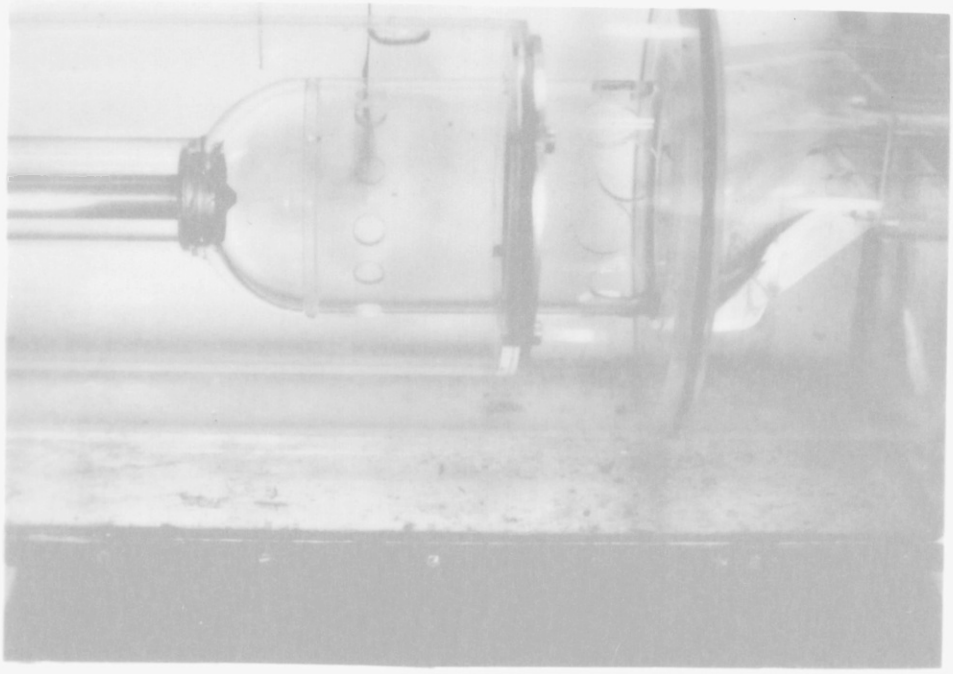
WOLFSHTEIN, M. [1968]. 'Numerical smearing in one-sided difference approximations to the equations of non-viscous flow'. Imperial College, Report No. EF/TN/A/3.

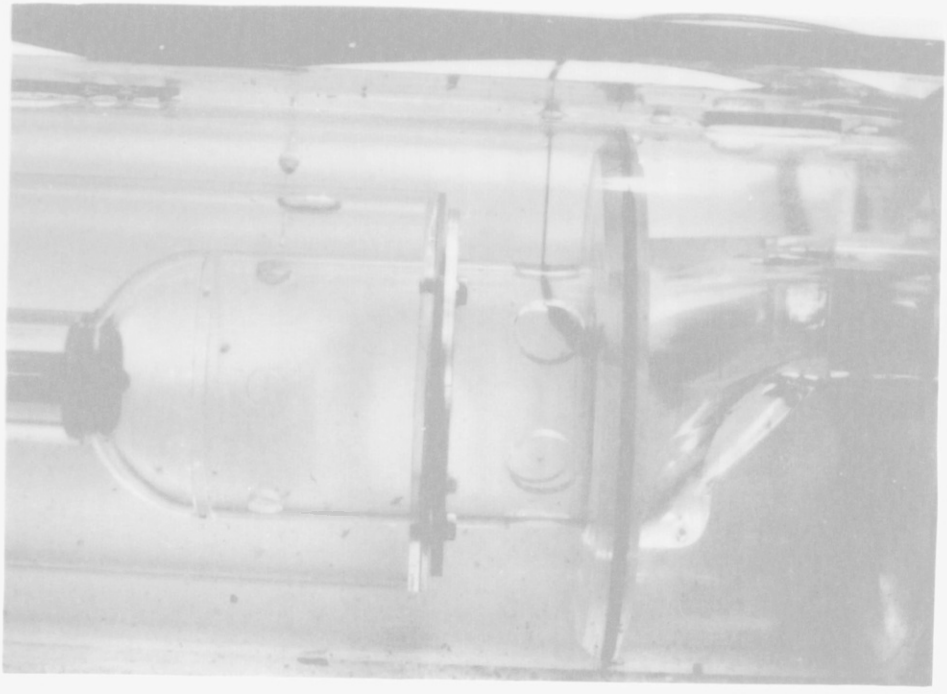
YANTA, W.J., and SMITH, R.A. [1973]. 'Measurements of turbulence transport properties with a laser-Doppler velocimeter'. AIAA Paper No.73-169.

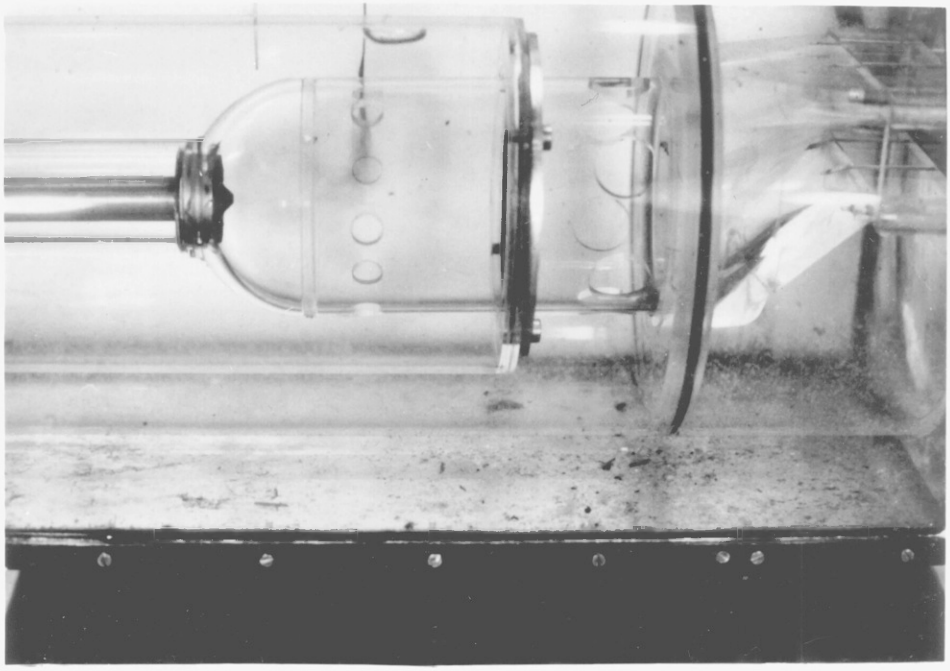
ZEDAN, M., and SCHNEIDER, G.E. [1983]. 'Investigation of the simultaneous variable solution for velocity and pressure in incompressible fluid flow problems'. AIAA Paper 83-1519.

ZEDAN, M., and SCHNEIDER, G.E. [1985]. 'A coupled strongly implicit procedure for velocity and pressure computation in fluid flow problems'. Numerical Heat Transfer, **8**, 537-557.

PLATE 1 - Flow visualization (still photography) by injection of a solution of nigrosine diluted in water through a small tube located at the centre of the primary (top) and dilution hole (bottom) - flow conditions corresponding to case 1 in Table 4.2. Flow from left to right rotating anticlockwise if viewed from the swirler towards the nozzle.







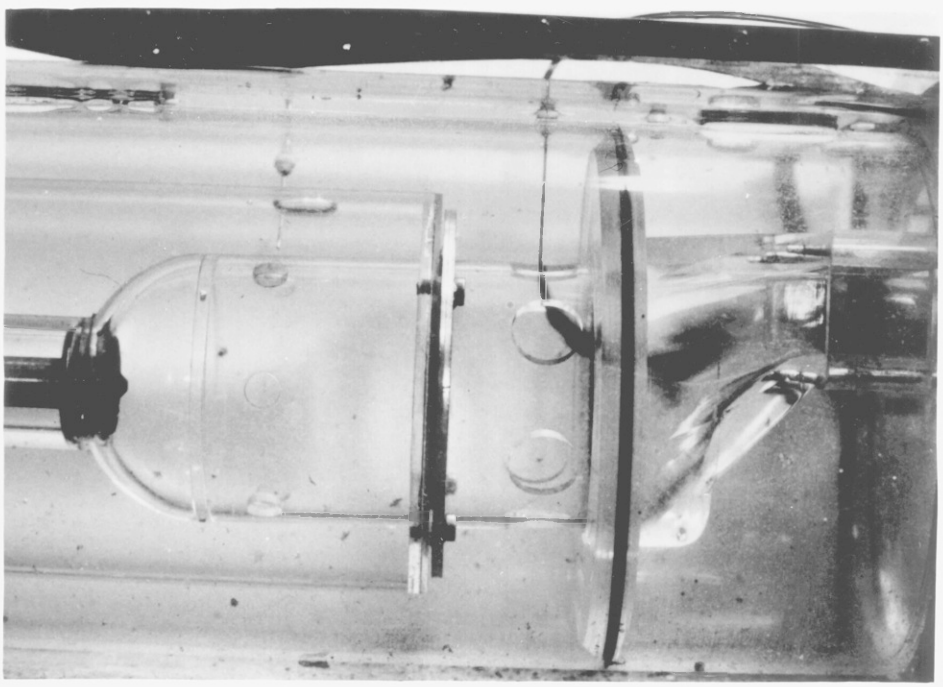
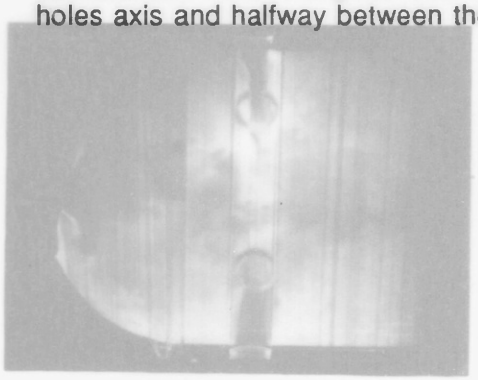


PLATE 2 - Flow visualization (still photography) by injection of a solution of rhodamine B diluted in water through the fuel injector - flow conditions corresponding to cases 5 and 6 in Table 4.2. Illumination obtained by a vertical laser sheet aligned with the combustor axis, containing the primary holes axis and halfway between the dilution holes axis.

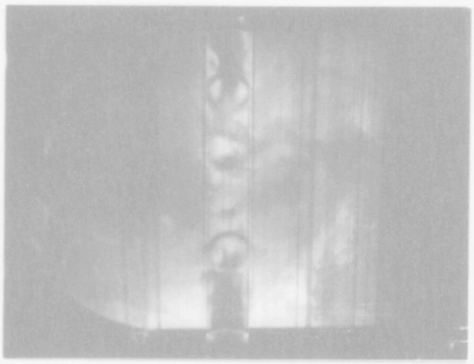
PRIMARY JETS



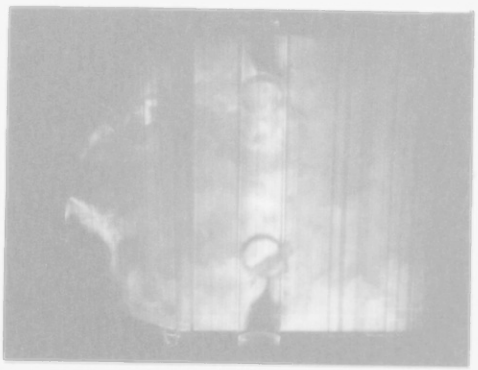
shutter speed = 1/500 sec.



shutter speed = 1/500 sec.



shutter speed = 1/1000 sec.

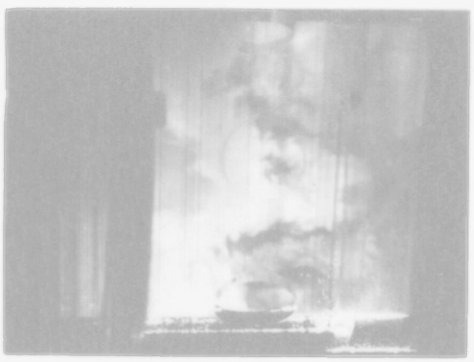


shutter speed = 1/1000 sec.

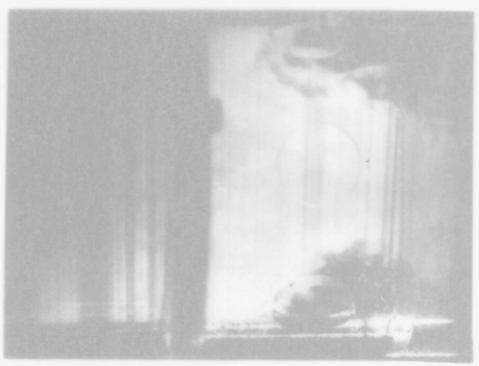
CASE 5 - Combustor flow with no flow through the swirler.

CASE 6 - Combustor flow with the highest swirler flow rate used in the present experiment.

DILUTION JETS



shutter speed = 1/500 sec.



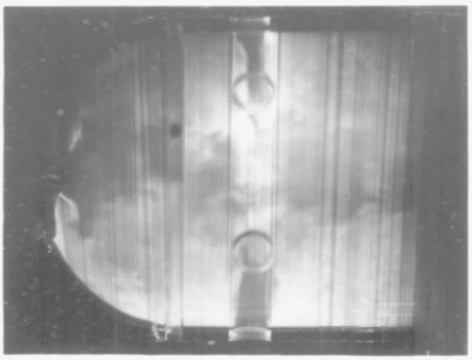
shutter speed = 1/500 sec.

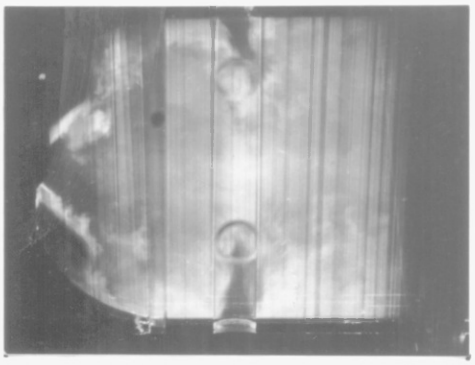


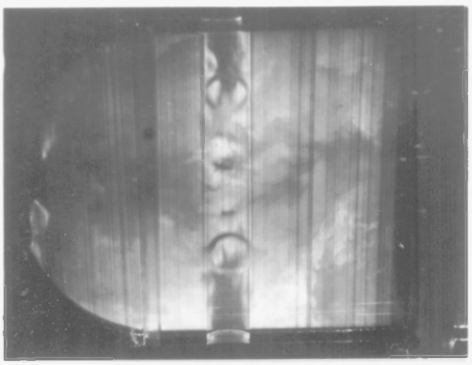
shutter speed = 1/1000 sec.

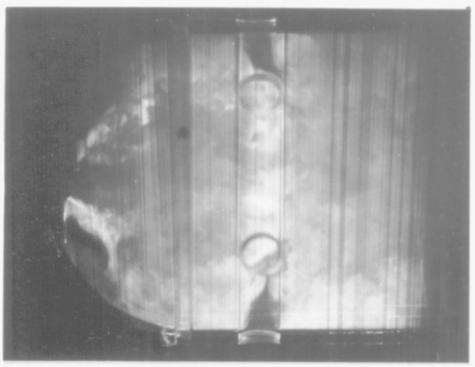


shutter speed = 1/1000 sec.

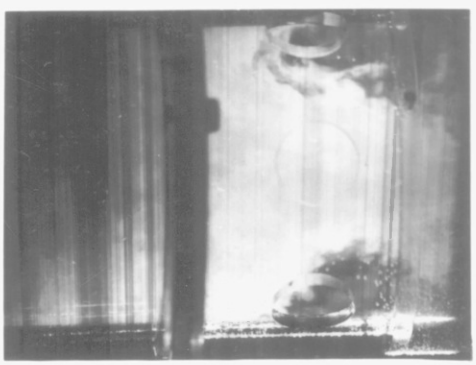


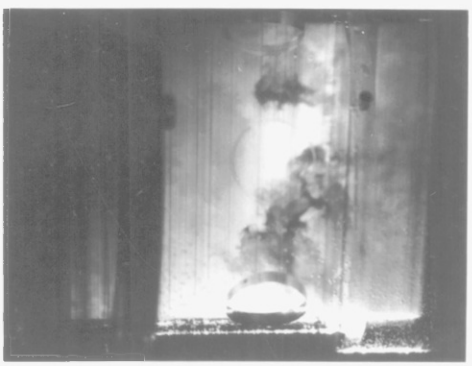












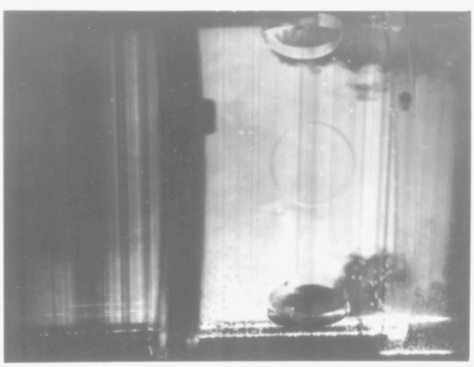
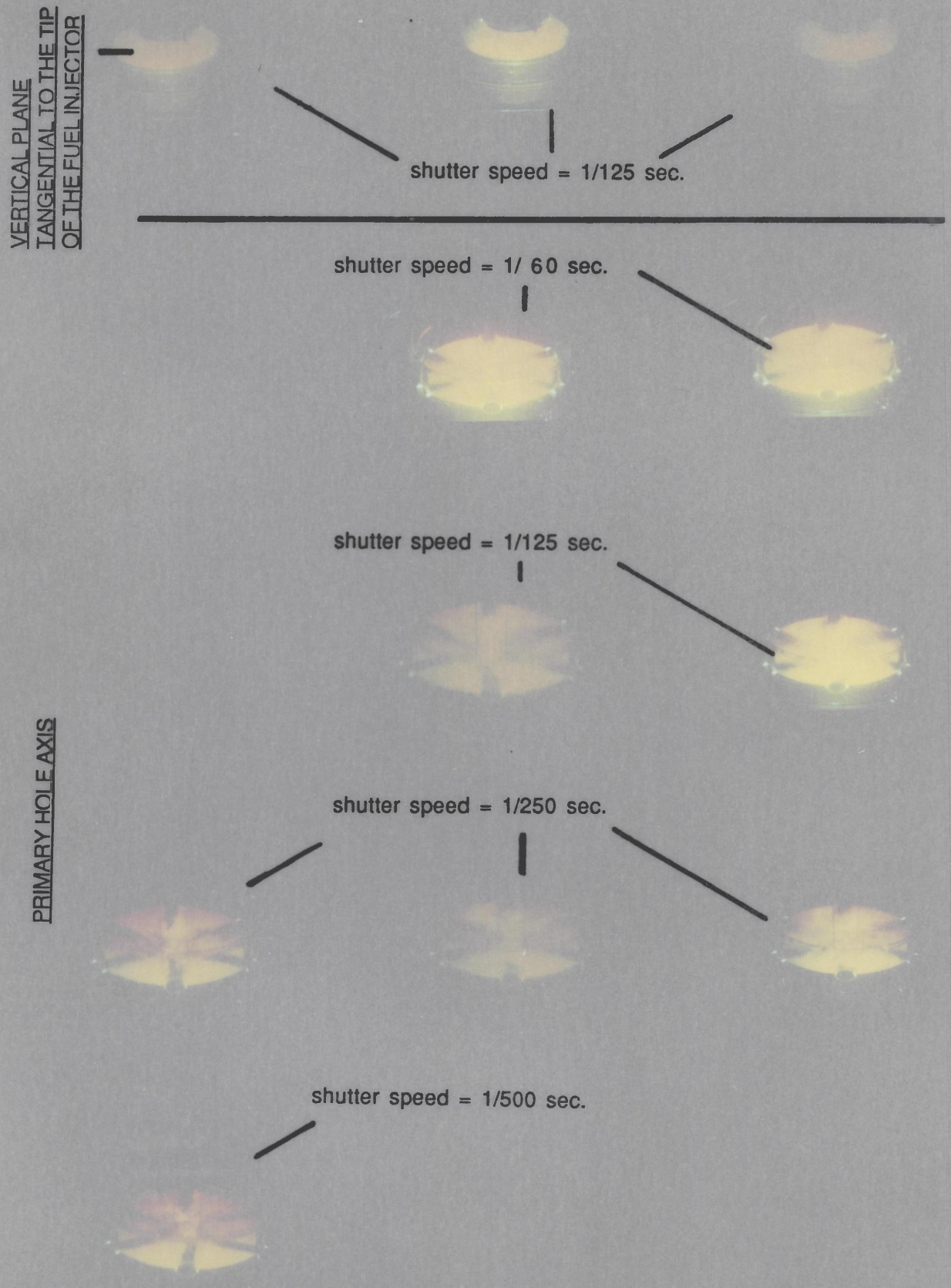


PLATE 3 - Flow visualization (still photography) by injection of a solution of rhodamine B diluted in water through the fuel injector - flow conditions corresponding to cases 1, 5 and 6 in Table 4.2. Illumination obtained by a vertical laser sheet perpendicular to the combustor axis at two different axial locations in the combustor. The photos were rotated by 90° relative to the photos in the two previous plates and the flow is now from top to bottom and, in case of combustor flow with swirl rotates anticlockwise if viewed from the top. Different flow conditions along columns and different shutter speeds along rows.



CASE 5 - Combustor flow with no flow through the swirler

CASE 1 - Combustor flow with standard conditions.

CASE 6 - Combustor flow with the highest swirler flow rate used in the present experiment.

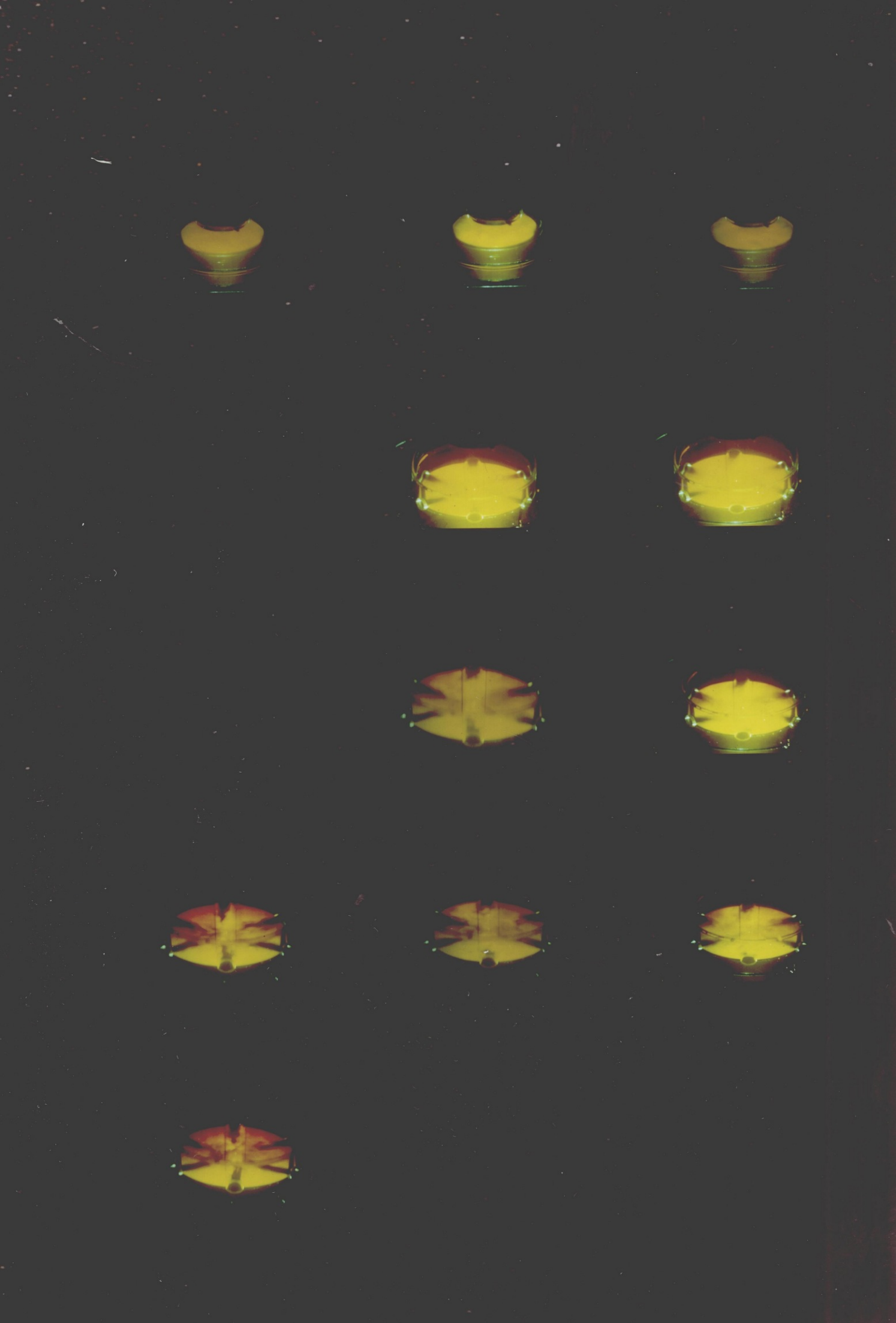
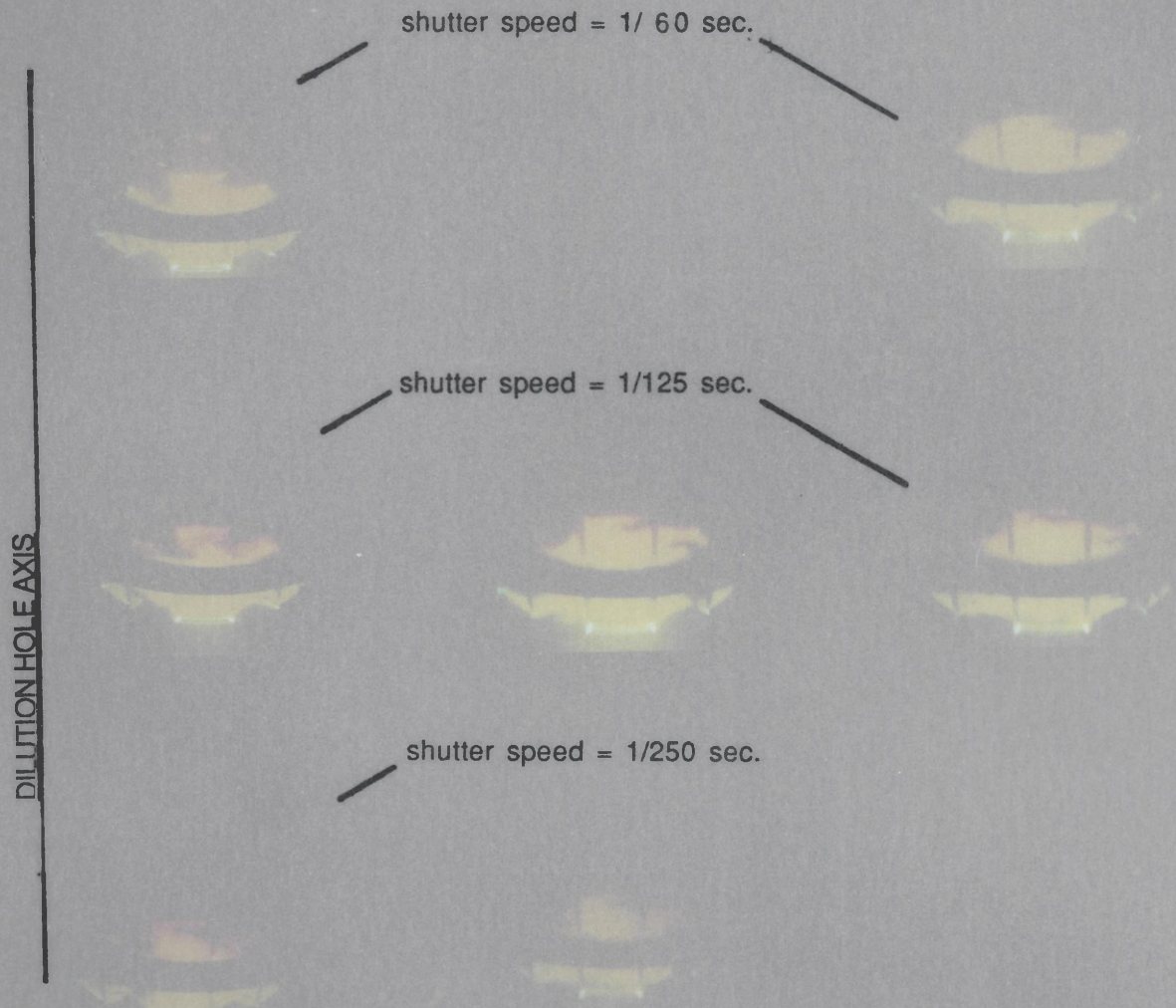


PLATE 4 - Flow visualization (still photography) by injection of a solution of rhodamine B diluted in water through the fuel injector - flow conditions corresponding to cases 1, 5 and 6 in Table 4.2. Illumination obtained by a vertical laser sheet perpendicular to the combustor axis and containing the dilution hole axis. See caption in previous plate also.



CASE 5 - Combustor flow with no flow through the swirler

CASE 1 - Combustor flow with standard conditions.

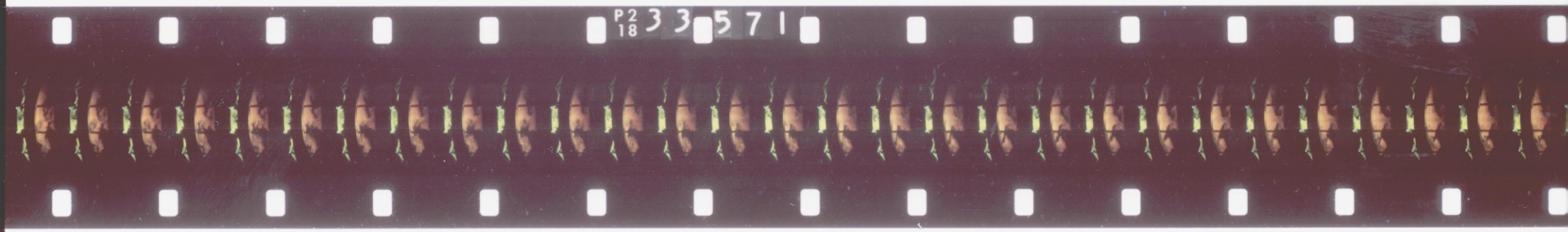
CASE 6 - Combustor flow with the highest swirler flow rate used in the present experiment.



PLATE 5 - Flow visualization (high speed photography) by injection of a solution of rhodamine B diluted in water through the fuel injector - flow conditions corresponding to case 5 (combustor without swirl flow) in Table 4.2. Illumination obtained by a vertical laser sheet perpendicular to the combustor axis and containing the primary and dilution hole axis. See also caption in plate 4.




P2 09 8 3 1 2 9


P2 18 3 3 5 7 1